MINISTRY OF EDUCATION AND TRAINING

HCMC UNIVERCITY OF TECHNOLOGY AND EDUCATION

VAN-THIEN TRAN

LIST OF PUBLICATIONS OF DISSERTATION: DEVELOPMENT OF STOCHASTIC COMPOSITE PLATE MODELS SUBJECTED TO MECHANICAL AND THERMAL LOADS

DOCTORAL DISSERTATION OF

ENGINEERING MECHANICS

Ho Chi Minh City, 7 /2025

BỘ GIÁO DỤC & ĐÀO TẠO
TRƯỜNG ĐẠI HỌC SƯ PHẠM KỸ THUẬT THÀNH PHỐ HỒ CHÍ MINH

CỘNG HÒA XÃ HỘI CHỦ NGHĨA VIỆT NAM
Độc lập – Tự do – Hạnh phúc

DANH MỤC CÁC BÀI BÁO KHOA HỌC ĐÃ CÔNG BỐ LIÊN QUAN KẾT QUẢ NGHIÊN CỨU CỦA LUẬN ÁN

Tên luận án: Phát triển mô hình tấm composite ngẫu nhiên dưới tác dụng tải trọng cơ học và nhiệt độ.

Họ & tên NCS: Trần Văn Thiên MSNCS: 2021001

Thuộc chuyên ngành: Cơ kỹ thuật Khóa: 2020 - 2023

Người hướng dẫn chính: GS.TS. Nguyễn Trung Kiên

Nơi công tác: Đại học Công nghệ TPHCM Điện thoại: 0933655425

Người hướng dẫn phụ: TS. Nguyễn Văn Hậu

Nơi công tác: Đại học Sư phạm Kỹ thuật TPHCM Điện thoại: 0908270222

Dưới đây là danh mục các bài báo khoa học về kết quả nghiên cứu của luận án đã được công bố:

Stt	Tên bài báo	Tác giả	Tên tạp chí/kỷ yếu, số/tập, số ISSN/ISBN	Thời gian xuất bản	Link/Doi	Ghi chú
I.	**Tạp chí khoa học trong danh mục WoS (SCIE, SSCI, AHCI, ESCI)**					
1	Stochastic collocation method for thermal buckling and vibration analysis of functionally graded sandwich microplates	**Van-Thien Tran,** Trung-Kien Nguyen, Phong T. T. Nguyen, and Thuc P. Vo	Journal of Thermal Stresses, vol. 46, p. 909-934 ISSN: 0149-5739	14/06/2023	https://doi.org/10.1080/01495739.2023.2217243	**SCIE (Q2)**
2	Vibration and buckling optimization of functionally graded porous microplates using BCMO-ANN algorithm	**Van-Thien Tran,** T.-K. Nguyen,H. Nguyen-Xuan, Magd Abdel Wahab	Thin- Walled Structures, vol. 182, p. 110267 ISSN: 0263-8231	01/11/2022	https://doi.org/10.1016/j.tws.2022.110267	**SCIE (Q1)**
3	Stochastic vibration and buckling analysis of functionally graded microplates with a unified higher-order shear deformation theory	**Van-Thien Tran,** T.-K. Nguyen,P. T. T. Nguyen, and T. P. Vo	Thin- Walled Structures, vol. 177, p.109473 ISSN: 0263-8231	04/6/2022	https://doi.org/10.1016/j.tws.2022.109473	**SCIE (Q1)**
4	An intelligent computational iBCMO-DNN	**Van-Thien Tran**, T.-K. Nguyen,H.	Journal of Thermal Stresses,	08/7/2024	https://doi.org/10.1080/01495739.2024.2368054	**SCIE (Q2)**

	algorithm for stochastic thermal buckling analysis of functionally graded porous microplates using modified strain gradient theory	Nguyen-Xuan	online, ISSN: 0149-5739			
5	Meta-heuristic optimization algorithms for vibration and buckling analysis of laminated composite plates	**Van-Thien Tran;** Trung-Kien Nguyen; H. Nguyen-Xuan, T. P. Vo	Engineering Analysis with Boundary Elements, vol.169, Part A, 12/ 2024, 105974, ISSN: 1873-197X	01/12/2024	https://doi.org/10.1016/j.enganabound.2024.105974	**SCIE (Q1)**
6	Novel computational algorithms for vibration, buckling, and transient analysis of porous metal foam microplates	**Van-Thien Tran;** Trung-Kien Nguyen; Van-Hau Nguyen, T. P. Vo	Journal of Vibration Engineering & Technologies , 13, 203 (2025). ISSN: 2523-3920	18/01/2025	https://doi.org/10.1007/s42417-024-01748-8	**SCIE (Q2)**
II	**Tạp chí khoa học trong danh mục Scopus**					
III	**Tạp chí khoa học quốc tế có ISSN, có phản biện nhưng chưa xếp hạng WoS/Sopus**					
1	Static and vibration analysis of functionally graded microplate with porosities based on higher-order shear deformation and modified strain gradient theory	**Van-Thien Tran,** Nguyen Van Hau, Trung-Kien Nguyen, T. P. Vo	Vietnam Journal of Mechanics, VOL. 45 NO. 1 ,2023 ISSN: 0866-7136	01/3/2023	https://doi.org/10.15625/0866-7136/17552	**ACI**
IV	**Kỷ yếu hội nghị khoa học quốc tế có phản biện và có ISBN**					
1	An Efficient Size-Dependent Computational Approach for Functionally Graded Porous Sandwich Microplates Based on Modified Couple Stress Theory	**Van-Thien Tran,** Trung-Kien Nguyen, Van- Hau Nguyen	Computational Intelligence Methods for Green Technology and Sustainable Development (GTSD 2022), Lecture Notes in Networks and Systems, vol 567, 82-96, 2023 ISSN: 2367-	15/12/2022	https://doi.org/10.1007/978-3-031-19694-2_8	**Scopus Index (Q4)**

			3370			
2	A general framework of higher-order shear deformation theory for free vibration analysis of functionally graded microplates	**Van-Thien Tran,** Trung-Kien Nguyen	Proceedin gs of the Second Internatio nal Conferenc e on Sustainabl e Civil Engineerin g and Architectu re (ICSCEA-2 021), Lecture Notes in Civil Engineerin g, vol.268, 713–727, 2023 ISSN: 2366-2557	21/9/2022	https://doi.org/10.1007/978-981-19-3303-5_64	**Scopus Index (Q4)**
V	**Kỷ yếu hội nghị khoa học quốc gia có phản biện và có ISBN**					
	A BCMO-DNN algorithm for vibration optimization of functionally graded porous microplates	Van-Hau Nguyen, **Van- Thien Tran,** Trung Kien Nguyen	Tuyển tập công trình khoa học Hội nghị Cơ học toàn quốc lần thứ XI(NACOME2 022), Nhà xuất bản Khoa học tự nhiênvà Công nghệ ,Tập 1,577-588	12/2022		

Thin-Walled Structures 177 (2022) 109473

Contents lists available at ScienceDirect

Thin-Walled Structures

journal homepage: www.elsevier.com/locate/tws

Full length article

Stochastic vibration and buckling analysis of functionally graded microplates with a unified higher-order shear deformation theory

Van-Thien Tran [a], Trung-Kien Nguyen [b,*], Phong T.T. Nguyen [c], Thuc P. Vo [d]

[a] Faculty of Civil Engineering, Ho Chi Minh City University of Technology and Education, 1 Vo Van Ngan Street, Thu Duc City, Ho Chi Minh City, Viet Nam
[b] CIRTech Institute, HUTECH University, 475A Dien Bien Phu Street, Binh Thanh District, Ho Chi Minh City, Viet Nam
[c] Faculty of International Education, Ho Chi Minh City University of Technology and Education, 1 Vo Van Ngan Street, Thu Duc City, Ho Chi Minh City, Viet Nam
[d] School of Computing, Engineering and Mathematical Sciences, La Trobe University, Bundoora, VIC 3086, Australia

ARTICLE INFO

Keywords:
Stochastic vibration and buckling
FG microplates
Higher-order shear deformation theory
Polynomial chaos expansion
Monte Carlo simulation
Modified couple stress theory

ABSTRACT

Based on equations of the elasticity, this paper proposes a unified higher-order shear deformation theory for stochastic vibration and buckling analysis of the functionally graded (FG) microplates. The governing equations of motions are derived from Hamilton's principle. The solutions are approximated by bi-directional series in which hybrid shape functions are proposed, then the stiffness and mass matrix are explicitly derived. In order to investigate the stochastic responses of the FG microplates, the polynomial chaos expansion (PCE) is used. The multiple uncertain material properties are randomly changed via the lognormal distributions. Numerical results are presented for different configurations of the FG microplates such as the power-law index, material length scale parameter, length-to-thickness ratio and boundary conditions on their critical buckling loads and natural frequencies. The results from PCE are evaluated by comparing with those from Monte Carlo simulation to show the efficiency and accuracy of the present approach. Some new results for stochastic analysis of the FG microplates are presented and can be used for future references.

1. Introduction

Functionally graded (FG) microplates with continuous variations of materials properties can be used for potential application in engineering fields such as atomic force microscopes (AFMs) [1], micro-electromechanical systems (MEMs) ([2,3]) and nano-electromechanical systems (NEMS) ([4,5]). It is known that classical elasticity theory could not accurately predict responses of these small scale structures; thus, different approaches have been developed. A number of studies have been performed to predict accurately static, buckling and vibration behaviours of the FG microplates ([6–16]) in which the modified coupled stress theory (MCT) and modified strain gradient theory (MST) are mostly used for various theories (classical plate theory (CPT), first-order shear deformation plate theory (FSDT), higher-order shear deformation plate theories (HSDTs), three dimensional elasticity theory). The MCT initiated by Yang et al. [17] was known as the simplest one to include the size effects with only one material length scale parameter (MLSP) associated with rotation gradient in the constitutive equations. The MST proposed by Lam et al. [18] modified the classical strain gradient theory of Mindlin [19], Mindlin and Eshel [20] to establish a new set of high-order metrics, where the total number of MLSP was reduced from five to three. The MST can be reduced to MCT if two MLSPs related to dilatation gradient and deviatoric stretch gradient were set to be zero. It should be mentioned that although the MST predicts more accurate than the MCT, it appears to be complicated to implement. Moreover, another way to capture size effects of nanostructures is to use the nonlocal elasticity theory (NET) known as Eringen's one ([21]). By involving the nonlocal parameter in constitutive equations, the NET has been employed for analysis of the FG nanoplates ([22–24]) and nanobeams ([25–27]). However, it is complicated to implement different boundary conditions for nanostructures.

Due to manufacturing process or other unexpected factors, the materials properties of the FG plates can be uncertain ([28–32]), which leads to the change on their static and dynamic behaviours. Literature review [33] shows that majority studies of the FG microplates focused on deterministic analysis, which provides only mean responses and neglects the deviation caused by their random material properties. Monte Carlo Simulation (MCS) method ([34]) is the simplest and most popular approach to solve this complicated problem. It was used for analysis of the FG and laminated composite plates ([35–38]). Nonetheless, this approach is infeasible in different cases due to its expensive computational cost, especially when a complicated physical model is considered. In order to overcome this adverse, Kumar et al. [39] proposed an artificial neural network-based-MCS approach for stochastic

* Corresponding author.
E-mail address: ntkien@hutech.edu.vn (T.-K. Nguyen).

https://doi.org/10.1016/j.tws.2022.109473
Received 14 February 2022; Received in revised form 8 May 2022; Accepted 19 May 2022
Available online xxxx
0263-8231/

buckling analysis of laminated composite sandwich plates. Another approach is to use polynomial chaos expansion (PCE) which speeds up the computing process while still maintains the accuracy. The key idea of this approach is to approximate the stochastic outputs as a series in an orthogonal space including the basis functions and their appropriate coefficients. This approach has been employed for static and dynamic analysis of laminated composite and FG plates with uncertainty of materials properties. Peng et al. [40] studied a uncertainty analysis of composite laminated plate with data-driven PCE method under insufficient input data of uncertain parameters based on finite element model (FEM) to solve the natural frequency. Umesh and Ganguli [41] presented the material uncertainty effect on vibration control of smart composite plate using PCE and FEM. Chakraborty et al. [42] analysed the stochastic free vibration analysis of laminated composite plates using polynomial correlated function expansion. Sasikumar et al. [43] proposed a data-driven PCE method for stochastic analysis of laminated composite plates. Shaker et al. [44] studied the stochastic FEM to perform reliability analysis of the free vibration of composite plates with material and fabrication uncertainties using the first-order and second-order reliability method based on the third-order shear deformation theory (TSDT). Li et al. [45] investigated stochastic thermal buckling characteristics of laminated composite plates with the random system properties using the first-order perturbation technique. For FG plates, Li et al. [46] investigated stochastic static responses of FG plates with uncertainty of material properties using the PCE, FSDT and isogeometric approach. García-Macías et al. [47] illustrated the meta model-based approach for stochastic free vibration analysis of FG carbon nanotube reinforced plates using the FEM. A literature review shows that although many studies on the stochastic analysis of composite/FG plates have been performed, as far as the authors are aware the similar research on the FG microplates is still very limited. Besides, it is well-known that the HSDT generally predicts more accurate than the FSDT, however, its accuracy depends on a choice of the shear functions ([48–55]). Thus, it is important to propose unified HSDT for various shear deformation plate theories and then apply for stochastic analysis of the FG microplates. These are the main novelty and contributions of this paper.

The main objective of this paper is to develop a stochastic model for free vibration and buckling analysis of the FG microplates using a combination of unified HSDT, which is derived from the fundamental of elasticity theory and PCE and MCT. The governing equations of motions are derived from Hamilton's principle and then bi-directional series-type solutions with hybrid shape functions are proposed. Numerical results are presented for different configurations of material distributions, multiple uncertain material properties, boundary conditions on the critical buckling loads and natural frequencies of the FG microplates. The MCS with 10,000 samples is also considered as the exact solutions and used to investigate the performance of the proposed PCE model. New results presented in this study can be of interests to the scientific and engineering community in the future.

2. Theoretical formulation

Consider a FG rectangle microplate in the coordinate system (x_1, x_2, x_3) with sides $a \times b$ and thickness h as shown in Fig. 1. It is composed of a mixture of ceramic and metal materials whose material properties vary continuously in the thickness direction. The material properties such as Young's modulus E, mass density ρ, Poisson's ratio ν can be approximated by the following expressions ([52,56]):

$$P(x_3) = (P_c - P_m)\left(\frac{2x_3 + h}{2h}\right)^p + P_m \tag{1}$$

where P_c and P_m are the material properties of ceramic and metal; p is the power-law index which is positive and $x_3 \in [-h/2, h/2]$.

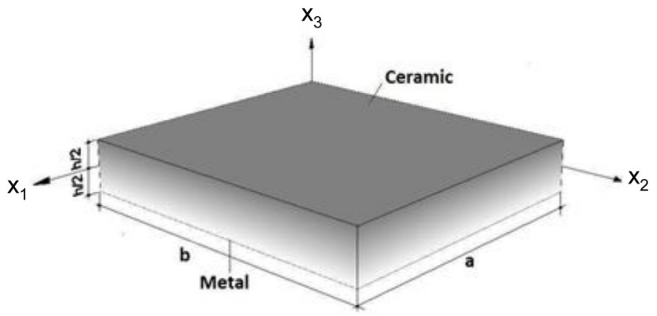

Fig. 1. Geometry of a FG microplate.

Table 1
Approximation functions of series solutions with different boundary conditions.

Boundary conditions (BCs)	Approximation functions	
	$R_j(x_1)$	$P_j(x_2)$
SFSF	$x_1 e^{-\frac{jx_1}{a}}$	$x_2 e^{-\frac{jx_2}{b}}$
SSSS	$x_1(a-x_1)e^{-\frac{jx_1}{a}}$	$x_2(b-x_2)e^{-\frac{jx_2}{b}}$
CFCF	$x_1^2 e^{-\frac{jx_1}{a}}$	$x_2^2 e^{-\frac{jx_1}{a}}$
CSCS	$x_1^2(a-x_1)e^{-\frac{jx_1}{a}}$	$x_2^2(b-x_2)e^{-\frac{jx_2}{b}}$
CCCC	$x_1^2(a-x_1)^2 e^{-\frac{jx_1}{a}}$	$x_2^2(b-x_2)^2 e^{-\frac{jx_2}{b}}$

Table 2
Convergence study of the series solution of the FG microplates (MAT 1) with different BCs ($a/h = 10$, $p = 1$, $h/l = 1$).

Solution	Number of series $N = N_1 = N_2$					
	2	4	6	8	10	12
Non-dimensional fundamental frequency						
SSSS	11.1861	11.0496	11.0085	11.0105	11.0100	11.0104
CSCS	17.3575	16.8286	16.8204	16.8195	16.8199	16.8196
CCCC	24.1572	24.0579	24.0530	24.0526	24.0524	24.0527
Non-dimensional critical buckling load with biaxial compression						
SSSS	29.8053	29.1773	28.9979	28.9879	28.9873	28.9878
CSCS	62.4027	57.1124	57.0130	57.0126	57.0129	57.0127
CCCC	109.5176	108.3697	108.1556	108.1545	108.1547	108.1544

2.1. Modified couple stress theory (MCT)

The total potential energy of the FG microplates is obtained by:

$$\Pi = \Pi_U + \Pi_V - \Pi_K \tag{2}$$

where Π_U, Π_V, Π_K are the strain energy, work done by membrane forces and kinetic energy of systems. Based on the MCT, the strain energy of the system Π_U is given by:

$$\Pi_U = \int_V (\boldsymbol{\sigma}\boldsymbol{\varepsilon} + \mathbf{m}\boldsymbol{\chi})\, dV \tag{3}$$

where $\boldsymbol{\varepsilon}, \boldsymbol{\chi}$ are strains and symmetric rotation gradients, respectively; $\boldsymbol{\sigma}$ is Cauchy stress; $\mathbf{m}$ is the high-order stress corresponding with strain gradients $\boldsymbol{\chi}$, respectively. The components of strain ε_{ij} and strain gradients χ_{ij} are defined as follows:

$$\varepsilon_{ij} = \frac{1}{2}(u_{i,j} + u_{j,i}) \tag{4a}$$

$$\chi_{ij} = \frac{1}{4}(u_{n,mj}e_{imn} + u_{n,mi}e_{jmn}) \tag{4b}$$

where δ_{ij}, e_{imn} are Kronecker delta and permutation symbol, respectively; the comma in subscript is used to indicate the derivative of variable that follows. The stress components are calculated from constitutive equations as follows:

$$\sigma_{ij} = \lambda\varepsilon_{kk}\delta_{ij} + 2\mu\varepsilon_{ij} \tag{5a}$$

$$m_{ij} = 2\mu l^2 \chi_{ij} \tag{5b}$$

Table 3
Non-dimensional natural frequency of the FG square microplates (MAT 1).

BCs	a/h	p	Theory	h/l				
				∞	5	2.5	1.25	1
SSSS	20	1	Present	4.5218	4.9612	6.0813	9.3027	11.1206
			RPT [56]	4.5228	4.9568	6.0756	9.2887	11.1042
			RPT [6]	4.5228	4.9568	6.0756	9.2887	11.1042
			RPT [9]	4.5228	4.9556	6.0714	9.2768	11.0882
		2	Present	4.1098	4.4980	5.5114	8.4121	10.0595
			RPT [56]	4.1100	4.5006	5.5082	8.4062	10.0450
		5	Present	3.8921	4.2000	5.0188	7.4385	8.8270
			RPT [56]	3.8884	4.2005	5.0199	7.4397	8.8286
		10	Present	3.7631	4.0302	4.7433	6.9005	8.1468
			RPT [56]	3.7622	4.0323	4.7488	6.9013	8.1494
			RPT [9]	3.7623	4.0299	4.7428	6.8914	8.1384
	10	1	Present	4.4209	4.8572	5.9865	9.1997	11.0105
			RPT [56]	4.4192	4.8526	5.9664	9.1537	10.9511
		2	Present	4.0104	4.4022	5.4165	8.3166	9.9495
			RPT [56]	4.0090	4.4006	5.4071	8.2863	9.9101
		5	Present	3.7681	4.0828	4.9083	7.3331	8.7203
			RPT [56]	3.7682	4.0876	4.9169	7.3338	8.7135
		10	Present	3.6387	3.9112	4.6331	6.7911	8.0442
			RPT [56]	3.6368	3.9162	4.6464	6.8030	8.0448
CCCC	5	1	Present	6.4417	7.9096	11.0832	19.0090	23.2057
			IGA [13]	6.3868	–	–	–	–
		2	Present	5.7789	7.1127	9.9861	17.1343	20.8920
			IGA [13]	5.7292	–	–	–	–
		5	Present	5.1524	6.2984	8.7539	14.9050	18.1416
			IGA [13]	5.1082	–	–	–	–
		10	Present	4.8661	5.8924	8.1005	13.6879	16.6596
			IGA [13]	4.8214	–	–	–	–
	10	1	Present	7.6557	8.9348	11.9381	19.7962	24.0526
			IGA [13]	7.6251	–	–	–	–
		2	Present	6.9136	8.0861	10.7890	17.8776	21.7236
			IGA [13]	6.8944	–	–	–	–
		5	Present	6.3989	7.3509	9.6103	15.6233	18.9125
			IGA [13]	6.3722	–	–	–	–
		10	Present	6.1521	6.9730	8.9756	14.3803	17.3596
			IGA [13]	6.1039	–	–	–	–

where λ, μ are Lamé constants; Latin indices in Eqs. (4) and (5) take values 1, 2 and 3; l is material length scale parameter (MLSP) which is used to measure the effect of couple stress ([58]). This parameter can be determined by experimental works ([18]).

The work done by membrane compressive loads (N_1^0, N_2^0, N_{12}^0) of the FG microplates is given by:

$$\Pi_V = -\int_A \left[N_1^0 \left(u_{3,1}^0\right)^2 + 2N_{12}^0 u_{3,1}^0 u_{3,2}^0 + N_2^0 \left(u_{3,2}^0\right)^2 \right] dA \tag{6}$$

The kinetic energy of the FG microplates Π_K is expressed by:

$$\Pi_K = \frac{1}{2}\int_V \rho\left(x_3\right)\left(\dot{u}_1^2 + \dot{u}_2^2 + \dot{u}_3^2\right) dV \tag{7}$$

where $\rho\left(x_3\right)$ is mass density; $\dot{u}_1 = u_{1,t}$, $\dot{u}_2 = u_{2,t}$, $\dot{u}_3 = u_{3,t}$ are velocities in x_1-, x_2- and x_3- directions, respectively.

2.2. Unified higher-order shear deformation theory (HSDT) of the FG microplates

For simplicity purpose, the effects of transverse normal strain are neglected, i.e. $u_3\left(x_1, x_2, x_3\right) = u_3^0\left(x_1, x_2\right)$ where $u_3^0\left(x_1, x_2\right)$ is transverse displacement at the mid-surface of the FG microplates. Moreover, it is supposed that the transverse shear stresses are expressed in terms of the transverse shear forces as follows:

$$\sigma_{13} = f_{,3}\left(x_3\right) Q_1\left(x_1, x_2\right) \tag{8a}$$

$$\sigma_{23} = f_{,3}\left(x_3\right) Q_2\left(x_1, x_2\right) \tag{8b}$$

where $f\left(x_3\right)$ is a higher-order term whose first derivative satisfies the free-stress boundary condition at the top and bottom surfaces of the microplates, i.e. $f_{,3}\left(x_3 = \pm\frac{h}{2}\right) = 0$; $Q_1\left(x_1, x_2\right), Q_2\left(x_1, x_2\right)$ are the transverse shear forces. Additionally, transverse shear strains are linearly related to the membrane displacements $u_1\left(x_1, x_2, x_3\right), u_2\left(x_1, x_2, x_3\right)$ and transverse one $u_3^0\left(x_1, x_2\right)$ by:

$$\gamma_{13} = u_{1,3} + u_{3,1}^0 = \frac{\sigma_{13}}{\mu} = \frac{f_{,3} Q_1}{\mu} \tag{9a}$$

$$\gamma_{23} = u_{2,3} + u_{3,2}^0 = \frac{\sigma_{23}}{\mu} = \frac{f_{,3} Q_2}{\mu} \tag{9b}$$

where $\mu\left(x_3\right) = \frac{E(x_3)}{2(1+\nu)}$ is the shear modulus. Furthermore, integrating Eq. (9) in x_3- direction leads to a general displacement field of the FG microplates as follows:

$$u_1\left(x_1, x_2, x_3\right) = u_1^0\left(x_1, x_2\right) - x_3 u_{3,1}^0 + \Psi\left(x_3\right) Q_1\left(x_1, x_2\right) \tag{10a}$$

$$u_2\left(x_1, x_2, x_3\right) = u_2^0\left(x_1, x_2\right) - x_3 u_{3,2}^0 + \Psi\left(x_3\right) Q_2\left(x_1, x_2\right) \tag{10b}$$

$$u_3\left(x_1, x_2, x_3\right) = u_3^0\left(x_1, x_2\right) \tag{10c}$$

where $\Psi\left(x_3\right) = \int_0^{x_3} \frac{f_{,3}}{\mu(x_3)} dx_3$. It is observed that Eq. (10) can be considered as a general zeroth-order shear deformation theory in which displacement field of Shimpi ([59]) can be obtained by the assumption of homogeneous materials and $f\left(x_3\right) = \frac{3}{2h}\left(z - \frac{4z^3}{3h^2}\right)$. Moreover, it is known that the transverse shear forces can be expressed in terms of the rotation $\left(\varphi_1, \varphi_2\right)$ and gradients of the transverse displacement as follows:

$$Q_1\left(x_1, x_2\right) = H^s\left(\varphi_1 + u_{3,1}^0\right) \tag{11a}$$

$$Q_2\left(x_1, x_2\right) = H^s\left(\varphi_2 + u_{3,2}^0\right) \tag{11b}$$

where $H^s = k^s \int_{-h/2}^{h/2} \mu\left(x_3\right) dx_3$ is the transverse shear stiffness of the FG microplates; $k^s = 5/6$ is shear coefficient factor. Substituting Eq. (11) into Eq. (10) leads to a general HSDT as follows:

$$u_1\left(x_1, x_2, x_3\right) = u_1^0\left(x_1, x_2\right) + \Phi_1\left(x_3\right) u_{3,1}^0 + \Phi_2\left(x_3\right) \varphi_1\left(x_1, x_2\right) \tag{12a}$$

Table 4
Comparison study between MCS (10.000 samples) and PCE (256 samples) for the mean, standard deviation (SD), Kurtosis and Skewness for the fundamental frequency of the FG plates ($a/h = 5$, MAT 1).

BCs	p	Theory	mean	SD	Kurtosis	Skewness	COV(%)	Time(s)	Present
SFSF	1	PCE	3.5550	0.1877	2.5916	0.0227	5.3	11.49	3.5559
		MCS	3.5551	0.1879	2.5914	0.0228	5.3	590.79	
	2	PCE	3.2106	0.2540	2.6438	0.1338	7.9	12.67	3.2076
		MCS	3.2121	0.2538	2.6439	0.1336	7.9	575.61	
	5	PCE	2.9792	0.3120	2.6835	0.1960	10.5	14.06	2.9722
		MCS	2.9819	0.3121	2.6835	0.1959	10.5	538.25	
	10	PCE	2.8668	0.3278	2.6921	0.2468	11.4	14.25	2.8571
		MCS	2.8689	0.3280	2.6922	0.2465	11.4	541.54	
SSSS	1	PCE	4.0790	0.2114	2.5845	0.0262	5.2	14.06	4.0782
		MCS	4.0787	0.2114	2.5844	0.0264	5.2	536.56	
	2	PCE	3.6839	0.2875	2.6374	0.1295	7.8	12.32	3.6811
		MCS	3.6849	0.2870	2.6377	0.1299	7.8	568.27	
	5	PCE	3.3997	0.3535	2.6737	0.2114	10.4	13.14	3.3950
		MCS	3.3988	0.3537	2.6734	0.2117	10.4	526.38	
	10	PCE	3.2601	0.3738	2.6984	0.2509	11.5	13.65	3.2511
		MCS	3.2577	0.3734	2.6983	0.2512	11.5	525.58	
CFCF	1	PCE	4.5089	0.2390	2.5653	0.0129	5.3	11.59	4.5082
		MCS	4.5100	0.2387	2.5657	0.0128	5.3	511.87	
	2	PCE	4.0469	0.3214	2.6253	0.1254	7.9	11.29	4.0431
		MCS	4.0473	0.3214	2.6255	0.1253	7.9	527.74	
	5	PCE	3.6776	0.3921	2.6732	0.2142	10.7	12	3.6696
		MCS	3.6803	0.3928	2.6734	0.2143	10.7	522.61	
	10	PCE	3.5154	0.4146	2.7044	0.2565	11.8	12	3.5051
		MCS	3.5148	0.4145	2.7049	0.2565	11.8	545.85	
CSCS	1	PCE	5.2247	0.2664	2.5709	0.0156	5.1	15	5.2238
		MCS	5.2272	0.2664	2.5707	0.0151	5.1	523.46	
	2	PCE	4.7038	0.3599	2.6277	0.1248	7.7	25	4.6999
		MCS	4.7045	0.3596	2.6278	0.1249	7.7	549.55	
	5	PCE	4.2712	0.4427	2.6774	0.2147	10.4	16	4.2627
		MCS	4.2687	0.4429	2.6775	0.2146	10.4	580.37	
	10	PCE	4.0666	0.4718	2.7066	0.2578	11.6	31	4.0550
		MCS	4.0656	0.4720	2.7064	0.2577	11.6	592.43	
CCCC	1	PCE	6.4425	0.3222	2.5557	0.0034	5.0	16.00	6.4417
		MCS	6.4429	0.3218	2.5550	0.0039	5.0	533.16	
	2	PCE	5.7829	0.4327	2.6171	0.1170	7.5	14.87	5.7789
		MCS	5.7815	0.4324	2.6179	0.1164	7.5	529.85	
	5	PCE	5.1638	0.5327	2.6805	0.2195	10.3	15.28	5.1524
		MCS	5.1649	0.5332	2.6811	0.2189	10.3	574.46	
	10	PCE	4.8807	0.5726	2.7155	0.2652	11.7	15.57	4.8661
		MCS	4.8811	0.5727	2.7150	0.2659	11.7	581.27	

$$u_2\left(x_1,x_2,x_3\right) = u_2^0\left(x_1,x_2\right) + \boldsymbol{\Phi}_1\left(x_3\right) u_{3,2}^0 + \boldsymbol{\Phi}_2\left(x_3\right)\varphi_2\left(x_1,x_2\right) \tag{12b}$$

$$u_3\left(x_1,x_2,x_3\right) = u_3^0\left(x_1,x_2\right) \tag{12c}$$

where $\boldsymbol{\Phi}_1\left(x_3\right) = H^s\Psi\left(x_3\right) - x_3, \boldsymbol{\Phi}_2\left(x_3\right) = H^s\Psi\left(x_3\right)$. Similarly, it is from Eq. (12) that the displacement field of Reissner [48], Shi et al. [55] can be derived with $f\left(x_3\right) = \frac{3}{2h}\left(z - \frac{4z^3}{3h^2}\right)$, and Reddy's theory [49] with $f\left(x_3\right) = \frac{6}{5h}\left(z - \frac{4z^3}{3h^2}\right)$.

Substituting Eq. (12) into Eq. (4), the in-plane and out-of-plane strains $\boldsymbol{\varepsilon}^T = \left[\boldsymbol{\varepsilon}^{(i)} \quad \boldsymbol{\varepsilon}^{(s)}\right]$ are obtained as follows:

$$\boldsymbol{\varepsilon}^{(i)} = \boldsymbol{\varepsilon}^{(0)} + \boldsymbol{\Phi}_1\left(x_3\right)\boldsymbol{\varepsilon}^{(1)} + \boldsymbol{\Phi}_2\left(x_3\right)\boldsymbol{\varepsilon}^{(2)} \tag{13a}$$

$$\boldsymbol{\varepsilon}^{(s)} = \boldsymbol{\Phi}_3\left(x_3\right)\boldsymbol{\varepsilon}^{(3)} \tag{13b}$$

where $\boldsymbol{\Phi}_3\left(x_3\right) = H^s\Psi_{,3}$ with $\Psi_{,3}\left(x_3\right) = \frac{f_{,3}(x_3)}{\mu(x_3)}$ and,

$$\boldsymbol{\varepsilon}^{(0)} = \begin{Bmatrix}\varepsilon_{11}^{(0)}\\ \varepsilon_{22}^{(0)}\\ \gamma_{12}^{(0)}\end{Bmatrix} = \begin{Bmatrix} u_{1,1}^0\\ u_{2,2}^0\\ u_{1,2}^0 + u_{2,1}^0\end{Bmatrix}, \boldsymbol{\varepsilon}^{(1)} = \begin{Bmatrix}\varepsilon_{11}^{(1)}\\ \varepsilon_{22}^{(1)}\\ \gamma_{12}^{(1)}\end{Bmatrix} = \begin{Bmatrix} u_{3,11}^0\\ u_{3,22}^0\\ 2u_{3,12}^0\end{Bmatrix},$$

$$\boldsymbol{\varepsilon}^{(2)} = \begin{Bmatrix}\varepsilon_{11}^{(2)}\\ \varepsilon_{22}^{(2)}\\ \gamma_{12}^{(2)}\end{Bmatrix} = \begin{Bmatrix} \varphi_{1,1}\\ \varphi_{2,2}\\ \varphi_{1,2} + \varphi_{2,1}\end{Bmatrix} \tag{14a}$$

$$\boldsymbol{\varepsilon}^{(3)} = \begin{Bmatrix}\gamma_{13}^{(0)}\\ \gamma_{23}^{(0)}\end{Bmatrix} = \begin{Bmatrix}\varphi_1 + u_{3,1}^0\\ \varphi_2 + u_{3,2}^0\end{Bmatrix} \tag{14b}$$

Moreover, the symmetric rotation gradients are given by:

$$\chi_{ij} = \frac{1}{2}\left(\overline{\theta}_{i,j} + \overline{\theta}_{j,i}\right) \tag{15}$$

where $\overline{\theta}_i$ is determined in terms of the displacements u_i as follows:

$$\overline{\theta}_1 = \frac{1}{2}\left(u_{3,2} - u_{2,3}\right) = \frac{1}{2}\left(u_{3,2}^0 - \boldsymbol{\Phi}_{1,3}u_{3,2}^0 - \boldsymbol{\Phi}_{2,3}\varphi_2\right) \tag{16a}$$

$$\overline{\theta}_2 = \frac{1}{2}\left(u_{1,3} - u_{3,1}\right) = \frac{1}{2}\left(-u_{3,1}^0 + \boldsymbol{\Phi}_{1,3}u_{3,1}^0 + \boldsymbol{\Phi}_{2,3}\varphi_1\right) \tag{16b}$$

$$\overline{\theta}_3 = \frac{1}{2}\left(u_{2,1} - u_{1,2}\right) = \frac{1}{2}\left[u_{2,1}^0 - u_{1,2}^0 + \boldsymbol{\Phi}_2\left(\varphi_{2,1} - \varphi_{1,2}\right)\right] \tag{16c}$$

Substituting Eq. (16) into Eq. (15), the rotation gradients are expressed as follows:

$$\boldsymbol{\chi} = \boldsymbol{\chi}^{(0)} + \boldsymbol{\Phi}_{1,3}\boldsymbol{\chi}^{(1)} + \boldsymbol{\Phi}_{2,3}\boldsymbol{\chi}^{(2)} + \boldsymbol{\Phi}_{1,33}\boldsymbol{\chi}^{(3)} + \boldsymbol{\Phi}_{2,33}\boldsymbol{\chi}^{(4)} + \boldsymbol{\Phi}_2\boldsymbol{\chi}^{(5)} \tag{17}$$

where $\boldsymbol{\chi}^T = \left[\chi_{11} \quad \chi_{22} \quad 2\chi_{12} \quad \chi_{33} \quad 2\chi_{13} \quad 2\chi_{23}\right]$ and,

$$\boldsymbol{\chi}^{(0)} = \frac{1}{2}\begin{Bmatrix} u_{3,12}^0\\ -u_{3,12}^0\\ u_{3,22}^0 - u_{3,11}^0\\ 0\\ u_{2,11}^0 - u_{1,12}^0\\ u_{2,12}^0 - u_{1,22}^0\end{Bmatrix}, \boldsymbol{\chi}^{(1)} = \frac{1}{2}\begin{Bmatrix} -u_{3,12}^0\\ u_{3,12}^0\\ u_{3,11}^0 - u_{3,22}^0\\ 0\\ 0\\ 0\end{Bmatrix},$$

Table 5
Comparison study between MCS (10.000 samples) and PCE (256 samples) for the mean, standard deviation (SD), Kurtosis and Skewness for the fundamental frequency of the FG microplates ($a/h = 10$, MAT 1).

BCs	p	Theory	Mean	SD	Kurtosis	$Skewness$	COV(%)	Time(s)	Present
$h/l = 1$									
SSSS	1	PCE	11.0107	0.5087	2.4628	−0.0532	4.6	17.02	11.0105
		MCS	11.0100	0.5087	2.4633	−0.0531	4.6	814.11	
	5	PCE	8.7431	0.8313	2.6301	0.1966	9.5	18.12	8.7203
		MCS	8.7456	0.8317	2.6308	0.1962	9.5	815.30	
	10	PCE	8.0719	0.8990	2.6953	0.2624	11.1	18.47	8.0442
		MCS	8.0747	0.8986	2.6949	0.2629	11.1	817.04	
CCCC	1	PCE	24.0519	1.1046	2.4451	−0.0594	4.6	17.68	24.0526
		MCS	24.0482	1.1041	2.4547	−0.0596	4.6	818.84	
	5	PCE	18.9599	1.7906	2.6265	0.1961	9.4	17.82	18.9125
		MCS	18.9631	1.7912	2.6260	0.1962	9.4	817.73	
	10	PCE	17.4222	1.9411	2.7025	0.2651	11.1	18.44	17.3596
		MCS	17.4209	1.9406	2.7031	0.2645	11.1	818.42	
$h/l = 5$									
SSSS	1	PCE	4.8590	0.2458	2.5788	0.0199	5.1	17.65	4.8572
		MCS	4.8565	0.2453	2.5779	0.0197	5.1	811.69	
	5	PCE	4.0912	0.4163	2.6649	0.2053	10.2	18.20	4.0828
		MCS	4.0913	0.4164	2.6648	0.2049	10.2	815.24	
	10	PCE	3.9210	0.4402	2.6852	0.2476	11.2	17.95	3.9112
		MCS	3.9213	0.4406	2.6855	0.2480	11.2	817.51	
CCCC	1	PCE	8.9385	0.4421	2.5478	0.0197	4.9	17.10	8.9348
		MCS	8.9356	0.4426	2.5481	0.0199	4.9	816.86	
	5	PCE	7.3712	0.7425	2.6682	0.2108	10.1	17.66	7.3509
		MCS	7.3723	0.7429	2.6675	0.2106	10.1	820.08	
	10	PCE	6.9934	0.7913	2.6981	0.2564	11.3	17.90	6.9730
		MCS	6.9955	0.7917	2.6987	0.2568	11.3	818.79	
$h/l = 10$									
SSSS	1	PCE	4.5341	0.2337	2.5998	0.0357	5.2	17.82	4.5338
		MCS	4.5330	0.2339	2.5995	0.0352	5.2	819.66	
	5	PCE	3.8564	0.3966	2.6671	0.2078	10.3	18.05	3.8502
		MCS	3.8580	0.3970	2.6675	0.2877	10.3	817.34	
	10	PCE	3.7169	0.4179	2.6889	0.2474	11.2	18.25	3.7072
		MCS	3.7199	0.4183	2.6891	0.2476	11.2	818.59	
CCCC	1	PCE	8.0048	0.4076	2.5525	0.0165	5.1	17.30	8.0090
		MCS	8.0032	0.4071	2.5520	0.0164	5.1	816.72	
	5	PCE	6.6760	0.6844	2.6616	0.2069	10.3	17.53	6.6562
		MCS	6.6778	0.6849	2.6611	0.2071	10.3	819.33	
	10	PCE	6.3784	0.7261	2.6906	0.2524	11.4	17.87	6.3648
		MCS	6.3783	0.7261	2.6905	0.2525	11.4	817.85	

Table 6
Non-dimensional critical buckling loads of the FG square plates (MAT 1).

BCs	a/h	Theory	p			
			1	2	5	10
Axial compression $\left(N_1^0, N_2^0, N_{12}^0 = 1, 0, 0\right)$						
SSSS	5	Present	8.2250	6.3433	5.0517	4.4807
		IGA [13]	8.2245	6.3432	5.0531	4.4807
		IGA-TSDT [57]	8.2245	6.3432	5.0531	4.4807
	10	Present	9.3395	7.2635	6.0352	5.4537
		IGA [13]	9.3391	7.2631	6.0353	5.4528
		IGA-TSDT [57]	9.3391	7.2631	6.0353	5.4529
CCCC	10	Present	21.0950	16.2860	13.0276	11.5736
		IGA [13]	20.9471	16.1682	12.9218	11.4711
Biaxial compression $\left(N_1^0, N_2^0, N_{12}^0 = 1, 1, 0\right)$						
SSSS	5	Present	4.1125	3.1717	2.5259	2.2404
		IGA [13]	4.1122	3.1716	2.5265	2.2403
		IGA-TSDT [57]	4.1123	3.1716	2.5265	2.2403
	10	Present	4.6697	3.6317	3.0176	2.7268
		IGA [13]	4.6696	3.6315	3.0177	2.7264
		IGA-TSDT [57]	4.6696	3.6315	3.0177	2.7264
CCCC	10	Present	11.4214	8.8376	7.1420	6.3759
		IGA [13]	11.3805	8.8028	7.1165	6.3518

Table 7
Non-dimensional critical buckling loads of SSSS FG square microplates (MAT 2) with biaxial compression.

a/h	p	Theory	h/l				
			∞	5	2.5	1.25	1
10	0	Present	18.0854	20.9253	29.4718	63.6538	88.2866
		IGA [13]	18.0754	20.9026	29.3735	63.1958	88.5417
		RPT [9]	18.0756	20.8497	29.1700	62.4358	87.3775
	1	Present	7.8281	9.3962	14.1003	32.9144	47.0226
		IGA- [13]	7.8276	9.3767	14.0232	32.6037	46.5372
		RPT [9]	7.8277	9.3581	13.9459	32.2693	45.9981
	10	Present	3.4988	4.0175	5.5737	11.7984	16.4669
		IGA- [13]	3.4969	4.0513	5.6631	11.9349	16.6033
		RPT [9]	3.4982	4.0246	5.5925	11.8036	16.4431
20	0	Present	18.9254	21.7833	30.3569	64.6505	90.3698
		IGA [13]	18.9243	21.7771	30.3324	64.5348	90.1804
		RPT [9]	18.9244	21.7628	30.2773	64.3321	89.8715
	1	Present	8.1147	9.6868	14.4033	33.2685	47.4168
		IGA [13]	8.1142	9.6815	14.3832	33.1882	47.2914
		RPT [9]	8.1143	9.6766	14.3626	33.0999	47.1494
	10	Present	3.7475	4.2674	5.8270	12.0655	16.7444
		IGA [13]	3.7450	4.2752	5.8505	12.1011	16.7793
		RPT [9]	3.7454	4.2677	5.8312	12.0666	16.7376

Table 8
Comparison study between MCS (10.000 samples) and PCE (16 samples) for the mean, standard deviation (SD), Kurtosis and Skewness for the critical buckling loads of the FG plates with axial compression (MAT 1).

BCs	a/h	p	Theory	Mean	SD	Kurtosis	Skewness	COV (%)	Time (s)	Present
SFSF	5	1	PCE	0.8844	0.1295	2.3679	0.3494	14.6	8.84	0.8814
			MCS	0.8848	0.1296	2.3675	0.3493	14.6	243.18	
		2	PCE	0.6872	0.0711	2.3260	0.2701	10.3	8.07	0.6846
			MCS	0.6868	0.0708	2.3264	0.2702	10.3	252.32	
		5	PCE	0.5666	0.0404	2.2600	0.1152	7.1	8.92	0.5660
			MCS	0.5659	0.0409	2.2605	0.1149	7.1	234.28	
		10	PCE	0.5112	0.0337	2.2556	0.1294	6.6	9.10	0.5106
			MCS	0.5112	0.0337	2.2555	0.1294	6.6	262.81	
SSSS		1	PCE	8.2320	1.2316	2.3684	0.3505	15.0	8.72	8.2250
			MCS	8.2314	1.2310	2.3688	0.3506	15.0	277.28	
		2	PCE	6.3687	0.6878	2.3295	0.2803	10.8	8.49	6.3433
			MCS	6.3664	0.6879	2.3291	0.2807	10.8	258.34	
		5	PCE	5.0478	0.3701	2.2547	0.1234	7.3	9.15	5.0517
			MCS	5.0531	0.3708	2.2543	0.1239	7.3	283.27	
		10	PCE	4.4855	0.2691	2.2591	0.1307	6.0	9.71	4.4807
			MCS	4.4853	0.2691	2.2593	0.1308	6.0	271.20	
CFCF		1	PCE	2.0177	0.2996	2.3536	0.3493	14.8	7.89	2.0053
			MCS	2.0115	0.2991	2.3534	0.3495	14.8	217.96	
		2	PCE	1.5574	0.1661	2.3261	0.2761	10.7	7.78	1.5511
			MCS	1.5543	0.1659	2.3264	0.2762	10.7	211.56	
		5	PCE	1.2547	0.0904	2.2668	0.1451	7.2	8.34	1.2535
			MCS	1.2509	0.0907	2.2663	0.1456	7.2	241.76	
		10	PCE	1.1203	0.0705	2.2563	0.1342	6.3	8.93	1.1188
			MCS	1.1183	0.0706	2.2565	0.1339	6.3	285.11	
SSSS	10	1	PCE	9.3424	1.3669	2.3676	0.3486	14.6	9.11	9.3395
			MCS	9.3427	1.3664	2.3679	0.3487	14.6	252.11	
		2	PCE	7.2897	0.7483	2.3244	0.2670	10.3	8.98	7.2635
			MCS	7.2763	0.7487	2.3245	0.2676	10.3	237.98	
		5	PCE	6.0415	0.4294	2.2585	0.1103	7.1	10.30	6.0352
			MCS	6.0410	0.4297	2.2586	0.1101	7.1	237.56	
		10	PCE	5.4599	0.3624	2.2551	0.1270	6.6	10.21	5.4537
			MCS	5.4544	0.3622	2.2553	0.1272	6.6	210.68	
CFCF		1	PCE	1.3561	0.1971	2.3655	0.3472	14.5	8.00	1.3470
			MCS	1.3462	0.1972	2.3655	0.3476	14.5	212.32	
		2	PCE	1.0518	0.1079	2.3223	0.2675	10.3	7.86	1.0480
			MCS	1.0431	0.1074	2.3227	0.2670	10.3	177.33	
		5	PCE	0.8734	0.0617	2.1885	0.0702	7.1	8.36	0.8729
			MCS	0.8778	0.0619	2.188	0.0708	7.1	243.65	
		10	PCE	0.7909	0.0531	2.2618	0.1271	6.7	8.69	0.7899
			MCS	0.7844	0.0533	2.2617	0.1274	6.7	255.65	

$$\chi^{(2)} = \frac{1}{2}\begin{Bmatrix} -\varphi_{2,1} \\ \varphi_{1,2} \\ \varphi_{1,1} - \varphi_{2,2} \\ \varphi_{2,1} - \varphi_{1,2} \\ 0 \\ 0 \end{Bmatrix} \tag{18a}$$

$$\chi^{(3)} = \frac{1}{2}\begin{Bmatrix} 0 \\ 0 \\ 0 \\ 0 \\ -u^0_{3,2} \\ u^0_{3,1} \end{Bmatrix}, \chi^{(4)} = \frac{1}{2}\begin{Bmatrix} 0 \\ 0 \\ 0 \\ 0 \\ -\varphi_2 \\ \varphi_1 \end{Bmatrix},$$

$$\chi^{(5)} = \frac{1}{2}\begin{Bmatrix} 0 \\ 0 \\ 0 \\ 0 \\ \varphi_{2,11} - \varphi_{1,12} \\ \varphi_{2,12} - \varphi_{1,22} \end{Bmatrix} \tag{18b}$$

Furthermore, the stresses and strains of the FG microplates are related by constitutive equations as follows:

$$\boldsymbol{\sigma}^{(i)} = \begin{Bmatrix} \sigma_{11} \\ \sigma_{22} \\ \sigma_{12} \end{Bmatrix} = \begin{bmatrix} Q_{11} & Q_{12} & 0 \\ Q_{12} & Q_{22} & 0 \\ 0 & 0 & Q_{66} \end{bmatrix} \begin{Bmatrix} \varepsilon_{11} \\ \varepsilon_{22} \\ \gamma_{12} \end{Bmatrix} = \mathbf{Q}^{(i)}_{\varepsilon}\boldsymbol{\varepsilon}^{(i)} \tag{19a}$$

$$\boldsymbol{\sigma}^{(o)} = \begin{Bmatrix} \sigma_{13} \\ \sigma_{23} \end{Bmatrix} = \begin{bmatrix} Q_{55} & 0 \\ 0 & Q_{44} \end{bmatrix} \begin{Bmatrix} \gamma_{13} \\ \gamma_{23} \end{Bmatrix} = \mathbf{Q}^{(o)}_{\varepsilon}\boldsymbol{\varepsilon}^{(s)} \tag{19b}$$

$$\mathbf{m} = \begin{Bmatrix} m_{11} \\ m_{22} \\ m_{12} \\ m_{33} \\ m_{23} \\ m_{13} \end{Bmatrix} = 2\mu l^2 \begin{bmatrix} 1 & 0 & 0 & 0 & 0 & 0 \\ 0 & 1 & 0 & 0 & 0 & 0 \\ 0 & 0 & 1 & 0 & 0 & 0 \\ 0 & 0 & 0 & 1 & 0 & 0 \\ 0 & 0 & 0 & 0 & 1 & 0 \\ 0 & 0 & 0 & 0 & 0 & 1 \end{bmatrix} \begin{Bmatrix} \chi_{11} \\ \chi_{22} \\ \chi_{12} \\ \chi_{33} \\ \chi_{23} \\ \chi_{13} \end{Bmatrix} = \alpha_{\chi}\mathbf{I}_{6\times 6}\chi \tag{19c}$$

where $\alpha_{\chi} = 2\mu l^2$, $Q_{11} = \frac{E(x_3)}{1-\nu^2}$, $Q_{22} = \frac{E(x_3)}{1-\nu^2}$, $Q_{12} = \frac{\nu E(x_3)}{1-\nu^2}$, $Q_{44} = Q_{55} = Q_{66} = \mu = \frac{E(x_3)}{2(1+\nu)}$.

In order to derive the equation of motion, Hamilton's principle is used:

$$\int_{t_1}^{t_2} \left(\delta\Pi_U + \delta\Pi_V - \delta\Pi_K\right) dt = 0 \tag{20}$$

where $\delta\Pi_U, \delta\Pi_V, \delta\Pi_K$ are the variations of strain energy, work done by membrane compressive forces and kinetic energy, respectively. The variation of the strain energy of FG microplates derived from Eq. (3)

Table 9
Comparison study between MCS (10.000 samples) and PCE (16 samples) for the mean, standard deviation (SD), Kurtosis and Skewness for the critical buckling loads of CCCC FG plates (MAT 1).

a/h	p	Theory	Mean	SD	Kurtosis	Skewness	COV (%)	Time (s)	Present
Axial compression $\left(N_1^0, N_2^0, N_{12}^0 = 1, 0, 0\right)$									
10	1	PCE	21.2503	3.1515	2.3684	0.3503	14.8	8.23	21.0950
		MCS	21.2089	3.1521	2.3678	0.3509	14.8	223.41	
	2	PCE	16.3498	1.7563	2.3279	0.2780	10.7	9.35	16.2860
		MCS	16.3320	1.7561	2.3282	0.2787	10.7	219.87	
	5	PCE	13.0542	0.9369	2.2711	0.1512	7.2	8.66	13.0276
		MCS	13.0527	0.9368	2.2715	0.1507	7.2	238.56	
	10	PCE	11.5863	0.7017	2.2578	0.1273	6.1	10.40	11.5736
		MCS	11.5920	0.7014	2.2581	0.1270	6.1	224.98	
20	1	PCE	23.8157	3.4591	2.3675	0.3488	14.5	12.09	23.6531
		MCS	23.7814	3.4585	2.3681	0.3494	14.5	236.52	
	2	PCE	18.4718	1.8916	2.3248	0.2670	10.2	9.27	18.4016
		MCS	18.4805	1.8912	2.3250	0.2671	10.2	231.35	
	5	PCE	15.3385	1.0897	2.2580	0.1081	7.1	10.10	15.3190
		MCS	15.2997	1.0895	2.2576	0.1088	7.1	227.63	
	10	PCE	13.8711	0.8991	2.1631	0.0328	6.5	9.98	13.8550
		MCS	13.7917	0.8998	2.1627	0.0331	6.5	240.74	
Biaxial compression $\left(N_1^0, N_2^0, N_{12}^0 = 1, 1, 0\right)$									
10	1	PCE	11.5002	1.6963	2.3681	0.3498	14.8	8.16	11.4214
		MCS	11.5036	1.6961	2.3683	0.3494	14.8	235.53	
	2	PCE	8.8696	0.9406	2.3275	0.2755	10.6	8.04	8.8376
		MCS	8.8668	0.9400	2.3277	0.2760	10.6	242.14	
	5	PCE	7.1544	0.5119	2.2670	0.1393	7.2	8.69	7.1420
		MCS	7.1579	0.5115	2.2676	0.1389	7.2	237.69	
	10	PCE	6.3870	0.3978	2.2578	0.1288	6.2	9.24	6.3759
		MCS	6.3884	0.3977	2.2580	0.1285	6.2	239.56	
20	1	PCE	12.6256	1.8307	2.3672	0.3481	14.5	7.98	12.5432
		MCS	12.6415	1.8311	2.3678	0.3489	14.5	243.86	
	2	PCE	9.7974	1.0001	2.3238	0.2659	10.2	8.21	9.7575
		MCS	9.7972	1.0002	2.3239	0.2657	10.2	241.38	
	5	PCE	8.1581	0.5792	2.2575	0.1051	7.1	8.84	8.1483
		MCS	8.1207	0.5798	2.2571	0.1057	7.1	246.90	
	10	PCE	7.3892	0.4961	2.2540	0.1267	6.7	8.94	7.3794
		MCS	7.3887	0.4959	2.2542	0.1270	6.7	244.81	

as follows:

$$\begin{aligned}\delta\prod_U &= \int_A (\boldsymbol{\sigma}\delta\boldsymbol{\varepsilon} + \mathbf{m}\delta\boldsymbol{\chi})\, dA \\ &= \int_A \Big[\mathbf{M}_\varepsilon^{(0)}\delta\boldsymbol{\varepsilon}^{(0)} + \mathbf{M}_\varepsilon^{(1)}\delta\boldsymbol{\varepsilon}^{(1)} + \mathbf{M}_\varepsilon^{(2)}\delta\boldsymbol{\varepsilon}^{(2)} + \mathbf{M}_\varepsilon^{(3)}\delta\boldsymbol{\varepsilon}^{(3)} \\ &+\mathbf{M}_\chi^{(0)}\delta\boldsymbol{\chi}^{(0)} + \mathbf{M}_\chi^{(1)}\delta\boldsymbol{\chi}^{(1)} + \mathbf{M}_\chi^{(2)}\delta\boldsymbol{\chi}^{(2)} + \mathbf{M}_\chi^{(3)}\delta\boldsymbol{\chi}^{(3)} \\ &+ \mathbf{M}_\chi^{(4)}\delta\boldsymbol{\chi}^{(4)} + \mathbf{M}_\chi^{(5)}\delta\boldsymbol{\chi}^{(5)}\Big]\, dA\end{aligned} \tag{21}$$

where the stress resultants are given by:

$$\left(\mathbf{M}_\varepsilon^{(0)}, \mathbf{M}_\varepsilon^{(1)}, \mathbf{M}_\varepsilon^{(2)}\right) = \int_{-h/2}^{h/2} \left(1, \Phi_1, \Phi_2\right) \boldsymbol{\sigma}^{(i)} dx_3 \tag{22a}$$

$$\mathbf{M}_\varepsilon^{(3)} = \int_{-h/2}^{h/2} \Phi_3 \boldsymbol{\sigma}^{(o)} dx_3 \tag{22b}$$

$$\begin{aligned}&\left(\mathbf{M}_\chi^{(0)}, \mathbf{M}_\chi^{(1)}, \mathbf{M}_\chi^{(2)}, \mathbf{M}_\chi^{(3)}, \mathbf{M}_\chi^{(4)}, \mathbf{M}_\chi^{(5)}\right) \\ &= \int_{-h/2}^{h/2} \left(1, \Phi_{1,3}, \Phi_{2,3}, \Phi_{1,33}, \Phi_{2,33}, \Phi_2\right) \mathbf{m} dx_3\end{aligned} \tag{22c}$$

These stress resultants can be expressed in terms of the strains and its gradients as follows:

$$\begin{Bmatrix}\mathbf{M}_\varepsilon^{(0)} \\ \mathbf{M}_\varepsilon^{(1)} \\ \mathbf{M}_\varepsilon^{(2)} \\ \mathbf{M}_\varepsilon^{(3)}\end{Bmatrix} = \begin{bmatrix}\mathbf{A}^\varepsilon & \mathbf{B}^\varepsilon & \mathbf{B}_s^\varepsilon & \mathbf{0} \\ \mathbf{B}^\varepsilon & \mathbf{D}^\varepsilon & \mathbf{D}_s^\varepsilon & \mathbf{0} \\ \mathbf{B}_s^\varepsilon & \mathbf{D}_s^\varepsilon & \mathbf{H}_s^\varepsilon & \mathbf{0} \\ \mathbf{0} & \mathbf{0} & \mathbf{0} & \mathbf{A}_s^\varepsilon\end{bmatrix} \begin{Bmatrix}\boldsymbol{\varepsilon}^{(0)} \\ \boldsymbol{\varepsilon}^{(1)} \\ \boldsymbol{\varepsilon}^{(2)} \\ \boldsymbol{\varepsilon}^{(3)}\end{Bmatrix} \tag{23a}$$

$$\begin{Bmatrix}\mathbf{M}_\chi^{(0)} \\ \mathbf{M}_\chi^{(1)} \\ \mathbf{M}_\chi^{(2)} \\ \mathbf{M}_\chi^{(3)} \\ \mathbf{M}_\chi^{(4)} \\ \mathbf{M}_\chi^{(5)}\end{Bmatrix} = \begin{bmatrix}\mathbf{A}^\chi & \overline{\mathbf{B}}^\chi & \overline{\mathbf{B}}_s^\chi & \overline{\overline{\mathbf{B}}}^\chi & \overline{\overline{\mathbf{B}}}_s^\chi & \mathbf{B}_s^\chi \\ \overline{\mathbf{B}}^\chi & \overline{\mathbf{D}}^\chi & \overline{\mathbf{D}}_s^\chi & \overline{\mathbf{E}}^\chi & \overline{\mathbf{E}}_s^\chi & \overline{\mathbf{F}}_s^\chi \\ \overline{\mathbf{B}}_s^\chi & \overline{\mathbf{D}}_s^\chi & \overline{\mathbf{H}}_s^\chi & \overline{\mathbf{G}}_s^\chi & \overline{\mathbf{I}}^\chi & \overline{\mathbf{J}}^\chi \\ \overline{\overline{\mathbf{B}}}^\chi & \overline{\mathbf{E}}^\chi & \overline{\mathbf{G}}_s^\chi & \overline{\overline{\mathbf{D}}}^\chi & \overline{\overline{\mathbf{D}}}_s^\chi & \overline{\overline{\mathbf{K}}}_s^\chi \\ \overline{\overline{\mathbf{B}}}_s^\chi & \overline{\mathbf{E}}_s^\chi & \overline{\mathbf{I}}^\chi & \overline{\overline{\mathbf{D}}}_s^\chi & \overline{\overline{\mathbf{H}}}_s^\chi & \overline{\overline{\mathbf{L}}} \\ \mathbf{B}_s^\chi & \overline{\mathbf{F}}_s^\chi & \overline{\mathbf{J}}^\chi & \overline{\overline{\mathbf{K}}}_s^\chi & \overline{\overline{\mathbf{L}}} & \mathbf{H}_s^\chi\end{bmatrix} \begin{Bmatrix}\boldsymbol{\chi}^{(0)} \\ \boldsymbol{\chi}^{(1)} \\ \boldsymbol{\chi}^{(2)} \\ \boldsymbol{\chi}^{(3)} \\ \boldsymbol{\chi}^{(4)} \\ \boldsymbol{\chi}^{(5)}\end{Bmatrix} \tag{23b}$$

where the stiffness components of the FG microplates are defined as follows:

$$\left(\mathbf{A}^\epsilon, \mathbf{B}^\epsilon, \mathbf{D}^\epsilon, \mathbf{H}_s^\epsilon, \mathbf{B}_s^\epsilon, \mathbf{D}_s^\epsilon\right) = \int_{-h/2}^{h/2} \left(1, \Phi_1, \Phi_1^2, \Phi_2^2, \Phi_2, \Phi_1\Phi_2\right) \mathbf{Q}_\epsilon^{(i)} dx_3 \tag{24a}$$

$$\mathbf{A}_s^\epsilon = \int_{-h/2}^{h/2} \Phi_3^2 \mathbf{Q}_\epsilon^{(o)} dx_3 \tag{24b}$$

$$\begin{aligned}&\left(\mathbf{A}^\chi, \overline{\mathbf{B}}^\chi, \overline{\mathbf{B}}_s^\chi, \overline{\overline{\mathbf{B}}}^\chi, \overline{\overline{\mathbf{B}}}_s^\chi, \mathbf{B}_s^\chi\right) = \left(A^\chi, \overline{B}^\chi, \overline{B}_s^\chi, \overline{\overline{B}}^\chi, \overline{\overline{B}}_s^\chi, B_s^\chi\right) \mathbf{I}_{6\times6} \\ &= \int_{-h/2}^{h/2} \left(1, \Phi_{1,3}, \Phi_{2,3}, \Phi_{1,33}, \Phi_{2,33}, \Phi_2\right) \alpha_\chi \mathbf{I}_{6\times6} dx_3\end{aligned} \tag{24c}$$

$$\begin{aligned}&\left(\overline{\mathbf{D}}^\chi, \overline{\mathbf{D}}_s^\chi, \overline{\mathbf{E}}^\chi, \overline{\mathbf{E}}_s^\chi, \overline{\mathbf{F}}_s^\chi\right) = \left(\overline{D}^\chi, \overline{D}_s^\chi, \overline{E}^\chi, \overline{E}_s^\chi, \overline{F}_s^\chi\right) \mathbf{I}_{6\times6} \\ &= \int_{-h/2}^{h/2} \Phi_{1,3} \left(\Phi_{1,3}, \Phi_{2,3}, \Phi_{1,33}, \Phi_{2,33}, \Phi_2\right) \alpha_\chi \mathbf{I}_{6\times6} dx_3\end{aligned} \tag{24d}$$

$$\begin{aligned}&\left(\overline{\mathbf{H}}_s^\chi, \overline{\mathbf{G}}_s^\chi, \overline{\mathbf{I}}^\chi, \overline{\mathbf{J}}^\chi\right) = \left(\overline{H}_s^\chi, \overline{G}_s^\chi, \overline{I}^\chi, \overline{J}^\chi\right) \mathbf{I}_{6\times6} \\ &= \int_{-h/2}^{h/2} \Phi_{2,3} \left(\Phi_{2,3}, \Phi_{1,33}, \Phi_{2,33}, \Phi_2\right) \alpha_\chi \mathbf{I}_{6\times6} dx_3\end{aligned} \tag{24e}$$

Table 10
Comparison study between MCS (10.000 samples) and PCE (16 samples) for the mean, standard deviation (SD), Kurtosis and Skewness for the critical buckling loads of the FG microplates with axial compression ($a/h = 10$, MAT 1).

BCs	p	Theory	Mean	SD	Kurtosis	Skewness	COV (%)	Time (s)	Present
$h/l = 1$									
SSSS	1	PCE	58.4624	9.8782	2.3812	0.3725	16.9	12.50	57.9757
		MCS	58.4657	9.8788	2.3809	0.3721	16.9	322.38	
	5	PCE	32.4824	3.2687	2.3614	0.3419	10.1	11.91	32.3346
		MCS	32.4856	3.2688	2.3615	0.3420	10.1	342.57	
	10	PCE	26.7580	1.9125	2.3526	0.3299	7.1	12.10	26.6745
		MCS	26.7544	1.9128	2.3529	0.3295	7.1	333.43	
CCCC	1	PCE	207.7745	35.5152	2.3821	0.3741	17.1	11.25	206.0174
		MCS	207.7809	35.5145	2.3815	0.3737	17.1	329.37	
	5	PCE	113.6983	11.7596	2.3717	0.3584	10.3	12.48	113.1408
		MCS	113.6748	11.7599	2.3722	0.3579	10.3	327.81	
	10	PCE	92.7044	6.6338	2.3664	0.3509	7.2	12.87	92.3964
		MCS	92.7008	6.6344	2.3659	0.3502	7.2	340.11	
$h/l = 5$									
SSSS	1	PCE	11.3652	1.7074	2.3706	0.3542	15.0	12.43	11.2853
		MCS	11.3660	1.7079	2.3712	0.3544	15.0	326.25	
	5	PCE	7.0992	0.5427	2.2761	0.1661	7.6	12.16	7.0872
		MCS	7.1011	0.5430	2.2766	0.1659	7.6	328.68	
	10	PCE	6.3119	0.4242	2.2682	0.1635	6.7	11.94	6.3026
		MCS	6.3131	0.4245	2.2686	0.1631	6.7	324.37	
CCCC	1	PCE	28.8815	4.4686	2.3726	0.3578	15.5	12.15	28.6604
		MCS	28.8786	4.4688	2.3721	0.3581	15.5	328.97	
	5	PCE	17.2289	1.3323	2.2976	0.2205	7.7	12.67	17.1832
		MCS	17.2301	1.3325	2.2977	0.2200	7.7	327.24	
	10	PCE	14.9834	0.9562	2.2820	0.1926	6.4	12.53	14.9497
		MCS	14.9864	0.9565	2.2826	0.1924	6.4	330.12	
$h/l = 10$									
SSSS	1	PCE	9.8931	1.4520	2.3685	0.3502	14.7	12.35	9.8259
		MCS	9.8878	1.4525	2.3688	0.3507	14.7	329.26	
	5	PCE	6.3059	0.4577	2.2632	0.1269	7.3	12.11	6.2982
		MCS	6.3113	0.4580	2.2628	0.1270	7.3	328.68	
	10	PCE	5.6729	0.3778	2.2586	0.1373	6.7	12.16	5.6659
		MCS	5.6803	0.3781	2.2590	0.1374	6.7	331.58	
CCCC	1	PCE	23.1786	3.4837	2.3697	0.3527	15.0	12.61	23.0067
		MCS	23.1818	3.4832	2.3700	0.3531	15.0	330.83	
	5	PCE	14.1185	1.0505	2.2789	0.1739	7.4	12.89	14.0846
		MCS	14.1109	1.0500	2.2783	0.1740	7.4	329.12	
	10	PCE	12.4604	0.8084	2.2651	0.1499	6.5	12.36	12.4363
		MCS	12.4581	0.8079	2.2655	0.1501	6.5	333.84	

$$\left(\overline{\overline{\mathbf{D}}}^{\chi}, \overline{\overline{\mathbf{D}}}_s^{\chi}, \overline{\mathbf{K}}_s^{\chi}, \overline{\overline{\mathbf{H}}}_s^{\chi}, \overline{\mathbf{L}}^{\chi}, \mathbf{H}_s^{\chi}\right) = \left(\overline{\overline{D}}^{\chi}, \overline{\overline{D}}_s^{\chi}, \overline{K}_s^{\chi}, \overline{\overline{H}}_s^{\chi}, \overline{L}^{\chi}, H_s^{\chi}\right)\mathbf{I}_{6\times6} = \int_{-h/2}^{h/2}\left(\Phi_{1,33}^2, \Phi_{1,33}\Phi_{2,33}, \Phi_{1,33}\Phi_2, \Phi_{2,33}^2, \Phi_{2,33}\Phi_2, \Phi_2^2\right)\alpha_{\chi}\mathbf{I}_{6\times6}dx_3 \tag{24f}$$

The variation of work done by membrane compressive loads derived from Eq. (6) is given by:

$$\delta\Pi_V = -\int_A N^0\left(u_{3,1}^0\delta u_{3,1}^0 + u_{3,2}^0\delta u_{3,2}^0\right)dA \tag{25}$$

where it is supposed that $N_1^0 = N_2^0 = N^0, N_{12}^0 = 0$. The variation of kinetic energy $\delta\prod_K$ derived from Eq. (9) is calculated by:

$$\begin{aligned}\delta\Pi_K &= \frac{1}{2}\int_V \rho\left(\dot{u}_1\delta\dot{u}_1 + \dot{u}_2\delta\dot{u}_2 + \dot{u}_3\delta\dot{u}_3\right)dV\\ &= \frac{1}{2}\int_A\Big[I_0\left(\dot{u}_1^0\delta\dot{u}_1^0 + \dot{u}_2^0\delta\dot{u}_2^0 + \dot{u}_3^0\delta\dot{u}_3^0\right)\\ &+I_1\left(\dot{u}_1^0\delta\dot{u}_{3,1}^0 + \dot{u}_{3,1}^0\delta\dot{u}_1^0 + \dot{u}_2^0\delta\dot{u}_{3,2}^0 + \dot{u}_{3,2}^0\delta\dot{u}_2^0\right)\\ &+J_2\left(\dot{u}_{3,1}^0\delta\dot{\varphi}_1 + \dot{\varphi}_1\delta\dot{u}_{3,1}^0 + \dot{u}_{3,2}^0\delta\dot{\varphi}_2 + \dot{\varphi}_2\delta\dot{u}_{3,2}^0\right) + K_2\left(\dot{\varphi}_1\delta\dot{\varphi}_1 + \dot{\varphi}_2\delta\dot{\varphi}_2\right)\\ &+J_1\left(\dot{u}_1^0\delta\dot{\varphi}_1 + \dot{\varphi}_1\delta\dot{u}_1^0 + \dot{u}_2^0\delta\dot{\varphi}_2 + \dot{\varphi}_2\delta\dot{u}_2^0\right) + I_2\left(\dot{u}_{3,1}^0\delta\dot{u}_{3,1}^0 + \dot{u}_{3,2}^0\delta\dot{u}_{3,2}^0\right)\Big]dA\end{aligned} \tag{26}$$

where $I_0, I_1, I_2, J_1, J_2, K_2$ are mass components of the FG microplates which are defined as follows:

$$\left(I_0, I_1, I_2, J_1, J_2, K_2\right) = \int_{-h/2}^{h/2}\left(1, \Phi_1, \Phi_1^2, \Phi_2, \Phi_1\Phi_2, \Phi_2^2\right)\rho dx_3 \tag{27}$$

3. Series-type solutions of the FG microplates

Based on the Ritz method, the membrane and transverse displacements, rotations $\left(u_1^0, u_2^0, u_3^0, \varphi_1, \varphi_2\right)$ of the FG microplates can be expressed in terms of the series of approximation functions and associated values of series as follows:

$$\left\{u_1^0(x_1, x_2, t), \varphi_1(x_1, x_2, t)\right\} = \sum_{i=1}^{N_1}\sum_{j=1}^{N_2}\left\{u_{1ij}(t), x_{ij}(t)\right\}R_{i,1}\left(x_1\right)P_j\left(x_2\right) \tag{28a}$$

$$\left\{u_2^0(x_1, x_2, t), \varphi_2(x_1, x_2, t)\right\} = \sum_{i=1}^{N_1}\sum_{j=1}^{N_2}\left\{u_{2ij}(t), y_{ij}(t)\right\}R_i\left(x_1\right)P_{j,2}\left(x_2\right) \tag{28b}$$

$$u_3^0(x_1, x_2, t) = \sum_{i=1}^{N_1}\sum_{j=1}^{N_2}u_{3ij}(t)R_i\left(x_1\right)P_j\left(x_2\right) \tag{28c}$$

where $u_{1ij}, u_{2ij}, u_{3ij}, x_{ij}, y_{ij}$ are variables to be determined; $R_i\left(x_1\right)$, $P_j\left(x_2\right)$ are the shape functions in x_1-, x_2- direction, respectively. As a result, five unknowns of the microplates only depend on two shape functions. It should be noted that the accuracy, convergence rates and numerical instabilities of the Ritz solution depends on the shape functions, which were discussed details in previous studies [50,60–62]. The functions $R_i\left(x_1\right)$ and $P_j\left(x_2\right)$ are chosen to satisfy the boundary conditions (BCs) in which the simply-supported and clamped ones are followed:

Table 11
Comparison study between MCS (10.000 samples) and PCE (16 samples) for the mean, standard deviation (SD), Kurtosis and Skewness for the critical buckling loads of the FG microplates with biaxial compression ($a/h = 10$, MAT 1).

BCs	p	Theory	Mean	SD	Kurtosis	Skewness	COV (%)	Time (s)	Present
$h/l = 1$									
SSSS	1	PCE	29.2312	4.9391	2.3812	0.3725	16.9	11.14	28.9879
		MCS	29.2307	4.9387	2.3813	0.3721	16.9	320.88	
	5	PCE	16.2412	1.6344	2.3614	0.3419	10.1	12.36	16.1673
		MCS	16.2435	1.6343	2.3619	0.3418	10.1	326.53	
	10	PCE	13.3790	0.9562	2.3526	0.3299	7.1	12.68	13.3372
		MCS	13.3822	0.9566	2.3527	0.3295	7.1	329.08	
CCCC	1	PCE	109.0762	18.6345	2.3820	0.3740	17.1	11.27	108.1545
		MCS	109.0770	18.6350	2.3826	0.3742	17.1	328.53	
	5	PCE	59.7307	6.1697	2.3713	0.3577	10.3	12.82	59.4389
		MCS	59.7422	6.1695	2.3715	0.3578	10.3	330.13	
	10	PCE	48.7194	3.4811	2.3708	0.3522	7.1	13.06	48.5635
		MCS	48.7209	3.4805	2.3711	03521	7.1	335.17	
$h/l = 5$									
SSSS	1	PCE	5.6826	0.8537	2.3706	0.3542	15.0	12.56	5.6427
		MCS	5.6897	0.8541	2.3711	0.3539	15.0	330.21	
	5	PCE	3.5496	0.2714	2.2761	0.1661	7.6	12.69	3.5436
		MCS	3.5574	0.2719	2.7657	0.1663	7.6	325.86	
	10	PCE	3.1560	0.2121	2.2682	0.1635	6.7	12.84	3.1513
		MCS	3.1495	0.2125	2.2675	0.1637	6.7	327.46	
CCCC	1	PCE	15.4284	2.3779	2.3724	0.3575	15.4	12.75	15.3135
		MCS	15.4356	2.3775	2.3720	0.3578	15.4	327.88	
	5	PCE	9.2723	0.7193	2.2942	0.2125	7.8	12.10	9.2498
		MCS	9.2688	0.7197	2.2948	0.2123	7.8	330.23	
	10	PCE	8.0932	0.5221	2.2796	0.1879	6.5	12.47	8.0786
		MCS	8.0844	0.5226	2.2799	0.1876	6.5	328.87	
$h/l = 10$									
SSSS	1	PCE	4.9466	0.7260	2.3685	0.3502	14.7	12.90	4.9130
		MCS	4.9508	0.7266	2.3688	0.3508	14.7	327.33	
	5	PCE	3.1530	0.2289	2.2631	0.1268	7.2	12.78	3.1491
		MCS	3.1603	0.2284	2.2637	0.1270	7.2	329.48	
	10	PCE	2.8364	0.1889	2.2586	0.1373	6.7	12.25	2.8330
		MCS	2.8294	0.1894	2.2590	0.1375	6.7	330.76	
CCCC	1	PCE	12.4847	1.8671	2.3695	0.3522	15.0	12.77	12.3969
		MCS	12.4846	1.8672	2.3694	0.3523	15.0	331.58	
	5	PCE	7.6855	0.5689	2.2750	0.1632	7.4	12.32	7.6723
		MCS	7.6890	0.5685	2.2725	0.1634	7.4	333.05	
	10	PCE	6.8149	0.4410	2.2638	0.1469	6.5	12.66	6.8047
		MCS	6.8201	0.4415	2.2634	0.1466	6.5	330.13	

- Simply supported (S): $u_2^0 = u_3^0 = \varphi_2 = 0$ at $x_1 = 0, a$ and $u_1^0 = u_3^0 = \varphi_1 = 0$ at $x_2 = 0, b$
- Clamped (C): $u_1^0 = u_2^0 = u_3^0 = \varphi_1 = \varphi_2 = 0$ at $x_1 = 0, a$ and $x_2 = 0, b$

The combination of S, C and Free (F) on the edges of the FG microplates leads to the various BCs as follows: SSSS, CSCS, CCCC, CFCF, SFSF which will be considered in the numerical examples. The hybrid shape functions $R_i(x_1)$ and $P_j(x_2)$ for different BCs used in this paper are listed in Table 1. Substituting Eq. (28) into Eqs. (21), (25) and (26) and then the subsequent results into Eq. (10) lead to the characteristic equations of motion of the FG microplates as follows:

$$\mathbf{Kd} + \mathbf{M}\ddot{\mathbf{d}} = \mathbf{0} \tag{29}$$

where $\mathbf{d} = \begin{bmatrix}\mathbf{u}_1 & \mathbf{u}_2 & \mathbf{u}_3 & \boldsymbol{\varphi}_1 & \boldsymbol{\varphi}_2\end{bmatrix}^T$ is the displacement vector to be determined; $\mathbf{K} = \mathbf{K}^{\epsilon} + \mathbf{K}^{\chi}$ is the stiffness matrix which is composed of that of the strains $\mathbf{K}^{\epsilon}$, symmetric rotation gradients $\mathbf{K}^{\chi}$; $\mathbf{M}$ is the mass matrix. These components are given more details as follows:

$$\mathbf{K}^{\zeta} = \begin{bmatrix} \mathbf{K}^{\zeta 11} & \mathbf{K}^{\zeta 12} & \mathbf{K}^{\zeta 13} & \mathbf{K}^{\zeta 14} & \mathbf{K}^{\zeta 15} \\ {}^T\mathbf{K}^{\zeta 12} & \mathbf{K}^{\zeta 22} & \mathbf{K}^{\zeta 23} & \mathbf{K}^{\zeta 24} & \mathbf{K}^{\zeta 25} \\ {}^T\mathbf{K}^{\zeta 13} & {}^T\mathbf{K}^{\zeta 23} & \mathbf{K}^{\zeta 33} & \mathbf{K}^{\zeta 34} & \mathbf{K}^{\zeta 35} \\ {}^T\mathbf{K}^{\zeta 14} & {}^T\mathbf{K}^{\zeta 24} & {}^T\mathbf{K}^{\zeta 34} & \mathbf{K}^{\zeta 44} & \mathbf{K}^{\zeta 45} \\ {}^T\mathbf{K}^{\zeta 15} & {}^T\mathbf{K}^{\zeta 25} & {}^T\mathbf{K}^{\zeta 35} & {}^T\mathbf{K}^{\zeta 45} & \mathbf{K}^{\zeta 55} \end{bmatrix} \quad \text{with } \zeta = \{\epsilon, \chi\} \tag{30}$$

where the components of stiffness matrix $\mathbf{K}^{\epsilon}$ are defined as follows:

$$K_{ijkl}^{\epsilon 11} = A_{11}^{\epsilon} T_{ik}^{22} S_{jl}^{00} + A_{66}^{\epsilon} T_{ik}^{11} S_{jl}^{11}, K_{ijkl}^{\epsilon 12} = A_{12}^{\epsilon} T_{ik}^{02} S_{jl}^{20} + A_{66}^{\epsilon} T_{ik}^{11} S_{jl}^{11}$$
$$K_{ijkl}^{\epsilon 13} = B_{11}^{\epsilon} T_{ik}^{22} S_{jl}^{00} + B_{12}^{\epsilon} T_{ik}^{02} S_{jl}^{20} + 2B_{66}^{\epsilon} T_{ik}^{11} S_{jl}^{11}$$
$$K_{ijkl}^{\epsilon 14} = B_{s11}^{\epsilon} T_{ik}^{22} S_{jl}^{00} + B_{s66}^{\epsilon} T_{ik}^{11} S_{jl}^{11}, K_{ijkl}^{\epsilon 15} = B_{s12}^{\epsilon} T_{ik}^{02} S_{jl}^{20} + B_{s66}^{\epsilon} T_{ik}^{11} S_{jl}^{11}$$
$$K_{ijkl}^{\epsilon 22} = A_{22}^{\epsilon} T_{ik}^{00} S_{jl}^{22} + A_{66}^{\epsilon} T_{ik}^{11} S_{jl}^{11}, K_{ijkl}^{\epsilon 23}$$
$$= B_{12}^{\epsilon} T_{ik}^{20} S_{jl}^{02} + B_{22}^{\epsilon} T_{ik}^{00} S_{jl}^{22} + 2B_{66}^{\epsilon} T_{ik}^{11} S_{jl}^{11}$$
$$K_{ijkl}^{\epsilon 24} = B_{s12}^{\epsilon} T_{ik}^{20} S_{jl}^{02} + B_{s66}^{\epsilon} T_{ik}^{11} S_{jl}^{11}, K_{ijkl}^{\epsilon 25} = B_{s22}^{\epsilon} T_{ik}^{00} S_{jl}^{22} + B_{s66}^{\epsilon} T_{ik}^{11} S_{jl}^{11}$$
$$K_{ijkl}^{\epsilon 33} = D_{11}^{\epsilon} T_{ik}^{22} S_{jl}^{00} + D_{12}^{\epsilon} \left(T_{ik}^{02} S_{jl}^{20} + T_{ik}^{20} S_{jl}^{02} \right) + D_{22}^{\epsilon} T_{ik}^{00} S_{jl}^{22} + 4D_{66}^{\epsilon} T_{ik}^{11} S_{jl}^{11}$$
$$+ A_{s44}^{\epsilon} T_{ik}^{00} S_{jl}^{11} + A_{s55}^{\epsilon} T_{ik}^{11} S_{jl}^{00} - N^0 \left(T_{ik}^{11} S_{jl}^{00} + T_{ik}^{00} S_{jl}^{11} \right)$$
$$K_{ijkl}^{\epsilon 34} = D_{s11}^{\epsilon} T_{ik}^{22} S_{jl}^{00} + D_{s12}^{\epsilon} T_{ik}^{20} S_{jl}^{02} + 2D_{s66}^{\epsilon} T_{ik}^{11} S_{jl}^{11} + A_{s55}^{\epsilon} T_{ik}^{11} S_{jl}^{00}$$
$$K_{ijkl}^{\epsilon 35} = D_{s12}^{\epsilon} T_{ik}^{02} S_{jl}^{20} + D_{s22}^{\epsilon} T_{ik}^{00} S_{jl}^{22} + 2D_{s66}^{\epsilon} T_{ik}^{11} S_{jl}^{11} + A_{s44}^{\epsilon} T_{ik}^{00} S_{jl}^{11}$$
$$K_{ijkl}^{\epsilon 44} = H_{s11}^{\epsilon} T_{ik}^{22} S_{jl}^{00} + H_{s66}^{\epsilon} T_{ik}^{11} S_{jl}^{11} + A_{s55}^{\epsilon} T_{ik}^{11} S_{jl}^{00}$$
$$K_{ijkl}^{\epsilon 45} = H_{s12}^{\epsilon} T_{ik}^{02} S_{jl}^{20} + H_{s66}^{\epsilon} T_{ik}^{11} S_{jl}^{11}, K_{ijkl}^{\epsilon 55} = H_{s22}^{\epsilon} T_{ik}^{00} S_{jl}^{22}$$
$$+ H_{s66}^{\epsilon} T_{ik}^{11} S_{jl}^{11} + A_{s44}^{\epsilon} T_{ik}^{00} S_{jl}^{11} \tag{31}$$

where

$$T_{ik}^{rs} = \int_0^a \frac{\partial^r R_i}{\partial x_1^r} \frac{\partial^s R_k}{\partial x_1^s} dx_1, S_{jl}^{rs} = \int_0^a \frac{\partial^r P_j}{\partial x_2^r} \frac{\partial^s P_l}{\partial x_2^s} dx_2 \tag{32}$$

The components of stiffness matrix $\mathbf{K}^{\chi}$ are defined as follows:

$$K_{ijkl}^{\chi 11} = \frac{A^{\chi}}{4} \left(T_{ik}^{22} S_{jl}^{11} + T_{ik}^{11} S_{jl}^{22} \right),$$
$$K_{ijkl}^{\chi 12} = -\frac{A^{\chi}}{4} \left(T_{ik}^{22} S_{jl}^{11} + T_{ik}^{11} S_{jl}^{22} \right)$$
$$K_{ijkl}^{\chi 13} = \frac{\overline{\overline{B}}^{\chi}}{4} \left(T_{ik}^{02} S_{jl}^{11} - T_{ik}^{11} S_{jl}^{02} \right),$$

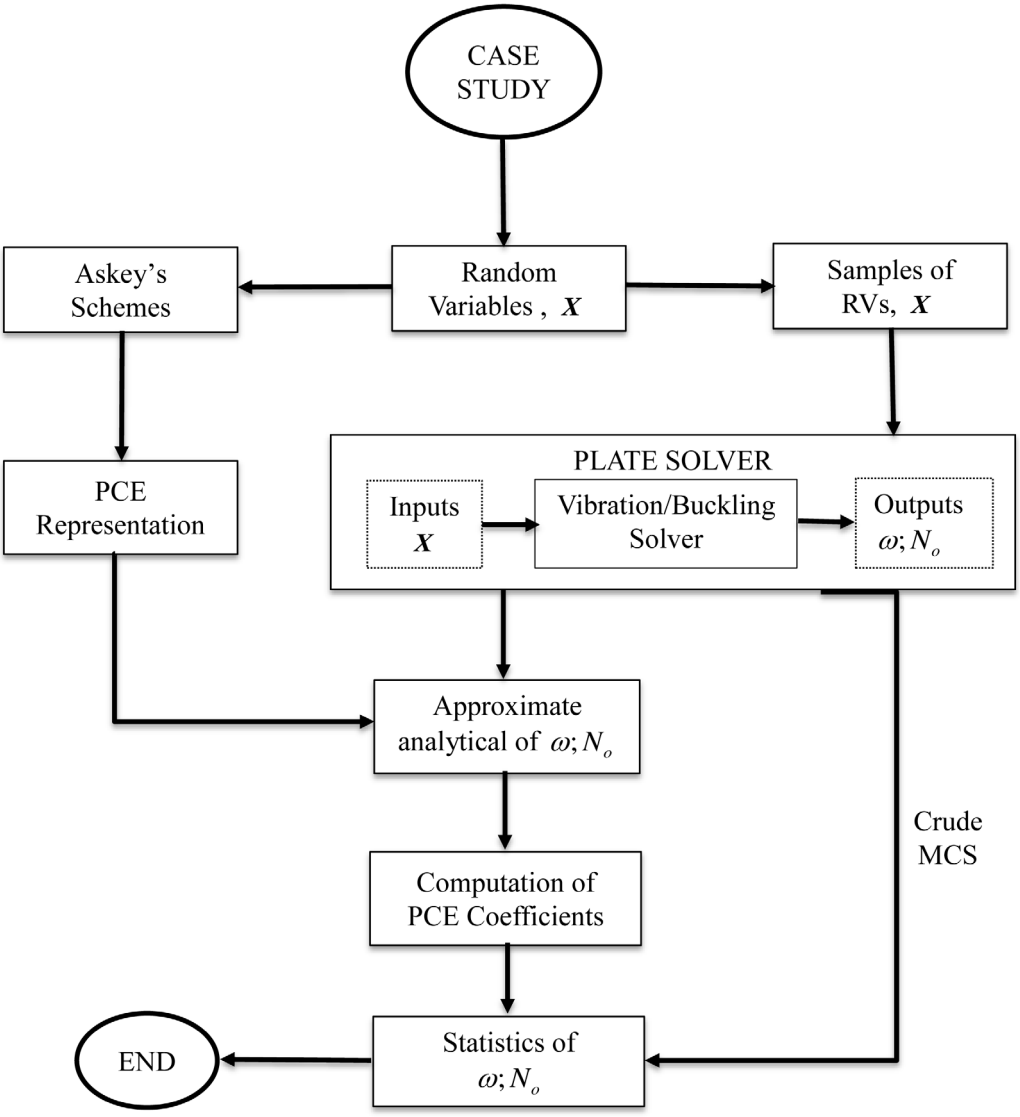

Fig. 2. Flowchart of stochastic free vibration and buckling analysis of the FG microplates using PCE and MCS.

$$K_{ijkl}^{\chi 14} = \frac{1}{4}\left(B_s^{\chi} T_{ik}^{22} S_{jl}^{11} + B_s^{\chi} T_{ik}^{11} S_{jl}^{22} - \overline{\overline{B}}_s^{\chi} T_{ik}^{11} S_{jl}^{02}\right)$$

$$K_{ijkl}^{\chi 15} = \frac{1}{4}\left(\overline{\overline{B}}_s^{\chi} T_{ik}^{02} S_{jl}^{11} - B_s^{\chi} T_{ik}^{22} S_{jl}^{11} - B_s^{\chi} T_{ik}^{11} S_{jl}^{22}\right),$$

$$K_{ijkl}^{\chi 22} = \frac{A^{\chi}}{4}\left(T_{ik}^{22} S_{jl}^{11} + T_{ik}^{11} S_{jl}^{22}\right)$$

$$K_{ijkl}^{\chi 23} = \frac{\overline{\overline{B}}^{\chi}}{4}\left(T_{ik}^{11} S_{jl}^{02} - T_{ik}^{02} S_{jl}^{11}\right),$$

$$K_{ijkl}^{\chi 24} = \frac{1}{4}\left(\overline{\overline{B}}_s^{\chi} T_{ik}^{11} S_{jl}^{02} - B_s^{\chi} T_{ik}^{22} S_{jl}^{11} - B_s^{\chi} T_{ik}^{11} S_{jl}^{22}\right)$$

$$K_{ijkl}^{\chi 25} = \frac{1}{4}\left(B_s^{\chi} T_{ik}^{22} S_{jl}^{11} + B_s^{\chi} T_{ik}^{11} S_{jl}^{22} - \overline{\overline{B}}_s^{\chi} T_{ik}^{02} S_{jl}^{11}\right)$$

$$K_{ijkl}^{\chi 33} = \frac{1}{4}\left(A^{\chi} - 2\overline{B}^{\chi} + \overline{D}^{\chi}\right)$$
$$\times \left(T_{ik}^{00} S_{jl}^{22} - T_{ik}^{20} S_{jl}^{02} - T_{ik}^{02} S_{jl}^{20} + T_{ik}^{22} S_{jl}^{00} + 2T_{ik}^{11} S_{jl}^{11}\right)$$
$$+ \frac{1}{4}\overline{\overline{D}}^{\chi}\left(T_{ik}^{00} S_{jl}^{11} + T_{ik}^{11} S_{jl}^{00}\right)$$

$$K_{ijkl}^{\chi 34} = \frac{1}{4}\left[\left(\overline{B}_s^{\chi} - \overline{D}_s^{\chi}\right)\left(T_{ik}^{20} S_{jl}^{02} - T_{ik}^{22} S_{jl}^{00} - T_{ik}^{11} S_{jl}^{11}\right)\right.$$
$$\left. + \overline{K}_s^{\chi}\left(T_{ik}^{20} S_{jl}^{11} - T_{ik}^{11} S_{jl}^{20}\right) + \overline{\overline{D}}_s^{\chi} T_{ik}^{11} S_{jl}^{00}\right]$$

$$K_{ijkl}^{\chi 35} = \frac{1}{4}\left[\left(\overline{B}_s^{\chi} - \overline{D}_s^{\chi}\right)\left(-T_{ik}^{00} S_{jl}^{22} + T_{ik}^{02} S_{jl}^{20} - T_{ik}^{11} S_{jl}^{11}\right)\right.$$
$$\left. + \overline{\overline{D}}_s^{\chi} T_{ik}^{00} S_{jl}^{11} + \overline{K}_s^{\chi}\left(T_{ik}^{11} S_{jl}^{20} - T_{ik}^{20} S_{jl}^{11}\right)\right]$$

$$K_{ijkl}^{\chi 44} = \frac{1}{4}\left[\overline{H}_s^{\chi}\left(T_{ik}^{22} S_{jl}^{00} + 2T_{ik}^{11} S_{jl}^{11}\right)\right.$$
$$\left. \overline{\overline{H}}_s^{\chi} T_{ik}^{11} S_{jl}^{00} - \overline{L}^{\chi}\left(T_{ik}^{11} S_{jl}^{20} + T_{ik}^{11} S_{jl}^{02}\right) + H_s^{\chi}\left(T_{ik}^{22} S_{jl}^{11} + T_{ik}^{11} S_{jl}^{22}\right)\right]$$

$$K_{ijkl}^{\chi 45} = \frac{1}{4}\left[\overline{L}^{\chi}\left(T_{ik}^{11} S_{jl}^{20} + T_{ik}^{02} S_{jl}^{11}\right)\right.$$
$$\left. - \overline{H}_s^{\chi}\left(T_{ik}^{02} S_{jl}^{20} + T_{ik}^{11} S_{jl}^{11}\right) - H_s^{\chi}\left(T_{ik}^{11} S_{jl}^{22} + T_{ik}^{22} S_{jl}^{11}\right)\right]$$

$$K_{ijkl}^{\chi 55} = \frac{1}{4}\left[\overline{H}_s^{\chi}\left(2T_{ik}^{11} S_{jl}^{11} + T_{ik}^{00} S_{jl}^{22}\right) + \overline{\overline{H}}_s^{\chi} T_{ik}^{00} S_{jl}^{11}\right.$$
$$\left. - \overline{L}^{\chi}\left(T_{ik}^{20} S_{jl}^{11} + T_{ik}^{02} S_{jl}^{11}\right) + H_s^{\chi}\left(T_{ik}^{11} S_{jl}^{22} + T_{ik}^{22} S_{jl}^{11}\right)\right] \quad (33)$$

The components of mass matrix **M** are given by:

$$M_{ijkl}^{11} = I_0 T_{ik}^{11} S_{jl}^{00}, M_{ijkl}^{13} = I_1 T_{ik}^{11} S_{jl}^{00}, M_{ijkl}^{14} = J_1 T_{ik}^{11} S_{jl}^{00}$$
$$M_{ijkl}^{22} = I_0 T_{ik}^{00} S_{jl}^{11}, M_{ijkl}^{23} = I_1 T_{ik}^{00} S_{jl}^{11}, M_{ijkl}^{25} = J_1 T_{ik}^{00} S_{jl}^{11}$$
$$M_{ijkl}^{33} = I_0 T_{ik}^{00} S_{jl}^{00} + I_2\left(T_{ik}^{11} S_{jl}^{00} + T_{ik}^{00} S_{jl}^{11}\right), M_{ijkl}^{34} = J_2 T_{ik}^{11} S_{jl}^{00},$$
$$M_{ijkl}^{35} = J_2 T_{ik}^{00} S_{jl}^{11}$$

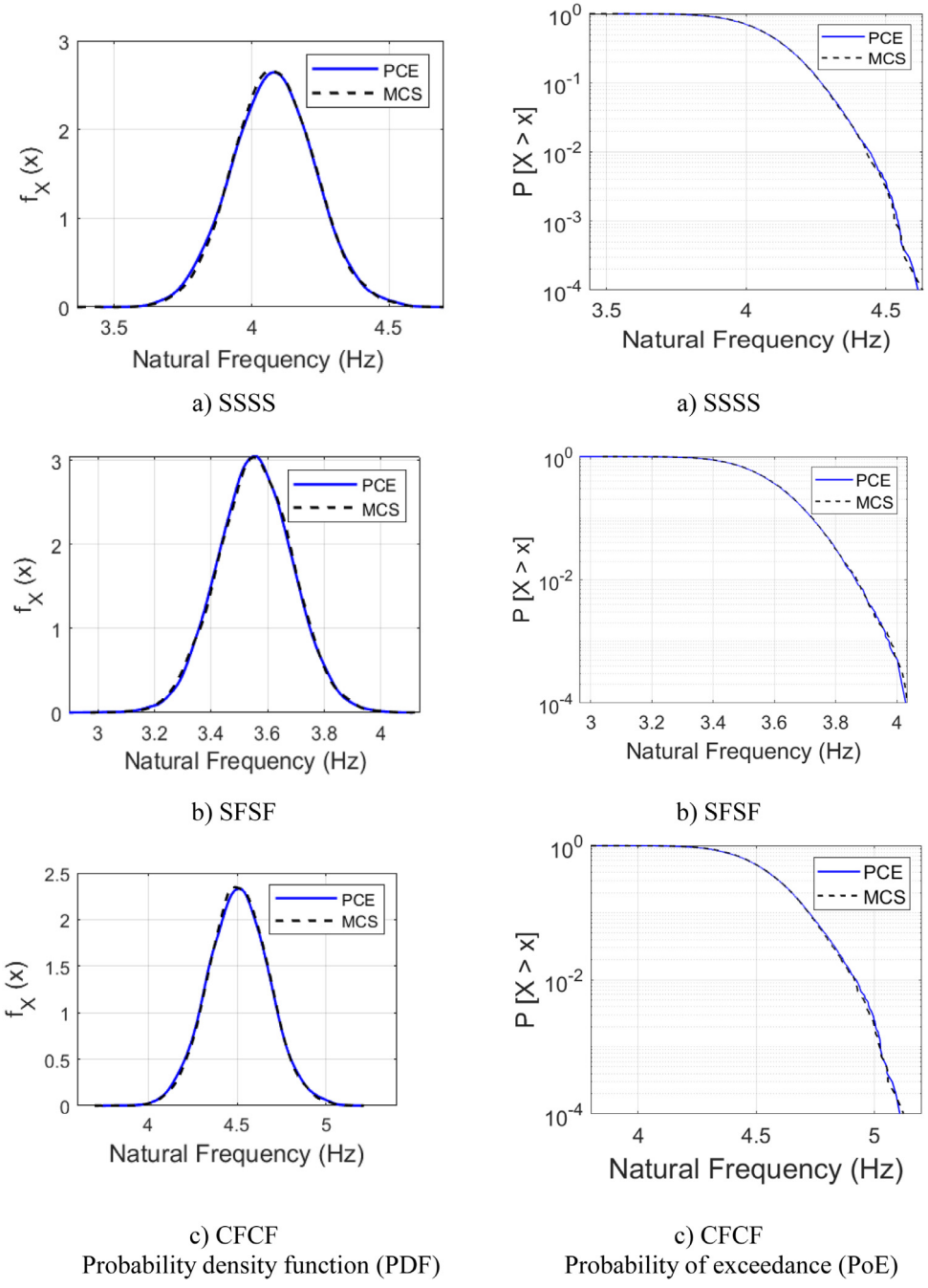

Fig. 3. PDF and PoE of MCS and PCE for the fundamental frequency (Hz) of FG plates with SSSS, SFSF and CFCF BCs ($p = 1$, $a/h = 5$).

$$M^{44}_{ijkl} = K_2 T^{11}_{ik} S^{00}_{jl}, M^{55}_{ijkl} = K_2 T^{00}_{ik} S^{11}_{jl} \tag{34}$$

The critical buckling loads of the FG microplates can be obtained from solving Eq. (29) by setting $\mathbf{M} = 0$. For free vibration analysis, the natural frequency ω of the FG microplates can be solved from the equation: $\left(\mathbf{K} - \omega^2 \mathbf{M}\right)\mathbf{d} = \mathbf{0}$ by denoting $\mathbf{d}(t) = \mathbf{d}e^{i\omega t}$ and $i^2 = -1$, which is imaginary unit.

4. Polynomial chaos expansion (PCE)

The PCE of real value random variables is investigated by starting from a univariate case and passing to a multivariate one. The first step of PCE is to approximate the responses, $\hat{u}$, which is a quantity of interest (QoI). In this paper, $\hat{u}$ is fundamental frequency or critical buckling load of the FG microplates in terms of a truncated orthogonal series as follows ([63,64]):

$$\hat{u} \approx \hat{u}_{PCE}(\mathbf{x}) = \sum_{i=0}^{P-1} c_i He_i(\mathbf{q}) + r \tag{35}$$

where $\hat{u}_{PCE}$ is the response of interest obtained from the PCE; $\mathbf{q}$ is a vector of independent random variables in PCE space mapped to physical random parameters $\mathbf{x}$; He_i are multivariate orthogonal basis functions; c_i are coefficients to be determined so that the residual r is minimized; P is the permutation of the qualified order of the polynomial n, and the number of random variable d, which is given

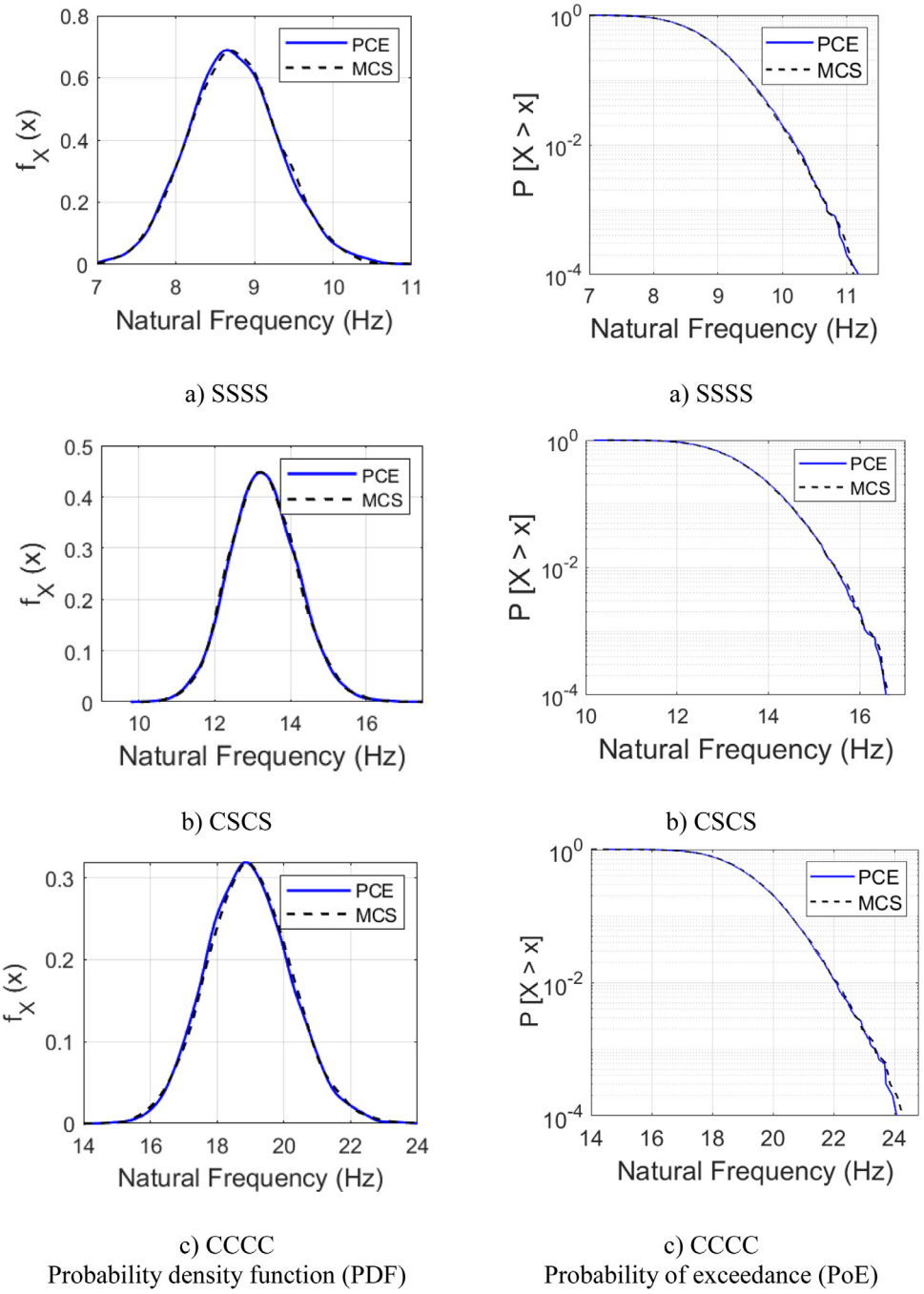

Fig. 4. PDF and PoE of MCS and PCE methods for the fundamental frequency (Hz) of FG microplates with SSSS, CSCS, CCCC BCs ($p = 5$, $h/l = 1$, $a/h = 10$).

by Askey's scheme ([63]):

$$P = \frac{(n+d)!}{n!d!} \tag{36}$$

The second step is to estimate all associated coefficients. This task can be easily obtained by forcing the residual minimum resulting in the inner product of the residual and each basis function He_i becomes zero. By taking the inner product of both sides of Eq. (35) with respect to He_j:

$$\left\langle \hat{u}, He_j \right\rangle = \sum_{i=0}^{P-1} c_i \left\langle He_i, He_j \right\rangle \tag{37}$$

then enforcing the orthogonality of He_j, Eq. (37) becomes:

$$c_i = \frac{\langle \hat{u}, He_i \rangle}{\langle He_i, He_i \rangle} = \frac{1}{\langle He_i, He_i \rangle} \int \hat{u} He_i \rho_Q(\mathbf{q})\, d\mathbf{q} \tag{38}$$

where He_i is Hermite polynomial, and the "truth" response $\hat{u}$ is unknown, thus Gauss–Hermite quadrature approach is implemented for computing c_i as follows:

$$c_i = \frac{1}{\gamma_i} \sum_{j_1=1}^{N_{gp}^1} \cdots \sum_{j_d=1}^{N_{gp}^d} \left(w_{j_1}^1 \times \cdots \times w_{j_d}^d \right) \times \hat{u}\left(q_{j_1}^1, \ldots, q_{j_d}^d \right) \times He_i\left(q_{j_1}^1, \ldots, q_{j_d}^d \right) \tag{39}$$

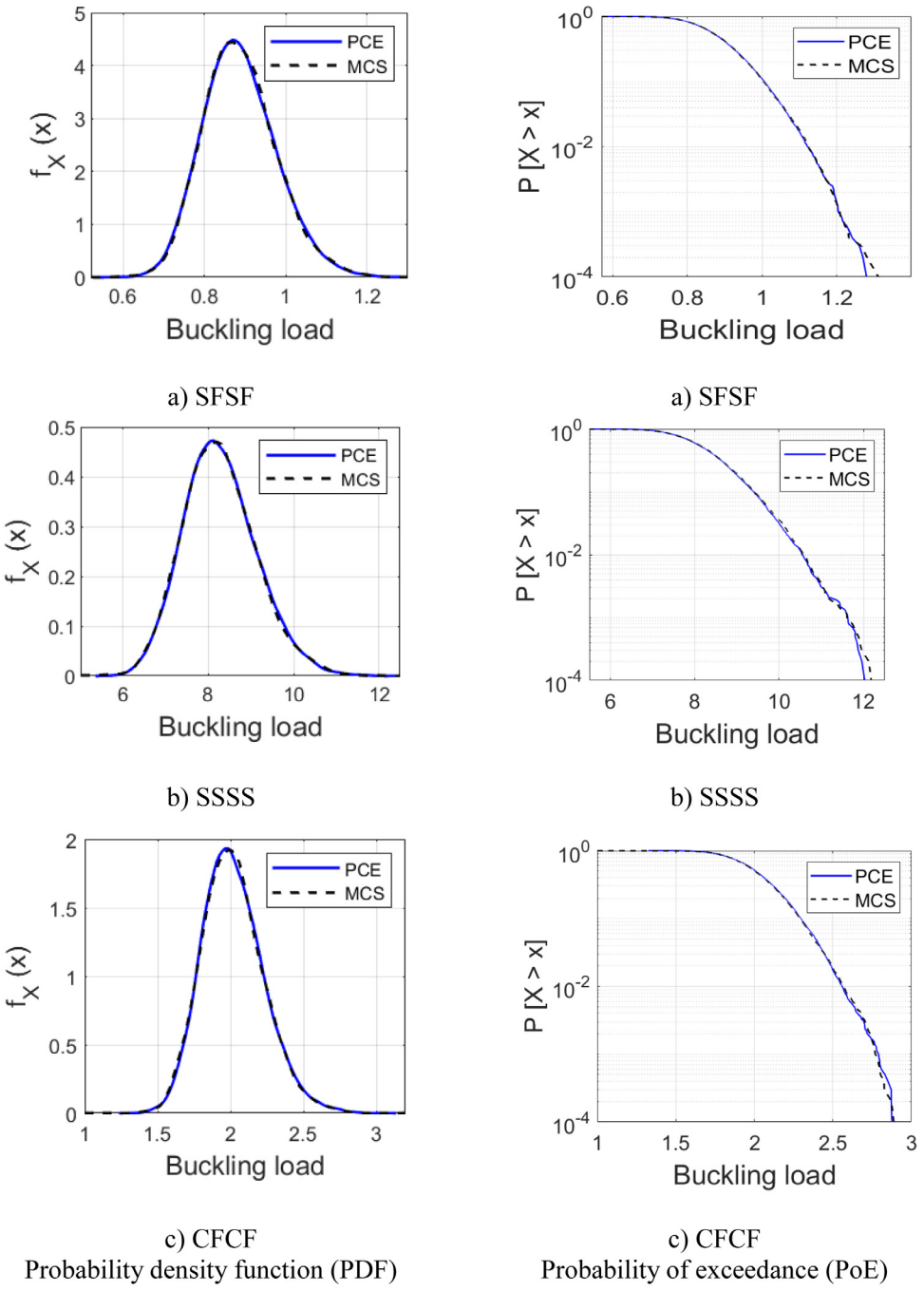

Fig. 5. PDF and PoE of MCS and PCE for the critical buckling load of FG plates with SFSF, SSSS, CFCF BCs under axial compression ($p = 1$, $a/h = 5$).

where $\gamma_i = \langle He_i, He_i \rangle$ can be analytically computed; N_{gp}^i is the number of quadrature point; q_j^i and w_j^i are the set of quadrature points and their weights, respectively for the random variable ith. For convenience, N_{gp}^i for each variable is chosen equally such that:

$$N_{gp}^1 = N_{gp}^2 = \cdots = N_{gp}^d = N_{gp} \tag{40}$$

where $N_{gp} = n + 1$ and the total number of Gauss points is at least $(n+1)^d$. Note that in Eq. (39), $\hat{u}\left(q_{j_1}^1, \ldots, q_{j_d}^d\right)$ is the "exact" response obtained from the "truth" computational model by solving Eq. (29). It means that in order to estimate all polynomial coefficients c_i, $(n+1)^d$ FG microplate models need to be run for $\hat{u}$. For the third-order PCE model of four random variables, for instance, $(3+1)^4 = 256$ "truth" samples (i.e., drawn from the FG microplate model represented in Eq. (29)), which is considered as the total computational cost of deriving PCE model, are needed.

Another advantage of PCE is that the mean and variance of the response can be analytical estimated from its coefficients as:

$$\mu_{\hat{u}} = E\left[\hat{u}_{PCE}\right] = c_0; \quad \overline{\sigma}_{\hat{u}}^2 = E\left[\left(\hat{u}_{PCE} - \mu_{\hat{u}}\right)^2\right] = \sum_{i=1}^{P-1} c_i^2 \langle He_i, He_i \rangle = \sum_{i=1}^{P-1} c_i^2 \gamma_i \tag{41}$$

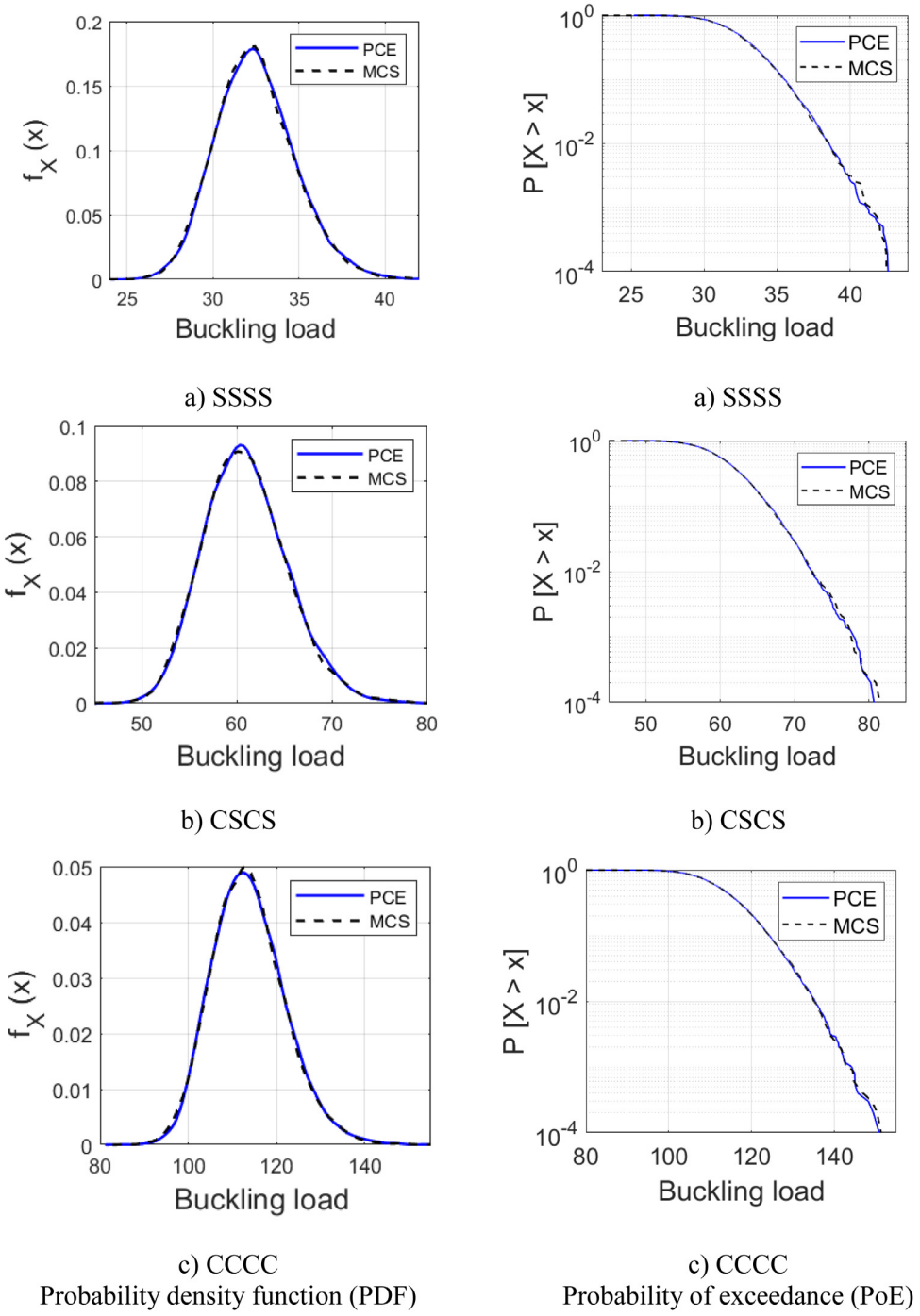

Fig. 6. PDF and PoE of MCS and PCE for the critical buckling load of FG microplates with SSSS, CSCS, CCCC BCs under axial compression ($p = 5$, $h/l = 1$, $a/h = 10$).

Moreover, Sobol' sensitivity indices can be also estimated directly from the PCE coefficients in which S_k is the first-order main effect, S_k^T is the total sensitivity index of a random variable X_k defined as follows ([65]):

$$S_k = \frac{D_k}{\sigma_{\hat{u}}^2}; S_k^T = \frac{D_k^T}{\sigma_{\hat{u}}^2} \tag{42}$$

where $D_k = \sum_{j \in \Gamma_k} c_j^2 \left\langle He_j(\mathbf{q}), He_j(\mathbf{q}) \right\rangle$ and $D_k^T = \sum_{j \in \Gamma_k^T} c_j^2 \left\langle He_j(\mathbf{q}), He_j(\mathbf{q}) \right\rangle$; Γ_k includes all j such that the multivariate function $He_j(\mathbf{q})$ only includes the variable q_k(i.e, $He_j(\mathbf{q}) = He_j(q_k)$), while Γ_k^T includes all j such that $He_j(\mathbf{q})$ must include the variable q_k(i.e, $He_j(\mathbf{q}) = He_j(q_1 \dots q_k \dots q_d)$).

Fig. 2 describes the framework for probabilistically assessing the responses of the FG microplates using both PCE and MCS.

5. Numerical examples

In this section, numerical examples are carried out to investigate stochastic buckling and free vibration behaviours of the FG microplates with different BCs in which the shear function $\Psi(x_3) = \cot^{-1}\left(\frac{h}{x_3}\right) -$

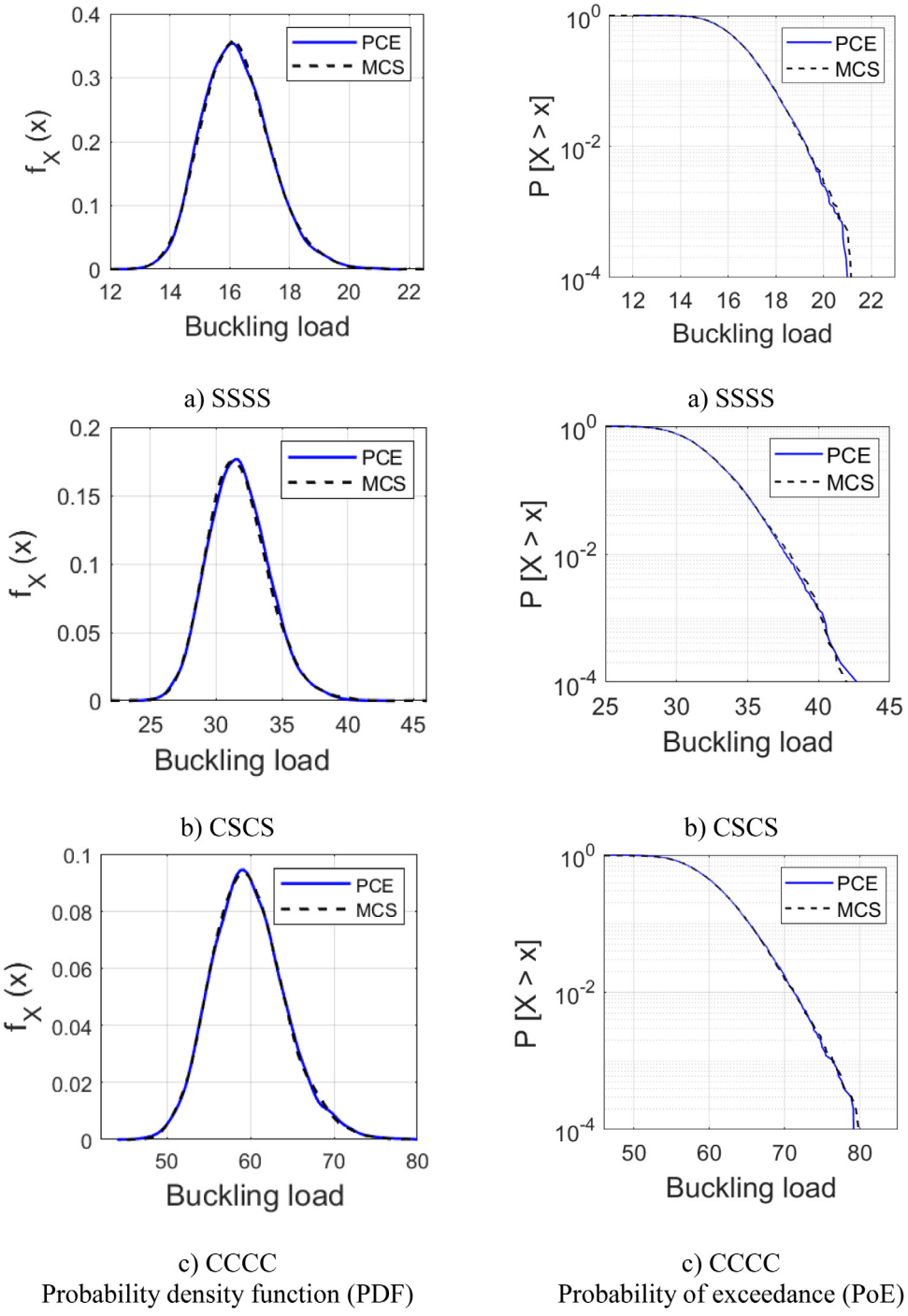

Fig. 7. PDF and PoE of MCS and PCE for the critical buckling load of FG microplates with SSSS, CSCS, CCCC BCs under biaxial compression ($p = 5$, $h/l = 1$, $a/h = 10$).

$\frac{16x_3^3}{15h^3}$ ([62]) is selected. The FG microplates are supposed to be made of a mixture of ceramic and metal whose mean material properties are given as follows:

- MAT 1: Al_2O_3 (E_c = 380 GPa, ρ_c = 3800 kg/m^3, ν_c = 0.3), Al (E_m = 70 GPa, ρ_m = 2702 kg/m^3, ν_m = 0.3).
- MAT 2: Al_2O_3 (E_c = 14.4 GPa, ν_c = 0.38), Al (E_m = 1.44 GPa, ν_m = 0.38).

In order to investigate of the stochastic responses of the FG microplates, the material properties (E_c, E_m, ρ_c, ρ_m) are assumed to be randomly distributed via the lognormal distributions, and the coefficient of variation (COV) for all random variables is set to equal 10%. The MCS with 10,000 samples is considered as the exact solutions for comparison purpose.

For convenience, the following non-dimensional parameters are used in the numerical examples:

$$\overline{\omega} = \frac{\omega a^2}{h}\sqrt{\frac{\rho_c}{E_c}} \tag{43a}$$

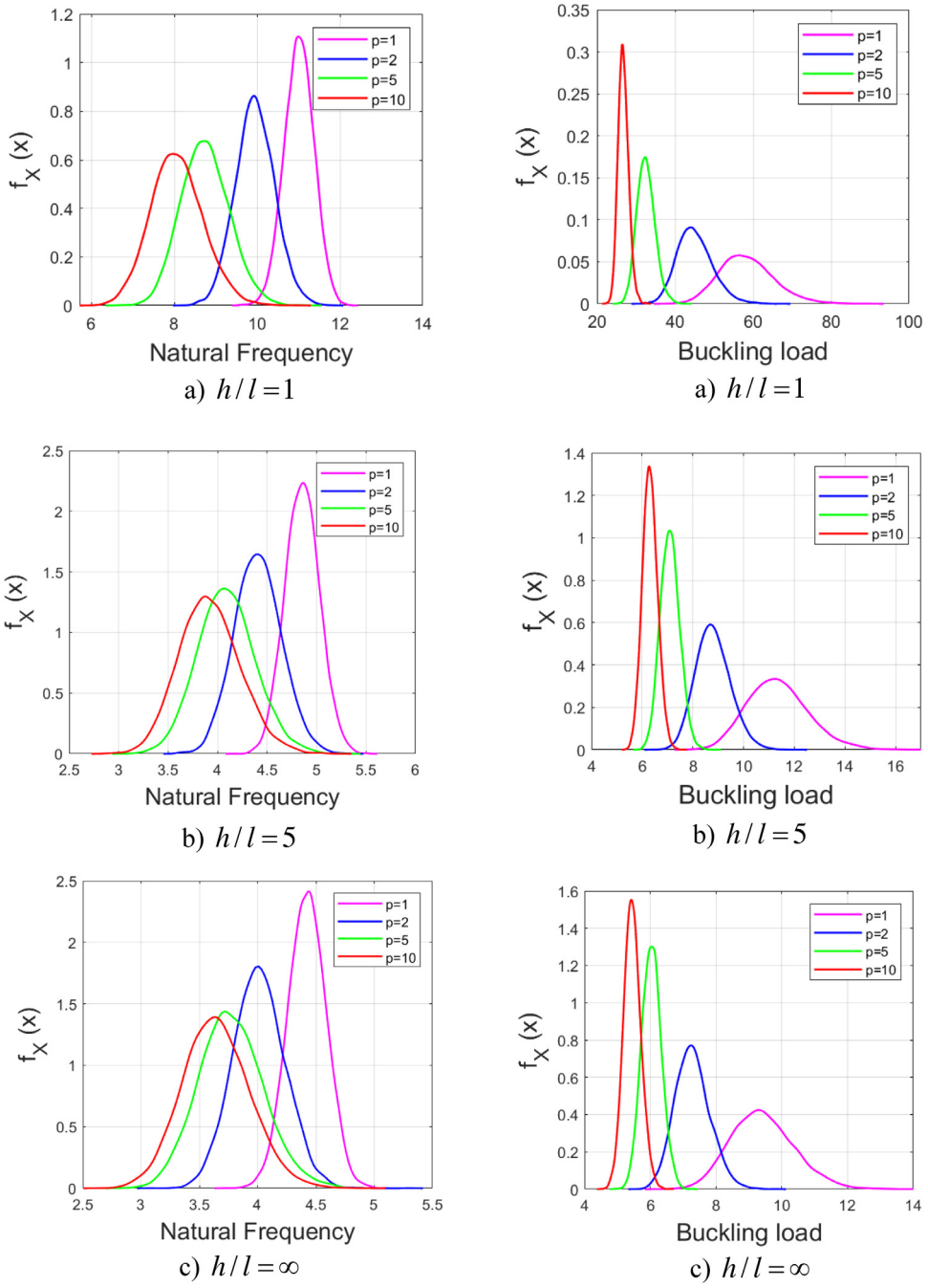

Fig. 8. Probability density function (PDF) for the natural frequency and critical buckling load of SSSS FG microplates ($a/h = 10$) with various power-law index p(PCE order-3).

$$\overline{N}_{cr} = \frac{N_{cr}a^2}{h^3 E_m} \tag{43b}$$

For the convergence study, Table 2 shows the critical buckling loads and fundamental frequencies of Al/Al_2O_3 (MAT 1) square microplates with length-to-thickness ratio ($a/h = 10$), power-law index ($p = 1$) and thickness to material length scale parameter ratio ($h/l = 1$). The results are calculated with various BCs and the same number of series in x_1- and x_2- direction ($N_1 = N_2 = N$). It can be seen from Table 2 that the results converge quickly, and the number of series $N = 8$ is sufficient for the convergence and therefore this number will be used in the following numerical examples.

5.1. Vibration analysis

In order to verify the accuracy of the present theory for vibration analysis, Table 3 displays non-dimensional deterministic fundamental frequencies of Al/Al_2O_3 (MAT 1) microplates with SSSS and CCCC BCs. Various values of p, h/l and a/h are considered. The obtained solutions are compared with those reported by refined plate theory (RPT) by He et al. [6] and Thai and Kim [56] using Navier solution and Nguyen et al. [9] based on isogeometric analysis (IGA-RPT), and by Thai et al. [13] using IGA-TSDT. It can be seen that there are good agreements among the models.

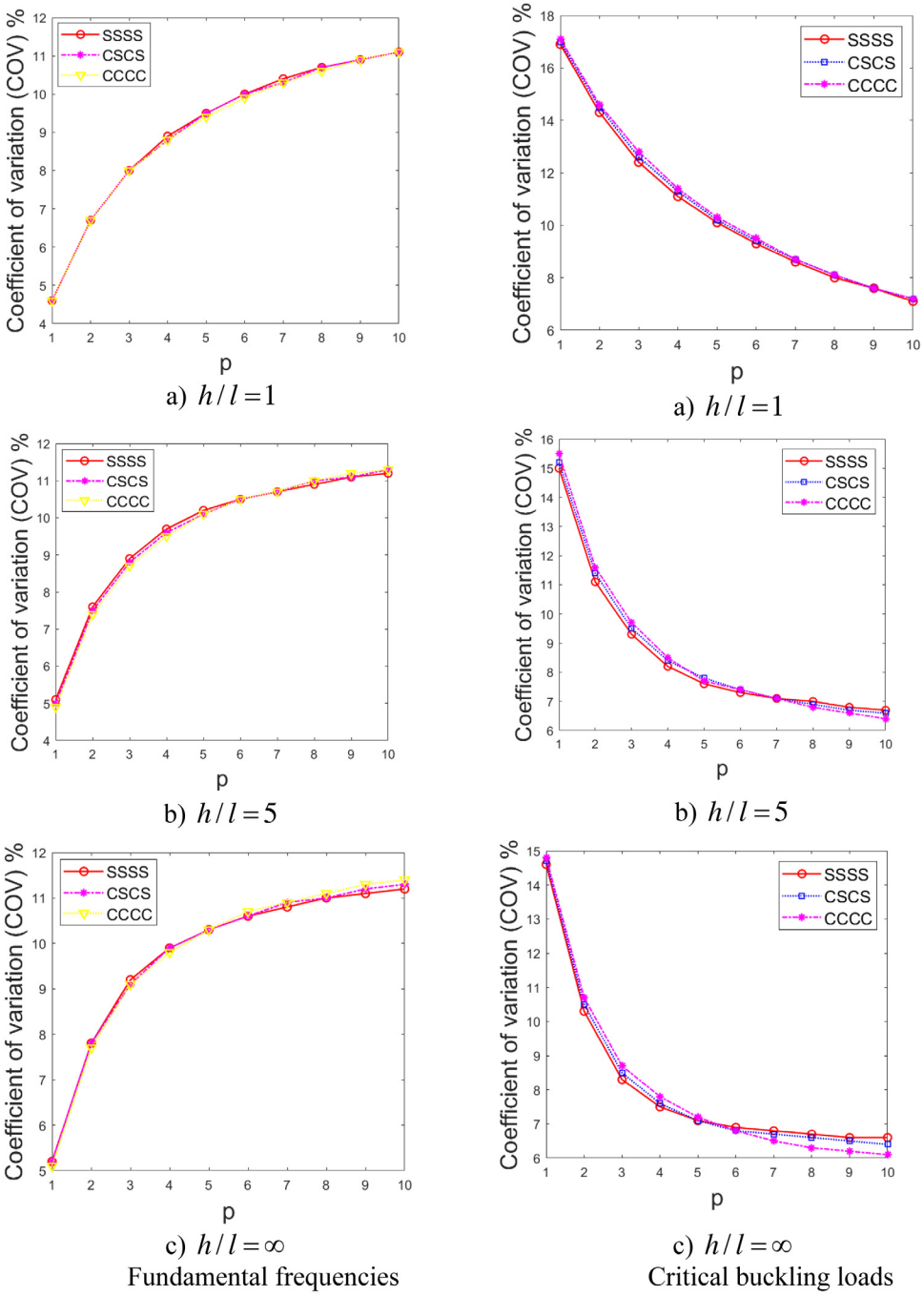

Fig. 9. Coefficient of variation (COV) with respect the power-law index p of the FG microplates ($a/h=10$) with various BCs and h/l.

Stochastic vibration analysis employs four random variables (E_m, E_c, ρ_m, ρ_c) with the mean values of MAT 1. The MCS with 10,000 samples is analysed for comparison purpose and used to investigate the performance of the proposed PCE model. It should be noted that only 256 samples (see Eq. (36) for details) are needed for third-order PCE model. The first four statistical moments of the fundamental frequency, namely the mean, standard deviation (SD), skewness and kurtosis obtained from the MCS and PCE models, for various values of p and a/h are compared in Tables 4 and 5. It can be observed that all statistical moments obtained from MCS and PCE show good agreements in all cases. The required computational time of the present approach is about 1/47 compared with direct MCS method. The mean values of fundamental frequencies for both PCE and MCS are close to the deterministic ones for all BCs and different values of p. Interestingly, although the COV of input random variables are kept the same, the COV of fundamental frequency increases with the increase of p.

5.2. Buckling analysis

Table 6 illustrates the non-dimensional deterministic critical buckling loads of Al/Al_2O_3 (MAT 1) plates with SSSS and CCCC BCs for various p and a/h. The obtained results are validated with those reported by Thai et al. [13] and Thai et al. [57]. An excellent agreement with previous ones can be observed. In order to further verify the

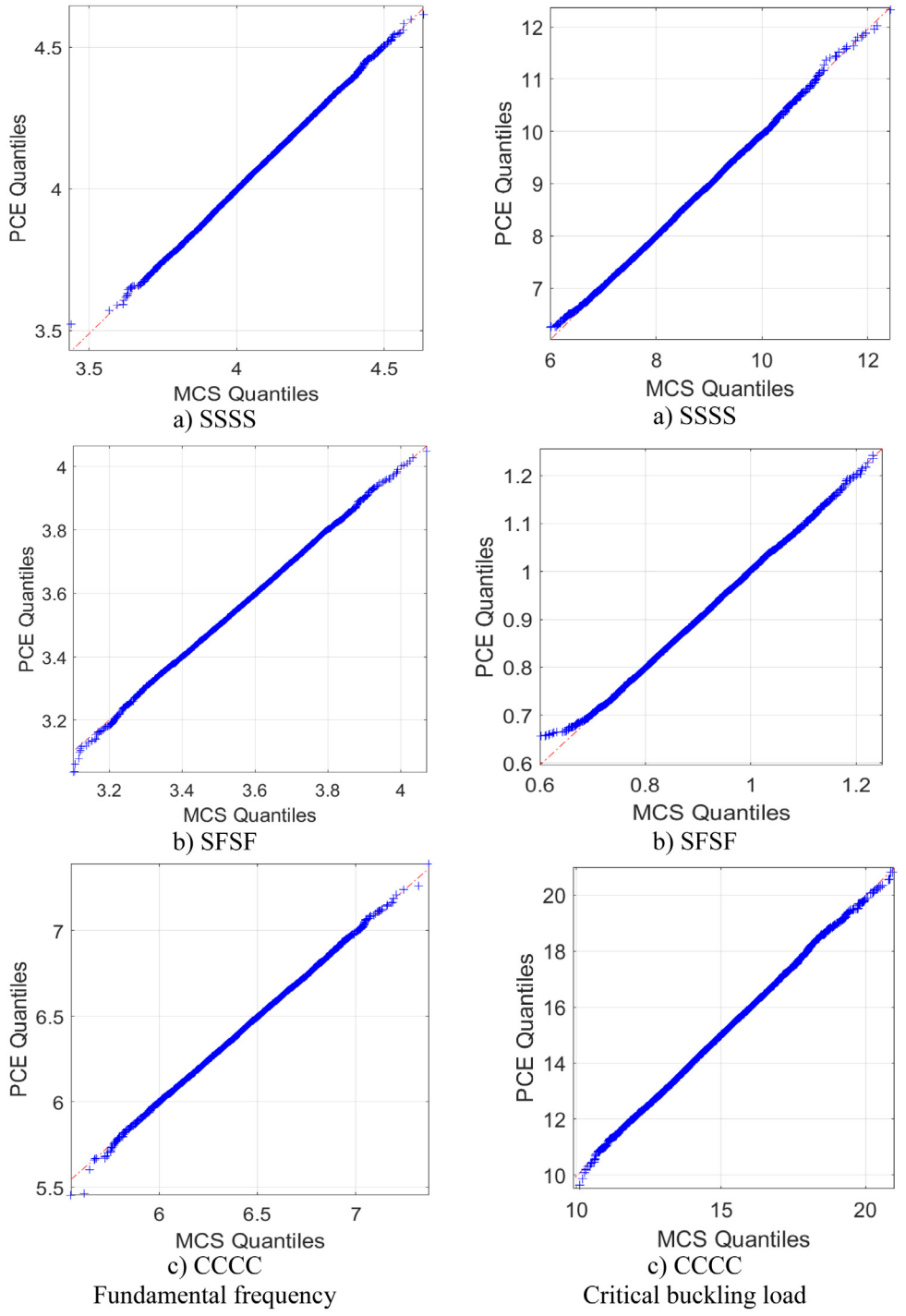

Fig. 10. Quantile–quantile plot of PCE and MCS method for the fundamental frequency and critical buckling load with axial compression of FG plates with various BCs ($p = 1$, $a/h = 5$).

proposed method, the deterministic critical buckling loads of SSSS FG microplates with MAT 2 under biaxial loads are also calculated. The results are compared with those from Thai et al. [13] (IGA-TSDT) and by Nguyen et al. [9] (IGA-RPT). It can be seen in Table 7 that the results predicted by proposed model are in good agreement with those from previous ones.

Two random variables E_m, E_c with the mean values of MAT 1 are considered for stochastic buckling analysis. It should be noted that only 16 samples required for third-order PCE model. The results of the FG plates and FG microplates with $h/l = 1$ for various BCs, p, a/h are given in Tables 8–11. The statistical moments obtained from MCS and PCE show good agreements. It is observed that the computational time in this case is about 1/28 compared with direct MCS method. Again, the mean values of critical buckling load for both PCE and MCS are close to the corresponding deterministic responses. In contrast to fundamental frequency, the COV of stochastic buckling loads decreases with the increase of p.

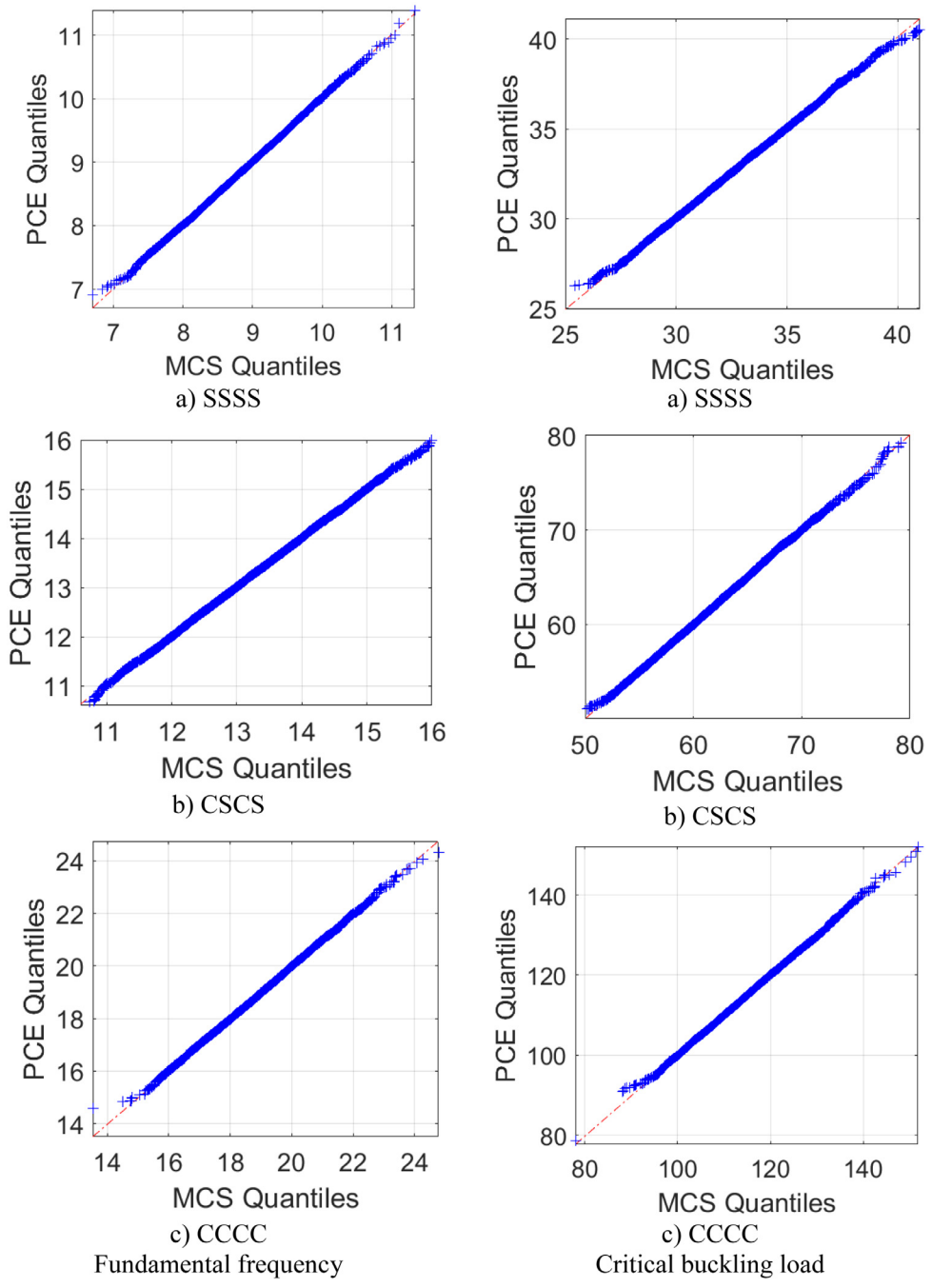

Fig. 11. Quantile–quantile plot of PCE and MCS method for the fundamental frequency and critical buckling load with axial compression of FG microplates with various BCs ($p = 5,\ h/l = 1,\ a/h = 10$).

5.3. Reliability estimation and sensitivity results

Figs. 3–7 compare the probability density function (PDF) and probability of exceedance (PoE) of MCS and PCE for the vibration and buckling analysis of the FG plates and microplates with various BCs. It can be observed again that the results of MCS are in good agreement with PCE. The effect of p on PDF for SSSS FG microplates with third-order PCE model is plotted in Fig. 8. Interestingly, the uncertainty in the buckling load appears larger (i.e., their distribution spreads wider) with the decrease of p, which are in contrast with the fundamental frequency. It is consistent with what is observed from the comparison of the COV of these stochastic responses shown in Fig. 9.

The linear quantile–quantile plots shown in Figs. 10 and 11 further confirm the matching statistical distribution of the fundamental frequencies and buckling loads computed from MCS and PCE. Thus, the PCE method gives an affordable alternative solution to predict the stochastic analysis of the FG microplates with multiple uncertain material properties. Figs. 12 and 13 compare the sensitivity indices based on the first-order and total Sobol indices for the vibration and buckling analysis using MCS and PCE. It is seen that the Sobol indices computed from the PCE are closely matched with those calculated from

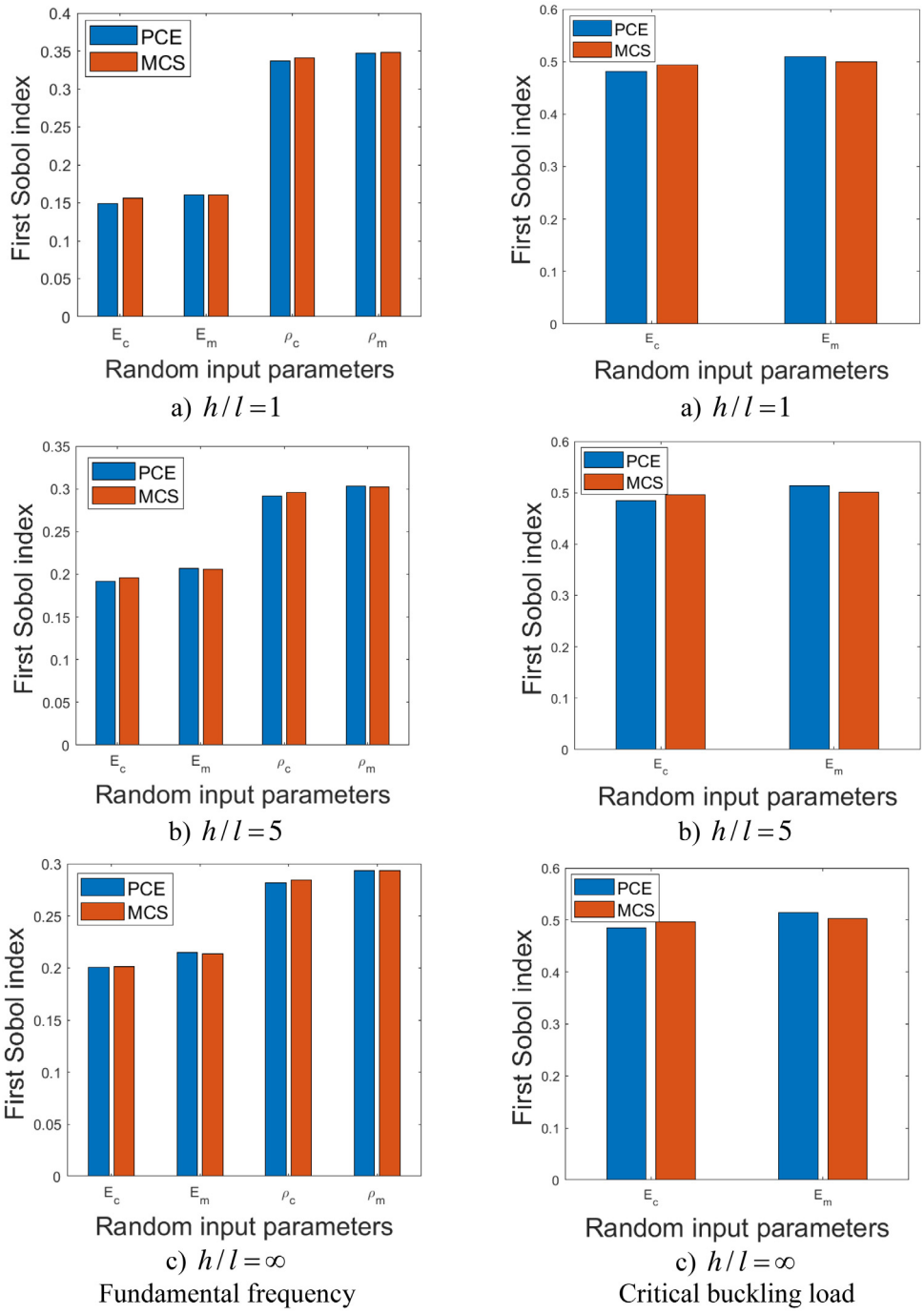

Fig. 12. First Sobol index of the random input variables with respect to the fundamental frequency and critical buckling load of SSSS FG microplates ($p = 5$, $a/h = 10$).

MCS. It is observed that the sensitivity indices of mass densities (ρ_c, ρ_m) are higher than those of Young's modulus (E_c, E_m) for all cases.

6. Conclusions

A unified higher-order shear deformation plate theory for stochastic vibration and buckling analysis of the FG microplates has been proposed in this paper. It is developed from fundamental equations of the elasticity theory. The solution field is approximated by bi-directional series in which hybrid shape functions are proposed, then the stiffness and mass matrix are explicitly derived. By applying the polynomial chaos expansion, only 256 and 16 samples are needed to compute stochastic fundamental frequency and critical buckling load, which is much less than the sample size of 10,000 of the Monte Carlo Simulation. Numerical examples are investigated for different configurations of material distribution, side-to-thickness ratio, and boundary conditions on the natural frequencies and critical buckling loads of the FG microplates. The proposed unified size dependent plate model presents the accuracy and efficiency in predicting stochastic vibration and buckling behaviours of the FG microplates.

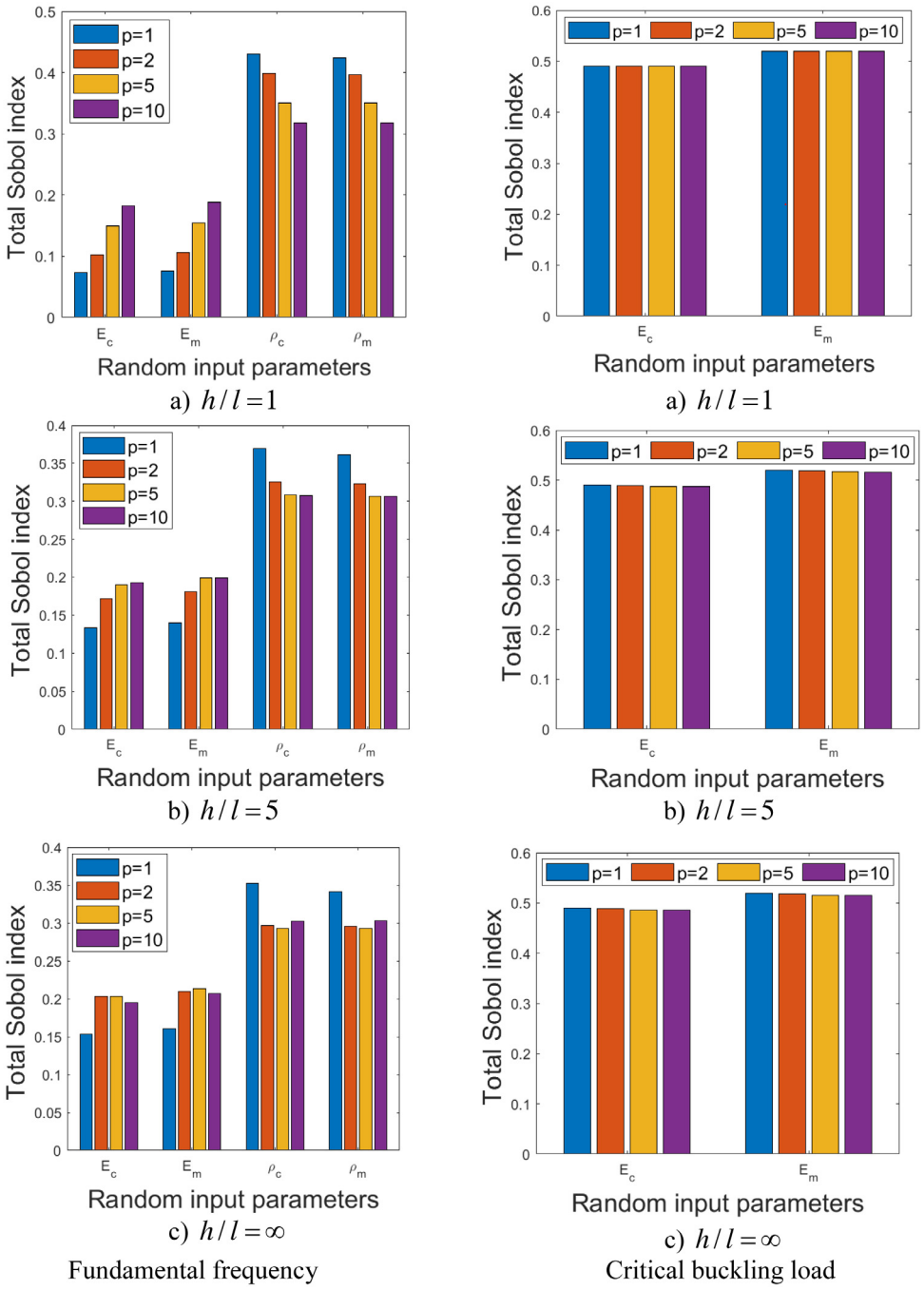

Fig. 13. Total Sobol index of the random input variables with respect to the fundamental frequency and critical buckling load of the CCCC FG microplates ($a/h = 10$).

CRediT authorship contribution statement

Van-Thien Tran: Software, Validation, Writing – review & editing, Data curation. **Trung-Kien Nguyen:** Writing – review & editing, Writing – original draft, Validation, Supervision, Methodology, Conceptualization. **Phong T.T. Nguyen:** Writing – review & editing. **Thuc P. Vo:** Writing – review & editing.

Declaration of competing interest

The authors declare that they have no known competing financial interests or personal relationships that could have appeared to influence the work reported in this paper.

References

[1] N. Jalili, K. Laxminarayana, A review of atomic force microscopy imaging systems: application to molecular metrology and biological sciences, Mechatronics 14 (8) (2004) 907–945.

[2] D. Ozevin, 10 - MIcro-electro-mechanical-systems (MEMS) for assessing and monitoring civil infrastructures, in: M.L. Wang, J.P. Lynch, H. Sohn (Eds.), Sensor Technologies for Civil Infrastructures, Woodhead Publishing, 2014, pp. 265–302e.

[3] B. Bahreyni, C. Shafai, Application of twin-beam structures for estimation of material properties and sensor fabrication, Can. J. Electr. Comput. Eng. 31 (2006) 85–88.

[4] B. Ilic, H.G. Craighead, S. Krylov, W. Senarante, C. Ober, O. Neuzil, Attogram detection using nanoelectromechanical oscillators, J. Appl. Phys. 95 (2004).

[5] I. Bargatin, I. Kozinsky, M. Roukes, Efficient electrothermal actuation of multiple modes of high-frequency nanoelectromechanical resonators, Appl. Phys. Lett. 9 (2007).

[6] L. He, J. Lou, E. Zhang, Y. Wang, Y. Bai, A size-dependent four variable refined plate model for functionally graded microplates based on modified couple stress theory, Compos. Struct. 130 (2015) 107–115.

[7] J. Fang, H. Wang, X. Zhang, On size-dependent dynamic behavior of rotating functionally graded Kirchhoff microplates, Int. J. Mech. Sci. 152 (2019) 34–50.

[8] A. Farzam, B. Hassani, Isogeometric analysis of in-plane functionally graded porous microplates using modified couple stress theory, Aerosp. Sci. Technol. 91 (2019) 508–524.

[9] H.X. Nguyen, T.N. Nguyen, M. Abdel-Wahab, S.P.A. Bordas, H. Nguyen-Xuan, T.P. Vo, A refined quasi-3D isogeometric analysis for functionally graded microplates based on the modified couple stress theory, Comput. Methods Appl. Mech. Engrg. 313 (2017) 904–940.

[10] J. Lou, L. He, J. Du, A unified higher order plate theory for functionally graded microplates based on the modified couple stress theory, Compos. Struct. 133 (2015) 1036–1047.

[11] L.C. Trinh, T.P. Vo, H.-T. Thai, J.L. Mantari, Size-dependent behaviour of functionally graded sandwich microplates under mechanical and thermal loads, Composites B 124 (2017) 218–241.

[12] C.H. Thai, A.J.M. Ferreira, P. Phung-Van, Free vibration analysis of functionally graded anisotropic microplates using modified strain gradient theory, Eng. Anal. Bound. Elem. 117 (2020) 284–298.

[13] S. Thai, H.-T. Thai, T.P. Vo, V.I. Patel, Size-dependant behaviour of functionally graded microplates based on the modified strain gradient elasticity theory and isogeometric analysis, Comput. Struct. 190 (2017) 219–241.

[14] S. Sahmani, R. Ansari, On the free vibration response of functionally graded higher-order shear deformable microplates based on the strain gradient elasticity theory, Compos. Struct. 95 (2013) 430–442.

[15] A. Karamanli, T.P. Vo, Size-dependent behaviour of functionally graded sandwich microbeams based on the modified strain gradient theory, Compos. Struct. 246 (2020) 112401.

[16] H. Salehipour, A. Shahsavar, A three dimensional elasticity model for free vibration analysis of functionally graded micro/nano plates: Modified strain gradient theory, Compos. Struct. 206 (2018) 415–424.

[17] F. Yang, A.C.M. Chong, D.C.C. Lam, P. Tong, Couple stress based strain gradient theory for elasticity, Int. J. Solids Struct. 39 (10) (2002) 2731–2743.

[18] D.C.C. Lam, F. Yang, A.C.M. Chong, J. Wang, P. Tong, Experiments and theory in strain gradient elasticity, J. Mech. Phys. Solids 51 (8) (2003) 1477–1508.

[19] R.D. Mindlin, Second gradient of strain and surface-tension in linear elasticity, Int. J. Solids Struct. 1 (4) (1965) 417–438.

[20] R.D. Mindlin, N.N. Eshel, On first strain-gradient theories in linear elasticity, Int. J. Solids Struct. 4 (1) (1968) 109–124.

[21] A.C. Eringen, Nonlocal polar elastic continua, Internat. J. Engrg. Sci. 10 (1) (1972) 1–16.

[22] A. Daneshmehr, A. Rajabpoor, A. Hadi, Size dependent free vibration analysis of nanoplates made of functionally graded materials based on nonlocal elasticity theory with high order theories, Internat. J. Engrg. Sci. 95 (2015) 23–35.

[23] A.R. Ashoori, E. Salari, S.A. Sadough Vanini, Size-dependent thermal stability analysis of embedded functionally graded annular nanoplates based on the nonlocal elasticity theory, Int. J. Mech. Sci. 119 (2016) 396–411.

[24] Q.-H. Pham, P.-C. Nguyen, T. Thanh Tran, Dynamic response of porous functionally graded sandwich nanoplates using nonlocal higher-order isogeometric analysis, Compos. Struct. 290 (2022) 115565.

[25] O. Rahmani, S.A.H. Hosseini, M. Parhizkari, Buckling of double functionally-graded nanobeam system under axial load based on nonlocal theory: an analytical approach, Microsyst. Technol. 23 (7) (2017) 2739–2751.

[26] S.A.H. Hosseini, O. Rahmani, Exact solution for axial and transverse dynamic response of functionally graded nanobeam under moving constant load based on nonlocal elasticity theory, Meccanica 52 (6) (2017) 1441–1457.

[27] S.A.H. Hosseini, O. Rahmani, Thermomechanical vibration of curved functionally graded nanobeam based on nonlocal elasticity, J. Therm. Stresses 39 (10) (2016) 1252–1267.

[28] Z. Lv, Z. Qiu, A direct probabilistic approach to solve state equations for nonlinear systems under random excitation, Acta Mech. Sinica 32 (5) (2016) 941–958.

[29] L. Nazarenko, H. Stolarski, H. Altenbach, Thermo-elastic properties of random particulate nano-materials for various models of interphase, Int. J. Mech. Sci. 126 (2017) 130–141.

[30] F. Scarpa, S. Adhikari, Uncertainty modeling of carbon nanotube terahertz oscillators, J. Non-Cryst. Solids (2008) 4151–4156, http://dx.doi.org/10.1016/j.jnoncrysol.2008.06.065.

[31] C. Jiang, G. Lu, X. Han, L. Liu, A new reliability analysis method for uncertain structures with random and interval variables, Int. J. Mech. Mater. Des. 8 (2012).

[32] J. Liu, X. Sun, X. Meng, K. Li, G. Zeng, X. Wang, A novel shape function approach of dynamic load identification for the structures with interval uncertainty, Int. J. Mech. Mater. Des. (2015).

[33] H.-T. Thai, T.P. Vo, T.-K. Nguyen, S.-E. Kim, A review of continuum mechanics models for size-dependent analysis of beams and plates, Compos. Struct. 177 (2017) 196–219.

[34] C.J. Mode, R.J. Gallop, A review on Monte Carlo simulation methods as they apply to mutation and selection as formulated in Wright–Fisher models of evolutionary genetics, Math. Biosci. 211 (2) (2008) 205–225.

[35] H.X. Nguyen, T. Duy Hien, J. Lee, H. Nguyen-Xuan, Stochastic buckling behaviour of laminated composite structures with uncertain material properties, Aerosp. Sci. Technol. 66 (2017) 274–283.

[36] K.R. Jagtap, A. Lal, B.N. Singh, Stochastic nonlinear bending response of functionally graded material plate with random system properties in thermal environment, Int. J. Mech. Mater. Des. 8 (2) (2012) 149–167.

[37] M.-C. Trinh, S.-N. Nguyen, H. Jun, T. Nguyen-Thoi, Stochastic buckling quantification of laminated composite plates using cell-based smoothed finite elements, Thin-Walled Struct. 163 (2021) 107674.

[38] R.A. Borges, L.F.F. Rodovalho, T.d.P. Sales, D.A. Rade, Stochastic eigenfrequency and buckling analyses of plates subjected to random temperature distributions, Mech. Syst. Signal Process. 147 (2021) 107088.

[39] R.R. Kumar, T. Mukhopadhyay, K.M. Pandey, S. Dey, Stochastic buckling analysis of sandwich plates: The importance of higher order modes, Int. J. Mech. Sci. 152 (2019) 630–643.

[40] X. Peng, D. Li, H. Wu, Z. Liu, J. Li, S. Jiang, J. Tan, Uncertainty analysis of composite laminated plate with data-driven polynomial chaos expansion method under insufficient input data of uncertain parameters, Compos. Struct. 209 (2019) 625–633.

[41] K. Umesh, R. Ganguli, Material uncertainty effect on vibration control of smart composite plate using polynomial chaos expansion, Mech. Adv. Mater. Struct. 20 (7) (2013) 580–591.

[42] S. Chakraborty, B. Mandal, R. Chowdhury, A. Chakrabarti, Stochastic free vibration analysis of laminated composite plates using polynomial correlated function expansion, Compos. Struct. 135 (2016) 236–249.

[43] P. Sasikumar, A. Venketeswaran, R. Suresh, S. Gupta, A data driven polynomial chaos based approach for stochastic analysis of CFRP laminated composite plates, Compos. Struct. 125 (2015) 212–227.

[44] A. Shaker, W. Abdelrahman, M. Tawfik, E.A. Sadek, Stochastic finite element analysis of the free vibration of laminated composite plates, Comput. Mech. 41 (2008) 493–501.

[45] J. Li, X. Tian, Z. Han, Y. Narita, Stochastic thermal buckling analysis of laminated plates using perturbation technique, Compos. Struct. 139 (2016) 1–12.

[46] K. Li, D. Wu, W. Gao, Spectral stochastic isogeometric analysis for static response of FGM plate with material uncertainty, Thin-Walled Struct. 132 (2018) 504–521.

[47] E. García-Macías, R. Castro-Triguero, M. Friswell, S. Adhikari, A. Sáez, Metamodel-based approach for stochastic free vibration analysis of functionally graded carbon nanotube reinforced plates, Compos. Struct. 152 (2016).

[48] E. Reissner, On transverse bending of plates, including the effect of transverse shear deformation, Int. J. Solids Struct. 11 (5) (1975) 569–573.

[49] J.N. Reddy, A simple higher-order theory for laminated composite plates, J. Appl. Mech. 51 (4) (1984) 745–752.

[50] T.-K. Nguyen, T.P. Vo, B.-D. Nguyen, J. Lee, An analytical solution for buckling and vibration analysis of functionally graded sandwich beams using a quasi-3D shear deformation theory, Compos. Struct. 156 (2016) 238–252.

[51] M. Touratier, An efficient standard plate theory, Internat. J. Engrg. Sci. 29 (8) (1991) 901–916.

[52] V.-H. Nguyen, T.-K. Nguyen, H.-T. Thai, T.P. Vo, A new inverse trigonometric shear deformation theory for isotropic and functionally graded sandwich plates, Composites B 66 (2014) 233–246.

[53] M. Aydogdu, A new shear deformation theory for laminated composite plates, Compos. Struct. 89 (1) (2009) 94–101.

[54] J.L. Mantari, A.S. Oktem, C. Guedes Soares, A new higher order shear deformation theory for sandwich and composite laminated plates, Composites B 43 (3) (2012) 1489–1499.

[55] G. Shi, K.Y. Lam, T.E. Tay, On efficient finite element modeling of composite beams and plates using higher-order theories and an accurate composite beam element, Compos. Struct. 41 (2) (1998) 159–165.

[56] H.-T. Thai, S.-E. Kim, A size-dependent functionally graded reddy plate model based on a modified couple stress theory, Composites B 45 (1) (2013) 1636–1645.

[57] C.H. Thai, A.J.M. Ferreira, H. Nguyen-Xuan, Isogeometric analysis of size-dependent isotropic and sandwich functionally graded microplates based on modified strain gradient elasticity theory, Compos. Struct. 192 (2018) 274–288.

[58] R.D. Mindlin, Influence of couple-stresses on stress concentrations, Exp. Mech. 3 (1) (1963) 1–7.

[59] R.P. Shimpi, Zeroth-order shear deformation theory for plates, 37 (4) (1999) 524–526.

[60] J.L. Mantari, F.G. Canales, Free vibration and buckling of laminated beams via hybrid Ritz solution for various penalized boundary conditions, Compos. Struct. 152 (2016) 306–315.

[61] P. Moreno-García, J.V. Dos Santos, H. Lopes, A review and study on ritz method admissible functions with emphasis on buckling and free vibration of isotropic and anisotropic beams and plates, Arch. Comput. Methods Eng. (2017).

[62] T.-K. Nguyen, T. Truong-Phong Nguyen, T.P. Vo, H.-T. Thai, Vibration and buckling analysis of functionally graded sandwich beams by a new higher-order shear deformation theory, Composites B 76 (2015) 273–285.

[63] D. Xiu, G. Karniadakis, The Wiener–Askey polynomial chaos for stochastic differential equations, SIAM J. Sci. Comput. 24 (2002) 619–644.

[64] T. Crestaux, O. Le Maître, J.-M. Martinez, Polynomial chaos expansion for sensitivity analysis, Reliab. Eng. Syst. Saf. 94 (7) (2009) 1161–1172.

[65] B. Sudret, Global sensitivity analysis using polynomial chaos expansions, Reliab. Eng. Syst. Saf. 93 (7) (2008) 964–979.

Thin-Walled Structures 182 (2023) 110267

Contents lists available at ScienceDirect

Thin-Walled Structures

journal homepage: www.elsevier.com/locate/tws

Full length article

Vibration and buckling optimization of functionally graded porous microplates using BCMO-ANN algorithm

Van-Thien Tran [a], Trung-Kien Nguyen [b,*], H. Nguyen-Xuan [b], Magd Abdel Wahab [c]

[a] Faculty of Civil Engineering, Ho Chi Minh City University of Technology and Education, 1 Vo Van Ngan Street, Thu Duc City, Ho Chi Minh City, Viet Nam
[b] CIRTech Institute, HUTECH University, 475A Dien Bien Phu Street, Binh Thanh District, Ho Chi Minh City, Viet Nam
[c] Laboratorium Soete, Faculty of Engineering and Architecture, Ghent University, B-9052 Zwijnaarde, Belgium

ARTICLE INFO

Keywords:
Vibration
Buckling
Functionally graded porous microplates
Optimization
Balancing composite motion optimization
Artificial neural network

ABSTRACT

A BCMO-ANN algorithm for vibration and buckling optimization of functionally graded porous (FGP) microplates is proposed in this paper. The theory is based on a unified framework of higher-order shear deformation theory and modified couple stress theory. A combination of artificial neural network (ANN) and balancing composite motion optimization (BCMO) is developed to solve the optimization problems and predict stochastic vibration and buckling behaviors of functionally graded porous microplates with uncertainties of material properties. The characteristic equations are derived from Hamilton's principle and approximation of field variables under Ritz-type exponential series. Numerical results are obtained to investigate the effects of the material distribution, material length scale, porosity density and boundary conditions on natural frequencies and critical buckling loads of functionally graded porous microplates. The novel results derived from this paper can be used as future references.

1. Introduction

The recent development of functionally graded porous (FGP) microplates with continuous material variations in a required direction and significant porosity density requires advanced computational theories and models. However, it is well known that the classical elasticity theory could not accurately predict the behaviors of such structures at a small scale [1]. To overcome this problem, the material size-dependent theory has been proposed to predict static and dynamic behaviors of nano- and micro-structures using different approaches. The nonlocal elasticity theory initiated by Eringen [2] can be used to capture the size effects of nanostructures, and has been used for analyzing functionally graded nanoplates [3–7], nano shells [8] and nanobeams [9–14]. Nevertheless, the implementation of this theory for microplates with different boundary conditions appears to be quite complicated. Another way to investigate the size effects is to use the modified couple stress theory (MCT) or modified strain gradient theory (MST). These theories have been employed to predict the behaviors of isotropic and functionally graded microplates with various displacement fields [15–27]. Literature shows that the study of size effects on static and dynamic responses of FGP microplates is still limited. Kim et al. [28] presented static, free vibration and buckling behaviors of FGP simply-supported microplates by using MCT, classical and first-order shear deformation theories (FSDT). Fan et al. [29], Thanh et al. [30] investigated the nonlinear buckling and vibration responses of FGP microplates using MCT, isogeometric approach and higher-order shear deformation theory (HSDT). Guo et al. [31] investigated forced vibration responses of exponentially FGP microplates under moving loads.

Moreover, to optimize static and dynamic behaviors of structures, meta-heuristic optimization methods [32] are recently considered as robust and reliable approaches for a wide range of complicated optimization problems, in which most of them was inspired by natural phenomena such as Moth-Fame Algorithm (MFA) [33], Gravitational Search Algorithm (GSA) [34], Firefly Algorithms (FA) [35], Memetic Algorithm (MA) [36], Ant Colony Optimization (ACO) [37], Particle Swarm Optimization (PSO) [38], Differential Evolution (DE) [39], Genetic Algorithms (GA) [40], Spotted Hyena Optimizer [41], etc. Owing to its advantages, these optimization algorithms have been applied for the optimization of functionally graded plates [42–46], nanoplates [47] and micro-beams [48]. In practice, the algorithms require dependent parameters and high computational costs. In order to overcome this adverse, the Balancing Composite Motion Optimization algorithm (BCMO) [49] has been recently developed, in which no dependent parameters are required. This method is inspired by the fact that the solution space is assumed to be in Cartesian coordinates and the searching movements of candidate solutions are compositely equalized in both global and local ones. In fact, a candidate solution can move closer to better ones to exploit the local regions, and move further to explore the search space. Thus, the best-ranked individual

* Corresponding author.
E-mail address: ntkien@hutech.edu.vn (T.-K. Nguyen).

https://doi.org/10.1016/j.tws.2022.110267
Received 6 September 2022; Received in revised form 10 October 2022; Accepted 11 October 2022
Available online xxxx
0263-8231/

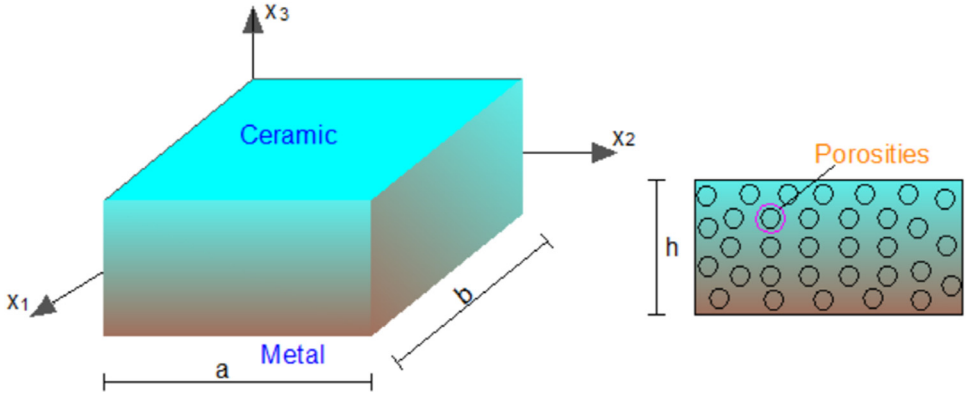

Fig. 1. Geometry of a FGP plate.

in each generation can jump immediately from space to space or intensify its current local space. The BCMO has been applied to optimize behaviors of functionally graded plates [50,51]. Furthermore, the machine learning, which involves an artificial neural network (ANN), has been used to predict the behaviors of materials [52–60]. A literature review shows that although many investigations on the optimization analysis of composite/functionally graded plates have been done, as far as the authors are aware, similar research on the FGP microplates with uncertain materials is still very limited. Besides, the combination between the BCMO algorithm and ANN to determine optimal responses for FGP microplates with uncertainties of material properties has not been developed yet. These are the main novelty and contributions of this paper.

The objective of this paper is to predict optimal responses of natural frequencies and critical buckling loads of FGP microplates subjected to uncertainties of material properties. The theory is based on a unified microplate model using a general framework of HSDT and MCT for analyzing FGP materials. A combination of BCMO-ANN is proposed to solve the optimization problems and predict stochastic vibration and buckling behaviors of FGP microplates. The characteristic equations are derived from Hamilton's principle, and the Ritz-type series method with hybrid shape functions is used to approximate the field variables. Various configurations of the material distribution, material length scale, porosity density and boundary conditions are investigated for natural frequencies and critical buckling loads of FGP microplates.

2. Theoretical formulation

Consider a FGP rectangle microplate in the coordinate system (x_1, x_2, x_3) with sides $a \times b$ and thickness h as shown in Fig. 1. The FGP microplate is composed of a mixture of ceramic and metallic materials, whose properties vary continuously in the thickness direction. The mixture has a porosity with the volume fraction β. The effective material properties of FGP microplates can be approximated by the following expression [6,30,61]:

$$P\left(x_3\right) = \left(P_c - P_m\right)\left(\frac{2x_3 + h}{2h}\right)^p + P_m - \frac{\beta}{2}\left(P_c + P_m\right) \tag{1}$$

where P_c and P_m are the properties of ceramic and metal materials, respectively, which include Young's moduli E, mass density ρ, Poisson's ratio ν; $\beta \leq 1$ is the porous volume fraction; p is the power-law index which is positive and $x_3 \in [-h/2, h/2]$.

2.1. Modified couple stress theory

The total potential energy of the FGP microplate is composed of the strain energy Π_{SE}, work done by membrane forces Π_W, and kinetic energy Π_{KE}. Based on the MCT, the strain energy of the FGP microplate is given by:

$$\Pi_{SE} = \int_V \left(\boldsymbol{\sigma\varepsilon} + \mathbf{m\chi}\right) dV \tag{2}$$

where ε_{ij} and χ_{ij} are components of strains and symmetric rotation gradients, respectively; σ_{ij} is the component of Cauchy stress; m_{ij} is the high-order stress associated to the strain gradient χ_{ij}. The components of strain and strain gradients are defined as follows:

$$\varepsilon_{ij} = \frac{1}{2}\left(u_{i,j} + u_{j,i}\right) \tag{3a}$$

$$\chi_{ij} = \frac{1}{4}\left(u_{n,mj}e_{imn} + u_{n,mi}e_{jmn}\right) \tag{3b}$$

where e_{imn} is permutation symbol; u_i is displacement. The stress components are calculated from the constitutive equations as follows:

$$\sigma_{ij} = \lambda\varepsilon_{kk}\delta_{ij} + 2\mu\varepsilon_{ij} \tag{4a}$$

$$m_{ij} = 2\mu l^2 \chi_{ij} \tag{4b}$$

where δ_{ij} is delta Kronecker; λ and μ are Lamé constants; l is material length scale parameter (MLSP) which is used to measure the effect of stress couple [62]. In practice, the MLSP depends on materials and size of structures [63], which can be determined by experimental works [64]. The work done by membrane compressive loads of the FGP microplate is given by:

$$\Pi_W = -\int_A \left[N_1^0\left(u_{3,1}^0\right)^2 + 2N_{12}^0 u_{3,1}^0 u_{3,2}^0 + N_2^0\left(u_{3,2}^0\right)^2\right] dA \tag{5}$$

where N_1^0, N_2^0 and N_{12}^0 are membrane compressive loads. The kinetic energy of the FGP microplate Π_{KE} is expressed by:

$$\Pi_K = \frac{1}{2}\int_V \rho\left(x_3\right)\left(\dot{u}_1^2 + \dot{u}_2^2 + \dot{u}_3^2\right) dV \tag{6}$$

where $\rho\left(x_3\right)$ is mass density of the FGP microplate; $\dot{u}_1 = u_{1,t}$, $\dot{u}_2 = u_{2,t}$, $\dot{u}_3 = u_{3,t}$ are velocities in x_1-, x_2- and x_3- directions, respectively.

2.2. Unified higher-order shear deformation theory

The general higher-order shear deformation theory for FGP microplates is given by [59]:

$$\begin{aligned} u_1\left(x_1, x_2, x_3\right) &= u_1^0\left(x_1, x_2\right) + \Phi_1\left(x_3\right)u_{3,1}^0 + \Phi_2\left(x_3\right)\varphi_1\left(x_1, x_2\right) \\ u_2\left(x_1, x_2, x_3\right) &= u_2^0\left(x_1, x_2\right) + \Phi_1\left(x_3\right)u_{3,2}^0 + \Phi_2\left(x_3\right)\varphi_2\left(x_1, x_2\right) \\ u_3\left(x_1, x_2, x_3\right) &= u_3^0\left(x_1, x_2\right) \end{aligned} \tag{7}$$

where $\Phi_1\left(x_3\right) = H^s\Psi\left(x_3\right) - x_3, \Phi_2\left(x_3\right) = H^s\Psi\left(x_3\right)$; H^s is the transverse shear stiffness of the FGP microplates; $f\left(x_3\right)$ is a higher-order term which must satisfy condition $f_{,3}\left(x_3 = \pm\frac{h}{2}\right) = 0$ and

$\Psi\left(x_3\right) = \int_0^{x_3} \frac{2(1+\nu)f_{,3}}{E(x_3)} dx_3 = \int_0^{x_3} \frac{f_{,3}}{\mu(x_3)} dx_3$. Substituting Eq. (7) into the strains and strain gradients in Eq. (3), the components of strains $\boldsymbol{\varepsilon}^T = \begin{bmatrix}\epsilon_{11} & \varepsilon_{22} & \gamma_{12} & \gamma_{13} & \gamma_{23}\end{bmatrix}$ and strain gradients $\boldsymbol{\chi}^T = \begin{bmatrix}\chi_{11} & \chi_{22} & 2\chi_{12} & \chi_{33} & 2\chi_{13} & 2\chi_{23}\end{bmatrix}$ are obtained as follows:

$$\boldsymbol{\varepsilon}^{(i)} = \boldsymbol{\varepsilon}^{(0)} + \boldsymbol{\Phi}_1\left(x_3\right)\boldsymbol{\varepsilon}^{(1)} + \boldsymbol{\Phi}_2\left(x_3\right)\boldsymbol{\varepsilon}^{(2)} + \boldsymbol{\Phi}_3\left(x_3\right)\boldsymbol{\varepsilon}^{(3)} \tag{8a}$$

$$\boldsymbol{\chi} = \boldsymbol{\chi}^{(0)} + \boldsymbol{\Phi}_{1,3}\boldsymbol{\chi}^{(1)} + \boldsymbol{\Phi}_{2,3}\boldsymbol{\chi}^{(2)} + \boldsymbol{\Phi}_{1,33}\boldsymbol{\chi}^{(3)} + \boldsymbol{\Phi}_{2,33}\boldsymbol{\chi}^{(4)} + \boldsymbol{\Phi}_2\boldsymbol{\chi}^{(5)} \tag{8b}$$

where $\boldsymbol{\Phi}_3\left(x_3\right) = H^s\Psi_{,3}$ with $\Psi_{,3}\left(x_3\right) = \frac{f_{,3}(x_3)}{\mu(x_3)}$ and,

$$\boldsymbol{\varepsilon}^{(0)} = \begin{Bmatrix}\varepsilon_{11}^{(0)}\\ \varepsilon_{22}^{(0)}\\ \gamma_{12}^{(0)}\\ \gamma_{13}^{(0)}\\ \gamma_{23}^{(0)}\end{Bmatrix} = \begin{Bmatrix}u_{1,1}^0\\ u_{2,2}^0\\ u_{1,2}^0 + u_{2,1}^0\\ 0\\ 0\end{Bmatrix}, \boldsymbol{\varepsilon}^{(1)} = \begin{Bmatrix}\varepsilon_{11}^{(1)}\\ \varepsilon_{22}^{(1)}\\ \gamma_{12}^{(1)}\\ \gamma_{13}^{(1)}\\ \gamma_{23}^{(1)}\end{Bmatrix} = \begin{Bmatrix}u_{3,11}^0\\ u_{3,22}^0\\ 2u_{3,12}^0\\ 0\\ 0\end{Bmatrix},$$

$$\boldsymbol{\varepsilon}^{(2)} = \begin{Bmatrix}\varepsilon_{11}^{(2)}\\ \varepsilon_{22}^{(2)}\\ \gamma_{12}^{(2)}\\ \gamma_{13}^{(2)}\\ \gamma_{23}^{(2)}\end{Bmatrix} = \begin{Bmatrix}\varphi_{1,1}\\ \varphi_{2,2}\\ \varphi_{1,2} + \varphi_{2,1}\\ 0\\ 0\end{Bmatrix} \tag{9a}$$

$$\boldsymbol{\varepsilon}^{(3)} = \begin{Bmatrix}\varepsilon_{11}^{(3)}\\ \varepsilon_{22}^{(3)}\\ \gamma_{12}^{(3)}\\ \gamma_{13}^{(3)}\\ \gamma_{23}^{(3)}\end{Bmatrix} = \begin{Bmatrix}0\\ 0\\ 0\\ \varphi_1 + u_{3,1}^0\\ \varphi_2 + u_{3,2}^0\end{Bmatrix} \tag{9b}$$

$$\boldsymbol{\chi}^{(0)} = \frac{1}{2}\begin{Bmatrix}u_{3,12}^0\\ -u_{3,12}^0\\ u_{3,22}^0 - u_{3,11}^0\\ 0\\ u_{2,11}^0 - u_{1,12}^0\\ u_{2,12}^0 - u_{1,22}^0\end{Bmatrix}, \boldsymbol{\chi}^{(1)} = \frac{1}{2}\begin{Bmatrix}-u_{3,12}^0\\ u_{3,12}^0\\ u_{3,11}^0 - u_{3,22}^0\\ 0\\ 0\\ 0\end{Bmatrix}, \boldsymbol{\chi}^{(2)} = \frac{1}{2}\begin{Bmatrix}-\varphi_{2,1}\\ \varphi_{1,2}\\ \varphi_{1,1} - \varphi_{2,2}\\ \varphi_{2,1} - \varphi_{1,2}\\ 0\\ 0\end{Bmatrix} \tag{9c}$$

$$\boldsymbol{\chi}^{(3)} = \frac{1}{2}\begin{Bmatrix}0\\ 0\\ 0\\ 0\\ -u_{3,2}^0\\ u_{3,1}^0\end{Bmatrix}, \boldsymbol{\chi}^{(4)} = \frac{1}{2}\begin{Bmatrix}0\\ 0\\ 0\\ 0\\ -\varphi_2\\ \varphi_1\end{Bmatrix}, \boldsymbol{\chi}^{(5)} = \frac{1}{2}\begin{Bmatrix}0\\ 0\\ 0\\ 0\\ \varphi_{2,11} - \varphi_{1,12}\\ \varphi_{2,12} - \varphi_{1,22}\end{Bmatrix} \tag{9d}$$

The relationship between the stresses and strains of FGP microplates is expressed as:

$$\boldsymbol{\sigma} = \begin{Bmatrix}\sigma_{11}\\ \sigma_{22}\\ \sigma_{12}\\ \sigma_{13}\\ \sigma_{23}\end{Bmatrix} = \begin{bmatrix}Q_{11} & Q_{12} & 0 & 0 & 0\\ Q_{12} & Q_{22} & 0 & 0 & 0\\ 0 & 0 & Q_{66} & 0 & 0\\ 0 & 0 & 0 & Q_{55} & 0\\ 0 & 0 & 0 & 0 & Q_{44}\end{bmatrix}\begin{Bmatrix}\varepsilon_{11}\\ \varepsilon_{22}\\ \gamma_{12}\\ \gamma_{13}\\ \gamma_{23}\end{Bmatrix} = \mathbf{Q}_\varepsilon\boldsymbol{\varepsilon} \tag{10a}$$

$$\mathbf{m} = \begin{Bmatrix}m_{11}\\ m_{22}\\ m_{12}\\ m_{33}\\ m_{23}\\ m_{13}\end{Bmatrix} = 2\mu l^2\begin{bmatrix}1 & 0 & 0 & 0 & 0 & 0\\ 0 & 1 & 0 & 0 & 0 & 0\\ 0 & 0 & 1 & 0 & 0 & 0\\ 0 & 0 & 0 & 1 & 0 & 0\\ 0 & 0 & 0 & 0 & 1 & 0\\ 0 & 0 & 0 & 0 & 0 & 1\end{bmatrix}\begin{Bmatrix}\chi_{11}\\ \chi_{22}\\ \chi_{12}\\ \chi_{33}\\ \chi_{23}\\ \chi_{13}\end{Bmatrix} = \alpha_\chi\mathbf{I}_{6\times6}\boldsymbol{\chi} \tag{10b}$$

where $\alpha_\chi = 2\mu l^2$, $Q_{11} = \frac{E(x_3)}{1-\nu^2}$, $Q_{22} = \frac{E(x_3)}{1-\nu^2}$, $Q_{12} = \frac{\nu E(x_3)}{1-\nu^2} Q_{44} = Q_{55} = Q_{66} = \mu = \frac{E(x_3)}{2(1+\nu)}$.

To derive the equation of motion, Hamilton's principle is used:

$$\int_{t_1}^{t_2}\left(\delta\Pi_{SE} + \delta\Pi_W - \delta\Pi_{KE}\right)dt = 0 \tag{11}$$

where the variation of the strain energy $\delta\Pi_{SE}$ of the FGP microplate is derived from Eq. (2) as follows:

$$\begin{aligned}\delta\Pi_{SE} &= \int_A\left(\boldsymbol{\sigma}\delta\boldsymbol{\varepsilon} + \mathbf{m}\delta\boldsymbol{\chi}\right)dA\\ &= \int_A\left[\mathbf{M}_\varepsilon^{(0)}\delta\boldsymbol{\varepsilon}^{(0)} + \mathbf{M}_\varepsilon^{(1)}\delta\boldsymbol{\varepsilon}^{(1)} + \mathbf{M}_\varepsilon^{(2)}\delta\boldsymbol{\varepsilon}^{(2)} + \mathbf{M}_\varepsilon^{(3)}\delta\boldsymbol{\varepsilon}^{(3)}\right.\\ &+\mathbf{M}_\chi^{(0)}\delta\boldsymbol{\chi}^{(0)} + \mathbf{M}_\chi^{(1)}\delta\boldsymbol{\chi}^{(1)} + \mathbf{M}_\chi^{(2)}\delta\boldsymbol{\chi}^{(2)}\\ &\left.+\mathbf{M}_\chi^{(3)}\delta\boldsymbol{\chi}^{(3)} + \mathbf{M}_\chi^{(4)}\delta\boldsymbol{\chi}^{(4)} + \mathbf{M}_\chi^{(5)}\delta\boldsymbol{\chi}^{(5)}\right]dA\end{aligned} \tag{12}$$

where the stress resultants are given by:

$$\left(\mathbf{M}_\varepsilon^{(0)}, \mathbf{M}_\varepsilon^{(1)}, \mathbf{M}_\varepsilon^{(2)}, \mathbf{M}_\varepsilon^{(3)}\right) = \int_{-h/2}^{h/2}\left(1, \boldsymbol{\Phi}_1, \boldsymbol{\Phi}_2, \boldsymbol{\Phi}_3\right)\boldsymbol{\sigma}dx_3 \tag{13a}$$

$$\begin{aligned}&\left(\mathbf{M}_\chi^{(0)}, \mathbf{M}_\chi^{(1)}, \mathbf{M}_\chi^{(2)}, \mathbf{M}_\chi^{(3)}, \mathbf{M}_\chi^{(4)}, \mathbf{M}_\chi^{(5)}\right)\\ &= \int_{-h/2}^{h/2}\left(1, \boldsymbol{\Phi}_{1,3}, \boldsymbol{\Phi}_{2,3}, \boldsymbol{\Phi}_{1,33}, \boldsymbol{\Phi}_{2,33}, \boldsymbol{\Phi}_2\right)\mathbf{m}dx_3\end{aligned} \tag{13b}$$

These stress resultants can be obtained in terms of the strains and its gradients as follows:

$$\begin{Bmatrix}\mathbf{M}_\varepsilon^{(0)}\\ \mathbf{M}_\varepsilon^{(1)}\\ \mathbf{M}_\varepsilon^{(2)}\\ \mathbf{M}_\varepsilon^{(3)}\end{Bmatrix} = \begin{bmatrix}\mathbf{A}^\varepsilon & \mathbf{B}^\varepsilon & \mathbf{B}_s^\varepsilon & \mathbf{0}\\ \mathbf{B}^\varepsilon & \mathbf{D}^\varepsilon & \mathbf{D}_s^\varepsilon & \mathbf{0}\\ \mathbf{B}_s^\varepsilon & \mathbf{D}_s^\varepsilon & \mathbf{H}_s^\varepsilon & \mathbf{0}\\ \mathbf{0} & \mathbf{0} & \mathbf{0} & \mathbf{A}_s^\varepsilon\end{bmatrix}\begin{Bmatrix}\boldsymbol{\varepsilon}^{(0)}\\ \boldsymbol{\varepsilon}^{(1)}\\ \boldsymbol{\varepsilon}^{(2)}\\ \boldsymbol{\varepsilon}^{(3)}\end{Bmatrix} \tag{14a}$$

$$\begin{Bmatrix}\mathbf{M}_\chi^{(0)}\\ \mathbf{M}_\chi^{(1)}\\ \mathbf{M}_\chi^{(2)}\\ \mathbf{M}_\chi^{(3)}\\ \mathbf{M}_\chi^{(4)}\\ \mathbf{M}_\chi^{(5)}\end{Bmatrix} = \begin{bmatrix}\mathbf{A}^\chi & \overline{\mathbf{B}}^\chi & \overline{\mathbf{B}}_s^\chi & \overline{\overline{\mathbf{B}}}^\chi & \overline{\mathbf{B}}_s^\chi & \mathbf{B}_s^\chi\\ \overline{\mathbf{B}}^\chi & \overline{\mathbf{D}}^\chi & \overline{\mathbf{D}}_s^\chi & \overline{\mathbf{E}}^\chi & \overline{\mathbf{E}}_s^\chi & \overline{\mathbf{F}}_s^\chi\\ \overline{\mathbf{B}}_s^\chi & \overline{\mathbf{D}}_s^\chi & \overline{\mathbf{H}}_s^\chi & \overline{\mathbf{G}}_s^\chi & \overline{\mathbf{I}}^\chi & \overline{\mathbf{J}}^\chi\\ \overline{\overline{\mathbf{B}}}^\chi & \overline{\mathbf{E}}^\chi & \overline{\mathbf{G}}_s^\chi & \overline{\overline{\mathbf{D}}}^\chi & \overline{\overline{\mathbf{D}}}_s^\chi & \overline{\overline{\mathbf{K}}}_s^\chi\\ \overline{\overline{\mathbf{B}}}_s^\chi & \overline{\mathbf{E}}_s^\chi & \overline{\mathbf{I}}^\chi & \overline{\overline{\mathbf{D}}}_s^\chi & \overline{\overline{\mathbf{H}}}_s^\chi & \overline{\mathbf{L}}\\ \mathbf{B}_s^\chi & \overline{\mathbf{F}}_s^\chi & \overline{\mathbf{J}}^\chi & \overline{\overline{\mathbf{K}}}_s^\chi & \overline{\mathbf{L}} & \mathbf{H}_s^\chi\end{bmatrix}\begin{Bmatrix}\boldsymbol{\chi}^{(0)}\\ \boldsymbol{\chi}^{(1)}\\ \boldsymbol{\chi}^{(2)}\\ \boldsymbol{\chi}^{(3)}\\ \boldsymbol{\chi}^{(4)}\\ \boldsymbol{\chi}^{(5)}\end{Bmatrix} \tag{14b}$$

where the stiffness components of the FGP microplate are defined as follows:

$$\left(\mathbf{A}^\varepsilon, \mathbf{B}^\varepsilon, \mathbf{D}^\varepsilon, \mathbf{H}_s^\varepsilon, \mathbf{B}_s^\varepsilon, \mathbf{D}_s^\varepsilon, \mathbf{A}_s^\varepsilon\right) = \int_{-h/2}^{h/2}\left(1, \boldsymbol{\Phi}_1, \boldsymbol{\Phi}_1^2, \boldsymbol{\Phi}_2^2, \boldsymbol{\Phi}_2, \boldsymbol{\Phi}_1\boldsymbol{\Phi}_2, \boldsymbol{\Phi}_3^2\right)\mathbf{Q}_\varepsilon dx_3 \tag{15a}$$

$$\begin{aligned}&\left(\mathbf{A}^\chi, \overline{\mathbf{B}}^\chi, \overline{\mathbf{B}}_s^\chi, \overline{\overline{\mathbf{B}}}^\chi, \overline{\overline{\mathbf{B}}}_s^\chi, \mathbf{B}_s^\chi\right) = \left(A^\chi, \overline{B}^\chi, \overline{B}_s^\chi, \overline{\overline{B}}^\chi, \overline{\overline{B}}_s^\chi, B_s^\chi\right)\mathbf{I}_{6\times6}\\ &= \int_{-h/2}^{h/2}\left(1, \boldsymbol{\Phi}_{1,3}, \boldsymbol{\Phi}_{2,3}, \boldsymbol{\Phi}_{1,33}, \boldsymbol{\Phi}_{2,33}, \boldsymbol{\Phi}_2\right)\alpha_\chi\mathbf{I}_{6\times6}dx_3\end{aligned} \tag{15b}$$

$$\left(\overline{\mathbf{D}}^{\chi},\overline{\mathbf{D}}_s^{\chi},\overline{\mathbf{E}}^{\chi},\overline{\mathbf{E}}_s^{\chi},\overline{\mathbf{F}}_s^{\chi}\right)=\left(\overline{D}^{\chi},\overline{D}_s^{\chi},\overline{E}^{\chi},\overline{E}_s^{\chi},\overline{F}_s^{\chi}\right)\mathbf{I}_{6\times6}$$
$$=\int_{-h/2}^{h/2}\boldsymbol{\Phi}_{1,3}\left(\boldsymbol{\Phi}_{1,3},\boldsymbol{\Phi}_{2,3},\boldsymbol{\Phi}_{1,33},\boldsymbol{\Phi}_{2,33},\boldsymbol{\Phi}_2\right)\alpha_{\chi}\mathbf{I}_{6\times6}dx_3 \tag{15c}$$

$$\left(\overline{\mathbf{H}}_s^{\chi},\overline{\mathbf{G}}_s^{\chi},\overline{\mathbf{I}}^{\chi},\overline{\mathbf{J}}^{\chi}\right)=\left(\overline{H}_s^{\chi},\overline{G}_s^{\chi},\overline{I}^{\chi},\overline{J}^{\chi}\right)\mathbf{I}_{6\times6}$$
$$=\int_{-h/2}^{h/2}\boldsymbol{\Phi}_{2,3}\left(\boldsymbol{\Phi}_{2,3},\boldsymbol{\Phi}_{1,33},\boldsymbol{\Phi}_{2,33},\boldsymbol{\Phi}_2\right)\alpha_{\chi}\mathbf{I}_{6\times6}dx_3 \tag{15d}$$

$$\left(\overline{\overline{\mathbf{D}}}^{\chi},\overline{\overline{\mathbf{D}}}_s^{\chi},\overline{\mathbf{K}}_s^{\chi},\overline{\overline{\mathbf{H}}}_s^{\chi},\overline{\mathbf{L}}^{\chi},\mathbf{H}_s^{\chi}\right)=\left(\overline{\overline{D}}^{\chi},\overline{\overline{D}}_s^{\chi},\overline{K}_s^{\chi},\overline{\overline{H}}_s^{\chi},\overline{L}^{\chi},H_s^{\chi}\right)\mathbf{I}_{6\times6}$$
$$=\int_{-h/2}^{h/2}\left(\boldsymbol{\Phi}_{1,33}^2,\boldsymbol{\Phi}_{1,33}\boldsymbol{\Phi}_{2,33},\boldsymbol{\Phi}_{1,33}\boldsymbol{\Phi}_2,\boldsymbol{\Phi}_{2,33}^2,\boldsymbol{\Phi}_{2,33}\boldsymbol{\Phi}_2,\boldsymbol{\Phi}_2^2\right)\alpha_{\chi}\mathbf{I}_{6\times6}dx_3 \tag{15e}$$

The variation of work done $\delta\Pi_W$ by membrane compressive loads derived from Eq. (5) is given by:

$$\delta\Pi_V=-\int_A N^0\left(u_{3,1}^0\delta u_{3,1}^0+u_{3,2}^0\delta u_{3,2}^0\right)dA \tag{16}$$

where it is assumed that $N_1^0=N_2^0=N^0,N_{12}^0=0$. The variation of kinetic energy $\delta\Pi_{KE}$ derived from Eq. (6) is calculated by:

$$\delta\Pi_K=\frac{1}{2}\int_V\rho\left(\dot{u}_1\delta\dot{u}_1+\dot{u}_2\delta\dot{u}_2+\dot{u}_3\delta\dot{u}_3\right)dV$$
$$=\frac{1}{2}\int_A\left[I_2\left(\dot{u}_{3,1}^0\delta\dot{u}_{3,1}^0+\dot{u}_{3,2}^0\delta\dot{u}_{3,2}^0\right)+K_2\left(\dot{\varphi}_1\delta\dot{\varphi}_1+\dot{\varphi}_2\delta\dot{\varphi}_2\right)\right.$$
$$I_0\left(\dot{u}_1^0\delta\dot{u}_1^0+\dot{u}_2^0\delta\dot{u}_2^0+\dot{u}_3^0\delta\dot{u}_3^0\right)+I_1\left(\dot{u}_1^0\delta\dot{u}_{3,1}^0+\dot{u}_{3,1}^0\delta\dot{u}_1^0+\dot{u}_2^0\delta\dot{u}_{3,2}^0+\dot{u}_{3,2}^0\delta\dot{u}_2^0\right)$$
$$+J_1\left(\dot{u}_1^0\delta\dot{\varphi}_1+\dot{\varphi}_1\delta\dot{u}_1^0+\dot{u}_2^0\delta\dot{\varphi}_2+\dot{\varphi}_2\delta\dot{u}_2^0\right)$$
$$\left.+J_2\left(\dot{u}_{3,1}^0\delta\dot{\varphi}_1+\dot{\varphi}_1\delta\dot{u}_{3,1}^0+\dot{u}_{3,2}^0\delta\dot{\varphi}_2+\dot{\varphi}_2\delta\dot{u}_{3,2}^0\right)\right]dA \tag{17}$$

where I_0,I_1,I_2,J_1,J_2,K_2 are mass components of the FGP microplate which are defined as:

$$\left(K_2,J_2,J_1,I_2,I_1,I_0\right)=\int_{-h/2}^{h/2}\left(\boldsymbol{\Phi}_2^2,\boldsymbol{\Phi}_1\boldsymbol{\Phi}_2,\boldsymbol{\Phi}_2,\boldsymbol{\Phi}_1^2,\boldsymbol{\Phi}_1,1\right)\rho dx_3 \tag{18}$$

3. Ritz method

Based on the Ritz method, the membrane and transverse displacements, rotations $\left(u_1^0,u_2^0,u_3^0,\varphi_1,\varphi_2\right)$ of the FGP microplate can be expressed in terms of the series of approximation functions and associated values of series as follows:

$$u_1^0(x_1,x_2,t)=\sum_{i=1}^{n_1}\sum_{j=1}^{n_2}u_{1ij}(t)R_{i,1}\left(x_1\right)P_j\left(x_2\right) \tag{19a}$$

$$u_2^0(x_1,x_2,t)=\sum_{i=1}^{n_1}\sum_{j=1}^{n_2}u_{2ij}(t)R_i\left(x_1\right)P_{j,2}\left(x_2\right) \tag{19b}$$

$$u_3^0(x_1,x_2,t)=\sum_{i=1}^{n_1}\sum_{j=1}^{n_2}u_{3ij}(t)R_i\left(x_1\right)P_j\left(x_2\right) \tag{19c}$$

$$\varphi_1(x_1,x_2,t)=\sum_{i=1}^{n_1}\sum_{j=1}^{n_2}x_{ij}(t)R_{i,1}\left(x_1\right)P_j\left(x_2\right) \tag{19d}$$

$$\varphi_2(x_1,x_2,t)=\sum_{i=1}^{n_1}\sum_{j=1}^{n_2}y_{ij}(t)R_i\left(x_1\right)P_{j,2}\left(x_2\right) \tag{19e}$$

where $u_{1ij},u_{2ij},u_{3ij},x_{ij},y_{ij}$ are variables to be determined; $R_i\left(x_1\right)$ and $P_j\left(x_2\right)$ are the shape functions in x_1-, x_2- direction, respectively. As a result, the five unknowns of the FGP microplate only depend on the two shape functions. It should be noted that the accuracy, convergence rates and numerical instabilities of the Ritz solution depend on the construction of shape functions, which has been discussed in [65–68]. The functions $R_i\left(x_1\right)$ and $P_j\left(x_2\right)$ are constructed to satisfy the boundary conditions (BCs) (see Table 1) in which the simply-supported and clamped–clamped BCs are as follows:

- Simply supported (S): $u_2^0=u_3^0=\varphi_2=0$ at $x_1=0,a$ and $u_1^0=u_3^0=\varphi_1=0$at $x_2=0,b$
- Clamped (C): $u_1^0=u_2^0=u_3^0=\varphi_1=\varphi_2=0$ at $x_1=0,a$ and $x_2=0,b$

The combination of simply-supported, clamped boundary conditions on the edges of the FGP microplate leads to the different BCs as follows: SSSS, CSCS and CCCC will be considered in the numerical examples. Substituting Eq. (19) into Eqs. (17), (16) and (12) and then the subsequent results into Eq. (11) lead to the following characteristic equations of motion of the FGP microplate:

$$\mathbf{Kd}+\mathbf{M}\ddot{\mathbf{d}}=\mathbf{0} \tag{20}$$

where $\mathbf{d}=\begin{bmatrix}\mathbf{u}_1 & \mathbf{u}_2 & \mathbf{u}_3 & \mathbf{x} & \mathbf{y}\end{bmatrix}^T$ is the displacement vector to be determined; $\mathbf{K}=\mathbf{K}^{\epsilon}+\mathbf{K}^{\chi}$ is the stiffness matrix which consists of the strains $\mathbf{K}^{\epsilon}$ and the symmetric rotation gradients $\mathbf{K}^{\chi}$; $\mathbf{M}$ is the mass matrix. The components of stiffness matrix and mass matrix are defined in details in [25]. Furthermore, it is worthy to note that for buckling analysis, the critical buckling loads of the FGP plate can be obtained from Eq. (20) by setting $\mathbf{M}=0$. For free vibration analysis, by denoting $\mathbf{d}(t)=\mathbf{d}e^{i\omega t}$ where ω is the natural frequencies of the FGP microplate and $i^2=-1$ is the imaginary unit, the natural frequencies can be derived by solving the following equation: $\left(\mathbf{K}-\omega^2\mathbf{M}\right)\mathbf{d}=\mathbf{0}$.

4. ANN-BCMO algorithm

4.1. Optimization problem

The objective of the optimization problem in this study is to search for the optimal material properties of the FGP microplate that can maximize the natural frequencies or critical buckling loads subjected to several constraints. The Young's modulus and mass densities are considered as design variables. The formulation of constrained objective functions for vibration optimization can be generally stated as:

$$\text{Maximize}\quad\overline{\omega}=f\left(E_{c,i},E_{m,i},\rho_{c,i},\rho_{m,i}\right)$$

$$\text{Subjected to}\begin{cases}\left(\mathbf{K}-\omega^2\mathbf{M}\right)\mathbf{d}=\mathbf{0}\\ E_{c,\min}\le E_{c,i}\le E_{c,\max}\\ E_{m,\min}\le E_{m,i}\le E_{m,\max}\\ \rho_{c,\min}\le\rho_{c,i}\le\rho_{c,\max}\\ \rho_{m,\min}\le\rho_{m,i}\le\rho_{m,\max}\end{cases} \tag{21}$$

The formulation of constrained objective functions for critical buckling loads of the FGP microplate can be expressed as follows:

$$\text{Maximize}\quad\overline{N}_{cr}=f\left(E_{c,i},E_{m,i}\right)$$

$$\text{Subjected to}\begin{cases}\mathbf{M}=\mathbf{0}\\ E_{c,\min}\le E_{c,i}\le E_{c,\max}\\ E_{m,\min}\le E_{m,i}\le E_{m,\max}\end{cases} \tag{22}$$

where $E_{,\min}=E_{,\text{mean}}-5\%E_{,\text{mean}}$, $E_{,\max}=E_{,\text{mean}}+5\%E_{,\text{mean}}$, $\rho_{,\min}=\rho_{,\text{mean}}-5\%\rho_{,\text{mean}}$ and $\rho_{,\max}=\rho_{,\text{mean}}+5\%\rho_{,\text{mean}}$; $E_{,\text{mean}}$ and $\rho_{,\text{mean}}$ are the mean values of Young's modulus and mass density of constituent materials, respectively.

4.2. Balancing composite motion optimization

Initiated by Le-Duc et al. [49], the BCMO is a population-based optimization method, in which the main idea of this approach is to balance individual composite motion properties in the global optimum. The

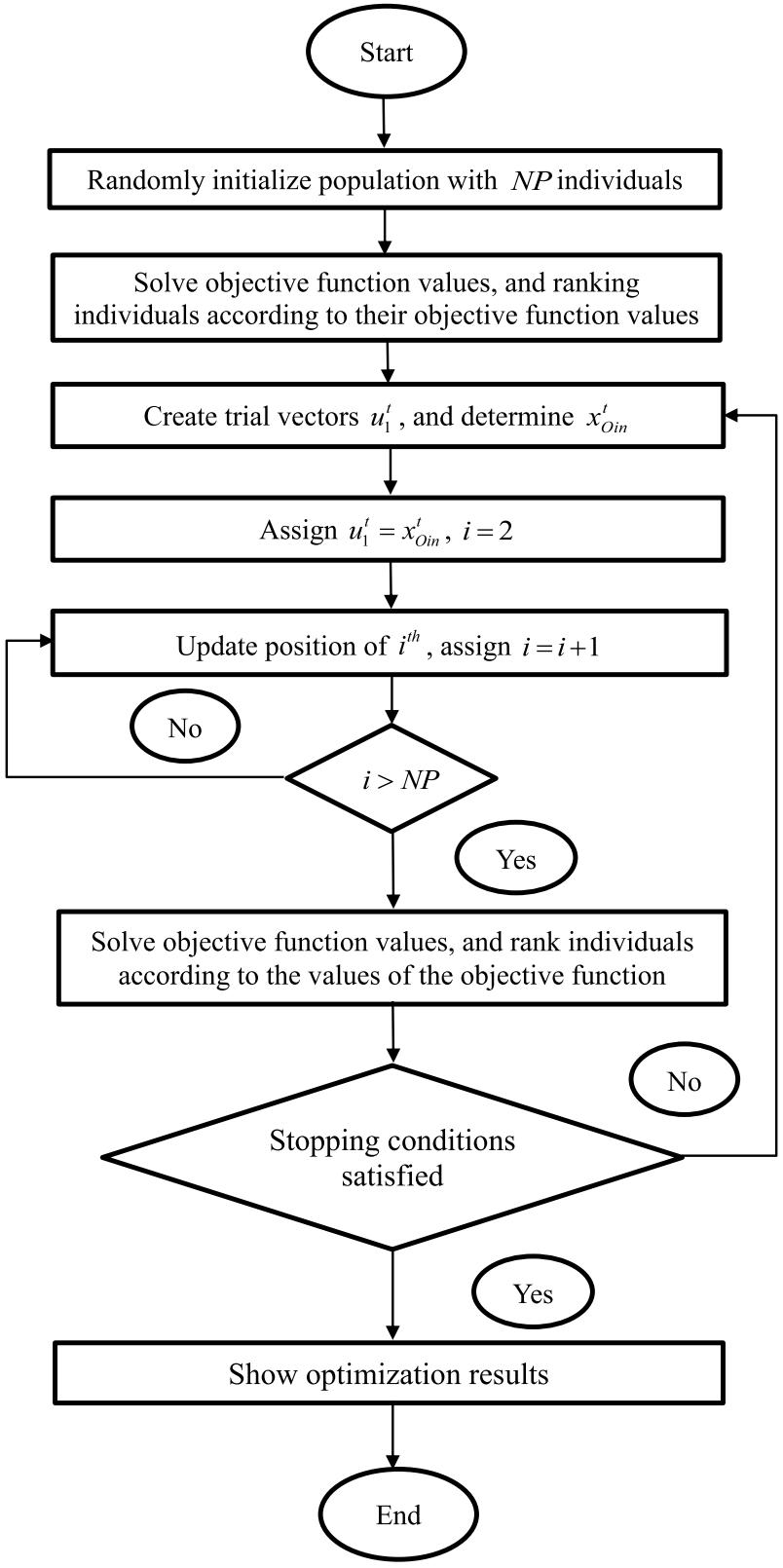

Fig. 2. Flowchart of the BCMO algorithm.

equalization of global and local searching through a probabilistic model of selection generates a movement mechanism for each individual.

Initialization: The population distribution is randomly initialized as follows:

$$x_i = x_j^L + rand\,(1,d) \times \left(x_i^U - x_j^L\right) \tag{23}$$

where x_i^L and x_i^U are the lower and upper bounds of the i^{th} individual; d is number of items. The objective function values of the population $f\,(x)$ is then evaluated and all individuals are ranked based on the sorting $f\,(x)$ as follows:

$$x = \arg sort\,\{f\,(x)\} \tag{24}$$

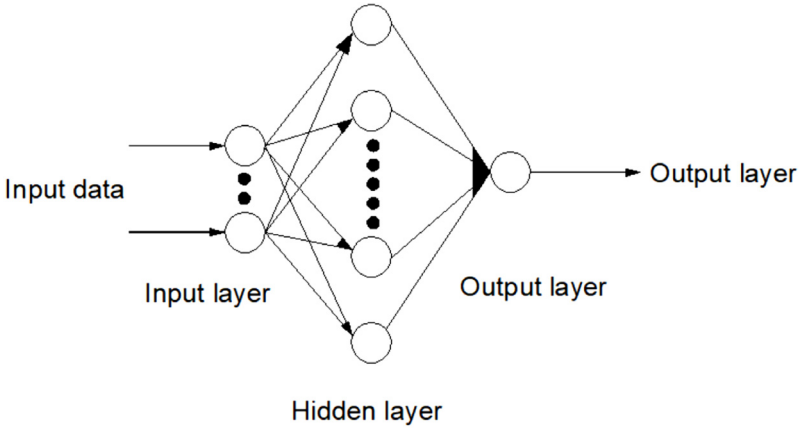

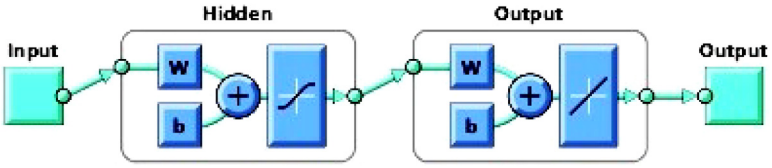

Fig. 3. An artificial neural network structure.

Table 1
Approximation functions of series solutions with different BCs.

Boundary conditions	Approximation functions	
	$R_j(x_1)$	$P_j(x_2)$
SSSS	$x_1(a-x_1)e^{-\frac{jx_1}{a}}$	$x_2(b-x_2)e^{-\frac{jx_2}{b}}$
CSCS	$x_1^2(a-x_1)e^{-\frac{jx_1}{a}}$	$x_2^2(b-x_2)e^{-\frac{jx_2}{b}}$
CCCC	$x_1^2(a-x_1)^2e^{-\frac{jx_1}{a}}$	$x_2^2(b-x_2)^2e^{-\frac{jx_2}{b}}$

Table 2
Convergence study of the series solution of Al/Al_2O_3 FGP plates with different boundary conditions ($a/h=10,\ p=10,\ \beta=0.1,\ h/l=1$).

Solution	Number of series $n=n_1=n_2$					
	2	4	6	8	10	12
Normalized fundamental frequency						
SSSS	7.6675	7.5748	7.5508	7.5531	7.5523	7.5529
CSCS	11.8257	11.4713	11.4652	11.4652	11.4652	11.4652
CCCC	16.4080	16.3353	16.3332	16.3281	16.3285	16.3283
Normalized critical buckling load with axial compression $(N_1^0, N_2^0, N_{12}^0 = 1,0,0)$						
SSSS	21.3756	21.1557	20.9383	20.8252	20.8263	20.8258
CSCS	42.7373	40.1757	39.0022	38.8722	38.8720	38.8721
CCCC	75.9027	74.8932	72.6642	72.4134	72.4140	72.4135

Table 3
Normalized fundamental frequency of simply supported FGP microplates with $a/h=20$.

β	h/l	Theory	p			
			1	2	5	10
0	∞	Present	4.5218	4.1098	3.8921	3.7631
		IGA [16]	4.5228	4.1101	3.8884	3.7622
	10	Present	4.6387	4.2122	3.9707	3.8305
		IGA [16]	4.6351	4.2111	3.9688	3.8316
	5	Present	4.9612	4.4980	4.2000	4.0302
		IGA [16]	4.9568	4.5006	4.2005	4.0324
	2	Present	6.7964	6.1561	5.5531	5.2202
		IGA [16]	6.7948	6.1565	5.5551	5.2212
	1	Present	11.1206	10.0595	8.8270	8.1468
		IGA [16]	11.1043	10.0451	8.8287	8.1496
0.2	∞	Present	4.2063	3.4877	3.0203	2.9228
		IGA [16]	4.2068	3.4871	3.0179	2.9184
	10	Present	4.3259	3.6089	3.1042	2.9862
		IGA [16]	4.3331	3.6038	3.1056	2.9849
	5	Present	4.6960	3.9324	3.3551	3.1733
		IGA [16]	4.6914	3.9330	3.3550	3.1752
	2	Present	6.6954	5.7322	4.7415	4.2613
		IGA [16]	6.6819	5.7303	4.7440	4.2686
	1	Present	11.2241	9.7475	7.9145	6.8643
		IGA [16]	11.2026	9.7395	7.9132	6.8669

Instant global point and best individual: The instant global point x_{Oin}^t is defined by the previous best of x_1^{t-1} with respect to a trial u_1^t using the objective function.

$$x_{Oin}^t = \begin{cases} u_1^t & if \quad f\left(u_1^t\right) < f\left(x_1^{t-1}\right) \\ x_1^{t-1} & otherwise \end{cases} \tag{25}$$

where u_1^t is determined using the current generation's population information as follows:

$$u_1^t = u_c + v_{k1/k2}^t + v_{k2/1}^t \tag{26}$$

where u_c is the midpoint of the design space $[LB, UB]$, which is expressed as follows:

$$u_c = \frac{LB+UB}{2} \tag{27}$$

where $v_{k1/k2}^t$ is the relative motions of the individual k_1th with respect to the individual k_2th; $v_{k2/1}^t$ is the relative motions of the individual k_2th with respect to the previous best one. $v_{k1/k2}^t$ and $v_{k2/1}^t$ are determined using $L_{LS}=1$ as follows:

$$v_{i/j} = \alpha_{ij}\left(x_j - x_i\right), \alpha_{ij} = L_{LS} \times dv_{ij} \tag{28}$$

where dv_{ij} is a vector that can be calculated by the trial number TV_j

$$dv_{ij} = \begin{cases} rand(1,d) & if \quad TV_j > 0.5 \\ -rand(1,d) & otherwise \end{cases} \tag{29}$$

Table 4
Mean and standard deviation (SD) of normalized fundamental frequency for FGP microplates with $a/h = 10$ and SSSS boundary condition.

β	p	h/l	Theory	Mean	SD	Time (s)	Present
0.1	1	10	Ritz-BCMO	4.4049	0.0496	615	4.4073
			BCMO-ANN	4.4090	0.0491	10	
		5	Ritz-BCMO	4.7449	0.0517	620	4.7485
			BCMO-ANN	4.7451	0.0513	9	
		1	Ritz-BCMO	11.0692	0.1051	617	11.0673
			BCMO-ANN	11.0745	0.1059	11	
	10	10	Ritz-BCMO	3.3994	0.0953	625	3.4012
			BCMO-ANN	3.4040	0.0961	10	
		5	Ritz-BCMO	3.5922	0.0997	623	3.6001
			BCMO-ANN	3.6037	0.0993	12	
		1	Ritz-BCMO	7.5662	0.1991	627	7.5531
			BCMO-ANN	7.5376	0.1983	10	
0.2	1	10	Ritz-BCMO	4.2436	0.0509	630	4.2482
			BCMO-ANN	4.2456	0.0512	11	
		5	Ritz-BCMO	4.6082	0.0522	624	4.6121
			BCMO-ANN	4.6074	0.0530	11	
		1	Ritz-BCMO	11.1087	0.1075	628	11.1145
			BCMO-ANN	11.1292	0.1066	12	
	10	10	Ritz-BCMO	2.8681	0.1277	631	2.8822
			BCMO-ANN	2.8645	0.1274	12	
		5	Ritz-BCMO	3.0547	0.1323	630	3.0723
			BCMO-ANN	3.0676	0.1309	10	
		1	Ritz-BCMO	6.7642	0.2269	628	6.7687
			BCMO-ANN	6.7623	0.2270	11	

Composite motion of individuals in solution space: In BCMO, v_j is the motion of the global search, which is determined by:

$$v_j = \alpha_j \left(x_{Oin} - x_j\right) \tag{30}$$

where α_j is considered as the first-order derivation of the motion distance $\left(x_{Oin} - x_j\right)$, that leads to:

$$\alpha_j = L_{GS} \times dv_j \tag{31}$$

where

$$L_{GS} = \begin{cases} e^{-\frac{1}{d}\frac{j}{NP}r_j^2} & if \quad TV_j > 0.5 \\ e^{-\frac{1}{d}\left(1-\frac{j}{NP}\right)r_j^2} & otherwise \end{cases} \tag{32}$$

where NP is the population size and dv_j is the vector that can be calculated by the trial number TV_j:

$$dv_{ij} = \begin{cases} rand(1,d) & if \quad TV_j > 0.5 \\ -rand(1,d) & otherwise \end{cases} \tag{33}$$

The distance from the jth individual to $\mathbf{O}_{in}$ call r_j is calculated by:

$$r_j = \left\| x_j - x_{Oin} \right\| \tag{34}$$

The probabilities of these v_{ik} cases are equal and can be determined as follows:

$$P\left(v_{ik}\right) = P\left(v_{i/j}\right) \times P\left(v_j\right) = 0.5 \times 0.5 = 0.25 \quad k = 1, \ldots, 4 \tag{35}$$

The updated position of the ith individual at the next generation is:

$$x_i^{t+1} = x_i^t + v_{i/j} + v_j \tag{36}$$

The flowchart of the BCMO algorithm is illustrated in Fig. 2 (more details about the BCMO algorithm can be found in [49]).

4.3. ANN-BCMO algorithm

The Artificial Neural Network (ANN) system shown in Fig. 3 contains three kinds of layers, namely, input layer, hidden layer, output layer in which each layer consists of neurons that are connected to each other in the previous layer. The input data from the outside are multiplied by the weights before they reach the nodes. Each node in the next layer will get a sum of the output values of the previous nodes multiplied with respective weights. The output data of the activation function for the sum is expressed as follows:

$$y_i^n = \varphi\left(x_i^n\right) = \varphi\left(\sum_{j=1}^{lm_{n-1}} w_{ij}^{n-1} \times y_j^{n-1} + b_i^n\right) \tag{37}$$

where y_i^n and x_i^n are data pair output and input of activation function of node i, respectively; w_{ij}^{n-1} is the weight between the output node i and input node j; b_i^n is the bias of node j; φ is the activation function. Moreover, it is known that the activation function plays an important role in defining the output signal of each neuron in each layer of a neural network. Different activation functions have been, therefore, developed in the literature [69]. For the present study, the activation function used to update weight and bias values is based on the Levenberg–Marquardt optimization [70,71].

Furthermore, a loss function is required to evaluate the performance of the prediction model. The objective of loss function is to measure the difference between target values and predicted ones, from which during the training process, the difference between the model outputs and the target values are converged to zeros. The loss functions are hence constructed to deal with different kinds of optimization problems. In practice, the mean square error (MSE) [72] is commonly used to evaluate the accuracy of the prediction model. It is also considered as a loss function during training process of the ANN. The statement of MSE is illustrated as follows:

$$MSE = \frac{1}{lm}\sum_{i}^{lm}\left(y_i - \widehat{y}_i\right)^2 \tag{38}$$

where lm is the number of training samples; y_i is the actual output data; $\widehat{y}_i$ is the predicted value of the $ith-$ sample.

5. Numerical examples

In this section, numerical examples are performed to investigate stochastic vibration and buckling responses of FGP microplates with three kinds of boundary conditions (SSSS, CSCS, CCCC), in which the shear function $\Psi\left(x_3\right) = \coth^{-1}\left(\frac{h}{x_3}\right) - \frac{16x_3^3}{15h^3}$ [67] is used. The FGP microplates are supposed to be composed of a mixture of ceramic and metal materials whose mean properties are: Al_2O_3 (E_c = 380 GPa, ρ_c = 3800 kg/m^3, ν_c = 0.3), Al (E_m = 70 GPa, ρ_m = 2702 kg/m^3, ν_m = 0.3), whereas for stochastic analysis, Young's moduli and mass densities are assumed to be randomly distributed via a uniform distribution.

For simplicity, the following normalized response parameters are used in the numerical examples:

$$\overline{\omega} = \frac{\omega a^2}{h}\sqrt{\frac{\rho_c}{E_c}} \tag{39a}$$

$$\overline{N}_{cr} = \frac{N_{cr}a^2}{h^3 E_m} \tag{39b}$$

In order to study the convergence of present solutions, Table 2 shows nondimensional deterministic critical buckling loads $\overline{N}_{cr}$ and fundamental frequencies $\overline{\omega}$ of the Al/Al_2O_3 square FGP microplates with a/h = 10, p = 10, h/l = 1 and β = 0.1. The results are calculated for three types of BCs (SSSS, CSCS and CCCC) and the same number of series type-solution in x_1- and x_2- direction ($n_1 = n_2 = n$). The responses show a rapid convergence for a number of series n = 8, hence this number will be used for the numerical examples.

5.1. Vibration analysis

In order to verify the accuracy of the present theory in predicting vibration behaviors, Table 3 displays normalized deterministic fundamental frequencies of Al/Al_2O_3 FGP microplates with simply supported

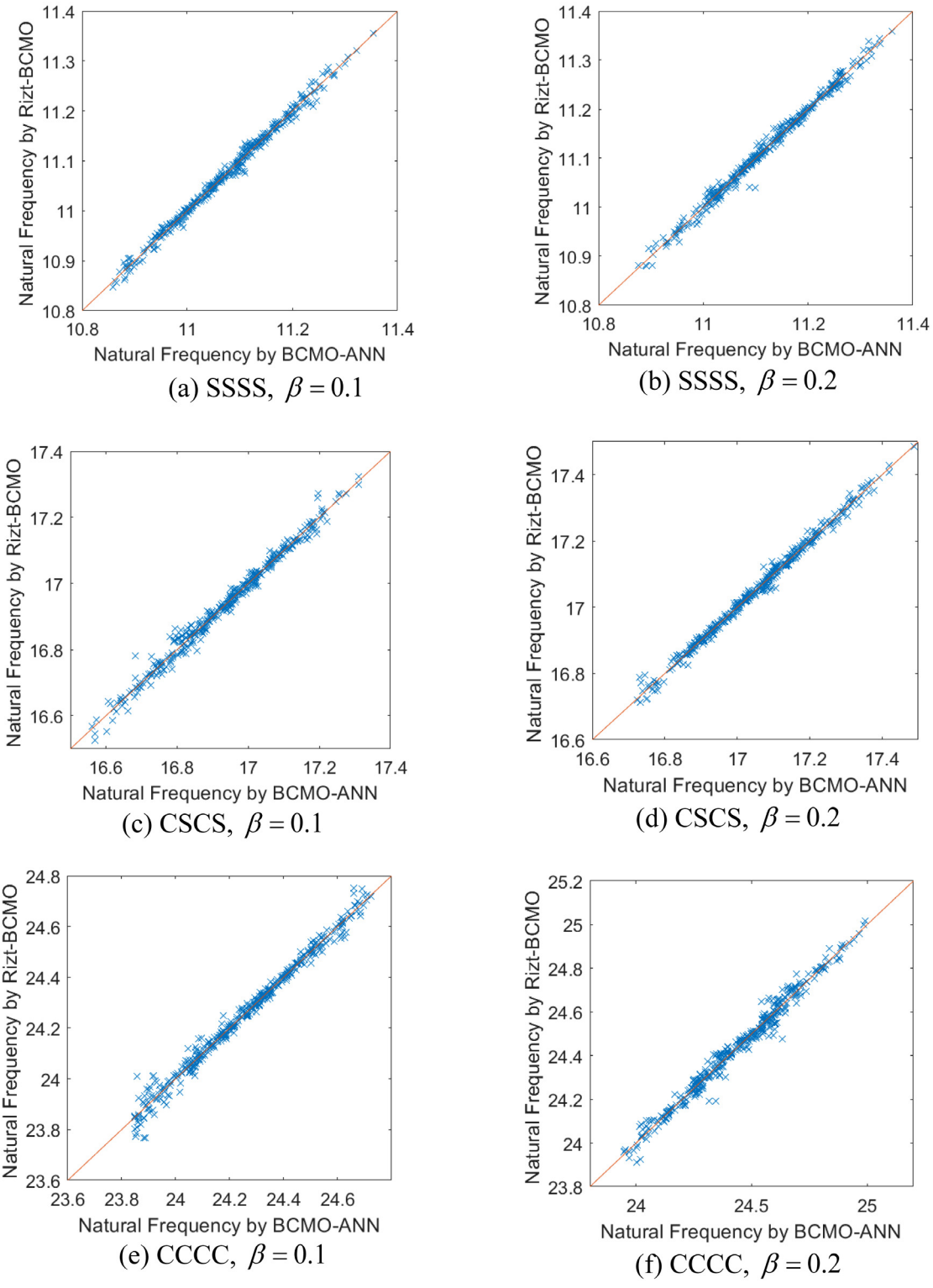

Fig. 4. Scatter plot of the Ritz-BCMO model with ANN-BCMO on the normalized fundamental frequency for FGP microplates with different boundary conditions, $p = 1$, $a/h = 10$ and $h/l = 1$.

boundary condition in which the results are computed with mean material properties, side-to-thickness ratio $a/h = 20$, power-law index $p = 1, 2, 5, 10$, porosity parameter $\beta = 0, 0.2$, and material length scale $h/l = \infty, 10, 5, 2, 1$. The obtained solutions are compared with those from Farzam et al. [16] using a refined HSDT (RPT) and isogeometric approach (IGA). It can be observed that there are good agreements between the two models for all cases. Therefore, the present model shows to be reliable to predict the dynamic behaviors of FGP microplates.

Moreover, in order to investigate stochastic behaviors of FGP microplates, four random variables of material properties ($E_{m,i}$, $E_{c,i}$, $p_{m,i}$,

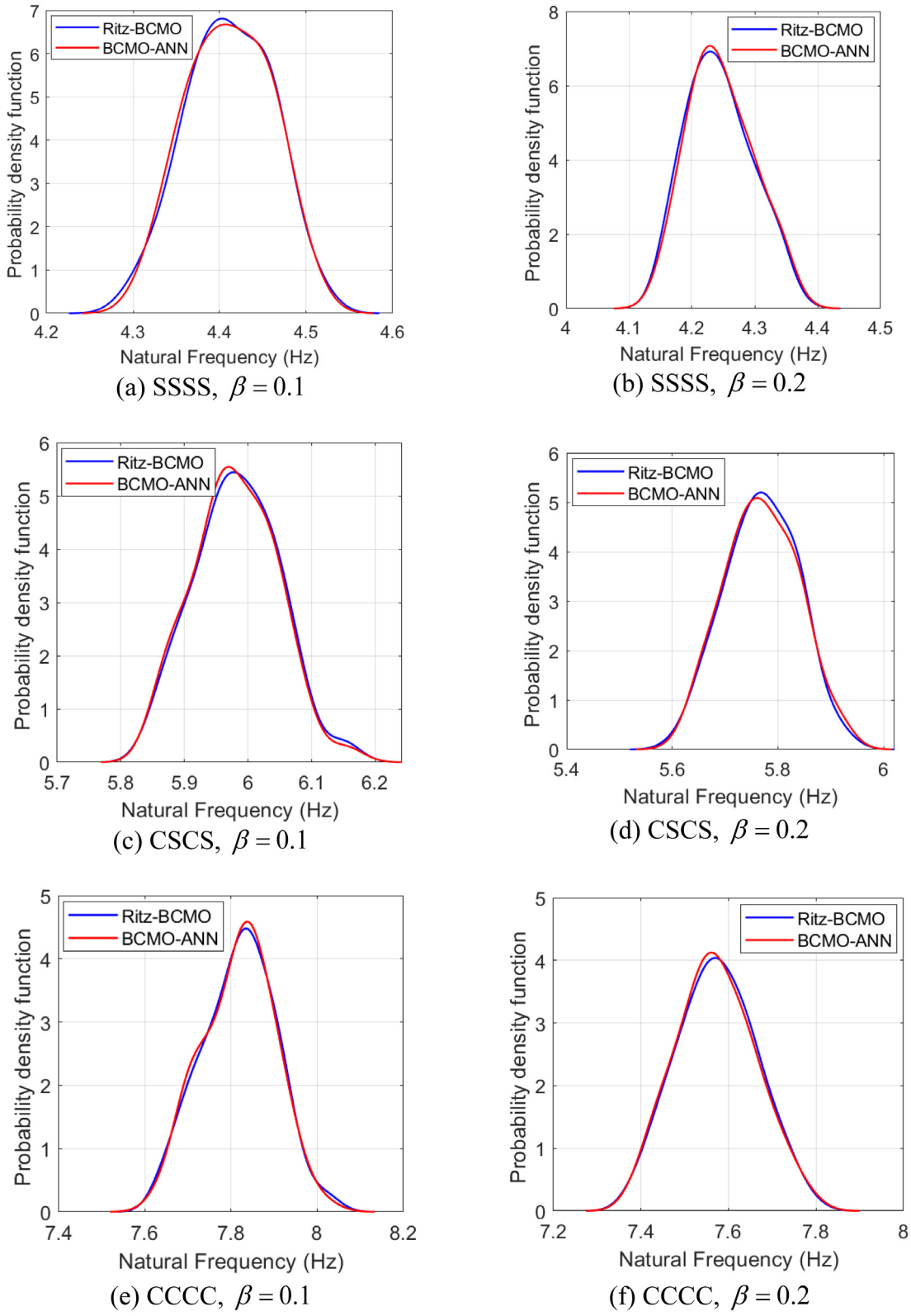

Fig. 5. Probability density function (PDF) of Ritz-BCMO and BCMO-ANN methods for normalized fundamental frequency of FGP microplates with different boundary conditions, $p = 1$, $a/h = 10$ and $h/l = 10$.

$p_{c,i}$) are employed with the population size $NP = 500$. It is noted that the weight and bias values are automatically updated according to Levenberg–Marquardt optimization, the number of nodes in each hidden layer is 21. The dataset, which consists of input–output pairs and training samples are randomly generated through iterations in the ANN training process. In addition, in the prediction process, training samples in the dataset are divided into two groups, in which 80% pairs in data is used for the training set and 20% for the test set. Tables 4–6 present the mean and standard deviation (SD) of normalized fundamental frequencies of Al/Al_2O_3 FGP microplates with different

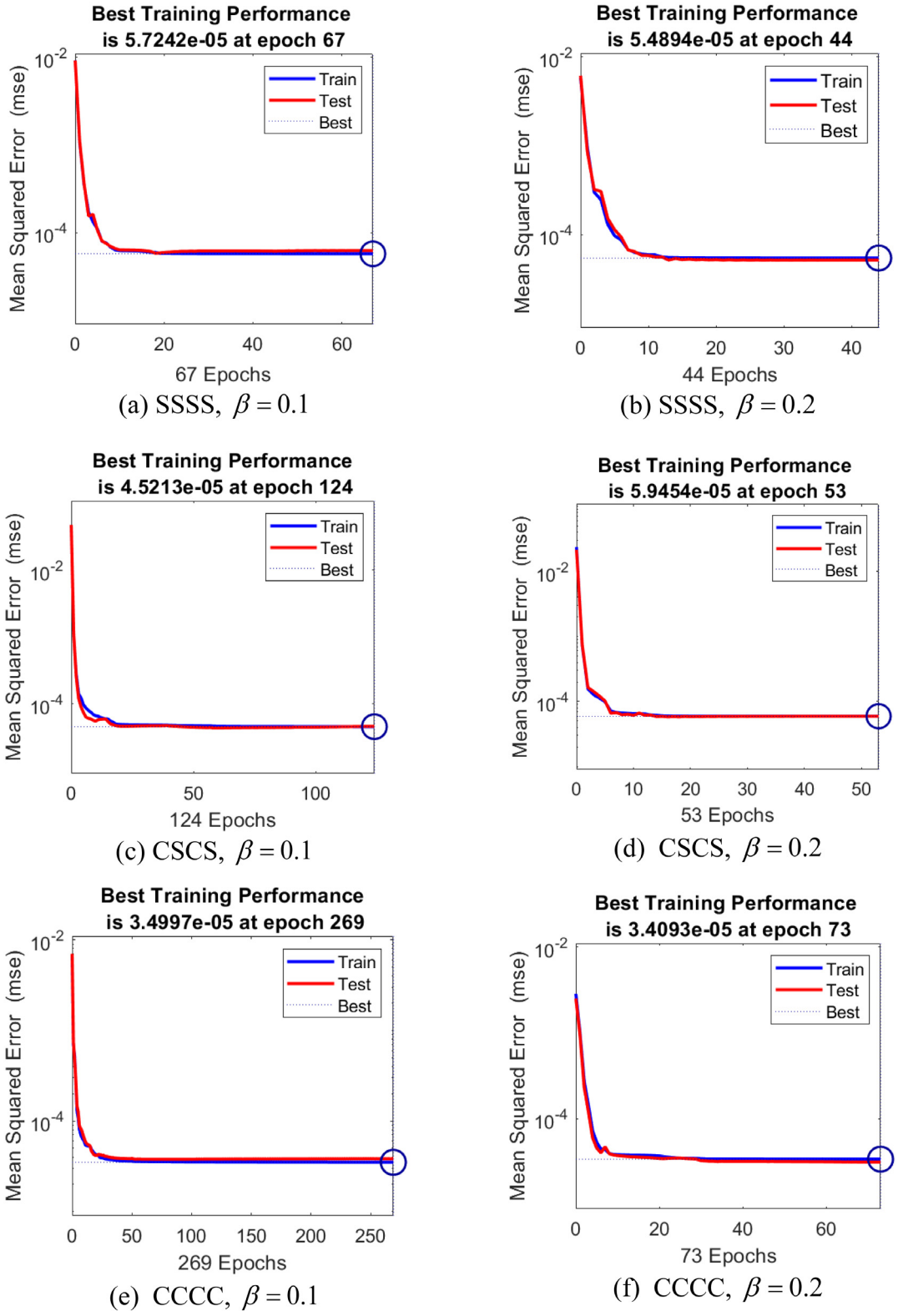

Fig. 6. Loss function of the normalized fundamental frequency for FGP microplates with different boundary conditions, $p = 10$, $a/h = 10$ and $h/l = 5$.

boundary conditions for both Ritz–BCMO and BCMO-ANN models. The solutions are computed with porous parameter $\beta = 0.1$ and 0.2, side-to-thickness ratio $a/h = 10$, two values of the power-law index $p = 1$ and $p = 10$, length scale parameter $h/l = 10$, 5, 1. It can be seen that the statistical moments of normalized fundamental frequencies obtained from the Ritz–BCMO and BCMO-ANN show great agreements in all cases. The mean values of nondimensional fundamental frequencies for both Ritz-BCMO and BCMO-ANN are close to the deterministic result for all BCs, different power-law index p and porosity parameter β. As expected, the natural frequencies decrease with an increase of the porosity density, power-law index and length scale parameter. Regarding the computational cost, it can be observed that the computational

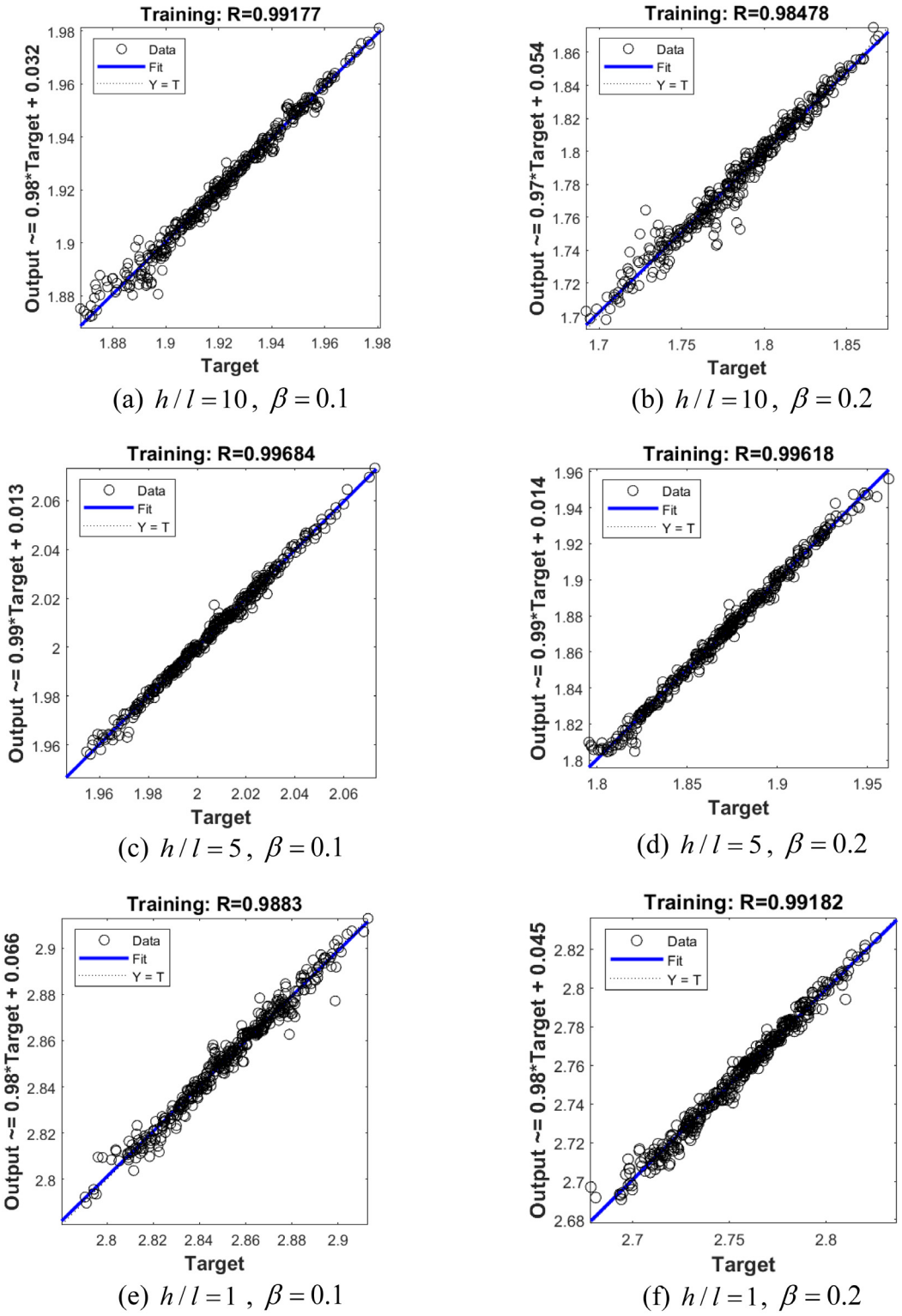

Fig. 7. Regression of the normalized fundamental frequency with log transfer function for FGP microplates with full clamped boundary condition, $p = 10$ and $a/h = 10$.

time required by the present Ritz-BCMO method is about 55 times larger than that by the present BCMO-ANN method.

In order to demonstrate the performance of present model further, Figs. 4 and 5 present the scatter plots and probability density function of the Ritz-BCMO model with BCMO-ANN one of the normalized fundamental frequencies for FGP microplates with different boundary conditions, $p = 1$, $a/h = 10$, $h/l = 1$ and $h/l = 10$, respectively. These graphs indicates that the present BCMO-ANN model can effectively substitute the Ritz-BCMO for stochastic analysis with accuracy and significant saving of computational time. Additionally, Figs. 6 and 7 show the loss function and linear regression of normalized fundamental frequencies of FGP microplates with $p = 10$, $a/h = 10$, $\beta = 0.1$ and 0.2. Obviously, MSE is smaller than 10^{-4} for both the training set and test set.

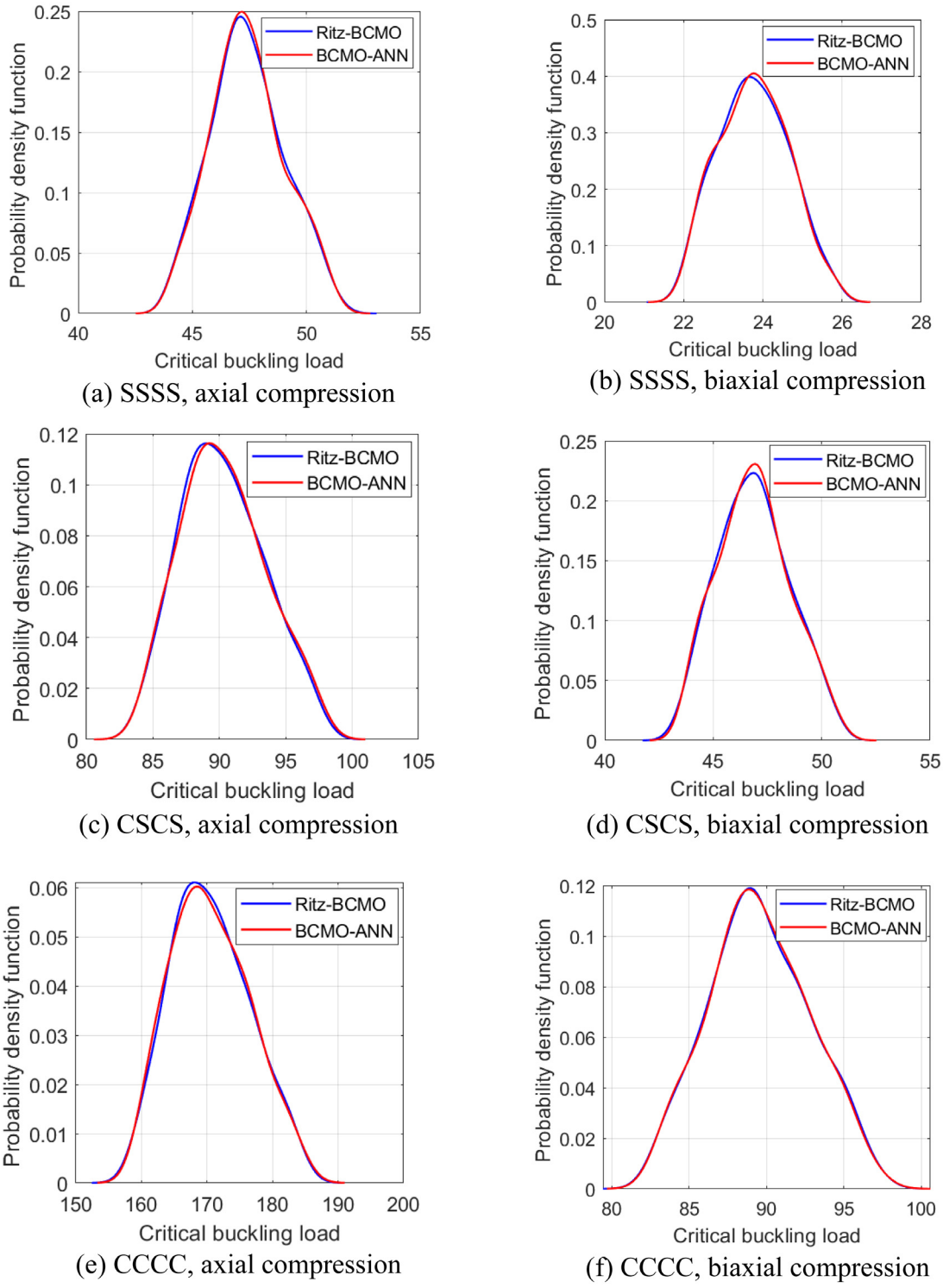

Fig. 8. Probability density function (PDF) of Ritz-BCMO and BCMO-ANN methods for the normalized critical buckling loads of FGP microplates with different boundary conditions, $p = 1$, $a/h = 10$, $h/l = 1$ and $\beta = 0.2$.

5.2. Buckling analysis

The accuracy study of present theory in predicting buckling behaviors is carried out in Table 7, which illustrates nondimensional deterministic critical buckling loads with biaxial compression of Al/Al_2O_3 FGP microplates with clamped boundary conditions on its edges. The results are reported with the side-to-thickness ratio $a/h = 20$, various values of the power-law index $p = 1, 2, 5, 10$, two porous parameters $\beta =$ 0 and 0.2, and compared to those derived from Farzam et al. [16]. It is observed that there are no significant differences between the models, it shows that the present theory is reliable in predicting buckling behaviors of FGP microplates.

Moreover, in order to investigate stochastic buckling behaviors of FGP microplates, two random variables of Young's moduli ($E_{m,i}$, $E_{c,i}$) are supposed to be randomly distributed with the same population size and number of nodes per hidden layer, training sample process as

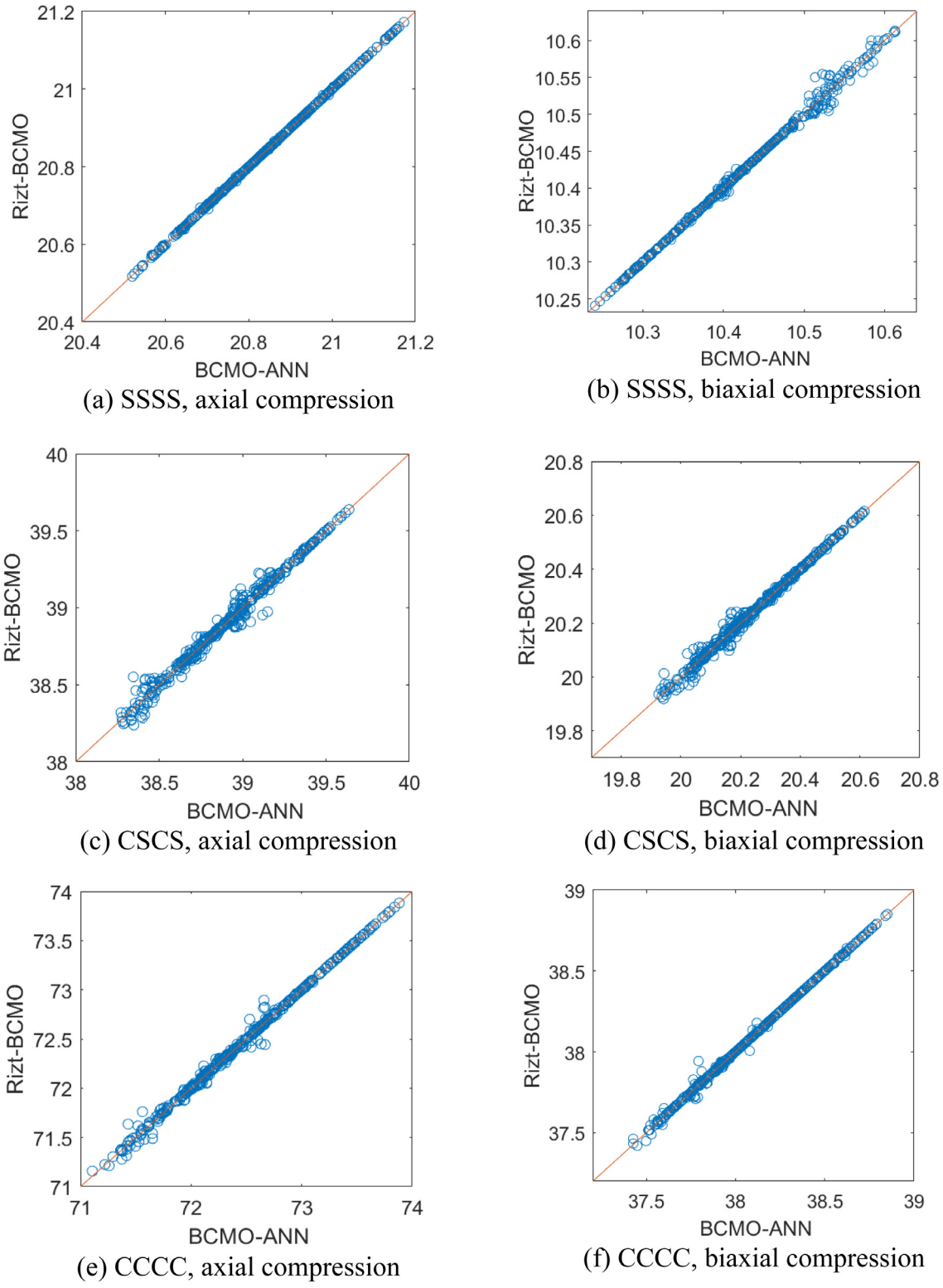

Fig. 9. Prediction of ANN of the normalized critical buckling loads for FGP microplates with different boundary conditions, $p = 10$, $a/h = 10$, $h/l = 1$ and $\beta = 0.1$.

the vibration analysis. Tables 8 and 9 present the mean and standard deviation of normalized critical buckling loads obtained from Ritz-BCMO and BCMO-ANN models for Al/Al_2O_3 FGP microplates with different boundary conditions. The buckling responses are computed for the side-to-thickness ratio $a/h = 10$, porous parameter $\beta = 0.1$ and 0.2, power-law index $p = 1$ and 10, length scale parameter $h/l = 1$ and 10. It can be seen that the statistical moments of the critical buckling loads obtained from the Ritz-BCMO and BCMO-ANN show good agreements in all cases. The mean values of nondimensional critical buckling loads for both Ritz-BCMO and BCMO-ANN are close to the deterministic results for all BCs, different power-law index p and porosity parameter β. Similar to the vibration behaviors, the critical buckling loads decrease with an increase of the porosity density, power-law index and length scale parameter. For the computational

Table 5
Mean and standard deviation (SD) of normalized fundamental frequency for FGP microplates with $a/h = 10$ and CSCS boundary condition.

BCs	β	p	h/l	Theory	Mean	SD	Time (s)	Present
CSCS	0.1	1	10	Ritz-BCMO	5.9709	0.0661	629	5.9773
				BCMO-ANN	5.9776	0.0666	11	
			5	Ritz-BCMO	6.5932	0.0697	628	6.5935
				BCMO-ANN	6.6068	0.0703	12	
			1	Ritz-BCMO	16.9205	0.1596	630	16.9323
				BCMO-ANN	16.9302	0.1595	11	
		10	10	Ritz-BCMO	4.5456	0.1275	628	4.5427
				Ritz-MCS	4.5391	0.1287	11	
			5	Ritz-BCMO	4.8913	0.1382	631	4.9086
				BCMO-ANN	4.9023	0.1370	10	
			1	Ritz-BCMO	11.4432	0.3015	630	11.4652
				BCMO-ANN	11.4558	0.3012	11	
	0.2	1	10	Ritz-BCMO	5.7790	0.0689	620	5.7776
				BCMO-ANN	5.7884	0.0683	11	
			5	Ritz-BCMO	6.4178	0.0737	625	6.4255
				BCMO-ANN	6.4172	0.0736	10	
			1	Ritz-BCMO	17.0373	0.1633	623	17.0376
				BCMO-ANN	17.0405	0.1631	10	
		10	10	Ritz-BCMO	3.8388	0.1654	619	3.8509
				BCMO-ANN	3.8154	0.1669	10	
			5	Ritz-BCMO	4.2145	0.1769	621	4.2046
				BCMO-ANN	4.2134	0.1762	12	
			1	Ritz-BCMO	10.3099	0.3396	623	10.3087
				BCMO-ANN	10.2909	0.3409	11	

Table 6
Mean and standard deviation (SD) of normalized fundamental frequency for FGP microplates with $a/h = 10$ and CCCC boundary condition.

BCs	β	p	h/l	Theory	Mean	SD	Time (s)	Present
CCCC	0.1	1	10	Ritz-BCMO	7.8171	0.0853	626	7.8053
				BCMO-ANN	7.8213	0.0848	11	
			5	Ritz-BCMO	8.7926	0.0918	628	8.7911
				BCMO-ANN	8.8009	0.0916	11	
			1	Ritz-BCMO	24.2602	0.2261	622	24.2394
				BCMO-ANN	24.2660	0.2246	10	
		10	10	Ritz-BCMO	5.8450	0.1658	629	5.8401
				Ritz-MCS	5.8386	0.1659	11	
			5	Ritz-BCMO	6.4137	0.1806	624	6.4284
				BCMO-ANN	6.4515	0.1806	12	
			1	Ritz-BCMO	16.3403	0.4260	630	16.3281
				BCMO-ANN	16.3219	0.4286	12	
	0.2	1	10	Ritz-BCMO	7.5722	0.0897	623	7.5793
				BCMO-ANN	7.5727	0.0884	10	
			5	Ritz-BCMO	8.5922	0.0947	625	8.6040
				BCMO-ANN	8.5938	0.0946	10	
			1	Ritz-BCMO	24.4008	0.2330	619	24.4211
				BCMO-ANN	24.3982	0.2328	12	
		10	10	Ritz-BCMO	4.9445	0.2153	631	4.9617
				BCMO-ANN	4.9350	0.2156	12	
			5	Ritz-BCMO	5.5006	0.2257	630	5.5266
				BCMO-ANN	5.4974	0.2265	12	
			1	Ritz-BCMO	14.6568	0.4808	628	14.7174
				BCMO-ANN	14.6502	0.4800	11	

Table 7
Normalized critical buckling loads of FGP plates with biaxial compression, $a/h = 20$ and CCCC boundary condition.

β	Theory	p			
		1	2	5	10
0	Present	12.5415	9.7627	8.1499	7.3803
	IGA [16]	12.5747	9.7903	8.1821	7.4115
0.2	Present	8.7149	5.5752	3.8308	3.4123
	IGA [16]	8.7341	5.5870	3.8437	3.4270

Table 8
Mean and standard deviation (SD) of normalized critical buckling loads for FGP microplates with axial compression, $a/h = 10$ and different boundary conditions.

BCs	β	p	h/l	Theory	Mean	SD	Time (s)	Present
SSSS	0.1	1	10	Ritz-BCMO	8.3720	0.2417	297	8.3650
				BCMO-ANN	8.3790	0.2436	9	
			1	Ritz-BCMO	52.8194	1.8771	300	52.7334
				BCMO-ANN	52.8290	1.8545	9	
		10	10	Ritz-BCMO	4.2241	0.0116	298	4.2227
				Ritz-MCS	4.2242	0.0116	10	
			1	Ritz-BCMO	20.8353	0.1537	301	20.8252
				BCMO-ANN	20.8384	0.1533	11	
	0.2	1	10	Ritz-BCMO	6.9308	0.1916	305	6.9123
				BCMO-ANN	6.9324	0.1919	10	
			1	Ritz-BCMO	47.4213	1.6199	299	47.3156
				BCMO-ANN	47.4764	1.6166	8	
		10	1	Ritz-BCMO	14.5998	0.1151	306	14.5857
				BCMO-ANN	14.6030	0.1147	9	
CSCS	0.1	1	10	Ritz-BCMO	12.7296	0.3869	304	12.7081
				BCMO-ANN	12.7162	0.3848	9	
			1	Ritz-BCMO	100.2965	3.7066	299	100.0118
				BCMO-ANN	100.1583	3.7333	10	
		10	10	Ritz-BCMO	6.2015	0.0138	298	6.2020
				BCMO-ANN	6.2013	0.0137	10	
			1	Ritz-BCMO	38.8945	0.3129	300	38.8722
				BCMO-ANN	38.9022	0.3105	10	
	0.2	1	10	Ritz-BCMO	10.5596	0.2964	303	10.5590
				BCMO-ANN	10.5602	0.2956	9	
			1	Ritz-BCMO	90.2539	3.1370	302	90.0581
				BCMO-ANN	90.2883	3.1192	9	
		10	1	Ritz-BCMO	27.4031	0.1820	307	27.4193
				BCMO-ANN	27.4036	0.1825	8	
CCCC	0.1	1	10	Ritz-BCMO	19.8302	0.6129	299	19.7962
				BCMO-ANN	19.8289	0.6077	10	
			1	Ritz-BCMO	188.9939	7.0268	301	188.4538
				BCMO-ANN	188.9322	7.0447	9	
		10	10	Ritz-BCMO	9.2737	0.0156	306	9.2742
				BCMO-ANN	9.2735	0.0155	10	
			1	Ritz-BCMO	72.4573	0.5968	304	72.4134
				BCMO-ANN	72.4720	0.5943	108	
	0.2	1	10	Ritz-BCMO	16.5572	0.4758	298	16.5561
				BCMO-ANN	16.5580	0.4750	9	
			1	Ritz-BCMO	170.5385	5.9719	302	170.1653
				BCMO-ANN	170.8541	5.9297	9	
		10	1	Ritz-BCMO	51.2885	0.3034	299	51.3261
				BCMO-ANN	51.2984	0.3020	8	

cost, the BCMO-ANN method again requires less computational time than the Ritz-BCMO method, in which the computational time of the BCMO-ANN method is about 1/30 times that of the Ritz-BCMO one. Furthermore, the performance in predicting buckling responses of the present BCMO-ANN is also illustrated in Figs. 8–11, in which the mean square error is smaller than 10^{-4} for both training and test sets.

6. Conclusions

Optimal behaviors of natural frequencies and critical buckling loads of FGP microplates with uncertainties of material properties has been presented in this paper. It is based on a unified framework of higher-order shear deformation theory and modified couple stress theory for analysis of FGP materials. A combination of BCMO-ANN has been proposed to solve the optimization problems and predict stochastic vibration and buckling behaviors of FGP microplates subjected to uncertainties of material properties. The effects of material distribution, material length scale, porosity density and boundary conditions on natural frequencies and critical buckling loads of FGP microplates have been investigated for both Ritz-BCMO and BCMO-ANN algorithm. Based on the obtained numerical results, the following important points can be derived:

- Hybrid series solutions with exponential shape functions converge quickly, number of series $n = 8$ assure the convergency of the solution field with different boundary conditions.

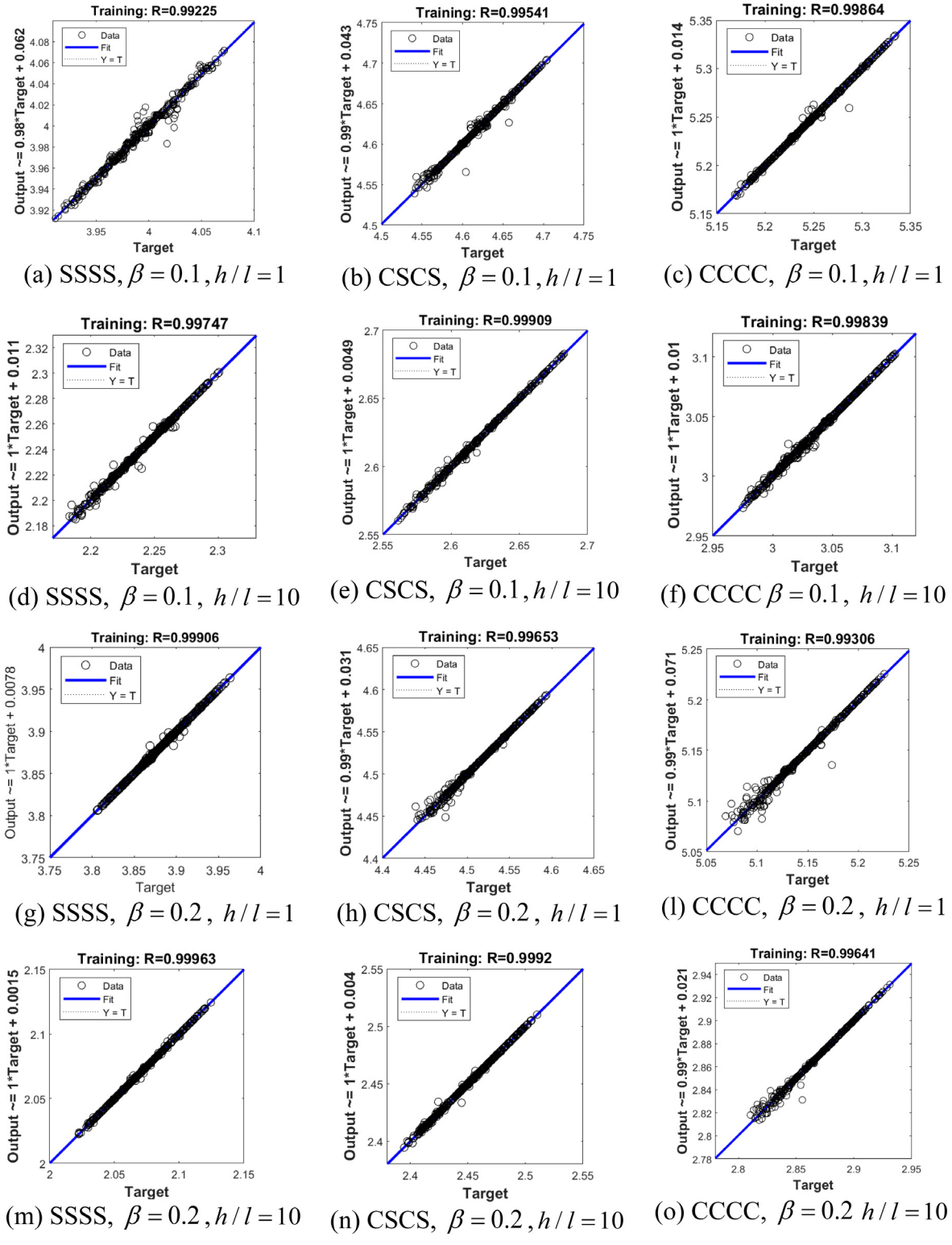

Fig. 10. Regression of the normalized critical buckling loads with log transfer function for FGP microplates with axial compression, different boundary conditions, $p = 1$ and $a/h = 10$.

- Present unified higher-order shear deformation theory and modified couple stress theory are found to be accurate and efficient in predicting stochastic behaviors of FGP microplates.
- Natural frequencies and critical buckling loads decrease with an increase of the porosity density, power-law index and material length scale parameter.
- Proposed BCMO-ANN algorithm allows to significantly save computational costs. The computational time of natural frequencies required by the BCMO-ANN method is about 1/55 times that of the Ritz-BCMO method, the computational time of critical buckling loads by the BCMO-ANN method is about 1/30 times that of the Ritz-BCMO method.

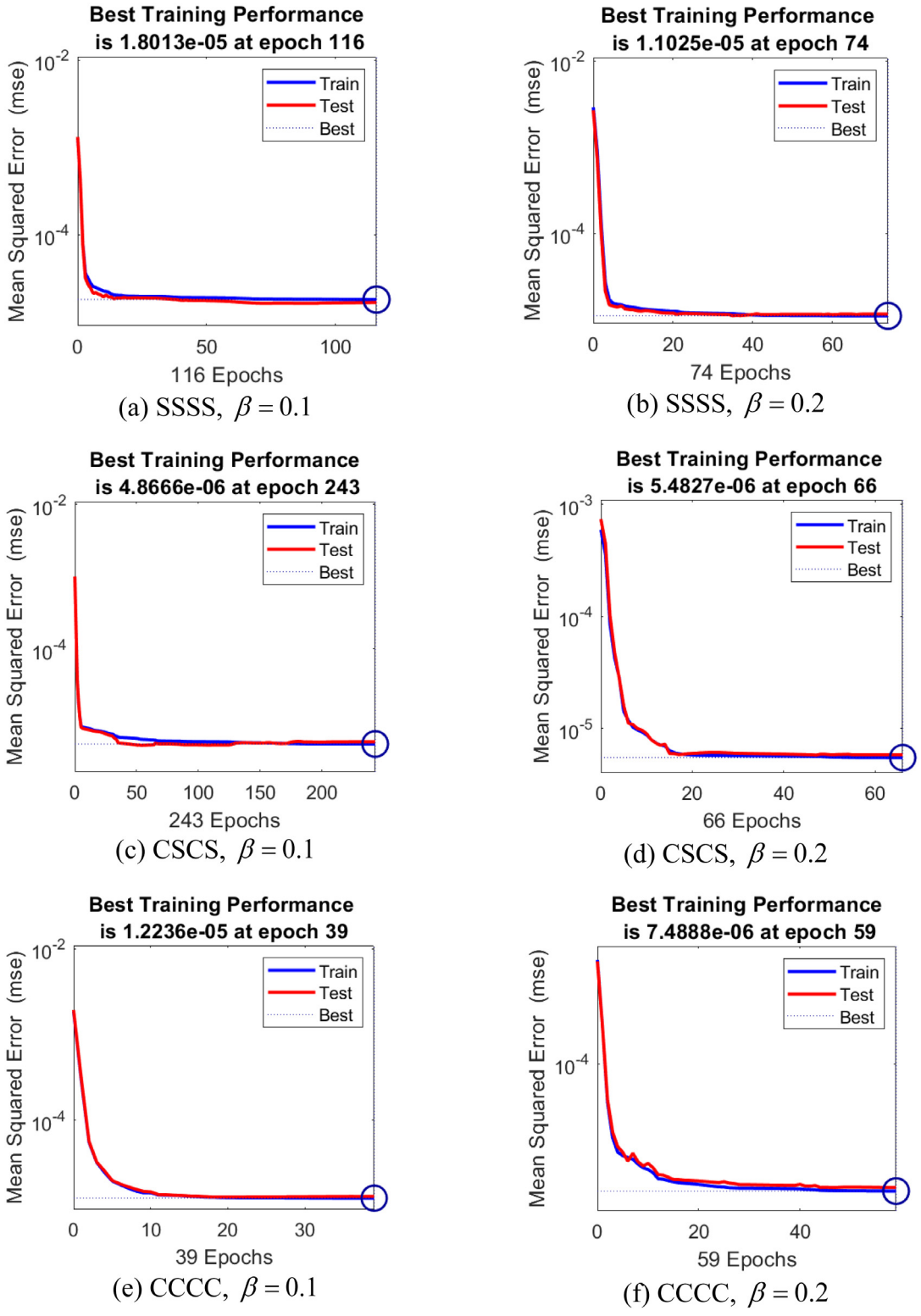

Fig. 11. Loss function of the normalized critical buckling loads with axial compression for FGP microplates with different boundary conditions, $p = 10$, $a/h = 10$ and $h/l = 1$.

CRediT authorship contribution statement

Van-Thien Tran: Writing – original draft, Visualization, Validation, Software, Investigation, Data curation. **Trung-Kien Nguyen:** Writing – review & editing, Writing – original draft, Supervision, Methodology, Conceptualization. **H. Nguyen-Xuan:** Writing – review & editing, Validation, Methodology. **Magd Abdel Wahab:** Writing – review & editing.

Declaration of competing interest

The authors declare that they have no known competing financial interests or personal relationships that could have appeared to influence the work reported in this paper.

Data availability

Data will be made available on request.

Table 9
Mean and standard deviation (SD) of normalized critical buckling loads for FGP microplates with biaxial compression, $a/h = 10$ and different boundary conditions.

BCs	β	p	h/l	Theory	Mean	SD	Time (s)	Present
SSSS	0.1	1	10	Ritz-BCMO	4.1910	0.1248	300	4.1847
				BCMO-ANN	4.1931	0.1244	10	
			1	Ritz-BCMO	26.4796	0.9498	303	26.3915
				BCMO-ANN	26.4859	0.9461	9	
		10	10	Ritz-BCMO	2.1124	0.0055	305	2.1124
				Ritz-MCS	2.1125	0.0054	10	
			1	Ritz-BCMO	10.4221	0.0848	302	10.4126
				BCMO-ANN	10.4204	0.0841	10	
	0.2	1	10	Ritz-BCMO	3.4483	0.1695	300	3.4580
				BCMO-ANN	3.4518	0.1680	9	
			1	Ritz-BCMO	23.7306	0.8426	299	23.6802
				BCMO-ANN	23.7248	0.8419	9	
		10	1	Ritz-BCMO	7.2935	0.0593	307	7.2996
				BCMO-ANN	7.2956	0.0590	10	
CSCS	0.1	1	10	Ritz-BCMO	6.7126	0.1933	301	6.6947
				BCMO-ANN	6.7152	0.1939	9	
			1	Ritz-BCMO	52.1365	1.8639	297	52.0159
				BCMO-ANN	52.1189	1.8692	9	
		10	10	Ritz-BCMO	3.2940	0.0078	302	3.2948
				BCMO-ANN	3.2943	0.0078	10	
			1	Ritz-BCMO	20.2335	0.1634	305	20.2364
				BCMO-ANN	20.2339	0.1624	9	
	0.2	1	10	Ritz-BCMO	5.5669	0.1480	301	5.5564
				BCMO-ANN	5.5687	0.1480	9	
			1	Ritz-BCMO	46.8068	1.7522	303	46.8299
				BCMO-ANN	46.8647	1.7555	8	
		10	1	Ritz-BCMO	14.2630	0.1006	300	14.2691
				BCMO-ANN	14.2676	0.0998	9	
CCCC	0.1	1	10	Ritz-BCMO	10.6631	0.3327	308	10.6407
				BCMO-ANN	10.6714	0.3348	11	
			1	Ritz-BCMO	99.3258	3.7428	304	98.9116
				BCMO-ANN	99.3542	3.7597	10	
		10	10	Ritz-BCMO	5.0716	0.0100	305	5.0732
				BCMO-ANN	5.0714	0.0100	9	
			1	Ritz-BCMO	38.0749	0.3189	301	38.0524
				BCMO-ANN	38.0630	0.3173	10	
	0.2	1	10	Ritz-BCMO	8.9167	0.2517	299	8.8781
				BCMO-ANN	8.9151	0.2516	10	
			1	Ritz-BCMO	89.5446	3.2452	301	89.2872
				BCMO-ANN	89.3834	3.2320	9	
		10	1	Ritz-BCMO	26.9385	0.1637	300	26.9569
				BCMO-ANN	26.9352	0.1641	9	

References

[1] F. Yang, A.C.M. Chong, D.C.C. Lam, P. Tong, Couple stress based strain gradient theory for elasticity, Int. J. Solids Struct. 39 (10) (2002) 2731–2743.

[2] A.C. Eringen, Nonlocal polar elastic continua, Internat. J. Engrg. Sci. 10 (1) (1972) 1–16.

[3] A. Daneshmehr, A. Rajabpoor, A. Hadi, Size dependent free vibration analysis of nanoplates made of functionally graded materials based on nonlocal elasticity theory with high order theories, Internat. J. Engrg. Sci. 95 (2015) 23–35.

[4] A.R. Ashoori, E. Salari, S.A. Sadough Vanini, Size-dependent thermal stability analysis of embedded functionally graded annular nanoplates based on the nonlocal elasticity theory, Int. J. Mech. Sci. 119 (2016) 396–411.

[5] Q.-H. Pham, P.-C. Nguyen, T. Thanh Tran, Dynamic response of porous functionally graded sandwich nanoplates using nonlocal higher-order isogeometric analysis, Compos. Struct. 290 (2022) 115565.

[6] A.M. Zenkour, M.H. Aljadani, Porosity effect on thermal buckling behavior of actuated functionally graded piezoelectric nanoplates, Eur. J. Mech. A Solids 78 (2019) 103835.

[7] S. Dastjerdi, B. Akgöz, New static and dynamic analyses of macro and nano FGM plates using exact three-dimensional elasticity in thermal environment, Compos. Struct. 192 (2018) 626–641.

[8] P. Van Vinh, A. Tounsi, M.-O. Belarbi, On the nonlocal free vibration analysis of functionally graded porous doubly curved shallow nanoshells with variable nonlocal parameters, Eng. Comput. (2022).

[9] O. Rahmani, S.A.H. Hosseini, M. Parhizkari, Buckling of double functionally-graded nanobeam system under axial load based on nonlocal theory: an analytical approach, Microsyst. Technol. 23 (7) (2017) 2739–2751.

[10] S.A.H. Hosseini, O. Rahmani, Exact solution for axial and transverse dynamic response of functionally graded nanobeam under moving constant load based on nonlocal elasticity theory, Meccanica 52 (6) (2017) 1441–1457.

[11] S.A.H. Hosseini, O. Rahmani, Thermomechanical vibration of curved functionally graded nanobeam based on nonlocal elasticity, J. Thermal Stresses 39 (10) (2016) 1252–1267.

[12] H. Darban, R. Luciano, A. Caporale, M. Basista, Modeling of buckling of nanobeams embedded in elastic medium by local-nonlocal stress-driven gradient elasticity theory, Compos. Struct. 297 (2022) 115907.

[13] M. Soltani, A. Soltani, O. Civalek, Interaction of the lateral buckling strength with the axial load for FG micro-sized I-section beam–columns, Thin-Walled Struct. 179 (2022) 109616.

[14] H.M. Numanoğlu, H. Ersoy, B. Akgöz, Ö. Civalek, A new eigenvalue problem solver for thermo-mechanical vibration of Timoshenko nanobeams by an innovative nonlocal finite element method, Math. Methods Appl. Sci. 45 (5) (2022) 2592–2614.

[15] J. Fang, H. Wang, X. Zhang, On size-dependent dynamic behavior of rotating functionally graded Kirchhoff microplates, Int. J. Mech. Sci. 152 (2019) 34–50.

[16] A. Farzam, B. Hassani, Isogeometric analysis of in-plane functionally graded porous microplates using modified couple stress theory, Aerosp. Sci. Technol. 91 (2019) 508–524.

[17] H.X. Nguyen, T.N. Nguyen, M. Abdel-Wahab, S.P.A. Bordas, H. Nguyen-Xuan, T.P. Vo, A refined quasi-3D isogeometric analysis for functionally graded microplates based on the modified couple stress theory, Comput. Methods Appl. Mech. Engrg. 313 (2017) 904–940.

[18] J. Lou, L. He, J. Du, A unified higher order plate theory for functionally graded microplates based on the modified couple stress theory, Compos. Struct. 133 (2015) 1036–1047.

[19] L.C. Trinh, T.P. Vo, H.-T. Thai, J.L. Mantari, Size-dependent behaviour of functionally graded sandwich microplates under mechanical and thermal loads, Composites B 124 (2017) 218–241.

[20] C.H. Thai, A.J.M. Ferreira, P. Phung-Van, Free vibration analysis of functionally graded anisotropic microplates using modified strain gradient theory, Eng. Anal. Bound. Elem. 117 (2020) 284–298.

[21] S. Thai, H.-T. Thai, T.P. Vo, V.I. Patel, Size-dependant behaviour of functionally graded microplates based on the modified strain gradient elasticity theory and isogeometric analysis, Comput. Struct. 190 (2017) 219–241.

[22] S. Sahmani, R. Ansari, On the free vibration response of functionally graded higher-order shear deformable microplates based on the strain gradient elasticity theory, Compos. Struct. 95 (2013) 430–442.

[23] A. Karamanli, T.P. Vo, Size-dependent behaviour of functionally graded sandwich microbeams based on the modified strain gradient theory, Compos. Struct. 246 (2020) 112401.

[24] H. Salehipour, A. Shahsavar, A three dimensional elasticity model for free vibration analysis of functionally graded micro/nano plates: Modified strain gradient theory, Compos. Struct. 206 (2018) 415–424.

[25] V.-T. Tran, T.-K. Nguyen, P.T.T. Nguyen, T.P. Vo, Stochastic vibration and buckling analysis of functionally graded microplates with a unified higher-order shear deformation theory, Thin-Walled Struct. 177 (2022) 109473.

[26] A.G. Shenas, S. Ziaee, P. Malekzadeh, Nonlinear free vibration of rotating FG trapezoidal microplates in thermal environment, Thin-Walled Struct. 170 (2022) 108614.

[27] B. Akgöz, Ö. Civalek, A microstructure-dependent sinusoidal plate model based on the strain gradient elasticity theory, Acta Mech. 226 (7) (2015) 2277–2294.

[28] J. Kim, K. Żur, J.N. Reddy, Bending, free vibration, and buckling of modified couples stress-based functionally graded porous micro-plates, Compos. Struct. (2018) 209.

[29] F. Fan, Y. Xu, S. Sahmani, B. Safaei, Modified couple stress-based geometrically nonlinear oscillations of porous functionally graded microplates using NURBS-based isogeometric approach, Comput. Methods Appl. Mech. Engrg. 372 (2020) 113400.

[30] C.-L. Thanh, L.V. Tran, T.Q. Bui, H.X. Nguyen, M. Abdel-Wahab, Isogeometric analysis for size-dependent nonlinear thermal stability of porous FG microplates, Compos. Struct. 221 (2019) 110838.

[31] L. Guo, X. Xin, D. Shahsavari, B. Karami, Dynamic response of porous E-FGM thick microplate resting on elastic foundation subjected to moving load with acceleration, Thin-Walled Struct. 173 (2022) 108981.

[32] S. Voß, Meta-heuristics: The state of the art, in: Local Search for Planning and Scheduling, Springer Berlin Heidelberg, Berlin, Heidelberg, 2001.

[33] S. Mirjalili, Moth-flame optimization algorithm: A novel nature-inspired heuristic paradigm, Knowl.-Based Syst. 89 (2015) 228–249.

[34] E. Rashedi, H. Nezamabadi-pour, S. Saryazdi, GSA: A gravitational search algorithm, Inform. Sci. 179 (13) (2009) 2232–2248.

[35] X.-S. Yang, Firefly algorithms for multimodal optimization, in: Stochastic Algorithms: Foundations and Applications, Springer Berlin Heidelberg, Berlin, Heidelberg, 2009.

[36] F. Neri, C. Cotta, Memetic algorithms and memetic computing optimization: A literature review, Swarm Evol. Comput. 2 (2012) 1–14.

[37] M. Dorigo, L.M. Gambardella, Ant colony system: a cooperative learning approach to the traveling salesman problem, IEEE Trans. Evol. Comput. 1 (1) (1997) 53–66.

[38] R. Eberhart, J. Kennedy, A new optimizer using particle swarm theory, in: MHS'95. Proceedings of the Sixth International Symposium on Micro Machine and Human Science, 1995.

[39] R. Storn, K. Price, Differential evolution – a simple and efficient heuristic for global optimization over continuous spaces, J. Global Optim. 11 (4) (1997) 341–359.
[40] Z. Michalewicz, Genetic Algorithms + Data Structures = Evolution Programs, Springer Berlin Heidelberg, Berlin, 1996.
[41] G. Dhiman, V. Kumar, Spotted hyena optimizer: A novel bio-inspired based metaheuristic technique for engineering applications, Adv. Eng. Softw. 114 (2017) 48–70.
[42] J.S. Moita, A.L. Araújo, V.F. Correia, C.M. Mota Soares, J. Herskovits, Material distribution and sizing optimization of functionally graded plate-shell structures, Composites B 142 (2018) 263–272.
[43] V.M. Franco Correia, J.F. Aguilar Madeira, A.L. Araújo, C.M. Mota Soares, Multiobjective optimization of ceramic–metal functionally graded plates using a higher order model, Compos. Struct. 183 (2018) 146–160.
[44] Q.X. Lieu, J. Lee, D. Lee, S. Lee, D. Kim, J. Lee, Shape and size optimization of functionally graded sandwich plates using isogeometric analysis and adaptive hybrid evolutionary firefly algorithm, Thin-Walled Struct. 124 (2018) 588–604.
[45] M. Ashjari, M.R. Khoshravan, Mass optimization of functionally graded plate for mechanical loading in the presence of deflection and stress constraints, Compos. Struct. 110 (2014) 118–132.
[46] D.T.T. Do, D. Lee, J. Lee, Material optimization of functionally graded plates using deep neural network and modified symbiotic organisms search for eigenvalue problems, Composites B 159 (2019) 300–326.
[47] P.V. Phuc, C. thai Hoang, M. Abdel Wahab, H. Nguyen-Xuan, Optimal design of FG sandwich nanoplates using size-dependent isogeometric analysis, Mech. Mater. (2019) 142.
[48] E. Taati, N. Sina, Multi-objective optimization of functionally graded materials, thickness and aspect ratio in micro-beams embedded in an elastic medium, Struct. Multidiscip. Optim. 58 (2018) 1–21.
[49] T. Le-Duc, Q.-H. Nguyen, H. Nguyen-Xuan, Balancing composite motion optimization, Inform. Sci. 520 (2020) 250–270.
[50] H. Thanh Duong, H. Chi Phan, T.-T. Le, N. Duc Bui, Optimization design of rectangular concrete-filled steel tube short columns with balancing composite motion optimization and data-driven model, Structures 28 (2020) 757–765.
[51] S. Khatir, S. Tiachacht, C. Le Thanh, E. Ghandourah, S. Mirjalili, M. Abdel Wahab, An improved artificial neural network using arithmetic optimization algorithm for damage assessment in FGM composite plates, Compos. Struct. 273 (2021) 114287.
[52] X. Liu, F. Tao, W. Yu, A neural network enhanced system for learning nonlinear constitutive law and failure initiation criterion of composites using indirectly measurable data, Compos. Struct. 252 (2020) 112658.
[53] B.A. Le, J. Yvonnet, Q.-C. He, Computational homogenization of nonlinear elastic materials using neural networks, Internat. J. Numer. Methods Engrg. 104 (12) (2015) 1061–1084.
[54] X. Lu, D.G. Giovanis, J. Yvonnet, V. Papadopoulos, F. Detrez, J. Bai, A data-driven computational homogenization method based on neural networks for the nonlinear anisotropic electrical response of graphene/polymer nanocomposites, Comput. Mech. 64 (2) (2019) 307–321.
[55] D.Z. Huang, K. Xu, C. Farhat, E. Darve, Learning constitutive relations from indirect observations using deep neural networks, J. Comput. Phys. 416 (2020) 109491.
[56] M. Stoffel, F. Bamer, B. Markert, Artificial neural networks and intelligent finite elements in non-linear structural mechanics, Thin-Walled Struct. 131 (2018) 102–106.
[57] M. Abouhamze, M. Shakeri, Multi-objective stacking sequence optimization of laminated cylindrical panels using a genetic algorithm and neural networks, Compos. Struct. 81 (2) (2007) 253–263.
[58] C. Bisagni, L. Lanzi, Post-buckling optimisation of composite stiffened panels using neural networks, Compos. Struct. 58 (2) (2002) 237–247.
[59] T.T. Tran, P.-C. Nguyen, Q.-H. Pham, Vibration analysis of FGM plates in thermal environment resting on elastic foundation using ES-MITC3 element and prediction of ANN, Case Stud. Therm. Eng. 24 (2021) 100852.
[60] L.H. Yam, Y.J. Yan, J.S. Jiang, Vibration-based damage detection for composite structures using wavelet transform and neural network identification, Compos. Struct. 60 (4) (2003) 403–412.
[61] P.A. Demirhan, V. Taskin, Bending and free vibration analysis of levy-type porous functionally graded plate using state space approach, Composites B 160 (2019) 661–676.
[62] R.D. Mindlin, Influence of couple-stresses on stress concentrations, Exp. Mech. 3 (1) (1963) 1–7.
[63] M. Akbarzadeh Khorshidi, The material length scale parameter used in couple stress theories is not a material constant, Internat. J. Engrg. Sci. 133 (2018) 15–25.
[64] D.C.C. Lam, F. Yang, A.C.M. Chong, J. Wang, P. Tong, Experiments and theory in strain gradient elasticity, J. Mech. Phys. Solids 51 (8) (2003) 1477–1508.
[65] J.L. Mantari, F.G. Canales, Free vibration and buckling of laminated beams via hybrid ritz solution for various penalized boundary conditions, Compos. Struct. 152 (2016) 306–315.
[66] P. Moreno-García, J.V. Dos Santos, H. Lopes, A review and study on ritz method admissible functions with emphasis on buckling and free vibration of isotropic and anisotropic beams and plates, Arch. Comput. Methods Eng. (2017).
[67] T.-K. Nguyen, T. Truong-Phong Nguyen, T.P. Vo, H.-T. Thai, Vibration and buckling analysis of functionally graded sandwich beams by a new higher-order shear deformation theory, Composites B 76 (2015) 273–285.
[68] T.-K. Nguyen, T.P. Vo, B.-D. Nguyen, J. Lee, An analytical solution for buckling and vibration analysis of functionally graded sandwich beams using a quasi-3D shear deformation theory, Compos. Struct. 156 (2016) 238–252.
[69] A. Apicella, F. Donnarumma, F. Isgrò, R. Prevete, A survey on modern trainable activation functions, Neural Netw. 138 (2021) 14–32.
[70] D.W. Marquardt, An algorithm for least-squares estimation of nonlinear parameters, J. Soc. Ind. Appl. Math. 11 (2) (1963) 431–441.
[71] K. Levenberg, A method for the solution of certain non-linear problems in least squares, Quart. Appl. Math. 2 (2) (1944) 164–168.
[72] S. Makridakis, A. Andersen, R. Carbone, R. Fildes, M. Hibon, R. Lewandowski, J. Newton, E. Parzen, R. Winkler, The accuracy of extrapolation (time series) methods: results of a forecasting competition, J. Forecast. 1 (2) (1982) 111–153.

JOURNAL OF THERMAL STRESSES
https://doi.org/10.1080/01495739.2023.2217243

Taylor & Francis
Taylor & Francis Group

Stochastic collocation method for thermal buckling and vibration analysis of functionally graded sandwich microplates

Van-Thien Tran[a], Trung-Kien Nguyen[b], Phong T. T. Nguyen[c], and Thuc P. Vo[d]

[a]Faculty of Civil Engineering, Ho Chi Minh City University of Technology and Education, Ho Chi Minh City, Vietnam; [b]CIRTech Institute, HUTECH University, Ho Chi Minh City, Vietnam; [c]Faculty of International Education, Ho Chi Minh City University of Technology and Education, Ho Chi Minh City, Vietnam; [d]School of Computing, Engineering and Mathematical Sciences, La Trobe University, Bundoora, VIC, Australia

ABSTRACT

Thermal buckling and vibration behaviors of functionally graded (FG) sandwich microplates are investigated by using a unified higher-order shear deformation theory and stochastic collocation (SC) method. Uniform and linear distributions are considered for thermal effect and lognormal distributions are used to characterize the variability of the materials properties. The governing equations are derived by using Hamilton's principle and solved by Ritz's approach. To demonstrate the effectiveness and accuracy of the current model, the results from SC are compared with those from Monte Carlo Simulation. The effects of boundary conditions, temperature distribution, thickness-to-length ratio, material scale characteristics and power-law index on the fundamental frequencies and critical buckling temperature of the FG sandwich microplates are investigated. The FG sandwich microplates' stochastic analysis provides some new findings that may be utilized as references in the future.

ARTICLE HISTORY
Received 18 January 2023
Accepted 28 April 2023

KEYWORDS
FG sandwich microplate; modified couple stress theory; Monte Carlo Simulation; stochastic collocation method; thermal buckling and vibration

1. Introduction

Potential engineering applications for functionally graded (FG) microplates with continually changing in material properties have been investigated in literatures [1–5]. Consequently, several methods have been proposed to consider the effects of small-scale phenomena using various nano- and micro-scale theories [6–9]. These methods with different displacement fields have been used to predict the static and dynamic behaviors of microplates [10–14] and nanostructures [15,16]. Bensaid et al. [17] presented the size-dependent of FG sandwich nanobeams with the Eringen's nonlocal elasticity theory. Daikh et al. [18–20] investigated the bending, free vibration and buckling analysis of sandwich FG nanoplates under different boundary conditions using the higher-order shear deformation theory (HSDT). Besides, temperature environment can have various effects on plates, depending on the material and temperature range it is exposed to. Thus, the study of size-dependent FG microstructures in this environment has been attracted by many researchers. Aria et al. [21] demonstrated the hygro-thermal behavior of FG sandwich microbeams using nonlocal elasticity theory. Shojaeefard et al. [22] used classical plate theory (CPT) and first-order shear deformation theory (FSDT) to investigate the temperature-dependent of FG porous circular microplates under a nonlinear thermal load. Thai et al. [23] analyzed the post-

CONTACT Trung-Kien Nguyen ntkien@hutech.edu.vn CIRTech Institute, HUTECH University, 475A Dien Bien Phu Street, Binh Thanh District, Ho Chi Minh City, Vietnam.

buckling of FG microplates subject to mechanical and thermal loads using isogeometric analysis and third-order shear deformation theory (IGA-TSDT) based on the modified strain gradient theory (MST). Farzam et al. [10] investigated the size-dependent analysis of FG microplates with temperature-dependent material properties using MST and IGA-refined plate theory (RPT). The study of how temperature affects the behavior of FG plates has generated significant interest [24–29]. Zenkour and Sobhy [30] studied the thermal buckling of various types of FG sandwich plates using the sinusoidal shear deformation theory. Fazzolari et al. [31] studied thermal buckling of FG sandwich plates using a refined quasi-3D theory. Daikh et al. [32–37] studied the thermal buckling, bending analysis of FG sandwich beams/plates resting on elastic foundations using a HSDT. The enhanced radial point interpolation mesh-free technique was used by Do et al. [38] to study the thermal buckling of FG sandwich plates. Sahoo et al. [39] investigated nonlinear vibration of FG sandwich structures under thermal loadings. The hydro-thermo-mechanical effects on static responses of FG plates have been studied by Mudhaffar et al. [40] by using a HSDT and Navier method. Daikh et al. [41] studied the thermal buckling of FG sandwich cylindrical shells with the simply supported boundary conditions by using the Donnell theory. It is important to remember that the properties of the material may be uncertain in actuality [42–46], owing to the manufacturing process or other unexpected situations. This uncertainty alters the static and dynamic behaviors of the structures, necessitating the use of sophisticated computational techniques. Almost all FG microplate research [47] has primarily concentrated on deterministic evaluation, disregarding the effect of random material properties. The most common and straightforward approach for addressing this challenging issue is the Monte Carlo Simulation (MCS) method [48], which was used for the laminated composite plates [49–51] and FG plates [52,53]. However, this method can result in high computing costs, especially when a complex physical model is considered. An alternative approach is to use polynomial chaos expansion (PCE), which can accelerate the computation while maintaining accuracy, as a way to overcome the limitations of MCS. The fundamental goal of this technique is to approximate random outputs as a series of basis functions and their corresponding coefficients in orthogonal space. The behaviors of FG plates and laminated composite with material uncertainty have been analyzed using this method [53–61]. Stochastic collocation (SC) [62–64] is known as one of stochastic expansion method similar to the popular PCE. This method allows for the efficient and accurate computation of statistics and solutions of mathematical models that involve stochastic input parameters. It is particularly useful in the field of uncertainty quantification, where it can be used to estimate the propagation of uncertainties in physical systems or to quantify the sensitivity of system response to uncertain parameters. It derives the Lagrange interpolation polynomials for a set of collocation points and reproduces the model responses at these collocation points as of expansion coefficients. After reviewing the literature, it becomes evident that although several studies have been conducted on the random reactions of FG plates, there is still a lack of research on the stochastic behavior of FG sandwich microplates in a temperature environment. Additionally, the SC method has not been extensively applied to address such complex issues. Thus, this paper seeks to fill this gap in previous studies and make unique contributions to the field.

The objective of this study is to propose a stochastic model by combining a general HSDT, SC, and MCT for free vibration and thermal buckling of FG sandwich microplates. The governing equations of motion are derived using Hamilton's principle, and after that, it is solved by the bidirectional series type with hybrid form functions. To assess the accuracy of the proposed SC model, a MCS with ten thousand samples is considered as a reliable benchmark. For various configurations of boundary conditions, material distribution, material uncertainty parameters on the thermal buckling load and fundamental frequencies of the FG sandwich microplates, numerical results are shown.

2. Theoretical formulation

In the coordinate system (x_1, x_2, x_3), the FG sandwich rectangular microplate is considered in Figure 1 with thickness h and sides $a \times b$. The microplate is made up of two FG faces comprised of ceramic-metal components and a homogenous core.

2.1. Material properties and temperature distribution

The following formulas can be used to evaluate the effective material properties of FG sandwich microplates:

$$Q(x_3) = (Q_c - Q_m)V_c(x_3) + Q_m \tag{1}$$

where the volume fraction of the ceramic material $V_c(x_3)$ across the plate thickness is determined by [65]:

$$V_c(x_3) = \begin{cases} \left(\frac{z_4 - x_3}{z_4 - z_3}\right)^p, & z_3 \le x_3 \le z_4 \quad FG \quad top \quad layer \\ 1 & z_2 \le x_3 \le z_3 \quad ceramic \quad core \quad layer \\ \left(\frac{x_3 - z_1}{z_2 - z_1}\right)^p & z_1 \le x_3 \le z_2 \quad FG \quad bottom \quad layer \end{cases} \tag{2}$$

with the power-law index p, Q_c and Q_m are the characteristics of ceramic and metal materials, respectively, such as the Young's moduli E, mass density ρ, and Poisson's ratio ν.

For the effect of the thermal field, two types of distribution temperature are considered as below [31, 66]:

- For uniform distribution (UTR): $T(z) = T_o + \Delta T$, the bottom surface's reference temperature is T_o.
- For linear distribution (LTR): $T(z) = (T_t - T_b)\left(\frac{z}{h} + \frac{1}{2}\right) + T_b$, temperatures at the top and bottom of the plate surface are represented by T_t and T_b, respectively.

2.2. A size-dependent model for FG sandwich microplates

The displacement field using a general HSDT as follows [66]:

$$u_1(x_1, x_2, x_3) = u_1^0(x_1, x_2) + \Phi_2(x_3)\varphi_1(x_1, x_2) + \Phi_1(x_3)u_{3,1}^0 \tag{3a}$$

$$u_2(x_1, x_2, x_3) = u_2^0(x_1, x_2) + \Phi_2(x_3)\varphi_2(x_1, x_2) + \Phi_1(x_3)u_{3,2}^0 \tag{3b}$$

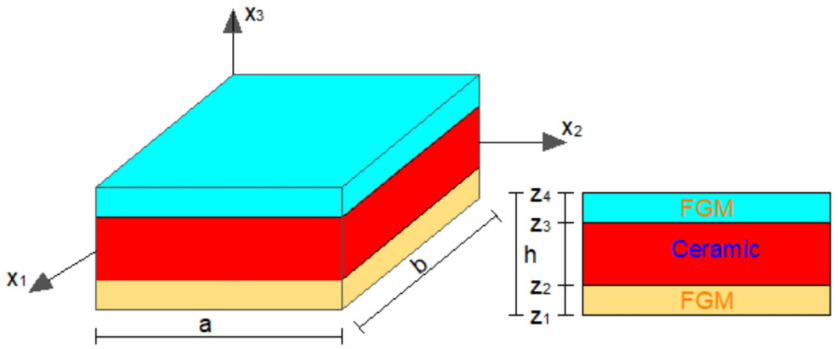

Figure 1. Geometry of a FG sandwich microplate.

$$u_3(x_1, x_2, x_3) = u_3^0(x_1, x_2) \tag{3c}$$

in which $\Phi_1(x_3) = H^s\Psi(x_3) - x_3, \Phi_2(x_3) = H^s\Psi(x_3)$; H^s is the FG sandwich microplates' transverse shear stiffness.

Total potential energy of system can be calculated by using Hamilton's principle:

$$\int_{t_1}^{t_2} (\delta\Pi_{UK} + \delta\Pi_{VK} - \delta\Pi_{KK})dt = 0 \tag{4}$$

where $\delta\Pi_{UK}, \delta\Pi_{KK}, \delta\Pi_{VK}$ are the variations of strain energy, kinetic energy, and work done by membrane compressive forces, respectively.

The variation of strain energy $\delta\Pi_{UK}$ is obtained by the modified couple stress theory (MCT) [8]:

$$\delta\prod\nolimits_{UK} = \int_A (\mathbf{m}\delta\boldsymbol{\chi} + \boldsymbol{\sigma}\delta\boldsymbol{\varepsilon})dA \tag{5}$$

where the high-order stress $\mathbf{m}$ is related to the strain gradients $\boldsymbol{\chi}$, and $\boldsymbol{\sigma}$ is Cauchy stress. The following definitions describe the elements of strain ε_{ij} and strain gradients χ_{ij} :

$$\varepsilon_{ij} = \frac{1}{2}(u_{i,j} + u_{j,i}) \tag{6a}$$

$$\chi_{ij} = \frac{1}{2}\left(\overline{\theta}_{i,j} + \overline{\theta}_{j,i}\right) \tag{6b}$$

$$\overline{\theta}_i = \frac{1}{2}curl(u_i) \tag{6c}$$

The following constitutive equations are used to determine the stress components:

$$\sigma_{ij} = \lambda\varepsilon_{kk}\delta_{ij} + 2\mu\varepsilon_{ij}; m_{ij} = 2\mu l^2\chi_{ij} \tag{7}$$

where λ, μ are Lamé constants; δ_{ij} is Kronecker delta and l is material length scale parameter (MLSP) which is used to measure the effect of coupled stress [67]. MLSP can be determined by experimental works [9] and has value of zero for macro plates.

Substituting Eq. (3) into Eq. (6a), the in-plane and out-of-plane strains $\boldsymbol{\varepsilon}^T = \left[\boldsymbol{\varepsilon}^{(i)} \quad \boldsymbol{\varepsilon}^{(s)}\right]$ are calculated as:

$$\boldsymbol{\varepsilon}^{(i)} = \boldsymbol{\varepsilon}^{(0)} + \Phi_1(x_3)\boldsymbol{\varepsilon}^{(1)} + \Phi_2(x_3)\boldsymbol{\varepsilon}^{(2)};\ \boldsymbol{\varepsilon}^{(s)} = \Phi_3(x_3)\boldsymbol{\varepsilon}^{(3)} \tag{8}$$

where $\Phi_3(x_3) = H^s \times \frac{f_{,3}(x_3)}{\mu(x_3)}$ and,

$$\boldsymbol{\varepsilon}^{(0)} = \begin{Bmatrix} \varepsilon_{11}^{(0)} \\ \varepsilon_{22}^{(0)} \\ \gamma_{12}^{(0)} \end{Bmatrix} = \begin{Bmatrix} u_{1,1}^0 \\ u_{2,2}^0 \\ u_{1,2}^0 + u_{2,1}^0 \end{Bmatrix}, \boldsymbol{\varepsilon}^{(1)} = \begin{Bmatrix} \varepsilon_{11}^{(1)} \\ \varepsilon_{22}^{(1)} \\ \gamma_{12}^{(1)} \end{Bmatrix} = \begin{Bmatrix} u_{3,11}^0 \\ u_{3,22}^0 \\ 2u_{3,12}^0 \end{Bmatrix}, \boldsymbol{\varepsilon}^{(2)} = \begin{Bmatrix} \varepsilon_{11}^{(2)} \\ \varepsilon_{22}^{(2)} \\ \gamma_{12}^{(2)} \end{Bmatrix} = \begin{Bmatrix} \varphi_{1,1} \\ \varphi_{2,2} \\ \varphi_{1,2} + \varphi_{2,1} \end{Bmatrix} \tag{9a}$$

$$\boldsymbol{\varepsilon}^{(3)} = \begin{Bmatrix} \gamma_{13}^{(0)} \\ \gamma_{23}^{(0)} \end{Bmatrix} = \begin{Bmatrix} \varphi_1 + u_{3,1}^0 \\ \varphi_2 + u_{3,2}^0 \end{Bmatrix} \tag{9b}$$

The symmetric rotation gradients are calculated by Eqs. (3) and (6c):

$$\overline{\theta}_1 = \frac{1}{2}(u_{3,2} - u_{2,3}) = \frac{1}{2}\left(u_{3,2}^0 - \Phi_{1,3}u_{3,2}^0 - \Phi_{2,3}\varphi_2\right) \tag{10a}$$

$$\overline{\theta}_2 = \frac{1}{2}(u_{1,3} - u_{3,1}) = \frac{1}{2}\left(-u^0_{3,1} + \Phi_{1,3}u^0_{3,1} + \Phi_{2,3}\varphi_1\right) \tag{10b}$$

$$\overline{\theta}_3 = \frac{1}{2}(u_{2,1} - u_{1,2}) = \frac{1}{2}\left[u^0_{2,1} - u^0_{1,2} + \Phi_2(\varphi_{2,1} - \varphi_{1,2})\right] \tag{10c}$$

The rotation gradients are stated as follows by substituting Eq. (10) into Eq. (6b):

$$\boldsymbol{\chi} = \Phi_2\boldsymbol{\chi}^{(5)} + \Phi_{2,33}\boldsymbol{\chi}^{(4)} + \Phi_{1,33}\boldsymbol{\chi}^{(3)} + \Phi_{2,3}\boldsymbol{\chi}^{(2)} + \Phi_{1,3}\boldsymbol{\chi}^{(1)} + \boldsymbol{\chi}^{(0)} \tag{11}$$

in which $\boldsymbol{\chi}^T = \begin{bmatrix}\chi_{11} & \chi_{22} & 2\chi_{12} & \chi_{33} & 2\chi_{13} & 2\chi_{23}\end{bmatrix}$ and,

$$\boldsymbol{\chi}^{(0)} = \frac{1}{2}\begin{Bmatrix} u^0_{3,12} \\ -u^0_{3,12} \\ u^0_{3,22} - u^0_{3,11} \\ 0 \\ u^0_{2,11} - u^0_{1,12} \\ u^0_{2,12} - u^0_{1,22} \end{Bmatrix},\ \boldsymbol{\chi}^{(1)} = \frac{1}{2}\begin{Bmatrix} -u^0_{3,12} \\ u^0_{3,12} \\ u^0_{3,11} - u^0_{3,22} \\ 0 \\ 0 \\ 0 \end{Bmatrix},\ \boldsymbol{\chi}^{(2)} = \frac{1}{2}\begin{Bmatrix} -\varphi_{2,1} \\ \varphi_{1,2} \\ \varphi_{1,1} - \varphi_{2,2} \\ \varphi_{2,1} - \varphi_{1,2} \\ 0 \\ 0 \end{Bmatrix} \tag{12a}$$

$$\boldsymbol{\chi}^{(3)} = \frac{1}{2}\begin{Bmatrix} 0 \\ 0 \\ 0 \\ 0 \\ -u^0_{3,2} \\ u^0_{3,1} \end{Bmatrix},\ \boldsymbol{\chi}^{(4)} = \frac{1}{2}\begin{Bmatrix} 0 \\ 0 \\ 0 \\ 0 \\ -\varphi_2 \\ \varphi_1 \end{Bmatrix},\ \boldsymbol{\chi}^{(5)} = \frac{1}{2}\begin{Bmatrix} 0 \\ 0 \\ 0 \\ 0 \\ \varphi_{2,11} - \varphi_{1,12} \\ \varphi_{2,12} - \varphi_{1,22} \end{Bmatrix} \tag{12b}$$

Additionally, the following constitutive equations connect the stresses and strains:

$$\boldsymbol{\sigma}^{(i)} = \begin{Bmatrix}\sigma_{11} \\ \sigma_{22} \\ \sigma_{12}\end{Bmatrix} = \begin{bmatrix} Q_{11} & Q_{12} & 0 \\ Q_{12} & Q_{22} & 0 \\ 0 & 0 & Q_{66}\end{bmatrix}\begin{Bmatrix}\varepsilon_{11} \\ \varepsilon_{22} \\ \gamma_{12}\end{Bmatrix} = \mathbf{Q}^{(i)}_{\varepsilon}\boldsymbol{\varepsilon}^{(i)} \tag{13a}$$

$$\boldsymbol{\sigma}^{(o)} = \begin{Bmatrix}\sigma_{13} \\ \sigma_{23}\end{Bmatrix} = \begin{bmatrix} Q_{55} & 0 \\ 0 & Q_{44}\end{bmatrix}\begin{Bmatrix}\gamma_{13} \\ \gamma_{23}\end{Bmatrix} = \mathbf{Q}^{(o)}_{\varepsilon}\boldsymbol{\varepsilon}^{(s)} \tag{13b}$$

$$\mathbf{m} = \begin{Bmatrix} m_{11} \\ m_{22} \\ m_{12} \\ m_{33} \\ m_{23} \\ m_{13} \end{Bmatrix} = 2\mu l^2\begin{bmatrix} 1 & 0 & 0 & 0 & 0 & 0 \\ 0 & 1 & 0 & 0 & 0 & 0 \\ 0 & 0 & 1 & 0 & 0 & 0 \\ 0 & 0 & 0 & 1 & 0 & 0 \\ 0 & 0 & 0 & 0 & 1 & 0 \\ 0 & 0 & 0 & 0 & 0 & 1 \end{bmatrix}\begin{Bmatrix} \chi_{11} \\ \chi_{22} \\ \chi_{12} \\ \chi_{33} \\ \chi_{23} \\ \chi_{13} \end{Bmatrix} = \alpha_\chi \mathbf{I}_{6\times 6}\boldsymbol{\chi} \tag{13c}$$

where $\alpha_\chi = 2\mu l^2$, $Q_{11} = \frac{E(x_3)}{1-\nu^2}$, $Q_{22} = \frac{E(x_3)}{1-\nu^2}$, $Q_{12} = \frac{\nu E(x_3)}{1-\nu^2}$, $Q_{44} = Q_{55} = Q_{66} = \mu = \frac{E(x_3)}{2(1+\nu)}$.

According to Eq. (5), the variation of strain energy varies as follows:

$$\begin{aligned}\delta\prod\nolimits_{UK} &= \int_A (\mathbf{m}\delta\boldsymbol{\chi} + \boldsymbol{\sigma}\delta\boldsymbol{\varepsilon})dA \\ &= \int_A \Big[\mathbf{P}_\varepsilon^{(0)}\delta\boldsymbol{\varepsilon}^{(0)} + \mathbf{P}_\varepsilon^{(1)}\delta\boldsymbol{\varepsilon}^{(1)} + \mathbf{P}_\varepsilon^{(2)}\delta\boldsymbol{\varepsilon}^{(2)} + \mathbf{P}_\varepsilon^{(3)}\delta\boldsymbol{\varepsilon}^{(3)} + \mathbf{P}_\chi^{(0)}\delta\boldsymbol{\chi}^{(0)} \\ &\quad + \mathbf{P}_\chi^{(1)}\delta\boldsymbol{\chi}^{(1)} + \mathbf{P}_\chi^{(2)}\delta\boldsymbol{\chi}^{(2)} + \mathbf{P}_\chi^{(3)}\delta\boldsymbol{\chi}^{(3)} + \mathbf{P}_\chi^{(4)}\delta\boldsymbol{\chi}^{(4)} + \mathbf{P}_\chi^{(5)}\delta\boldsymbol{\chi}^{(5)}\Big]dA\end{aligned} \tag{14}$$

where

$$\left(\mathbf{P}_\varepsilon^{(0)}, \mathbf{P}_\varepsilon^{(1)}, \mathbf{P}_\varepsilon^{(2)}\right) = \int_{-h/2}^{h/2} (1, \Phi_1, \Phi_2)\boldsymbol{\sigma}^{(i)}dx_3; \mathbf{P}_\varepsilon^{(3)} = \int_{-h/2}^{h/2} \Phi_3\boldsymbol{\sigma}^{(o)}dx_3 \tag{15a}$$

$$\left(\mathbf{P}_\chi^{(0)}, \mathbf{P}_\chi^{(1)}, \mathbf{P}_\chi^{(2)}, \mathbf{P}_\chi^{(3)}, \mathbf{P}_\chi^{(4)}, \mathbf{P}_\chi^{(5)}\right) = \int_{-h/2}^{h/2} (1, \Phi_{1,3}, \Phi_{2,3}, \Phi_{1,33}, \Phi_{2,33}, \Phi_2)\mathbf{m}dx_3 \tag{15b}$$

The stress resultants can be defined as follows:

$$\begin{Bmatrix} \mathbf{P}_\varepsilon^{(0)} \\ \mathbf{P}_\varepsilon^{(1)} \\ \mathbf{P}_\varepsilon^{(2)} \\ \mathbf{P}_\varepsilon^{(3)} \end{Bmatrix} = \begin{bmatrix} \mathbf{A}^\varepsilon & \mathbf{B}^\varepsilon & \mathbf{B}_s^\varepsilon & \mathbf{0} \\ \mathbf{B}^\varepsilon & \mathbf{D}^\varepsilon & \mathbf{D}_s^\varepsilon & \mathbf{0} \\ \mathbf{B}_s^\varepsilon & \mathbf{D}_s^\varepsilon & \mathbf{H}_s^\varepsilon & \mathbf{0} \\ \mathbf{0} & \mathbf{0} & \mathbf{0} & \mathbf{A}_s^\varepsilon \end{bmatrix} \begin{Bmatrix} \boldsymbol{\varepsilon}^{(0)} \\ \boldsymbol{\varepsilon}^{(1)} \\ \boldsymbol{\varepsilon}^{(2)} \\ \boldsymbol{\varepsilon}^{(3)} \end{Bmatrix} \tag{16a}$$

$$\begin{Bmatrix} \mathbf{P}_\chi^{(0)} \\ \mathbf{P}_\chi^{(1)} \\ \mathbf{P}_\chi^{(2)} \\ \mathbf{P}_\chi^{(3)} \\ \mathbf{P}_\chi^{(4)} \\ \mathbf{P}_\chi^{(5)} \end{Bmatrix} = \begin{bmatrix} \mathbf{A}^\chi & \overline{\mathbf{B}}^\chi & \overline{\mathbf{B}}_s^\chi & \overline{\overline{\mathbf{B}}}^\chi & \overline{\overline{\mathbf{B}}}_s^\chi & \mathbf{B}_s^\chi \\ \overline{\mathbf{B}}^\chi & \overline{\mathbf{D}}^\chi & \overline{\mathbf{D}}_s^\chi & \overline{\mathbf{E}}^\chi & \overline{\mathbf{E}}_s^\chi & \overline{\mathbf{F}}_s^\chi \\ \overline{\mathbf{B}}_s^\chi & \overline{\mathbf{D}}_s^\chi & \overline{\mathbf{H}}_s^\chi & \overline{\mathbf{G}}_s^\chi & \overline{\mathbf{I}}^\chi & \overline{\mathbf{J}}^\chi \\ \overline{\overline{\mathbf{B}}}^\chi & \overline{\mathbf{E}}^\chi & \overline{\mathbf{G}}_s^\chi & \overline{\overline{\mathbf{D}}}^\chi & \overline{\overline{\mathbf{D}}}_s^\chi & \overline{\mathbf{K}}_s^\chi \\ \overline{\overline{\mathbf{B}}}_s^\chi & \overline{\mathbf{E}}_s^\chi & \overline{\mathbf{I}}^\chi & \overline{\overline{\mathbf{D}}}_s^\chi & \overline{\overline{\mathbf{H}}}_s^\chi & \overline{\mathbf{L}} \\ \mathbf{B}_s^\chi & \overline{\mathbf{F}}_s^\chi & \overline{\mathbf{J}}^\chi & \overline{\mathbf{K}}_s^\chi & \overline{\mathbf{L}} & \mathbf{H}_s^\chi \end{bmatrix} \begin{Bmatrix} \boldsymbol{\chi}^{(0)} \\ \boldsymbol{\chi}^{(1)} \\ \boldsymbol{\chi}^{(2)} \\ \boldsymbol{\chi}^{(3)} \\ \boldsymbol{\chi}^{(4)} \\ \boldsymbol{\chi}^{(5)} \end{Bmatrix} \tag{16b}$$

where the stiffness components are defined by:

$$\left(\mathbf{A}^\varepsilon, \mathbf{B}^\varepsilon, \mathbf{D}^\varepsilon, \mathbf{H}_s^\varepsilon, \mathbf{B}_s^\varepsilon, \mathbf{D}_s^\varepsilon\right) = \int_{-h/2}^{h/2} \left(1, \Phi_1, \Phi_1^2, \Phi_2^2, \Phi_2, \Phi_1\Phi_2\right)\mathbf{Q}_\varepsilon^{(i)}dx_3 \tag{17a}$$

$$\mathbf{A}_s^\varepsilon = \int_{-h/2}^{h/2} \Phi_3^2\mathbf{Q}_\varepsilon^{(o)}dx_3 \tag{17b}$$

$$\begin{aligned}\left(\mathbf{A}^\chi, \overline{\mathbf{B}}^\chi, \overline{\mathbf{B}}_s^\chi, \overline{\overline{\mathbf{B}}}^\chi, \overline{\overline{\mathbf{B}}}_s^\chi, \mathbf{B}_s^\chi\right) &= \left(A^\chi, \overline{B}^\chi, \overline{B}_s^\chi, \overline{\overline{B}}^\chi, \overline{\overline{B}}_s^\chi, B_s^\chi\right)\mathbf{I}_{6\times 6} \\ &= \int_{-h/2}^{h/2} (1, \Phi_{1,3}, \Phi_{2,3}, \Phi_{1,33}, \Phi_{2,33}, \Phi_2)\alpha_\chi\mathbf{I}_{6\times 6}dx_3\end{aligned} \tag{17c}$$

$$\begin{aligned}\left(\overline{\mathbf{D}}^{\chi},\overline{\mathbf{D}}_s^{\chi},\overline{\mathbf{E}}^{\chi},\overline{\mathbf{E}}_s^{\chi},\overline{\mathbf{F}}_s^{\chi}\right) &= \left(\overline{D}^{\chi},\overline{D}_s^{\chi},\overline{E}^{\chi},\overline{E}_s^{\chi},\overline{F}_s^{\chi}\right)\mathbf{I}_{6\times6}\\ &= \int_{-h/2}^{h/2}\Phi_{1,3}(\Phi_{1,3},\Phi_{2,3},\Phi_{1,33},\Phi_{2,33},\Phi_2)\alpha_\chi\mathbf{I}_{6\times6}dx_3\end{aligned} \tag{17d}$$

$$\left(\overline{\mathbf{H}}_s^{\chi},\overline{\mathbf{G}}_s^{\chi},\overline{\mathbf{I}}^{\chi},\overline{\mathbf{J}}^{\chi}\right) = \left(\overline{H}_s^{\chi},\overline{G}_s^{\chi},\overline{I}^{\chi},\overline{J}^{\chi}\right)\mathbf{I}_{6\times6} = \int_{-h/2}^{h/2}\Phi_{2,3}(\Phi_{2,3},\Phi_{1,33},\Phi_{2,33},\Phi_2)\alpha_\chi\mathbf{I}_{6\times6}dx_3 \tag{17e}$$

$$\begin{aligned}\left(\overline{\overline{\mathbf{D}}}^{\chi},\overline{\overline{\mathbf{D}}}_s^{\chi},\overline{\mathbf{K}}_s^{\chi},\overline{\overline{\mathbf{H}}}_s^{\chi},\overline{\mathbf{L}}^{\chi},\mathbf{H}_s^{\chi}\right) &= \left(\overline{\overline{D}}^{\chi},\overline{\overline{D}}_s^{\chi},\overline{K}_s^{\chi},\overline{\overline{H}}_s^{\chi},\overline{L}^{\chi},H_s^{\chi}\right)\mathbf{I}_{6\times6}\\ &= \int_{-h/2}^{h/2}\left(\Phi_{1,33}^2,\Phi_{1,33}\Phi_{2,33},\Phi_{1,33}\Phi_2,\Phi_{2,33}^2,\Phi_{2,33}\Phi_2,\Phi_2^2\right)\alpha_\chi\mathbf{I}_{6\times6}dx_3\end{aligned} \tag{17f}$$

The variation of work produced by in-plane thermal load (N_0^t) as follows:

$$\delta\Pi_{VK} = -\int_A N_0^t\left(u_{3,1}^0\delta u_{3,1}^0 + u_{3,2}^0\delta u_{3,2}^0\right)dA \tag{18}$$

where

$$N_0^t = \int_{z_i}^{z_j}(Q_{11}+Q_{12})\alpha\Delta T dz; \quad i=1,2,3; \quad j=2,3,4 \tag{19}$$

in which α is the coefficient of thermal expansion; $\Delta T = T(z) - T_o$ is the current temperature's deviation from reference one T^o.

The variation of kinetic energy $\delta\prod_{KK}$ is represented as follows:

$$\begin{aligned}\delta\Pi_{KK} &= \frac{1}{2}\int_V \rho(\dot{u}_1\delta\dot{u}_1 + \dot{u}_2\delta\dot{u}_2 + \dot{u}_3\delta\dot{u}_3)dV\\ &= \frac{1}{2}\int_A\Big[I_0\left(\dot{u}_1^0\delta\dot{u}_1^0 + \dot{u}_2^0\delta\dot{u}_2^0 + \dot{u}_3^0\delta\dot{u}_3^0\right) + I_1\left(\dot{u}_1^0\delta\dot{u}_{3,1}^0 + \dot{u}_{3,1}^0\delta\dot{u}_1^0 + \dot{u}_2^0\delta\dot{u}_{3,2}^0 + \dot{u}_{3,2}^0\delta\dot{u}_2^0\right)\\ &\quad + J_2\left(\dot{u}_{3,1}^0\delta\dot{\varphi}_1 + \dot{\varphi}_1\delta\dot{u}_{3,1}^0 + \dot{u}_{3,2}^0\delta\dot{\varphi}_2 + \dot{\varphi}_2\delta\dot{u}_{3,2}^0\right) + K_2(\dot{\varphi}_1\delta\dot{\varphi}_1 + \dot{\varphi}_2\delta\dot{\varphi}_2)\\ &\quad + J_1\left(\dot{u}_1^0\delta\dot{\varphi}_1 + \dot{\varphi}_1\delta\dot{u}_1^0 + \dot{u}_2^0\delta\dot{\varphi}_2 + \dot{\varphi}_2\delta\dot{u}_2^0\right) + I_2\left(\dot{u}_{3,1}^0\delta\dot{u}_{3,1}^0 + \dot{u}_{3,2}^0\delta\dot{u}_{3,2}^0\right)\Big]dA\end{aligned} \tag{20}$$

where $\rho(x_3)$ is mass density; $\dot{u}_1 = u_{1,t}$, $\dot{u}_2 = u_{2,t}$, $\dot{u}_3 = u_{3,t}$ are velocities in x_1-, x_2- and x_3- directions, respectively, and $I_0, I_1, I_2, J_1, J_2, K_2,$ are defined as:

$$(I_0, I_1, I_2, J_1, J_2, K_2) = \int_{-h/2}^{h/2}\left(1, \Phi_1, \Phi_1^2, \Phi_2, \Phi_1\Phi_2, \Phi_2^2\right)\rho dx_3 \tag{21}$$

3. Series of approximation functions of the FG sandwich microplate

According to the Ritz technique, the following series type solution of approximation functions and related series values may be used to represent the transverse and membrane displacements, rotations, $(u_1^0, u_2^0, u_3^0, \varphi_1, \varphi_2)$ of the FG sandwich microplates:

Table 1. The shape function for three types of boundary conditions (BCs).

	Approximation functions	
BCs	$R_j(x_1)$	$P_j(x_2)$
SSSS	$x_1(a-x_1)e^{-\frac{jx_1}{a}}$	$x_2(b-x_2)e^{-\frac{jx_2}{b}}$
CSCS	$x_1^2(a-x_1)e^{-\frac{jx_1}{a}}$	$x_2^2(b-x_2)e^{-\frac{jx_2}{b}}$
CCCC	$x_1^2(a-x_1)^2e^{-\frac{jx_1}{a}}$	$x_2^2(b-x_2)^2e^{-\frac{jx_2}{b}}$

Table 2. Convergence study for critical buckling temperatures analysis of FG sandwich microplates for various BCs ($h/l = 5$, $a/h = 10$, $p = 0.5$) under uniform distribution with biaxial compression.

Solution	Number of series $N = N_1 = N_2$					
	2	4	6	8	10	12
(MAT 1, 1-2-1)						
SSSS	0.9955	0.9777	0.9774	0.9771	0.9770	0.9772
CSCS	1.7221	1.6223	1.6203	1.6198	1.6196	1.6197
CCCC	2.6960	2.6709	2.6639	2.6636	2.6638	2.6637

$$\left\{u_1^0(x_1,x_2,t),\varphi_1(x_1,x_2,t)\right\} = \sum_{i=1}^{N_1}\sum_{j=1}^{N_2}\left\{u_{1ij}(t),x_{ij}(t)\right\}R_{i,1}(x_1)P_j(x_2) \tag{22a}$$

$$\left\{u_2^0(x_1,x_2,t),\varphi_2(x_1,x_2,t)\right\} = \sum_{i=1}^{N_1}\sum_{j=1}^{N_2}\left\{u_{2ij}(t),y_{ij}(t)\right\}R_i(x_1)P_{j,2}(x_2) \tag{22b}$$

$$u_3^0(x_1,x_2,t) = \sum_{i=1}^{N_1}\sum_{j=1}^{N_2}u_{3ij}(t)R_i(x_1)P_j(x_2) \tag{22c}$$

where $u_{1ij}, u_{2ij}, u_{3ij}, x_{ij}, y_{ij}$ are variables that need to be calculated; the shape functions in the x_1- and x_2- directions are represented by $R_i(x_1), P_j(x_2)$. Thus, just two shape functions are required to find five unknowns of the microplate. It should be clearly explained that the shape functions have an impact on the Ritz solution's precision, convergence rates, and numerical instabilities, as detailed in prior research [68–71]. The boundary conditions (BCs) that the clamped (C) and simply-supported (S) ones follow are satisfied by the functions $R_i(x_1)$ and $P_j(x_2)$:

- Simply supported (S): $u_2^0 = u_3^0 = \varphi_2 = 0$ at $x_1 = 0, a$ and $u_1^0 = u_3^0 = \varphi_1 = 0$ at $x_2 = 0, b$
- Clamped (C): $u_1^0 = u_2^0 = u_3^0 = \varphi_1 = \varphi_2 = 0$ at $x_1 = 0, a$ and $x_2 = 0, b$

The following BCs: SSSS, CSCS, and CCCC are produced when S and C are present on the edges of FG sandwich microplates and will be examined in the numerical examples. Table 1 contains a list of the hybrid shape functions $R_i(x_1)$ and $P_j(x_2)$ for the various BCs in this study. The characteristic equations of motion of the FG sandwich microplates are given by substituting Eq. (22) into Eqs. (20), (18), and (5) and then incorporating the outcomes into Eq. (4) as follows:

$$\mathbf{Kd} + \mathbf{M}\ddot{\mathbf{d}} = \mathbf{0} \tag{23}$$

where $\mathbf{d} = \begin{bmatrix}\mathbf{u}_1 & \mathbf{u}_2 & \mathbf{u}_3 & \boldsymbol{\varphi}_1 & \boldsymbol{\varphi}_2\end{bmatrix}^T$ is the displacements vector to be calculated; $\mathbf{K} = \mathbf{K}^{\varepsilon} + \mathbf{K}^{\chi}$ is the stiffness matrix which is made from the symmetric rotation gradients $\mathbf{K}^{\chi}$, strains $\mathbf{K}^{\varepsilon}$ and mass matrix is $\mathbf{M}$. The following details are provided:

Table 3. Non-dimensional critical buckling loads of square SSSS FG sandwich microplates (MAT 2) ($a/h = 10$) with biaxial compression.

p	h/l	Theory	1-0-1	2-1-2	2-1-1	1-1-1	2-2-1	1-2-1
0	∞	Present	6.5028	6.5028	6.5028	6.5028	6.5028	6.5028
		MCT [74]	6.5244	6.5244	6.5244	6.5244	6.5244	6.5244
	5	Present	7.6525	7.6525	7.6525	7.6525	7.6525	7.6525
		MCT [74]	7.6507	7.6507	7.6507	7.6507	7.6507	7.6507
	5/3	Present	16.8490	16.8490	16.8490	16.8490	16.8490	16.8490
		MCT [74]	16.6536	16.6536	16.6536	16.6536	16.6536	16.6536
	1	Present	35.2385	35.2385	35.2385	35.2385	35.2385	35.2385
		MCT [74]	34.6404	34.6404	34.6404	34.6404	34.6404	34.6404
1	∞	Present	2.5838	2.9203	3.0972	3.2326	3.4749	3.7534
		MCT [74]	2.5925	2.9301	3.1077	3.2435	3.4867	3.7662
	5	Present	3.2653	3.6956	3.8959	4.0704	4.3440	4.6693
		MCT [74]	3.2609	3.6906	3.8908	4.0649	4.3383	4.6632
	5/3	Present	8.7161	9.8974	10.2848	10.7723	11.2954	11.9955
		MCT [74]	8.5680	9.7282	10.1120	10.5884	11.1065	11.7939
	1		19.6139	22.2967	23.0585	24.1715	25.1938	26.6433
		MCT [74]	19.0532	21.6545	22.4164	23.4849	24.5068	25.9187
5	∞	Present	1.3294	1.5215	1.7020	1.7900	2.0562	2.3675
		MCT [74]	1.3337	1.5266	1.7077	1.7960	2.0632	2.3756
	5	Present	1.6980	2.0469	2.2664	2.4197	2.7380	3.1275
		MCT [74]	1.6960	2.0445	2.2636	2.4168	2.7346	3.1231
	5/3	Present	4.6463	6.2490	6.7810	7.4568	8.1917	9.2066
		MCT [74]	4.5696	6.1430	6.6668	7.3276	8.0512	9.0429
	1	Present	10.5408	14.6501	15.8069	17.5270	19.0950	21.3603
		MCT [74]	10.2367	14.1766	15.3203	16.9495	18.4979	20.6714
10	∞	Present	1.2439	1.3734	1.5461	1.5976	1.8540	2.1401
		MCT [74]	1.2479	1.3779	1.5514	1.6029	1.8603	2.1474
	5	Present	1.4413	1.7118	1.9372	2.0199	2.3532	2.6647
		MCT [74]	1.4115	1.6816	1.8885	1.9710	2.2723	2.6059
	5/3	Present	3.9196	5.5886	6.1450	6.8379	7.6059	8.6601
		MCT [74]	3.8578	5.4951	6.0425	6.7211	7.4766	8.5067
	1	Present	8.6748	13.0792	14.3174	16.1503	17.8273	20.2462
		MCT [74]	8.4504	12.6622	13.8814	15.6153	17.2662	19.5807

$$\mathbf{K}^{\xi} = \begin{bmatrix} \mathbf{K}^{\xi 11} & \mathbf{K}^{\xi 12} & \mathbf{K}^{\xi 13} & \mathbf{K}^{\xi 14} & \mathbf{K}^{\xi 15} \\ {}^{T}\mathbf{K}^{\xi 12} & \mathbf{K}^{\xi 22} & \mathbf{K}^{\xi 23} & \mathbf{K}^{\xi 24} & \mathbf{K}^{\xi 25} \\ {}^{T}\mathbf{K}^{\xi 13} & {}^{T}\mathbf{K}^{\xi 23} & \mathbf{K}^{\xi 33} & \mathbf{K}^{\xi 34} & \mathbf{K}^{\xi 35} \\ {}^{T}\mathbf{K}^{\xi 14} & {}^{T}\mathbf{K}^{\xi 24} & {}^{T}\mathbf{K}^{\xi 34} & \mathbf{K}^{\xi 44} & \mathbf{K}^{\xi 45} \\ {}^{T}\mathbf{K}^{\xi 15} & {}^{T}\mathbf{K}^{\xi 25} & {}^{T}\mathbf{K}^{\xi 35} & {}^{T}\mathbf{K}^{\xi 45} & \mathbf{K}^{\xi 55} \end{bmatrix} \quad \text{with } \xi = \{\varepsilon, \chi\} \tag{24}$$

where the components of the stiffness matrix $\mathbf{K}^{\xi}$ and mass matrix $\mathbf{M}$ can be found more details in [61].

By solving Eq. (23) with $\mathbf{M} = 0$ and accounting for Eq. (19), it is possible to determine the thermal buckling of the FG sandwich microplates. Their natural frequency ω can be computed using equation: $(\mathbf{K} - \omega^2\mathbf{M})\mathbf{d} = \mathbf{0}$ by designating $\mathbf{d}(t) = \mathbf{d}e^{i\omega t}$ and $i^2 = -1$, which is imaginary unit.

4. Stochastic collocation (SC)

In this paper, material properties are treated as random variables, which leads to random responses of the model, such as fundamental frequency or thermal buckling load. These stochastic responses can be effectively represented using a SC method.

For 1-D problem (i.e., one random input X) and n_i interpolation points, it approximates the stochastic response u by forming the Lagrange functions and estimating the model response at interpolation points $u(q_i)$ as follows [72,73]:

Table 4. Non-dimensional critical buckling temperature $\overline{T}_{cr}$ of square SSSS FG sandwich microplates (MAT 1) under uniform distribution with biaxial compression.

a/h	p	h/l	Theory	1-0-1	2-1-2	2-2-1	1-1-1	1-2-1
5	0.5	∞	Present	2.8652	2.8237	2.8582	2.8263	2.8652
			HPT [30]	–	–	2.8632	2.8322	2.8697
			HPT[32]	2.8707	2.8302	–	2.8322	2.8697
		10	Present	3.0391	2.9952	3.0275	2.9963	3.0336
		5	Present	3.5609	3.5097	3.5356	3.5064	3.5387
		2	Present	7.2172	7.1128	7.0927	7.0784	7.0753
		1	Present	20.2608	19.9707	19.7861	19.8241	19.6944
	2	∞	Present	2.6301	2.3961	2.4177	2.3595	2.4279
			HPT [30]	–	–	2.4183	2.3599	2.4287
			HPT[32]	2.6345	2.3963	–	2.3599	2.4287
		10	Present	2.8142	2.5734	2.5903	2.5336	2.5987
		5	Present	3.3664	3.1055	3.1083	3.0558	3.1111
		2	Present	7.2302	6.8289	6.7329	6.7105	6.6972
		1	Present	21.0124	20.1094	19.6617	19.7458	19.4885
10	0.5	∞	Present	0.8006	0.7895	0.8036	0.7920	0.8072
			HPT [30]	–	–	0.8059	0.7945	0.8092
			HPT[32]	0.8031	0.7922	–	0.7945	0.8092
		10	Present	0.8445	0.8327	0.8464	0.8349	0.8496
		5	Present	0.9761	0.9625	0.9745	0.9636	0.9771
		2	Present	1.8983	1.8713	1.8719	1.8646	1.8694
		1	Present	5.1908	5.1170	5.0767	5.0822	5.0556
	2	∞	Present	0.7169	0.6498	0.6612	0.6414	0.6656
			HPT [30]	–	–	0.6621	0.6423	0.6668
			HPT[32]	0.7178	0.6507	–	0.6423	0.6668
		10	Present	0.7633	0.6945	0.7047	0.6853	0.7089
		5	Present	0.9024	0.8285	0.8351	0.8168	0.8381
		2	Present	1.8758	1.7663	1.7484	1.7374	1.7418
		1	Present	5.1513	5.1143	5.0090	5.0241	4.9683

Table 5. Non-dimensional critical buckling temperature $\overline{T}_{cr}$ of square SSSS FG sandwich microplates under linear distribution with biaxial compression, $T_b = 25^oC$.

a/h	p	h/l	Theory	1-0-1	2-1-2	2-2-1	1-1-1	1-2-1
5	0.5	∞	Present	5.6189	5.5292	5.3622	5.5293	5.5998
			HPT [30]	–	–	5.4417	5.6144	5.6894
			HPT[32]	5.6914	5.6105	–	5.6144	5.6894
		10	Present	5.9600	5.8650	5.6798	5.8620	5.9289
		5	Present	6.9831	6.8723	6.6328	6.8598	6.9160
		2	Present	14.1524	13.9264	13.3052	13.8469	13.8268
		1	Present	39.7280	39.0998	37.1151	38.7782	38.4860
	2	∞	Present	5.1581	4.6895	4.3583	4.6133	4.7424
			HPT [30]	–	–	4.4071	4.6699	4.8074
			HPT[32]	5.2103	4.7427	–	4.6699	4.8074
		10	Present	5.5190	5.0366	4.6695	4.9536	5.0760
		5	Present	6.6017	6.0777	5.6031	5.9745	6.0768
		2	Present	14.1778	13.3634	12.1359	13.1187	13.0802
		1	Present	41.2017	39.3500	35.4382	38.6005	38.0611
10	0.5	∞	Present	1.5708	1.5466	1.5167	1.5502	1.5782
			HPT [30]	–	–	1.4972	1.5391	1.5685
			HPT[32]	1.5562	1.5344	–	1.5391	1.5685
		10	Present	1.6569	1.6313	1.5885	1.6341	1.6613
		5	Present	1.9149	1.8853	1.8289	1.8857	1.9101
		2	Present	3.7231	3.6646	3.5122	3.6483	3.6539
		1	Present	10.1790	10.0190	9.5235	9.9421	9.8801
	2	∞	Present	1.4067	1.2725	1.1925	1.2549	1.3014
			HPT [30]	–	–	1.1731	1.2347	1.2837
			HPT[32]	1.3856	1.2515	–	1.2347	1.2837
		10	Present	1.4976	1.3599	1.2708	1.3406	1.3855
		5	Present	1.7703	1.6221	1.5060	1.5977	1.6376
		2	Present	3.6790	3.4571	3.1521	3.3973	3.4026
		1	Present	10.4936	10.0084	9.0288	9.8221	9.7038

Table 6. Non-dimensional critical buckling temperature $\overline{T}_{cr}$ of square FG sandwich microplates (MAT 1) under uniform distribution with biaxial compression.

BCs	p	h/l	Theory	1-0-1	2-1-2	2-2-1	1-1-1	1-2-1
CSCS	0.5	∞	Present	4.2188	4.1548	4.1877	4.1550	4.1920
		10	Present	4.5793	4.5102	4.5388	4.5036	4.5412
		5	Present	5.6498	5.5657	5.5812	5.5502	5.5776
		2	Present	13.0949	12.9023	12.8237	12.8234	12.7779
		1	Present	39.5812	39.0115	38.5968	38.7035	38.3992
	2	∞	Present	3.9457	3.6089	3.6173	3.5456	3.6242
		10	Present	4.3266	3.9758	3.9747	3.9069	3.9778
		5	Present	5.4591	5.0670	5.0370	4.9780	5.0287
		2	Present	13.3304	12.6528	12.4203	12.4232	12.3328
		1	Present	41.3300	39.6361	38.6845	38.9069	38.3152
CCCC	0.5	∞	Present	6.0403	5.9696	5.9703	5.9712	5.9830
		10	Present	6.7604	6.6550	6.6614	6.6319	6.6559
		5	Present	8.8280	8.6919	8.6757	8.6523	8.6555
		2	Present	23.2428	22.8973	22.6967	22.7331	22.5951
		1	Present	74.4843	73.4092	72.5563	72.8005	72.1597
	2	∞	Present	5.8827	5.3268	5.2999	5.2335	5.2793
		10	Present	6.5364	6.0414	5.9914	5.9246	5.9784
		5	Present	8.7276	8.1530	8.0464	7.9963	8.0113
		2	Present	23.9800	22.8551	22.3528	22.4250	22.1628
		1	Present	78.1686	75.0826	73.1813	73.6825	72.4412
$a/h = 10$								
CSCS	0.5	∞	Present	1.2629	1.2447	1.2646	1.2478	1.2698
		10	Present	1.3546	1.3340	1.3533	1.3364	1.3576
		5	Present	1.6242	1.6010	1.6170	1.6011	1.6198
		2	Present	3.5111	3.4605	3.4532	3.4448	3.4456
		1	Present	10.2315	10.0853	9.9942	10.0122	9.9487
	2	∞	Present	1.1380	1.0329	1.0486	1.0189	1.0553
		10	Present	1.2337	1.1251	1.1384	1.1094	1.1441
		5	Present	1.5198	1.4006	1.4067	1.3799	1.4097
		2	Present	3.5114	3.3192	3.2751	3.2633	3.2585
		1	Present	10.6067	10.1548	9.9316	9.9733	9.8451
CCCC	0.5	$h/l = 1$	Present	1.9793	1.9499	1.9779	1.9508	1.9854
		10	Present	2.1554	2.1239	2.1499	2.1253	2.1541
		5	Present	2.6817	2.6424	2.6614	2.6319	2.6636
		2	Present	6.3550	6.2624	6.2357	6.2286	6.2173
		1	Present	19.4421	19.1633	18.9723	19.0172	18.8798
	2	∞	Present	1.7995	1.6372	1.6558	1.6148	1.6632
		10	Present	1.9849	1.8154	1.8306	1.7888	1.8377
		5	Present	2.5416	2.3515	2.3524	2.3146	2.3540
		2	Present	6.4214	6.0892	5.9919	5.9838	5.9545
		1	Present	20.2446	19.4079	18.9595	19.0571	18.7855

$$u(X) \approx \hat{u}(X) = \sum_{i=1}^{n_i} u(q_i) L_i(q) \tag{25}$$

where q is a standard variable mapping to the physical variable X and for maximizing performance of this approach, q_i are defined as appropriate Gauss quadrature points corresponding to the distribution of q. More specifically, q could be normal, uniform or exponential variable, and q_i are probabilistic Gauss-Hermite, Gauss-Legendre or Gauss-Laguerre quadrature points, respectively. The 1-D Lagrange interpolation $L_i(q)$ is defined as:

$$L_i(q) = \prod_{\substack{j=1 \\ j \neq i}}^{n_i} \frac{q - q_j}{q_i - q_j} \tag{26}$$

A tensor product of 1-D functions is applied to expand the SC approximation to the multi-dimensional space. Particularly, the expansion of d-variable and n_k collocation points for the k^{th} variable can be expressed as:

Table 7. Non-dimensional critical buckling temperature $\overline{T}_{cr}$ of square FG sandwich microplates (MAT 1) under linear distribution with biaxial compression, $T_b = 25^oC$.

BCs	p	h/l	Theory	1-0-1	2-1-2	2-2-1	1-1-1	1-2-1
$a/h = 5$								
CSCS	0.5	∞	Present	8.2731	8.1351	7.8562	8.1208	8.1926
		10	Present	8.9800	8.8310	8.5147	8.8104	8.8749
		5	Present	11.0790	10.8976	10.4700	10.8576	10.9002
		2	Present	25.6773	25.2613	24.0553	25.0843	24.9704
		1	Present	77.6111	76.3782	72.3996	75.7077	75.0373
	2	∞	Present	7.7376	7.0658	6.5206	6.9356	7.0788
		10	Present	8.4844	7.7805	7.1646	7.6383	7.7694
		5	Present	10.7051	9.9158	9.0793	9.7320	9.8218
		2	Present	26.1390	24.7593	22.3865	24.2862	24.0863
		1	Present	81.0401	77.5589	69.7241	76.0570	74.8287
CCCC	0.5	∞	Present	11.3498	11.6886	11.0893	11.5192	11.6801
		10	Present	13.2567	13.0291	12.4996	12.9769	13.0029
		5	Present	17.3110	17.0191	16.2743	16.9250	16.9179
		2	Present	45.5751	44.8296	42.5747	44.4686	44.1542
		1	Present	146.0485	143.7224	140.0998	142.4044	141.0091
	2	∞	Present	11.3820	10.4687	9.5652	10.4857	10.3737
		10	Present	12.8190	11.8248	10.8069	11.5793	11.6859
		5	Present	17.1112	15.9533	14.5040	15.6295	15.6496
		2	Present	47.0206	44.7227	40.2883	43.8378	43.2838
		1	Present	153.2727	146.9189	139.8997	143.0374	141.4751
$a/h = 10$								
CSCS	0.5	∞	Present	2.4771	2.4377	2.3737	2.4416	2.4823
		10	Present	2.6548	2.6122	2.5393	2.6150	2.6538
		5	Present	3.1858	3.1354	2.0526	3.1329	3.1664
		2	Present	6.8856	6.7759	6.4783	6.7391	6.7339
		1	Present	20.0628	19.7461	18.7476	19.5854	19.4417
	2	∞	Present	2.2323	2.0222	1.8907	1.9928	2.0618
		10	Present	2.4200	2.2026	2.0526	2.1697	2.2354
		5	Present	2.9809	2.7417	2.5362	2.6985	2.7540
		2	Present	6.8860	6.4958	5.9037	6.3800	6.3647
		1	Present	20.7985	19.8714	17.9010	19.4970	19.2279
CCCC	0.5	∞	Present	3.8819	3.8270	3.4247	3.8245	3.8766
		10	Present	4.2267	4.1577	4.0323	4.1589	4.2104
		5	Present	5.2592	5.1741	4.9934	5.1644	5.2064
		2	Present	12.4618	12.2613	11.6975	12.1844	12.1503
		1	Present	38.1228	37.5191	35.5885	37.1999	36.8942
	2	∞	Present	3.5242	3.2014	2.9860	3.1533	3.2524
		10	Present	3.8936	3.5540	3.3005	3.4976	3.5894
		5	Present	4.9846	4.6020	4.2407	4.5257	4.5983
		2	Present	12.5920	11.9164	10.8003	11.6984	11.6310
		1	Present	39.6963	37.9774	34.1725	37.2542	36.6881

$$\hat{u}(\mathbf{q}) = \sum_{j_1=1}^{n_1} \ldots \sum_{j_d=1}^{n_d} u\left(q_{j_1}^1, \ldots, q_{j_d}^d\right) \times \left(L_{j_1}^1 \otimes \ldots \otimes L_{j_d}^d\right) \tag{27}$$

where $\mathbf{q} = \left[q^1, q^2, \ldots, q^d\right]^T$ is a vector of random inputs and $L_{j_k}^k = \prod_{\substack{s=1 \\ s \neq j_k}}^{n_k} \frac{q^k - q_s^k}{q_{j_k}^k - q_s^k}$ in which q_s^k is a collocation point of the variable q^k. Note that in this paper, q^k is the standard normal variable and q_s^k is Gauss-Hermite quadrature point. For convenience, the number of quadrature points for each variable is chosen equally such that:

$$n_1 = n_2 = \ldots = n_d = N_{gp} \tag{28}$$

The total number of Gauss point for the full tensor product is $(N_{gp})^d$. Note that in Eq. (27), $u(q_{j_1}^1, \ldots, q_{j_d}^d)$ is the "correct" response achieved from the "right" model by solving Eq. (23). When the SC model is constructed, MCS can perform directly from Eq. (27) to facilitate the probabilistic characteristics of the output, u. The cost for evaluating the approximate u using Eq. (27) is

Table 8. The standard deviation (SD), mean, Skewness, Kurtosis for the biaxial thermal buckling of FG sandwich microplates (MAT 1, $a/h = 10$) under uniform distribution of SC (256 samples) and MCS (10,000 samples).

BCs	p	Theory	Mean	SD	Kurtosis	Skewness	COV (%)	Time (s)	Present
1-1-1									
$h/l = 1$									
SSSS	0.5	SC	5.1240	0.4618	3.7233	0.5720	9.0	35	5.0822
		MCS	5.1272	0.4625	3.7173	0.5728	9.0	345	
	2	SC	5.0582	0.4206	3.3517	0.4612	8.3	40	5.0241
		MCS	5.0586	0.4199	3.3488	0.4622	8.3	337	
CCCC	0.5	SC	19.1480	1.7282	3.6560	0.5447	9.0	40	19.0172
		MCS	19.1660	1.7298	3.6663	0.5463	9.0	333	
	2	SC	19.2059	1.5587	3.3783	0.4601	8.1	41	19.0571
		MCS	19.1902	1.5537	3.3739	0.4625	8.1	338	
$h/l = 5$									
SSSS	0.5	SC	0.9702	0.0896	3.9393	0.4313	9.2	34	0.9636
		MCS	0.9711	0.0889	3.9440	0.4318	9.2	338	
	2	SC	0.8229	0.0758	3.5360	0.4483	9.1	35	0.8168
		MCS	0.8239	0.0753	3.5357	0.4481	9.1	335	
CCCC	0.5	SC	2.6516	0.2388	3.7487	0.6004	9.0	36	2.6319
		MCS	2.6437	0.2373	3.7387	0.6016	9.0	341	
	2	SC	2.3275	0.2043	3.4008	0.4579	8.8	37	2.3146
		MCS	2.3244	0.2038	3.4017	0.4598	8.8	339	
2-1-2									
$h/l = 1$									
SSSS	0.5	SC	5.1575	0.4437	3.6578	0.5488	8.6	33	5.1170
		MCS	5.1630	0.4431	3.6507	0.5451	8.6	330	
	2	SC	5.1476	0.3989	3.3984	0.4576	7.7	35	5.1143
		MCS	5.1497	0.3972	3.3867	0.4550	7.7	336	
CCCC	0.5	SC	19.2746	1.7223	4.0047	0.4794	8.9	36	19.1633
		MCS	19.3199	1.7202	4.0166	0.4751	8.9	337	
	2	SC	19.5098	1.5476	3.7307	0.3735	7.9	34	19.4079
		MCS	19.4620	1.5415	3.7325	0.3733	7.9	339	
$h/l = 5$									
SSSS	0.5	SC	0.9701	0.0848	3.6716	0.4538	8.7	33	0.9625
		MCS	0.9694	0.0845	3.6585	0.4554	8.7	334	
	2	SC	0.8354	0.0738	3.3880	0.3847	8.8	33	0.8285
		MCS	0.8359	0.0740	3.3960	0.3858	8.8	329	
CCCC	0.5	SC	2.6647	0.2316	3.6160	0.5683	8.7	37	2.6424
		MCS	2.6566	0.2312	3.6124	0.5677	8.7	331	
	2	SC	2.3663	0.2010	3.4978	0.4153	8.5	35	2.3515
		MCS	2.3593	0.2001	3.4965	0.4160	8.5	334	

considerably lower than that for the original model in Eq. (23); hence, the total cost when using the SC model may be thought of as simply the cost of $(N_{gp})^d$ truth model runs. To assess the accuracy of the proposed SC model, 10,000 samples of MCS drawn from the original computational model represented in Eq. (23) are also generated. To distinguish between MCS carried out on the SC model (Eq. (27)) and MCS performed with the model in Eq. (23), the former is referred to simply as the SC method. It is demonstrated in the following section that to achieve sufficient accuracy, the computational cost of the SC model is much lower than that of MCS (i.e., $N_{gp}^d = 10,000$). It is also noted that for high-dimensional problems (i.e., the number of random variable, d is large), the SC method is also expensive compared to MCS, then alternative surrogate models with or without dimension reduction techniques should be adopted. This paper only considers four random variables for buckling analysis, six random variables for vibration analysis, and because of its well-known theoretical development, straightforward implementation, the SC approach is employed here.

Table 9. The standard deviation (SD), mean, Skewness, Kurtosis for the biaxial thermal buckling of FG sandwich microplates (MAT 1, $a/h = 10$) under linear distribution of SC (256 samples) and MCS (10,000 samples), $T_b = 25^oC$.

BCs	p	Theory	Mean	SD	Kurtosis	Skewness	COV (%)	Time (s)	Present
1-1-1									
$h/l = 1$									
SSSS	0.5	SC	10.0239	0.8972	3.7410	0.5955	8.9	30	9.9421
		MCS	10.0179	0.8962	3.7306	0.5927	8.9	325	
	2	SC	9.8862	0.8221	3.4865	0.5257	8.3	33	9.8221
		MCS	9.9028	0.8225	3.4923	0.5270	8.3	330	
CCCC	0.5	SC	37.4986	3.3337	3.4160	0.5005	9.0	40	37.1999
		MCS	37.4981	3.3363	3.4145	0.4994	9.0	342	
	2	SC	37.4604	3.1073	3.4426	0.4919	8.3	41	37.2542
		MCS	37.4520	3.1061	3.4461	0.4912	8.3	340	
$h/l = 5$									
SSSS	0.5	SC	1.9025	0.1750	3.5750	0.5379	9.2	31	1.8857
		MCS	1.8990	0.1741	3.5568	0.5388	9.2	331	
	2	SC	1.6121	0.1451	3.4563	0.4883	9.0	32	1.5977
		MCS	1.6120	0.1459	3.4534	0.4870	9.0	343	
CCCC	0.5	SC	5.2057	0.4802	3.7467	0.5627	9.2	35	5.1644
		MCS	5.2083	0.4811	3.7479	0.5611	9.2	339	
	2	SC	4.5258	0.4083	3.5553	0.5651	9.0	33	4.5257
		MCS	4.5315	0.4093	3.5512	0.5664	9.0	342	
2-1-2									
$h/l = 1$									
SSSS	0.5	SC	10.1009	0.8765	3.6702	0.5612	8.7	36	10.0190
		MCS	10.1144	0.8751	3.6789	0.5680	8.7	336	
	2	SC	10.0814	0.7879	3.6023	0.4996	7.8	32	10.0084
		MCS	10.0814	0.7875	3.6088	0.4978	7.8	340	
CCCC	0.5	SC	37.8308	3.2790	3.4421	0.4947	8.7	38	37.5191
		MCS	37.7803	3.2773	3.4489	0.4940	8.7	345	
	2	SC	38.1656	2.9707	3.3935	0.4623	7.8	35	37.9774
		MCS	38.0900	2.9685	3.3911	0.4637	7.8	339	
$h/l = 5$									
SSSS	0.5	SC	1.9006	0.1756	3.6637	0.5696	9.2	32	1.8853
		MCS	1.8996	0.1749	3.6758	0.5677	9.2	330	
	2	SC	1.6355	0.1449	3.4050	0.4536	8.9	31	1.6221
		MCS	1.6344	0.1459	3.4225	0.4503	8.9	342	
CCCC	0.5	SC	5.2082	0.4516	3.6203	0.5790	8.7	37	5.1741
		MCS	5.2046	0.4527	3.6243	0.5781	8.7	336	
	2	SC	4.6453	0.3921	3.2125	0.3540	8.4	33	4.6020
		MCS	4.6464	0.3925	3.2137	0.3433	8.4	335	

5. Numerical examples

In this part, FG sandwich microplates with various BCs are utilized to analyze stochastic thermal buckling and vibration, where the shear function $\Psi(x_3) = \cot^{-1}\left(\frac{h}{x_3}\right) - \frac{16x_3^3}{15h^3}$ [70] is chosen. They are made from a ceramic and metal whose mean material properties are given by:

- MAT 1: ZrO_2 ($E_c = 244.27$ GPa, $\alpha_c = 12.766 \times 10^{-6}$1/C, $\nu_c = 0.3$), $Ti-Al6-4V$ ($E_m = 66.2$ GPa, $\alpha_m = 10.3 \times 10^{-6}$ 1/C, $\nu_m = 0.3$).
- MAT 2: Al_2O_3 ($E_c = 380$ GPa, $\rho_c = 3800$ kg/m^3, $\alpha_c = 7.4 \times 10^{-6}$1/C, $\nu_c = 0.3$), Al ($E_m = 70$ GPa, $\rho_m = 2702$ kg/m^3, $\alpha_m = 23 \times 10^{-6}$1/C, $\nu_m = 0.3$).

The following normalized parameters are used:

$$\overline{\omega} = \frac{\omega a^2}{h}\sqrt{\frac{\rho_0}{E_0}}; \overline{\omega}_T = \frac{\omega a^2}{h}\sqrt{\frac{\rho_m\left(1-\nu_m^2\right)}{E_m}}; (E_0 = 1\text{GPa}, \rho_0 = 1\ \text{kg/m}^3) \tag{29a}$$

Table 10. Comparison of non-dimensional fundamental frequency $\overline{\omega}$ of square SSSS FG sandwich microplates (MAT 2, $a/h = 10$).

p	h/l	Theory	1-0-1	2-1-2	2-1-1	1-1-1	2-2-1	1-2-1
0.5	∞	Present	1.4414	1.4814	1.5044	1.5182	1.5448	1.5728
		MCT [74]	1.4462	1.4861	1.5084	1.5213	1.5492	1.5766
	5	Present	1.5978	1.6412	1.6639	1.6793	1.7059	1.7345
		MCT [74]	1.5987	1.6423	1.6643	1.6788	1.7064	1.7345
	5/3	Present	2.5192	2.5876	2.6090	2.6353	2.6650	2.6996
		MCT [74]	2.5006	2.5667	2.5900	2.6142	2.6437	2.6787
	1	Present	3.7337	3.8305	3.8583	3.8965	3.9337	3.9800
		MCT [74]	3.6872	3.7836	3.8126	3.8488	3.8885	3.9325
1	∞	Present	1.2428	1.3002	1.3330	1.3536	1.3951	1.4398
		MCT [74]	1.2449	1.3019	1.3352	1.3552	1.3975	1.4413
	5	Present	1.3972	1.4622	1.4948	1.5189	1.5610	1.6054
		MCT [74]	1.3963	1.4612	1.4941	1.4941	1.5590	1.6038
	5/3	Present	2.2831	2.3940	2.4305	2.4687	2.5162	2.5745
		MCT [74]	2.2638	2.3729	2.4092	2.4492	2.4950	2.5512
	1	Present	3.4251	3.5941	3.6398	3.7004	3.7575	3.8367
		MCT [74]	3.3769	3.5413	3.5882	3.6486	3.7072	3.7830
5	∞	Present	0.9468	0.9822	1.0308	1.0442	1.1094	1.1739
		MCT [74]	0.9473	0.9832	1.0320	1.0461	1.1105	1.1756
	5	Present	1.0994	1.1394	1.1886	1.2156	1.2796	1.3500
		MCT [74]	1.1083	1.1379	1.1882	1.2136	1.2785	1.3480
	5/3	Present	1.7689	1.9910	2.0574	2.1321	2.2139	2.3144
		MCT [74]	1.7540	1.9730	2.0398	2.1137	2.1944	2.2944
	1	Present	2.6648	3.0474	3.1405	3.2691	3.3784	3.5261
		MCT [74]	2.6261	2.9984	3.0933	3.2160	3.3274	3.4702
10	∞	Present	0.9284	0.9430	0.9922	0.9960	1.0605	1.1229
		MCT [74]	0.9296	0.9443	0.9935	0.9969	1.0625	1.1247
	5	Present	1.0338	1.0924	1.1448	1.1626	1.2313	1.2991
		MCT [74]	1.0326	1.0912	1.1434	1.1619	1.2294	1.2982
	5/3	Present	1.6480	1.9024	1.9786	2.0600	2.1486	2.2601
		MCT [74]	1.6350	1.8863	1.9614	2.0420	2.1309	2.2392
	1	Present	2.4530	2.9105	3.0198	3.1652	3.2897	3.4536
		MCT [74]	2.4205	2.8645	2.9739	3.1138	3.2394	3.3986

$$\overline{N}_{cr} = \frac{N_{cr}a^2}{100h^3E_0}; \overline{T}_{cr} = \Delta T_{cr} \times 10^{-3}, \tag{29b}$$

The material properties (E_c, E_m, ρ_c, ρ_m and α_c, α_m) are taken to be used at random using the lognormal distributions with their coefficient of variation (COV) of 10% as a case-study. The proposed method can work for any continuous probability distributions with different values of COV. It should be mentioned that these distributions must be calibrated using experimental data for real application. The assumptions of lognormal distributions are appropriate for non-negative values. For comparison, 10,000 samples of the MCS are utilized.

Non-dimensional critical buckling temperatures of FG sandwich square microplates with $p = 0.5$, $a/h = 10$ and $h/l = 5$ are shown in Table 2 for the convergence investigation. The number of series in the x_1- and x_2- directions is the same ($N_1 = N_2 = N$) for different BCs. It can be seen that the results converge extremely rapidly, and since $N = 8$ is the requisite number of series to achieve convergence and it is used in the following numerical examples.

5.1. Buckling analysis

The biaxial of non-dimensional deterministic critical buckling loads of SSSS Al/Al_2O_3 microplates (MAT 2) are shown in Table 3 for various values of $a/h = 10$, p and h/l, and compared with those published by Thai et al. [74]. An excellent agreement with earlier ones can be observed. The deterministic critical buckling temperature of SSSS FG sandwich microplates with MAT 1

Table 11. Non-dimensional natural frequency $\overline{\omega}_T$ of square FG sandwich microplates under uniform distribution (MAT 2, $a/h = 10$), $\Delta T = 600^oC$.

p	h/l	Theory	2-1-1	1-1-1	2-2-1	1-2-1	1-8-1
SSSS							
0.5	∞	Present	5.2828	5.5053	5.8330	6.1849	7.5599
	10	Present	5.6804	5.9002	6.2190	6.5494	7.8887
	5	Present	6.7502	6.9571	7.2390	7.5427	8.7866
	1	Present	21.7290	21.9876	22.2244	22.5426	23.5853
1	∞	Present	3.3546	3.7458	4.3526	4.9427	7.0961
	10	Present	3.9058	4.2720	4.8168	5.3696	7.4425
	5	Present	5.2381	5.5431	6.0010	6.4990	8.3592
	1	Present	20.3576	20.7811	21.1600	21.6622	23.2434
2	∞	Present	1.0349	1.3045	2.6476	3.6014	6.6425
	10	Present	1.6559	2.3509	3.3179	4.1329	6.9974
	5	Present	3.6867	4.1199	4.7776	5.4491	7.9550
	1	Present	18.9069	19.5118	20.0411	20.7504	22.9113
CSCS							
0.5	∞	Present	9.2418	9.4377	9.7615	10.0928	11.5272
	10	Present	9.8156	10.0126	10.3226	10.6504	12.0520
	5	Present	11.3549	11.5560	11.8480	12.1655	13.4940
	1	Present	34.1543	34.5217	34.8508	35.2996	36.7173
1	∞	Present	7.4475	7.7481	8.2590	8.7898	10.9900
	10	Present	8.0847	8.3837	8.8720	9.3889	11.5307
	5	Present	9.7417	10.0445	10.4945	10.9918	13.0024
	1	Present	32.1924	32.7971	33.3236	34.0426	36.2349
2	∞	Present	5.6557	6.0253	6.7434	7.4690	10.4629
	10	Present	6.3822	6.7506	7.4232	8.1226	11.0151
	5	Present	8.1803	8.5594	9.1656	9.8283	12.5190
	1	Present	30.0657	30.9575	31.7100	32.7355	35.7494
CCCC							
0.5	∞	Present	13.4057	13.6605	13.9256	14.3084	15.9403
	10	Present	14.2449	14.4422	14.7806	15.1027	16.6347
	5	Present	16.4696	16.7153	17.0222	17.4042	18.8916
	1	Present	49.4877	49.9962	50.4376	51.0499	52.9363
1	∞	Present	11.4477	11.7521	12.3305	12.8608	15.2125
	10	Present	12.3330	12.6339	13.1914	13.6853	16.0937
	5	Present	14.6262	14.9790	15.4730	16.0375	18.2948
	1	Present	46.7919	47.6390	48.3560	49.3432	52.2943
2	∞	Present	9.5184	9.8784	10.5923	11.3128	14.7131
	10	Present	10.4395	10.8537	11.5183	12.2454	15.4720
	5	Present	12.7946	13.2360	13.8757	14.6515	17.7552
	1	Present	43.8247	45.0873	46.1175	47.5447	51.6388

under biaxial compression is also estimated in order to further validate the proposed technique with uniform and linear distribution. The outcomes are compared with those obtained by Zenkour et al. [30] and Daikh et al. [32]. As seen in Tables 4 and 5, the present solutions match well with those from earlier ones. Tables 6 and 7 provide some new results of the thermal buckling of CSCS and CCCC FG sandwich microplates.

Stochastic thermal buckling analysis takes into account four random variables $E_m, E_c,\ \alpha_c,\ \alpha_m$ that are presumptively distributed lognormally with MAT 1 mean values. For the SC model with the Gauss quadrature point $N_{gp} = 4$, only 256 samples are needed. Tables 8 and 9 list the results of the FG sandwich microplates with $h/l = 1$ and $h/l = 5$ for two types of BCs, a/h and p. The statistical moments derived from SC and MCS exhibit strong concordance. It is noted that this case's computing time is around 1/10 of the time required by the direct MCS technique. Again, for both SC and MCS, the mean values of the critical buckling temperature are quite similar to the corresponding deterministic responses.

Table 12. The standard deviation (SD), mean, Skewness, Kurtosis for the natural frequencies $\overline{\omega}_T$ of FG sandwich microplates (1-2-1) under uniform distribution of SC (4096 samples) and MCS (10,000 samples) (MAT 2, $a/h = 10$), $\Delta T = 600^oC$.

BCs	p	Theory	Mean	SD	Kurtosis	Skewness	COV (%)	Time (s)	Present
$h/l = 1$									
SSSS	0.5	SC	22.6602	2.0772	3.1872	0.2472	9.2	101	22.5426
		MCS	22.6515	2.0821	3.2086	0.2464	9.2	1425	
	1	SC	21.7469	1.9354	3.1576	0.2720	8.9	99	21.6622
		MCS	21.7353	1.9309	3.1168	0.2674	8.9	1421	
	2	SC	20.8142	1.7360	3.0883	0.2400	8.3	102	20.7504
		MCS	20.8017	1.7312	3.0987	0.2384	8.3	1427	
CSCS	0.5	SC	35.4451	3.3220	3.1932	0.2635	9.4	100	35.2996
		MCS	35.4430	3.3328	3.1935	0.2667	9.4	1419	
	1	SC	34.1428	2.9795	3.0064	0.1946	8.7	104	34.0426
		MCS	34.1526	2.9763	3.0023	0.1958	8.7	1425	
	2	SC	32.8265	2.7542	3.1626	0.2596	8.4	102	32.7355
		MCS	32.8231	2.7507	3.1633	0.2583	8.4	1426	
CCCC	0.5	SC	51.2987	4.7779	3.0567	0.2155	9.3	103	51.0499
		MCS	51.2902	4.7786	3.0478	0.2161	9.3	1423	
	1	SC	49.5010	4.4544	3.1195	0.2677	9.0	101	49.3432
		MCS	49.5012	4.4578	3.1212	0.2664	9.0	1424	
	2	SC	47.7206	3.9214	3.1770	0.2183	8.2	99	47.5447
		MCS	47.7163	3.9259	3.1798	0.2177	8.2	1427	
$h/l = 5$									
SSSS	0.5	SC	7.5787	0.7032	3.1579	0.2657	9.3	103	7.5427
		MCS	7.5762	0.7048	3.1580	0.2655	9.3	1423	
	1	SC	6.5071	0.5581	2.9883	0.2181	8.6	104	6.4990
		MCS	6.5097	0.5595	2.9870	0.2196	8.6	1422	
	2	SC	5.4565	0.4318	3.1400	0.2212	7.9	105	5.4491
		MCS	5.4497	0.4329	3.1363	0.2222	7.9	1429	
CSCS	0.5	SC	12.2202	1.1289	3.2599	0.3121	9.2	105	12.1655
		MCS	12.2159	1.1254	3.2554	0.3160	9.2	1425	
	1	SC	11.0292	0.9435	3.2227	0.2880	8.6	104	10.9918
		MCS	11.0278	0.9453	3.2207	0.2892	8.6	1427	
	2	SC	9.8561	0.7592	3.1190	0.1959	7.7	102	9.8283
		MCS	9.8528	0.7555	3.1193	0.1952	7.7	1426	
CCCC	0.5	SC	17.4699	1.6109	3.1958	0.2921	9.2	102	17.4042
		MCS	17.4736	1.6157	3.1948	0.2928	9.2	1428	
	1	SC	16.0781	1.3699	3.0924	0.2469	8.5	101	16.0375
		MCS	16.0823	1.3742	3.0888	0.2477	8.5	1425	
	2	SC	14.6956	1.1520	3.1677	0.2234	7.8	104	14.6515
		MCS	14.7067	1.1541	3.1697	0.2241	7.8	1422	

5.2. Vibration analysis

Non-dimensional deterministic fundamental frequencies of SSSS Al/Al_2O_3 sandwich microplates (MAT 2) are shown in Table 10 to demonstrate the correctness of the current theory for vibration analysis. It is noted that the results are computed without temperature effects and validated with those from Thai et al. [74]. Table 11 presents some new results of FG sandwich microplates under uniform temperature distribution for three boundary conditions (SSSS, CSCS, CCCC).

Six random variables ($E_m, E_c, \rho_m, \rho_c,\ \alpha_c,\ \alpha_m$) used in stochastic vibration analysis are assumed to follow lognormal distributions and their mean values are taken from MAT 2. It should be noticed that just 4096 samples are required for the SC model, whereas 10,000 samples are required to estimate the cost of the MCS. Table 12 compares the standard deviation (SD), mean, kurtosis and skewness, which are the first four statistical moments of the natural frequencies as calculated by the SC and MCS models for a range of p and a/h values. It is clear that there is consistently strong agreement between all statistical moments derived from two models. Comparing the current technique to the direct MCS method, the computing time is around 1/14. For all boundary conditions and various values of power index p, the mean fundamental frequency values for SC and MCS are nearly identical to the deterministic values.

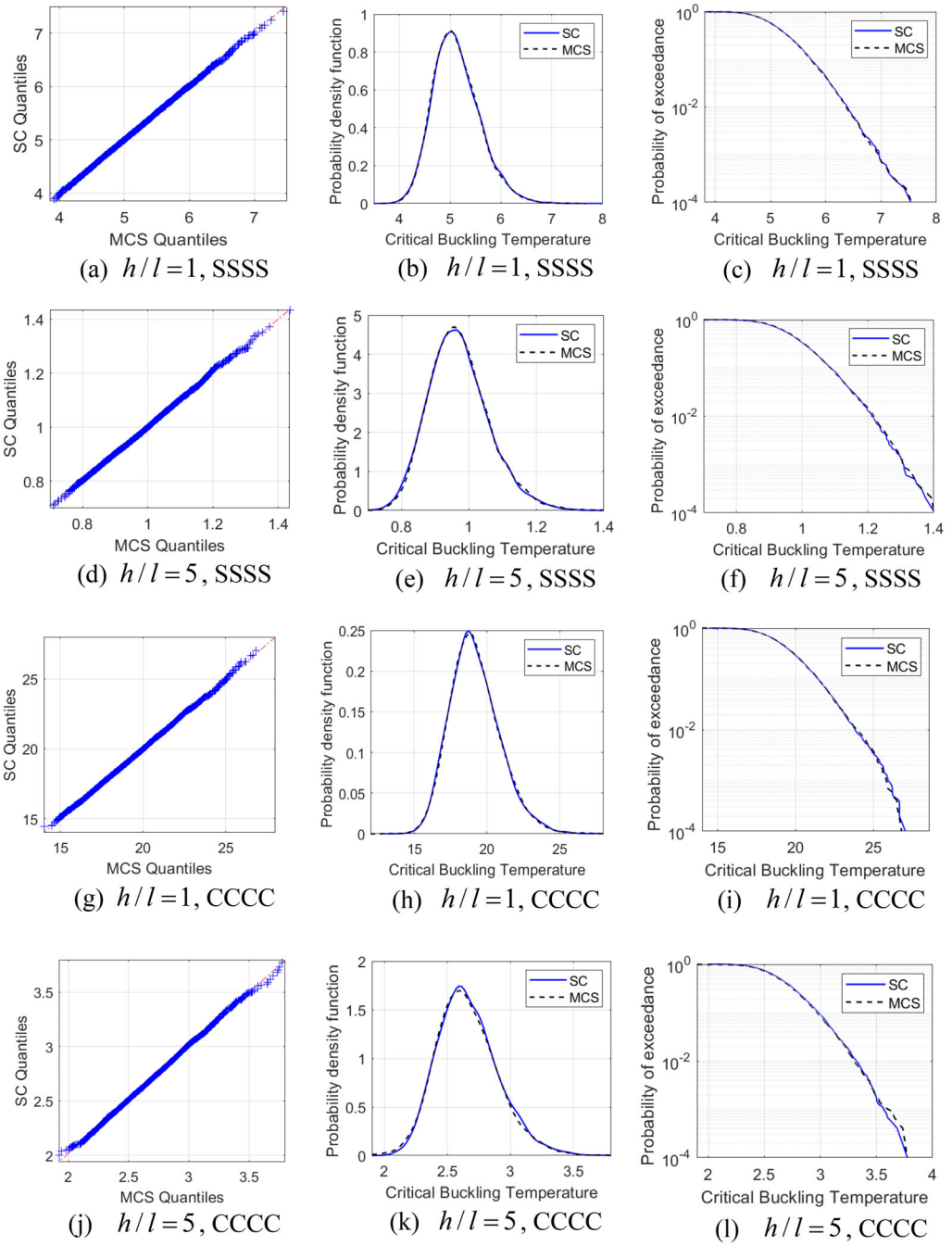

Figure 2. Quantile-quantile, PDF and PoE of MCS and SC for the critical buckling temperature of the (1-1-1) FG sandwich microplates under uniform distribution with SSSS, CCCC BCs (MAT 1, $p=0.5$, $\alpha/h=10$).

5.3. Results of reliability estimation

Figures 2–4 compare the linear quantile–quantile, probability of exceeding (PoE), and probability density function (PDF) of SC and MCS for the fundamental frequency and thermal buckling of the FG sandwich microplates with various BCs. It is clear that the SC method offers a feasible

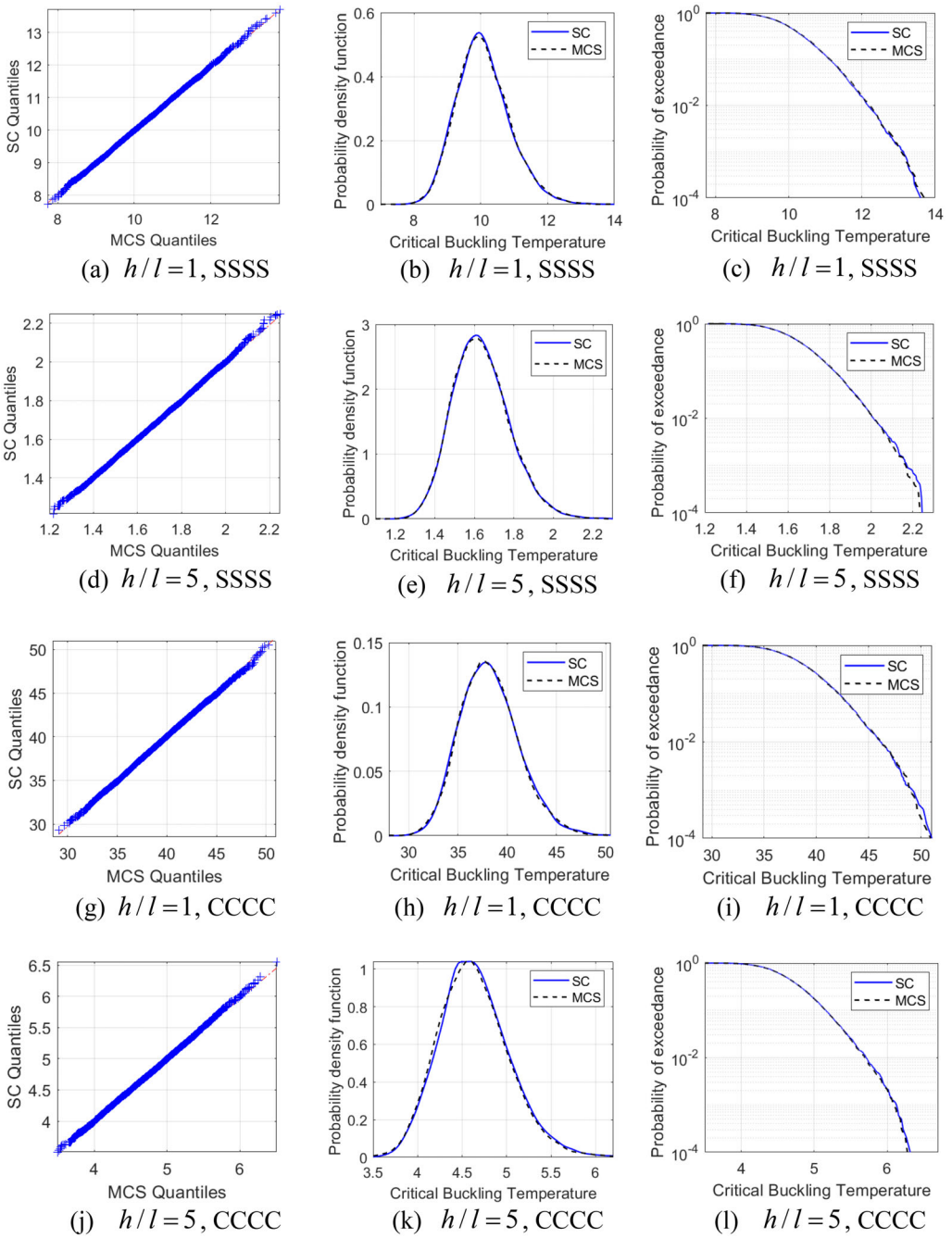

Figure 3. Quantile-quantile, PDF and PoE of MCS and SC for the critical buckling temperature of the (2-1-2) FG sandwich microplates under linear distribution with SSSS, CCCC BCs (MAT 1, $p=2$, $\alpha/h=10$).

alternative approach for simulating the uncertainties of various material characteristics. A decrease in frequency and critical buckling temperature is observed with an increase in the material length scale parameter with $h/l=\infty$ being the minimal value (Figure 5). Additionally, this graph interestingly shows that a decrease of h/l leads to the uncertainty expansion of the frequency and critical buckling temperature. It is interesting to see in Figure 6 that when p

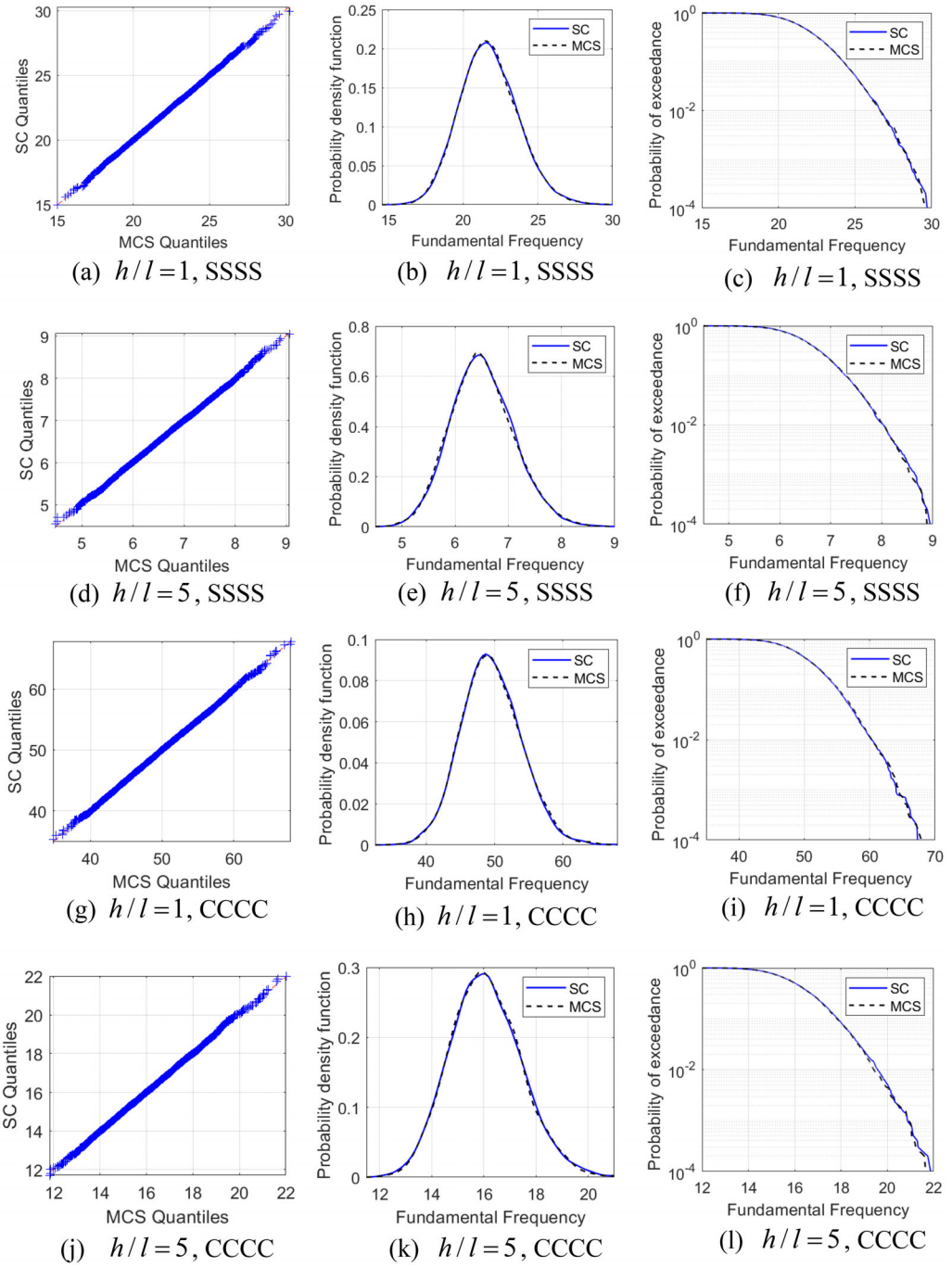

Figure 4. Quantile-quantile, PDF and PoE of MCS and SC for the free vibration of the (1-2-1) FG sandwich microplates under uniform distribution with SSSS, CCCC BCs (MAT 2, $p=1$, $\alpha/h=10$).

decreases, the frequency and thermal buckling uncertainty appears to expand. It is similar when comparing the COV of these stochastic responses in Figure 7. It is worth noting that even when maintaining a constant COV of the input random variables, the fundamental frequency's COV drops as p increases. As p rises, the COV of stochastic thermal buckling temperatures falls.

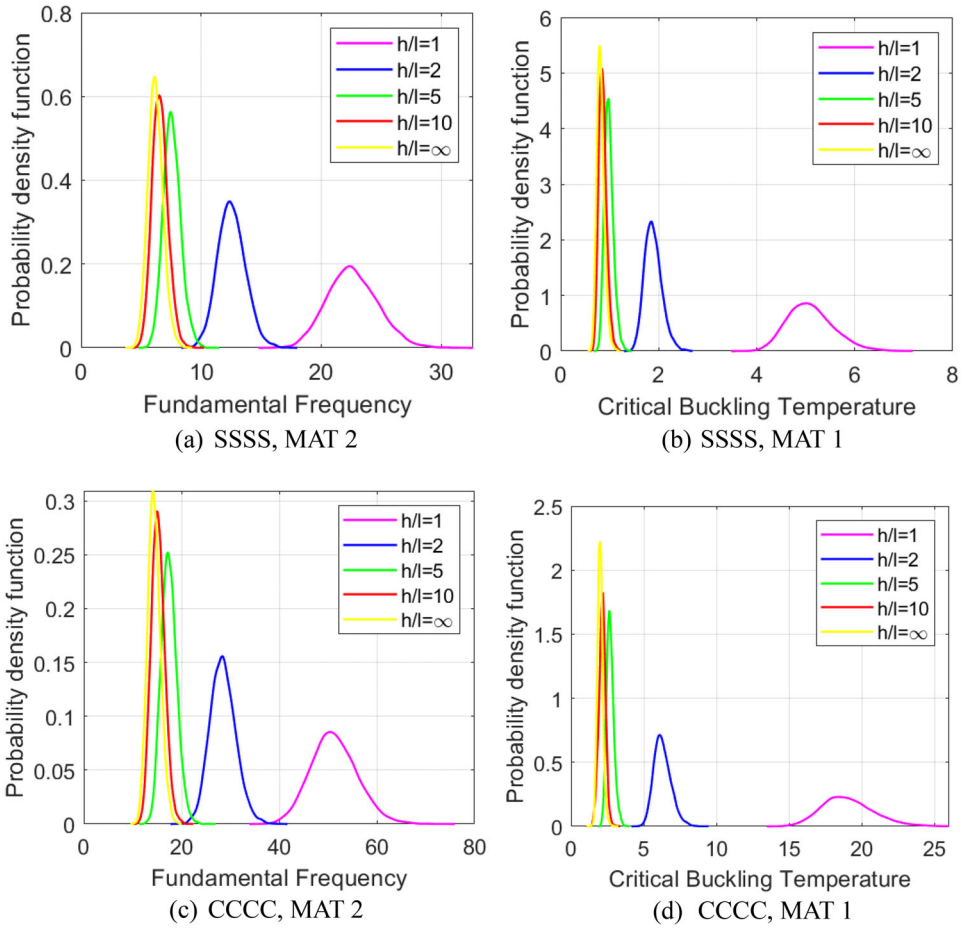

Figure 5. Probability density function (PDF) for the critical buckling temperature and free vibration of (1-2-1) FG sandwich microplates under uniform distribution with various ratio thickness to material h/l, ($\alpha/h = 10$, $p = 0.5$).

6. Conclusions

A higher-order shear deformation microplate model for stochastic thermal buckling and vibration analysis of functionally graded sandwich microplates is investigated in this study. The governing equations are developed using Hamilton's principle and solved by Ritz's approach using a hybrid shape function. The stochastic collocation method is utilized and the obtained results are compared with those from Monte Carlo Simulation. The effects of material distribution, ratio of side-to-thickness, and boundary conditions on the natural frequencies and thermal buckling of FG sandwich microplates are investigated. The following important points can be derived from the numerical results obtained:

- The accuracy and efficiency of predicting stochastic thermal buckling and fundamental frequencies of FG sandwich microplates have been demonstrated.
- In contrast to the Monte Carlo Simulation, which requires 10,000 samples, the stochastic collocation approach requires just 256 samples to calculate stochastic thermal buckling, the fundamental frequencies are 4096 samples, respectively.
- It is also interesting to note that when the power-law index p and ratio of thickness-to-MLSP h/l decrease, the frequency and thermal buckling uncertainty appears to expand.

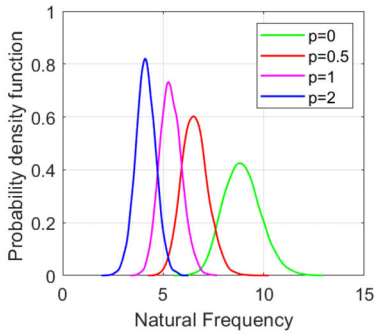

(a) $h/l=10$, SSSS, MAT 2

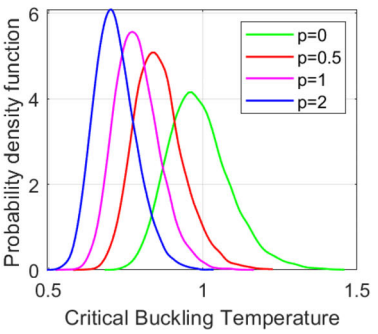

(b) $h/l=10$, SSSS, MAT 1

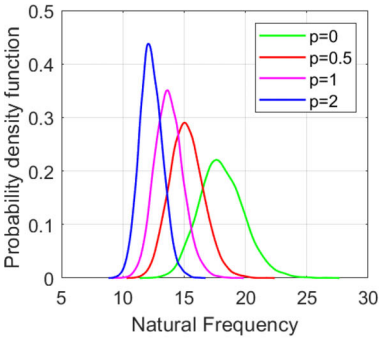

(c) $h/l=10$, CCCC, MAT 2

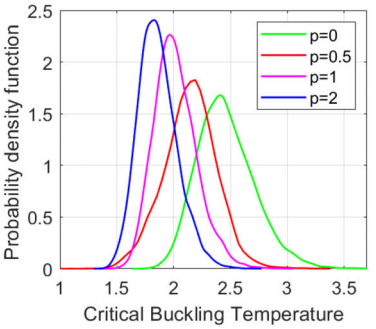

(d) $h/l=10$, CCCC, MAT 1

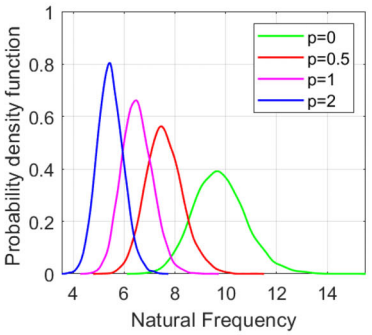

(e) $h/l=5$, SSSS, MAT 2

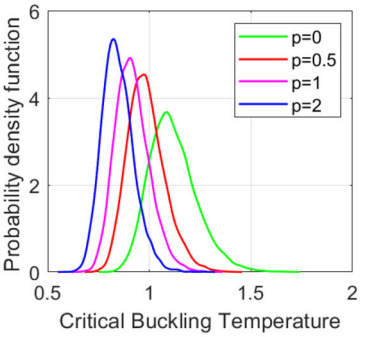

(f) $h/l=5$, SSSS, MAT 1

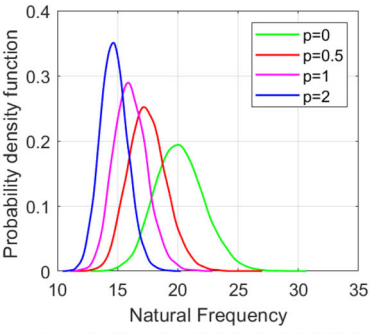

(g) $h/l=5$, CCCC, MAT 2

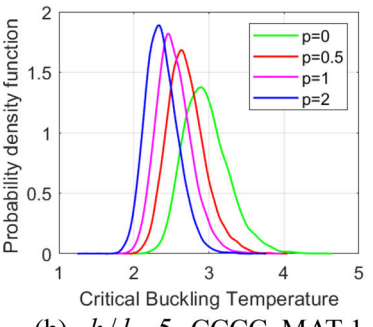

(h) $h/l=5$, CCCC, MAT 1

Figure 6. Probability density function (PDF) for the natural frequencies and critical buckling temperature of (1-2-1) FG sandwich microplates under uniform distribution with various power-law index p ($\alpha/h=10$).

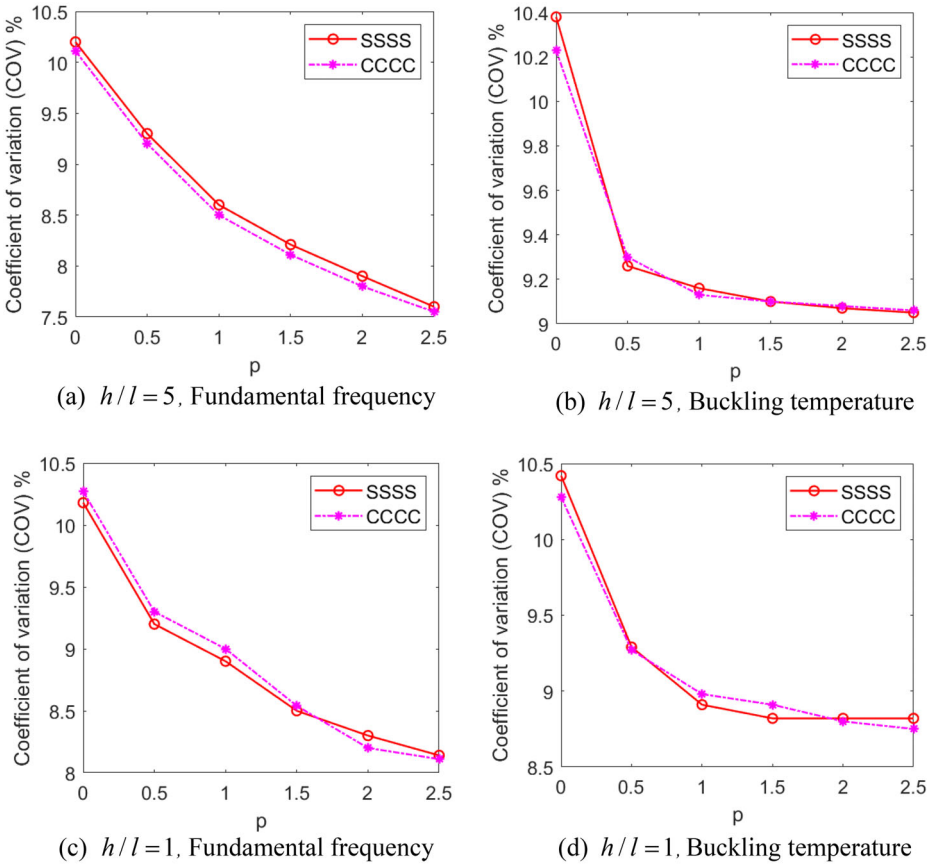

Figure 7. Coefficient of variation (COV) of fundamental frequency (MAT 2) and critical buckling temperature (MAT 1) with respect to the power-law index *p* of the FG sandwich microplates (1-2-1) with various BCs and *h/l*, $\alpha/h = 10$ under uniform distribution.

References

[1] N. Jalili and K. Laxminarayana, "A review of atomic force microscopy imaging systems: application to molecular metrology and biological sciences," *Mechatronics*, vol. 14, no. 8, pp. 907–945, 2004. DOI: 10.1016/j.mechatronics.2004.04.005.

[2] D. Ozevin, "10 - Micro-electro-mechanical-systems (MEMS) for assessing and monitoring civil infrastructures," In *Woodhead Publishing Series in Electronic and Optical Materials, Sensor Technologies for Civil Infrastructures*, vol. 55, M. L. Wang, J. P. Lynch, and H. Sohn, Eds. Woodhead Publishing, 2014, pp. 265–302e.

[3] B. Bahreyni and C. Shafai, "Application of twin-beam structures for estimation of material properties and sensor fabrication," *Can. J. Electr. Comput. Eng.*, vol. 31, no. 2, pp. 85–88, 2006. DOI: 10.1109/CJECE.2006.259189.

[4] B. Ilic, H. G. Craighead, S. Krylov, W. Senaratne, C. Ober, and P. Neuzil, "Attogram detection using nanoelectromechanical oscillators," *J. Appl. Phys.*, vol. 95, no. 7, pp. 3694–3703, 2004. DOI: 10.1063/1.1650542.

[5] I. Bargatin, I. Kozinsky, and M. Roukes, "Efficient electrothermal actuation of multiple modes of high-frequency nanoelectromechanical resonators," *Appl. Phys. Lett.*, vol. 90, no. 9, p. 093116, 2007. DOI: 10.1063/1.2709620.

[6] R. D. Mindlin and H. F. Tiersten, "Effects of couple-stresses in linear elasticity," *Arch. Rational Mech. Anal.*, vol. 11, no. 1, pp. 415–448, 1962. DOI: 10.1007/BF00253946.

[7] A. C. Eringen, "Nonlocal polar elastic continua," *Int. J. Eng. Sci.*, vol. 10, no. 1, pp. 1–16, 1972. DOI: 10.1016/0020-7225(72)90070-5.

[8] F. Yang, A. C. M. Chong, D. C. C. Lam, and P. Tong, "Couple stress based strain gradient theory for elasticity," *Int. J. Solids Struct.*, vol. 39, no. 10, pp. 2731–2743, 2002. DOI: 10.1016/S0020-7683(02)00152-X.

[9] D. C. C. Lam, F. Yang, A. C. M. Chong, J. Wang, and P. Tong, "Experiments and theory in strain gradient elasticity," *J. Mech. Phys. Solids*, vol. 51, no. 8, pp. 1477–1508, 2003. DOI: 10.1016/S0022-5096(03)00053-X.

[10] A. Farzam and B. Hassani, "Size-dependent analysis of FG microplates with temperature-dependent material properties using modified strain gradient theory and isogeometric approach," *Compos. B: Eng.*, vol. 161, pp. 150–168, 2019. DOI: 10.1016/j.compositesb.2018.10.028.

[11] H. X. Nguyen, T. N. Nguyen, M. Abdel-Wahab, S. P. A. Bordas, H. Nguyen-Xuan, and T. P. Vo, "A refined quasi-3D isogeometric analysis for functionally graded microplates based on the modified couple stress theory," *Comput. Methods Appl. Mech. Eng.*, vol. 313, pp. 904–940, 2017. DOI: 10.1016/j.cma.2016.10.002.

[12] L. C. Trinh, T. P. Vo, H.-T. Thai, and J. L. Mantari, "Size-dependent behaviour of functionally graded sandwich microplates under mechanical and thermal loads," *Compos. B: Eng.*, vol. 124, pp. 218–241, 2017. DOI: 10.1016/j.compositesb.2017.05.042.

[13] C. H. Thai, A. J. M. Ferreira, and P. Phung-Van, "Free vibration analysis of functionally graded anisotropic microplates using modified strain gradient theory," *Eng. Anal. Bound. Elem.*, vol. 117, pp. 284–298, 2020. DOI: 10.1016/j.enganabound.2020.05.003.

[14] A. Karamanli and T. P. Vo, "Size-dependent behaviour of functionally graded sandwich microbeams based on the modified strain gradient theory," *Compos. Struct.*, vol. 246, p. 112401, 2020. DOI: 10.1016/j.compstruct.2020.112401.

[15] L. Li and Y. Hu, "Post-buckling analysis of functionally graded nanobeams incorporating nonlocal stress and microstructure-dependent strain gradient effects," *Int. J. Mech. Sci.*, vol. 120, pp. 159–170, 2017. DOI: 10.1016/j.ijmecsci.2016.11.025.

[16] L. Li, R. Lin, and T. Y. Ng, "Contribution of nonlocality to surface elasticity," *Int. J. Eng. Sci.*, vol. 152, p. 103311, 2020. DOI: 10.1016/j.ijengsci.2020.103311.

[17] I. Bensaid, A. A. Daikh, and A. Drai, "Size-dependent free vibration and buckling analysis of sigmoid and power law functionally graded sandwich nanobeams with microstructural defects," *Proc. Inst. Mech. Eng., C: J. Mech. Eng. Sci.*, vol. 234, no. 18, pp. 3667–3688, 2020. DOI: 10.1177/0954406220916481.

[18] A. A. Daikh, M. S. A. Houari, and A. Tounsi, "Buckling analysis of porous FGM sandwich nanoplates due to heat conduction via nonlocal strain gradient theory," *Eng. Res. Express*, vol. 1, no. 1, p. 015022, 2019. DOI: 10.1088/2631-8695/ab38f9.

[19] A. A. Daikh and A. M. Zenkour, "Bending of functionally graded sandwich nanoplates resting on Pasternak foundation under different boundary conditions," *J. Appl. Comput. Mech.*, vol. 6, no. Special Issue, pp. 1245–1259, 2020.

[20] A. A. Daikh, A. Drai, I. Bensaid, M. S. A. Houari, and A. Tounsi, "On vibration of functionally graded sandwich nanoplates in the thermal environment," *J. Sandw. Struct. Mater.*, vol. 23, no. 6, pp. 2217–2244, 2020. DOI: 10.1177/1099636220909790.

[21] A. I. Aria and M. I. Friswell, "Computational hygro-thermal vibration and buckling analysis of functionally graded sandwich microbeams," *Compos. B: Eng.*, vol. 165, pp. 785–797, 2019. DOI: 10.1016/j.compositesb.2019.02.028.

[22] M. H. Shojaeefard, H. Saeidi Googarchin, M. Ghadiri, and M. Mahinzare, "Micro temperature-dependent FG porous plate: free vibration and thermal buckling analysis using modified couple stress theory with CPT and FSDT," *Appl. Math. Modell.*, vol. 50, pp. 633–655, 2017. DOI: 10.1016/j.apm.2017.06.022.

[23] S. Thai, H.-T. Thai, T. P. Vo, and J. N. Reddy, "Post-buckling of functionally graded microplates under mechanical and thermal loads using isogeomertic analysis," *Eng. Struct.*, vol. 150, pp. 905–917, 2017. DOI: 10.1016/j.engstruct.2017.07.073.

[24] W. Lanhe, "Thermal buckling of a simply supported moderately thick rectangular FGM plate," *Compos. Struct.*, vol. 64, no. 2, pp. 211–218, 2004. DOI: 10.1016/j.compstruct.2003.08.004.

[25] Y. Kiani and M. R. Eslami, "An exact solution for thermal buckling of annular FGM plates on an elastic medium," *Compos. B: Eng.*, vol. 45, no. 1, pp. 101–110, 2013. DOI: 10.1016/j.compositesb.2012.09.034.

[26] D. V. Dung and L. K. Hoa, "Nonlinear torsional buckling and postbuckling of eccentrically stiffened FGM cylindrical shells in thermal environment," *Compos. B: Eng.*, vol. 69, pp. 378–388, 2015. DOI: 10.1016/j.compositesb.2014.10.018.

[27] L. S. Ma and T. J. Wang, "Nonlinear bending and post-buckling of a functionally graded circular plate under mechanical and thermal loadings," *Int. J. Solids Struct.*, vol. 40, no. 13–14, pp. 3311–3330, 2003. DOI: 10.1016/S0020-7683(03)00118-5.

[28] H. V. Tung, "Thermal and thermomechanical postbuckling of FGM sandwich plates resting on elastic foundations with tangential edge constraints and temperature dependent properties," *Compos. Struct.*, vol. 131, pp. 1028–1039, 2015. DOI: 10.1016/j.compstruct.2015.06.043.

[29] N. D. Duc, N. D. Tuan, P. Tran, N. T. Dao, and N. T. Dat, "Nonlinear dynamic analysis of Sigmoid functionally graded circular cylindrical shells on elastic foundations using the third order shear deformation theory in thermal environments," *Int. J. Mech. Sci.*, vol. 101–102, pp. 338–348, 2015. DOI: 10.1016/j.ijmecsci.2015.08.018.

[30] A. M. Zenkour and M. Sobhy, "Thermal buckling of various types of FGM sandwich plates," *Compos. Struct.*, vol. 93, no. 1, pp. 93–102, 2010. DOI: 10.1016/j.compstruct.2010.06.012.

[31] F. A. Fazzolari and E. Carrera, "Thermal stability of FGM sandwich plates under various through-the-thickness temperature distributions," *J. Therm. Stresses*, vol. 37, no. 12, pp. 1449–1481, 2014. DOI: 10.1080/01495739.2014.937251.

[32] A. A. Daikh and A. Megueni, "Thermal buckling analysis of functionally graded sandwich plates," *J. Therm. Stresses*, vol. 41, no. 2, pp. 139–159, 2018. DOI: 10.1080/01495739.2017.1393644.

[33] A. A. Daikh, "Temperature dependent vibration analysis of functionally graded sandwich plates resting on Winkler/Pasternak/Kerr foundation," *Mater. Res. Express*, vol. 6, no. 6, p. 065702, 2019. DOI: 10.1088/2053-1591/ab097b.

[34] A. A. Daikh, M. Guerroudj, M. El Adjrami, and A. Megueni, "Thermal buckling of functionally graded sandwich beams," *AMR*, vol. 1156, pp. 43–59, 2020. DOI: 10.4028/www.scientific.net/AMR.1156.43.

[35] A. A. Daikh, I. Bensaid, and A. M. Zenkour, "Temperature dependent thermomechanical bending response of functionally graded sandwich plates," *Eng. Res. Express*, vol. 2, no. 1, p. 015006, 2020. DOI: 10.1088/2631-8695/ab638c.

[36] A. Bakora and A. Tounsi, "Thermo-mechanical post-buckling behavior of thick functionally graded plates resting on elastic foundations," *Struct. Eng. Mech.*, vol. 56, no. 1, pp. 85–106, 2015. DOI: 10.12989/sem.2015.56.1.085.

[37] A.-A. Daikh *et al.*, "Static analysis of functionally graded plate structures resting on variable elastic foundation under various boundary conditions," *Acta Mech.*, vol. 234, no. 2, pp. 775–806, 2023. DOI: 10.1007/s00707-022-03405-1.

[38] V. N. V. Do and C.-H. Lee, "Thermal buckling analyses of FGM sandwich plates using the improved radial point interpolation mesh-free method," *Compos. Struct.*, vol. 177, pp. 171–186, 2017. DOI: 10.1016/j.compstruct.2017.06.054.

[39] B. Sahoo, N. Sharma, B. Sahoo, P. Malhari Ramteke, S. Kumar Panda, and S. R. Mahmoud, "Nonlinear vibration analysis of FGM sandwich structure under thermal loadings," *Structures*, vol. 44, pp. 1392–1402, 2022. DOI: 10.1016/j.istruc.2022.08.081.

[40] I. M. Mudhaffar, A. Tounsi, A. Chikh, M. A. Al-Osta, M. M. Al-Zahrani, and S. U. Al-Dulaijan, "Hygro-thermo-mechanical bending behavior of advanced functionally graded ceramic metal plate resting on a viscoelastic foundation," *Structures*, vol. 33, pp. 2177–2189, 2021. DOI: 10.1016/j.istruc.2021.05.090.

[41] A. A. Daikh, "Thermal buckling analysis of functionally graded sandwich cylindrical shells," *Adv. Aircr. Spacecr. Sci.*, vol. 7, no. 4, pp. 335–351, 2020.

[42] Z. Lv and Z. Qiu, "A direct probabilistic approach to solve state equations for nonlinear systems under random excitation," *Acta Mech. Sin.*, vol. 32, no. 5, pp. 941–958, 2016. DOI: 10.1007/s10409-016-0594-y.

[43] L. Nazarenko, H. Stolarski, and H. Altenbach, "Thermo-elastic properties of random particulate nano-materials for various models of interphase," *Int. J. Mech. Sci.*, vol. 126, pp. 130–141, 2017. DOI: 10.1016/j.ijmecsci.2017.03.021.

[44] F. Scarpa and S. Adhikari, "Uncertainty modeling of carbon nanotube terahertz oscillators," *J. Non-Cryst. Solids*, vol. 354, no. 35–39, pp. 4151–4156, 2008. : DOI: 10.1016/j.jnoncrysol.2008.06.065.

[45] C. Jiang, G. Lu, X. Han, and L. Liu, "A new reliability analysis method for uncertain structures with random and interval variables," *Int. J. Mech. Mater. Des.*, vol. 8, no. 2, pp. 169–182, 2012. DOI: 10.1007/s10999-012-9184-8.

[46] J. Liu, X. Sun, X. Meng, K. Li, G. Zeng, and X. Wang, "A novel shape function approach of dynamic load identification for the structures with interval uncertainty," *Int. J. Mech. Mater. Des.*, vol. 12, no. 3, pp. 375–386, 2016. DOI: 10.1007/s10999-015-9304-3.

[47] H.-T. Thai, T. P. Vo, T.-K. Nguyen, and S.-E. Kim, "A review of continuum mechanics models for size-dependent analysis of beams and plates," *Compos. Struct.*, vol. 177, pp. 196–219, 2017. DOI: 10.1016/j.compstruct.2017.06.040.

[48] C. J. Mode and R. J. Gallop, "A review on Monte Carlo simulation methods as they apply to mutation and selection as formulated in Wright–Fisher models of evolutionary genetics," *Math. Biosci.*, vol. 211, no. 2, pp. 205–225, 2008. DOI: 10.1016/j.mbs.2007.05.015.

[49] H. X. Nguyen, T. Duy Hien, J. Lee, and H. Nguyen-Xuan, "Stochastic buckling behaviour of laminated composite structures with uncertain material properties," *Aerosp. Sci. Technol.*, vol. 66, pp. 274–283, 2017. DOI: 10.1016/j.ast.2017.01.028.

[50] M.-C. Trinh, S.-N. Nguyen, H. Jun, and T. Nguyen-Thoi, "Stochastic buckling quantification of laminated composite plates using cell-based smoothed finite elements," *Thin-Walled Struct.*, vol. 163, p. 107674, 2021. DOI: 10.1016/j.tws.2021.107674.

[51] N. Grover, R. Sahoo, B. N. Singh, and D. K. Maiti, "Influence of parametric uncertainties on the deflection statistics of general laminated composite and sandwich plates," *Compos. Struct.*, vol. 171, pp. 158–169, 2017. DOI: 10.1016/j.compstruct.2017.03.036.

[52] K. R. Jagtap, A. Lal, and B. N. Singh, "Stochastic nonlinear free vibration analysis of elastically supported functionally graded materials plate with system randomness in thermal environment," *Compos. Struct.*, vol. 93, no. 12, pp. 3185–3199, 2011. DOI: 10.1016/j.compstruct.2011.06.010.

[53] E. García-Macías, R. Castro-Triguero, M. I. Friswell, S. Adhikari, and A. Sáez, "Metamodel-based approach for stochastic free vibration analysis of functionally graded carbon nanotube reinforced plates," *Compos. Struct.*, vol. 152, pp. 183–198, 2016. DOI: 10.1016/j.compstruct.2016.05.019.

[54] K. Li, D. Wu, and W. Gao, "Spectral stochastic isogeometric analysis for static response of FGM plate with material uncertainty," *Thin-Walled Struct.*, vol. 132, pp. 504–521, 2018. DOI: 10.1016/j.tws.2018.08.028.

[55] X. Peng *et al.*, "Uncertainty analysis of composite laminated plate with data-driven polynomial chaos expansion method under insufficient input data of uncertain parameters," *Compos. Struct.*, vol. 209, pp. 625–633, 2019. DOI: 10.1016/j.compstruct.2018.11.015.

[56] K. Umesh and R. Ganguli, "Material uncertainty effect on vibration control of smart composite plate using polynomial chaos expansion," *Mech. Adv. Mater. Struct.*, vol. 20, no. 7, pp. 580–591, 2013. DOI: 10.1080/15376494.2011.643279.

[57] S. Chakraborty, B. Mandal, R. Chowdhury, and A. Chakrabarti, "Stochastic free vibration analysis of laminated composite plates using polynomial correlated function expansion," *Compos. Struct.*, vol. 135, pp. 236–249, 2016. DOI: 10.1016/j.compstruct.2015.09.044.

[58] P. Sasikumar, A. Venketeswaran, R. Suresh, and S. Gupta, "A data driven polynomial chaos based approach for stochastic analysis of CFRP laminated composite plates," *Compos. Struct.*, vol. 125, pp. 212–227, 2015. DOI: 10.1016/j.compstruct.2015.02.010.

[59] A. Shaker, W. Abdelrahman, M. Tawfik, and E. A. Sadek, "Stochastic finite element analysis of the free vibration of laminated composite plates," *Comput. Mech.*, vol. 41, no. 4, pp. 493–501, 2008. DOI: 10.1007/s00466-007-0205-7.

[60] J. Li, X. Tian, Z. Han, and Y. Narita, "Stochastic thermal buckling analysis of laminated plates using perturbation technique," *Compos. Struct.*, vol. 139, pp. 1–12, 2016. DOI: 10.1016/j.compstruct.2015.11.076.

[61] V.-T. Tran, T.-K. Nguyen, P. T. T. Nguyen, and T. P. Vo, "Stochastic vibration and buckling analysis of functionally graded microplates with a unified higher-order shear deformation theory," *Thin-Walled Struct.*, vol. 177, p. 109473, 2022. DOI: 10.1016/j.tws.2022.109473.

[62] D. Xiu and J. S. Hesthaven, "High-order collocation methods for differential equations with random inputs," *SIAM J. Sci. Comput.*, vol. 27, no. 3, pp. 1118–1139, 2005. DOI: 10.1137/040615201.

[63] P. Bressolette, M. Fogli, and C. Chauvière, "A stochastic collocation method for large classes of mechanical problems with uncertain parameters," *Probabilist. Eng. Mech.*, vol. 25, no. 2, pp. 255–270, 2010. DOI: 10.1016/j.probengmech.2010.01.002.

[64] P. T. T. Nguyen, L. C. Trinh, and T.-K. Nguyen, "Probabilistic free vibration analysis of functionally graded beams using stochastic finite element methods," In *Computational Intelligence Methods for Green Technology and Sustainable Development. GTSD 2020. Advances in Intelligent Systems and Computing,* vol. 1284, Y. P. Huang, W. J. Wang, H. A. Quoc, L. H. Giang, and N. L. Hung, Eds. Cham: Springer, 2020, pp. 517–531. DOI: 10.1007/978-3-030-62324-1_44.

[65] Q. Li, V. P. Iu, and K. P. Kou, "Three-dimensional vibration analysis of functionally graded material sandwich plates," *J. Sound Vib.*, vol. 311, no. 1–2, pp. 498–515, 2008. DOI: 10.1016/j.jsv.2007.09.018.

[66] T.-K. Nguyen, H.-T. Thai, and T. P. Vo, "A novel general higher-order shear deformation theory for static, vibration and thermal buckling analysis of the functionally graded plates," *J. Therm. Stresses*, vol. 44, no. 3, pp. 1–21, 2021. DOI: 10.1080/01495739.2020.1869127.

[67] R. D. Mindlin, "Influence of couple-stresses on stress concentrations," *Exp. Mech.*, vol. 3, no. 1, pp. 1–7, 1963. DOI: 10.1007/BF02327219.

[68] J. L. Mantari and F. G. Canales, "Free vibration and buckling of laminated beams via hybrid Ritz solution for various penalized boundary conditions," *Compos. Struct.*, vol. 152, pp. 306–315, 2016. DOI: 10.1016/j.compstruct.2016.05.037.

[69] P. Moreno-García, J. V. Dos Santos, and H. Lopes, "A review and study on Ritz method admissible functions with emphasis on buckling and free vibration of isotropic and anisotropic beams and plates," *Arch. Computat. Methods Eng.*, vol. 25, no. 3, pp. 785–815, 2018. DOI: 10.1007/s11831-017-9214-7.

[70] T.-K. Nguyen, T. Truong-Phong Nguyen, T. P. Vo, and H.-T. Thai, "Vibration and buckling analysis of functionally graded sandwich beams by a new higher-order shear deformation theory," *Compos. B: Eng.*, vol. 76, pp. 273–285, 2015. DOI: 10.1016/j.compositesb.2015.02.032.

[71] T.-K. Nguyen, T. P. Vo, B.-D. Nguyen, and J. Lee, "An analytical solution for buckling and vibration analysis of functionally graded sandwich beams using a quasi-3D shear deformation theory," *Compos. Struct.*, vol. 156, pp. 238–252, 2016. DOI: 10.1016/j.compstruct.2015.11.074.

[72] F. Nobile, R. Tempone, and C. G. Webster, "An anisotropic sparse grid stochastic collocation method for partial differential equations with random input data," *SIAM J. Numer. Anal.*, vol. 46, no. 5, pp. 2411–2442, 2008. DOI: 10.1137/070680540.

[73] F. Nobile, R. Tempone, and C. G. Webster, "A sparse grid stochastic collocation method for partial differential equations with random input data," *SIAM J. Numer. Anal.*, vol. 46, no. 5, pp. 2309–2345, 2008. DOI: 10.1137/060663660.

[74] C. Thai Hoang, A. Ferreira, J. Lee, and H. Nguyen-Xuan, "An efficient size-dependent computational approach for functionally graded isotropic and sandwich microplates based on modified couple stress theory and moving Kriging-based meshfree method," *Int. J. Mech. Sci.*, vol. 142–143, pp. 322–338, 2018. DOI: 10.1016/j.ijmecsci.2018.04.040.

JOURNAL OF THERMAL STRESSES
https://doi.org/10.1080/01495739.2024.2368054

An intelligent computational iBCMO-DNN algorithm for stochastic thermal buckling analysis of functionally graded porous microplates using modified strain gradient theory

Van-Thien Tran[a], Trung-Kien Nguyen[b], and H. Nguyen-Xuan[b]

[a]Faculty of Civil Engineering, Ho Chi Minh City University of Technology and Education, Ho Chi Minh City, Vietnam; [b]CIRTech Institute, HUTECH University, Ho Chi Minh City, Vietnam

ABSTRACT

The authors propose an intelligent computational method using the deep feedforward neural network integrated with an improved balance composite motion optimization algorithm to formulate a so-called iBCMO-DNN for solving the stochastic thermal buckling problems of functionally graded porous microplates. In the present approach, the deterministic behaviors of the functionally graded porous microplates were firstly analyzed by the combination of a unified higher-order shear deformation theory, modified strain gradient theory, and Ritz-type series solutions, and then stochastic responses under uncertainty of material properties are obtained by the iBCMO-DNN algorithm. The deep neural network with the long short-term memory model is used as a surrogate method to replace the time-consuming computational model, while the improved balance composite motion optimization is used to search for the optimal solutions. The obtained numerical results for various boundary conditions, uncertainty parameters, and three types of temperature distribution indicated that the proposed method achieves its accuracy and effectiveness in predicting stochastic thermal buckling of the functionally graded porous microplates. The improved balance composite motion optimization algorithm demonstrates a computational time ∼1.7 times faster than its predecessor. Furthermore, integrating a deep neural network into the improved algorithm reduces computational time to about 2/5 compared to the method without it.

ARTICLE HISTORY
Received 13 December 2023
Accepted 5 June 2024

KEYWORDS
Balance composite motion optimization algorithm; deep neural network; functionally graded porous microplates; modified strain gradient theory; thermal buckling

1. Introduction

The functionally graded materials (FGMs) have been increasingly studied for applications in different engineering fields, such as nano-electromechanical systems (NEMS) [1], micro-electromechanical systems (MEMs) [2,3], and atomic force microscopes (AFMs) [4] since its smooth variation of material properties could meet severe thermo-mechanical conditions in comparison with conventional multilayered materials. However, in practice, the FGMs may contain internal defects, such as pores, uncertainty in material properties, and size effects at small-scale structures, which result in its behavior variations and therefore require efficient computational methods. These interesting topics have attracted numerous researchers with different approaches.

For analysis of functionally graded porous (FGP) plates at macro scale in thermo-mechanical environments, many investigations on behaviors of FGP plates have been performed with various approaches [5–7] in which it could be noted that the effects of porosities impacted importantly

CONTACT Trung-Kien Nguyen ntkien@hutech.edu.vn CIRTech Institute, HUTECH University, 475A Dien Bien Phu Street, Binh Thanh District, Ho Chi Minh City, Vietnam.

on responses of the FGP plates. Nevertheless, when considering such structures at a small scale, the standard elasticity theory would be not able to forecast accurately, hence the nano and micro theories were developed to capture the size effects. Based on this approach, several researches have been carried out to examine thermo-mechanical behaviors of FGM nanostructures [8–10] using nonlocal strain gradient theory [11,12], FGM microplates [13–16], and FGP microplates [17]. It is worth noticing that to examine the size effects of isotropic microplates, the modified coupled stress theory (MCT) [18] including one material length scale parameter (MLSP) and additional strain gradient in constitutive equations has been commonly employed by its simplicity. Alternatively, by introducing the dilatation and deviatoric stretch gradients in constitutive equations, the modified strain gradient theory (MST) [19,20] derived from the five-MLSP strain gradient theory [21,22] appeared to be more accurate than the MCT. Furthermore, in practice, the material properties of FGP microplates could be uncertain due to manufacture processing or other unexpected phenomena, it led to changes of behaviors of the FGP microplates and therefore required advanced computational methods to quantify the solution field. Practically, to predict stochastic responses of structures, Monte Carlo Simulation (MCS) method is the simplest one to solve this complicated problem. Nonetheless, this approach is infeasible in different cases due to its expensive computational cost, especially when a complicated physical model is considered. Another approach is to use polynomial chaos expansion (PCE) which speeds up the computing process while still maintains the accuracy. Several earlier studies have been conducted for stochastic analysis of FGM and FGP plates [23,24], and FG/FGP microplates [25,26].

In addition, there has been a significant interest in the optimal design of FGM plates, as evidenced by numerous studies [27–29]. Optimization algorithms can be classified into two primary categories: gradient-based methods, such as sequential quadratic programming, optimality criterion, force method, and non-gradient-based methods. The algorithms in the first group [30–32] quickly find the best solutions. However, a common limitation of these algorithms is their tendency to become stuck at local optimal solutions. Furthermore, it is imperative to conduct the sensitivity analysis of both the fitness and constraint functions, as they play a crucial role in the optimization process. However, it is worth noting that those analyses can be intricate and resource-intensive. To mitigate these limitations, a variety of alternative algorithms have been devised, such as the Firefly Algorithms (FA) [33], Memetic Algorithm (MA) [34], Ant Colony Optimization (ACO) [35], Particle Swarm Optimization (PSO) [36], and modified symbiotic organism search (mSOS) [37], Balancing composite motion optimization method (BCMO) [38], etc. The candidates within this particular group are generated in a random manner within the search domain without any reliance on gradient information. As a result, these algorithms have the potential to achieve a solution that is globally optimal. However, a notable drawback is the high computational cost associated with them, particularly when dealing with optimization problems that involve a large number of design variables. Moreover, it should be noted that the machine learning and balancing composite motion optimization method (BCMO) have been developed for different optimization problems of structure behaviors, which could be considered in enhancing computational costs. The BCMO [38] is an optimization approach based on the fact that the search motions of potential solutions are compositely balanced in both local and global. A candidate solution can advance both to further explore the search space and to approach better ones in the local areas. Thereby, the best individual generated in each generation after ranking could jump from one space to another right away or strengthen its existing local space. In practice, the BCMO could be integrated with the artificial neural network (ANN) to optimize behaviors of the composite structures and reduce computational costs. Thanh Duong et al. [39] presented the BCMO-ANN algorithm for the optimization design of rectangular concrete-filled steel tube short columns. Khatir et al. [40] used the BCMO-ANN for damage assessment of FGM plates. Tran et al. [41] recently investigated stochastic vibration and buckling optimization of FGP microplates using the BCMO-ANN and MCT. A literature review shows that the effects of

porosity, uncertainty in material properties, and size effects of FGP microplates have been a challenging topic that needs to be studied further. Particularly, when confronted with the uncertain and naturally variable mechanical properties of the materials, these factors present major difficulties that necessitate more deep study. So, in the present work, we focus on improving the BCMO algorithm and combining it with deep learning (DNN) to resolve this problem. The main contribution of this paper is a novel intelligent computation algorithm iBCMO-DNN for solving the stochastic thermal buckling problems of FGP microplates using the MST, unified higher-order shear deformation theory (HSDT), and Ritz method.

With the aim of reducing the computational time in dealing with stochastic problems, this study proposes a novel intelligent computational algorithm, namely iBCMO-DNN, for handling stochastic thermal buckling analysis of FGP microplates. The theory is developed *via* the improved BCMO, DNN, MST, and unified higher-order shear deformation theory (HSDT). The deterministic responses of FGP microplates are derived from the Ritz-based solver, a general HSDT, and MST. The approximation functions of the Ritz approach are shown as a hybrid with a sequence of exponential functions mixed with a polynomial to meet the boundary conditions. The solution field is then generated randomly and optimally selected by a modified BCMO, and the subsequent results are trained *via* the DNN. Numerical results are displayed for various configurations of boundary conditions, uncertainty parameters, and three types of temperature distribution on the critical buckling temperature of FGP microplates.

2. Theoretical formulation

Considering a rectangle FGP microplate in the coordinate system (x_1, x_2, x_3) with thickness h, sides $a \times b$ as provided in Figure 1.

2.1. Material properties and temperature distribution

The effective material properties of FGP microplates are given by [42]:

$$P(x_3) = (P_c - P_m)\left(\frac{2x_3 + h}{2h}\right)^p + P_m - \frac{\beta}{2}(P_c + P_m) \tag{1}$$

where P_c and P_m are the Poisson's ratio ν, Young's moduli E of ceramic and metal materials, respectively; p is the power-law index; $0 \leq \beta \ll 1$ is the porosity volume fraction; $x_3 \in [-h/2, h/2]$. Moreover, to investigate the effect of temperature on the buckling responses, three types of temperature distribution are considered below [43,44]:

- For uniform temperature distribution (UTR): $T(z) = T_o + \Delta T$ where the bottom surface's reference temperature is T_o.

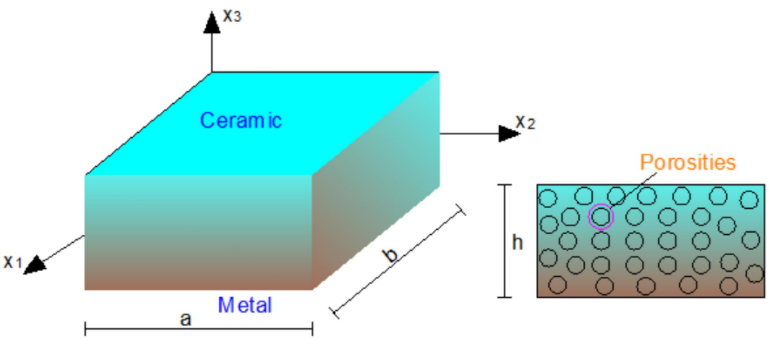

Figure 1. Geometry of FGP microplates.

- For linear temperature distribution (LTR): $T(z) = (T_t - T_b)\left(\frac{z}{h} + \frac{1}{2}\right) + T_b$ where the temperatures at the top and bottom surfaces of FGP microplates are represented by T_t and T_b, respectively.
- For the nonlinear temperature rise (NLTR): the expression of the current temperature is derived from the Fourier equation of steady-state heat conduction as follows: $T(z) = T(b) + \frac{T_t - T_b}{\int_{-h/2}^{h/2} 1/k(z)dz} \int_{-h/2}^{z} \frac{1}{k(\xi)d\xi}$ where $k(z)$ is the coefficient of thermal conductivity. It is noted that, in the present work, the material properties are supposed to be temperature-independent, and the effects of temperature dependency on the thermal buckling of FGM microplates could be referred to Refs. [45,46] for more details.

2.2. FGP microplates' unified kinematics

A general HSDT kinematic of FGP microplates is generated from Refs. [25,44] as follows:

$$u_1(x_1, x_2, x_3) = \Phi_2(x_3)\varphi_1(x_1, x_2) + \Phi_1(x_3)u^0_{3,1} + u^0_1(x_1, x_2) \tag{2a}$$

$$u_2(x_1, x_2, x_3) = \Phi_2(x_3)\varphi_2(x_1, x_2) + \Phi_1(x_3)u^0_{3,2} + u^0_2(x_1, x_2) \tag{2b}$$

$$u_3(x_1, x_2, x_3) = u^0_3(x_1, x_2) \tag{2c}$$

with $\Phi_2(x_3) = H^s\Psi(x_3), \Phi_1(x_3) = H^s\Psi(x_3) - x_3$, $\Psi(x_3) = \int_0^{x_3} \frac{f,_3}{\mu(x_3)} dx_3$; u_j $(j = 1, 2, 3)$ are displacements in x_1-, x_2-, and x_3- directions, respectively; u^0_1, u^0_2 and u^0_3 are membrane and transverse displacements at neutral plane; φ_1, φ_2 are rotations at neutral plane with respect to the x_1- and x_2- axis, respectively; H^s is the transverse shear stiffness; $f(x_3)$ is a higher-order term which satisfies the boundary condition $f,_3\left(x_3 = \pm\frac{h}{2}\right) = 0$.

The FGP microplates' total potential energy is calculated by using Hamilton's principle as follows [47]:

$$\int_{t_1}^{t_2} (\delta\Pi_{UB} + \delta\Pi_{VB})dt = 0 \tag{3}$$

where $\delta\Pi_{VB}, \delta\Pi_{UB}$ are the variations of work done by membrane compressive forces, and strain energy, respectively.

The strain energy variation of the system $\delta\Pi_{UB}$ is obtained by the modified strain gradient theory (MST) [19,48,49]:

$$\delta\Pi_{UB} = \int_A (\boldsymbol{\sigma}\delta\boldsymbol{\varepsilon} + \mathbf{p}\delta\boldsymbol{\xi} + \boldsymbol{\tau}\delta\boldsymbol{\eta} + \mathbf{m}\delta\boldsymbol{\chi})dA \tag{4}$$

where $\boldsymbol{\varepsilon}, \boldsymbol{\chi}, \boldsymbol{\xi}, \boldsymbol{\eta}$ are strains, symmetric rotation gradients, dilatation gradient, and deviation stretch gradient, respectively; $\boldsymbol{\sigma}$ is Cauchy stress; $\mathbf{m}, \mathbf{p}, \boldsymbol{\tau}$ are high-order stresses corresponding with strain gradients $\boldsymbol{\chi}, \boldsymbol{\xi}, \boldsymbol{\eta}$, respectively. The components of strain ε_{ij} and strain gradients $\xi_i, \eta_{ijk}, \chi_{ij}$ are defined as follows:

$$\varepsilon_{ij} = (u_{i,j} + u_{j,i})/2;\ \xi_i = \varepsilon_{mm,i};\ \chi_{ij} = (u_{n,mj}e_{imn} + u_{n,mi}e_{jmn})/4 \tag{5a}$$

$$\eta_{ijk} = (\varepsilon_{jk,i} + \varepsilon_{ki,j} + \varepsilon_{ij,k})/3 - \left[(\xi_i + 2\varepsilon_{mi,m})\delta_{jk} + (\xi_k + 2\varepsilon_{mk,m})\delta_{ij} + \left(\xi_j + 2\varepsilon_{mj,m}\right)\delta_{ki}\right]/15 \tag{5b}$$

where δ_{ij} is Kronecker delta; e_{imn} is permutation symbol. The constitutive equations are used to determine the stress components as follows:

$$\sigma_{ij} = \lambda\varepsilon_{kk}\delta_{ij} + 2\mu\varepsilon_{ij};\ m_{ij} = 2\mu l_1^2\chi_{ij};\ p_j = 2\mu l_2^2\xi_j;\ \tau_{ijk} = 2\mu l_3^2\eta_{ijk} \tag{6}$$

where λ, μ are Lamé constants; l_1, l_2, l_3 are three material length scale parameters (MLSP) that should be practically determined by experimental works. Substituting Eq. (2) into Eq. (5a), the strains $\boldsymbol{\varepsilon}^T = \begin{bmatrix} \boldsymbol{\varepsilon}^{(i)} & \boldsymbol{\varepsilon}^{(ss)} \end{bmatrix}$ are achieved as follows:

$$\boldsymbol{\varepsilon}^{(ss)} = \Phi_3(x_3)\boldsymbol{\varepsilon}^{(3)};\ \boldsymbol{\varepsilon}^{(i)} = \Phi_2(x_3)\boldsymbol{\varepsilon}^{(2)} + \Phi_1(x_3)\boldsymbol{\varepsilon}^{(1)} + \boldsymbol{\varepsilon}^{(0)} \tag{7}$$

where $\Phi_3(x_3) = H^s f_{,3}(x_3)/\mu(x_3)$. The non-zero components of dilatation gradients $\boldsymbol{\xi} = \begin{bmatrix} \xi_1 & \xi_2 & \xi_3 \end{bmatrix}^T$ are given by:

$$\boldsymbol{\xi} = \boldsymbol{\xi}^{(0)} + \Phi_1\boldsymbol{\xi}^{(1)} + \Phi_2\boldsymbol{\xi}^{(2)} + \Phi_{1,3}\boldsymbol{\xi}^{(3)} + \Phi_{2,3}\boldsymbol{\xi}^{(4)} \tag{8}$$

The expressions of deviatoric stretch gradient and strain gradient components are as follows:

$$\boldsymbol{\eta} = \boldsymbol{\eta}^{(0)} + \Phi_1\boldsymbol{\eta}^{(1)} + \Phi_2\boldsymbol{\eta}^{(2)} + \Phi_3\boldsymbol{\eta}^{(3)} + \Phi_{1,3}\boldsymbol{\eta}^{(4)} + \Phi_{2,3}\boldsymbol{\eta}^{(5)} + \Phi_{3,3}\boldsymbol{\eta}^{(6)} \tag{9a}$$

$$\boldsymbol{\chi} = \boldsymbol{\chi}^{(0)} + \boldsymbol{\chi}^{(1)}\Phi_{1,3} + \boldsymbol{\chi}^{(2)}\Phi_{2,3} + \boldsymbol{\chi}^{(3)}\Phi_{1,33} + \boldsymbol{\chi}^{(4)}\Phi_{2,33} + \boldsymbol{\chi}^{(5)}\Phi_2 \tag{9b}$$

where

$$\boldsymbol{\eta}^T = \begin{bmatrix} \eta_{111} & \eta_{222} & \eta_{333} & 3\eta_{331} & 3\eta_{332} & 3\eta_{221} & 3\eta_{112} & 3\eta_{113} & 3\eta_{223} & 6\eta_{123} \end{bmatrix},$$
$$\boldsymbol{\chi}^T = \begin{bmatrix} \chi_{11} & \chi_{22} & 2\chi_{12} & \chi_{33} & 2\chi_{13} & 2\chi_{23} \end{bmatrix}$$

The strain components of the FGP microplates are described in Appendix A. The stress-strain relationship of FGP microplates is represented as follows:

$$\boldsymbol{\sigma}^{(i)} = \begin{Bmatrix} \sigma_{11} \\ \sigma_{22} \\ \sigma_{12} \end{Bmatrix} = \mathbf{Q}_\varepsilon^{(i)}\boldsymbol{\varepsilon}^{(i)} = \begin{bmatrix} Q_{11} & Q_{12} & 0 \\ Q_{12} & Q_{22} & 0 \\ 0 & 0 & Q_{66} \end{bmatrix} \begin{Bmatrix} \varepsilon_{11} \\ \varepsilon_{22} \\ \gamma_{12} \end{Bmatrix} \tag{10a}$$

$$\boldsymbol{\sigma}^{(o)} = \begin{Bmatrix} \sigma_{13} \\ \sigma_{23} \end{Bmatrix} = \mathbf{Q}_\varepsilon^{(o)}\boldsymbol{\varepsilon}^{(ss)} = \begin{bmatrix} Q_{55} & 0 \\ 0 & Q_{44} \end{bmatrix} \begin{Bmatrix} \gamma_{13} \\ \gamma_{23} \end{Bmatrix} \tag{10b}$$

$$\mathbf{m} = \begin{Bmatrix} m_{11} \\ m_{22} \\ m_{12} \\ m_{33} \\ m_{23} \\ m_{13} \end{Bmatrix} = \alpha_\chi \mathbf{I}_{6\times 6}\boldsymbol{\chi} = 2\mu l_1^2 \begin{bmatrix} 1 & 0 & 0 & 0 & 0 & 0 \\ 0 & 1 & 0 & 0 & 0 & 0 \\ 0 & 0 & 1 & 0 & 0 & 0 \\ 0 & 0 & 0 & 1 & 0 & 0 \\ 0 & 0 & 0 & 0 & 1 & 0 \\ 0 & 0 & 0 & 0 & 0 & 1 \end{bmatrix} \begin{Bmatrix} \chi_{11} \\ \chi_{22} \\ \chi_{12} \\ \chi_{33} \\ \chi_{23} \\ \chi_{13} \end{Bmatrix} \tag{10c}$$

$$\mathbf{p} = \begin{Bmatrix} p_1 \\ p_2 \\ p_3 \end{Bmatrix} = \alpha_\xi \mathbf{I}_{3\times 3}\boldsymbol{\xi} = 2\mu l_2^2 \begin{bmatrix} 1 & 0 & 0 \\ 0 & 1 & 0 \\ 0 & 0 & 1 \end{bmatrix} \begin{Bmatrix} \xi_1 \\ \xi_2 \\ \xi_3 \end{Bmatrix} \tag{10d}$$

$$\boldsymbol{\tau} = \begin{Bmatrix} \tau_{111} \\ \tau_{222} \\ \tau_{112} \\ \tau_{221} \\ \tau_{331} \\ \tau_{332} \\ \tau_{333} \\ \tau_{113} \\ \tau_{223} \\ \tau_{123} \end{Bmatrix} = \alpha_\eta \mathbf{I}_{10\times 10}\boldsymbol{\eta} = 2\mu l_3^2 \begin{bmatrix} 1 & 0 & 0 & 0 & 0 & 0 & 0 & 0 & 0 & 0 \\ 0 & 1 & 0 & 0 & 0 & 0 & 0 & 0 & 0 & 0 \\ 0 & 0 & 1 & 0 & 0 & 0 & 0 & 0 & 0 & 0 \\ 0 & 0 & 0 & 1 & 0 & 0 & 0 & 0 & 0 & 0 \\ 0 & 0 & 0 & 0 & 1 & 0 & 0 & 0 & 0 & 0 \\ 0 & 0 & 0 & 0 & 0 & 1 & 0 & 0 & 0 & 0 \\ 0 & 0 & 0 & 0 & 0 & 0 & 1 & 0 & 0 & 0 \\ 0 & 0 & 0 & 0 & 0 & 0 & 0 & 1 & 0 & 0 \\ 0 & 0 & 0 & 0 & 0 & 0 & 0 & 0 & 1 & 0 \\ 0 & 0 & 0 & 0 & 0 & 0 & 0 & 0 & 0 & 1 \end{bmatrix} \begin{Bmatrix} \eta_{111} \\ \eta_{222} \\ \eta_{112} \\ \eta_{221} \\ \eta_{331} \\ \eta_{332} \\ \eta_{333} \\ \eta_{113} \\ \eta_{223} \\ \eta_{123} \end{Bmatrix} \tag{10e}$$

where $\alpha_\chi = 2\mu l_1^2$, $\alpha_\xi = 2\mu l_2^2$, $\alpha_\eta = 2\mu l_3^2$, $Q_{44} = Q_{55} = Q_{66} = \mu = \frac{E(x_3)}{2(1+\nu)}$, $Q_{12} = \frac{\nu E(x_3)}{1-\nu^2}$, $Q_{22} = \frac{E(x_3)}{1-\nu^2}$, $Q_{11} = \frac{E(x_3)}{1-\nu^2}$.

The variation of the strain energy of FGP microplates is hence derived from Eq. (4) as follows:

$$\begin{aligned}\delta\Pi_{UB} &= \int_A (\boldsymbol{\sigma}\delta\boldsymbol{\varepsilon} + \mathbf{p}\delta\boldsymbol{\xi} + \boldsymbol{\tau}\delta\boldsymbol{\eta} + \mathbf{m}\delta\boldsymbol{\chi})dA \\ &= \int_A [\ \mathbf{P}_{\varepsilon}^{(3)}\delta\boldsymbol{\varepsilon}^{(3)} + \mathbf{P}_{\varepsilon}^{(2)}\delta\boldsymbol{\varepsilon}^{(2)} + \mathbf{P}_{\varepsilon}^{(1)}\delta\boldsymbol{\varepsilon}^{(1)} + \mathbf{P}_{\varepsilon}^{(0)}\delta\boldsymbol{\varepsilon}^{(0)} \\ &\quad + \mathbf{P}_{\xi}^{(4)}\delta\boldsymbol{\xi}^{(4)} + \mathbf{P}_{\xi}^{(3)}\delta\boldsymbol{\xi}^{(3)} + \mathbf{P}_{\xi}^{(2)}\delta\boldsymbol{\xi}^{(2)} + \mathbf{P}_{\xi}^{(1)}\delta\boldsymbol{\xi}^{(1)} + \mathbf{P}_{\xi}^{(0)}\delta\boldsymbol{\xi}^{(0)} \\ &\quad + \mathbf{P}_{\chi}^{(5)}\delta\boldsymbol{\chi}^{(5)} + \mathbf{P}_{\chi}^{(4)}\delta\boldsymbol{\chi}^{(4)} + \mathbf{P}_{\chi}^{(3)}\delta\boldsymbol{\chi}^{(3)} + \mathbf{P}_{\chi}^{(2)}\delta\boldsymbol{\chi}^{(2)} + \mathbf{P}_{\chi}^{(1)}\delta\boldsymbol{\chi}^{(1)} + \mathbf{P}_{\chi}^{(0)}\delta\boldsymbol{\chi}^{(0)} \\ &\quad + \mathbf{P}_{\eta}^{(6)}\delta\boldsymbol{\eta}^{(6)} + \mathbf{P}_{\eta}^{(5)}\delta\boldsymbol{\eta}^{(5)} + \mathbf{P}_{\eta}^{(4)}\delta\boldsymbol{\eta}^{(4)} + \mathbf{P}_{\eta}^{(3)}\delta\boldsymbol{\eta}^{(3)} + \mathbf{P}_{\eta}^{(2)}\delta\boldsymbol{\eta}^{(2)} + \mathbf{P}_{\eta}^{(1)}\delta\boldsymbol{\eta}^{(1)} + \mathbf{P}_{\eta}^{(0)}\delta\boldsymbol{\eta}^{(0)}]dA\end{aligned} \tag{11}$$

where the stress resultants are given by:

$$\left(\mathbf{P}_{\varepsilon}^{(0)}, \mathbf{P}_{\varepsilon}^{(1)}, \mathbf{P}_{\varepsilon}^{(2)}\right) = \int_{-h/2}^{h/2} (1, \Phi_1, \Phi_2)\boldsymbol{\sigma}^{(i)}dx_3;\ \mathbf{P}_{\varepsilon}^{(3)} = \int_{-h/2}^{h/2} \Phi_3\boldsymbol{\sigma}^{(o)}dx_3 \tag{12a}$$

$$\left(\mathbf{P}_{\xi}^{(0)}, \mathbf{P}_{\xi}^{(1)}, \mathbf{P}_{\xi}^{(2)}, \mathbf{P}_{\xi}^{(3)}, \mathbf{P}_{\xi}^{(4)}\right) = \int_{-h/2}^{h/2} (1, \Phi_1, \Phi_2, \Phi_{1,3}, \Phi_{2,3})\mathbf{p}dx_3 \tag{12b}$$

$$\left(\mathbf{P}_{\chi}^{(0)}, \mathbf{P}_{\chi}^{(1)}, \mathbf{P}_{\chi}^{(2)}, \mathbf{P}_{\chi}^{(3)}, \mathbf{P}_{\chi}^{(4)}, \mathbf{P}_{\chi}^{(5)}\right) = \int_{-h/2}^{h/2} (1, \Phi_{1,3}, \Phi_{2,3}, \Phi_{1,33}, \Phi_{2,33}, \Phi_2)\mathbf{m}dx_3 \tag{12c}$$

$$\left(\mathbf{P}_{\eta}^{(0)}, \mathbf{P}_{\eta}^{(1)}, \mathbf{P}_{\eta}^{(2)}, \mathbf{P}_{\eta}^{(3)}, \mathbf{P}_{\eta}^{(4)}, \mathbf{P}_{\eta}^{(5)}, \mathbf{P}_{\eta}^{(6)}\right) = \int_{-h/2}^{h/2} (1, \Phi_1, \Phi_2, \Phi_3, \Phi_{1,3}, \Phi_{2,3}, \Phi_{3,3})\boldsymbol{\eta}dx_3 \tag{12d}$$

The following stress resultants could be derived in terms of gradients and strains:

$$\begin{Bmatrix} \mathbf{P}_{\varepsilon}^{(0)} \\ \mathbf{P}_{\varepsilon}^{(1)} \\ \mathbf{P}_{\varepsilon}^{(2)} \\ \mathbf{P}_{\varepsilon}^{(3)} \end{Bmatrix} = \begin{bmatrix} \mathbf{A}^{\varepsilon} & \mathbf{B}^{\varepsilon} & \mathbf{B}_s^{\varepsilon} & \mathbf{0} \\ \mathbf{B}^{\varepsilon} & \mathbf{D}^{\varepsilon} & \mathbf{D}_s^{\varepsilon} & \mathbf{0} \\ \mathbf{B}_s^{\varepsilon} & \mathbf{D}_s^{\varepsilon} & \mathbf{H}_s^{\varepsilon} & \mathbf{0} \\ \mathbf{0} & \mathbf{0} & \mathbf{0} & \mathbf{A}_s^{\varepsilon} \end{bmatrix} \begin{Bmatrix} \boldsymbol{\varepsilon}^{(0)} \\ \boldsymbol{\varepsilon}^{(1)} \\ \boldsymbol{\varepsilon}^{(2)} \\ \boldsymbol{\varepsilon}^{(3)} \end{Bmatrix} \tag{13a}$$

$$\begin{Bmatrix} \mathbf{P}_{\xi}^{(0)} \\ \mathbf{P}_{\xi}^{(1)} \\ \mathbf{P}_{\xi}^{(2)} \\ \mathbf{P}_{\xi}^{(3)} \\ \mathbf{P}_{\xi}^{(4)} \end{Bmatrix} \begin{bmatrix} \mathbf{A}^{\xi} & \mathbf{B}^{\xi} & \mathbf{B}_s^{\xi} & \bar{\mathbf{B}}^{\xi} & \bar{\mathbf{B}}_s^{\xi} \\ \mathbf{B}^{\xi} & \mathbf{D}^{\xi} & \mathbf{D}_s^{\xi} & \bar{\mathbf{O}}^{\xi} & \bar{\mathbf{P}}_s^{\xi} \\ \mathbf{B}_s^{\xi} & \mathbf{D}_s^{\xi} & \mathbf{H}_s^{\xi} & \bar{\mathbf{F}}_s^{\xi} & \bar{\mathbf{J}}^{\xi} \\ \bar{\mathbf{B}}^{\xi} & \bar{\mathbf{O}}^{\xi} & \bar{\mathbf{F}}_s^{\xi} & \bar{\mathbf{D}}^{\xi} & \bar{\mathbf{D}}_s^{\xi} \\ \bar{\mathbf{B}}_s^{\xi} & \bar{\mathbf{P}}_s^{\xi} & \bar{\mathbf{J}}^{\xi} & \bar{\mathbf{D}}_s^{\xi} & \bar{\mathbf{H}}_s^{\xi} \end{bmatrix} \begin{Bmatrix} \boldsymbol{\xi}^{(0)} \\ \boldsymbol{\xi}^{(1)} \\ \boldsymbol{\xi}^{(2)} \\ \boldsymbol{\xi}^{(3)} \\ \boldsymbol{\xi}^{(4)} \end{Bmatrix} \tag{13b}$$

$$\begin{Bmatrix} \mathbf{P}_{\chi}^{(0)} \\ \mathbf{P}_{\chi}^{(1)} \\ \mathbf{P}_{\chi}^{(2)} \\ \mathbf{P}_{\chi}^{(3)} \\ \mathbf{P}_{\chi}^{(4)} \\ \mathbf{P}_{\chi}^{(5)} \end{Bmatrix} = \begin{bmatrix} \mathbf{A}^{\chi} & \bar{\mathbf{B}}^{\chi} & \bar{\mathbf{B}}_s^{\chi} & \overline{\bar{\mathbf{B}}}^{\chi} & \overline{\bar{\mathbf{B}}}_s^{\chi} & \mathbf{B}_s^{\chi} \\ \bar{\mathbf{B}}^{\chi} & \bar{\mathbf{D}}^{\chi} & \bar{\mathbf{D}}_s^{\chi} & \bar{\mathbf{E}}^{\chi} & \bar{\mathbf{E}}_s^{\chi} & \bar{\mathbf{F}}_s^{\chi} \\ \bar{\mathbf{B}}_s^{\chi} & \bar{\mathbf{D}}_s^{\chi} & \bar{\mathbf{H}}_s^{\chi} & \bar{\mathbf{G}}_s^{\chi} & \bar{\mathbf{I}}^{\chi} & \bar{\mathbf{J}}^{\chi} \\ \overline{\bar{\mathbf{B}}}^{\chi} & \bar{\mathbf{E}}^{\chi} & \bar{\mathbf{G}}_s^{\chi} & \overline{\bar{\mathbf{D}}}^{\chi} & \overline{\bar{\mathbf{D}}}_s^{\chi} & \bar{\mathbf{K}}_s^{\chi} \\ \overline{\bar{\mathbf{B}}}_s^{\chi} & \bar{\mathbf{E}}_s^{\chi} & \bar{\mathbf{I}}^{\chi} & \overline{\bar{\mathbf{D}}}_s^{\chi} & \overline{\bar{\mathbf{H}}}_s^{\chi} & \bar{\mathbf{L}} \\ \mathbf{B}_s^{\chi} & \bar{\mathbf{F}}_s^{\chi} & \bar{\mathbf{J}}^{\chi} & \bar{\mathbf{K}}_s^{\chi} & \bar{\mathbf{L}} & \mathbf{H}_s^{\chi} \end{bmatrix} \begin{Bmatrix} \boldsymbol{\chi}^{(0)} \\ \boldsymbol{\chi}^{(1)} \\ \boldsymbol{\chi}^{(2)} \\ \boldsymbol{\chi}^{(3)} \\ \boldsymbol{\chi}^{(4)} \\ \boldsymbol{\chi}^{(5)} \end{Bmatrix} \tag{13c}$$

$$\begin{Bmatrix} \mathbf{P}_{\eta}^{(0)} \\ \mathbf{P}_{\eta}^{(1)} \\ \mathbf{P}_{\eta}^{(2)} \\ \mathbf{P}_{\eta}^{(3)} \\ \mathbf{P}_{\eta}^{(4)} \\ \mathbf{P}_{\eta}^{(5)} \\ \mathbf{P}_{\eta}^{(6)} \end{Bmatrix} = \begin{bmatrix} \mathbf{A}^{\eta} & \mathbf{B}^{\eta} & \mathbf{B}_{s}^{\eta} & \mathbf{A}_{s}^{\eta} & \bar{\mathbf{B}}^{\eta} & \bar{\mathbf{B}}_{s}^{\eta} & \bar{\mathbf{A}}_{s}^{\eta} \\ \mathbf{B}^{\eta} & \mathbf{D}^{\eta} & \mathbf{D}_{s}^{\eta} & \mathbf{D}_{ts}^{\eta} & \bar{\mathbf{O}}^{\eta} & \bar{\mathbf{P}}_{s}^{\eta} & \bar{\mathbf{Q}}_{s}^{\eta} \\ \mathbf{B}_{s}^{\eta} & \mathbf{D}_{s}^{\eta} & \mathbf{H}_{s}^{\eta} & \mathbf{D}_{hs}^{\eta} & \bar{\mathbf{F}}_{s}^{\eta} & \bar{\mathbf{J}}^{\eta} & \bar{\mathbf{F}}_{hs}^{\eta} \\ \mathbf{A}_{s}^{\eta} & \mathbf{D}_{ts}^{\eta} & \mathbf{D}_{hs}^{\eta} & \mathbf{H}_{ts}^{\eta} & \bar{\mathbf{F}}_{ts}^{\eta} & \bar{\mathbf{J}}_{hs}^{\eta} & \bar{\mathbf{R}}^{\eta} \\ \bar{\mathbf{B}}^{\eta} & \bar{\mathbf{O}}^{\eta} & \bar{\mathbf{F}}_{s}^{\eta} & \bar{\mathbf{F}}_{ts}^{\eta} & \bar{\mathbf{D}}^{\eta} & \bar{\mathbf{D}}_{s}^{\eta} & \bar{\mathbf{D}}_{ts}^{\eta} \\ \bar{\mathbf{B}}_{s}^{\eta} & \bar{\mathbf{P}}_{s}^{\eta} & \bar{\mathbf{J}}^{\eta} & \bar{\mathbf{J}}_{hs}^{\eta} & \bar{\mathbf{D}}_{s}^{\eta} & \bar{\mathbf{H}}_{s}^{\eta} & \bar{\mathbf{D}}_{hs}^{\eta} \\ \bar{\mathbf{A}}_{s}^{\eta} & \bar{\mathbf{Q}}_{s}^{\eta} & \bar{\mathbf{F}}_{hs}^{\eta} & \bar{\mathbf{R}}^{\eta} & \bar{\mathbf{D}}_{ts}^{\eta} & \bar{\mathbf{D}}_{hs}^{\eta} & \bar{\mathbf{H}}_{ts}^{\eta} \end{bmatrix} \begin{Bmatrix} \boldsymbol{\eta}^{(0)} \\ \boldsymbol{\eta}^{(1)} \\ \boldsymbol{\eta}^{(2)} \\ \boldsymbol{\eta}^{(3)} \\ \boldsymbol{\eta}^{(4)} \\ \boldsymbol{\eta}^{(5)} \\ \boldsymbol{\eta}^{(6)} \end{Bmatrix} \tag{13d}$$

where the FGP microplate stiffness components are described in Appendix B. The variation of work done by membrane compressive loads in thermo-mechanical environments is determined by:

$$\delta\Pi_{VB} = -\int_{A} N^{(tr)}\left(u^0_{3,1}\delta u^0_{3,1} + u^0_{3,2}\delta u^0_{3,2}\right)dA - \int_{A}\left(N_1^{(m)}u^0_{3,1}\delta u^0_{3,1} + N_2^{(m)}u^0_{3,2}\delta u^0_{3,2}\right)dA \tag{14}$$

where $N_1^{(m)}$ and $N_2^{(m)}$ are in-plane edge loads, $N_{12}^{(m)} = 0$; $N_1^{(tr)} = N_2^{(tr)} = N^{(tr)}, N_{12}^{(tr)} = 0$ are the pre-buckling in-plane thermal loads given by:

$$N^{(tr)} = \int_{-h/2}^{h/2}(Q_{11} + Q_{12})\alpha\Delta T dz \tag{15}$$

in which α is the coefficient of thermal expansion; $\Delta T = T(z) - T_o$ is the current temperature's deviation from the reference one T^o.

2.3. Ritz-type series solution

According to the Ritz approach, the following series of approximation functions and associated series values can be used to describe the membrane and transverse displacements $(u_1^0, u_2^0, u_3^0, \varphi_1, \varphi_2)$ of the FGP microplates:

$$u_1^0(x_1,x_2) = \sum_{i=1}^{n_1}\sum_{j=1}^{n_2} u_{1ij}R_{i,1}(x_1)P_j(x_2); \quad u_2^0(x_1,x_2) = \sum_{i=1}^{n_1}\sum_{j=1}^{n_2} u_{2ij}R_i(x_1)P_{j,2}(x_2) \tag{16a}$$

$$u_3^0(x_1,x_2) = \sum_{i=1}^{n_1}\sum_{j=1}^{n_2} u_{3ij}R_i(x_1)P_j(x_2); \quad \varphi_2(x_1,x_2) = \sum_{i=1}^{n_1}\sum_{j=1}^{n_2} y_{ij}R_i(x_1)P_{j,2}(x_2) \tag{16b}$$

$$\varphi_1(x_1,x_2) = \sum_{i=1}^{n_1}\sum_{j=1}^{n_2} x_{ij}R_{i,1}(x_1)P_j(x_2) \tag{16c}$$

where $u_{1ij}, u_{2ij}, u_{3ij}, x_{ij}, y_{ij}$ represent unknown variables which need to determined; the shape functions in x_1- and x_2- direction are $R_i(x_1), P_j(x_2)$, respectively. As a consequence, only two shape functions affect the five unknowns of the microplates. It should be noted that the decision of the shape functions affects the accuracy, convergence rates, and numerical instabilities of the Ritz solution, which was discussed in detail in Refs. [50,51]. The functions $R_i(x_1)$ and $P_j(x_2)$ are generated to satisfy the boundary conditions (BCs) at the microplate edges as follows:

- Clamped (C): $\varphi_2 = \varphi_1 = u_3^0 = u_2^0 = u_1^0 = 0$ at $x_2 = 0, b$ and $x_1 = 0, a$
- Simply supported (S): $\varphi_2 = u_3^0 = u_2^0 = 0$ at $x_1 = 0, a$ and $\varphi_1 = u_3^0 = u_1^0 = 0$ at $x_2 = 0, b$.

Noting that the use of modified strain gradient theory to capture the size effects could lead to an increase in the order of differential characteristic equations and additional higher-order

boundary conditions [48,49,52]. However, for the simplicity purpose, the effect of non-classical boundary conditions is not considered in this paper.

The combination of clamped and simply-supported BCs on the edges of the microplates leads to the various ones as follows: SSSS, SCSC, CCCC which will be taken into account in the numerical examples as follows:

- For SSSS BC: $R_i(x_1) = x_1(a-x_1)e^{-\frac{ix_1}{a}}$, $P_j(x_2) = x_2(b-x_2)e^{-\frac{jx_2}{b}}$
- For CCCC BC: $R_i(x_1) = x_1^2(a-x_1)^2e^{-\frac{ix_1}{a}}$, $P_j(x_2) = x_2^2(b-x_2)^2e^{-\frac{jx_2}{b}}$
- For SCSC BC: $R_i(x_1) = x_1(a-x_1)^2e^{-\frac{ix_1}{a}}$, $P_j(x_2) = x_2(b-x_2)^2e^{-\frac{jx_2}{b}}$.

Additionally, to construct characteristic equations of motion for the FGP microplates, substituting the approximations in Eq. (16) into Eq. (3) by accounting for Eqs. (11) and (14) leads to:

$$\mathbf{Kd} = \mathbf{0} \tag{17}$$

where $\mathbf{d} = \begin{bmatrix} \mathbf{u}_1 & \mathbf{u}_2 & \mathbf{u}_3 & \mathbf{x} & \mathbf{y} \end{bmatrix}^T$ is the displacement vector to be determined; $\mathbf{K} = \mathbf{K}^{\varepsilon} + \mathbf{K}^{\chi} + \mathbf{K}^{\xi} + \mathbf{K}^{\eta}$ is the stiffness matrix which is composed of those of the strains $\mathbf{K}^{\varepsilon}$, symmetric rotation gradients $\mathbf{K}^{\chi}$, dilatation gradient $\mathbf{K}^{\xi}$, and deviation stretch gradient $\mathbf{K}^{\eta}$. These components are given in more detail as follows:

$$\mathbf{K}^{\kappa} = \begin{bmatrix} \mathbf{K}^{\kappa 11} & \mathbf{K}^{\kappa 12} & \mathbf{K}^{\kappa 13} & \mathbf{K}^{\kappa 14} & \mathbf{K}^{\kappa 15} \\ {}^{T}\mathbf{K}^{\kappa 12} & \mathbf{K}^{\kappa 22} & \mathbf{K}^{\kappa 23} & \mathbf{K}^{\kappa 24} & \mathbf{K}^{\kappa 25} \\ {}^{T}\mathbf{K}^{\kappa 13} & {}^{T}\mathbf{K}^{\kappa 23} & \mathbf{K}^{\kappa 33} & \mathbf{K}^{\kappa 34} & \mathbf{K}^{\kappa 35} \\ {}^{T}\mathbf{K}^{\kappa 14} & {}^{T}\mathbf{K}^{\kappa 24} & {}^{T}\mathbf{K}^{\kappa 34} & \mathbf{K}^{\kappa 44} & \mathbf{K}^{\kappa 45} \\ {}^{T}\mathbf{K}^{\kappa 15} & {}^{T}\mathbf{K}^{\kappa 25} & {}^{T}\mathbf{K}^{\kappa 35} & {}^{T}\mathbf{K}^{\kappa 45} & \mathbf{K}^{\kappa 55} \end{bmatrix} \quad \text{with } \kappa = \{\varepsilon, \xi, \chi, \eta\} \tag{18}$$

where the components of the stiffness matrix $\mathbf{K}^{\varepsilon}$ and $\mathbf{K}^{\chi}$ can be referenced to the earlier work [25]. The stiffness matrix's components $\mathbf{K}^{\xi}$ and $\mathbf{K}^{\eta}$ are given in Appendix C.

2.4. iBCMO-DNN algorithm

It is known that the material properties may be uncertain due to the manufacturing process or other major circumstances. Because of this uncertainty, structures' static and dynamic behaviors are fluctuated, it hence required the advanced computational methods to predict its stochastic behaviors. As mentioned in the introduction, many approaches could be used with different degrees of success, the present section proposes an intelligent computational iBCMO-DNN algorithm which enables to capture uncertain responses of the FGP microplates.

2.4.1. An improved balancing composite motion optimization (iBCMO)

The balancing composite motion optimization (BCMO) is a meta-heuristic algorithm technique which was initially developed by Le-Duc et al. [38] in which the key idea of this approach is to balance the individual composite motion features within the global optimum. Balancing global and local search *via* a probabilistic decision model creates a mechanism of mobility for each individual.

Initialization: As follows, a random initialization is used to create the population distribution,

$$x_i = x_j^L + rand(1,d) \times \left(x_i^U - x_j^L\right) \tag{19}$$

where x_i^L is the lower bound and x_i^U is the upper bound of the $i^{th}-$ individual; the number of items is d.

Best individual and instant global point: The instant global point x_{Oin}^{t} is determined as the prior best of x_1^{t-1} with regard to a trial u_1^t, where u_1^t is calculated using population information from the current generation as follows:

$$u_1^t = (LB + UB)/2 + v_{k1/k2}^t + v_{k2/1}^t \tag{20}$$

where $v_{k1/k2}^t$ is the relative motions of the individual k_1^{th} with respect to the individual k_2^{th}; $v_{k2/1}^t$ is the relative motions of the individual k_2^{th} with respect to the previous best one. $v_{k1/k2}^t$ and $v_{k2/1}^t$

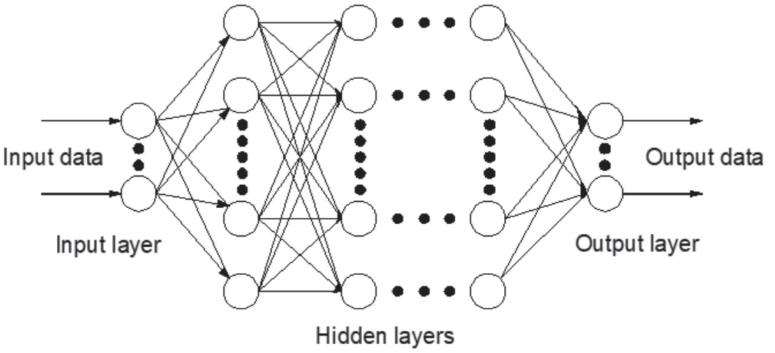

Figure 2. Deep neural network.

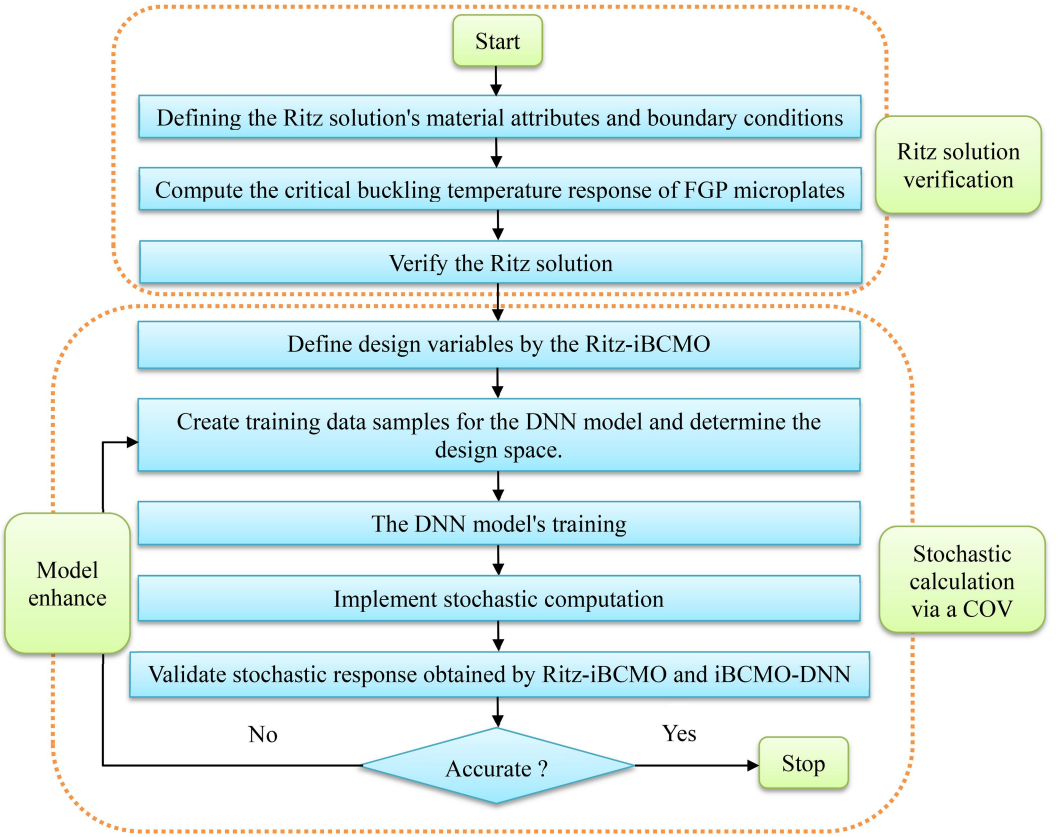

Figure 3. The flowchart of the stochastic response of FGP microplates.

are determined as follows:

$$v_{i/j} = (x_j - x_i)\begin{cases} rand(1,d) & if \quad TV_j > \zeta \\ -rand(1,d) & otherwise \end{cases} \tag{21}$$

where ζ is the probability threshold in selecting the mutation and crossover phases. The value of $\zeta = 0.5$ has been chosen for the balance of global and local search phases as well as mutation and crossover mechanisms for solving general optimization problems [38]. Instant global point is defined as follows:

$$x_{Oin}^t = \begin{cases} u_1^t & if\ f\left(u_1^t\right) < f\left(x_1^{t-1}\right) \\ x_1^{t-1} & otherwise \end{cases} \tag{22}$$

Individuals' composite mobility in the solution space: In BCMO, v_j represents the global search motion, which is governed by:

$$v_j = L_{GS} \times dv_j \times (x_{Oin} - x_j) \tag{23}$$

where

$$L_{GS} = \begin{cases} e^{-\frac{1}{dNP}\frac{j}{r_j^2}} & if\ TV_j > \zeta \\ e^{-\frac{1}{d}\left(1-\frac{j}{NP}\right)r_j^2} & otherwise \end{cases};\ dv_{ij} = \begin{cases} rand(1,d) & if\ TV_j > \zeta \\ -rand(1,d) & otherwise \end{cases} \tag{24}$$

where NP is the population size. These v_{ik} instances have equal probability and can be calculated as follows:

$$P(v_{ik}) = P(v_{i/j}) \times P(v_j) = \zeta^2 \quad \text{with} \quad k = 1, \ldots, 4 \tag{25}$$

The i^{th} individual's position is updated as follows:

$$x_i^{t+1} = x_i^t + v_{i/j} + v_j \tag{26}$$

It is noted that in the original BCMO, the function *rand* is a random number which is uniformly distributed in the range $[0, 1]$, the present iBCMO tries to enhance convergence speed

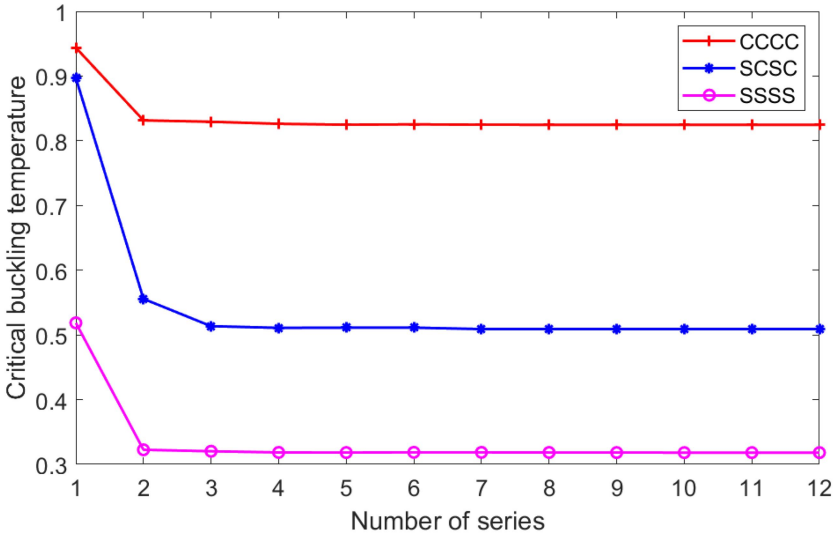

Figure 4. Convergence study of series solution of Al/Al_2O_3 FGP microplates with different boundary conditions ($a/h = 20$, $p = 5$, $\beta = 0.1$, $h/l = 5$).

while guarantees the solution accuracy by defining a subset $[a_1, b_1] \in [0, 1]$ which gives the most optimal values. Moreover, it is worthy to noticing that the probabilistic threshold ζ for choosing its mutation and crossover phases might be changed with different problems, therefore which will be selected throughout numerical simulations.

2.4.2. iBCMO-DNN algorithm

A deep feedforward neural network is shown in Figure 2 in which the input data of the neural network is passed through the input layer, hidden layers, and output layer. Before reaching the nodes, the input data from the outside is multiplied by the weights. Each node in the succeeding layers will get the total of the preceding nodes' output values multiplied by their respective

Table 1. Normalized critical buckling load $\bar{N}_{cr} = (N^m_{cr}a^2/h^3E_m)$ of Al/Al_2O_3 FGP square microplates ($\beta = 0$, $a/h = 10$, SSSS).

		h/l				
p	Theory	∞	10	5	2	1
Axial compression $(N_1^{(m)}, N_2^{(m)}, N_{12}^{(m)} = 1, 0, 0)$						
0.5	Present	12.1593	14.1562	20.1595	62.2324	212.5038
	MST [60]	12.1236	14.1490	20.1999	62.1669	211.1461
	RPT [62]	12.1213	14.1543	20.2387	62.6144	213.5682
	IGA [61]	12.1230	14.0850	19.9551	60.8187	206.3342
1	Present	9.3724	11.0035	15.9002	50.1979	172.6696
	MST [60]	9.3391	10.9906	15.9260	50.1870	171.9637
	RPT [62]	9.3391	10.9968	15.9590	50.5419	173.7865
	IGA [61]	9.3391	10.9375	15.7204	49.0315	167.6943
2	Present	7.2889	8.5648	12.3864	39.0974	134.4300
	MST [60]	7.2631	8.5419	12.3708	39.0731	134.2383
	RPT [62]	7.2631	8.5479	12.4000	39.3331	135.4673
	IGA [61]	7.2631	8.4979	12.1985	38.0563	130.3251
5	Present	6.0563	7.0017	9.7751	28.8861	96.9485
	MST [60]	6.0353	6.9468	9.6789	28.7840	96.9802
	RPT [62]	6.0353	6.9549	9.7100	28.9617	97.6728
	IGA [61]	6.0353	6.9131	9.5425	27.9155	93.4952
10	Present	5.4723	6.2570	8.5295	24.0504	79.2548
	MST [60]	5.4529	6.1945	8.4150	23.9178	79.2302
	RPT [62]	5.4528	6.2026	8.4445	24.0660	79.7717
	IGA [61]	5.4528	6.1674	8.3032	23.1847	76.2541
Biaxial compression $(N_1^{(m)}, N_2^{(m)}, N_{12}^{(m)} = 1, 1, 0)$						
0.5	Present	6.0800	7.0780	10.0781	31.1022	106.1940
	MST [60]	6.0618	7.0745	10.1000	31.0834	105.6232
	RPT [62]	6.0606	7.0772	10.1193	31.3072	106.7841
	IGA [61]	6.0615	7.0425	9.9775	30.4094	103.1673
1	Present	4.6865	5.5017	7.9490	25.0897	86.2975
	MST [60]	4.6696	5.4953	7.9630	25.0935	85.9820
	RPT [62]	4.6695	5.4984	7.9795	25.2710	86.8932
	IGA [61]	4.6696	5.4688	7.8602	24.5158	83.8473
2	Present	3.6447	4.2824	6.1925	19.5433	67.1946
	MST [60]	3.6315	4.2710	6.1854	19.5365	67.1192
	RPT [62]	3.6315	4.2740	6.2000	19.6665	67.7337
	IGA [61]	3.6315	4.2490	6.0993	19.0282	65.1626
5	Present	3.0284	3.5007	4.8868	14.4394	48.4615
	MST [60]	3.0177	3.4734	4.8395	14.3920	48.4902
	RPT [62]	3.0177	3.4774	4.8550	14.4808	48.8364
	IGA [61]	3.0177	3.4565	4.7712	13.9578	46.7476
10	Present	2.7363	3.1284	4.2640	12.0217	39.6153
	MST [60]	2.7264	3.0972	4.2075	11.9589	39.6151
	RPT [62]	2.7264	3.1013	4.2222	12.0330	39.8858
	IGA [61]	2.7264	3.0837	4.1516	11.5924	38.1271

Table 2. Normalized critical buckling load $\bar{N}_{cr} = (N^m_{cr}a^2/h^3E_m)$ of Al/Al_2O_3 FGP square microplates with axial compression $(N_1^{(m)}, N_2^{(m)}, N_{12}^{(m)} = 1, 0, 0)$, $\beta = 0$, $a/h = 10$, SCSC and CCCC boundary conditions

		h/l				
p	Theory	∞	10	5	2	1
SCSC						
0.5	Present	20.4079	23.9355	34.5293	106.2774	360.4446
	IGA [61]	20.7870	24.2336	34.4511	104.9240	355.0073
1	Present	15.7470	18.6220	27.2586	87.4220	300.6437
	IGA [61]	16.0781	18.9077	27.2924	85.1205	290.3734
2	Present	12.2120	14.4381	21.1388	68.0160	234.9042
	IGA [61]	12.4183	14.6427	21.2445	67.0440	230.0893
5	Present	10.0014	11.5889	16.3775	50.0462	170.4489
	IGA [61]	9.9661	11.6057	16.4530	50.0703	169.7890
10	Present	8.9785	10.2705	14.1665	41.5532	139.4981
	IGA [61]	8.8672	10.2203	14.1983	41.6312	139.1741
CCCC						
0.5	Present	27.2737	31.9314	45.8300	140.3232	477.7048
	IGA [61]	27.0706	31.6036	45.0313	137.6734	466.5827
1	Present	21.0949	24.8790	36.1457	114.3872	391.8628
	IGA [61]	20.9471	24.6676	35.6870	111.7391	381.8401
2	Present	16.2844	19.2023	27.8882	88.3252	302.6476
	IGA [61]	16.1682	19.0964	27.7817	88.0910	302.9154
5	Present	13.0268	15.1511	21.4006	64.5835	219.5999
	IGA [61]	12.9218	15.0971	21.5034	65.8642	223.8079
10	Present	11.5736	13.3378	18.4901	53.8684	179.6851
	IGA [61]	11.4711	13.2770	18.5512	54.7761	183.4780

Table 3. Normalized critical buckling load $\bar{N}_{cr} = (N^m_{cr}a^2/h^3E_m)$ of Al/Al_2O_3 FGP square microplates $(a/h = 10$, SSSS), $(N_1^{(m)}, N_2^{(m)}, N_{12}^{(m)} = 1, 0, 0)$.

			h/l				
β	p	Theory	∞	10	5	2	1
SSSS							
0.1	0.5	Present	10.7948	12.6701	18.3088	57.8304	198.9871
	1	Present	7.9448	9.4448	13.9488	45.4984	158.1497
	2	Present	5.7630	6.8953	10.2914	34.0529	118.8672
	5	Present	4.5302	5.3182	7.6301	23.5858	80.4325
	10	Present	4.0691	4.6990	6.5045	18.7935	62.4979
0.2	0.5	Present	9.4762	11.2247	16.4823	53.3286	184.9203
	1	Present	6.5272	7.8908	11.9841	40.6488	142.9793
	2	Present	4.1773	5.1601	8.1107	28.7696	102.5064
	5	Present	2.8570	3.4750	5.2956	17.9166	62.9178
	10	Present	2.5287	2.9923	4.2978	13.1640	44.7111
SCSC							
0.1	0.5	Present	18.1615	21.4830	31.4557	100.8126	346.1531
	1	Present	13.3906	16.0431	24.0094	79.4346	275.5905
	2	Present	9.6990	11.6851	17.6630	59.4432	208.0289
	5	Present	7.5049	8.8335	12.8445	41.0540	141.9227
	10	Present	6.6698	7.6989	10.8027	32.6080	110.5416
0.2	0.5	Present	15.9821	19.0868	28.4059	93.1467	321.8675
	1	Present	11.0405	13.4593	20.7214	71.1660	249.3802
	2	Present	7.0742	8.8085	14.0286	50.4483	179.7521
	5	Present	4.7670	5.8212	9.0096	31.4459	111.6549
	10	Present	4.1405	4.8922	7.1593	23.0534	79.7902
CCCC							
0.1	0.5	Present	24.3601	28.7527	41.8178	132.4741	453.8002
	1	Present	18.0333	21.5132	31.8839	103.7666	358.2498
	2	Present	13.0317	15.6155	23.3124	76.7932	264.9759
	5	Present	9.8266	11.5830	16.7471	52.3538	179.5735
	10	Present	8.5850	9.9884	14.0572	41.8132	123.2950
0.2	0.5	Present	21.5197	25.6169	37.8204	122.3423	421.5245
	1	Present	14.9569	18.1229	27.5534	92.7331	322.8644
	2	Present	9.6040	11.8409	18.4980	64.5556	221.4257
	5	Present	6.3170	7.6725	11.6563	38.6637	132.2340
	10	Present	5.3232	6.3350	9.2270	26.8966	92.8254

weights, and the activation function's output data for the sum is supplied as follows [53]:

$$y_i^n = \varphi\left(x_i^n\right) = \varphi\left(\sum_{j=1}^{L_{n-1}} w_{ij}^{n-1} \times y_j^{n-1} + b_i^n\right) \tag{27}$$

where a data pair with output and input of activation function of node i which are y_i^n and x_i^n, respectively; b_i^n is the bias of node j; w_{ij}^{n-1} is the weight between the output node i and input

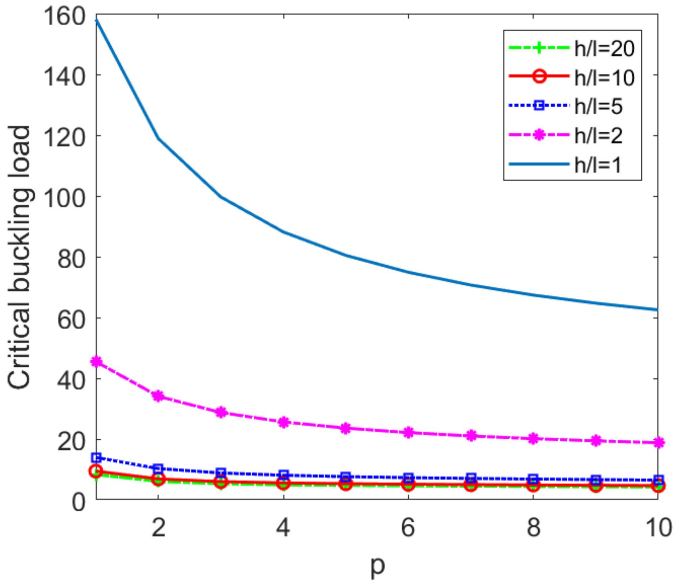

(a) SSSS

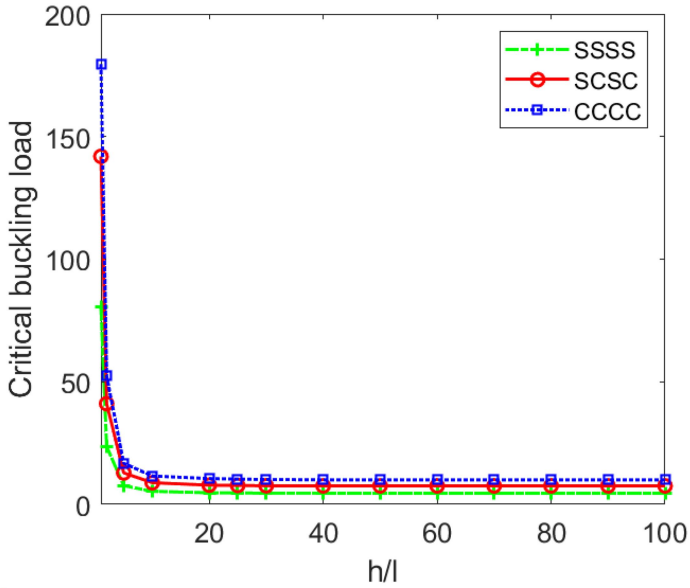

(b) $p = 5$

Figure 5. Variation of normalized critical buckling load for axial compression with respect the power index p and length scale-to-thickness ratio h/l ($a/h = 10,\ \beta = 0.1$).

node j; φ is the activation function. Many kinds of activation functions are available in the literature [54], in the present study, the long short-term memory network (LSTM) [55] will be applied in which the tanh activation function is used for nodes of the input layer and hidden layers, and the sigmoid activation function for the output nodes. The LSTM algorithm enhances the conventional recurrent neural network (RNN) by addressing memory storage and gradient dispersion issues. With its long short-term memory capabilities, the LSTM finds extensive application in time-series prediction tasks. Depth series and time series share fundamental characteristics, with each data point's relationship extending from the past to the future. Consequently, the LSTM models are suitable for forecasting deep formation penetration rates.

The flowchart of iBCMO-DNN algorithm is presented in Figure 3. It is noted that the input and associated output of a data pair is namely a training data. A goal value will be estimated from the corresponding input data in the training data, this goal value is compared with the corresponding output one to estimate the error value of the loss function. Moreover, in the present study, the mean square error (MSE) [56] will be used for the process of training as follows:

$$MSE = \frac{1}{L}\sum_{i}^{L}\left(y_i - \widehat{y}_i\right)^2 \tag{28}$$

where L is number of samples; y_i is output data; $\widehat{y}_i$ is goal data to be predicted. Furthermore, the adaptive moment estimation (Adam) [57] to adjust weights and bias for minimizing the cost function is determined by the gradient of the loss function. The batch gradient descent (BGD) calculates gradients using the whole data set in the dataset and updates them only after all training data has been assessed. As a result, various deficiencies in memory, training speed, and stability appear. Hence, in the current task, mini-batch gradient descent (mBGD) [58] was used.

3. Numerical results

In this section, numerical examples with the shear function $f(x_3) = x_3 - 4x_3^3/3h^2$ [47] are performed to explore the deterministic and stochastic responses of FGP microplates with various BCs. The FGP microplates are expected to be made of a combination of ceramic and metal mate-

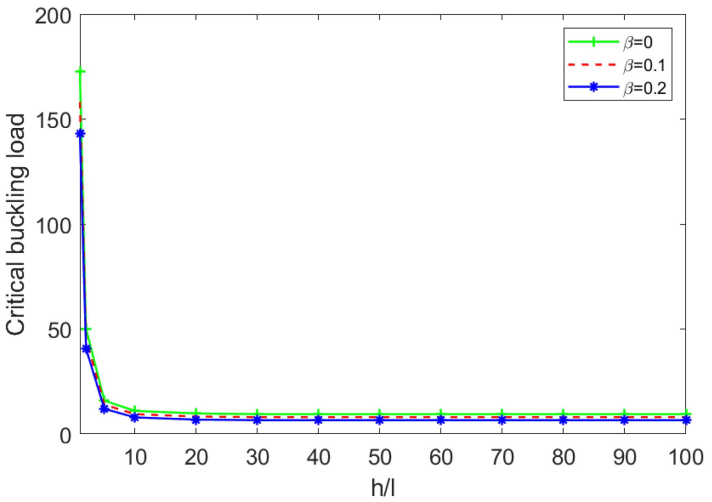

Figure 6. Size effect of the MST for the normalized critical buckling load with respect to the length scale-to-thickness ratio h/l under axial compression, $a/h = 10$, and power–law index $p = 1$, SSSS boundary condition.

rials with mean properties as follows: Al_2O_3 ($E_c = 380$ GPa, $\rho_c = 3800$ kg/m^3, $\alpha_c = 7.4 \times 10^{-6}$1/C, $\nu_c = 0.3$), Al ($E_m = 70$ GPa, $\rho_m = 2702$ kg/m^3, $\alpha_m = 23 \times 10^{-6}$1/C, $\nu_m = 0.3$). For simplification purposes, all three length scale parameters are considered to have the same value, i.e., $l_1 = l_2 = l_3 = l$. In practice, these material length scale values should be derived mainly *via* experimental data. Unless special mention, square FGP microplates with three BCs (SSSS, SCSC, CCCC) are considered in numerical examples, and for convenience, the following normalized parameters are used in the computations:

$$\bar{T}_{cr} = T_{cr} \times 10^{-3} \tag{29}$$

It is worth to noticing that the stretching-bending coupling effect appears in functionally graded microplates due to the change of material properties in its thickness. This coupling produces deflection and bending moments when the microplate is subjected to in-plane compressive

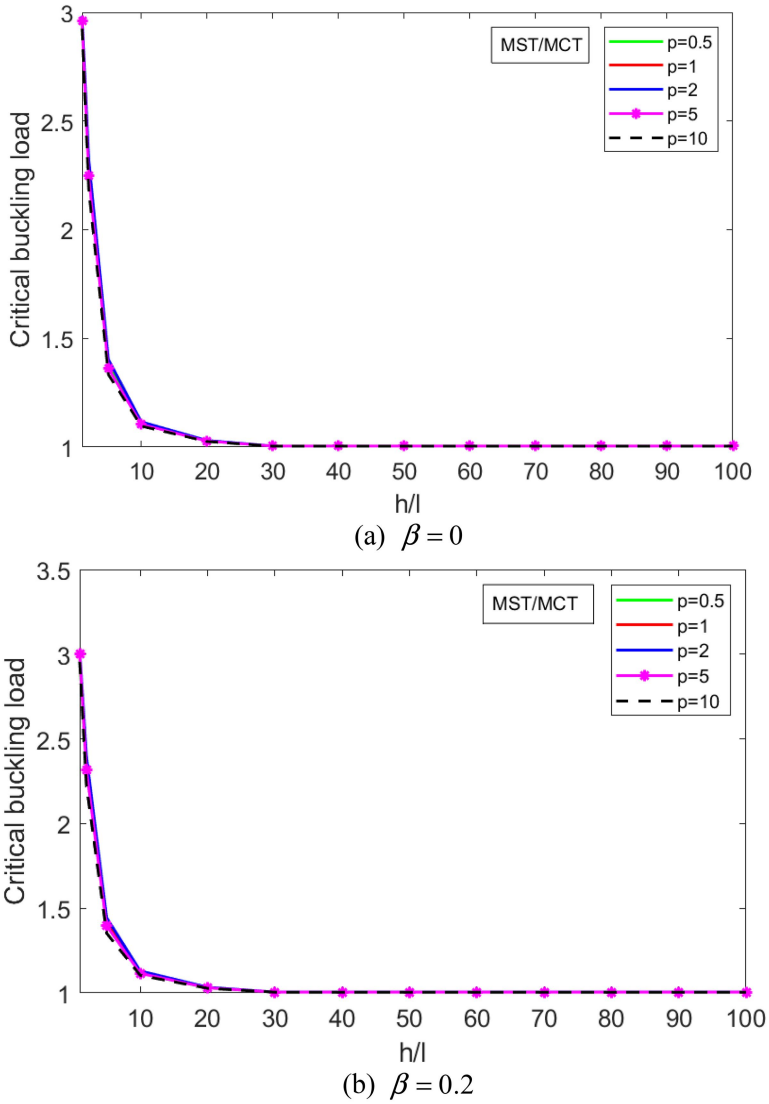

Figure 7. Size effect of the MCT and MST for the normalized critical buckling load with respect to the length scale-to-thickness ratio h/l under axial compression, $a/h = 10$, SSSS boundary condition.

loads. Earlier work [59] on buckling behaviors of functionally graded plates revealed that the bifurcation-type buckling occurs when the functionally graded plate is fully clamped. For movable-edge functionally graded plates, the bifurcation-type buckling occurs when the in-plane loads are applied at the neutral surface. For the present FGP microplates, it is supposed that the buckling analysis is performed for FGP microplates subjected to in-plane mechanical and thermal loads (Eq. 14) acting on the neutral surface.

For stochastic analysis, the material characteristics $(E_m, E_c, \alpha_c, \alpha_m, p)$ are assumed to be distributed randomly using uniform distributions, and the coefficient of variation (COV) is set at 10% for all random variables.

For the convergence study of the present solution, Figure 4 shows the normalized critical buckling temperatures $\bar{T}_{cr}$ of Al/Al_2O_3 FGP microplates under biaxial compression with $a/h = 20$, $p = 5$, $\beta = 0.1$ and $h/l = 5$. The results are calculated with three types of BCs (SSSS, SCSC, CCCC) and the same number of series in x_1- and x_2- direction $(n_1 = n_2 = n)$. It is observed from Figure 4 that the results converge quickly for a small number of series in which the CCCC and SCSC boundary conditions having more kinematic constraints converge lower than the SSSS one. Obviously, the number of series $n = 8$ can be ensure the stability and convergence of the present solution, hence this value will be used for following numerical computations.

3.1. Deterministic buckling analysis

Example 1: This example aims to present a deterministic buckling analysis of FGP microplates with unchanged material properties and subjected to mechanical membrane loads. To verify the accuracy of the present theory in predicting buckling behaviors with deterministic material properties, Table 1 presents normalized critical buckling loads of simply supported FGM microplates under mechanical loads in which the responses are calculated with both axial compression $(N_1^{(m)}, N_2^{(m)}, N_{12}^{(m)} = 1, 0, 0)$ and biaxial compression $(N_1^{(m)}, N_2^{(m)}, N_{12}^{(m)} = 1, 1, 0)$, different values of $h/l = \infty$, 10, 5, 2, 1, and no porosity effect is accounted $(\beta = 0)$. These results are then compared with those reported by Thai et al. [60], Thai et al. [61], and Zhang et al. [62]. It can be seen from Table 1 that there are good agreements among models, the effects of thickness-to-MLSP ratio impacted importantly on critical buckling loads of FGM microplates. Similarly, the

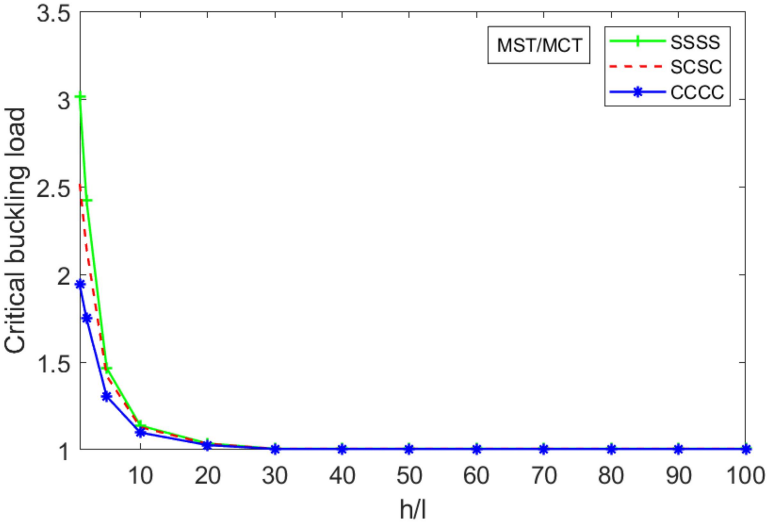

Figure 8. The normalized critical buckling under impacting size effect of the MST and MCT with axial compression, $a/h = 10$, $\beta = 0.2$, $p = 1$.

accuracy of the present model in predicting buckling behaviors is also verified as expected in Table 2 for SCSC and CCCC boundary conditions of FGM microplates. Moreover, to investigate the effects of porosity, material distribution, boundary conditions, and size effects in mechanical buckling responses further, Table 3 introduces new numerical results of critical buckling loads for the FGP microplates under uniaxial compression with porous parameter $\beta = 0.1$ and 0.2, side-to-thickness ratio $a/h = 10$, different power indices $p = 0.5, 1, 2, 5, 10$, various values of $h/l = \infty$, 10, 5, 2, 1, and three boundary conditions (SSSS, SCSC, CCCC). The variation of normalized critical buckling loads with respect to p and h/l is also plotted in Figures 5 and 6. It is observed that the critical buckling loads decrease with an increase in the power-law index p, porosity parameter β, and thickness-to-MLSP ratio h/l. This phenomena can be explained by the fact that the increase of p, β and h/l leads to the decrease of stiffness of the FGP microplates. It is interesting

Table 4. Normalized thermal critical buckling load $\bar{T}_{cr}$ of Al/Al_2O_3 FGP square microplates with biaxial compression $(N_1^{(tr)}, N_2^{(tr)}, N_{12}^{(tr)} = 1, 1, 0)$ and $a/h = 20$ under uniform temperature distribution.

			h/l				
BCs	p	Theory	∞	10	5	2	1
SSSS							
$\beta = 0$	0	Present	0.4218	0.4835	0.6691	1.9704	6.6189
		HSDT [63]	0.4215	–	–	–	–
	1	Present	0.1964	0.2303	0.3324	1.0482	3.6054
		HSDT [63]	0.1962	–	–	–	–
	5	Present	0.1786	0.2046	0.2823	0.8242	2.7581
		HSDT [63]	0.1785	–	–	–	–
	10	Present	0.1834	0.2073	0.2784	0.7736	2.5401
		HSDT [63]	0.1831	–	–	–	–
$\beta = 0.1$	0	Present	0.5437	0.6265	0.8758	2.6239	8.8690
	1	Present	0.2206	0.2622	0.3871	1.2629	4.3917
	5	Present	0.1930	0.2244	0.3182	0.9728	3.3096
	10	Present	0.2067	0.2354	0.3207	0.9130	3.0261
$\beta = 0.2$	0	Present	0.7513	0.8705	1.2289	3.7427	12.7232
	1	Present	0.2494	0.3015	0.4583	1.5576	5.4844
	5	Present	0.1924	0.2318	0.3496	1.1726	4.1113
	10	Present	0.2235	0.2596	0.3663	1.1071	3.7505
SCSC							
$\beta = 0$	0	Present	0.6778	0.7785	1.0805	3.1951	10.7448
	1	Present	0.3161	0.3716	0.5381	1.7036	5.8633
	5	Present	0.2865	0.3282	0.4532	1.3291	4.4592
	10	Present	0.2936	0.3317	0.4458	1.2450	4.1022
$\beta = 0.1$	0	Present	0.8743	1.0093	1.4151	4.2562	14.4002
	1	Present	0.3554	0.4233	0.6271	2.0541	7.1462
	5	Present	0.3098	0.3601	0.5112	1.5695	5.3516
	10	Present	0.3310	0.3764	0.5129	1.4686	4.8856
$\beta = 0.2$	0	Present	1.2081	1.4029	1.9864	6.0725	20.6616
	1	Present	0.4020	0.4873	0.7434	2.5356	8.9306
	5	Present	0.3092	0.3726	0.5627	1.8936	6.6505
	10	Present	0.3577	0.4146	0.5853	1.7804	6.0543
CCCC							
$\beta = 0.0$	0	Present	1.0893	1.2534	1.7454	5.1862	17.4462
	1	Present	0.5092	0.5997	0.8710	2.7683	9.5260
	5	Present	0.4587	0.5266	0.7303	2.1551	7.2379
	10	Present	0.4691	0.5310	0.7169	2.0168	6.6553
$\beta = 0.1$	0	Present	1.4057	1.6260	2.2871	6.9105	23.3840
	1	Present	0.5731	0.6839	1.0162	3.3393	11.6128
	5	Present	0.4965	0.5786	0.8248	2.5465	8.6892
	10	Present	0.5285	0.6026	0.8249	2.3793	7.9270
$\beta = 0.2$	0	Present	1.9443	2.2614	3.2123	9.8621	33.5549
	1	Present	0.6491	0.7883	1.2057	4.1243	14.5162
	5	Present	0.4969	0.6002	0.9100	3.0767	10.8067
	10	Present	0.5710	0.6638	0.9419	2.8862	9.8272

to see that the size effects of FGP microplates are importantly significant from $h/l < 20$ for both FGM microplates ($\beta = 0$) and FGP microplates ($\beta = 0.1, 0.2$). Figure 6 also shows that the porosity effect does not impact significantly on the size effects of FGP microplates with boundary condition. This can be explained by the fact that the effective properties of functionally graded porous materials are calculated in Eq. (1) based on the volume average approximation in which the effect of geometric size of porosity has not been considered.

To examine the size effects of FGP microplates further, Figures 7 and 8 provide the variation of the proportion of critical buckling loads derived from the MST and MCT with respect to h/l. The results are computed for FGP microplates with $a/h = 10$, $\beta = 0.2$, $p = 1$ and different boundary conditions. Three curves are observed in which the highest and lowest curves correspond to the SSSS and CCCC boundary conditions, respectively. It is clear from these graphs that

Table 5. Normalized thermal critical buckling load $\bar{T}_{cr}$ of Al/Al_2O_3 FGP square microplates with biaxial compression $(N_1^{(tr)}, N_2^{(tr)}, N_{12}^{(tr)} = 1, 1, 0)$ and $a/h = 20$ under linear temperature distribution.

			h/l				
BCs	p	Theory	∞	10	5	2	1
SSSS							
$\beta = 0$	0	Present	0.8325	0.9543	1.3206	3.8889	13.0637
		HSDT [63]	0.8330	–	–	–	–
	1	Present	0.3638	0.4266	0.6157	1.9416	6.6783
		HSDT [63]	0.3587	–	–	–	–
	5	Present	0.3040	0.3483	0.4804	1.4026	4.6940
		HSDT [63]	0.2987	–	–	–	–
	10	Present	0.3213	0.3632	0.4879	1.3556	4.4515
		HSDT [63]	0.3156	–	–	–	–
$\beta = 0.1$	0	Present	1.0730	1.2366	1.7286	5.1788	17.5047
	1	Present	0.4050	0.4813	0.7106	2.3183	8.0619
	5	Present	0.3141	0.3652	0.5178	1.5831	5.3857
	10	Present	0.3468	0.3949	0.5379	1.5314	5.0761
$\beta = 0.2$	0	Present	1.4829	1.7181	2.4255	7.3868	25.1115
	1	Present	0.4521	0.5467	0.8310	2.8240	9.9438
	5	Present	0.3095	0.3488	0.5261	1.7647	6.1874
	10	Present	0.3436	0.3992	0.5633	1.7023	5.7669
SCSC							
$\beta = 0$	0	Present	1.3378	1.5366	2.1325	6.3061	21.2068
	1	Present	0.5856	0.6883	0.9967	3.1556	10.8606
	5	Present	0.4876	0.5585	0.7713	2.2619	7.5890
	10	Present	0.5146	0.5812	0.7812	2.1818	7.1888
$\beta = 0.1$	0	Present	1.7258	1.9921	2.7929	8.4005	28.4214
	1	Present	0.6524	0.7771	1.1513	3.7707	13.1183
	5	Present	0.5041	0.5860	0.8319	2.5540	8.7086
	10	Present	0.5552	0.6315	0.8604	2.4634	8.1952
$\beta = 0.2$	0	Present	2.3846	2.7688	3.9205	11.9852	40.7795
	1	Present	0.7289	0.8836	1.3478	4.5974	16.1921
	5	Present	0.4953	0.5607	0.8468	2.8499	10.0089
	10	Present	0.5501	0.6375	0.9000	2.7376	9.3093
CCCC							
$\beta = 0.0$	0	Present	2.1500	2.4738	3.4449	10.2358	34.4334
	1	Present	0.9432	1.1108	1.6134	5.1277	17.6450
	5	Present	0.7806	0.8962	1.2429	3.6677	12.3179
	10	Present	0.8220	0.9306	1.2564	3.5343	11.6630
$\beta = 0.1$	0	Present	2.7744	3.2092	4.5141	13.6392	46.1527
	1	Present	1.0521	1.2554	1.8654	6.1301	21.3176
	5	Present	0.8079	0.9416	1.3422	4.1440	14.1401
	10	Present	0.8865	1.0109	1.3838	3.9911	13.2970
$\beta = 0.2$	0	Present	3.8373	4.4632	6.3400	19.4646	66.2268
	1	Present	1.1769	1.4292	2.1860	7.4777	26.3194
	5	Present	0.7878	0.9033	1.3695	4.6303	16.2639
	10	Present	0.8779	1.0207	1.4484	4.4380	15.1107

the MST with three MLSPs generates the critical buckling loads much larger than the MCT with one MLSP, especially when the MLSP is close to the microplate thickness. As seen in Figures 7 and 8, for $h/l = 1$ and SSSS boundary condition, the critical buckling loads obtained from the MST are greater than three times than those from the MCT. The differences between these theories are sharply decreased up to $h/l = 20$ from which the size effects can be neglected. It underlines how crucial it is to take into account three MLSPs while dealing with microplate problems.

Example 2: The next example is to consider deterministic critical buckling temperatures. Tables 4–6 present normalized critical buckling temperatures of FGP microplates with three types of temperature distribution (UTR, LTR, NLTR), $a/h = 20$, $p = 0, 1, 5, 10$ and $h/l = \infty$, 10, 5, 2, 1. For verification purposes, the obtained critical buckling temperatures for FGM plates without porous parameters ($\beta = 0$) and size effect are compared to those provided by Zenkour et al. [63], Yaghoobi et al. [64]. It is seen that there are good agreements among the models. The porosity

Table 6. Normalized thermal critical buckling load $\bar{T}_{cr}$ of Al/Al_2O_3 FGP square microplates with biaxial compression $(N_1^{(tr)}, N_2^{(tr)}, N_{12}^{(tr)} = 1, 1, 0)$ and $a/h = 20$ under nonlinear temperature distribution.

			h/l				
BCs	p	Theory	∞	10	5	2	1
SSSS							
$\beta = 0$	0	Present	0.8436	0.9670	1.3382	3.9407	13.2379
		FSDT [64]	0.8330	–	–	–	–
	1	Present	0.6554	0.7687	1.1094	3.4982	12.0321
	5	Present	0.4326	0.4955	0.6836	1.9956	6.6784
		FSDT [64]	0.3746	–	–	–	–
	10	Present	0.4042	0.4569	0.6137	1.7051	5.5989
		FSDT [64]	0.3660	–	–	–	–
$\beta = 0.1$	0	Present	1.0873	1.2531	1.7517	5.2479	17.7381
	1	Present	0.7327	0.8706	1.2855	4.1939	14.5842
	5	Present	0.4449	0.5173	0.7335	2.2425	7.6292
	10	Present	0.4347	0.4951	0.6744	1.9199	6.3640
$\beta = 0.2$	0	Present	1.5027	1.7410	2.4579	7.4853	25.4463
	1	Present	0.8232	0.9954	1.5131	5.1421	18.1060
	5	Present	0.4372	0.4907	0.7401	2.4824	8.7039
	10	Present	0.4283	0.4976	0.7020	2.1216	7.1875
SCSC							
$\beta = 0$	0	Present	1.3557	1.5569	2.1610	6.3902	21.4896
	1	Present	1.0550	1.2402	1.7957	5.6854	19.5674
	5	Present	0.6937	0.7946	1.0974	3.2182	10.7974
	10	Present	0.6473	0.7311	0.9826	2.7443	9.0419
$\beta = 0.1$	0	Present	1.7486	2.0186	2.8301	8.5125	28.8004
	1	Present	1.1802	1.4058	2.0827	6.8214	23.7315
	5	Present	0.7141	0.8301	1.1785	3.6179	12.3362
	10	Present	0.6960	0.7917	1.0787	3.0884	10.2745
$\beta = 0.2$	0	Present	2.4162	2.8058	3.9728	12.1451	41.3232
	1	Present	1.3272	1.6089	2.4541	8.3710	29.4832
	5	Present	0.6976	0.7987	1.1912	4.0090	14.0796
	10	Present	0.6856	0.7946	1.1217	3.4120	11.6025
CCCC							
$\beta = 0.0$	0	Present	2.1787	2.5067	3.4908	10.3723	34.8925
	1	Present	1.6994	2.0013	2.9068	9.2386	31.7907
	5	Present	1.1107	1.2751	1.7684	5.2183	17.5254
	10	Present	1.0341	1.1705	1.5802	4.4453	14.6694
$\beta = 0.1$	0	Present	2.8114	3.2520	4.5743	13.8211	46.7680
	1	Present	1.9033	2.2712	3.3745	11.0895	38.5645
	5	Present	1.1445	1.3338	1.9013	5.8702	20.0301
	10	Present	1.1114	1.2674	1.7348	5.0036	16.6705
$\beta = 0.2$	0	Present	3.8886	4.5227	6.4246	19.7241	67.1098
	1	Present	1.2290	2.6023	3.9804	13.6157	47.9233
	5	Present	1.1218	1.2907	1.9265	6.5135	22.8785
	10	Present	1.0944	1.2722	1.8052	5.5312	18.8330

and size effects on critical buckling temperatures reporting new numerical results are presented in Tables 4–6 and will be used as benchmarks for future researches. Figures 9–11 also display the variation of the critical buckling temperature with respect to the power-law index p, porosity parameter β, different temperature distributions (UTR, LTR, NLTR), and boundary conditions. It is interesting to observe from these graphs that the critical buckling temperatures increase with the porosity parameter β, this can be explained by the fact that an increase of the porous parameter led to the increase of the thermal conductivity coefficient and therefore it requires a higher critical buckling load. Furthermore, the effect of three types of temperatures (UTR, LTR, NLTR) with respect to h/l is also displayed in Figures 9–11 for the microplates. The highest and lowest values are associated with the NLTR and UTR, respectively.

3.2. Stochastic analysis of critical buckling temperature

Example 3: The objective of this example is to examine the optimal random range $[a_1, b_1]$ and probability threshold ζ serving for studying stochastic critical buckling temperatures of FGP

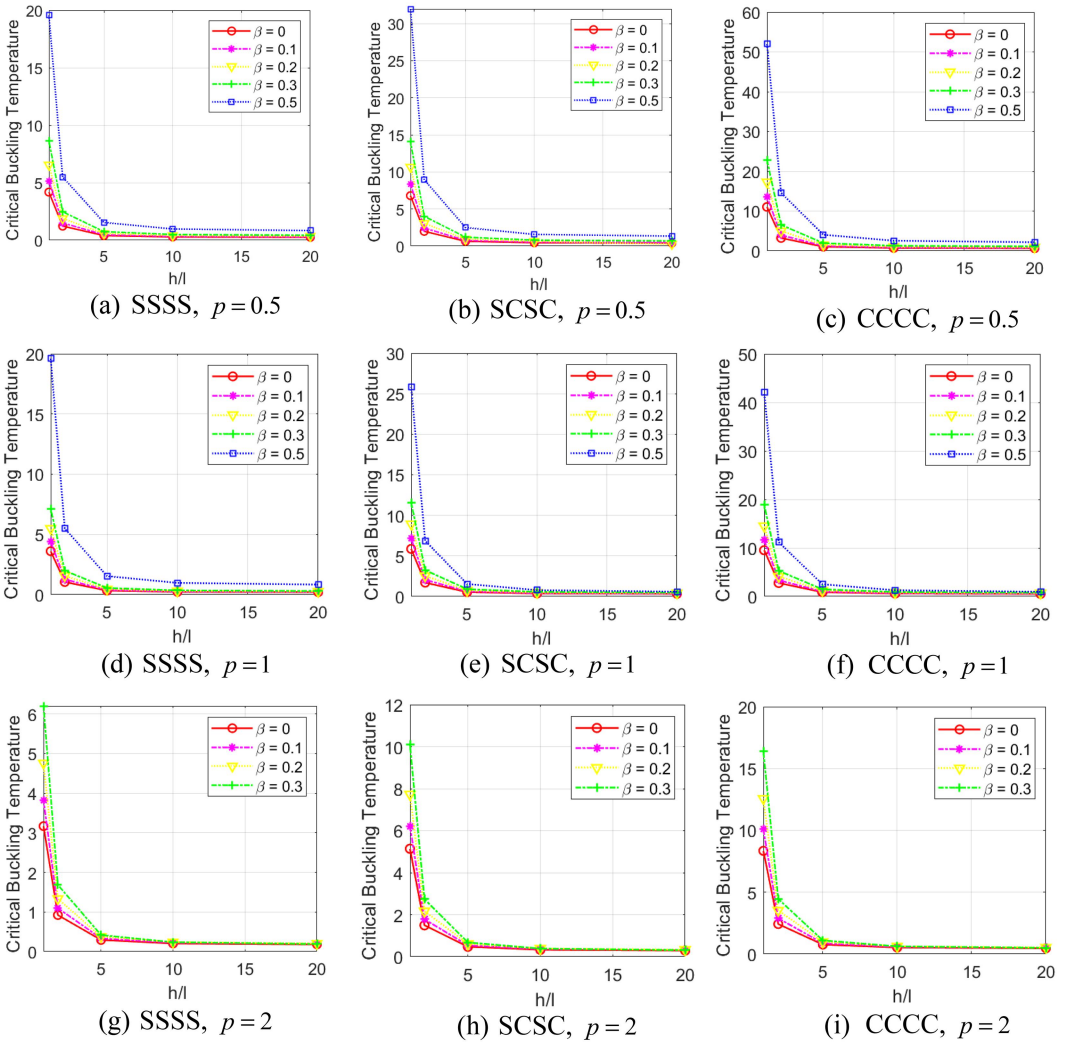

Figure 9. Variation of normalized thermal buckling load with respect the length scale-to-thickness ratio h/l ($a/h = 20$) with biaxial compression and uniform temperature distribution.

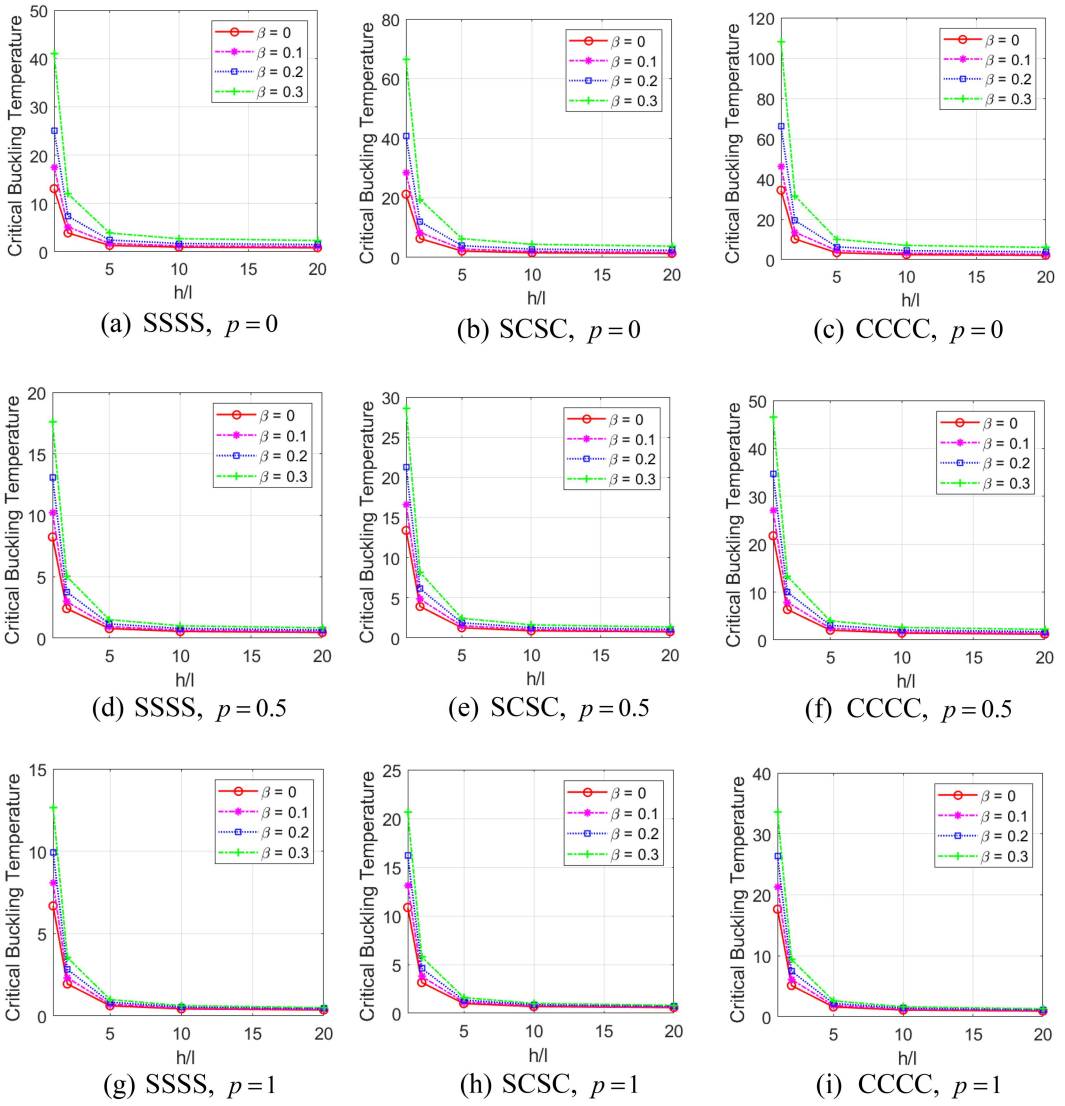

Figure 10. Variation of normalized thermal buckling load with respect the length scale-to-thickness ratio h/l ($a/h = 20$) with biaxial compression and linear temperature distribution.

microplates. As explained in the introduction section, the BCMO is a meta-heuristic algorithm that enables to optimize responses and saves the computational costs [38]. However, in practice, the original BCMO algorithm will take a long time to tackle complicated problems, such as stochastic size effects. Alternatively, by narrowing the random range in $[a_1, b_1] \in [0, 1]$ and changing the probabilistic threshold ζ in the optimization process of solution field, and using the DNN for learning behaviors, the present iBCMO-DNN provides a novel intelligent computational algorithm for solving stochastic problems.

To determine the optimal random range $[a_1, b_1]$, Table 7 presents the comparison of the normalized critical buckling temperature $\bar{T}_{cr}$ of simply supported Al/Al_2 O_3 FGP square microplates under uniform temperature distribution. The results are computed with different random ranges $[a_1, b_1]$, side to thickness ratio $a/h = 20$, porous coefficient $\beta = 0.1$, power-index $p = 1$, thickness-to-MLSP ratio $h/l = 10$, biaxial compression $(N_1^{(tr)}, N_2^{(tr)}, N_{12}^{(tr)} = 1, 1, 0)$, and probability

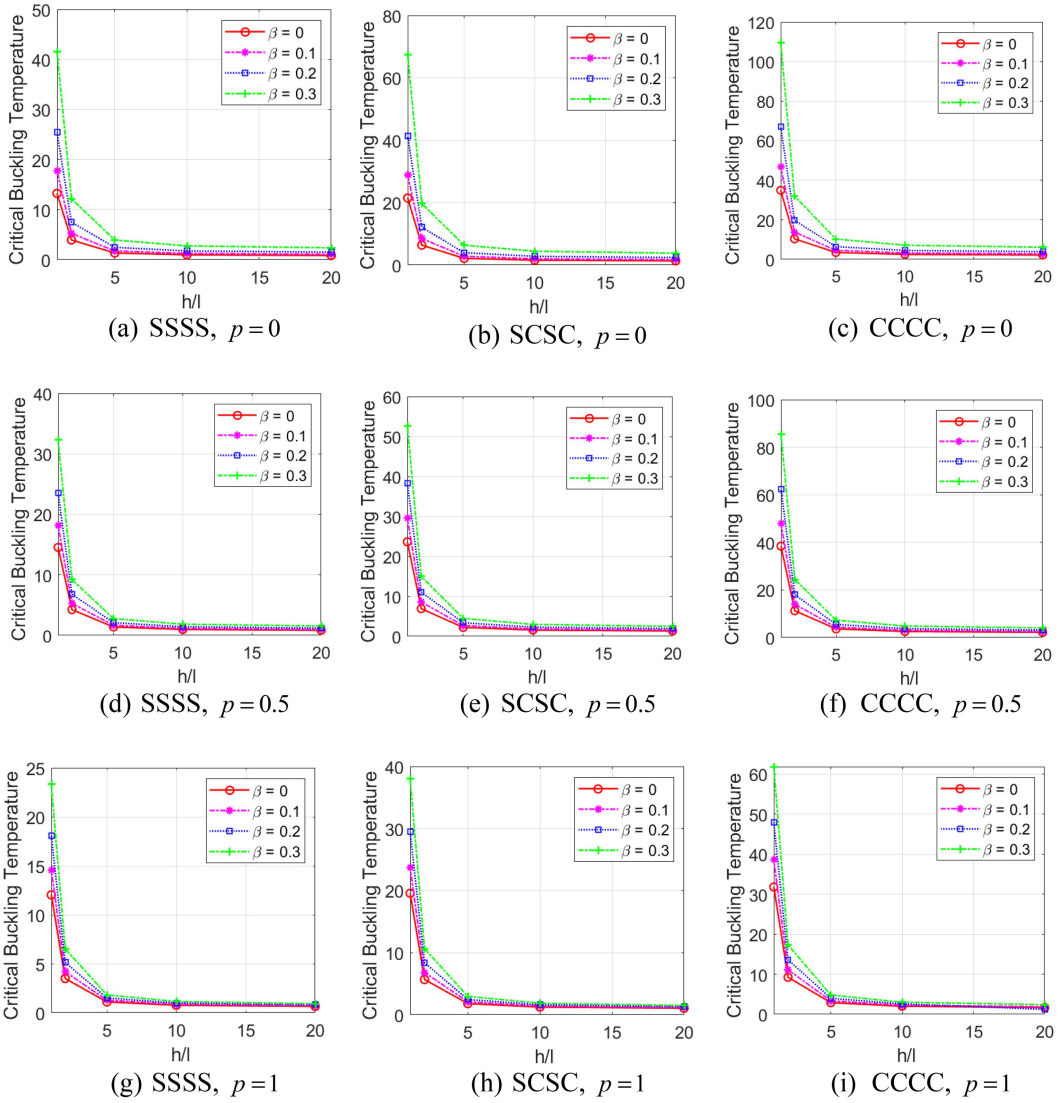

Figure 11. Variation of normalized thermal buckling load with respect the length scale-to-thickness ratio h/l ($a/h = 20$) with biaxial compression and nonlinear temperature distribution.

Table 7. Comparison of the *rand* coefficient of the Ritz-iBCMO algorithm for the normalized critical buckling temperature $\bar{T}_{cr}$ of Al/Al_2O_3 FGP square microplates with $a/h = 20$, $\beta = 0.1$, $p = 1$, $h/l = 10$ with biaxial compression $(N_1^{(tr)}, N_2^{(tr)}, N_{12}^{(tr)} = 1, 1, 0)$ under uniform temperature distribution and simply supported boundary condition.

Theory	Mean	*SD*	Time(s)	Present
rand(0, 1)	0.2630	0.0124	3611	0.2622
rand(0.1, 0.9)	0.2628	0.0099	2156	
rand(0.2, 0.8)	0.2624	0.0073	2116	
rand(0.3, 0.7)	0.2624	0.0051	2107	
rand(0.4, 0.6)	0.2623	0.0026	2066	
rand(0.4, 0.7)	0.2589	0.0036	1952	
rand(0.4, 0.9)	0.2523	0.0056	1999	

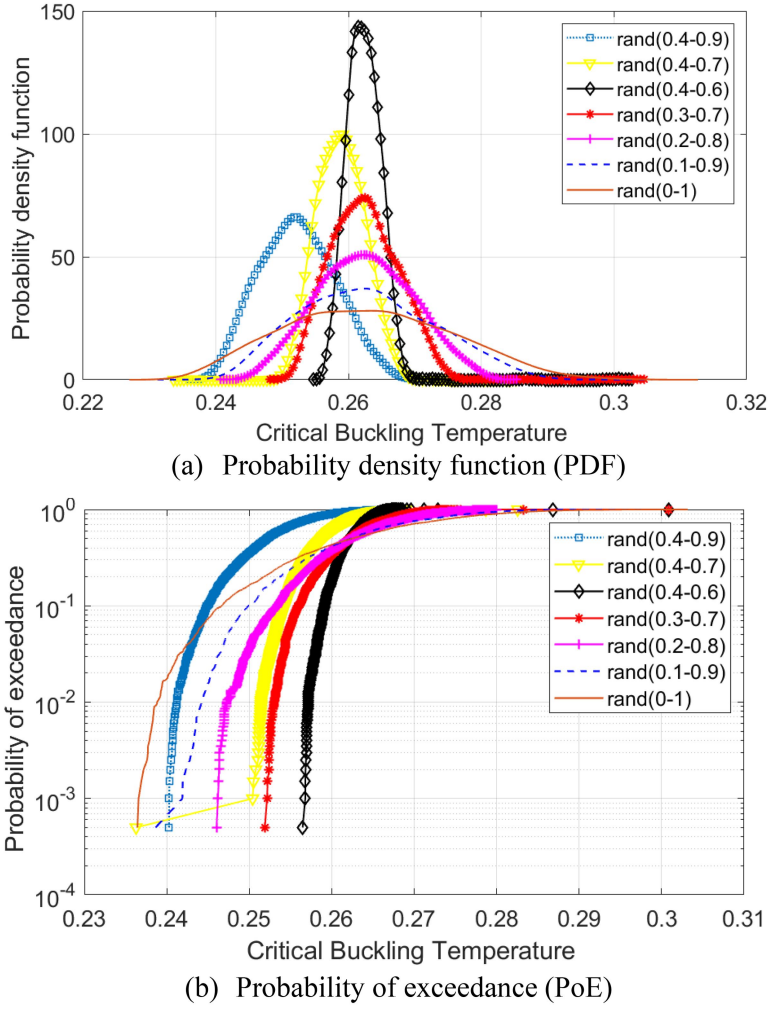

Figure 12. Comparison of the efficiency of the *rand* coefficient differences for iBCMO algorithm of normalized thermal buckling load with biaxial compression, $a/h = 20$, $p = 1$, $h/l = 10$, $\beta = 0.1$, uniform temperature distribution, SSSS boundary condition.

threshold $\zeta = 0.6$. It can be seen that as the random range steadily narrows, the standard deviation (SD) and computational time decreases. In comparison, the symmetric cases with $rand(0.2, 0.8)$, $rand(0.3, 0.7)$, and $rand(0.4, 0.6)$ show the rationality of the mean value and computational cost. Moreover, in order to investigate the choice of random range further, Figure 12 displays the probability density function (PDF) and probability of exceedance (PoE) of normalized critical buckling temperature with various values of the random ranges. It is observed that the asymmetric ranges (0.4,0.7) and (0.4,0.9) provide significant deviations of the mean values with the exact value, therefore the asymmetric ranges are not suitable for the present stochastic analysis. For the symmetric cases, it appears that the ranges of (0.3,0.7) and (0.4,0.6) present uneven graphs, while the random range (0.2,0.8) is found to be appropriate for stochastic responses, therefore the random range $[a_1, b_1] = [0.2, 0.8]$ will be selected for the following numerical examples.

Furthermore, Figure 13 plots the probability density function of critical buckling loads of FGP microplates for different values of probabilistic threshold. It can be observed from this graph that

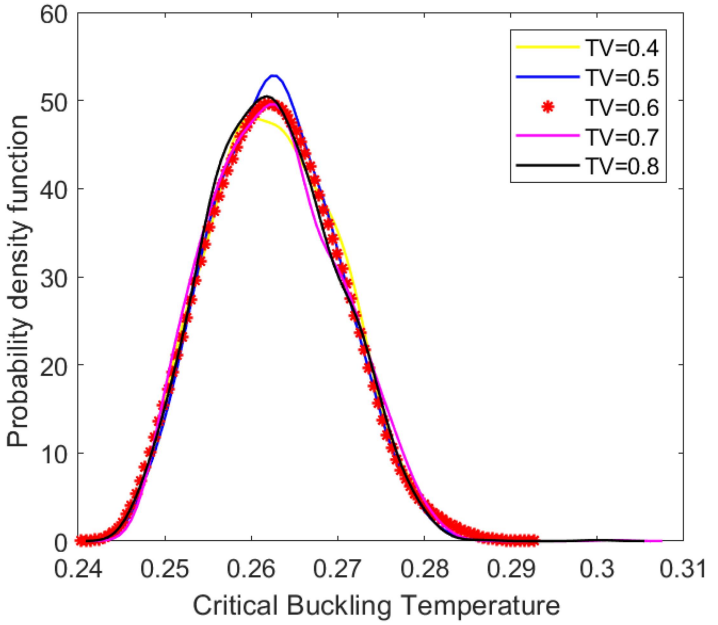

Figure 13. Comparison of the efficiency of the probabilistic threshold (TV) differences for iBCMO algorithm of normalized thermal buckling load with biaxial compression, $a/h = 20,\ p = 1,\ h/l = 10,\ \beta = 0.1,$ uniform temperature distribution, SSSS boundary condition.

Table 8. Comparison between BCMO and iBCMO algorithms for the normalized critical buckling temperature $\bar{T}_{cr}$ of Al/Al_2O_3 FGP square microplates with $a/h = 20,\ \beta = 0.1,\ p = 1$ with biaxial compression and uniform temperature distribution

BCs	h/l	Theory	Mean	*SD*	Time(s)	Present
SSSS	10	Ritz-BCMO	0.2634	0.0120	3611	0.2622
		Ritz-iBCMO	0.2624	0.0073	2116	
	1	Ritz-BCMO	4.4061	0.1996	3618	4.3917
		Ritz-iBCMO	4.3999	0.1169	2124	
SCSC	10	Ritz-BCMO	0.4250	0.0195	3683	0.4233
		Ritz-iBCMO	0.4243	0.0117	2127	
	1	Ritz-BCMO	7.1609	0.3134	3651	7.1462
		Ritz-iBCMO	7.1610	0.1900	2133	
CCCC	10	Ritz-BCMO	0.6860	0.0312	3653	0.6839
		Ritz-iBCMO	0.6850	0.0195	2123	
	1	Ritz-BCMO	11.6378	0.5202	3652	11.6128
		Ritz-iBCMO	11.6345	0.3095	2119	

the probability threshold coefficient $\zeta = 0.6$ has the most uniform data density, that numerically confirms the correctness of this coefficient in the computations.

Example 4: To demonstrate the performance of the present theory in predicting stochastic buckling temperatures of FGP microplates further, Table 8 introduces the comparison of both BCMO and iBCMO algorithm for normalized critical buckling temperature $\bar{T}_{cr}$ of FGP microplates under uniform temperature distribution with $a/h = 20,\ \beta = 0.1,$ and $p = 1$. It can be seen that the computational cost from the iBCMO is lower about 1.7 times than that of the BCMO for different boundary conditions, with same mean values, the standard deviation from the iBCMO is much smaller than that from the BCMO. This is also verified by Figure 14 which displays the probability density function of thermal buckling loads of FGP microplates under uniform temperature distribution with $a/h = 20,\ p = 1,$ and $h/l = 10$.

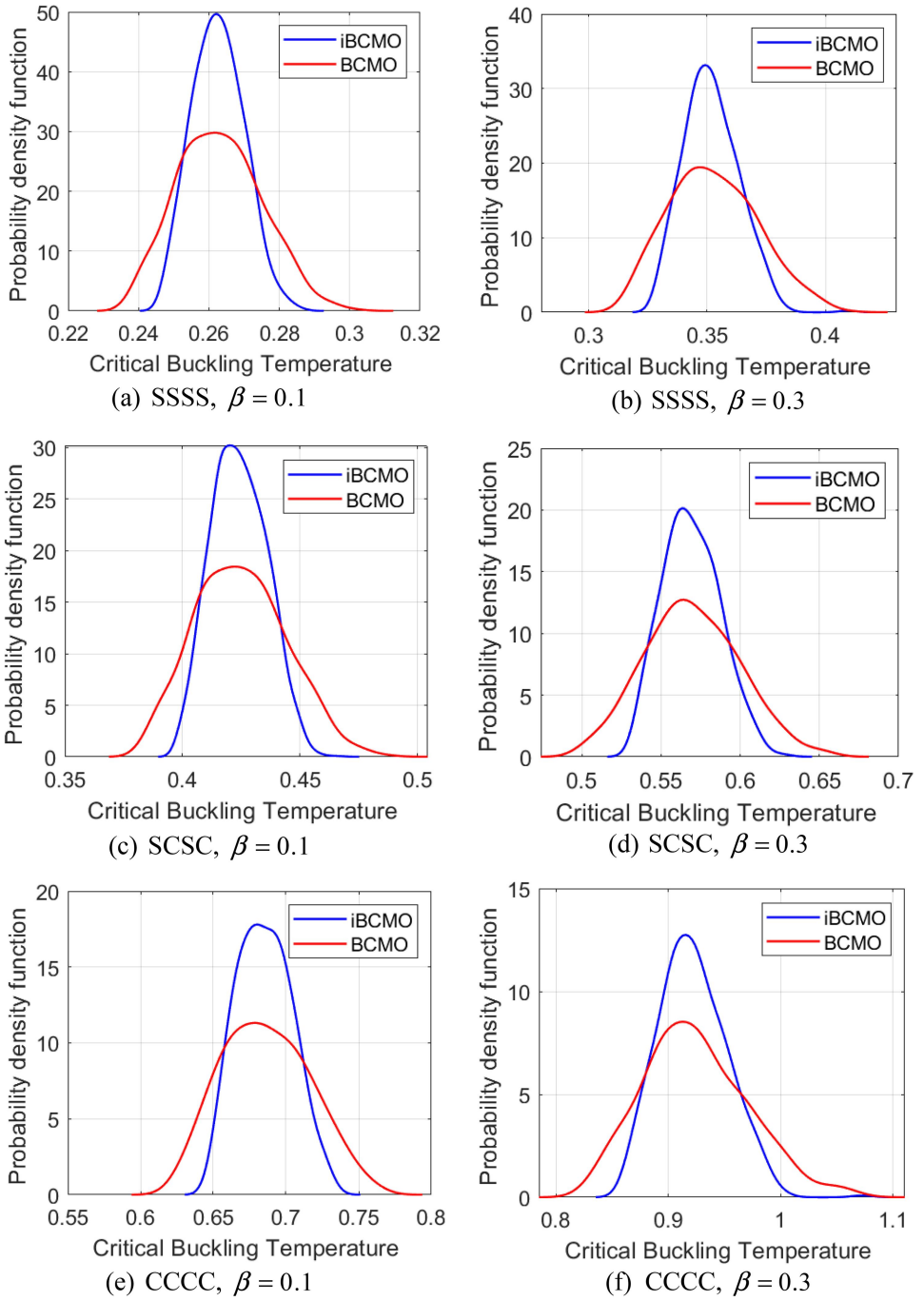

Figure 14. Comparison of the efficiency of iBCMO with the BCMO algorithm of normalized thermal buckling load, $a/h = 20$, $p = 1$, $h/l = 10$, biaxial compression and uniform temperature distribution.

To investigate stochastic critical buckling temperatures of FGP microplates, it is noted that five random variables of material properties $(E_{m,i}, E_{c,i}, \alpha_{t,i}, \alpha_{m,i}, \rho)$ are designed to be randomly distributed with the same population size $NP = 2000$. Additionally, the data training was generated

Table 9. Mean and standard deviation (*SD*) of normalized critical buckling temperature for FGP microplates with biaxial compression, $a/h = 20$, SSSS boundary condition and uniform temperature distribution.

β	p	h/l	Theory	Mean	*SD*	Time(s)	Present
0.1	0.5	10	Ritz-iBCMO	0.3291	0.0089	2123	0.3284
			iBCMO-DNN	0.3307	0.0091	845	
		1	Ritz-iBCMO	5.1633	0.1343	2125	5.1596
			iBCMO-DNN	5.1688	0.1347	844	
	2	10	Ritz-iBCMO	0.2239	0.0066	2124	0.2236
			iBCMO-DNN	0.2259	0.0071	845	
		1	Ritz-iBCMO	3.8358	0.1084	2123	3.8278
			iBCMO-DNN	3.8315	0.1082	846	
0.3	0.5	10	Ritz-iBCMO	0.4960	0.0152	2121	0.4952
			iBCMO-DNN	0.4995	0.0151	840	
		1	Ritz-iBCMO	8.6618	0.2454	2126	8.6440
			iBCMO-DNN	8.6669	0.2460	841	
	2	10	Ritz-iBCMO	0.2373	0.0122	2127	0.2370
			iBCMO-DNN	0.2389	0.0124	842	
		1	Ritz-iBCMO	6.2104	0.1712	2123	6.2009
			iBCMO-DNN	6.2155	0.1718	843	

Table 10. Mean and standard deviation (*SD*) of normalized critical buckling for FGP microplates with biaxial compression, $a/h = 20$, SCSC boundary condition and uniform temperature distribution.

β	p	h/l	Theory	Mean	*SD*	Time(s)	Present
0.1	0.5	10	Ritz-iBCMO	0.5307	0.0147	2129	0.5299
			iBCMO-DNN	0.5311	0.0146	841	
		1	Ritz-iBCMO	8.4103	0.2165	2127	8.3968
			iBCMO-DNN	8.4133	0.2173	845	
	2	10	Ritz-iBCMO	0.3614	0.0106	2124	0.3607
			iBCMO-DNN	0.3658	0.0108	843	
		1	Ritz-iBCMO	6.2261	0.1744	2122	6.2152
			iBCMO-DNN	6.2249	0.1740	840	
0.3	0.5	10	Ritz-iBCMO	0.8008	0.0243	2133	0.7999
			iBCMO-DNN	0.8014	0.0244	842	
		1	Ritz-iBCMO	14.1140	0.3999	2128	14.0821
			iBCMO-DNN	14.1184	0.4009	844	
	2	10	Ritz-iBCMO	0.3843	0.0195	2127	0.3839
			iBCMO-DNN	0.3849	0.0197	843	
		1	Ritz-iBCMO	10.1095	0.2818	2124	10.0882
			iBCMO-DNN	10.1109	0.2826	841	

Table 11. Mean and standard deviation (*SD*) of normalized critical buckling for FGP microplates with biaxial compression, $a/h = 20$, CCCC boundary condition and uniform temperature distribution.

β	p	h/l	Theory	Mean	*SD*	Time(s)	Present
0.1	0.5	10	Ritz-iBCMO	0.8568	0.0229	2122	0.8555
			iBCMO-DNN	0.8575	0.0231	840	
		1	Ritz-iBCMO	13.6636	0.3535	2125	13.6417
			iBCMO-DNN	13.6659	0.3541	841	
	2	10	Ritz-iBCMO	0.5831	0.0170	2124	0.5825
			iBCMO-DNN	0.5838	0.0172	840	
		1	Ritz-iBCMO	10.1182	0.2835	2124	10.1004
			iBCMO-DNN	10.1197	0.2842	843	
0.3	0.5	10	Ritz-iBCMO	1.2957	0.0395	2119	1.2936
			iBCMO-DNN	1.2967	0.0398	844	
		1	Ritz-iBCMO	22.9234	0.6409	2121	22.8856
			iBCMO-DNN	22.9287	0.6413	843	
	2	10	Ritz-iBCMO	0.6249	0.0316	2127	0.6233
			iBCMO-DNN	0.6255	0.0318	842	
		1	Ritz-iBCMO	16.4441	0.4720	2126	16.4167
			iBCMO-DNN	16.4458	0.4726	844	

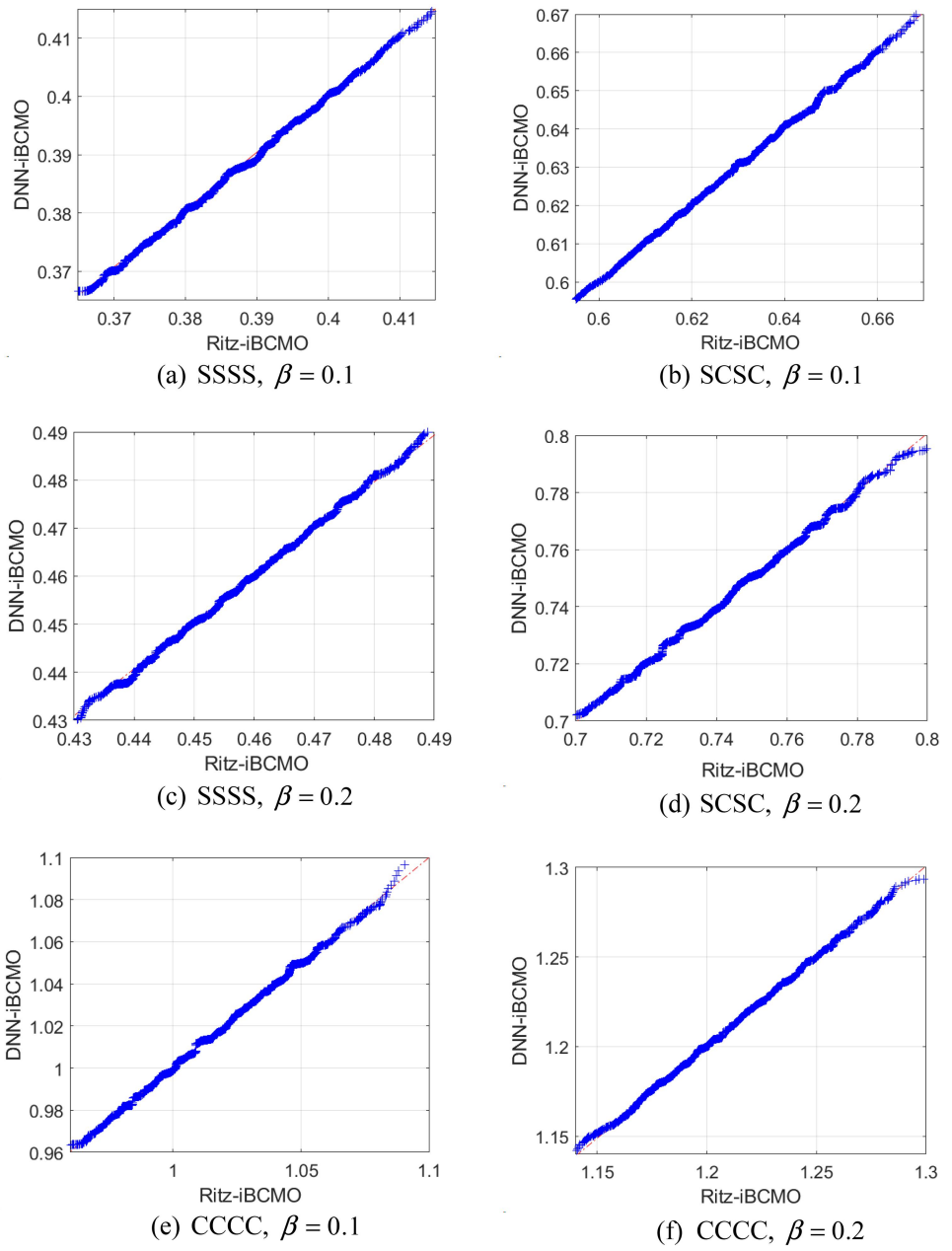

Figure 15. Quantile-quantile plot of the Ritz-iBCMO model with DNN-iBCMO, $a/h = 20$, $p = 1$, $h/l = 5$, $\beta = 0.1$, 0.2, biaxial compression and uniform temperature distribution.

from the earlier analysis of Ritz-iBCMO solution. These values will be evaluated for the accuracy through the training process using the long short time memory model of the deep learning network. The initial normalization of the critical buckling temperatures is used as the output data for training samples, and these design factors are taken into consideration as the input data. Input-output pairs and randomly generated training samples are included in the data set, which is used to train *via* the DNN. It is worth noticing that the DNN processing involves 500 iterations with one epoch between each one, the DNN structure is 110-110-4. The data was divided into two groups

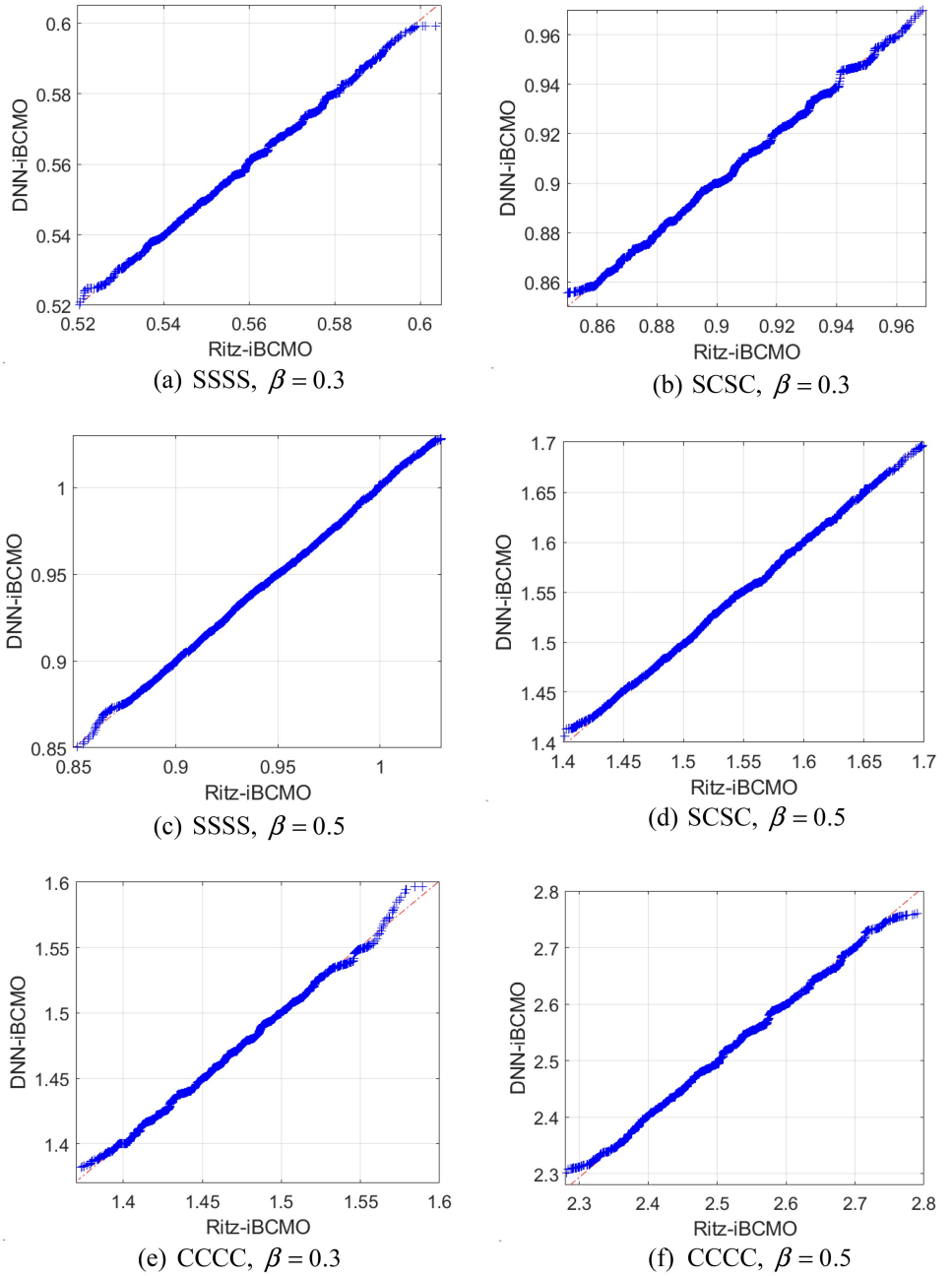

Figure 16. Quantile-quantile plot of the Ritz-iBCMO model with DNN-iBCMO, $a/h = 20$, $p = 1$, $h/l = 5$, $\beta = 0.3$, 0.5, biaxial compression and uniform temperature distribution.

with 80% for the training set and 20% for the test set. The type of DNN is the long short time memory with tanh function for hidden layers and sigmoid function for output layer.

For Al/Al_2O_3 FGP microplates with three boundary conditions, the mean and standard deviation of normalized critical buckling temperatures from the Ritz-iBCMO and iBCMO-DNN models are shown in Tables 9–11. The critical buckling temperature responses are computed for the side-to-thickness ratio $a/h = 20$, porous parameter $\beta = 0.1$ and 0.3, power-law index $p = 0.5$ and 2, thickness-to-MLSP ratio $h/l = 1$ and 10. Obviously, the statistical moments of the critical buckling temperatures

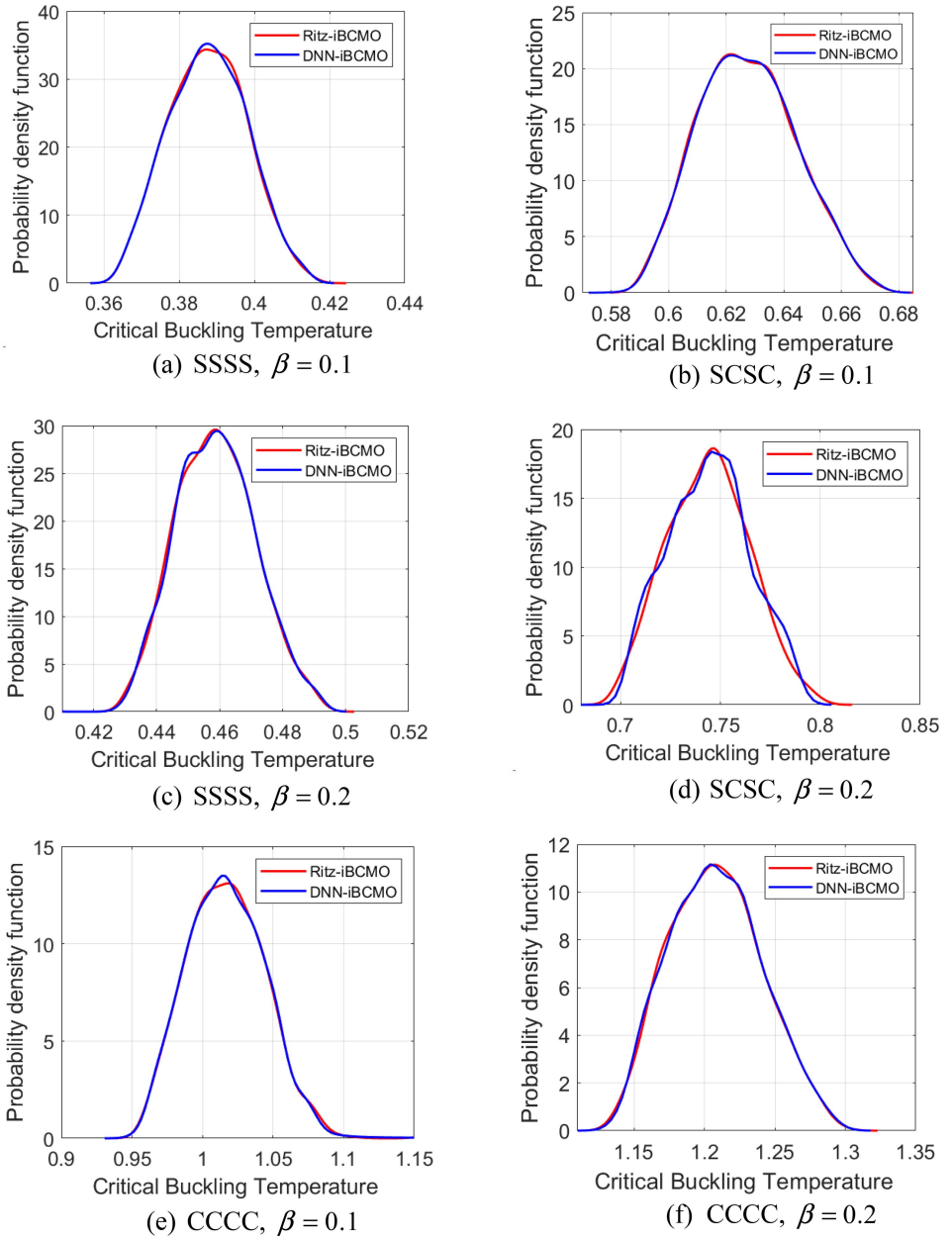

Figure 17. Probability density function (PDF) of Ritz-iBCMO and iBCMO-DNN methods the normalized thermal buckling with $a/h = 20$, $p = 1$, $h/l = 5$, $\beta = 0.1$, 0.2, biaxial compression and uniform temperature distribution.

derived from the Ritz-iBCMO and iBCMO-DNN show good agreements for all cases. For all BCs, varied power-law indexes p and porosity parameters β, the mean values of the critical buckling temperatures for the Ritz-iBCMO and iBCMO-DNN are close to the deterministic responses. As expected, the critical buckling temperatures rise with the increase of β and h/l. In the comparison of the computational time between the theories, the iBCMO-DNN approach takes less computational times than the Ritz-iBCMO method. The computational time of the iBCMO-DNN method is about 2/5 that of the Ritz-iBCMO method. Additionally, the performance of the current iBCMO-DNN algorithm in predicting buckling temperature responses is also shown in Figures 15–19 in which the mean square error is

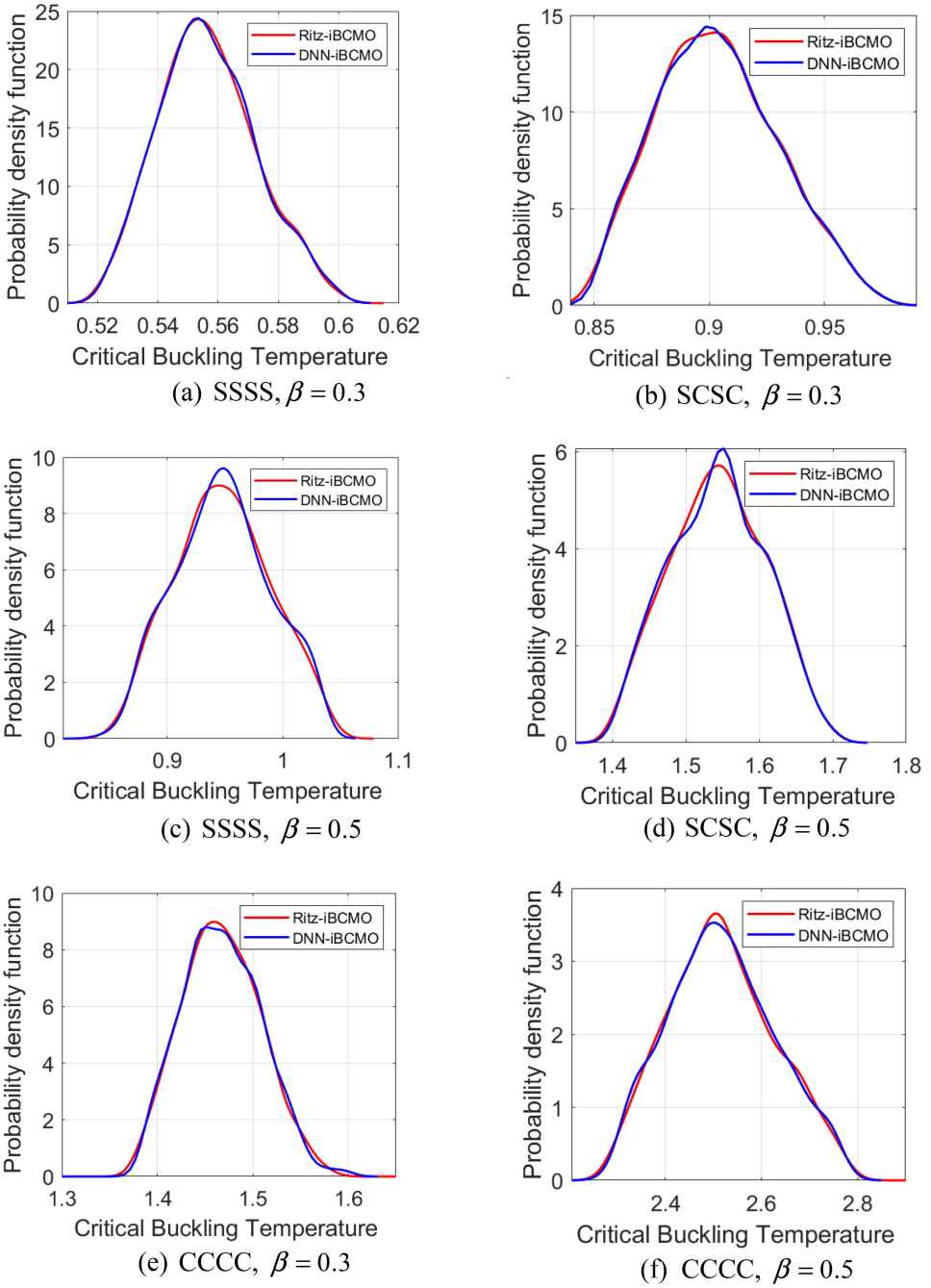

Figure 18. Probability density function (PDF) of Ritz-iBCMO and iBCMO-DNN methods the normalized thermal buckling with $a/h = 20$, $p = 1$, $h/l = 5$, $\beta = 0.3$, 0.5, biaxial compression and uniform temperature distribution.

almost nil for both training and test sets. Figures 17 and 18 describe the probability density function of the critical buckling temperatures generated from the Ritz-iBCMO and iBCMO-DNN analysis. It can be seen again that the results of iBCMO-DNN are in good agreement with the Ritz-iBCMO. This proves that the present model in capturing size effects with the uncertainty of material properties based on the unified HSDT, Ritz solution and iBCMO-DNN is completely reliable. Finally, it can be seen

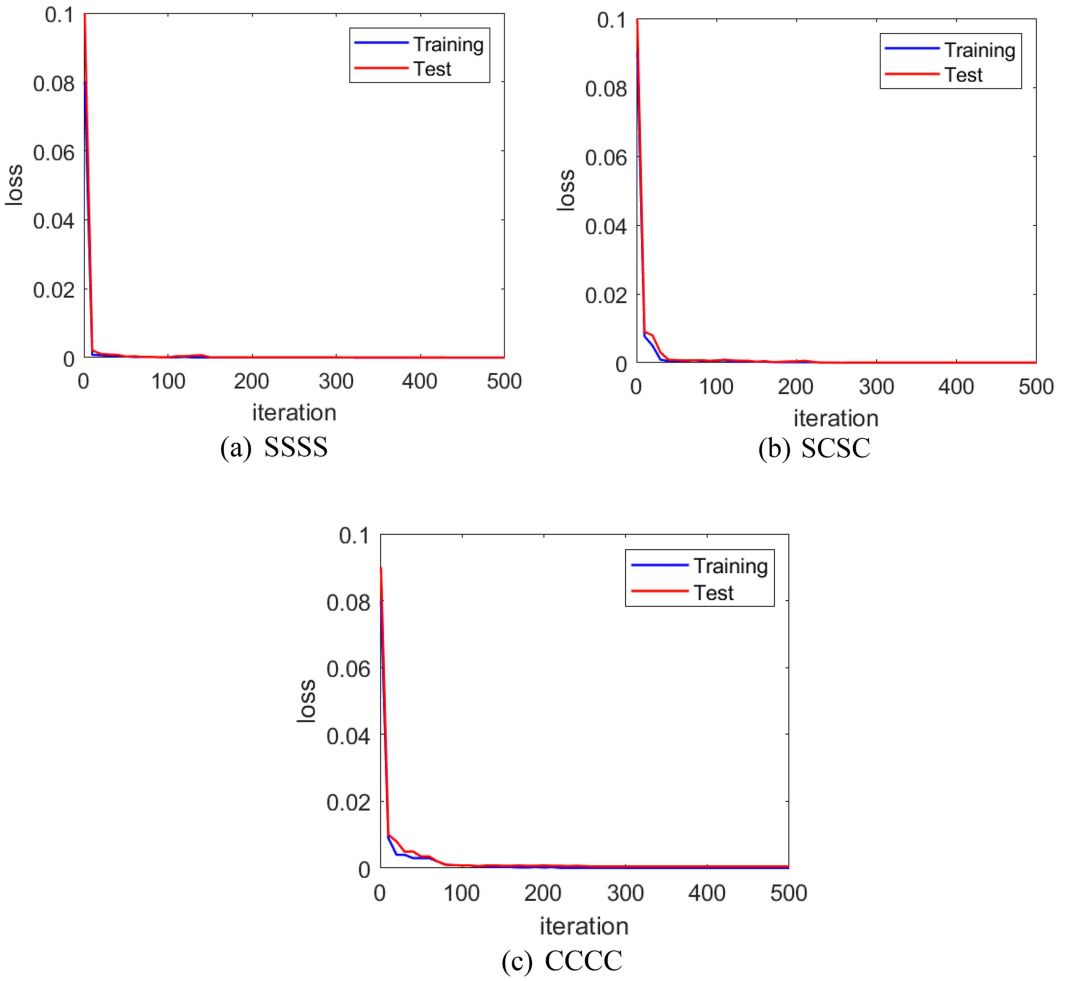

Figure 19. Loss function of the normalized critical buckling temperature with $a/h = 20,\ h/l = 5,\ \beta = 0.3$.

that the improved balance composite motion optimization algorithm demonstrates a computational time faster than its predecessor. Furthermore, integrating a deep neural network into the improved algorithm reduces computational time compared to the method without it. The iBCMO-DNN method presented in this paper significantly helps save time and cost in predicting stochastic buckling behaviors of FGP microplates.

4. Conclusions

This research proposed a novel intelligent computational algorithm, namely iBCMO-DNN, for stochastic buckling temperature analysis of FGP microplates with uncertainty of material properties. It utilized a deep feedforward neural network made with the long short-term memory model to replace time-consuming computational methods. An improved BCMO algorithm was also used to search for optimal solutions. Deterministic responses of the microplates were obtained using a unified HSDT and MST approach. Ritz-iBCMO and iBCMO-DNN were two algorithms created to study how different factors affect the critical buckling temperatures of FGP microplates. The

numerical results demonstrated the accuracy and efficiency of the proposed model in predicting stochastic buckling temperatures. The following significant points might be deduced as follows:

- The current unified HSDT and MST are proven to be accurate and effective in predicting the buckling responses of FGP microplates.
- An important difference in critical buckling loads is derived from the MST and MCT for the MLSP-to-thickness ratio $h/l \leq 20$, the MST hence showed its accuracy for capturing the size effects of FGP microplates.
- The porosity does not impact significantly on size effects of the FGP microplates.
- The critical buckling temperature increases with an increase in the porosity density. Meanwhile, critical buckling temperature decreases with an increase in the power-law index and thickness-to-MLSP ratio h/l.
- The computational cost of the proposed iBCMO algorithm is lower 1.7 times than that of the existing BCMO method.
- The proposed iBCMO-DNN algorithm provides for substantial cost savings in computing stochastic buckling responses of FGP microplates. The computational time of critical buckling temperatures from the iBCMO-DNN approach requires ∼2/5 that from the Ritz-iBCMO method.

Disclosure statement

No potential conflict of interest was reported by the author(s).

References

[1] B. Ilic, H. G. Craighead, S. Krylov, W. Senaratne, C. Ober, and P. Neuzil, "Attogram detection using nanoelectromechanical oscillators," *J. Appl. Phys.*, vol. 95, no. 7, pp. 3694–3703, 2004. DOI: 10.1063/1.1650542.

[2] D. Ozevin, "10 – Micro-electro-mechanical-systems (MEMS) for assessing and monitoring civil infrastructures," in *Sensor Technologies for Civil Infrastructures*, M. L. Wang, J. P. Lynch, and H. Sohn, Eds., Woodhead Publishing, 2014, pp. 265–302.

[3] B. Bahreyni and C. Shafai, "Application of twin-beam structures for estimation of material properties and sensor fabrication," *Can. J. Electr. Comput. Eng.*, vol. 31, pp. 85–88, 2006. DOI: 10.1109/CJECE.2006.259189.

[4] N. Jalili and K. Laxminarayana, "A review of atomic force microscopy imaging systems: application to molecular metrology and biological sciences," *Mechatronics*, vol. 14, no. 8, pp. 907–945, 2004. DOI: 10.1016/j.mechatronics.2004.04.005.

[5] P. A. Demirhan and V. Taskin, "Bending and free vibration analysis of Levy-type porous functionally graded plate using state space approach," *Compos. Part B Eng.*, vol. 160, pp. 661–676, 2019. DOI: 10.1016/j.compositesb.2018.12.020.

[6] K. Li *et al.*, "Isogeometric Analysis of functionally graded porous plates reinforced by graphene platelets," *Compos. Struct.*, vol. 204, pp. 114–130, 2018. DOI: 10.1016/j.compstruct.2018.07.059.

[7] D. Chen, J. Yang, and S. Kitipornchai, "Buckling and bending analyses of a novel functionally graded porous plate using Chebyshev-Ritz method," *Archiv. Civil Mech. Eng.*, vol. 19, no. 1, pp. 157–170, 2019. DOI: 10.1016/j.acme.2018.09.004.

[8] N. V. Nguyen, H. Nguyen-Xuan, D. Lee, and J. Lee, "A novel computational approach to functionally graded porous plates with graphene platelets reinforcement," *Thin Walled Struct.*, vol. 150, pp. 106684, 2020. DOI: 10.1016/j.tws.2020.106684.

[9] A. R. Ashoori, E. Salari, and S. A. Sadough Vanini, "Size-dependent thermal stability analysis of embedded functionally graded annular nanoplates based on the nonlocal elasticity theory," *Int. J. Mech. Sci.*, vol. 119, pp. 396–411, 2016. DOI: 10.1016/j.ijmecsci.2016.10.035.

[10] A. Daneshmehr, A. Rajabpoor, and A. Hadi, "Size dependent free vibration analysis of nanoplates made of functionally graded materials based on nonlocal elasticity theory with high order theories," *Int. J. Eng. Sci.*, vol. 95, pp. 23–35, 2015. DOI: 10.1016/j.ijengsci.2015.05.011.

[11] A. C. Eringen, "On differential equations of nonlocal elasticity and solutions of screw dislocation and surface waves," *J. Appl. Phys.*, vol. 54, no. 9, pp. 4703–4710, 1983. DOI: 10.1063/1.332803.

[12] Y. Gholami, R. Ansari, R. Gholami, and H. Rouhi, "Nonlinear bending analysis of nanoplates made of FGMs based on the most general strain gradient model and 3D elasticity theory," *Eur. Phys. J. Plus*, vol. 134, no. 4, pp. 167, 2019. DOI: 10.1140/epjp/i2019-12501-x.

[13] R. Ansari, R. Gholami, M. Faghih Shojaei, V. Mohammadi, and M. A. Darabi, "Size-dependent nonlinear bending and postbuckling of functionally graded Mindlin rectangular microplates considering the physical neutral plane position," *Compos. Struct.*, vol. 127, pp. 87–98, 2015. DOI: 10.1016/j.compstruct.2015.02.082.

[14] R. Ansari, R. Gholami, M. Faghih Shojaei, V. Mohammadi, and M. A. Darabi, "Coupled longitudinal-transverse-rotational free vibration of post-buckled functionally graded first-order shear deformable micro- and nano-beams based on the Mindlin's strain gradient theory," *Appl. Math. Model.*, vol. 40, no. 23–24, pp. 9872–9891, 2016. DOI: 10.1016/j.apm.2016.06.042.

[15] R. Ansari, R. Gholami, and A. Shahabodini, "Size-dependent geometrically nonlinear forced vibration analysis of functionally graded first-order shear deformable microplates," *J. Mech.*, vol. 32, no. 5, pp. 539–554, 2016. DOI: 10.1017/jmech.2016.10.

[16] R. Gholami, R. Ansari, and H. Rouhi, "Nonlinear pull-in instability of strain gradient microplates made of functionally graded materials," *Int. J. Struct. Stab. Dyn.*, vol. 19, no. 2, pp. 1950007, 2018. DOI: 10.1142/S021945541950007X.

[17] M. H. Shojaeefard, H. Saeidi Googarchin, M. Ghadiri, and M. Mahinzare, "Micro temperature-dependent FG porous plate: free vibration and thermal buckling analysis using modified couple stress theory with CPT and FSDT," *Appl. Math. Model.*, vol. 50, pp. 633–655, 2017. DOI: 10.1016/j.apm.2017.06.022.

[18] F. Yang, A. C. M. Chong, D. C. C. Lam, and P. Tong, "Couple stress based strain gradient theory for elasticity," *Int. J. Solids Struct.*, vol. 39, no. 10, pp. 2731–2743, 2002. DOI: 10.1016/S0020-7683(02)00152-X.

[19] D. C. C. Lam, F. Yang, A. C. M. Chong, J. Wang, and P. Tong, "Experiments and theory in strain gradient elasticity," *J. Mech. Phys. Solids*, vol. 51, no. 8, pp. 1477–1508, 2003. DOI: 10.1016/S0022-5096(03)00053-X.

[20] R. Ansari, M. F. Shojaei, and R. Gholami, "Size-dependent nonlinear mechanical behavior of third-order shear deformable functionally graded microbeams using the variational differential quadrature method," *Compos. Struct.*, vol. 136, pp. 669–683, 2016. DOI: 10.1016/j.compstruct.2015.10.043.

[21] R. D. Mindlin, "Second gradient of strain and surface-tension in linear elasticity," *Int. J. Solids Struct.*, vol. 1, no. 4, pp. 417–438, 1965. DOI: 10.1016/0020-7683(65)90006-5.

[22] R. D. Mindlin and N. N. Eshel, "On first strain-gradient theories in linear elasticity," *Int. J. Solids Struct.*, vol. 4, no. 1, pp. 109–124, 1968. DOI: 10.1016/0020-7683(68)90036-X.

[23] M.-C. Trinh, T. Mukhopadhyay, and S.-E. Kim, "A semi-analytical stochastic buckling quantification of porous functionally graded plates," *Aerospace Sci. Technol.*, vol. 105, pp. 105928, 2020. DOI: 10.1016/j.ast.2020.105928.

[24] X. Sun, R. Gao, and Y. Zhang, "Spectral stochastic isogeometric analysis of bending and free vibration of porous functionally graded plates," *Appl. Math. Model.*, vol. 116, pp. 711–734, 2023. DOI: 10.1016/j.apm.2022.12.017.

[25] V.-T. Tran, T.-K. Nguyen, P. T. T. Nguyen, and T. P. Vo, "Stochastic vibration and buckling analysis of functionally graded microplates with a unified higher-order shear deformation theory," *Thin Walled Struct.*, vol. 177, pp. 109473, 2022. DOI: 10.1016/j.tws.2022.109473.

[26] V.-T. Tran, T.-K. Nguyen, P. T. T. Nguyen, and T. P. Vo, "Stochastic collocation method for thermal buckling and vibration analysis of functionally graded sandwich microplates," *J. Therm. Stress.*, vol. 46, no. 9, pp. 909–934, 2023. DOI: 10.1080/01495739.2023.2217243.

[27] Q. X. Lieu, J. Lee, D. Lee, S. Lee, D. Kim, and J. Lee, "Shape and size optimization of functionally graded sandwich plates using isogeometric analysis and adaptive hybrid evolutionary firefly algorithm," *Thin Walled Struct.*, vol. 124, pp. 588–604, 2018. DOI: 10.1016/j.tws.2017.11.054.

[28] J. S. Moita, A. L. Araújo, V. F. Correia, C. M. Mota Soares, and J. Herskovits, "Material distribution and sizing optimization of functionally graded plate-shell structures," *Compos. Part B Eng.*, vol. 142, pp. 263–272, 2018. DOI: 10.1016/j.compositesb.2018.01.023.

[29] V. M. Franco Correia, J. F. Aguilar Madeira, A. L. Araújo, and C. M. Mota Soares, "Multiobjective optimization of ceramic-metal functionally graded plates using a higher order model," *Compos. Struct.*, vol. 183, pp. 146–160, 2018. DOI: 10.1016/j.compstruct.2017.02.013.

[30] A. Kaveh and V. Kalatjari, "Topology optimization of trusses using genetic algorithm, force method and graph theory," *Numer. Methods Eng.*, vol. 58, no. 5, pp. 771–791, 2003. DOI: 10.1002/nme.800.

[31] N. S. Khot, L. Berke, and V. B. Venkayya, "Comparison of optimality criteria algorithms for minimum weight design of structures," *AIAA J.*, vol. 17, no. 2, pp. 182–190, 1979. DOI: 10.2514/3.61093.

[32] R. Sedaghati, "Benchmark case studies in structural design optimization using the force method," *Int. J. Solids Struct.*, vol. 42, no. 21–22, pp. 5848–5871, 2005. DOI: 10.1016/j.ijsolstr.2005.03.030.

[33] X.-S. Yang, "Firefly algorithms for multimodal optimization," in *Stochastic Algorithms: Foundations and Applications*, Berlin; Heidelberg: Springer Berlin Heidelberg, 2009.

[34] F. Neri and C. Cotta, "Memetic algorithms and memetic computing optimization: a literature review," *Swarm Evol. Comput.*, vol. 2, pp. 1–14, 2012. DOI: 10.1016/j.swevo.2011.11.003.
[35] M. Dorigo and L. M. Gambardella, "Ant colony system: a cooperative learning approach to the traveling salesman problem," *IEEE Trans. Evol. Comput.*, vol. 1, no. 1, pp. 53–66, 1997. DOI: 10.1109/4235.585892.
[36] R. Eberhart and J. Kennedy, "A new optimizer using particle swarm theory," MHS'95. Proceedings of the Sixth International Symposium on Micro Machine and Human Science, 1995. DOI: 10.1109/MHS.1995.494215.
[37] D. T. T. Do, H. Nguyen-Xuan, and J. Lee, "Material optimization of tri-directional functionally graded plates by using deep neural network and isogeometric multimesh design approach," *Appl. Math. Model.*, vol. 87, pp. 501–533, 2020. DOI: 10.1016/j.apm.2020.06.002.
[38] T. Le-Duc, Q.-H. Nguyen, and H. Nguyen-Xuan, "Balancing composite motion optimization," *Inform. Sci.*, vol. 520, pp. 250–270, 2020. DOI: 10.1016/j.ins.2020.02.013.
[39] H. Thanh Duong, H. Chi Phan, T.-T. Le, and N. Duc Bui, "Optimization design of rectangular concrete-filled steel tube short columns with balancing composite motion optimization and data-driven model," *Structures*, vol. 28, pp. 757–765, 2020. DOI: 10.1016/j.istruc.2020.09.013.
[40] S. Khatir, S. Tiachacht, C. Le Thanh, E. Ghandourah, S. Mirjalili, and M. Abdel Wahab, "An improved artificial neural network using arithmetic optimization algorithm for damage assessment in FGM composite plates," *Compos. Struct.*, vol. 273, pp. 114287, 2021. DOI: 10.1016/j.compstruct.2021.114287.
[41] V.-T. Tran, T.-K. Nguyen, H. Nguyen-Xuan, and M. Abdel Wahab, "Vibration and buckling optimization of functionally graded porous microplates using BCMO-ANN algorithm," *Thin Walled Struct.*, vol. 182, pp. 110267, 2023. DOI: 10.1016/j.tws.2022.110267.
[42] A. M. Zenkour and M. H. Aljadani, "Porosity effect on thermal buckling behavior of actuated functionally graded piezoelectric nanoplates," *Eur. J. Mech. A/Solids*, vol. 78, pp. 103835, 2019. DOI: 10.1016/j.euromechsol.2019.103835.
[43] F. A. Fazzolari and E. Carrera, "Thermal stability of FGM sandwich plates under various through-the-thickness temperature distributions," *J. Therm. Stress.*, vol. 37, no. 12, pp. 1449–1481, 2014. DOI: 10.1080/01495739.2014.937251.
[44] T.-K. Nguyen, H.-T. Thai, and T. P. Vo, "A novel general higher-order shear deformation theory for static, vibration and thermal buckling analysis of the functionally graded plates," *J. Therm. Stress.*, vol. 44, no. 3, pp. 1–21, 2021. DOI: 10.1080/01495739.2020.1869127.
[45] L. C. Trinh *et al.*, "Size-dependent behaviour of functionally graded sandwich microplates under mechanical and thermal loads," *Compos. Part B Eng.*, vol. 124, pp. 218–241, 2017. DOI: 10.1016/j.compositesb.2017.05.042.
[46] A. Farzam and B. Hassani, "Size-dependent analysis of FG microplates with temperature-dependent material properties using modified strain gradient theory and isogeometric approach," *Compos. Part B Eng.*, vol. 161, pp. 150–168, 2019. DOI: 10.1016/j.compositesb.2018.10.028.
[47] J. N. Reddy, *Mechanics of Laminated Composite Plates and Shells*. 2nd ed., Boca Raton, FL: CRC Press, 2003.
[48] S. Sahmani and R. Ansari, "On the free vibration response of functionally graded higher-order shear deformable microplates based on the strain gradient elasticity theory," *Compos. Struct.*, vol. 95, pp. 430–442, 2013. DOI: 10.1016/j.compstruct.2012.07.025.
[49] R. Gholami and R. Ansari, "A most general strain gradient plate formulation for size-dependent geometrically nonlinear free vibration analysis of functionally graded shear deformable rectangular microplates," *Nonlin. Dyn.*, vol. 84, no. 4, pp. 2403–2422, 2016. DOI: 10.1007/s11071-016-2653-0.
[50] M. Aydogdu, "Vibration analysis of cross-ply laminated beams with general boundary conditions by Ritz method," *Int. J. Mech. Sci.*, vol. 47, no. 11, pp. 1740–1755, 2005. DOI: 10.1016/j.ijmecsci.2005.06.010.
[51] T.-K. Nguyen, T. P. Vo, B.-D. Nguyen, and J. Lee, "An analytical solution for buckling and vibration analysis of functionally graded sandwich beams using a quasi-3D shear deformation theory," *Compos. Struct.*, vol. 156, pp. 238–252, 2016. DOI: 10.1016/j.compstruct.2015.11.074.
[52] A. Jafari and M. Ezzati, "Investigating the non-classical boundary conditions relevant to strain gradient theories," *Phys. E Low Dimens. Syst. Nanostruct.*, vol. 86, pp. 88–102, 2017. DOI: 10.1016/j.physe.2016.09.012.
[53] S. Makridakis *et al.*, "The accuracy of extrapolation (time series) methods: results of a forecasting competition," *J. Forecast.*, vol. 1, no. 2, pp. 111–153, 1982. DOI: 10.1002/for.3980010202.
[54] T. Szandała, "Review and comparison of commonly used activation functions for deep neural networks," in *Bio-inspired Neurocomputing*, A. K. Bhoi, P. K. Mallick, C. M. Liu, and V. E. Balas, Eds. Singapore: Springer, 2021, pp. 203–224.
[55] G. Van Houdt, C. Mosquera, and G. Nápoles, "A review on the long short-term memory model," *Artif. Intell. Rev.*, vol. 53, no. 8, pp. 5929–5955, 2020. DOI: 10.1007/s10462-020-09838-1.
[56] S. Makridakis *et al.*, "The accuracy extrapolation (time series) methods: results a forecasting competition," *J. Forecast.*, vol. 1, no. 2, pp. 111–153, 1982.

[57] D. Kingma and J. Ba, "Adam: a method for stochastic optimization," International Conference on Learning Representations, 2014.
[58] G. E. Hinton, "A practical guide to training restricted Boltzmann machines," in *Neural Networks: Tricks of the Trade*, 2nd ed., G. Montavon, G. B. Orr, and K.-R. Müller, Eds. Berlin; Heidelberg: Springer Berlin Heidelberg, 2012, pp. 599–619.
[59] M. Aydogdu, "Conditions for functionally graded plates to remain flat under in-plane loads by classical plate theory," *Compos. Struct.*, vol. 82, no. 1, pp. 155–157, 2008. DOI: 10.1016/j.compstruct.2006.10.004.
[60] C. H. Thai, A. J. M. Ferreira, and H. Nguyen-Xuan, "Isogeometric analysis of size-dependent isotropic and sandwich functionally graded microplates based on modified strain gradient elasticity theory," *Compos. Struct.*, vol. 192, pp. 274–288, 2018. DOI: 10.1016/j.compstruct.2018.02.060.
[61] S. Thai, H.-T. Thai, T. P. Vo, and V. I. Patel, "Size-dependent behaviour of functionally graded microplates based on the modified strain gradient elasticity theory and isogeometric analysis," *Comput. Struct.*, vol. 190, pp. 219–241, 2017. DOI: 10.1016/j.compstruc.2017.05.014.
[62] B. Zhang, Y. He, D. Liu, L. Shen, and J. Lei, "An efficient size-dependent plate theory for bending, buckling and free vibration analyses of functionally graded microplates resting on elastic foundation," *Appl. Math. Model.*, vol. 39, no. 13, pp. 3814–3845, 2015. DOI: 10.1016/j.apm.2014.12.001.
[63] A. M. Zenkour and A. F. Radwan, "Hygrothermo-mechanical buckling of FGM plates resting on elastic foundations using a quasi-3D model," *Int. J. Comput. Methods Eng. Sci. Mech.*, vol. 20, no. 2, pp. 85–98, 2019. DOI: 10.1080/15502287.2019.1568618.
[64] H. Yaghoobi and M. Torabi, "Exact solution for thermal buckling of functionally graded plates resting on elastic foundations with various boundary conditions," *J. Therm. Stress.*, vol. 36, no. 9, pp. 869–894, 2013. DOI: 10.1080/01495739.2013.770356.

Appendix A

The strain components of the FGP microplates.

$$\boldsymbol{\varepsilon}^{(0)} = \begin{Bmatrix} \varepsilon_{11}^{(0)} \\ \varepsilon_{22}^{(0)} \\ \gamma_{12}^{(0)} \end{Bmatrix} = \begin{Bmatrix} u_{1,1}^{0} \\ u_{2,2}^{0} \\ u_{1,2}^{0} + u_{2,1}^{0} \end{Bmatrix}; \quad \boldsymbol{\varepsilon}^{(1)} = \begin{Bmatrix} \varepsilon_{11}^{(1)} \\ \varepsilon_{22}^{(1)} \\ \gamma_{12}^{(1)} \end{Bmatrix} = \begin{Bmatrix} u_{3,11}^{0} \\ u_{3,22}^{0} \\ 2u_{3,12}^{0} \end{Bmatrix} \tag{A.1a}$$

$$\boldsymbol{\varepsilon}^{(3)} = \begin{Bmatrix} \gamma_{13}^{(0)} \\ \gamma_{23}^{(0)} \end{Bmatrix} = \begin{Bmatrix} \varphi_1 + u_{3,1}^{0} \\ \varphi_2 + u_{3,2}^{0} \end{Bmatrix}; \quad \boldsymbol{\varepsilon}^{(2)} = \begin{Bmatrix} \varepsilon_{11}^{(2)} \\ \varepsilon_{22}^{(2)} \\ \gamma_{12}^{(2)} \end{Bmatrix} = \begin{Bmatrix} \varphi_{1,1} \\ \varphi_{2,2} \\ \varphi_{1,2} + \varphi_{2,1} \end{Bmatrix} \tag{A.1b}$$

$$\boldsymbol{\xi}^{(0)} = \begin{Bmatrix} \xi_1^{(0)} \\ \xi_2^{(0)} \\ \xi_3^{(0)} \end{Bmatrix} = \begin{Bmatrix} u_{1,11}^{0} + u_{2,12}^{0} \\ u_{1,12}^{0} + u_{2,22}^{0} \\ 0 \end{Bmatrix}; \quad \boldsymbol{\xi}^{(1)} = \begin{Bmatrix} \xi_1^{(1)} \\ \xi_2^{(1)} \\ \xi_3^{(1)} \end{Bmatrix} = \begin{Bmatrix} u_{3,111}^{0} + u_{3,122}^{0} \\ u_{3,112}^{0} + u_{3,222}^{0} \\ 0 \end{Bmatrix} \tag{A.1c}$$

$$\boldsymbol{\xi}^{(2)} = \begin{Bmatrix} \xi_1^{(2)} \\ \xi_2^{(2)} \\ \xi_3^{(2)} \end{Bmatrix} = \begin{Bmatrix} \varphi_{1,11} + \varphi_{2,12} \\ \varphi_{1,12} + \varphi_{2,22} \\ 0 \end{Bmatrix}; \quad \boldsymbol{\xi}^{(3)} = \begin{Bmatrix} \xi_1^{(3)} \\ \xi_2^{(3)} \\ \xi_3^{(3)} \end{Bmatrix} = \begin{Bmatrix} 0 \\ 0 \\ u_{3,11}^{0} + u_{3,22}^{0} \end{Bmatrix}; \quad \boldsymbol{\xi}^{(4)} = \begin{Bmatrix} \xi_1^{(4)} \\ \xi_2^{(4)} \\ \xi_3^{(4)} \end{Bmatrix} = \begin{Bmatrix} 0 \\ 0 \\ \varphi_{1,1} + \varphi_{2,2} \end{Bmatrix} \tag{A.1d}$$

The non-zero components of deviatoric stretch gradients η_{ijk} are given by:

$$\eta_{111} = \varepsilon_{11,1} - \frac{1}{5}\left(\xi_1 + 2\varepsilon_{11,1} + \gamma_{12,2} + \gamma_{13,3}\right) \tag{A.2a}$$

$$\eta_{222} = \varepsilon_{22,2} - \frac{1}{5}\left(\xi_2 + 2\varepsilon_{22,2} + \gamma_{12,1} + \gamma_{23,3}\right); \quad \eta_{333} = -\frac{1}{5}\left(\xi_3 + \gamma_{13,1} + \gamma_{23,2}\right) \tag{A.2b}$$

$$\eta_{112} = \eta_{211} = \eta_{121} = \frac{1}{3}(\varepsilon_{11,2} + \gamma_{12,1}) - \frac{1}{15}(\xi_2 + \gamma_{12,1} + 2\varepsilon_{22,2} + \gamma_{23,3}) \tag{A.2c}$$

$$\eta_{113} = \eta_{311} = \eta_{131} = \frac{1}{3}(\gamma_{13,1} + \varepsilon_{11,3}) - \frac{1}{15}(\xi_3 + \gamma_{13,1} + \gamma_{23,2}) \tag{A.2d}$$

$$\eta_{221} = \eta_{122} = \eta_{212} = \frac{1}{3}(\gamma_{12,2} + \varepsilon_{22,1}) - \frac{1}{15}(\xi_1 + 2\varepsilon_{11,1} + \gamma_{12,2} + \gamma_{13,3}) \tag{A.2e}$$

$$\eta_{223} = \eta_{322} = \eta_{232} = \frac{1}{3}(\gamma_{23,2} + \varepsilon_{22,3}) - \frac{1}{15}(\xi_3 + \gamma_{13,1} + \gamma_{23,2}) \tag{A.2f}$$

$$\eta_{331} = \eta_{133} = \eta_{313} = \frac{1}{3}\gamma_{13,3} - \frac{1}{15}(\xi_1 + 2\varepsilon_{11,1} + \gamma_{12,2} + \gamma_{13,3}) \tag{A.2g}$$

$$\eta_{332} = \eta_{233} = \eta_{323} = \frac{1}{3}\gamma_{23,3} - \frac{1}{15}(\xi_2 + \gamma_{12,1} + 2\varepsilon_{22,2} + \gamma_{23,3}) \tag{A.2h}$$

$$\eta_{123} = \eta_{231} = \eta_{312} = \eta_{132} = \eta_{321} = \eta_{213} = \frac{1}{6}(\gamma_{23,1} + \gamma_{13,2} + \gamma_{12,3}) \tag{A.2i}$$

with

$$\boldsymbol{\eta}^{(0)} = \frac{1}{5}\begin{Bmatrix} 2u^0_{1,11} - 2u^0_{2,12} - u^0_{1,22} \\ 2u^0_{2,22} - 2u^0_{1,12} - u^0_{2,11} \\ 0 \\ -\left(3u^0_{1,11} + 2u^0_{2,12} + u^0_{1,22}\right) \\ -\left(3u^0_{2,22} + 2u^0_{1,12} + u^0_{2,11}\right) \\ 4u^0_{1,22} + 8u^0_{2,12} - 3u^0_{1,11} \\ 4u^0_{2,11} + 8u^0_{1,12} - 3u^0_{2,22} \\ 0 \\ 0 \\ 0 \end{Bmatrix}, \boldsymbol{\eta}^{(1)} = \frac{1}{5}\begin{Bmatrix} 2u^0_{3,111} - 3u^0_{3,122} \\ 2u^0_{3,222} - 3u^0_{3,112} \\ 0 \\ -3\left(u^0_{3,111} + u^0_{3,122}\right) \\ -3\left(u^0_{3,112} + u^0_{3,222}\right) \\ 3\left(4u^0_{3,122} - u^0_{3,111}\right) \\ 3\left(4u^0_{3,112} - u^0_{3,222}\right) \\ 0 \\ 0 \\ 0 \end{Bmatrix} \tag{A.3a}$$

$$\boldsymbol{\eta}^{(2)} = \frac{1}{5}\begin{Bmatrix} 2\varphi_{1,11} - 2\varphi_{2,12} - \varphi_{1,22} \\ 2\varphi_{2,22} - 2\varphi_{1,12} - \varphi_{2,11} \\ 0 \\ -(3\varphi_{1,11} + 2\varphi_{2,12} + \varphi_{1,22}) \\ -(3\varphi_{2,22} + 2\varphi_{1,12} + \varphi_{2,11}) \\ 4\varphi_{1,22} + 8\varphi_{2,12} - 3\varphi_{1,11} \\ 4\varphi_{2,11} + 8\varphi_{1,12} - 3\varphi_{2,22} \\ 0 \\ 0 \\ 0 \end{Bmatrix}, \boldsymbol{\eta}^{(3)} = \frac{1}{5}\begin{Bmatrix} 0 \\ 0 \\ -\left(u^0_{3,11} + u^0_{3,22} + \varphi_{1,1} + \varphi_{2,2}\right) \\ 0 \\ 0 \\ 0 \\ 0 \\ 4u^0_{3,11} - u^0_{3,22} + 4\varphi_{1,1} - \varphi_{2,2} \\ 4u^0_{3,22} - u^0_{3,11} + 4\varphi_{2,2} - \varphi_{1,1} \\ 5\left(\varphi_{1,2} + \varphi_{2,1} + 2u^0_{3,12}\right) \end{Bmatrix} \tag{A.3b}$$

$$\boldsymbol{\eta}^{(4)}=\frac{1}{5}\begin{Bmatrix}0\\0\\-\left(u^0_{3,11}+u^0_{3,22}\right)\\0\\0\\0\\0\\4u^0_{3,11}-u^0_{3,22}\\4u^0_{3,22}-u^0_{3,11}\\10u^0_{3,12}\end{Bmatrix},\boldsymbol{\eta}^{(5)}=\frac{1}{5}\begin{Bmatrix}0\\0\\-(\varphi_{1,1}+\varphi_{2,2})\\0\\0\\0\\0\\4\varphi_{1,1}-\varphi_{2,2}\\4\varphi_{2,2}-\varphi_{1,1}\\5(\varphi_{1,2}+\varphi_{2,1})\end{Bmatrix},\boldsymbol{\eta}^{(6)}=\frac{1}{5}\begin{Bmatrix}-\left(\varphi_1+u^0_{3,1}\right)\\-\left(\varphi_2+u^0_{3,2}\right)\\0\\4\left(\varphi_1+u^0_{3,1}\right)\\4\left(\varphi_2+u^0_{3,2}\right)\\-\left(\varphi_1+u^0_{3,1}\right)\\-\left(\varphi_2+u^0_{3,2}\right)\\0\\0\\0\end{Bmatrix} \tag{A.3c}$$

$$\boldsymbol{\chi}^{(0)}=\frac{1}{2}\begin{Bmatrix}u^0_{3,12}\\-u^0_{3,12}\\u^0_{3,22}-u^0_{3,11}\\0\\u^0_{2,11}-u^0_{1,12}\\u^0_{2,12}-u^0_{1,22}\end{Bmatrix},\ \boldsymbol{\chi}^{(1)}=\frac{1}{2}\begin{Bmatrix}-u^0_{3,12}\\u^0_{3,12}\\u^0_{3,11}-u^0_{3,22}\\0\\0\\0\end{Bmatrix},\ \boldsymbol{\chi}^{(2)}=\frac{1}{2}\begin{Bmatrix}-\varphi_{2,1}\\\varphi_{1,2}\\\varphi_{1,1}-\varphi_{2,2}\\\varphi_{2,1}-\varphi_{1,2}\\0\\0\end{Bmatrix} \tag{A.3d}$$

$$\boldsymbol{\chi}^{(3)}=\frac{1}{2}\begin{Bmatrix}0\\0\\0\\0\\-u^0_{3,2}\\u^0_{3,1}\end{Bmatrix},\ \boldsymbol{\chi}^{(4)}=\frac{1}{2}\begin{Bmatrix}0\\0\\0\\0\\-\varphi_2\\\varphi_1\end{Bmatrix},\ \boldsymbol{\chi}^{(5)}=\frac{1}{2}\begin{Bmatrix}0\\0\\0\\0\\\varphi_{2,11}-\varphi_{1,12}\\\varphi_{2,12}-\varphi_{1,22}\end{Bmatrix} \tag{A.3e}$$

Appendix B

The FGP microplates stiffness components are described as follows:

$$\left(\mathbf{D}^{\varepsilon}_s,\mathbf{B}^{\varepsilon}_s,\mathbf{H}^{\varepsilon}_s,\mathbf{D}^{\varepsilon},\mathbf{B}^{\varepsilon},\mathbf{A}^{\varepsilon}\right)=\int_{-h/2}^{h/2}\left(\Phi_1\Phi_2,\Phi_2,\Phi_2^2,\Phi_1^2,\Phi_1,1\right)\mathbf{Q}^{(i)}_{\varepsilon}dx_3;\quad \mathbf{A}^{\varepsilon}_s=\int_{-h/2}^{h/2}\Phi_3^2\mathbf{Q}^{(o)}_{\varepsilon}dx_3 \tag{B.1a}$$

$$\left(\mathbf{A}^{\xi},\mathbf{B}^{\xi},\mathbf{B}^{\xi}_s,\bar{\mathbf{B}}^{\xi},\bar{\mathbf{B}}^{\xi}_s\right)=\left(A^{\xi},B^{\xi},B^{\xi}_s,\bar{B}^{\xi},\bar{B}^{\xi}_s\right)\mathbf{I}_{3\times3}=\int_{-h/2}^{h/2}(1,\Phi_1,\Phi_2,\Phi_{1,3},\Phi_{2,3})\alpha_{\xi}\mathbf{I}_{3\times3}dx_3 \tag{B.1b}$$

$$\left(\mathbf{D}^{\xi},\mathbf{D}^{\xi}_s,\bar{\mathbf{O}}^{\xi},\bar{\mathbf{P}}^{\xi}_s\right)=\left(D^{\xi},D^{\xi}_s,\bar{O}^{\xi},\bar{P}^{\xi}_s\right)\mathbf{I}_{3\times3}=\int_{-h/2}^{h/2}\Phi_1(\Phi_1,\Phi_2,\Phi_{1,3},\Phi_{2,3})\alpha_{\xi}\mathbf{I}_{3\times3}dx_3 \tag{B.1c}$$

$$\begin{aligned}\left(\mathbf{H}^{\xi}_s,\bar{\mathbf{F}}^{\xi}_s,\bar{\mathbf{J}}^{\xi},\bar{\mathbf{D}}^{\xi},\bar{\mathbf{D}}^{\xi}_s,\bar{\mathbf{H}}^{\xi}_s\right)&=\left(H^{\xi}_s,\bar{F}^{\xi}_s,\bar{J}^{\xi},\bar{D}^{\xi},\bar{D}^{\xi}_s,\bar{H}^{\xi}_s\right)\mathbf{I}_{3\times3}\\&=\int_{-h/2}^{h/2}\left(\Phi_2^2,\Phi_2\Phi_{1,3},\Phi_2\Phi_{2,3},\Phi_{1,3}^2,\Phi_{1,3}\Phi_{2,3},\Phi_{2,3}^2\right)\alpha_{\xi}\mathbf{I}_{3\times3}dx_3\end{aligned} \tag{B.1d}$$

$$\left(\mathbf{A}^{\eta},\mathbf{B}^{\eta},\mathbf{B}_{s}^{\eta},\mathbf{A}_{s}^{\eta},\bar{\mathbf{B}}^{\eta},\bar{\mathbf{B}}_{s}^{\eta},\bar{\mathbf{A}}_{s}^{\eta}\right)=\left(A^{\eta},B^{\eta},B_{s}^{\eta},A_{s}^{\eta},\bar{B}^{\eta},\bar{B}_{s}^{\eta},\bar{A}_{s}^{\eta}\right)\mathbf{I}_{10\times10}=\int_{-h/2}^{h/2}\left(1,\Phi_{1},\Phi_{2},\Phi_{3},\Phi_{1,3},\Phi_{2,3},\Phi_{3,3}\right)\alpha_{\eta}\mathbf{I}_{10\times10}dx_{3} \tag{B.1e}$$

$$\left(\mathbf{D}^{\eta},\mathbf{D}_{s}^{\eta},\mathbf{D}_{ts}^{\eta},\bar{\mathbf{O}}^{\eta},\bar{\mathbf{P}}_{s}^{\eta},\bar{\mathbf{Q}}_{s}^{\eta}\right)=\left(D^{\eta},D_{s}^{\eta},D_{ts}^{\eta},\bar{O}^{\eta},\bar{P}_{s}^{\eta},\bar{Q}_{s}^{\eta}\right)\mathbf{I}_{10\times10}=\int_{-h/2}^{h/2}\Phi_{1}\left(\Phi_{1},\Phi_{2},\Phi_{3},\Phi_{1,3},\Phi_{2,3},\Phi_{3,3}\right)\alpha_{\eta}\mathbf{I}_{10\times10}dx_{3} \tag{B.1f}$$

$$\left(\mathbf{H}_{s}^{\eta},\bar{\mathbf{D}}_{hs}^{\eta},\bar{\mathbf{F}}_{s}^{\eta},\bar{\mathbf{J}}^{\eta},\bar{\mathbf{F}}_{hs}^{\eta}\right)=\left(H_{s}^{\eta},\bar{D}_{hs}^{\eta},\bar{F}_{s}^{\eta},\bar{J}^{\eta},\bar{F}_{hs}^{\eta}\right)\mathbf{I}_{10\times10}=\int_{-h/2}^{h/2}\Phi_{2}\left(\Phi_{2},\Phi_{3},\Phi_{1,3},\Phi_{2,3},\Phi_{3,3}\right)\alpha_{\eta}\mathbf{I}_{10\times10}dx_{3} \tag{B.1g}$$

$$\left(\mathbf{H}_{ts}^{\eta},\bar{\mathbf{F}}_{ts}^{\eta},\bar{\mathbf{J}}_{hs}^{\eta},\bar{\mathbf{R}}^{\eta}\right)=\left(H_{ts}^{\eta},\bar{F}_{ts}^{\eta},\bar{J}_{hs}^{\eta},\bar{R}^{\eta}\right)\mathbf{I}_{10\times10}=\int_{-h/2}^{h/2}\Phi_{3}\left(\Phi_{3},\Phi_{1,3},\Phi_{2,3},\Phi_{3,3}\right)\alpha_{\eta}\mathbf{I}_{10\times10}dx_{3} \tag{B.1h}$$

$$\left(\bar{\mathbf{D}}^{\eta},\bar{\mathbf{D}}_{s}^{\eta},\bar{\mathbf{D}}_{ts}^{\eta},\bar{\mathbf{H}}_{s}^{\eta},\bar{\mathbf{D}}_{hs}^{\eta},\bar{\mathbf{H}}_{ts}^{\eta}\right)=\left(\bar{D}^{\eta},\bar{D}_{s}^{\eta},\bar{D}_{ts}^{\eta},\bar{H}_{s}^{\eta},\bar{D}_{hs}^{\eta},\bar{H}_{ts}^{\eta}\right)\mathbf{I}_{10\times10}=\int_{-h/2}^{h/2}\left(\Phi_{1,3}^{2},\Phi_{1,3}\Phi_{2,3},\Phi_{1,3}\Phi_{3,3},\Phi_{2,3}^{2},\Phi_{2,3}\Phi_{3,3},\Phi_{3,3}^{2}\right)\alpha_{\eta}\mathbf{I}_{10\times10}dx_{3} \tag{B.1i}$$

$$\left(\mathbf{A}^{\chi},\bar{\mathbf{B}}^{\chi},\bar{\mathbf{B}}_{s}^{\chi},\overline{\mathbf{B}}^{\chi},\overline{\mathbf{B}}_{s}^{\chi},\mathbf{B}_{s}^{\chi}\right)=\left(A^{\chi},\bar{B}^{\chi},\bar{B}_{s}^{\chi},\overline{B}^{\chi},\overline{B}_{s}^{\chi},B_{s}^{\chi}\right)\mathbf{I}_{6\times6}=\int_{-h/2}^{h/2}\left(1,\Phi_{1,3},\Phi_{2,3},\Phi_{1,33},\Phi_{2,33},\Phi_{2}\right)\alpha_{\chi}\mathbf{I}_{6\times6}dx_{3} \tag{B.1j}$$

$$\left(\bar{\mathbf{D}}^{\chi},\bar{\mathbf{D}}_{s}^{\chi},\bar{\mathbf{E}}^{\chi},\bar{\mathbf{E}}_{s}^{\chi},\bar{\mathbf{F}}_{s}^{\chi}\right)=\left(\bar{D}^{\chi},\bar{D}_{s}^{\chi},\bar{E}^{\chi},\bar{E}_{s}^{\chi},\bar{F}_{s}^{\chi}\right)\mathbf{I}_{6\times6}=\int_{-h/2}^{h/2}\left(\Phi_{1,3}\Phi_{1,3},\Phi_{2,3}\Phi_{1,3},\Phi_{1,33}\Phi_{1,3},\Phi_{2,33}\Phi_{1,3},\Phi_{2}\Phi_{1,3}\right)\alpha_{\chi}\mathbf{I}_{6\times6}dx_{3} \tag{B.1k}$$

$$\left(\bar{\mathbf{H}}_{s}^{\chi},\bar{\mathbf{G}}_{s}^{\chi},\bar{\mathbf{I}}^{\chi},\bar{\mathbf{J}}^{\chi}\right)=\left(\bar{H}_{s}^{\chi},\bar{G}_{s}^{\chi},\bar{I}^{\chi},\bar{J}^{\chi}\right)\mathbf{I}_{6\times6}=\int_{-h/2}^{h/2}\left(\Phi_{2,3}\Phi_{2,3},\Phi_{1,33}\Phi_{2,3},\Phi_{2,33}\Phi_{2,3},\Phi_{2}\Phi_{2,3}\right)\alpha_{\chi}\mathbf{I}_{6\times6}dx_{3} \tag{B.1l}$$

$$\left(\overline{\mathbf{D}}^{\chi},\overline{\bar{\mathbf{D}}}_{s}^{\chi},\bar{\mathbf{K}}_{s}^{\chi},\overline{\bar{\mathbf{H}}}_{s}^{\chi},\bar{\mathbf{L}}^{\chi},\mathbf{H}_{s}^{\chi}\right)=\left(\overline{D}^{\chi},\overline{\bar{D}}_{s}^{\chi},\bar{K}_{s}^{\chi},\overline{\bar{H}}_{s}^{\chi},\bar{L}^{\chi},H_{s}^{\chi}\right)\mathbf{I}_{6\times6}=\int_{-h/2}^{h/2}\left(\Phi_{1,33}^{2},\Phi_{1,33}\Phi_{2,33},\Phi_{1,33}\Phi_{2},\Phi_{2,33}^{2},\Phi_{2,33}\Phi_{2},\Phi_{2}^{2}\right)\alpha_{\chi}\mathbf{I}_{6\times6}dx_{3} \tag{B.1m}$$

Appendix C

The stiffness matrix's components $\mathbf{K}^{\xi}$ are given as follows:

$$K_{ijkl}^{\xi 11} = A^{\xi}\left(T_{ik}^{33}S_{jl}^{00} + T_{ik}^{22}S_{jl}^{11}\right), K_{ijkl}^{\xi 12} = A^{\xi}\left(T_{ik}^{13}S_{jl}^{20} + T_{ik}^{02}S_{jl}^{31}\right) \tag{C.1a}$$

$$K_{ijkl}^{\xi 13} = B^{\xi}\left(T_{ik}^{33}S_{jl}^{00} + T_{ik}^{13}S_{jl}^{20} + T_{ik}^{02}S_{jl}^{31} + T_{ik}^{22}S_{jl}^{11}\right) \tag{C.1b}$$

$$K_{ijkl}^{\xi 14} = B_s^{\xi}\left(T_{ik}^{33}S_{jl}^{00} + T_{ik}^{22}S_{jl}^{11}\right),\ K_{ijkl}^{\xi 15} = B_s^{\xi}\left(T_{ik}^{13}S_{jl}^{20} + T_{ik}^{02}S_{jl}^{31}\right) \tag{C.1c}$$

$$K_{ijkl}^{\xi 22} = A^{\xi}\left(T_{ik}^{11}S_{jl}^{22} + T_{ik}^{00}S_{jl}^{33}\right),\ K_{ijkl}^{\xi 23} = B^{\xi}\left(T_{ik}^{31}S_{jl}^{02} + T_{ik}^{11}S_{jl}^{22} + T_{ik}^{20}S_{jl}^{13} + T_{ik}^{00}S_{jl}^{33}\right) \tag{C.1d}$$

$$K_{ijkl}^{\xi 24} = B_s^{\xi}\left(T_{ik}^{31}S_{jl}^{02} + T_{ik}^{20}S_{jl}^{13}\right),\ K_{ijkl}^{\xi 25} = B_s^{\xi}\left(T_{ik}^{11}S_{jl}^{22} + T_{ik}^{00}S_{jl}^{33}\right) \tag{C.1e}$$

$$\begin{aligned} K_{ijkl}^{\xi 33} = {} & D^{\xi}\left(T_{ik}^{33}S_{jl}^{00} + T_{ik}^{00}S_{jl}^{33} + T_{ik}^{31}S_{jl}^{02} + T_{ik}^{02}S_{jl}^{31} + T_{ik}^{13}S_{jl}^{20} + T_{ik}^{20}S_{jl}^{13} + T_{ik}^{11}S_{jl}^{22} + T_{ik}^{22}S_{jl}^{11}\right) \\ & + \bar{D}^{\xi}\left(T_{ik}^{22}S_{jl}^{00} + T_{ik}^{20}S_{jl}^{02} + T_{ik}^{02}S_{jl}^{20} + T_{ik}^{00}S_{jl}^{22}\right) \end{aligned} \tag{C.1f}$$

$$K_{ijkl}^{\xi 34} = D_s^{\xi}\left(T_{ik}^{33}S_{jl}^{00} + T_{ik}^{31}S_{jl}^{02} + T_{ik}^{22}S_{jl}^{11} + T_{ik}^{20}S_{jl}^{13}\right) + \bar{D}_s^{\xi}\left(T_{ik}^{22}S_{jl}^{00} + T_{ik}^{20}S_{jl}^{02}\right) \tag{C.1g}$$

$$K_{ijkl}^{\xi 35} = D_s^{\xi}\left(T_{ik}^{13}S_{jl}^{20} + T_{ik}^{11}S_{jl}^{22} + T_{ik}^{02}S_{jl}^{31} + T_{ik}^{00}S_{jl}^{33}\right) + \bar{D}_s^{\xi}\left(T_{ik}^{02}S_{jl}^{20} + T_{ik}^{00}S_{jl}^{22}\right) \tag{C.1h}$$

$$K_{ijkl}^{\xi 44} = H_s^{\xi}T_{ik}^{33}S_{jl}^{00} + H_s^{\xi}T_{ik}^{22}S_{jl}^{11} + \bar{H}_s^{\xi}T_{ik}^{22}S_{jl}^{00},\ K_{ijkl}^{\xi 45} = H_s^{\xi}T_{ik}^{13}S_{jl}^{20} + H_s^{\xi}T_{ik}^{02}S_{jl}^{31} + \bar{H}_s^{\xi}T_{ik}^{02}S_{jl}^{20} \tag{C.1i}$$

$$K_{ijkl}^{\xi 55} = H_s^{\xi}T_{ik}^{00}S_{jl}^{33} + H_s^{\xi}T_{ik}^{11}S_{jl}^{22} + \bar{H}_s^{\xi}T_{ik}^{00}S_{jl}^{22} \tag{C.1j}$$

The components of stiffness matrix $\mathbf{K}^{\eta}$ are defined as follows:

$$K_{ijkl}^{\eta 11} = \frac{A^{\eta}}{25}\left(22T_{ik}^{33}S_{jl}^{00} - 11T_{ik}^{31}S_{jl}^{02} - 11T_{ik}^{13}S_{jl}^{20} + 18T_{ik}^{11}S_{jl}^{22} + 72T_{ik}^{22}S_{jl}^{11}\right) \tag{C.2a}$$

$$K_{ijkl}^{\eta 12} = \frac{2A^{\eta}}{25}\left(-11T_{ik}^{13}S_{jl}^{20} - 11T_{ik}^{02}S_{jl}^{31} + 18T_{ik}^{11}S_{jl}^{22} + 18T_{ik}^{22}S_{jl}^{11}\right) \tag{B.2a}$$

$$\begin{aligned} K_{ijkl}^{\eta 13} = {} & \frac{B^{\eta}}{25}\left(22T_{ik}^{33}S_{jl}^{00} - 11T_{ik}^{31}S_{jl}^{02} - 33T_{ik}^{13}S_{jl}^{20} + 54T_{ik}^{11}S_{jl}^{22} - 22T_{ik}^{02}S_{jl}^{31} + 108T_{ik}^{22}S_{jl}^{11}\right) \\ & - \frac{\bar{A}_s^{\eta}}{25}\left(11T_{ik}^{13}S_{jl}^{00} + 7T_{ik}^{11}S_{jl}^{02} + 14T_{ik}^{02}S_{jl}^{11}\right) \end{aligned} \tag{C.2b}$$

$$K_{ijkl}^{\eta 14} = \frac{B_s^{\eta}}{25}\left(22T_{ik}^{33}S_{jl}^{00} - 11T_{ik}^{31}S_{jl}^{02} - 11T_{ik}^{13}S_{jl}^{20} + 18T_{ik}^{11}S_{jl}^{22} + 72T_{ik}^{22}S_{jl}^{11}\right) - \frac{\bar{A}_s^{\eta}}{25}\left(11T_{ik}^{13}S_{jl}^{00} + 7T_{ik}^{11}S_{jl}^{02}\right) \tag{C.2c}$$

$$K_{ijkl}^{\eta 15} = \frac{2B_s^{\eta}}{25}\left(18T_{ik}^{11}S_{jl}^{22} - 11T_{ik}^{13}S_{jl}^{20} + 18T_{ik}^{22}S_{jl}^{11} - 11T_{ik}^{02}S_{jl}^{31}\right) - \frac{14\bar{A}_s^{\eta}}{25}T_{ik}^{02}S_{jl}^{11} \tag{C.2d}$$

$$K_{ijkl}^{\eta 22} = \frac{A^{\eta}}{25}\left(72T_{ik}^{11}S_{jl}^{22} + 22T_{ik}^{00}S_{jl}^{33} - 11T_{ik}^{02}S_{jl}^{31} - 11T_{ik}^{20}S_{jl}^{13} + 18T_{ik}^{22}S_{jl}^{11}\right) \tag{C.2e}$$

$$\begin{aligned} K_{ijkl}^{\eta 23} = {} & \frac{B^{\eta}}{25}\left(22T_{ik}^{00}S_{jl}^{33} - 22T_{ik}^{31}S_{jl}^{02} + 108T_{ik}^{11}S_{jl}^{22} - 11T_{ik}^{02}S_{jl}^{31} - 33T_{ik}^{20}S_{jl}^{13} + 54T_{ik}^{22}S_{jl}^{11}\right) \\ & - \frac{\bar{A}_s^{\eta}}{25}\left(14T_{ik}^{11}S_{jl}^{02} + 7T_{ik}^{02}S_{jl}^{11} + 11T_{ik}^{00}S_{jl}^{13}\right) \end{aligned} \tag{C.2f}$$

$$K_{ijkl}^{\eta 24} = \frac{2B_s^{\eta}}{25}\left(-11T_{ik}^{31}S_{jl}^{02} + 18T_{ik}^{11}S_{jl}^{22} + 18T_{ik}^{22}S_{jl}^{11} - 11T_{ik}^{20}S_{jl}^{13}\right) - \frac{14\bar{A}_s^{\eta}}{25}T_{ik}^{11}S_{jl}^{02} \tag{B.2a}$$

$$K_{ijkl}^{\eta 25} = \frac{B_s^{\eta}}{25}\left(72T_{ik}^{11}S_{jl}^{22} + 22T_{ik}^{00}S_{jl}^{33} - 11T_{ik}^{02}S_{jl}^{31} - 11T_{ik}^{20}S_{jl}^{13} + 18T_{ik}^{22}S_{jl}^{11}\right) - \frac{\bar{A}_s^{\eta}}{25}\left(7T_{ik}^{02}S_{jl}^{11} + 11T_{ik}^{00}S_{jl}^{13}\right) \tag{C.2g}$$

$$\begin{aligned} K_{ijkl}^{\eta 33} = {} & \frac{D^{\eta}}{25}\left(22T_{ik}^{33}S_{jl}^{00} - 33T_{ik}^{31}S_{jl}^{02} - 33T_{ik}^{13}S_{jl}^{20} + 162T_{ik}^{11}S_{jl}^{22} + 162T_{ik}^{22}S_{jl}^{11}\right) \\ & + \frac{D^{\eta}}{25}\left(22T_{ik}^{00}S_{jl}^{33} - 33T_{ik}^{02}S_{jl}^{31} - 33T_{ik}^{20}S_{jl}^{13}\right) \\ & - \frac{\bar{Q}_s^{\eta}}{25}\left(11T_{ik}^{00}S_{jl}^{13} + 11T_{ik}^{13}S_{jl}^{00} + 11T_{ik}^{31}S_{jl}^{00} + 11T_{ik}^{00}S_{jl}^{31}\right) \\ & - \frac{\bar{Q}_s^{\eta}}{25}\left(21T_{ik}^{02}S_{jl}^{11} + 21T_{ik}^{11}S_{jl}^{02} + 21T_{ik}^{11}S_{jl}^{20} + 21T_{ik}^{20}S_{jl}^{11}\right) \\ & + \frac{H_{ts}^{\eta} + 2\bar{F}_{ts}^{\eta} + \bar{D}^{\eta}}{25}\left(18T_{ik}^{22}S_{jl}^{00} - 7T_{ik}^{20}S_{jl}^{02} - 7T_{ik}^{02}S_{jl}^{20} + 18T_{ik}^{00}S_{jl}^{22} + 100T_{ik}^{11}S_{jl}^{11}\right) \\ & + \frac{18\bar{H}_{ts}^{\eta}}{25}\left(T_{ik}^{11}S_{jl}^{00} + T_{ik}^{00}S_{jl}^{11}\right) \end{aligned} \tag{C.2h}$$

$$\begin{aligned} K_{ijkl}^{\eta 34} = {} & \frac{D_s^{\eta}}{25}\left(22T_{ik}^{33}S_{jl}^{00} - 33T_{ik}^{31}S_{jl}^{02} - 11T_{ik}^{13}S_{jl}^{20} + 54T_{ik}^{11}S_{jl}^{22} - 22T_{ik}^{20}S_{jl}^{13} + 108T_{ik}^{22}S_{jl}^{11}\right) \\ & - \frac{\bar{Q}_s^{\eta}}{25}\left(11T_{ik}^{13}S_{jl}^{00} + 21T_{ik}^{11}S_{jl}^{02}\right) + \frac{H_{ts}^{\eta} + \bar{J}_{hs}^{\eta} + \bar{F}_{ts}^{\eta} + \bar{D}_s^{\eta}}{25}\left(18T_{ik}^{22}S_{jl}^{00} - 7T_{ik}^{20}S_{jl}^{02} + 50T_{ik}^{11}S_{jl}^{11}\right) \\ & - \frac{\bar{F}_{hs}^{\eta}}{25}\left(14T_{ik}^{20}S_{jl}^{11} + 11T_{ik}^{31}S_{jl}^{00} + 7T_{ik}^{11}S_{jl}^{20}\right) + \frac{18\bar{H}_{ts}^{\eta}}{25}T_{ik}^{11}S_{jl}^{00} \end{aligned} \tag{C.2i}$$

$$\begin{aligned} K_{ijkl}^{\eta 35} = {} & \frac{D_s^{\eta}}{25}\left(108T_{ik}^{11}S_{jl}^{22} + 54T_{ik}^{22}S_{jl}^{11} + 22T_{ik}^{00}S_{jl}^{33} - 33T_{ik}^{02}S_{jl}^{31} - 11T_{ik}^{20}S_{jl}^{13} - 22T_{ik}^{13}S_{jl}^{20}\right) \\ & - \frac{\bar{Q}_s^{\eta}}{25}\left(21T_{ik}^{02}S_{jl}^{11} + 11T_{ik}^{00}S_{jl}^{13}\right) + \frac{H_{ts}^{\eta} + \bar{J}_{hs}^{\eta} + \bar{F}_{ts}^{\eta} + \bar{D}_s^{\eta}}{25}\left(18T_{ik}^{00}S_{jl}^{22} - 7T_{ik}^{02}S_{jl}^{20} + 50T_{ik}^{11}S_{jl}^{11}\right) \\ & - \frac{\bar{F}_{hs}^{\eta}}{25}\left(14T_{ik}^{11}S_{jl}^{20} + 11T_{ik}^{00}S_{jl}^{31} + 7T_{ik}^{20}S_{jl}^{11}\right) + \frac{18\bar{H}_{ts}^{\eta}}{25}T_{ik}^{00}S_{jl}^{11} \end{aligned} \tag{C.2j}$$

$$\begin{aligned} K_{ijkl}^{\eta 44} = {} & \frac{H_s^{\eta}}{25}\left(22T_{ik}^{33}S_{jl}^{00} - 11T_{ik}^{31}S_{jl}^{02} - 11T_{ik}^{13}S_{jl}^{20} + 18T_{ik}^{11}S_{jl}^{22} + 72T_{ik}^{22}S_{jl}^{11}\right) + \frac{18\bar{H}_{ts}^{\eta}}{25}T_{ik}^{11}S_{jl}^{00} \\ & + \frac{H_{ts}^{\eta} + 2\bar{J}_{hs}^{\eta} + \bar{H}_s^{\eta}}{25}\left(18T_{ik}^{22}S_{jl}^{00} + 25T_{ik}^{11}S_{jl}^{11}\right) - \frac{\bar{F}_{hs}^{\eta}}{25}\left(11T_{ik}^{31}S_{jl}^{00} + 7T_{ik}^{11}S_{jl}^{20} + 11T_{ik}^{13}S_{jl}^{00} + 7T_{ik}^{11}S_{jl}^{02}\right) \end{aligned} \tag{C.2k}$$

$$\begin{aligned} K_{ijkl}^{\eta 45} = {} & \frac{H_s^{\eta}}{25}\left(36T_{ik}^{11}S_{jl}^{22} + 36T_{ik}^{22}S_{jl}^{11} - 22T_{ik}^{13}S_{jl}^{20} - 22T_{ik}^{02}S_{jl}^{31}\right) - \frac{14\bar{F}_{hs}^{\eta}}{25}\left(T_{ik}^{02}S_{jl}^{11} + T_{ik}^{11}S_{jl}^{20}\right) \\ & + \frac{H_{ts}^{\eta} + 2\bar{J}_{hs}^{\eta} + \bar{H}_s^{\eta}}{25}\left(25T_{ik}^{11}S_{jl}^{11} - 7T_{ik}^{02}S_{jl}^{20}\right) \end{aligned} \tag{C.2l}$$

$$\begin{aligned} K_{ijkl}^{\eta 55} = {} & \frac{H_s^{\eta}}{25}\left(72T_{ik}^{11}S_{jl}^{22} + 22T_{ik}^{00}S_{jl}^{33} - 11T_{ik}^{02}S_{jl}^{31} - 11T_{ik}^{20}S_{jl}^{13} + 18T_{ik}^{22}S_{jl}^{11}\right) + \frac{18\bar{H}_{ts}^{\eta}}{25}T_{ik}^{00}S_{jl}^{11} \\ & + \frac{H_{ts}^{\eta} + 2\bar{J}_{hs}^{\eta} + \bar{H}_s^{\eta}}{25}\left(18T_{ik}^{00}S_{jl}^{22} + 25T_{ik}^{11}S_{jl}^{11}\right) - \frac{\bar{F}_{hs}^{\eta}}{25}\left(11T_{ik}^{00}S_{jl}^{13} + 7T_{ik}^{02}S_{jl}^{11} + 11T_{ik}^{00}S_{jl}^{31} + 7T_{ik}^{20}S_{jl}^{11}\right) \end{aligned} \tag{C.2m}$$

with $T_{ik}^{rs} = \int_0^a \frac{\partial^r R_i}{\partial x_1^r}\frac{\partial^s R_k}{\partial x_1^s}dx_1, S_{jl}^{rs} = \int_0^b \frac{\partial^r P_j}{\partial x_2^r}\frac{\partial^s P_l}{\partial x_2^s}dx_2$.

Journal of Vibration Engineering & Technologies (2025)13:203
https://doi.org/10.1007/s42417-024-01748-8

ORIGINAL PAPER

Novel Computational Algorithms for Vibration, Buckling, and Transient Analysis of Porous Metal Foam Microplates

Van-Thien Tran[1] · Trung-Kien Nguyen[2] · Van-Hau Nguyen[1] · Thuc P. Vo[3]

Received: 25 April 2024 / Revised: 3 December 2024 / Accepted: 23 December 2024

Abstract

Purpose This research proposes novel computational methods, namely the Ritz–Hermite and Ritz–Laguerre methods, for the analysis of porous metal foam (PMF) microplates.

Method The analysis is based on higher-order shear deformation theory and modified couple stress theory, incorporating a constant material length scale parameter. The dynamic responses of the microplates under an explosive blast load are determined using Newmark's technique. The proposed Ritz method employs orthogonal polynomial-generated shape functions, constructed as hybrid functions by combining a base polynomial with a series of orthogonal polynomials (Hermite and Laguerre), ensuring compliance with required boundary conditions.

Results and Conclusion The proposed methods exhibit superior convergence speed and stability compared to alternative shape functions. The study presents, for the first time, the dynamic responses of PMF microplates under various loads, including explosive blasts, triangular, and rectangular patterns. The research investigates the effects of the material length scale parameter, damping factor, side-to-thickness ratio, porosity coefficient, porosity distribution, and boundary conditions on the vibration, buckling, and transient responses of PMF microplates. The findings, supported by numerical results, highlight the efficiency and accuracy of the proposed computational methods in predicting the structural characteristics of PMF microplates.

Keywords Porous metal foam microplates · Ritz solution · Higher-order shear deformation theory · Vibration · Buckling · Transient analysis

Abbreviations

BCs	Boundary conditions
FSDT	First-other shear deformation theory
HSDT	High-other shear deformation theory
PMF	Porous metal foam
MAT	Material
MCT	Modified couple stress theory
MLSP	Material length scale parameter
OP	Orthogonal polynomials and
NOP	Non-orthogonal polynomials

List of Symbols

$\mathbf{C}$	Damping matrix
$\mathbf{M}$	Mass matrix
$\mathbf{K}$	Stiffness matrix
$\mathbf{F}$	Force
$\mathbf{d}$	Displacement field
$\dot{\mathbf{d}}$	Velocity
$\ddot{\mathbf{d}}$	Acceleration
E	Young's modulus
h	The thickness
ρ	Mass density
β	The porosity volume fraction
x_1, x_2, x_3	The coordinate system
v	Poisson's ratio
Π_{SE}	The strain energy
Π_W	Work done by membrane forces
Π_{KE}	Kinetic energy

✉ Trung-Kien Nguyen
ntkien@hutech.edu.vn

[1] Faculty of Civil Engineering, Ho Chi Minh City University of Technology and Education, 1 Vo Van Ngan Street, Thu Duc City, Ho Chi Minh City, Viet Nam

[2] Faculty of Civil Engineering, HUTECH University, 475A Dien Bien Phu Street, Binh Thanh District, Ho Chi Minh City, Viet Nam

[3] School of Computing, Engineering and Mathematical Sciences, La Trobe University, Bundoora, VIC 3086, Australia

Published online: 18 February 2025

$\boldsymbol{\varepsilon}$	Strains
$\boldsymbol{\chi}$	Symmetric rotation gradients
$\boldsymbol{\sigma}$	Cauchy stress
$\mathbf{m}$	The high-order stress corresponding with strain gradients $\boldsymbol{\chi}$
l	Material length scale parameters
$T_i(x_1), F_j(x_2)$	The shape functions in direction in x_1-, x_2-

Introduction

Owing to their distinctive properties in energy absorption capacity, high strength, and lightweight design, porous materials have been applied in various engineering fields, such as aerospace and the petrochemical industry [1–4]. In practice, the development of such materials accompanied efficiently computational methods and models in order to predict accurately their responses at different structural scales.

Earlier experimental work has shown that constituent size effects need to be considered when computing the responses of micro and nanoscale structures. In this context, it is well known that classical elasticity theory is inadequate; therefore, surrogate theories accounting for size effects have been explored to calculate their responses. One such theory is the modified couple stress theory (MCT) proposed by Yang [5], which used a single material length scale parameter (MLSP) to account for the size effects. Because of its simplicity, the MCT has been used for size dependent analysis of functionally graded (FG) and functionally graded porous (FGP) microplates with different porosity densities. Li et al. [6] investigated thermal-electric effects on dynamic behaviors of FG piezoelectric sandwich microplates by using the MCT and hyperbolic tangential mixed shear deformation theory. Tran et al. [7, 8] developed a unified higher-order shear deformation theory (HSDT) using the MCT and Ritz method to analyze vibration and buckling behaviors of FGP microplates. Fan et al. [9] employed isogeometric analysis (IGA) and HSDT to investigate the nonlinear vibrations of FGP microplates. Farzam and Hassani [10] investigated the structural responses of FGP microplates using the IGA and a refined HSDT. Using the classical plate theory (CPT), first-order shear deformation theory (FSDT), MCT and Navier's solution, Kim et al. [11] demonstrated the structural responses of FGP microplates. The nonlinear buckling and vibration responses of FGP microplates were examined by Thanh et al. [12] utilizing the MCT, IGA and a HSDT**.** An alternative approach for exploring the size effects is to utilize the modified strain gradient theory (MST) by introducing the effects of rotation, dilatation and deviatoric stretch gradients in constitutive equations [13], which incorporates three MLSPs. This methodology has been applied to forecast the behaviors of microstructures [14–17]. In comparison, the MST could predict microstructures' responses more accurate than the MCT owing to accounting for three MLSPs, however this method is complicated in theoretical formulation and implementation. Moreover, the nonlocal elasticity theory (NET), also known as Eringen's theory, is another method for capturing the size effects for nanostructures [18]. The NET has been applied to analyze FGP nanoplates [19–23] by including the nonlocal parameter in constitutive equations.

The exceptional material properties of porous metal foams (PMF) have increasingly attracted researchers to explore their characteristics and behaviors for various applications. Wang et al. [24] investigated static and buckling behaviors of 3D PMF plates within the context of a refined HSDT, and Galerkin method. Pham et al. [25] examined bending, free vibration, and forced vibration transient responses of PMF plate by using the IGA and a refined HSDT. Tu et al. [26] analyzed the buckling and post-buckling responses of thin PMF plates using Galerkin's analytical solution and CPT. Phung-Van et al. [27] studied behaviors of PMF nanoplates using the IGA. Sobhy et al. [28] investigated the phase velocity of the waves and wave frequency of PMF nanoplates using a refined HSDT and wave propagation analysis. Pham et al. [25] analyzed PMF microplates using a refined HSDT, MST and IGA. Le et al. [29] utilized the MCT and IGA to investigate the linear bending and geometrically nonlinear responses of PMF microplates.

In addition to plate models and size-dependent theories, computational methods have also significantly impacted the behavior of porous structures, which can be categorised into numerical and analytical methods. Among these, the Ritz approach is an efficient technique that enables the approximation of the solution field with high accuracy and simplicity in formulation and programming. Initially introduced by Walter Ritz [30], this method was designed to analyse the free vibrations of structures. Since then, several researchers have used this method to investigate the structural responses of beams, plates, and shells. It is important to note that the accuracy, numerical stability, and convergence rates of the Ritz method heavily rely on the choice of approximation functions. Therefore, careful selection of these functions is crucial to ensure both accuracy and favourable numerical properties. The functions must be linearly independent, complete, and compatible with the geometric boundary conditions (BCs) [31]. The Ritz method also faces challenges when applied to systems with irregular geometries. In order to overcome

this adverse, the *pb*2-Ritz method [32, 33] with a combination of two-dimensional polynomial function and basic boundary function, or Ritz method with mapping technique [34, 35] could solve different shaped plate problems. A brief literature review shows that polynomial methods can be categorised into two typical types: orthogonal polynomials (OP) and non-orthogonal polynomials (NOP). For the OP shape function, Chebyshev's polynomial [36] is commonly used for analysis of composite structures due to its convergence rate and numerical robustness [37–39] and it can be formulated using the Gram-Schmidt procedure [40–43]. In practice, the approximation functions of Ritz method can also be expressed as a series of NOP [44, 45]. This particular set does not exhibit orthogonality, resulting in the loss of certain computational benefits. However, the primary advantage of these functions lies in their ability to simplify the generation process compared to orthogonal counterparts. The evaluation of integrals is significantly easier than that involving their orthogonal equivalents. Moreover, it is worth noting that the shape functions should be selected to satisfy the boundary conditions (BCs) [46–48], which have been found to be efficient in terms of convergence rate. Alternatively, the penalty function method can be used to incorporate the BCs; however, it leads to an increase in the size of the mass and stiffness matrices, thereby raising computational costs. A literature review reveals that although OP offer significant advantages in numerical computations, there remains a gap in their development for the analysis of PMF microplates. The novelty of this paper lies in the development and application of the Hermite–Ritz and Laguerre–Ritz methods in combination with the unified HSDT and MCT for the free vibration, buckling, and transient analysis of PMF microplates. This approach offers a significant advancement by achieving faster convergence, enhanced numerical stability, and reduced computational complexity through the innovative use of orthogonal polynomials. The recursive properties of these polynomials facilitate the development of efficient algorithms, while their algebraic simplicity ensures ease of implementation without compromising accuracy. To the best of the authors' knowledge, this is the first study to comprehensively investigate such analyses using this unique combination of methodologies. This paper addresses a critical gap in the literature on PMF microplate behavior, and this is the primary motivation behind the study.

This paper proposes two new computational algorithms, namely Ritz–Hermite and Ritz–Laguerre, in conjunction with HSDT and MCT for the analysis of PMF microplates. The characteristic equations are derived using Hamilton's principle. The study investigates the responses of PMF microplates under various dynamic loads, including explosive blasts, triangular, and rectangular patterns, using Newmark's technique. The influence of the MLSP, damping factor, side-to-thickness ratio, porosity coefficient, porosity distribution, and BCs on the vibration, buckling, and transient responses of the PMF microplates is examined.

Theoretical Formulation

Porous Metal Foam Material (PMF)

Consider PMF rectangular microplate, which has three types of porosity distributions, with the thickness h and sides $a \times b$ as seen in Fig. 1. The effective material properties are expressed via porosity parameter β and maximum

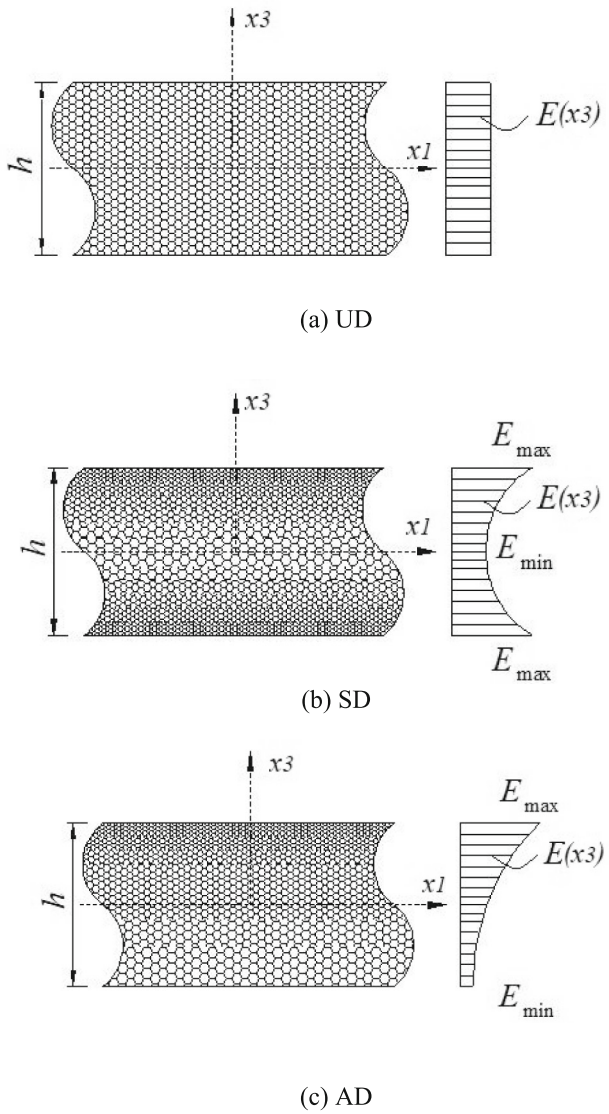

Fig. 1 Three types of PMF microplates

Young's modulus $E_{\max}$ as well as the corresponding coefficients β_m and $\rho_{\max}$ of mass density as follows [49]:

- Distribution of uniform porosity (UD)

$$\rho(z) = \rho_{\max}\sqrt{(1-\beta\upsilon)} \tag{1a}$$

$$E(z) = E_{\max}(1-\beta\upsilon) \tag{1b}$$

- Distribution of asymmetric porosity (AD)

$$\rho(z) = \rho_{\max}\left[1-\beta_m\cos\left(\frac{\pi z}{2h}+\frac{\pi}{4}\right)\right] \tag{2a}$$

$$E(z) = E_{\max}\left[1-\beta\cos\left(\frac{\pi z}{2h}+\frac{\pi}{4}\right)\right] \tag{2b}$$

- Distribution of symmetric porosity (SD)

$$\rho(z) = \rho_{\max}\left(1-\beta_m\cos\left(\frac{\pi z}{h}\right)\right) \tag{3a}$$

$$E(z) = E_{\max}\left(1-\beta\cos\left(\frac{\pi z}{h}\right)\right) \tag{3b}$$

where β and β_m denote the porosity parameters of Young's modulus and mass density, which are given by:

$$\beta = 1-\frac{E_{\min}}{E_{\max}}, 0<\beta<1 \tag{4a}$$

$$\beta_m = 1-\frac{\rho_{\min}}{\rho_{\max}}, 0<\beta_m<1 \tag{4b}$$

$$\beta_m = 1-\sqrt{1-\beta} \tag{4c}$$

where $E_{\max}$, $E_{\min}$ and $\rho_{\max}$, $\rho_{\min}$ are maximum/minimum values of Young's modulus and mass density, respectively. It is noted that the material characteristics for UD remain constant in the thickness direction and depend only on β. Thereafter, the coefficient υ in Eq. (1) is written as follows:

$$\upsilon = \frac{1}{\beta}-\frac{1}{\beta}\left(\frac{2}{\pi}\sqrt{1-\beta}-\frac{2}{\pi}+1\right)^2 \tag{5}$$

Unified High-Order Shear Deformation Theory (HSDT) of Porous Metal Foam Microplate

This paper proposes a novel unified shear deformation theory [50] based on the fundamental equations of elasticity, featuring fewer unknown variables. The displacement field is expressed in a unified form, allowing for the recovery of several shear deformation plate theories, including zeroth-order, third-order, various HSDTs, and refined four-unknown HSDTs. The Carrera Unified Formulation (CUF), proposed by Carrera et al. [51, 52], provides a comprehensive framework that unifies various structural theories, offering high flexibility and accuracy in modeling complex structures. The proposed theory can be viewed as a simplified model that can be derived from the CUF. For the analysis of PMF microplates, the kinematic of HSDT [50] is written by:

$$\begin{aligned}\mathbf{u}(x_1,x_2,x_3) &= (H^s\Psi(x_3))\mathbf{u}_3(x_1,x_2)+(H^s\Psi(x_3)-x_3)\mathbf{u}_2\\ &\quad+\mathbf{u}_1(x_1,x_2)\\ &= \Upsilon_2(x_3)\mathbf{u}_3(x_1,x_2)+\Upsilon_1(x_3)\mathbf{u}_2+\mathbf{u}_1(x_1,x_2)\end{aligned} \tag{6}$$

where $\mathbf{u}=\begin{Bmatrix}u_1\\u_2\\u_3\end{Bmatrix}$, $\mathbf{u}_1=\begin{Bmatrix}u_1^0\\u_2^0\\u_3^0\end{Bmatrix}$, $\mathbf{u}_2=\begin{Bmatrix}u_{3,1}^0\\u_{3,2}^0\\0\end{Bmatrix}$, $\mathbf{u}_3=\begin{Bmatrix}\varphi_1\\\varphi_2\\0\end{Bmatrix}$; $u_j\,(j=1,2,3)$ are displacements in x_1-, x_2- and x_3- directions, respectively; u_1^0, u_2^0 and u_3^0 are membrane and transverse displacements at neutral plane; φ_1, φ_2 are rotations at neutral plane with respect to the x_1- and x_2- axis, respectively; H^s is the transverse shear stiffness;

$$\Psi(x_3) = \int_0^{x_3}\frac{2(1+v)f_{,3}}{E(x_3)}dx_3 = \int_0^{x_3}\frac{f_{,3}}{\mu(x_3)}dx_3$$

where $f(x_3)$ is a higher-order shear function with $f_{,3}\left(x_3=\pm\frac{h}{2}\right)=0$; the comma in index indicates the differentiation of variable that follows. It is noted that the accuracy of HSDT depends on the selection of shear functions [53–56].

Modified Couple Stress Theory (MCT)

Hamilton's principle is applied to compute the variation of total potential energy:

$$\delta\Pi = \int_{t_1}^{t_2}(\delta\Pi_{SE}+\delta\Pi_W-\delta\Pi_{KE})dt = 0 \tag{7}$$

where Π_{KE}, Π_W and Π_{SE} are the kinetic energy, work done by external force and strain energy, respectively.

Moreover, following the MCT [5], the strain energy of the microplate is defined as:

$$\delta\Pi_{SE} = \int_A(\boldsymbol{\sigma}\delta\boldsymbol{\varepsilon}+\mathbf{m}\delta\boldsymbol{\chi})dA \tag{8}$$

where ε_{ij} and χ_{ij}, respectively, are strain and symmetric rotation gradient components; σ_{ij} are Cauchy's stress component; m_{ij} are the high-order stresses connected to the strain gradient χ_{ij}.

The components of the strain tensor are given by:

$$\varepsilon_{ij} = \frac{1}{2}\left(u_{j,i}+u_{i,j}\right) \tag{9}$$

By substituting Eq. (6) into Eq. (9), the strain field is written under compact form as follows:

$$\boldsymbol{\varepsilon}^T = [\,\varepsilon_{11} \quad \varepsilon_{22} \quad \gamma_{12} \quad \gamma_{13} \quad \gamma_{23}\,] \tag{10a}$$

$$\boldsymbol{\varepsilon}^{(i)} = \Upsilon_3(x_3)\boldsymbol{\varepsilon}^{(3)} + \Upsilon_2(x_3)\boldsymbol{\varepsilon}^{(2)} + \Upsilon_1(x_3)\boldsymbol{\varepsilon}^{(1)} + \boldsymbol{\varepsilon}^{(0)} \tag{10b}$$

where $\Upsilon_3(x_3) = \frac{f_3(x_3)}{\mu(x_3)}H^s$.

Moreover, the symmetric rotation gradient tensor $\boldsymbol{\chi}$ is written as:

$$\chi_{ij} = \frac{1}{2}\left(\overline{\theta}_{j,i} + \overline{\theta}_{i,j}\right) \tag{11}$$

where $\overline{\theta}_i$ is calculated using the displacements u_i as shown in:

$$\begin{aligned}\overline{\theta} &= \begin{Bmatrix}\overline{\theta}_1\\ \overline{\theta}_2\\ \overline{\theta}_3\end{Bmatrix} = -\frac{1}{2}\begin{Bmatrix}u_{2,3} - u_{3,2}\\ u_{3,1} - u_{1,3}\\ u_{1,2} - u_{2,1}\end{Bmatrix}\\ &= \frac{1}{2}\begin{Bmatrix}u^0_{3,2} - \Upsilon_{1,3}u^0_{3,2} - \Upsilon_{2,3}\varphi_2\\ -u^0_{3,1} + \Upsilon_{1,3}u^0_{3,1} + \Upsilon_{2,3}\varphi_1\\ u^0_{2,1} - u^0_{1,2} + \Upsilon_2\left(\varphi_{2,1} - \varphi_{1,2}\right)\end{Bmatrix}\end{aligned} \tag{12}$$

Substituting Eq. (12) into Eq. (11), the rotation gradients are represented as follows:

$$\begin{aligned}\boldsymbol{\chi} =& \Upsilon_2\boldsymbol{\chi}^{(5)} + \Upsilon_{2,33}\boldsymbol{\chi}^{(4)} + \Upsilon_{1,33}\boldsymbol{\chi}^{(3)} + + \Upsilon_{2,3}\boldsymbol{\chi}^{(2)}\\ &+ \Upsilon_{1,3}\boldsymbol{\chi}^{(1)} + \boldsymbol{\chi}^{(0)}\end{aligned} \tag{13}$$

The strain components of the PMF microplates are described in Appendix 1. The relationship between the conventional stress and strain is illustrated as:

$$\boldsymbol{\sigma} = \mathbf{Q}_\varepsilon\boldsymbol{\varepsilon} \tag{14}$$

where the stiffness $\mathbf{Q}_\varepsilon$ is represented by:

$$\mathbf{Q}_\varepsilon = \begin{bmatrix} Q_{11} & Q_{12} & 0 & 0 & 0\\ Q_{12} & Q_{22} & 0 & 0 & 0\\ 0 & 0 & Q_{66} & 0 & 0\\ 0 & 0 & 0 & Q_{55} & 0\\ 0 & 0 & 0 & 0 & Q_{44}\end{bmatrix} \tag{15}$$

and $Q_{44} = Q_{55} = Q_{66} = \mu = \frac{E(x_3)}{2(1+\nu)}$, $Q_{11} = Q_{22} = \frac{E(x_3)}{1-\nu^2}$, $Q_{12} = \frac{\nu E(x_3)}{1-\nu^2}$, $\alpha_\chi = 2\mu l^2$ and l is material length scale parameter (MLSP) which is used to measure the size effect.

According to the MCT [5], the higher-order stress components are as follows:

$$\begin{aligned}\mathbf{m} &= \begin{Bmatrix}m_{11}\\ m_{22}\\ m_{12}\\ m_{33}\\ m_{23}\\ m_{13}\end{Bmatrix} = 2\mu l^2\begin{bmatrix}1&0&0&0&0&0\\ 0&1&0&0&0&0\\ 0&0&1&0&0&0\\ 0&0&0&1&0&0\\ 0&0&0&0&1&0\\ 0&0&0&0&0&1\end{bmatrix}\begin{Bmatrix}\chi_{11}\\ \chi_{22}\\ \chi_{12}\\ \chi_{33}\\ \chi_{23}\\ \chi_{13}\end{Bmatrix}\\ &= \alpha_\chi\mathbf{I}_{6\times6}\boldsymbol{\chi}\end{aligned} \tag{16}$$

Substituting Eqs. (16) and (14) into Eq. (8), the strain energy $\delta\Pi_{SE}$ could be expressed in the following way:

$$\begin{aligned}\delta\Pi_{SE} =& \int_A (\mathbf{m}\delta\boldsymbol{\chi} + \boldsymbol{\sigma}\delta\boldsymbol{\varepsilon})dA\\ =& \int_A \Big[\mathbf{N}^{(3)}_\varepsilon\delta\boldsymbol{\varepsilon}^{(3)} + \mathbf{N}^{(2)}_\varepsilon\delta\boldsymbol{\varepsilon}^{(2)} + \mathbf{N}^{(1)}_\varepsilon\delta\boldsymbol{\varepsilon}^{(1)} + \mathbf{N}^{(0)}_\varepsilon\delta\boldsymbol{\varepsilon}^{(0)}\\ &+ \mathbf{N}^{(5)}_\chi\delta\boldsymbol{\chi}^{(5)} + \mathbf{N}^{(4)}_\chi\delta\boldsymbol{\chi}^{(4)} + \mathbf{N}^{(3)}_\chi\delta\boldsymbol{\chi}^{(3)}\\ &+ \mathbf{N}^{(2)}_\chi\delta\boldsymbol{\chi}^{(2)} + \mathbf{N}^{(1)}_\chi\delta\boldsymbol{\chi}^{(1)} + \mathbf{N}^{(0)}_\chi\delta\boldsymbol{\chi}^{(0)}\Big]dA\end{aligned} \tag{17}$$

where the stress resultants are supplied by:

$$\left(\mathbf{N}^{(3)}_\varepsilon, \mathbf{N}^{(2)}_\varepsilon, \mathbf{N}^{(1)}_\varepsilon, \mathbf{N}^{(0)}_\varepsilon\right) = \int_{-h/2}^{h/2}\left(\Upsilon_3, \Upsilon_2, \Upsilon_1, 1\right)\boldsymbol{\sigma}dx_3 \tag{18a}$$

$$\begin{aligned}&\left(\mathbf{N}^{(5)}_\chi, \mathbf{N}^{(4)}_\chi, \mathbf{N}^{(3)}_\chi, \mathbf{N}^{(2)}_\chi, \mathbf{N}^{(1)}_\chi, \mathbf{N}^{(0)}_\chi\right)\\ &= \int_{-h/2}^{h/2}\left(\Upsilon_2, \Upsilon_{2,33}, \Upsilon_{1,33}, \Upsilon_{2,3}, \Upsilon_{1,3}, 1\right)\mathbf{m}dx_3\end{aligned} \tag{18b}$$

The stress results could be calculated using strains and its gradients as shown in Appendix 2. The variation of work produced by membrane compressive loads is presented as:

$$\delta\Pi_W = -\int_A N^0\left(u^0_{3,1}\delta u^0_{3,1} + u^0_{3,2}\delta u^0_{3,2}\right)dA \tag{19}$$

where $N^0_1 = N^0_2 = N^0, N^0_{12} = 0$.

The variation of kinetic energy $\delta\Pi_{KE}$ is calculated by:

$$\begin{aligned}\delta\Pi_{KE} =& \frac{1}{2}\int_V \rho\left(\dot{u}_1\delta\dot{u}_1 + \dot{u}_2\delta\dot{u}_2 + \dot{u}_3\delta\dot{u}_3\right)dV \\ =& \frac{1}{2}\int_A \Big[I_2\left(\dot{u}^0_{3,1}\delta\dot{u}^0_{3,1} + \dot{u}^0_{3,2}\delta\dot{u}^0_{3,2}\right) \\ &+ K_2(\dot{\varphi}_1\delta\dot{\varphi}_1 + \dot{\varphi}_2\delta\dot{\varphi}_2)I_0\left(\dot{u}^0_1\delta\dot{u}^0_1 + \dot{u}^0_2\delta\dot{u}^0_2 + \dot{u}^0_3\delta\dot{u}^0_3\right) \\ &+ I_1\left(\dot{u}^0_1\delta\dot{u}^0_{3,1} + \dot{u}^0_{3,1}\delta\dot{u}^0_1 + \dot{u}^0_2\delta\dot{u}^0_{3,2} + \dot{u}^0_{3,2}\delta\dot{u}^0_2\right) \\ &+ J_1\left(\dot{u}^0_1\delta\dot{\varphi}_1 + \dot{\varphi}_1\delta\dot{u}^0_1 + \dot{u}^0_2\delta\dot{\varphi}_2 + \dot{\varphi}_2\delta\dot{u}^0_2\right) \\ &+ J_2\left(\dot{u}^0_{3,1}\delta\dot{\varphi}_1 + \dot{\varphi}_1\delta\dot{u}^0_{3,1} + \dot{u}^0_{3,2}\delta\dot{\varphi}_2 + \dot{\varphi}_2\delta\dot{u}^0_{3,2}\right)\Big]dA\end{aligned} \tag{20}$$

where $I_0, I_1, I_2, J_1, J_2, K_2$ are the mass components described as:

$$(K_2, J_2, J_1, I_2, I_1, I_0) = \int_{-h/2}^{h/2} \left(\Upsilon_2^2, \Upsilon_1\Upsilon_2, \Upsilon_2, \Upsilon_1^2, \Upsilon_1, 1\right)\rho dx_3 \tag{21}$$

Ritz Formulation

Based on the Ritz approach and variational formulation, a series of approximation functions and associated values can be utilized to represent the membrane and transverse displacements $\left(\varphi_1, \varphi_2, u^0_1, u^0_2, u^0_3\right)$ of the PMF microplates, as follows:

$$\begin{aligned}&\left(\varphi_1(x_1,x_2,t), u^0_1(x_1,x_2,t)\right) \\ &= R(x_1,x_2)\sum_{i=1}^{n_1}\sum_{j=1}^{n_2}\left(x_{ij}(t), u_{1ij}(t)\right)F_j(x_2)T_{i,1}(x_1)\end{aligned} \tag{22a}$$

$$\begin{aligned}&\left(\varphi_2(x_1,x_2,t), u^0_2(x_1,x_2,t)\right) \\ &= R(x_1,x_2)\sum_{i=1}^{n_1}\sum_{j=1}^{n_2}\left(y_{ij}(t), u_{2ij}(t)\right)F_{j,2}(x_2)T_i(x_1)\end{aligned} \tag{22b}$$

$$u^0_3(x_1,x_2,t) = R(x_1,x_2)\sum_{i=1}^{n_1}\sum_{j=1}^{n_2}u_{3ij}(t)F_j(x_2)T_i(x_1) \tag{22c}$$

Table 1 Admissible functions for various BCs

BCs	Solutions	$T_j(x_1)$	$F_j(x_2)$
SSSS	Hermite	$x_1(a-x_1)He_j$	$x_2(b-x_2)He_j$
	Laguerre	$x_1(a-x_1)L_j$	$x_2(b-x_2)L_j$
SCSC	Hermite	$x_1(a-x_1)^2He_j$	$x_2(b-x_2)^2He_j$
	Laguerre	$x_1(a-x_1)^2L_j$	$x_2(b-x_2)^2L_j$
CCCC	Hermite	$x_1^2(a-x_1)^2He_j$	$x_2^2(b-x_2)^2He_j$
	Laguerre	$x_1^2(a-x_1)^2L_j$	$x_2^2(b-x_2)^2L_j$

where $x_{ij}, y_{ij}, u_{3ij}, u_{2ij}, u_{1ij}$ are the unknown variables; $R(x_1,x_2) = R_1(x_1)R_2(x_2)$ is the admissible function that satisfies BCs (Table 1). It is noted that two shape functions in the x_1- and x_2- directions, namely $T_i(x_1)$ and $F_j(x_2)$, are sufficient to determine five unknowns variables. In this study, the Hermite and Laguerre polynomials are used to develop Ritz solutions, namely Hermite–Ritz, Laguerre–Ritz.

The Hermite polynomials are characterized by the following recursion formula:

$$\begin{cases} He_0(x) = 1, & He_1(x) = 2x, \\ He_n(x) = 2x & He_{n-1}(x) - 2(n-1)He_{n-2}(x) \end{cases} \tag{23}$$

where x denotes the coordinate x_1 or x_2. It is noted that the Hermite polynomials satisfy the normalization as follows:

$$\int_{-\infty}^{\infty}(He(x))^2e^{-x^2}dx = 2^n\sqrt{\pi}n! \tag{24}$$

Moreover, the hypergeometric functions define the generalized Laguerre function as follows:

$$\mathrm{L}(n,a,x) = \binom{n+a}{a}{}_1F_1(-n;a+1;x) \tag{25}$$

where these functions return orthogonal generalized Laguerre polynomials for nonnegative integer values of n:

$$\langle f1, f2\rangle = \int_0^{\infty} e^{-x}x^a f_1(x)f_2(x)dx \tag{26}$$

Furthermore, generalized Laguerre polynomials fulfill this normalization:

$$\langle \mathrm{L}(n,a,x), \mathrm{L}(m,a,x)\rangle = \begin{cases} 0 & if \quad n \neq m \\ \dfrac{\Gamma(a+n+1)}{n!} & if \quad n = m \end{cases} \tag{27}$$

The first five Hermite polynomials, Laguerre polynomials are displayed in Fig. 2. It is noted that the approximation functions $F_j(x_2)$ and $T_i(x_1)$ are combined with the admissible functions to fulfill the following clamped–clamped and simply-supported BCs:

- Clamped (C): $\varphi_1 = \varphi_2 = u^0_1 = u^0_2 = u^0_3 = 0$ at $x_2 = 0, b$ and $x_1 = 0, a$
- Simply-supported (S): $\varphi_1 = u^0_1 = u^0_3 = 0$ at $x_2 = 0, b$ and $\varphi_2 = u^0_3 = u^0_2 = 0$ at $x_1 = 0, a$.

The following BCs result from the combination of fully clamped and simply-supported BCs on the borders of the PMF microplates. The numerical examples will hence include three representative BCs, namely SSSS, SCSC, and CCCC.

By using Lagrange's equations $\frac{\delta\Pi}{\delta d} - \frac{d}{dt}\frac{\delta\Pi}{\delta\dot{d}} = 0$, substituting Eq. (22) into Eqs. (20), (19) and (17) and then the

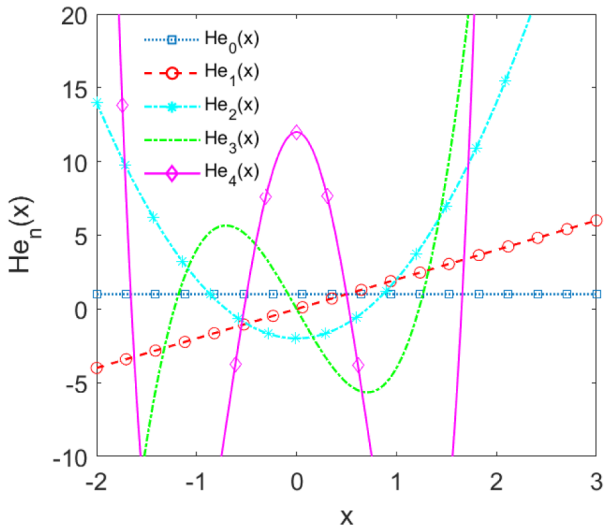

(a) The first five Hermite polynomials

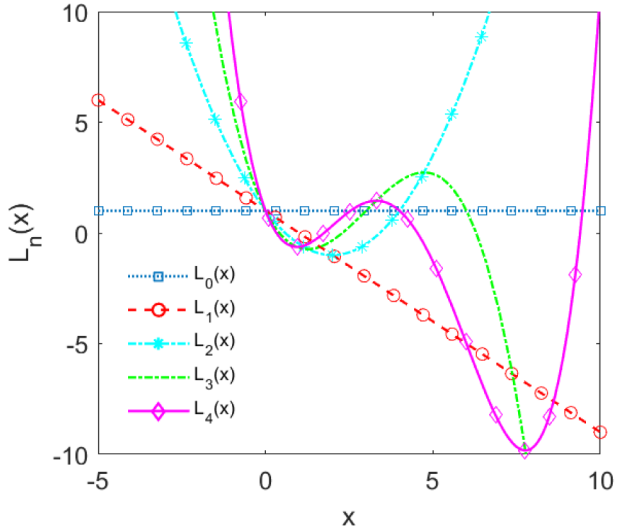

(b) The first five Laguerre polynomials

Fig. 2 The first five polynomials of approximation

subsequent results into Eq. (7), the characteristic equations of motion are obtained as follows:

$$\left(\mathbf{K}-N^0\mathbf{K}^g\right)\mathbf{d}+\mathbf{C}\dot{\mathbf{d}}+\mathbf{M}\ddot{\mathbf{d}}=\mathbf{F}(t) \tag{28}$$

where $\mathbf{d}=[\mathbf{u}_1 \quad \mathbf{u}_2 \quad \mathbf{u}_3 \quad \mathbf{x} \quad \mathbf{y}]^T$ is the displacement vector; the stiffness matrix $\mathbf{K}=\mathbf{K}^{\varepsilon}+\mathbf{K}^{\chi}$ is composed of the stiffness matrix of the strains $\mathbf{K}^{\varepsilon}$ and the stiffness matrix of the symmetric rotation gradients $\mathbf{K}^{\chi}$; $\mathbf{K}^g$ is the geometric stiffness matrix; $\mathbf{M}$ is the mass matrix; $\mathbf{C}=2\zeta\omega\mathbf{M}$ is the damping matrix; $\mathbf{F}(t)$ is the external load vector. For the transient vibration analysis, a sinusoidal transverse dynamic load is defined as follows [57]:

$$\mathbf{F}(t)=q_0\sin\left(\frac{\pi x_1}{a}\right)\sin\left(\frac{\pi x_2}{b}\right)\begin{bmatrix} e^{-\gamma_d(t)} & \textit{Explosive blast pulse}\\ \begin{cases}1-t/t_0 & 0\le t\le t_0\\ 0 & t>t_0\end{cases} & \textit{Triangular pulse}\\ \begin{cases}1 & 0\le t\le t_0\\ 0 & t>t_0\end{cases} & \textit{Rectangular pulse}\end{bmatrix} \tag{29}$$

where $\gamma_d=330\ \mathrm{s}^{-1}$ is the decay coefficient of the waveform; $q_0=16$ is the load intensity.

The components of stiffness and mass matrix are described in further in detail as follows:

$$\mathbf{K}^{\lambda}=\begin{bmatrix}\mathbf{K}^{\lambda 11} & \mathbf{K}^{\lambda 12} & \mathbf{K}^{\lambda 13} & \mathbf{K}^{\lambda 14} & \mathbf{K}^{\lambda 15}\\ {}^T\mathbf{K}^{\lambda 12} & \mathbf{K}^{\lambda 22} & \mathbf{K}^{\lambda 23} & \mathbf{K}^{\lambda 24} & \mathbf{K}^{\lambda 25}\\ {}^T\mathbf{K}^{\lambda 13} & {}^T\mathbf{K}^{\lambda 23} & \mathbf{K}^{\lambda 33} & \mathbf{K}^{\lambda 34} & \mathbf{K}^{\lambda 35}\\ {}^T\mathbf{K}^{\lambda 14} & {}^T\mathbf{K}^{\lambda 24} & {}^T\mathbf{K}^{\lambda 34} & \mathbf{K}^{\lambda 44} & \mathbf{K}^{\lambda 45}\\ {}^T\mathbf{K}^{\lambda 15} & {}^T\mathbf{K}^{\lambda 5} & {}^T\mathbf{K}^{\lambda 35} & {}^T\mathbf{K}^{\lambda 45} & \mathbf{K}^{\lambda 55}\end{bmatrix} \quad \text{with } \lambda=\{\chi,\varepsilon\} \tag{30a}$$

$$\mathbf{K}^g=\begin{bmatrix}\mathbf{0} & \mathbf{0} & \mathbf{0} & \mathbf{0} & \mathbf{0}\\ \mathbf{0} & \mathbf{0} & \mathbf{0} & \mathbf{0} & \mathbf{0}\\ \mathbf{0} & \mathbf{0} & \mathbf{K}^{g33} & \mathbf{0} & \mathbf{0}\\ \mathbf{0} & \mathbf{0} & \mathbf{0} & \mathbf{0} & \mathbf{0}\\ \mathbf{0} & \mathbf{0} & \mathbf{0} & \mathbf{0} & \mathbf{0}\end{bmatrix} \quad \text{with } K^{g33}_{ijkl}=H^{11}_{ik}S^{00}_{jl}+H^{00}_{ik}S^{11}_{jl} \tag{30b}$$

where the stiffness matrix components, $\mathbf{K}^{\varepsilon}$ and $\mathbf{K}^{\chi}$, are described in Appendix 3. The mass matrix's constituents $\mathbf{M}$ are provided by:

$$\begin{aligned}
&M^{11}_{ijkl}=I_0H^{11}_{ik}S^{00}_{jl},M^{13}_{ijkl}=I_1H^{11}_{ik}S^{00}_{jl},M^{14}_{ijkl}=J_1H^{11}_{ik}S^{00}_{jl}\\
&M^{22}_{ijkl}=I_0H^{00}_{ik}S^{11}_{jl},M^{23}_{ijkl}=I_1H^{00}_{ik}S^{11}_{jl},M^{25}_{ijkl}=J_1H^{00}_{ik}S^{11}_{jl}\\
&M^{33}_{ijkl}=I_0H^{00}_{ik}S^{00}_{jl}+I_2\left(H^{11}_{ik}S^{00}_{jl}+H^{00}_{ik}S^{11}_{jl}\right),\\
&M^{34}_{ijkl}=J_2H^{11}_{ik}S^{00}_{jl},M^{35}_{ijkl}=J_2H^{00}_{ik}S^{11}_{jl}\\
&M^{44}_{ijkl}=K_2H^{11}_{ik}S^{00}_{jl},M^{55}_{ijkl}=K_2H^{00}_{ik}S^{11}_{jl}
\end{aligned} \tag{31}$$

It is noted that the components of the stiffness and mass matrices will be calculated using numerical integration via adaptive Simpson's quadrature [58]. Based on Eq. (28), the critical buckling loads N^{cr} of the PMF microplate can be obtained by disregarding the mass inertia components, damping ratio and solving the characteristic equation $(\mathbf{K}-N^0\mathbf{K}^g)\mathbf{d}=\mathbf{0}$. For free vibration analysis, it is supposed that $N^0=0$ and $\mathbf{d}(t)=\mathbf{d}e^{i\omega t}$, where $i^2=-1$ represents the imaginary unit, and ω denotes the natural frequency of the PMF microplate. By solving the equation

$(\mathbf{K}-\omega^2\mathbf{M})\mathbf{d}=\mathbf{0}$, the natural frequencies will be determined. For transient analysis, it is assumed that $N^0=0$, and therefore the transient responses can be obtained from Eq. (28) by using the Newmark's method [59], as shown:

$$\mathbf{d}_{i+1}=\mathbf{d}_i+\Delta t\dot{\mathbf{d}}_i+(0.5-\eta)\Delta t^2\ddot{\mathbf{d}}_i+\eta\ddot{\mathbf{d}}_{i+1}\Delta t^2 \tag{32a}$$

$$\dot{\mathbf{d}}_{i+1}=\dot{\mathbf{d}}_i+(1-\gamma)\Delta t\ddot{\mathbf{d}}_i+\gamma\Delta t\ddot{\mathbf{d}}_{i+1} \tag{32b}$$

Substituting Eq. (32) into Eq. (28) leads to:

$$[\mathbf{K}\eta\Delta t^2+\mathbf{C}\gamma\Delta t+\mathbf{M}]\ddot{\mathbf{d}}_{i+1}=\mathbf{F}_{i+1}-\mathbf{C}[\dot{\mathbf{d}}_i+(1-\gamma)\Delta t\ddot{\mathbf{d}}_i]-\mathbf{K}[\mathbf{d}_i+\Delta t\dot{\mathbf{d}}_i+(0.5-\eta)\Delta t^2\ddot{\mathbf{d}}_i] \tag{33a}$$

$$\hat{\mathbf{K}}\ddot{\mathbf{d}}_{i+1}=\hat{\mathbf{f}}_{i+1} \tag{33b}$$

where

$$\hat{\mathbf{K}}=[\mathbf{K}\eta\Delta t^2+\mathbf{C}\gamma\Delta t+\mathbf{M}] \tag{34a}$$

$$\hat{\mathbf{f}}_{i+1}=\mathbf{F}_{i+1}-\mathbf{C}[\dot{\mathbf{d}}_i+(1-\gamma)\Delta t\ddot{\mathbf{d}}_i]-\mathbf{K}[\mathbf{d}_i+\Delta t\dot{\mathbf{d}}_i+(0.5-\eta)\Delta t^2\ddot{\mathbf{d}}_i] \tag{34b}$$

with $\Delta t=0.01,\eta=\frac{1}{4},\gamma=\frac{1}{2}$.

Numerical Results

In this part, numerical examples are performed to explore free vibration, buckling, and transient analysis of PMF microplates with different BCs and three porosity distributions (UD, AD, SD) in which the shear function $\Psi(x_3)=\cot^{-1}\left(\frac{h}{x_3}\right)-\frac{16x_3^3}{15h^3}$ [60] is used. The PMF microplates are designed to be made of metal foam materials whose characteristics are followed:

- MAT 1 [25]:$E_{\max}=200$ GPa, $\rho_{\max}=7850$ kg/m.^{3}, $\nu_{\max}=0.33$
- MAT 2 [61]: $E_{\max}=90$ GPa, $\rho_{\max}=2700$ kg/m.^{3},$\nu_{\max}=0.23$

The numerical results obtained in this work is performed in an Intel® Core™ i7 at 2.8 GHz, 8 GB of RAM. For simplicity purpose, the numerical examples utilize the following normalized response parameters:

$$\overline{\omega}=100\omega h\sqrt{\frac{\rho_{\max}}{E_{\max}}};\ \overline{N}_{cr}=\frac{N_{cr}a^2}{h^3E_{\max}} \tag{35}$$

Example 1 To evaluate the convergence and efficiency of the current computational method, this example compares the convergence speed and stability of the proposed Hermite–Ritz and Laguerre–Ritz solutions with those obtained from other shape functions in the Ritz method. The following approximation functions will be used in Eq. (22) for the computations:

a. Chebyshev polynomials [36]:

The Chebyshev polynomials are characterized by the following recursion formula:

$$\begin{cases}F_0(x_2)=1, & F_1(x_2)=x_2,\\ F_j(x_2)=2x_2F_{j-1}(x_2)-F_{j-2}(x_2)\end{cases} \tag{36}$$

where $-1\le x_2\le 1$. It is noted that the Chebyshev polynomials satisfy the normalization as follows:

$$\int_{-1}^{1}\frac{F_i(x_2)F_j(x_2)}{\sqrt{1-x_2^2}}dx_2=\begin{cases}0 & if \quad i\neq j\\ \pi & if \quad i=j=0\\ \frac{\pi}{2} & if \quad i=j\neq 0\end{cases} \tag{37}$$

b. Static Beam Functions (SBF) [62]:

$$F_j(x_2)=A_j+B_jx_2+C_jx_2^2+D_jx_2^3+\sin\left(\frac{jx_2}{b}\right) \tag{38}$$

with $A_j=0;B_j=-\frac{j\pi}{b};C_j=\frac{j\pi\left((-1)^j+2\right)}{b^2};D_j=-\frac{j\pi\left((-1)^j+1\right)}{b^3}$

c. Non-Orthogonal Polynomials (NOP) [63]:

$$F_j(x_2)=(b-x_2)^2x_2^{j+1} \tag{39}$$

d. Product of Trigonometric Functions (PTF) [64]:

$$F_j(x_2)=\sin\left(\frac{\pi x_2}{b}\right)\sin\left(\frac{j\pi x_2}{b}\right) \tag{40}$$

e. Characteristic Functions (CF) [65]:

$$F_j(x_2)=\sin\alpha_jx_2-\sinh\alpha_jx_2-\phi_j\left(\cos\alpha_jx_2-\cosh\alpha_jx_2\right) \tag{41}$$

with $\phi_j=\frac{\sin\alpha_jb-\sinh\alpha_jb}{\cos\alpha_jb-\cosh\alpha_jb};\alpha_j=\frac{(j+0.5)\pi}{b}$.

It is noted that the shape functions $T_i(x_1)$ in the x_1-direction are defined in a similar way by replacing in Eqs. (36)–(41) the coordinate x_2 by x_1, the length b by the width a.

Moreover, for the purpose of investigating the convergence of approximation functions, the reference distance is defined as follows:

$$d_f=\omega_{i+1}-\omega_i \tag{42}$$

where ω_i and ω_{i+1} are the fundamental frequencies at number of series n_i and n_{i+1}.

In order to evaluate the convergence of the proposed Ritz solutions, Table 2 and Fig. 3 compare the convergence speed of fundamental frequencies of the PMF CCCC plates with side-to-thickness ratio $a/h=10$ and porous parameter $\beta=0.3$. It is worthy to noticing that the results

Table 2 Comparison of the convergence speed of the series solution for normalized fundamental frequencies of PMF CCCC plates ($a/h = 10$ and $\beta = 0.3$)

Solution	Number of series $n = n_1 = n_2$									
	2	3	5	6	8	9	10	15	16	17
SBF	11.765	11.27	10.681	10.125	9.905	9.858	9.772	9.4444	9.444	9.444
NOP	9.455	9.44	9.382	9.373	9.362	9.363	9.362	9.364	9.362	9.362
PTF	9.784	9.486	9.401	9.400	9.362	9.364	9.362	9.364	9.363	9.362
CF	9.560	9.545	9.503	9.467	9.402	9.388	9.388	9.388	9.388	9.388
Chebyshev	9.649	9.382	9.382	9.383	9.381	9.384	9.383	9.383	9.382	9.382
Hermite	9.649	9.382	9.382	9.382	9.381	9.383	9.384	9.381	9.382	9.382
Laguerre	9.534	9.364	9.364	9.364	9.364	9.364	9.364	9.364	9.364	9.364
IGA [25]	9.520									

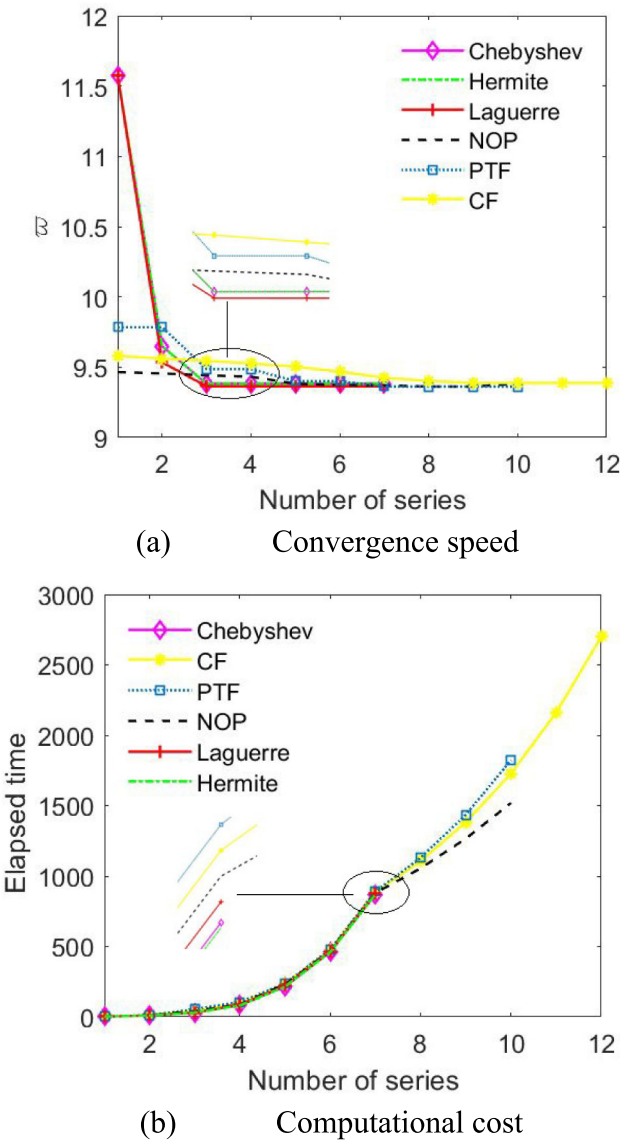

Fig. 3 Comparison of the convergence speed and computational cost of normalized fundamental frequencies of PMF CCCC plates with respect to the number of series ($a/h = 10$ and $\beta = 0.3$)

are computed with seven types of shape functions (Hermite–Ritz, Laguerre–Ritz, Chebyshev–Ritz, SBF, NOP, CF and PTF), the number of series in x_2- and x_1- direction are supposed to be similar, i.e. $n_1 = n_2 = n$. The tabular data and graph illustrate that the overall trend of the solutions is a decrease as the number of series increases, eventually reaching a converged value, after which the graphs stabilize. In comparison, it is observed that the responses derived from the SBF function require the largest number of series $n = 15$, while the proposed Hermite, Laguerre, and Chebyshev orthogonal polynomials achieve convergence with the lowest number of series $n = 3$. The responses from NOP and PTF and CF functions are obviously converged at $n = 8$ and $n = 9$, respectively. Figure 3 shows the elapsed time required to compute the natural frequencies for various shape functions, where the computational cost logically increases with the number of series. Consequently, the proposed model demonstrates significantly faster convergence compared to other methods like SBF, NOP, PTF, and CF, resulting in more efficient numerical computations. Additionally, the use of orthogonal polynomials enhances numerical efficiency by improving stability and reducing computational complexity, especially when compared to non-orthogonal polynomials. These polynomials also possess algebraic simplicity, making them easier to implement in numerical models without compromising accuracy. Notably, the performance of the proposed Hermite–Ritz and Laguerre–Ritz methods is comparable to that of the well-known Chebyshev polynomials, which are widely recognised for their accuracy and efficiency, making the proposed model a highly competitive and promising approach for enhancing the Ritz method.

In order to examine the convergence of buckling and free vibration responses of PMF microplates with $a/h = 10$, $\beta = 0.1$ and $h/l = 1$. The results in Table 3 demonstrate rapid convergence of the proposed solution across all cases, with a convergence point observed at $n = 3$. This value will be used in the following numerical examples. The current Hermite–Ritz and Laguerre–Ritz solutions show greater efficiency in terms of both

Table 3 Convergence study of the series solution of Hermite and Laguerre polynomials for UD CCCC microplates with different BCs (MAT 1, $a/h = 10$, $\beta = 0.1$, $h/l = 1$)

BCs	Solution	Number of series $n = n_1 = n_2$						
		1	2	3	4	5	6	7
Normalized fundamental frequency								
SSSS	Hermite	15.6713	13.6135	13.6004	13.6005	13.6016	13.6008	13.6005
	Laguerre	15.6197	13.5862	13.5604	13.5603	13.5604	13.5605	13.5604
SCSC	Hermite	22.2541	20.2237	20.2040	20.2040	20.2042	20.2043	20.2041
	Laguerre	22.1756	20.0831	20.0677	20.0679	20.0677	20.0678	20.0677
CCCC	Hermite	29.6893	28.9057	28.6386	28.6385	28.6388	28.6387	28.6386
	Laguerre	29.6589	28.8648	28.6135	28.6137	28.6136	28.6135	28.6135
Normalized critical buckling load for biaxial compression								
SSSS	Hermite	12.5538	10.7729	9.1169	9.1170	9.1169	9.1171	9.1170
	Laguerre	12.5497	10.7654	9.1132	9.1133	9.1131	9.1132	9.1132
SCSC	Hermite	19.9021	18.2037	17.3403	17.3426	17.3412	17.3408	17.3404
	Laguerre	19.7828	18.1026	17.2474	17.2426	27.2424	27.2425	17.2424
CCCC	Hermite	32.9265	31.8104	31.7498	31.7498	31.7499	31.7499	31.7498
	Laguerre	32.9873	31.8926	31.8486	31.8487	31.8488	31.8486	31.8486

convergence and computational time compared to earlier shape functions [36, 62–65].

Example 2 In this example, free vibration behaviors of the square PMF microplates with various BCs such as SSSS, CCCC and SCSC are analysed. The results of the present model in Table 4 are compared with those from previous study [61] for PMF SSSS microplate with $\beta = 0.1, 0.3, 0.5$, $l/h = 0$, 0.2, 0.4, 0.6, 0.8, $a/h = 10$, and three porosity distributions (UD, AD, SD) using the MAT2. There are good agreements between the two models for all cases. Moreover, the fundamental frequencies for PMF microplate with various configurations are reported in Tables 5, 6 and 7. The obtained results are compared with those from the earlier work of Pham et al. [25] for PMF macroplates without the size effects, i.e. $h/l = \infty$. It can be seen from Tables 5 and 6 that there are good agreements between the two models for all cases. It is also observed from these tables that the results vary with the porosity distribution in which the largest and smallest frequencies correspond to SD and UD. Some new results for microplates are given in Tables 5, 6 and 7 can be used for the benchmark in future research (Fig. 4).

Figures 5 and 6 illustrate the effect of the porosity coefficients, porosity distribution, size effects and BCs on the vibrational characteristics of square PMF microplates. As observed, the frequencies decrease with increasing porosity coefficients and thickness-to- MLSP ratios for all BCs and porosity contributions. The curves become flat when the ratio of h/l reaches to 20, indicating that size effects become insignificant beyond this point. Notably, the size effect is most pronounced at $h/l = 1$ and decreases sharply as the ratio increases from $h/l = 1$ to $h/l = 10$.

Example 3 In this example, buckling behaviors of the square PMF microplates (MAT1) with various configurations are considered and their buckling loads are given in Tables 8, 9, 10 and 11. It is noted that the obtained results in Tables 8 and 9 for PMF SSSS microplates under biaxial compression $\left(N_1^{(0)}, N_2^{(0)}, N_{12}^{(0)} = 1, 1, 0\right)$ and uniaxial compression $\left(N_1^{(0)}, N_2^{(0)}, N_{12}^{(0)} = 1, 0, 0\right)$ are verified with those derived from Pham et al. [25] without the size effects ($h/l = \infty$). It is observed that two models are in good agreements for different cases. New results with different thickness-to-MLSP ratios and BCs are provided in Tables 8, 9, 10 and 11 for future benchmarks.

Moreover, Fig. 7 displays the normalized critical buckling loads of PMF SD microplates with respect to the thickness-to-MLSP ratio. It is interesting to observe that the porosity does not significantly impact on the size effect, when the thickness-to-MLSP ratio increases, the curves of critical buckling loads decrease suddenly from $h/l \leq 10$ and then become stable from $h/l \geq 20$. As expected, the normalized critical buckling loads slightly decrease with an increase in the porous parameter due to the reduction in stiffness. When comparing porosity distribution types, it is observed that the UD requires a lower critical buckling load than the SD one, similar to the trend seen in free vibration responses. This confirms that symmetric porosity distribution provides greater stiffness advantages over the uniform arrangement.

Example 4 This example focuses on the responses of PMF microplates under three types of dynamic load, namely explosive blast load, rectangular load, and triangular load. Since there is no available results of PMF microplates

Table 4 Normalized fundamental frequencies of square PMF SSSS microplates (MAT 2,$a/h = 10$)

Type distribution	β	Theory	l/h				
			0	0.2	0.4	0.6	0.8
UD	0.1	Ritz–Hermite	5.5729	6.0854	7.4391	9.2658	11.3390
		Ritz–Laguerre	5.5647	6.0886	7.4423	9.2689	11.3423
		IGA [61]	5.5753	6.0852	7.4069	9.1964	11.2321
	0.3	Ritz–Hermite	5.3231	5.8425	7.1786	8.9737	11.0054
		Ritz–Laguerre	5.3262	5.8456	7.1816	8.9769	11.0087
		IGA [61]	5.3658	5.8566	7.1287	8.8509	10.8101
	0.5	Ritz–Hermite	5.0481	5.5585	6.8658	8.6144	10.5878
		Ritz–Laguerre	5.0511	5.5614	6.8688	8.6175	10.5911
		IGA [61]	5.1129	5.5806	6.7927	8.4337	10.3006
SD	0.1	Ritz–Hermite	5.6465	6.1634	7.5032	9.3176	11.3817
		Ritz–Laguerre	5.6499	6.1666	7.5066	9.3209	11.3851
		IGA [61]	5.6517	6.1564	7.4679	9.2483	11.2774
	0.3	Ritz–Hermite	5.6125	6.1092	7.4020	9.1598	11.1650
		Ritz–Laguerre	5.6158	6.1126	7.4055	9.1634	11.1690
		IGA [61]	5.6300	6.1062	7.3500	9.0477	10.9906
	0.5	Ritz–Hermite	5.6119	6.0834	7.3177	9.0066	10.9415
		Ritz–Laguerre	5.6151	6.0868	7.3214	9.0108	10.9462
		IGA [61]	5.6364	6.0839	7.2570	8.8666	10.7168
AD	0.1	Ritz–Hermite	5.5777	6.1005	7.4519	9.2765	11.3484
		Ritz–Laguerre	5.5810	6.1037	7.4550	9.2798	11.3518
		IGA [61]	5.5896	6.0988	7.4192	9.2076	11.2428
	0.3	Ritz–Hermite	5.3696	5.8871	7.2205	9.0146	11.0472
		Ritz–Laguerre	5.3727	5.8903	7.2237	9.0178	11.0507
		IGA [61]	5.4055	5.8971	7.1717	8.8985	10.8638
	0.5	Ritz–Hermite	5.1129	5.6269	6.9441	8.7073	10.6982
		Ritz–Laguerre	5.1159	5.6298	6.9472	8.7106	10.7017
		IGA [61]	5.1658	5.6431	6.8785	8.5487	10.4470

under dynamic loads, the verification is carried for PMF plates. It can be seen in Fig. 8 that the present results agree well with those from the previous study published by Pham et al. [25] for PMF SSSS plates under triangular load with $a/h = 10$ and $\beta = 0.1$.

It is noted that since the dynamic load refers to an intensely high load that occurs for a relatively short period of time, hence the time step of $\Delta t = 0.01$ seconds is chosen. Moreover, in order to examine the effects of porosity coefficient on dynamic responses of PMF microplates, the normalized dynamic deflections $\overline{w} = w/(1000h)$ are calculated for three types of porosity distribution (UD, SD, AD) with $a/h = 10$. Figure 9 shows the time-dependent variation of nonlinear defections of PMF UD SSSS microplates with $\beta = 0.1$, 0.2, 0.3 and 0.4 under explosive blast load. It is observed that for $h/l = 10$ and $\zeta = 0.05$, an increase in the porosity coefficient results in a reduction in the microplate's stiffness, which leads to an increase in transverse displacement. Moreover, the nonlinear displacement response of PMF microplates increases as the ratio h/l decreases and reaches its maximum at $h/l = 1$. Figure 10 illustrates the influence of the damping factor on the nonlinear dynamic characteristics of UD microplates under explosive blast load. To quantify this, seven different damping coefficient values $\zeta = 0\%$, 1%, 2%, 3%, 4%, 6% and 10% are used and the results are computed with $h/l =$ 5 and 1. It is noted that a damping coefficient of $\zeta = 0\%$ implies the absence of structural damping in the equation of motion, the transverse displacements of PMF microplates are reported for porosity coefficient $\beta = 0.2$. As depicted in Fig. 10, the damping coefficient profoundly affects the nonlinear dynamic behavior of the structure. Specifically, disregarding damping ($\zeta = 0\%$) leads to a sustained deflection amplitude over time post-load removal. Conversely, increasing the damping parameter substantially mitigates nonlinear dynamic responses. Moreover, although higher damping ratios effectively diminish deflection amplitudes, they have only a marginal impact on motion periods. This underscores the substantial role of structural damping in dissipating vibrational energy.

Table 5 Normalized fundamental frequencies of square PMF SSSS microplates (MAT 1, $a/h = 10$)

Type distribution	β	Theory	h/l				
			∞	10	5	2	1
UD	0.1	Ritz–Hermite	5.7950	5.9242	6.2959	8.4518	13.6004
		Ritz–Laguerre	5.7850	5.9136	6.2836	8.4305	13.5604
		IGA [25]	5.7276	–	–	–	–
	0.2	Ritz–Hermite	5.6551	5.7849	6.1579	8.3123	13.4323
		Ritz–Laguerre	5.6453	5.7745	6.1458	8.2914	13.3928
		IGA [25]	5.6244	–	–	–	–
	0.3	Ritz–Hermite	5.5103	5.6404	6.0140	8.1634	13.2463
		Ritz–Laguerre	5.5007	5.6302	6.0021	8.1428	13.2073
		IGA [25]	5.5125	–	–	–	–
	0.4	Ritz–Hermite	5.3583	5.4886	5.8620	8.0019	13.0374
		Ritz–Laguerre	5.3490	5.4786	5.8504	7.9815	12.9990
SD	0.1	Ritz–Hermite	5.8931	6.0203	6.3864	8.5195	13.6430
		Ritz–Laguerre	5.8830	6.0095	6.3740	8.4983	13.6031
		IGA [25]	5.8052	–	–	–	–
	0.2	Ritz–Hermite	5.8614	5.9868	6.3482	8.4562	13.5258
		Ritz–Laguerre	5.8513	5.9761	6.3359	8.4351	13.4864
		IGA [25]	5.7905	–	–	–	–
	0.3	Ritz–Hermite	5.8373	5.9607	6.3164	8.3945	13.4030
		Ritz–Laguerre	5.8273	5.9501	6.3042	8.3737	13.3641
		IGA [25]	5.7806	–	–	–	–
	0.4	Ritz–Hermite	5.8227	5.9437	6.2927	8.3360	13.2752
		Ritz–Laguerre	5.8127	5.9332	6.2806	8.3154	13.2369
AD	0.1	Ritz–Hermite	5.8142	5.9431	6.3138	8.4655	13.6100
		Ritz–Laguerre	5.8042	5.9324	6.3014	8.4443	13.5701
		IGA [25]	5.7422	–	–	–	–
	0.2	Ritz–Hermite	5.6935	5.8226	6.1937	8.3414	13.4558
		Ritz–Laguerre	5.6836	5.8121	6.1816	8.3204	13.4163
		IGA [25]	5.6527	–	–	–	–
	0.3	Ritz–Hermite	5.5665	5.6958	6.0673	8.2097	13.2901
		Ritz–Laguerre	5.5568	5.6856	6.0554	8.1890	13.2511
		IGA [25]	5.5529	–	–	–	–
	0.4	Ritz–Hermite	5.4297	5.5594	5.9313	8.0680	13.1114
		Ritz–Laguerre	5.4203	5.5493	5.9195	8.0475	13.0729

Similar results for PMF SD microplates under explosive blast load are also observed in Fig. 11. Finally, the influence of two types of dynamic load (rectangular and triangular) on the nonlinear deflections of PMF AD microplates is shown in Figs. 12 and 13. Various porosity parameters and damping ratios, specifically $\beta = 0.1$, 0.3, 0.5 and 0.6, and $\zeta = 1\%$, 3%, 5%, and 7%, are employed while maintaining h/l of 1, 2, and 5. Increasing the damping parameter significantly reduces nonlinear dynamic responses, highlighting the vital role of structural damping in minimizing and controlling oscillations in engineering structures. Furthermore, although higher damping ratios effectively reduce deflection amplitudes, their impact on motion periods remains marginal.

Conclusions

This paper proposes two new computational algorithms, namely Ritz–Hermite and Ritz–Laguerre, in conjunction with HSDT and MCT for the analysis of PMF microplates. It is based on the higher-order shear deformation theory and the modified couple stress theory with a constant material length scale parameter. The dynamic responses of the microplates under an explosive blast load are determined using Newmark's technique. The influence of the porosity parameters, shape functions, and boundary conditions on the frequency, buckling, and dynamic responses have been examined. The proposed model demonstrates significantly faster convergence compared to other

Table 6 Normalized fundamental frequencies of square PMF CCCC microplates (MAT 1, $a/h = 10$)

Type distribution	β	Theory	h/l				
			∞	10	5	2	1
UD	0.1	Ritz–Hermite	9.8398	10.2084	11.2347	16.6898	28.6386
		Ritz–Laguerre	9.8202	10.1891	11.2161	16.6711	28.6135
		IGA [25]	9.8918	–	–	–	–
	0.2	Ritz–Hermite	9.7059	9.9853	11.0126	16.4507	28.2951
		Ritz–Laguerre	9.6968	9.9666	10.9945	16.4325	28.2804
		IGA [25]	9.7136	–	–	–	–
	0.3	Ritz–Hermite	9.3824	9.7521	10.7786	16.1909	27.4022
		Ritz–Laguerre	9.3639	9.7339	10.7610	16.1731	27.4001
		IGA [25]	9.5202	–	–	–	–
	0.4	Ritz–Hermite	9.2358	9.5050	10.5287	15.9042	26.9741
		Ritz–Laguerre	9.2178	9.4874	10.5117	15.8868	26.9688
SD	0.1	Ritz–Hermite	9.9853	10.3490	11.3634	16.7781	28.6911
		Ritz–Laguerre	9.9653	10.3293	11.3444	16.7591	28.6658
		IGA [25]	10.0044	–	–	–	–
	0.2	Ritz–Hermite	9.9215	10.2809	11.2836	16.6400	28.4350
		Ritz–Laguerre	9.9015	10.2612	11.2647	16.6211	28.4099
		IGA [25]	9.9537	–	–	–	–
	0.3	Ritz–Hermite	9.8661	10.2205	11.2095	16.4985	28.1614
		Ritz–Laguerre	9.8462	10.2009	11.1906	16.4797	28.1365
		IGA [25]	9.9063	–	–	–	–
	0.4	Ritz–Hermite	9.8213	10.1698	11.1428	16.3549	27.8712
		Ritz–Laguerre	9.8013	10.1501	11.1238	16.3361	27.8465
AD	0.1	Ritz–Hermite	9.8687	10.2363	11.2605	16.7085	28.6519
		Ritz–Laguerre	9.8524	10.2195	11.2422	16.6814	28.6226
		IGA [25]	9.9133	–	–	–	–
	0.2	Ritz–Hermite	9.7140	10.0418	11.0654	16.4925	28.3518
		Ritz–Laguerre	9.7080	10.0253	11.0474	16.4660	28.3035
		IGA [25]	9.7558	–	–	–	–
	0.3	Ritz–Hermite	9.4686	9.8365	10.8590	16.2617	27.9877
		Ritz–Laguerre	9.4531	9.8205	10.8415	16.2358	27.9804
		IGA [25]	9.5816	–	–	–	–
	0.4	Ritz–Hermite	9.2470	9.6151	10.6365	16.0129	27.6375
		Ritz–Laguerre	9.2319	9.5994	10.6195	15.9877	27.6314

methods such as static beam functions, non-orthogonal polynomials, products of trigonometric functions, characteristic functions, and comparable to the well-known Chebyshev polynomials. This results in more efficient numerical computations, making the proposed model a highly competitive and promising approach for enhancing the Ritz method. Some findings are followed:

- The increase of the porosity coefficient and thickness-to-MLSP ratio leads to the reduction of the stiffness, natural frequencies and critical buckling loads of the porous metal foam microplates.
- Among the porosity arrangements, the symmetric porosity distribution reports a largest stiffness for porous material foam microplates.
- The size effects are significant when the thickness-to-MLSP ratio is smaller than 20, the porosity does not impact importantly on the size effects of porous metal foam microplates.
- Increasing the damping parameter significantly reduces nonlinear dynamic responses, highlighting the vital role of structural damping in minimizing and controlling oscillations in engineering structures.

Table 7 Normalized fundamental frequencies of square PMF SCSC microplates (MAT 1, $a/h = 10$)

Type distribution	β	Theory	h/l				
			∞	10	5	2	1
UD	0.1	Ritz–Hermite	7.6602	7.8896	8.5375	12.1058	20.2040
		Ritz–Laguerre	7.6430	7.8683	8.5058	12.0348	20.0677
	0.2	Ritz–Hermite	7.4797	7.7099	8.3591	11.9203	19.9663
		Ritz–Laguerre	7.4625	7.6886	8.3275	11.8498	19.8314
	0.3	Ritz–Hermite	7.2922	7.5229	8.1724	11.7204	19.7014
		Ritz–Laguerre	7.2751	7.5016	8.1409	11.6506	19.5679
	0.4	Ritz–Hermite	7.0950	7.3256	7.9741	11.5015	19.4016
		Ritz–Laguerre	7.0779	7.3045	7.9429	11.4326	19.2700
SD	0.1	Ritz–Hermite	7.7830	8.0090	8.6483	12.1852	20.2524
		Ritz–Laguerre	7.7662	7.9881	8.6170	12.1143	20.1162
	0.2	Ritz–Hermite	7.7377	7.9609	8.5924	12.0894	20.0745
		Ritz–Laguerre	7.7213	7.9404	8.5615	12.0193	19.9396
	0.3	Ritz–Hermite	7.7011	7.9209	8.5430	11.9935	19.8859
		Ritz–Laguerre	7.6852	7.9010	8.5128	11.9242	19.7525
	0.4	Ritz–Hermite	7.6752	7.8911	8.5022	11.8989	19.6876
		Ritz–Laguerre	7.6601	7.8718	8.4727	11.8306	19.5557
AD	0.1	Ritz–Hermite	7.6843	7.9132	8.5594	12.1223	20.2155
		Ritz–Laguerre	7.6767	7.9007	8.5350	12.0520	20.0710
	0.2	Ritz–Hermite	7.5280	7.7572	8.4037	11.9558	19.9961
		Ritz–Laguerre	7.5201	7.7445	8.3791	11.8861	19.8530
	0.3	Ritz–Hermite	7.3635	7.5929	8.2393	11.7786	19.7597
		Ritz–Laguerre	7.3554	7.5800	8.2147	11.7094	19.6182
	0.4	Ritz–Hermite	7.1861	7.4158	8.0622	11.5877	19.5045
		Ritz–Laguerre	7.1778	7.4028	8.0376	11.5192	19.3646

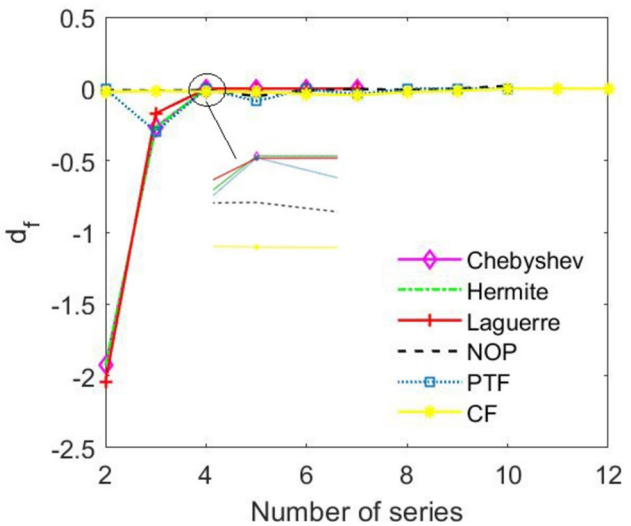

Fig. 4 Distance of normalized fundamental frequency of PMF CCCC plates with respect to the number of series ($a/h = 10$ and $\beta = 0.3$)

Appendix 1

The strain components of the PMF microplates are given by:

$$\boldsymbol{\varepsilon}^{(0)} = \begin{Bmatrix} \varepsilon_{11}^{(0)} \\ \varepsilon_{22}^{(0)} \\ \gamma_{12}^{(0)} \\ \gamma_{13}^{(0)} \\ \gamma_{23}^{(0)} \end{Bmatrix} = \begin{Bmatrix} u_{1,1}^{0} \\ u_{2,2}^{0} \\ u_{1,2}^{0} + u_{2,1}^{0} \\ 0 \\ 0 \end{Bmatrix}, \boldsymbol{\varepsilon}^{(1)} = \begin{Bmatrix} \varepsilon_{11}^{(1)} \\ \varepsilon_{22}^{(1)} \\ \gamma_{12}^{(1)} \\ \gamma_{13}^{(1)} \\ \gamma_{23}^{(1)} \end{Bmatrix} = \begin{Bmatrix} u_{3,11}^{0} \\ u_{3,22}^{0} \\ 2u_{3,12}^{0} \\ 0 \\ 0 \end{Bmatrix},$$

$$\boldsymbol{\varepsilon}^{(2)} = \begin{Bmatrix} \varepsilon_{11}^{(2)} \\ \varepsilon_{22}^{(2)} \\ \gamma_{12}^{(2)} \\ \gamma_{13}^{(2)} \\ \gamma_{23}^{(2)} \end{Bmatrix} = \begin{Bmatrix} \varphi_{1,1} \\ \varphi_{2,2} \\ \varphi_{1,2} + \varphi_{2,1} \\ 0 \\ 0 \end{Bmatrix} \tag{A.1a}$$

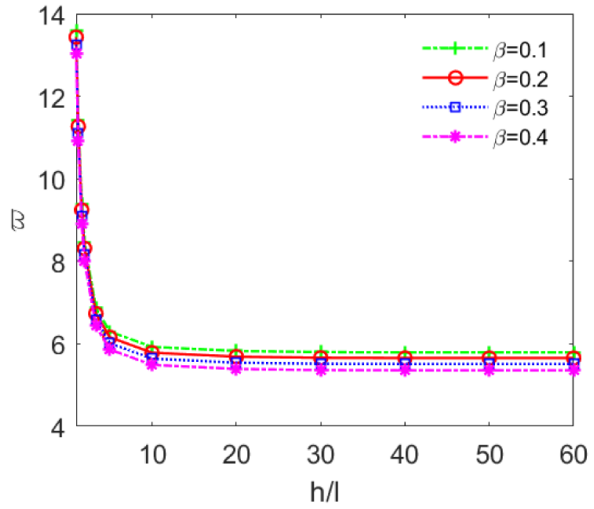

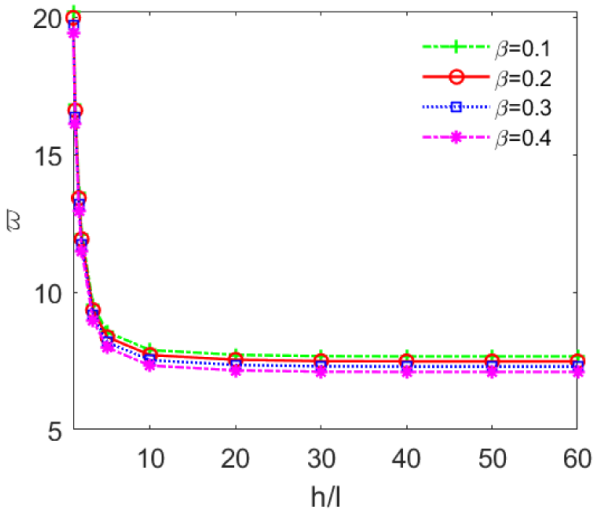

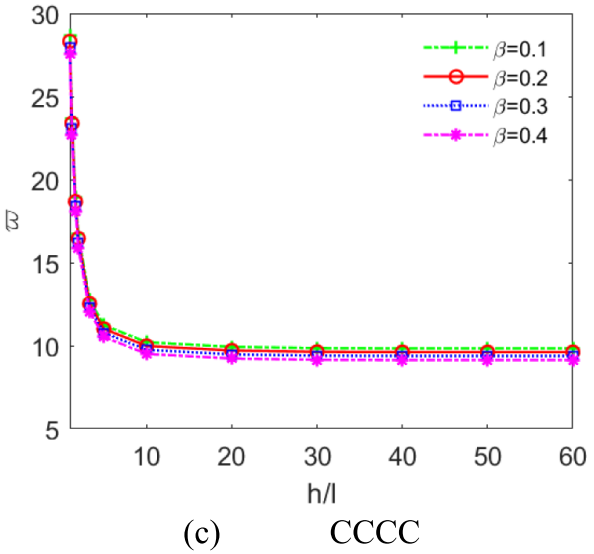

Fig. 5 Variation of normalized fundamental frequencies of PMF UD microplates with respect to h/l $(a/h = 10)$

$$\boldsymbol{\varepsilon}^{(3)} = \begin{Bmatrix} \varepsilon_{11}^{(3)} \\ \varepsilon_{22}^{(3)} \\ \gamma_{12}^{(3)} \\ \gamma_{13}^{(3)} \\ \gamma_{23}^{(3)} \end{Bmatrix} = \begin{Bmatrix} 0 \\ 0 \\ 0 \\ \varphi_1 + u_{3,1}^0 \\ \varphi_2 + u_{3,2}^0 \end{Bmatrix} \tag{A.1b}$$

$$\boldsymbol{\chi}^T = \begin{Bmatrix} \chi_{11} \\ \chi_{22} \\ 2\chi_{12} \\ \chi_{33} \\ 2\chi_{13} \\ 2\chi_{23} \end{Bmatrix}, \ \boldsymbol{\chi}^{(0)} = \frac{1}{2} \begin{Bmatrix} u_{3,12}^0 \\ -u_{3,12}^0 \\ u_{3,22}^0 - u_{3,11}^0 \\ 0 \\ u_{2,11}^0 - u_{1,12}^0 \\ u_{2,12}^0 - u_{1,22}^0 \end{Bmatrix},$$

$$\boldsymbol{\chi}^{(1)} = \frac{1}{2} \begin{Bmatrix} -u_{3,12}^0 \\ u_{3,12}^0 \\ u_{3,11}^0 - u_{3,22}^0 \\ 0 \\ 0 \\ 0 \end{Bmatrix}, \ \boldsymbol{\chi}^{(2)} = \frac{1}{2} \begin{Bmatrix} -\varphi_{2,1} \\ \varphi_{1,2} \\ \varphi_{1,1} - \varphi_{2,2} \\ \varphi_{2,1} - \varphi_{1,2} \\ 0 \\ 0 \end{Bmatrix} \tag{A.1c}$$

$$\boldsymbol{\chi}^{(5)} = \frac{1}{2} \begin{Bmatrix} 0 \\ 0 \\ 0 \\ 0 \\ \varphi_{2,11} - \varphi_{1,12} \\ \varphi_{2,12} - \varphi_{1,22} \end{Bmatrix}, \ \boldsymbol{\chi}^{(4)} = \frac{1}{2} \begin{Bmatrix} 0 \\ 0 \\ 0 \\ 0 \\ -\varphi_2 \\ \varphi_1 \end{Bmatrix} \tag{A.1d}$$

$$\boldsymbol{\chi}^{(3)} = \frac{1}{2} \begin{Bmatrix} 0 \\ 0 \\ 0 \\ 0 \\ -u_{3,2}^0 \\ u_{3,1}^0 \end{Bmatrix}$$

Appendix 2

The stress results could be calculated using strains and its gradients as shown:

$$\begin{Bmatrix} \mathbf{N}_{\varepsilon}^{(0)} \\ \mathbf{N}_{\varepsilon}^{(1)} \\ \mathbf{N}_{\varepsilon}^{(2)} \\ \mathbf{N}_{\varepsilon}^{(3)} \end{Bmatrix} = \begin{bmatrix} \mathbf{A}^{\varepsilon} & \mathbf{B}^{\varepsilon} & \mathbf{B}_s^{\varepsilon} & \mathbf{0} \\ \mathbf{B}^{\varepsilon} & \mathbf{D}^{\varepsilon} & \mathbf{D}_s^{\varepsilon} & \mathbf{0} \\ \mathbf{B}_s^{\varepsilon} & \mathbf{D}_s^{\varepsilon} & \mathbf{H}_s^{\varepsilon} & \mathbf{0} \\ \mathbf{0} & \mathbf{0} & \mathbf{0} & \mathbf{A}_s^{\varepsilon} \end{bmatrix} \begin{Bmatrix} \boldsymbol{\varepsilon}^{(0)} \\ \boldsymbol{\varepsilon}^{(1)} \\ \boldsymbol{\varepsilon}^{(2)} \\ \boldsymbol{\varepsilon}^{(3)} \end{Bmatrix} \tag{B.1a}$$

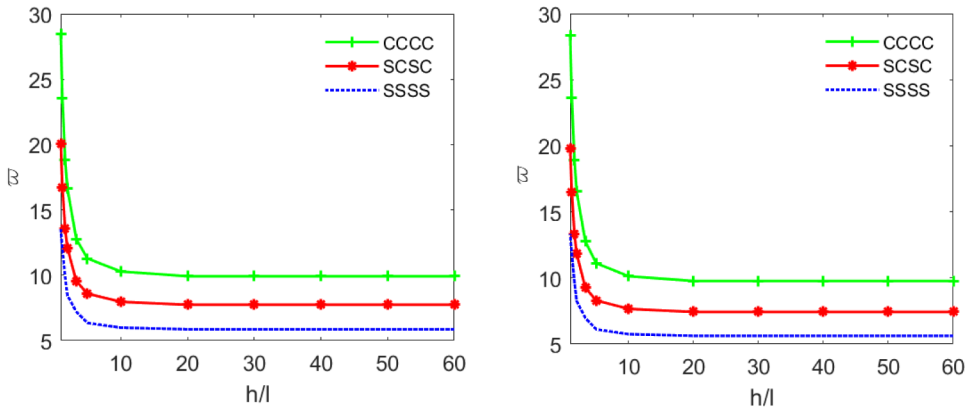

Fig. 6 Variation of normalized fundamental frequencies of PMF microplates with respect to h/l ($a/h = 10$ and $\beta = 0.2$)

$$\begin{Bmatrix} \mathbf{N}_{\chi}^{(0)} \\ \mathbf{N}_{\chi}^{(1)} \\ \mathbf{N}_{\chi}^{(2)} \\ \mathbf{N}_{\chi}^{(3)} \\ \mathbf{N}_{\chi}^{(4)} \\ \mathbf{N}_{\chi}^{(5)} \end{Bmatrix} = \begin{bmatrix} \mathbf{A}^{\chi} & \overline{\mathbf{B}}^{\chi} & \overline{\mathbf{B}}_s^{\chi} & \overline{\overline{\mathbf{B}}}^{\chi} & \overline{\overline{\mathbf{B}}}_s^{\chi} & \mathbf{B}_s^{\chi} \\ \overline{\mathbf{B}}^{\chi} & \overline{\mathbf{D}}^{\chi} & \overline{\mathbf{D}}_s^{\chi} & \overline{\mathbf{E}}^{\chi} & \overline{\mathbf{E}}_s^{\chi} & \overline{\mathbf{F}}_s^{\chi} \\ \overline{\mathbf{B}}_s^{\chi} & \overline{\mathbf{D}}_s^{\chi} & \overline{\mathbf{H}}_s^{\chi} & \overline{\mathbf{G}}_s^{\chi} & \overline{\mathbf{I}}^{\chi} & \overline{\mathbf{J}}^{\chi} \\ \overline{\overline{\mathbf{B}}}^{\chi} & \overline{\mathbf{E}}^{\chi} & \overline{\mathbf{G}}_s^{\chi} & \overline{\overline{\mathbf{D}}}^{\chi} & \overline{\overline{\mathbf{D}}}_s^{\chi} & \overline{\mathbf{K}}_s^{\chi} \\ \overline{\overline{\mathbf{B}}}_s^{\chi} & \overline{\mathbf{E}}_s^{\chi} & \overline{\mathbf{I}}^{\chi} & \overline{\overline{\mathbf{D}}}_s^{\chi} & \overline{\overline{\mathbf{H}}}_s^{\chi} & \overline{\mathbf{L}} \\ \mathbf{B}_s^{\chi} & \overline{\mathbf{F}}_s^{\chi} & \overline{\mathbf{J}}^{\chi} & \overline{\mathbf{K}}_s^{\chi} & \overline{\mathbf{L}} & \mathbf{H}_s^{\chi} \end{bmatrix} \begin{Bmatrix} \boldsymbol{\chi}^{(0)} \\ \boldsymbol{\chi}^{(1)} \\ \boldsymbol{\chi}^{(2)} \\ \boldsymbol{\chi}^{(3)} \\ \boldsymbol{\chi}^{(4)} \\ \boldsymbol{\chi}^{(5)} \end{Bmatrix} \tag{B.1b}$$

where the PMF microplate's stiffness components are described as follows:

$$\left(\mathbf{A}_s^{\varepsilon}, \mathbf{D}_s^{\varepsilon}, \mathbf{B}_s^{\varepsilon}, \mathbf{B}_s^{\varepsilon}, \mathbf{H}_s^{\varepsilon}, \mathbf{D}^{\varepsilon}, \mathbf{B}^{\varepsilon}, \mathbf{A}^{\varepsilon}\right) = \int_{-h/2}^{h/2} \left(\Upsilon_3^2, \Upsilon_1\Upsilon_2, \Upsilon_2, \Upsilon_2^2, \Upsilon_1^2, \Upsilon_1, 1\right)\mathbf{Q}_{\varepsilon} dx_3 \tag{B.2a}$$

$$\left(\mathbf{B}_s^{\chi}, \overline{\overline{\mathbf{B}}}_s^{\chi}, \overline{\overline{\mathbf{B}}}^{\chi}, \overline{\mathbf{B}}_s^{\chi}, \overline{\mathbf{B}}^{\chi}, \mathbf{A}^{\chi}\right) = \left(B_s^{\chi}, \overline{\overline{B}}_s^{\chi}, \overline{\overline{B}}^{\chi}, \overline{B}_s^{\chi}, \overline{B}^{\chi}, A^{\chi}\right)\mathbf{I}_{6\times 6} = \int_{-h/2}^{h/2} \left(\Upsilon_2, \Upsilon_{2,33}, \Upsilon_{1,33}, \Upsilon_{2,3}, \Upsilon_{1,3}, 1\right)\alpha_{\chi}\mathbf{I}_{6\times 6} dx_3 \tag{B.2b}$$

$$\left(\overline{\mathbf{D}}^{\chi}, \overline{\mathbf{D}}_s^{\chi}, \overline{\mathbf{E}}^{\chi}, \overline{\mathbf{E}}_s^{\chi}, \overline{\mathbf{F}}_s^{\chi}\right) = \left(\overline{D}^{\chi}, \overline{D}_s^{\chi}, \overline{E}^{\chi}, \overline{E}_s^{\chi}, \overline{F}_s^{\chi}\right)\mathbf{I}_{6\times 6} = \int_{-h/2}^{h/2} \Upsilon_{1,3}\left(\Upsilon_{1,3}, \Upsilon_{2,3}, \Upsilon_{1,33}, \Upsilon_{2,33}, \Upsilon_2\right)\alpha_{\chi}\mathbf{I}_{6\times 6} dx_3 \tag{B.2c}$$

$$\left(\overline{\mathbf{J}}^{\chi}, \overline{\mathbf{I}}^{\chi}, \overline{\mathbf{G}}_s^{\chi}, \overline{\mathbf{H}}_s^{\chi}\right) = \left(\overline{J}^{\chi}, \overline{I}^{\chi}, \overline{G}_s^{\chi}, \overline{H}_s^{\chi}\right)\mathbf{I}_{6\times 6} = \int_{-h/2}^{h/2} \Upsilon_{2,3}\left(\Upsilon_2, \Upsilon_{2,33}, \Upsilon_{1,33}, \Upsilon_{2,3}\right)\alpha_{\chi}\mathbf{I}_{6\times 6} dx_3 \tag{B.2d}$$

$$\left(\overline{\overline{\mathbf{D}}}^{\chi}, \overline{\overline{\mathbf{D}}}_s^{\chi}, \overline{\mathbf{K}}_s^{\chi}, \overline{\overline{\mathbf{H}}}_s^{\chi}, \overline{\mathbf{L}}^{\chi}, \mathbf{H}_s^{\chi}\right) = \left(\overline{\overline{D}}^{\chi}, \overline{\overline{D}}_s^{\chi}, \overline{K}_s^{\chi}, \overline{\overline{H}}_s^{\chi}, \overline{L}^{\chi}, H_s^{\chi}\right)\mathbf{I}_{6\times 6} = \int_{-h/2}^{h/2} \left(\Upsilon_{1,33}^2, \Upsilon_{1,33}\Upsilon_{2,33}, \Upsilon_{1,33}\Upsilon_2, \Upsilon_{2,33}^2, \Upsilon_{2,33}\Upsilon_2, \Upsilon_2^2\right)\alpha_{\chi}\mathbf{I}_{6\times 6} dx_3 \tag{B.2e}$$

Appendix 3

The stiffness matrix $\mathbf{K}^{\varepsilon}$ components are described as belows:

$$\begin{aligned}
K_{ijkl}^{\varepsilon 11} &= A_{11}^{\varepsilon} H_{ik}^{22} S_{jl}^{00} + A_{66}^{\varepsilon} H_{ik}^{11} S_{jl}^{11}, K_{ijkl}^{\varepsilon 12} = A_{12}^{\varepsilon} H_{ik}^{02} S_{jl}^{20} + A_{66}^{\varepsilon} H_{ik}^{11} S_{jl}^{11} \\
K_{ijkl}^{\varepsilon 13} &= B_{11}^{\varepsilon} H_{ik}^{22} S_{jl}^{00} + B_{12}^{\varepsilon} H_{ik}^{02} S_{jl}^{20} + 2B_{66}^{\varepsilon} H_{ik}^{11} S_{jl}^{11} \\
K_{ijkl}^{\varepsilon 14} &= B_{s11}^{\varepsilon} H_{ik}^{22} S_{jl}^{00} + B_{s66}^{\varepsilon} H_{ik}^{11} S_{jl}^{11}, K_{ijkl}^{\varepsilon 15} = B_{s12}^{\varepsilon} H_{ik}^{02} S_{jl}^{20} + B_{s66}^{\varepsilon} H_{ik}^{11} S_{jl}^{11} \\
K_{ijkl}^{\varepsilon 22} &= A_{22}^{\varepsilon} H_{ik}^{00} S_{jl}^{22} + A_{66}^{\varepsilon} H_{ik}^{11} S_{jl}^{11}, K_{ijkl}^{\varepsilon 23} = B_{12}^{\varepsilon} H_{ik}^{20} S_{jl}^{02} + B_{22}^{\varepsilon} H_{ik}^{00} S_{jl}^{22} + 2B_{66}^{\varepsilon} H_{ik}^{11} S_{jl}^{11} \\
K_{ijkl}^{\varepsilon 24} &= B_{s12}^{\varepsilon} H_{ik}^{20} S_{jl}^{02} + B_{s66}^{\varepsilon} H_{ik}^{11} S_{jl}^{11}, K_{ijkl}^{\varepsilon 25} = B_{s22}^{\varepsilon} H_{ik}^{00} S_{jl}^{22} + B_{s66}^{\varepsilon} H_{ik}^{11} S_{jl}^{11} \\
K_{ijkl}^{\varepsilon 33} &= D_{11}^{\varepsilon} H_{ik}^{22} S_{jl}^{00} + D_{12}^{\varepsilon}\left(H_{ik}^{02} S_{jl}^{20} + H_{ik}^{20} S_{jl}^{02}\right) + D_{22}^{\varepsilon} H_{ik}^{00} S_{jl}^{22} + 4D_{66}^{\varepsilon} H_{ik}^{11} S_{jl}^{11} \\
&\quad + A_{s44}^{\varepsilon} H_{ik}^{00} S_{jl}^{11} + A_{s55}^{\varepsilon} H_{ik}^{11} S_{jl}^{00} \\
K_{ijkl}^{\varepsilon 34} &= D_{s11}^{\varepsilon} H_{ik}^{22} S_{jl}^{00} + D_{s12}^{\varepsilon} H_{ik}^{20} S_{jl}^{02} + 2D_{s66}^{\varepsilon} H_{ik}^{11} S_{jl}^{11} + A_{s55}^{\varepsilon} H_{ik}^{11} S_{jl}^{00} \\
K_{ijkl}^{\varepsilon 35} &= D_{s12}^{\varepsilon} H_{ik}^{02} S_{jl}^{20} + D_{s22}^{\varepsilon} H_{ik}^{00} S_{jl}^{22} + 2D_{s66}^{\varepsilon} H_{ik}^{11} S_{jl}^{11} + A_{s44}^{\varepsilon} H_{ik}^{00} S_{jl}^{11} \\
K_{ijkl}^{\varepsilon 44} &= H_{s11}^{\varepsilon} H_{ik}^{22} S_{jl}^{00} + H_{s66}^{\varepsilon} H_{ik}^{11} S_{jl}^{11} + A_{s55}^{\varepsilon} H_{ik}^{11} S_{jl}^{00} \\
K_{ijkl}^{\varepsilon 45} &= H_{s12}^{\varepsilon} H_{ik}^{02} S_{jl}^{20} + H_{s66}^{\varepsilon} H_{ik}^{11} S_{jl}^{11}, K_{ijkl}^{\varepsilon 55} = H_{s22}^{\varepsilon} H_{ik}^{00} S_{jl}^{22} + H_{s66}^{\varepsilon} H_{ik}^{11} S_{jl}^{11} + A_{s44}^{\varepsilon} H_{ik}^{00} S_{jl}^{11}
\end{aligned} \tag{C.1}$$

where

$$H_{ik}^{rs} = \int_0^a \frac{\partial^r T_i}{\partial x_1^r}\frac{\partial^s T_k}{\partial x_1^s} dx_1, S_{jl}^{rs} = \int_0^b \frac{\partial^r F_j}{\partial x_2^r}\frac{\partial^s F_l}{\partial x_2^s} dx_2 \tag{C.2}$$

with $i,k = 1,...,n_1$; $j,l = 1,...,n_2$; r,s are the order of partial derivatives.

The components of the stiffness matrix $\mathbf{K}^{\chi}$ are expressed as follows:

Table 8 Normalized critical buckling loads of the square PMF SSSS microplates under uniaxial compression (MAT 1, $a/h = 10$)

Type distribution	β	Theory	h/l				
			∞	10	5	2	1
UD	0.1	Ritz–Hermite	3.2565	3.4002	3.8312	6.8477	17.6179
		Ritz–Laguerre	3.2576	3.4013	3.8324	6.8499	17.6228
		IGA [25]	3.2625	–	–	–	–
	0.2	Ritz–Hermite	2.9905	3.1263	3.5339	6.3864	16.5708
		Ritz–Laguerre	2.9915	3.1274	3.5351	6.3884	16.5753
		IGA [25]	3.0337	–	–	–	–
	0.3	Ritz–Hermite	2.7274	2.8549	3.2376	5.9161	15.4791
		Ritz–Laguerre	2.7282	2.8559	3.2387	5.9179	15.4833
		IGA [25]	2.7992	–	–	–	–
	0.4	Ritz–Hermite	2.5627	2.7348	3.1309	5.6331	14.9277
		Ritz–Laguerre	2.5679	2.7400	3.1363	5.6478	14.9290
		IGA [25]	2.5578	–	–	–	–
	0.5	Ritz–Hermite	2.3250	2.4465	2.8109	5.3608	14.4634
		Ritz–Laguerre	2.3297	2.4512	2.8157	5.3651	14.4632
		IGA [25]	2.3076	–	–	–	–
	0.6	Ritz–Hermite	2.0427	2.1526	2.4824	4.7904	13.0289
		Ritz–Laguerre	2.0468	2.1568	2.4867	4.7941	13.0286
		IGA [25]	2.0459	–	–	–	–
	0.7	Ritz–Hermite	1.7507	1.8478	2.1393	4.1788	11.4591
		Ritz–Laguerre	1.7542	1.8515	2.1430	4.1820	11.4588
		IGA [25]	1.7679	–	–	–	–
SD	0.1	Ritz–Hermite	3.3825	3.5275	3.9626	7.0081	17.8820
		Ritz–Laguerre	3.3891	3.5345	3.9706	7.0230	17.9206
		IGA [25]	3.3520	–	–	–	–
	0.2	Ritz–Hermite	3.2272	3.3645	3.7764	6.6593	16.9527
		Ritz–Laguerre	3.2335	3.3712	3.7841	6.6736	16.9900
		IGA [25]	3.2164	–	–	–	–
	0.3	Ritz–Hermite	3.0753	3.2046	3.5923	6.3057	15.9944
		Ritz–Laguerre	3.0814	3.2109	3.5996	6.3194	16.0303
		IGA [25]	3.0796	–	–	–	–
	0.4	Ritz–Hermite	2.9259	3.0467	3.4092	5.9459	15.0038
		Ritz–Laguerre	2.9315	3.0526	3.4160	5.9588	15.0384
		IGA [25]	2.9410	–	–	–	–
	0.5	Ritz–Hermite	2.7781	2.8901	3.2262	5.5785	14.5779
		Ritz–Laguerre	2.7833	2.8957	3.2326	5.5908	14.5613
		IGA [25]	2.8000	–	–	–	–
	0.6	Ritz–Hermite	2.6304	2.7332	3.0418	5.2012	13.2126
		Ritz–Laguerre	2.6354	2.7385	3.0479	5.2132	13.2452
		IGA [25]	2.6555	–	–	–	–
	0.7	Ritz–Hermite	2.4808	2.5741	2.8538	4.8117	11.8035
		Ritz–Laguerre	2.4854	2.5789	2.8595	4.8232	11.8355
		IGA [25]	2.5054	–	–	–	–

Table 9 Normalized critical buckling loads of the square PMF SSSS microplates under biaxial compression (MAT 1, $a/h = 10$)

Type distribution	β	Theory	h/l				
			∞	10	5	2	1
UD	0.1	Ritz–Hermite	1.6598	1.7344	1.9582	3.5245	9.1169
		Ritz–Laguerre	1.6617	1.7362	1.9599	3.5252	9.1132
		IGA [25]	1.6313	–	–	–	–
	0.2	Ritz–Hermite	1.5242	1.5948	1.8064	3.2876	8.5757
		Ritz–Laguerre	1.5260	1.5965	1.8080	3.2881	8.5722
		IGA [25]	1.5169	–	–	–	–
	0.3	Ritz–Hermite	1.3901	1.4564	1.6551	3.0459	8.0114
		Ritz–Laguerre	1.3917	1.4580	1.6566	3.0464	8.0081
		IGA [25]	1.3996	–	–	–	–
	0.4	Ritz–Hermite	1.2566	1.3182	1.5032	2.7976	7.4187
		Ritz–Laguerre	1.2581	1.3197	1.5045	2.7980	7.4157
		IGA [25]	1.2789	–	–	–	–
	0.5	Ritz–Hermite	1.1284	1.1791	1.3492	2.5398	6.7905
		Ritz–Laguerre	1.1298	1.1804	1.3505	2.5403	6.7876
		IGA [25]	1.1538	–	–	–	–
SD	0.1	Ritz–Hermite	1.6919	1.7645	1.9821	3.5452	9.1437
		Ritz–Laguerre	1.6958	1.7685	1.9866	3.5434	9.1447
		IGA [25]	1.6760	–	–	–	–
	0.2	Ritz–Hermite	1.6143	1.6830	1.8890	3.3308	8.6189
		Ritz–Laguerre	1.6179	1.6868	1.8933	3.3386	8.6191
		IGA [25]	1.6082	–	–	–	–
	0.3	Ritz–Hermite	1.5383	1.6029	1.7968	3.1539	8.0996
		Ritz–Laguerre	1.5418	1.6066	1.8010	3.1614	8.0991
		IGA [25]	1.5398	–	–	–	–
	0.4	Ritz–Hermite	1.4636	1.5240	1.7053	2.9740	7.5042
		Ritz–Laguerre	1.4668	1.5274	1.7091	2.9811	7.5229
		IGA [25]	1.4705	–	–	–	–
	0.5	Ritz–Hermite	1.3896	1.4457	1.6138	2.7902	6.9911
		Ritz–Laguerre	1.3927	1.4489	1.6174	2.7970	7.0091
		IGA [25]	1.4000	–	–	–	–

Table 10 Normalized critical buckling loads of the square PMF microplates under biaxial compression with different BCs (MAT 1, $a/h = 10$)

BCs	Type distribution	β	Theory	h/l				
				∞	10	5	2	1
SCSC	UD	0.1	Ritz–Hermite	2.5725	2.7218	3.1684	6.2766	17.3403
			Ritz–Laguerre	2.5757	2.7225	3.1620	6.2673	17.2474
		0.2	Ritz–Hermite	2.3649	2.5061	2.9284	5.8675	16.3300
			Ritz–Laguerre	2.3678	2.5066	2.9223	5.8509	16.2477
		0.3	Ritz–Hermite	2.1591	2.2916	2.6882	5.4480	15.2726
			Ritz–Laguerre	2.1616	2.2920	2.6823	5.4343	15.1917
		0.4	Ritz–Hermite	1.9536	2.0770	2.4460	5.0145	14.0583
			Ritz–Laguerre	1.9559	2.0772	2.4405	4.9939	13.9994
		0.5	Ritz–Hermite	1.7467	1.8602	2.1996	4.5622	12.9731
			Ritz–Laguerre	1.7487	1.8603	2.1945	4.5549	12.8973
	SD	0.1	Ritz–Hermite	2.6373	2.7851	3.2271	6.3035	17.3759
			Ritz–Laguerre	2.6396	2.7852	3.2212	6.2680	17.2914
		0.2	Ritz–Hermite	2.5144	2.6542	3.0727	5.9848	16.3627
			Ritz–Laguerre	2.5166	2.6545	3.0672	5.9450	16.2989
		0.3	Ritz–Hermite	2.3934	2.5250	2.9189	5.6599	15.4188
			Ritz–Laguerre	2.3956	2.5253	2.9138	5.6229	15.2963
		0.4	Ritz–Hermite	2.2735	2.3966	2.7648	5.3274	14.4510
			Ritz–Laguerre	2.2757	2.3971	2.7603	5.2934	14.3806
		0.5	Ritz–Hermite	2.1539	2.2680	2.6095	4.9858	13.4462
			Ritz–Laguerre	2.1561	2.2686	2.6055	4.9551	13.3688
CCCC	UD	0.1	Ritz–Hermite	3.8964	4.1769	5.0167	10.8758	31.7498
			Ritz–Laguerre	3.8916	4.1732	5.0160	10.8953	31.8486
		0.2	Ritz–Hermite	3.5870	3.8523	4.6465	10.1878	29.9295
			Ritz–Laguerre	3.5828	3.8490	4.6460	10.2061	30.0218
		0.3	Ritz–Hermite	3.2794	3.5285	4.2743	9.4783	28.0183
			Ritz–Laguerre	3.2755	3.5254	4.2739	9.4952	28.1040
		0.4	Ritz–Hermite	2.9713	3.2031	3.8974	8.7412	25.9982
			Ritz–Laguerre	2.9678	3.2004	3.8970	8.7567	26.0769
		0.5	Ritz–Hermite	2.6601	2.8734	3.5121	7.9681	23.8437
			Ritz–Laguerre	2.6569	2.8709	3.5117	7.9821	23.9152
	SD	0.1	Ritz–Hermite	4.0128	4.2937	5.1346	11.0014	31.9071
			Ritz–Laguerre	4.0101	4.2911	5.1323	11.0004	31.9084
		0.2	Ritz–Hermite	3.8218	4.0876	4.8836	10.4371	30.2273
			Ritz–Laguerre	3.8192	4.0851	4.8815	10.4361	30.2285
		0.3	Ritz–Hermite	3.6324	3.8826	4.6318	9.8587	28.4864
			Ritz–Laguerre	3.6299	3.8802	4.6298	9.8578	28.4875
		0.4	Ritz–Hermite	3.4431	3.6771	4.3775	9.2638	26.6787
			Ritz–Laguerre	3.4407	3.6748	4.3755	9.2628	26.6797
		0.5	Ritz–Hermite	3.2524	3.4693	4.1187	8.6494	24.7981
			Ritz–Laguerre	3.2501	3.4672	4.1169	8.6485	24.7990

Table 11 Normalized critical buckling loads of the square PMF microplates under uniaxial compression with different BCs (MAT 1, $a/h = 10$)

BCs	Type distribution	β	Theory	h/l				
				∞	10	5	2	1
SCSC	UD	0.1	Ritz–Hermite	4.7816	5.0648	5.9094	11.7613	32.5557
			Ritz–Laguerre	4.7944	5.0757	5.9164	11.7602	32.5554
		0.2	Ritz–Hermite	4.3975	4.6651	5.4635	10.9965	30.6609
			Ritz–Laguerre	4.4087	4.6747	5.4694	10.9948	30.6594
		0.3	Ritz–Hermite	4.0162	4.2675	5.0169	10.2118	28.6774
			Ritz–Laguerre	4.0261	4.2757	5.0218	10.2096	28.6749
		0.4	Ritz–Hermite	3.6353	3.8691	4.5663	9.4006	26.5867
			Ritz–Laguerre	3.6439	3.8761	4.5703	9.3980	26.5831
		0.5	Ritz–Hermite	3.2515	3.4664	4.1075	8.5539	24.3627
			Ritz–Laguerre	3.2587	3.4723	4.1106	8.5508	24.3584
	SD	0.1	Ritz–Hermite	4.9348	5.2183	6.0637	11.9181	32.7184
			Ritz–Laguerre	4.9488	5.2303	6.0716	11.9175	32.7172
		0.2	Ritz–Hermite	4.7033	4.9718	5.7723	11.3150	31.0072
			Ritz–Laguerre	4.7171	4.9837	5.7802	11.3142	31.0035
		0.3	Ritz–Hermite	4.4751	4.7279	5.4817	10.6997	29.2375
			Ritz–Laguerre	4.4885	4.7395	5.4895	10.6987	29.2309
		0.4	Ritz–Hermite	4.2482	4.4848	5.1900	10.0696	27.4035
			Ritz–Laguerre	4.2617	4.4966	5.1979	10.0685	27.3939
		0.5	Ritz–Hermite	4.0211	4.2408	4.8954	9.4221	25.4996
			Ritz–Laguerre	4.0348	4.2528	4.9036	9.4207	25.4861
CCCC	UD	0.1	Ritz–Hermite	7.2066	7.7529	9.3772	20.5925	60.5079
			Ritz–Laguerre	7.2087	7.7607	9.3998	20.6066	60.5522
		0.2	Ritz–Hermite	6.6402	7.1564	8.6914	19.2962	56.1332
			Ritz–Laguerre	6.6424	7.1637	8.7125	19.3026	56.1381
		0.3	Ritz–Hermite	6.0758	6.5601	8.0006	17.9581	51.9046
			Ritz–Laguerre	6.0778	6.5668	8.0200	18.0165	51.9990
		0.4	Ritz–Hermite	5.5495	5.9598	7.2997	16.5666	48.0675
			Ritz–Laguerre	5.5513	5.9660	7.3175	16.6068	48.0901
	SD	0.1	Ritz–Hermite	7.4160	7.9634	9.5899	20.8101	60.6146
			Ritz–Laguerre	7.4182	7.9713	9.6128	20.9251	61.0770
		0.2	Ritz–Hermite	7.0582	7.5769	9.1175	19.7408	57.4269
			Ritz–Laguerre	7.0605	7.5846	9.1394	19.8490	57.8579
		0.3	Ritz–Hermite	6.7020	7.1909	8.6423	18.6441	54.1228
			Ritz–Laguerre	6.7040	7.1980	8.6627	18.7448	54.5204
		0.4	Ritz–Hermite	6.3440	6.8020	8.1607	17.5149	50.6915
			Ritz–Laguerre	6.3462	6.8089	8.1800	17.6081	51.0542

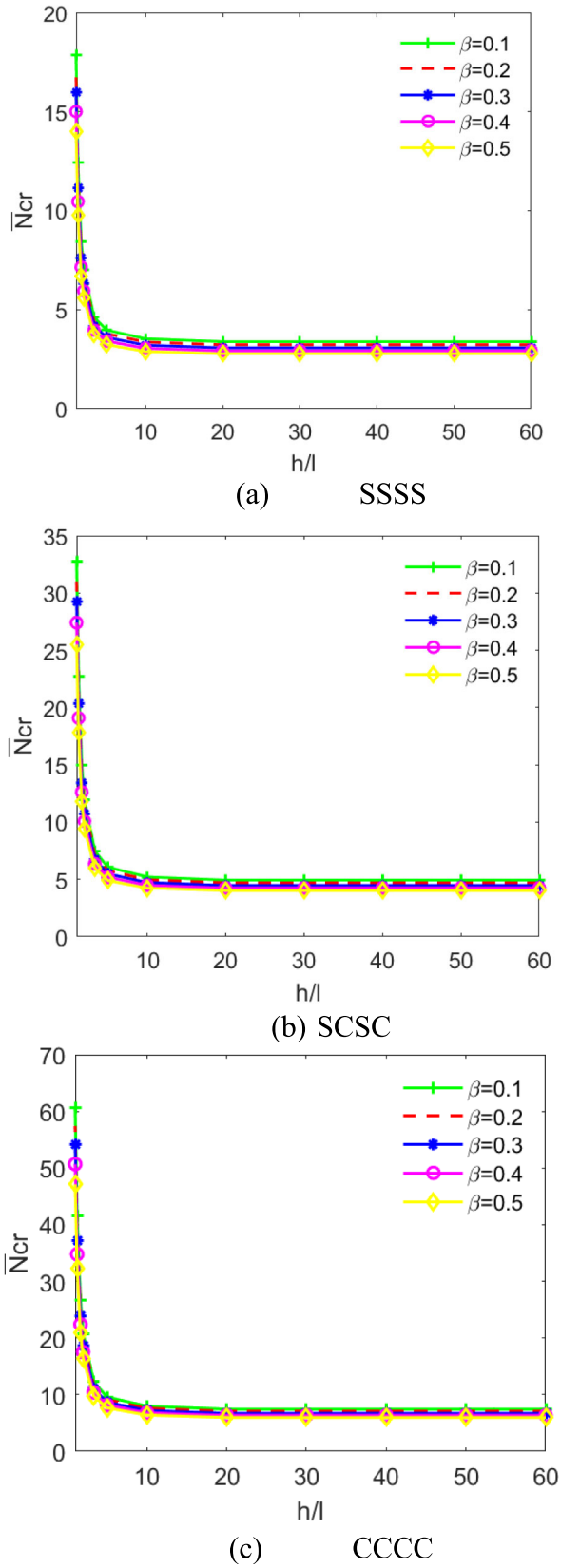

◀**Fig. 7** Variation of normalized critical buckling loads of PMF SD microplates under uniaxial compression with respect to h/l ($a/h = 10$)

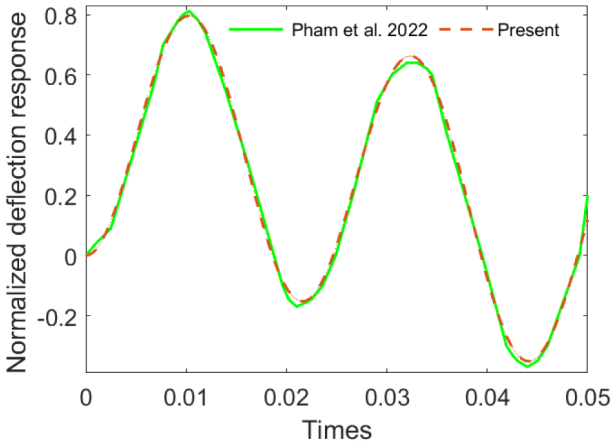

Fig. 8 Deflection response of the square PMF SD SSSS plate under triangular load ($a/h = 10$ and $\beta = 0.1$)

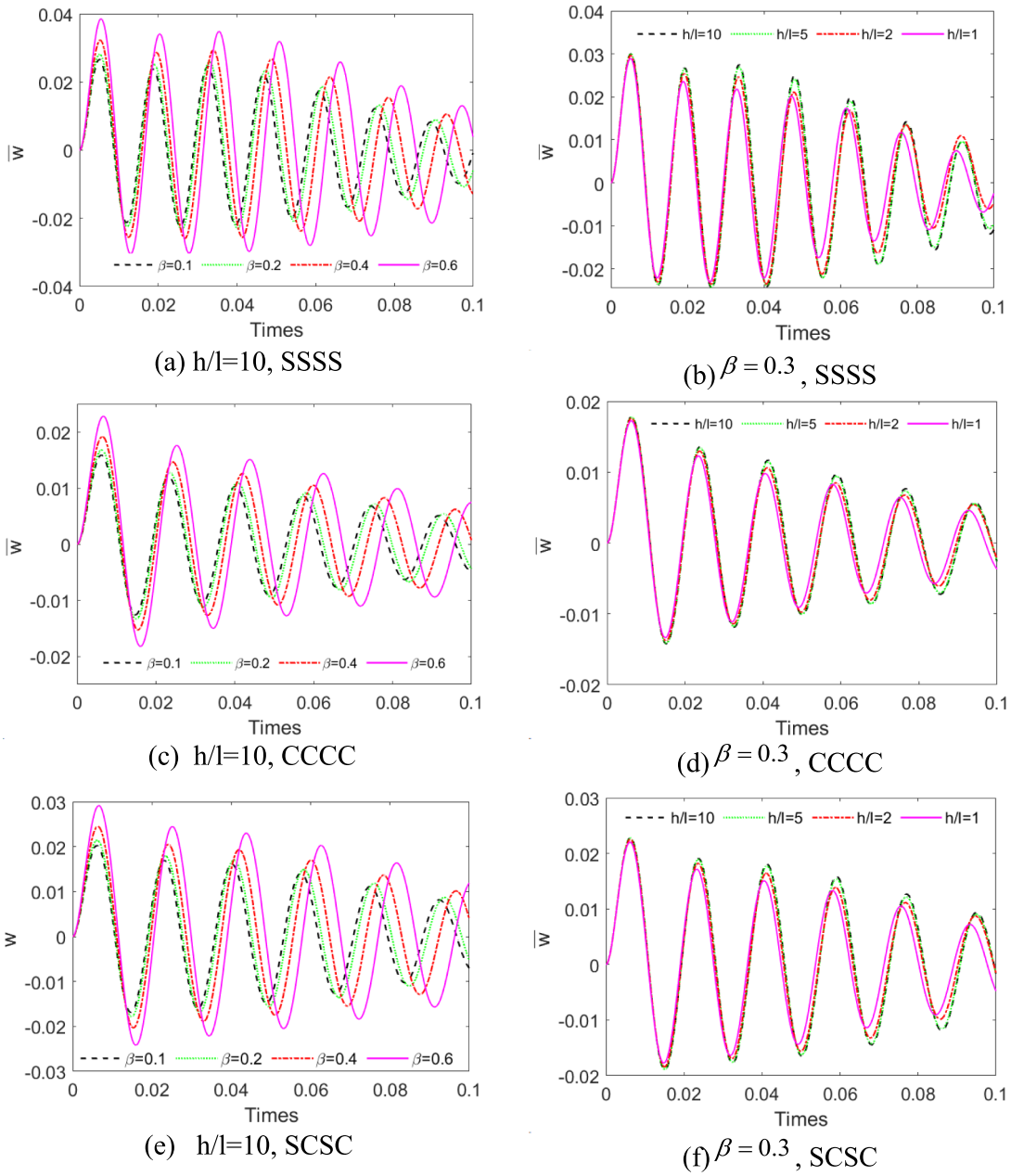

Fig. 9 Deflection response of the square PMF UD microplate under explosive blast loading ($a/h = 10$ and $\zeta = 0.05$)

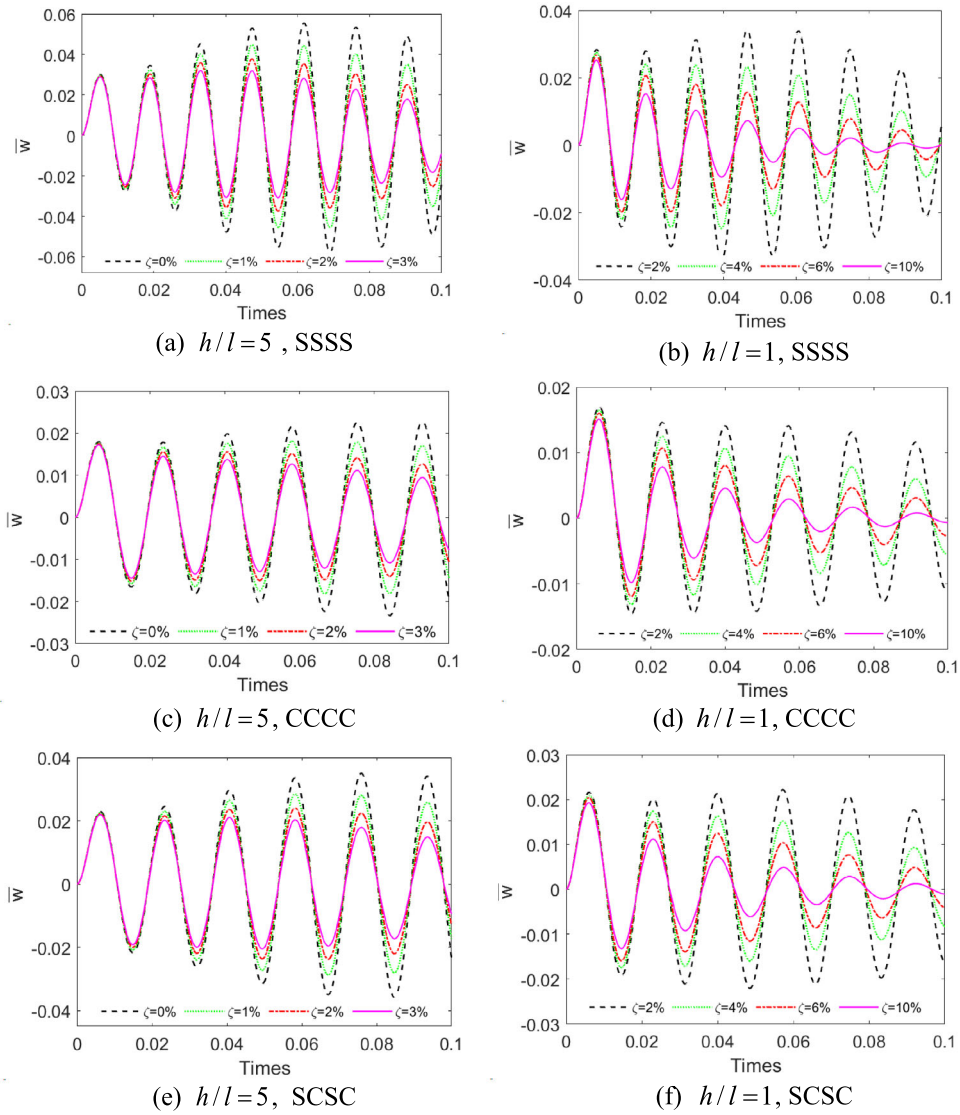

Fig. 10 Deflection response of the square PMF UD microplate under explosive blast loading for various damping ratios ($a/h = 10$ and $\beta = 0.2$)

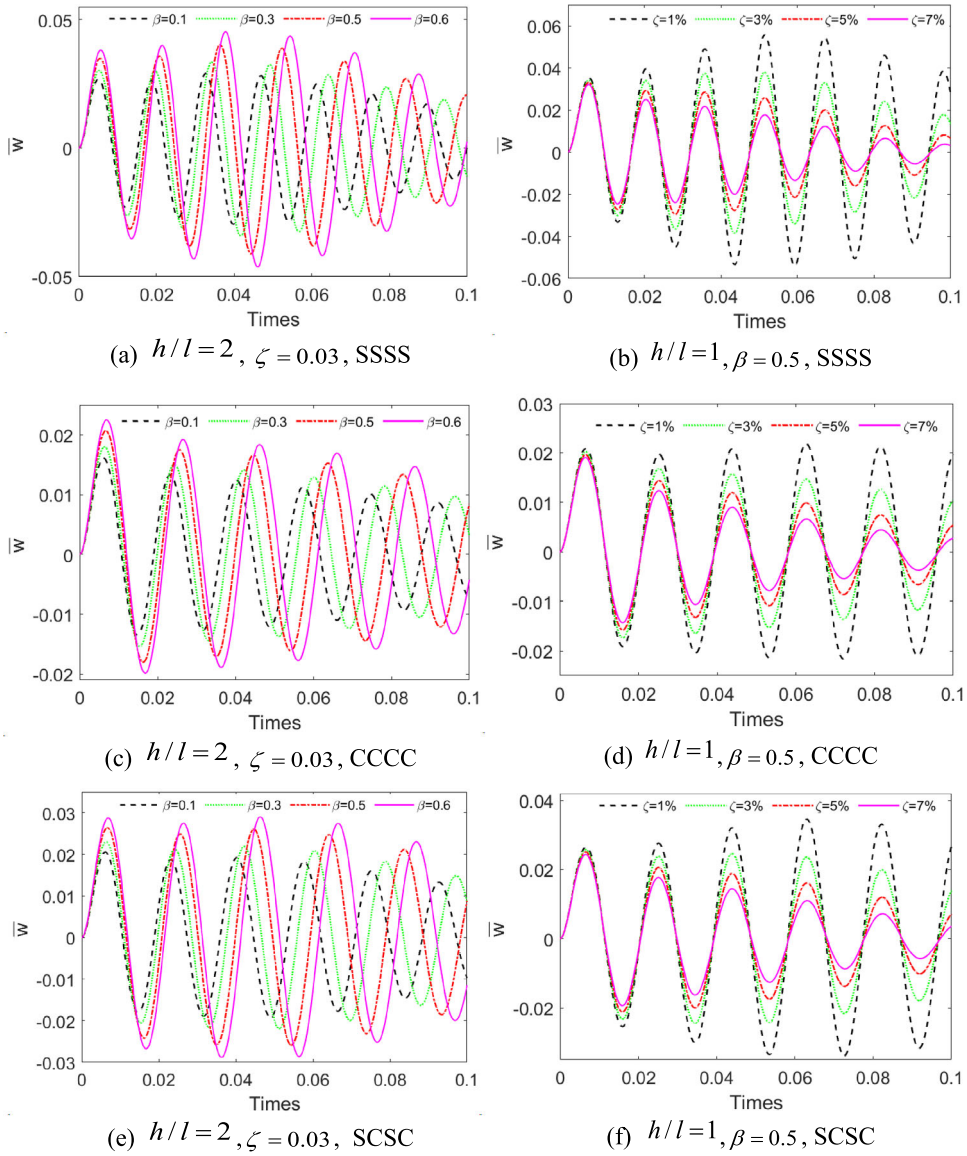

(a) $h/l=2$, $\zeta=0.03$, SSSS (b) $h/l=1$, $\beta=0.5$, SSSS

(c) $h/l=2$, $\zeta=0.03$, CCCC (d) $h/l=1$, $\beta=0.5$, CCCC

(e) $h/l=2$, $\zeta=0.03$, SCSC (f) $h/l=1$, $\beta=0.5$, SCSC

Fig. 11 Deflection response of the square PMF SD microplate under explosive blast loading ($a/h=10$)

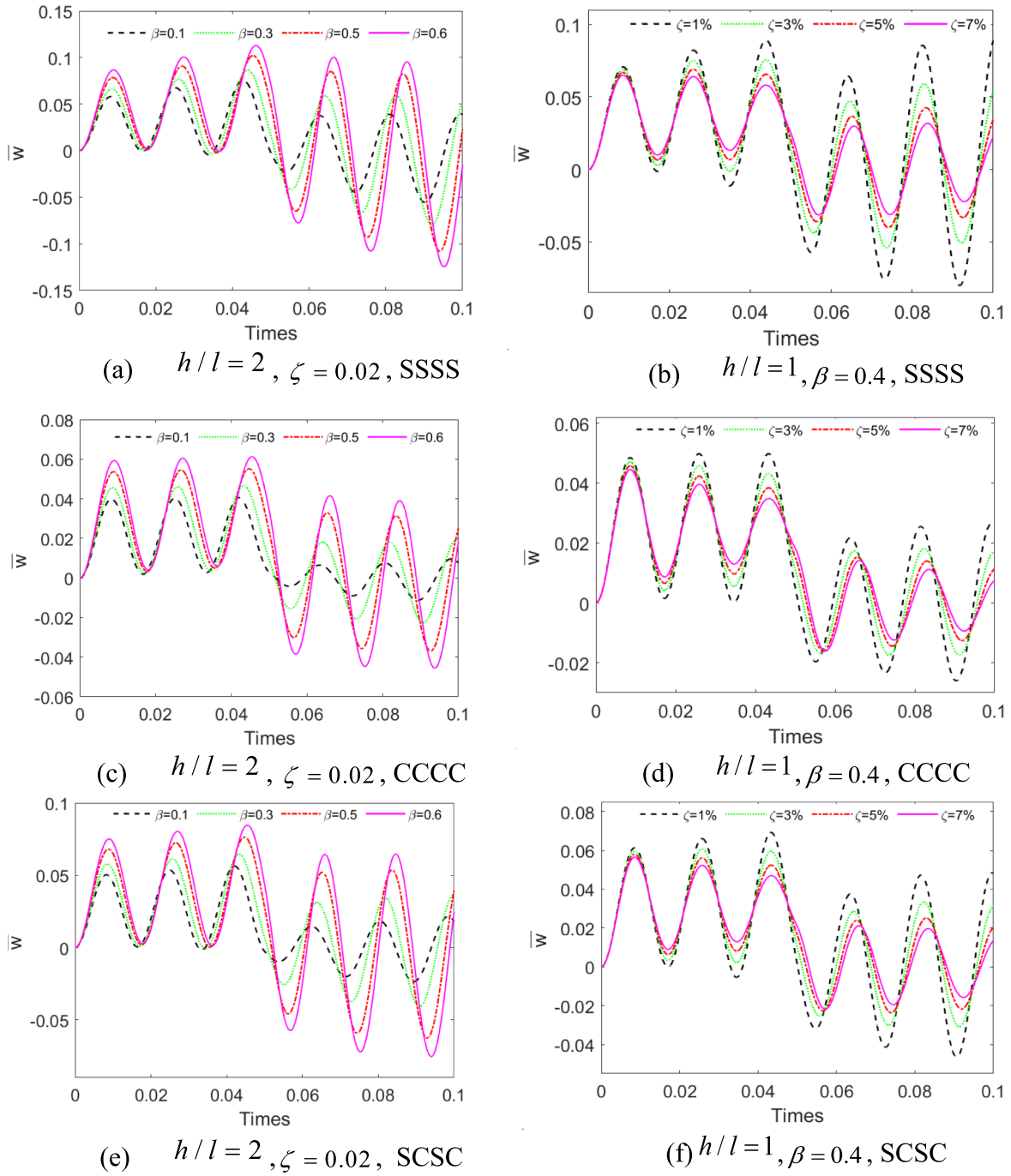

Fig. 12 Deflection response of the square PMF AD microplate under rectangular load ($a/h = 10$)

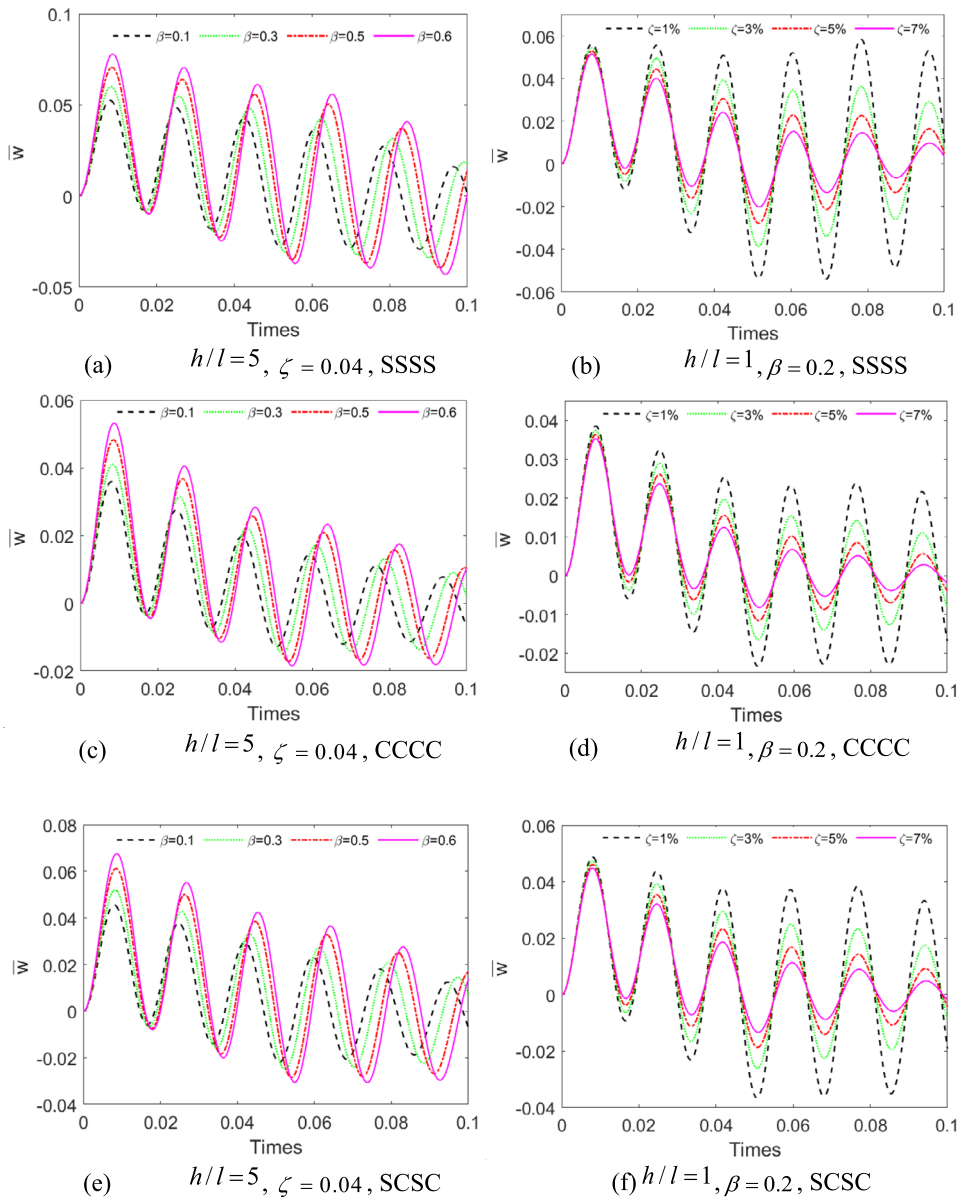

Fig. 13 Deflection response of the square PMF AD microplate under triangular load $(a/h = 10)$

$$K_{ijkl}^{\chi 11} = \frac{A^{\chi}}{4}\left(H_{ik}^{22}S_{jl}^{11} + H_{ik}^{11}S_{jl}^{22}\right),$$

$$K_{ijkl}^{\chi 12} = -\frac{A^{\chi}}{4}\left(H_{ik}^{22}S_{jl}^{11} + H_{ik}^{11}S_{jl}^{22}\right)$$

$$K_{ijkl}^{\chi 13} = \frac{\overline{\overline{B}}^{\chi}}{4}\left(H_{ik}^{02}S_{jl}^{11} - H_{ik}^{11}S_{jl}^{02}\right),$$

$$K_{ijkl}^{\chi 14} = \frac{1}{4}\left(B_s^{\chi}H_{ik}^{22}S_{jl}^{11} + B_s^{\chi}H_{ik}^{11}S_{jl}^{22} - \overline{\overline{B}}_s^{\chi}H_{ik}^{11}S_{jl}^{02}\right)$$

$$K_{ijkl}^{\chi 15} = \frac{1}{4}\left(\overline{\overline{B}}_s^{\chi}H_{ik}^{02}S_{jl}^{11} - B_s^{\chi}H_{ik}^{22}S_{jl}^{11} - B_s^{\chi}H_{ik}^{11}S_{jl}^{22}\right),$$

$$K_{ijkl}^{\chi 22} = \frac{A^{\chi}}{4}\left(H_{ik}^{22}S_{jl}^{11} + H_{ik}^{11}S_{jl}^{22}\right)$$

$$K_{ijkl}^{\chi 23} = \frac{\overline{\overline{B}}^{\chi}}{4}\left(H_{ik}^{11}S_{jl}^{02} - H_{ik}^{02}S_{jl}^{11}\right),$$

$$K_{ijkl}^{\chi 24} = \frac{1}{4}\left(\overline{\overline{B}}_s^{\chi}H_{ik}^{11}S_{jl}^{02} - B_s^{\chi}H_{ik}^{22}S_{jl}^{11} - B_s^{\chi}H_{ik}^{11}S_{jl}^{22}\right)$$

$$K_{ijkl}^{\chi 25} = \frac{1}{4}\left(B_s^{\chi}H_{ik}^{22}S_{jl}^{11} + B_s^{\chi}H_{ik}^{11}S_{jl}^{22} - \overline{\overline{B}}_s^{\chi}H_{ik}^{02}S_{jl}^{11}\right)$$

$$K_{ijkl}^{\chi 33} = \frac{1}{4}\left(A^{\chi} - 2\overline{B}^{\chi} + \overline{D}^{\chi}\right)\left(H_{ik}^{00}S_{jl}^{22} - H_{ik}^{20}S_{jl}^{02} - H_{ik}^{02}S_{jl}^{20} + H_{ik}^{22}S_{jl}^{00} + 2H_{ik}^{11}S_{jl}^{11}\right) + \frac{1}{4}\overline{\overline{D}}^{\chi}\left(H_{ik}^{00}S_{jl}^{11} + H_{ik}^{11}S_{jl}^{00}\right)$$

$$K_{ijkl}^{\chi 34} = \frac{1}{4}\left[\left(\overline{B}_s^{\chi} - \overline{D}_s^{\chi}\right)\left(H_{ik}^{20}S_{jl}^{02} - H_{ik}^{22}S_{jl}^{00} - H_{ik}^{11}S_{jl}^{11}\right) + \overline{K}_s^{\chi}\left(H_{ik}^{20}S_{jl}^{11} - H_{ik}^{11}S_{jl}^{20}\right) + \overline{\overline{D}}_s^{\chi}H_{ik}^{11}S_{jl}^{00}\right]$$

$$K_{ijkl}^{\chi 35} = \frac{1}{4}\left[\left(\overline{B}_s^{\chi} - \overline{D}_s^{\chi}\right)\left(-H_{ik}^{00}S_{jl}^{22} + H_{ik}^{02}S_{jl}^{20} - H_{ik}^{11}S_{jl}^{11}\right) + \overline{\overline{D}}_s^{\chi}H_{ik}^{00}S_{jl}^{11} + \overline{K}_s^{\chi}\left(H_{ik}^{11}S_{jl}^{20} - H_{ik}^{20}S_{jl}^{11}\right)\right]$$

$$K_{ijkl}^{\chi 44} = \frac{1}{4}\left[\overline{H}_s^{\chi}\left(H_{ik}^{22}S_{jl}^{00} + 2H_{ik}^{11}S_{jl}^{11}\right) + \overline{\overline{H}}_s^{\chi}H_{ik}^{11}S_{jl}^{00} - \overline{L}^{\chi}\left(H_{ik}^{11}S_{jl}^{20} + H_{ik}^{11}S_{jl}^{02}\right) + H_s^{\chi}\left(H_{ik}^{22}S_{jl}^{11} + H_{ik}^{11}S_{jl}^{22}\right)\right]$$

$$K_{ijkl}^{\chi 45} = \frac{1}{4}\left[\overline{L}^{\chi}\left(H_{ik}^{11}S_{jl}^{20} + H_{ik}^{02}S_{jl}^{11}\right) - \overline{H}_s^{\chi}\left(H_{ik}^{02}S_{jl}^{20} + H_{ik}^{11}S_{jl}^{11}\right) - H_s^{\chi}\left(H_{ik}^{11}S_{jl}^{22} + H_{ik}^{22}S_{jl}^{11}\right)\right]$$

$$K_{ijkl}^{\chi 55} = \frac{1}{4}\left[\overline{H}_s^{\chi}\left(2H_{ik}^{11}S_{jl}^{11} + H_{ik}^{00}S_{jl}^{22}\right) + \overline{\overline{H}}_s^{\chi}H_{ik}^{00}S_{jl}^{11} + -\overline{L}^{\chi}\left(H_{ik}^{20}S_{jl}^{11} + H_{ik}^{02}S_{jl}^{11}\right) + H_s^{\chi}\left(H_{ik}^{11}S_{jl}^{22} + H_{ik}^{22}S_{jl}^{11}\right)\right] \tag{C.3}$$

Data availability The data that support the findings of this study are available from the corresponding author upon reasonable request.

References

1. Banhart J (2001) Manufacture, characterisation and application of cellular metals and metal foams. Prog Mater Sci 46(6):559–632
2. Salimon A, Bréchet Y, Ashby MF, Greer AL (2005) Potential applications for steel and titanium metal foams. J Mater Sci 40(22):5793–5799
3. Wu H, Yang J, Kitipornchai S (2020) Mechanical analysis of functionally graded porous structures: a review. Int J Struct Stab Dyn 20(13):2041015
4. Kuruneru STW, Vafai K, Sauret E, Gu Y (2020) Application of porous metal foam heat exchangers and the implications of particulate fouling for energy-intensive industries. Chem Eng Sci 228:115968
5. Yang F, Chong ACM, Lam DCC, Tong P (2002) Couple stress based strain gradient theory for elasticity. Int J Solids Struct 39(10):2731–2743
6. Li F-L, Fan S-J, Hao Y-X, Yang L, Lv M (2023) Dynamic behaviors of thermal-electric imperfect functionally graded piezoelectric sandwich microplates based on modified couple stress theory. J Vib Eng Technol 11(5):2387–2401
7. Tran V-T, Nguyen T-K, Phong TT, Vo TP (2022) Stochastic vibration and buckling analysis of functionally graded microplates with a unified higher-order shear deformation theory. Thin-Walled Struct 177:109473
8. Tran V-T, Nguyen T-K, Phong TT, Vo TP (2023) Stochastic collocation method for thermal buckling and vibration analysis of functionally graded sandwich microplates. J Thermal Stress 46(9):909–934
9. Fan F, Xu Y, Sahmani S, Safaei B (2020) Modified couple stress-based geometrically nonlinear oscillations of porous functionally graded microplates using NURBS-based isogeometric approach. Comput Methods Appl Mech Eng 372:113400
10. Farzam A, Hassani B (2019) Isogeometric analysis of in-plane functionally graded porous microplates using modified couple stress theory. Aerosp Sci Technol 91:508–524
11. Kim J, Żur K, Reddy JN (2018) Bending, free vibration, and buckling of modified couples stress-based functionally graded porous micro-plates. Compos Struct 209:879
12. Thanh C-L, Tran LV, Bui TQ, Nguyen HX, Abdel-Wahab M (2019) Isogeometric analysis for size-dependent nonlinear thermal stability of porous FG microplates. Compos Struct 221:110838
13. Lam DCC, Yang F, Chong ACM, Wang J, Tong P (2003) Experiments and theory in strain gradient elasticity. J Mech Phys Solids 51(8):1477–1508
14. Tran V-T, Nguyen V-H, Nguyen T-K, Vo TP (2023) Static and vibration analysis of functionally graded microplate with porosities based on higher-order shear deformation and modified strain gradient theory. Vietnam J Mech 45(1):36–59
15. Fang J, Wang H, Zhang X (2019) On size-dependent dynamic behavior of rotating functionally graded Kirchhoff microplates. Int J Mech Sci 152:34–50
16. Thai S, Thai H-T, Vo TP, Patel VI (2017) Size-dependant behaviour of functionally graded microplates based on the modified strain gradient elasticity theory and isogeometric analysis. Comput Struct 190:219–241
17. Tran V-T, Nguyen T-K, Nguyen-Xuan H (2024) An intelligent computational iBCMO-DNN algorithm for stochastic thermal buckling analysis of functionally graded porous microplates using modified strain gradient theory. J Therm Stresses 47(9):1188–1227
18. Eringen AC (1972) Nonlocal polar elastic continua. Int J Eng Sci 10(1):1–16
19. Daneshmehr A, Rajabpoor A, Hadi A (2015) Size dependent free vibration analysis of nanoplates made of functionally graded materials based on nonlocal elasticity theory with high order theories. Int J Eng Sci 95:23–35
20. Ashoori AR, Salari E, Sadough Vanini SA (2016) Size-dependent thermal stability analysis of embedded functionally graded

annular nanoplates based on the nonlocal elasticity theory. Int J Mech Sci 119:396–411
21. Pham Q-H, Nguyen P-C, Thanh Tran T (2022) Dynamic response of porous functionally graded sandwich nanoplates using nonlocal higher-order isogeometric analysis. Compos Struct 290:115565
22. Wang Q, Yao A, Dindarloo MH (2021) New higher-order shear deformation theory for bending analysis of the two-dimensionally functionally graded nanoplates. Proc Inst Mech Eng Part C: J Mech Eng Sci 235(16):3015–3028
23. Thi T-TT, Tran VK, Pham QH (2024) Static and dynamic analyses of multi-directional functionally graded porous nanoplates with variable nonlocal parameter using MITC3 + element. J Vib Eng Technol 12(3):5147–5171
24. Wang YQ, Zhang ZY (2019) Bending and buckling of three-dimensional graphene foam plates. Results Phys 13:102136
25. Pham-Tan H, Thai CH, Phung-Van P (2022) NURBS-based refined plate theory for metal foam plates with porosities. Thin-Walled Struct 175:109246
26. Tu TM, Hoa LK, Hung DX, Hai LT (2018) Nonlinear buckling and post-buckling analysis of imperfect porous plates under mechanical loads. J Sandw Struct Mater 22(6):1910–1930
27. Phung-Van P, Ferreira AJM, Nguyen-Xuan H, Thai Chien H (2021) A nonlocal strain gradient isogeometric nonlinear analysis of nanoporous metal foam plates. Eng Anal Boundary Elements 130:58–68
28. Sobhy M, Zenkour AM, Abazid MA (2022) Hygrothermal wave dispersion analysis of metal foam microplates strengthened by graphene embedded in a viscoelastic medium under 2D magnetic field effect. Mech Adv Mater Struct 29(28):7592–7604
29. Cuong-Le T, Hoang-Le M, Ferreira AJM, Abdel Wahab M (2022) Small size-effect isogeometric analysis for linear and nonlinear responses of porous metal foam microplate. Compos Struct 285:115189
30. Ritz W (2009) Über eine neue Methode zur Lösung gewisser Variationsprobleme der mathematischen Physik. J für die reine und Angew Math 1909:1–61
31. Reddy JN (2003) Mechanics of laminated composite plates and shells: theory and analysis. Second Edition ed. CRC Press, Boca Raton
32. Liew KM (1992) Response of plates of arbitrary shape subject to static loading. J Eng Mech 118(9):1783–1794
33. Liew KM, Wang CM (1992) Vibration analysis of plates by the pb-2 Rayleigh–Ritz method: mixed boundary conditions, reentrant corners, and internal curved supports⁎. Mech Struct Mach 20(3):281–292
34. Nallim LG, Martinez SO, Grossi RO (2005) Statical and dynamical behaviour of thin fibre reinforced composite laminates with different shapes. Comput Methods Appl Mech Eng 194(17):1797–1822
35. Rango RF, Bellomo FJ, Nallim LG (2015) A variational Ritz formulation for vibration analysis of thick quadrilateral laminated plates. Int J Mech Sci 104:60–74
36. Mason JC, Handscomb DC (2002) Chebyshev polynomials. CRC Press
37. Li Q, Iu VP, Kou KP (2008) Three-dimensional vibration analysis of functionally graded material sandwich plates. J Sound Vib 311(1):498–515
38. Chen D, Yang J, Kitipornchai S (2019) Buckling and bending analyses of a novel functionally graded porous plate using Chebyshev–Ritz method. Arch Civil Mech Eng 19(1):157–170
39. Zhu J, Fang Z, Liu X, Zhang J, Kiani Y (2023) Vibration characteristics of skew sandwich plates with functionally graded metal foam core. Structures 55:370–378
40. Sun S, Cao D, Han Q (2013) Vibration studies of rotating cylindrical shells with arbitrary edges using characteristic orthogonal polynomials in the Rayleigh–Ritz method. Int J Mech Sci 68:180–189
41. Song X, Zhai J, Chen Y, Han Q (2015) Traveling wave analysis of rotating cross-ply laminated cylindrical shells with arbitrary boundaries conditions via Rayleigh–Ritz method. Compos Struct 133:1101–1115
42. Parashar SK, Kumar A (2015) Three-dimensional analytical modeling of vibration behavior of piezoceramic cylindrical shells. Arch Appl Mech 85(5):641–656
43. Tran V-T, Nguyen T-K, Nguyen-Xuan H, Vo TP (2024) Metaheuristic optimization algorithms for vibration and buckling analysis of laminated composite plates. Eng Anal Boundary Elem 169:105974
44. Nguyen T-K, Vo TP, Nguyen B-D, Lee J (2016) An analytical solution for buckling and vibration analysis of functionally graded sandwich beams using a quasi-3D shear deformation theory. Compos Struct 156:238–252
45. Aydogdu M (2006) Buckling analysis of cross-ply laminated beams with general boundary conditions by Ritz method. Compos Sci Technol 66(10):1248–1255
46. Nguyen N-D, Vo TP, Nguyen T-K (2020) An improved shear deformable theory for bending and buckling response of thin-walled FG sandwich I-beams resting on the elastic foundation. Compos Struct 254:112823
47. Nguyen N-D, Nguyen T-K, Vo TP, Nguyen T-N, Lee S (2019) Vibration and buckling behaviours of thin-walled composite and functionally graded sandwich I-beams. Compos Part B: Eng 166:414–427
48. Tran V-T, Nguyen T-K, Nguyen-Xuan H, Abdel Wahab M (2023) Vibration and buckling optimization of functionally graded porous microplates using BCMO-ANN algorithm. Thin-Walled Struct 182:110267
49. Barati MR, Zenkour AM (2017) Investigating post-buckling of geometrically imperfect metal foam nanobeams with symmetric and asymmetric porosity distributions. Compos Struct 182:91–98
50. Nguyen T-K, Thai H-T, Vo TP (2021) A novel general higher-order shear deformation theory for static, vibration and thermal buckling analysis of the functionally graded plates. J Therm Stresses 44(3):377–394
51. Carrera E, Brischetto S, Cinefra M, Soave M (2011) Effects of thickness stretching in functionally graded plates and shells. Compos B Eng 42(2):123–133
52. Carrera E, Zappino E (2015) Carrera unified formulation for free-vibration analysis of aircraft structures. AIAA J 54(1):280–292
53. Reddy JN (1984) A simple higher-order theory for laminated composite plates. J Appl Mech 51(4):745–752
54. Nguyen TN, Thai CH, Nguyen-Xuan H (2016) On the general framework of high order shear deformation theories for laminated composite plate structures: a novel unified approach. Int J Mech Sci 110:242–255
55. Nguyen V-H, Nguyen T-K, Thai H-T, Vo TP (2014) A new inverse trigonometric shear deformation theory for isotropic and functionally graded sandwich plates. Compos Part B: Eng 66:233–246
56. Aydogdu M (2009) A new shear deformation theory for laminated composite plates. Compos Struct 89(1):94–101
57. Nguyen NV, Tran KQ, Nguyen-Xuan H (2023) A refined quasi-3D isogeometric nonlinear model of functionally graded triply periodic minimal surface plates. Eng Comput 40:2161
58. Nouriani H, Ezzati R (2020) Application of Simpson quadrature rule and iterative method for solving nonlinear fuzzy delay integral equations. Fuzzy Sets Syst 400:147–161
59. Newmark Nathan M (1959) A method of computation for structural dynamics. J Eng Mech Div 85(3):67–94
60. Nguyen T-K, Truong-Phong Nguyen T, Vo TP, Thai H-T (2015) Vibration and buckling analysis of functionally graded sandwich

beams by a new higher-order shear deformation theory. Compos Part B: Eng 76:273–285
61. Shi P, Dong C, Shou H, Li B (2023) Bending, vibration and buckling isogeometric analysis of functionally graded porous microplates based on the TSDT incorporating size and surface effects. Thin-Walled Struct 191:111027
62. Ding Z (1996) Natural frequencies of rectangular plates using a set of static beam functions in Rayleigh–Ritz method. J Sound Vib 189(1):81–87
63. Kim CS, Young PG, Dickinson SM (1990) On the flexural vibration of rectangular plates approached by using simple polynomials in the Rayleigh–Ritz method. J Sound Vib 143(3):379–394
64. Chai Gin B (1993) Free vibration of rectangular isotropic plates with and without a concentrated mass. Comput Struct 48(3):529–533
65. Sobhy M (2013) Buckling and free vibration of exponentially graded sandwich plates resting on elastic foundations under various boundary conditions. Compos Struct 99:76–87

Engineering Analysis with Boundary Elements 169 (2024) 105974

Contents lists available at ScienceDirect

Engineering Analysis with Boundary Elements

journal homepage: www.elsevier.com/locate/enganabound

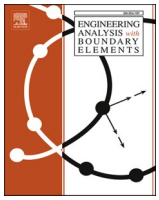

Meta-heuristic optimization algorithms for vibration and buckling analysis of laminated composite plates

Van-Thien Tran [a], Trung-Kien Nguyen [b,*], H. Nguyen-Xuan [c], Thuc P. Vo [d,*]

[a] Faculty of Civil Engineering, Ho Chi Minh City University of Technology and Education, 1 Vo Van Ngan Street, Thu Duc City, Ho Chi Minh City, Vietnam
[b] Faculty of Civil Engineering, HUTECH University, 475A Dien Bien Phu Street, Binh Thanh District, Ho Chi Minh City, Vietnam
[c] CIRTech Institute, HUTECH University, 475A Dien Bien Phu Street, Binh Thanh District, Ho Chi Minh City, Vietnam
[d] School of Computing, Engineering and Mathematical Sciences, La Trobe University, Bundoora, VIC 3086, Australia

ARTICLE INFO

Keywords:
Laminated composite plates
Vibration and buckling optimization
Unified higher-order shear deformation theory
Balance composite motion optimization
Shrimp and goby association search algorithm

ABSTRACT

The authors propose meta-heuristic optimization algorithms for the vibration and buckling analysis of laminated composite plates. This approach combines unified higher-order shear deformation theory, the Ritz method, and three optimization algorithms: the Shrimp and Goby Association Search Algorithm (SGA), Balancing Composite Motion Optimization (BCMO), and Differential Evolution (DE). The Ritz method, utilizing hybrid shape functions, is employed to solve optimization problems by using the Gram-Schmidt process to construct approximation functions. The SGA and BCMO are applied for the first time to determine the optimal buckling loads and frequencies of laminated composite plates. Numerical examples are provided to explore the influence of fiber angle, modulus ratio, and various boundary conditions on the optimal results. The findings demonstrate that BCMO and SGA are efficient and robust algorithms for addressing the optimization problems of laminated composite plates.

1. Introduction

Laminated composite plates have found extensive applications in engineering fields such as mechanical engineering, aerospace, construction, and more ([1-5]). Among the critical factors influencing their mechanical properties, the customization of fiber orientation is a pivotal element in shaping structural stiffness. In practice, achieving optimal fiber orientation demands a complex computational process, which has drawn the interest of numerous researchers employing various computational approaches.

In order to optimize responses of the laminated composite structures, meta-heuristic optimization methods have been recently considered as robust and reliable approaches for a wide range of complicated optimization problems. The core components of metaheuristic algorithms are exploration and exploitation. Exploration involves thoroughly searching the entire solution space to generate a variety of potential solutions, while exploitation focuses on refining the search within specific regions to identify the best solutions based on the knowledge gained from previous candidates. Randomization plays a crucial role in exploration, helping to avoid getting stuck in local optima. By such a way, metaheuristic optimization algorithms could approach to global optimization solutions. In general, meta-heuristic optimization algorithms [6] could be divided in three popular categories. The first category is inspired by the phenomenon of evolution observed in the natural world in which the algorithms are generally derived from the principles of Charles Darwin. Based on this approach, a number of optimization algorithms have been developed such as differential evolution (DE) [7,8], genetic algorithm (GA) [9], genetic programming [10], non-dominated sorting genetic algorithm II (NSGA-II) [11]. In general, they directly utilize the objective function and constraints to seek optimal solutions. The selection of an optimal candidate for the next generation necessitates consideration of their capacity to adapt and thrive within their ecological surroundings. Some representative earlier works are herein cited for optimization of laminated composite plates. Karakaya et al. [12] compared the optimal buckling results obtained using the GA algorithm with those obtained using the generalized pattern search algorithm. Ho-Huu et al. [13] employed the DE algorithm and the smoothed Finite Element Method (FEM) to analyze optimal buckling responses, taking into account fiber angle and layer thickness as design variables. By using the NSGA-II and GA algorithms, Kalantari et al. [14] investigated the minimum flexural strength of composite laminates with design variables being fiber angle and fiber volume fraction. Drosopoulos et al. [15] used NSGA-II and FEM to scrutinize the maximum frequency of laminate composite plate with layer thickness,

* Corresponding author.
E-mail addresses: ntkien@hutech.edu.vn (T.-K. Nguyen), t.vo@latrobe.edu.au (T.P. Vo).

https://doi.org/10.1016/j.enganabound.2024.105974
Received 28 June 2024; Received in revised form 20 August 2024; Accepted 17 September 2024

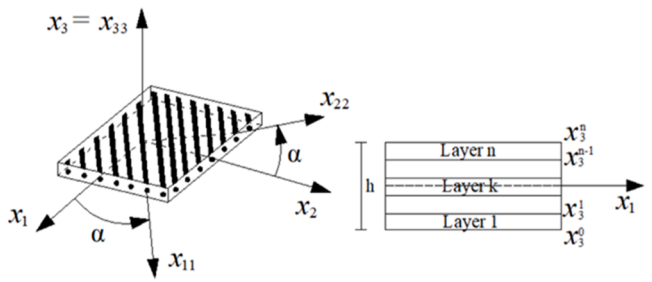

Fig. 1. Geometry of laminated composite plates

fiber distribution, and fiber angles as design variables. Moreover, the second type of meta-heuristic optimization algorithms encompasses swarm-based approaches, from which a number of optimization algorithms have been developed such as Ant colony optimization (ACO) [16], shrimp and goby association search algorithm (SGA) [17], dragonfly algorithm (DA) [18], particle swarm optimization (PSO) [19], salp swarm algorithm (SSA) [20]. The SGA is developed without depending on input parameters. Its concept is inspired by the symbiotic relationship between shrimp and goby fishes in their natural habitat. In this ecosystem, the goby uses the shrimp's burrow as a haven during the day and a regular resting place at night. Essentially, the security level of the shelter is contingent upon the shrimp's capacity to allure the gobiid fish. It is noted that the efficacy of these algorithms relies on the synchronization of a collective of particles, which impedes the ability to discern and independently assess individual particles. Instead, particles participate in collective communication to determine their subsequent course of action. A collective of agents engaged in continuous movement and interaction across several activities is often known as a particle swarm. The use of these algorithms for optimization of laminated composite plates could be mentioned in the following earlier works. By using a higher-order shear deformation theory (HSDT), isogeometric method (IGA) and the PSO algorithm, Shafei et al. [21] investigated the minimum frequency of laminated composite plates. Based on the HSDT, FEM and PSO, Vosoughi et al. ([22,23]) studied the optimal buckling loads of composite laminated plates with design variables as fiber orientations. Finally, the third set of meta-heuristic optimization algorithms comprises those influenced by physical principles. In order to direct the movement of particles throughout the optimization process, these algorithms take their cues from the most fundamental scientific laws. Some examples of these types of algorithms are the balancing composite motion optimization (BCMO) [24], the curved space optimization (CSO) [25], and the water wave optimization (WWO) [26]. These principles include the dynamics of magnetic fields, the gravitational interactions among celestial bodies, electron charge transfers, chemical processes. More importantly, these algorithms typically necessitate interrelated parameters and involve substantial computational expenses. Besides, it can be observed that the recent development of the BCMO eliminates the need for interdependent parameters to address this challenge. This approach draws inspiration from assuming the solution space operates within Cartesian coordinates, balancing the global and local search movements of potential solutions. Indeed, a potential solution can approach superior solutions to exploit local areas and extend further to explore the search landscape. Consequently, the highest-ranked individual in each generation can swiftly transition between spaces or enhance its existing local exploration.

In the realm of computational methods for structural analysis, various approaches have been employed. Among these, the Ritz method [27] can be considered as an efficient and accurate approximate solution. Due to its advantages, researchers have widely applied this method to explore static and dynamic responses in beams, plates, and shells. However, it is noted that the precision, stability, and convergence of Ritz solutions rely on the construction of approximation functions, which must satisfy geometric boundary conditions (BCs) and be computationally stable [28]. Many researchers have typically employed orthogonal polynomials (OP) due to their convergence and numerical robustness. For example, Zhou et al. [29] studied the free vibration of rectangular plates using the Chebyshev polynomial for series type solution. Chen et al. [30] studied the bending and stability of functionally graded (FG) porous plates based on the Chebyshev-Ritz method. Non-orthogonal polynomial (NOP) series offer computational simplicity but sacrifice orthogonality, impacting certain advantages. For instance, Nguyen et al. ([31]) analysed the structural responses of FG sandwich beams based on the NOP for admissible function. In addition, the penalty function method [32] offers an alternative for integrating the BCs. However, this technique results in augmented dimensions of the mass and stiffness matrices, consequently escalating computational expenses. In addition, there has been development in the utilization of the admissible function as a hybrid form ([33,34]). Moreover, the Gram-Schmidt (GS) procedure can make the admissible OP function. Liew et al. [35] studied the frequency of regular polygonal plates using the shape function created from the GS process with the initialization function chosen to satisfy at least the geometrical BCs. Based on this approach, there are some studies for laminated cylindrical shells ([36-38]) with shape functions created from the GS technique within the first function satisfying the BCs, which has caused difficulty for structures with complex geometric designs.

A brief literature survey indicates that the BCMO and SGA algorithms are recognized as efficient methods for structural optimization. However, no research has been identified that specifically employs these algorithms for solving optimization problems of laminated composite plates. This study aims to address this gap by proposing meta-heuristic optimization algorithms to minimize the critical buckling loads and fundamental frequencies of laminated composite plates. Additionally, a new hybrid shape function for the Ritz method is also presented in this study. The theoretical framework incorporates a unified HSDT, Ritz method, three optimization algorithms: BCMO, SGA and DE. To address the problems, the series-type solution employs OP generated through the Gram-Schmidt process. SGA and BCMO are employed to optimize vibration and buckling analysis of laminated composite plates, and their performance is compared with the DE algorithm. Numerical examples explore the impact of fiber angle, modulus ratio, and various BCs on the optimum results.

2. Theoretical formulation

To address shear deformation in plates, the first-order shear deformation theory is the simplest method, but it requires a shear correction factor to properly handle the free-traction boundary conditions for shear stresses [39]. In contrast, the HSDTs ([33,40-44]) with higher-order variations of in-plane displacements or both in-plane and out-of-plane displacements (Quasi-3D) ([45-49]) do not need such correction factors. However, the HSDTs ignore the thickness-stretching effect, resulting in a uniform transverse displacement across the plate's thickness. The significance of considering the thickness-stretching effect has been highlighted by Carrera et al. [50]. Although plate models incorporating higher-order variations of both in-plane and out-of-plane displacements generally provide more accurate predictions than the HSDTs, they are more complex and costly to implement due to the increased number of variables. For simplicity purpose, in the present study, the unified HSDT for laminated composite plates in Fig. 1 is referenced by ([33]) as follows:

$$\begin{aligned} u_1(x_1,x_2,x_3,t) &= \theta_1(x_1,x_2)\Psi_2(x_3) + u^0_{3,1}\Psi_1(x_3) + u^0_1(x_1,x_2) \\ u_2(x_1,x_2,x_3,t) &= \theta_2(x_1,x_2)\Psi_2(x_3) + u^0_{3,2}\Psi_1(x_3) + u^0_2(x_1,x_2) \\ u_3(x_1,x_2,x_3,t) &= u^0_3(x_1,x_2) \end{aligned} \tag{1}$$

where $\Psi_2(x_3) = H^s\Phi(x_3), \Psi_1(x_3) = H^s\Phi(x_3) - x_3$; H^s is the transverse shear stiffness; $\Phi(x_3) = \int_0^{x_3} \frac{2(1+\nu)f_{,3}}{E(x_3)}dx_3 = \int_0^{x_3} \frac{f_{,3}}{\mu(x_3)}dx_3$, and $f(x_3)$ is a higher-order component that needs to fulfill a specific condition $f_{,3}\left(x_3 =\right.$

$\pm\frac{h}{2}\Big) = 0$; u_1^0, u_2^0 and u_3^0 are membrane and transverse displacements at neutral plane; θ_1, θ_2 are rotations at neutral plane with respect to the x_1- and x_2- axis, respectively; the comma in the subscript is used to indicate the differentiation of the variable that follows.

The components of strains $\boldsymbol{\varepsilon}^T = [\,\varepsilon_{11} \quad \varepsilon_{22} \quad \gamma_{12} \quad \gamma_{13} \quad \gamma_{23}\,]$ are found as follows:

$$\boldsymbol{\varepsilon}^{(i)} = \Psi_3(x_3)\boldsymbol{\varepsilon}^{(3)} + \Psi_2(x_3)\boldsymbol{\varepsilon}^{(2)} + \Psi_1(x_3)\boldsymbol{\varepsilon}^{(1)} + \boldsymbol{\varepsilon}^{(0)} \tag{2}$$

where $\Psi_3(x_3) = \Phi_{,3}H^s$ with $\Phi_{,3}(x_3) = \frac{f_{,3}(x_3)}{\mu(x_3)}$ and,

$$\boldsymbol{\varepsilon}^{(0)} = \begin{Bmatrix} \varepsilon_{11}^{(0)} \\ \varepsilon_{22}^{(0)} \\ \gamma_{12}^{(0)} \\ \gamma_{13}^{(0)} \\ \gamma_{23}^{(0)} \end{Bmatrix} = \begin{Bmatrix} u_{1,1}^0 \\ u_{2,2}^0 \\ u_{1,2}^0 + u_{2,1}^0 \\ 0 \\ 0 \end{Bmatrix},\ \boldsymbol{\varepsilon}^{(1)} = \begin{Bmatrix} \varepsilon_{11}^{(1)} \\ \varepsilon_{22}^{(1)} \\ \gamma_{12}^{(1)} \\ \gamma_{13}^{(1)} \\ \gamma_{23}^{(1)} \end{Bmatrix} = \begin{Bmatrix} u_{3,11}^0 \\ u_{3,22}^0 \\ 2u_{3,12}^0 \\ 0 \\ 0 \end{Bmatrix} \tag{3a}$$

$$\boldsymbol{\varepsilon}^{(2)} = \begin{Bmatrix} \varepsilon_{11}^{(2)} \\ \varepsilon_{22}^{(2)} \\ \gamma_{12}^{(2)} \\ \gamma_{13}^{(2)} \\ \gamma_{23}^{(2)} \end{Bmatrix} = \begin{Bmatrix} \theta_{1,1} \\ \theta_{2,2} \\ \theta_{1,2} + \theta_{2,1} \\ 0 \\ 0 \end{Bmatrix}, \boldsymbol{\varepsilon}^{(3)} = \begin{Bmatrix} \varepsilon_{11}^{(3)} \\ \varepsilon_{22}^{(3)} \\ \gamma_{12}^{(3)} \\ \gamma_{13}^{(3)} \\ \gamma_{23}^{(3)} \end{Bmatrix} = \begin{Bmatrix} 0 \\ 0 \\ 0 \\ \theta_1 + u_{3,1}^0 \\ \theta_2 + u_{3,2}^0 \end{Bmatrix} \tag{3b}$$

The relationship between the strains and stresses for the k layer is expressed as:

$$\boldsymbol{\sigma} = \begin{Bmatrix} \sigma_{11} \\ \sigma_{22} \\ \sigma_{12} \\ \sigma_{13} \\ \sigma_{23} \end{Bmatrix} = \begin{bmatrix} \overline{Q}^{(k)}_{11} & \overline{Q}^{(k)}_{12} & \overline{Q}^{(k)}_{16} & 0 & 0 \\ \overline{Q}^{(k)}_{12} & \overline{Q}^{(k)}_{22} & \overline{Q}^{(k)}_{26} & 0 & 0 \\ \overline{Q}^{(k)}_{16} & \overline{Q}^{(k)}_{22} & \overline{Q}^{(k)}_{66} & 0 & 0 \\ 0 & 0 & 0 & \overline{Q}^{(k)}_{55} & \overline{Q}^{(k)}_{45} \\ 0 & 0 & 0 & \overline{Q}^{(k)}_{45} & \overline{Q}^{(k)}_{44} \end{bmatrix} \begin{Bmatrix} \varepsilon_{11} \\ \varepsilon_{22} \\ \gamma_{12} \\ \gamma_{13} \\ \gamma_{23} \end{Bmatrix} = \overline{\mathbf{Q}}_\varepsilon \boldsymbol{\varepsilon} \tag{4}$$

where

$$\overline{Q}_{11}^{(k)} = Q_{22}^{(k)}\sin^4\alpha + Q_{11}^{(k)}\cos^4\alpha + 2\left(2Q_{66}^{(k)} + Q_{12}^{(k)}\right)\cos^2\alpha\sin^2\alpha \tag{5a}$$

$$\overline{Q}_{12}^{(k)} = Q_{12}^{(k)}\left(\cos^4\alpha + \sin^4\alpha\right) + \left(Q_{11}^{(k)} - 4Q_{66}^{(k)} + Q_{22}^{(k)}\right)\cos^2\alpha\sin^2\alpha \tag{5b}$$

$$\overline{Q}_{22}^{(k)} = 2\left(2Q_{66}^{(k)} + Q_{12}^{(k)}\right)\cos^2\alpha\sin^2\alpha + Q_{11}^{(k)}\sin^4\alpha + Q_{22}^{(k)}\cos^4\alpha \tag{5c}$$

$$\overline{Q}_{16}^{(k)} = \left(2Q_{66}^{(k)} + Q_{12}^{(k)} - Q_{22}^{(k)}\right)\sin^3\alpha\cos\alpha + \left(Q_{11}^{(k)} - \left(Q_{12}^{(k)} + 2Q_{66}^{(k)}\right)\right)\sin\alpha\cos^3\alpha \tag{5d}$$

$$\overline{Q}_{26}^{(k)} = \left(2Q_{66}^{(k)} + Q_{12}^{(k)} - Q_{22}^{(k)}\right)\sin\alpha\cos^3\alpha + \left(Q_{11}^{(k)} - \left(Q_{12}^{(k)} + 2Q_{66}^{(k)}\right)\right)\sin^3\alpha\cos\alpha \tag{5e}$$

$$\overline{Q}_{66}^{(k)} = \left(Q_{22}^{(k)} + Q_{11}^{(k)} - 2\left(Q_{12}^{(k)} + Q_{66}^{(k)}\right)\right)\cos^2\alpha\sin^2\alpha + Q_{66}^{(k)}\left(\cos^4\alpha + \sin^4\alpha\right) \tag{5f}$$

$$\overline{Q}_{44}^{(k)} = Q_{44}^{(k)}\cos^2\alpha + Q_{55}^{(k)}\sin^2\alpha \tag{5g}$$

$$\overline{Q}_{55}^{(k)} = Q_{44}^{(k)}\sin^2\alpha + Q_{55}^{(k)}\cos^2\alpha \tag{5h}$$

$$\overline{Q}_{45}^{(k)} = \left(Q_{55}^{(k)} - Q_{44}^{(k)}\right)\cos\alpha\sin\alpha \tag{5k}$$

with α is the fiber angle in each layer (Fig. 1); $Q_{ij}^{(k)}$ of the orthotropic composite plates in the local coordinate system are given by:

$$Q_{11}^{(k)} = \frac{E_1}{1-\nu_{12}\nu_{21}}, Q_{12}^{(k)} = \frac{\nu_{12}E_2}{1-\nu_{12}\nu_{21}}, Q_{22}^{(k)} = \frac{E_2}{1-\nu_{12}\nu_{21}}, Q_{66}^{(k)} = G_{12}, Q_{44}^{(k)} = G_{23}, Q_{55}^{(k)} = G_{13} \tag{6}$$

To obtain the equations of motion, Hamilton's principle is employed:

$$\int_{t_1}^{t_2} (\delta\Pi_{SE} + \delta\Pi_V - \delta\Pi_K)dt = 0 \tag{7}$$

The variation of the strain energy $\delta\Pi_{SE}$ is given by:

$$\delta\Pi_{SE} = \int_A \boldsymbol{\sigma}\delta\boldsymbol{\varepsilon}dA = \int_A \left[\mathbf{N}_\varepsilon^{(0)}\delta\boldsymbol{\varepsilon}^{(0)} + \mathbf{N}_\varepsilon^{(1)}\delta\boldsymbol{\varepsilon}^{(1)} + \mathbf{N}_\varepsilon^{(2)}\delta\boldsymbol{\varepsilon}^{(2)} + \mathbf{N}_\varepsilon^{(3)}\delta\boldsymbol{\varepsilon}^{(3)}\right]dA \tag{8}$$

where the stress resultants can be derived based on the strains and their gradients using the following expressions:

$$\left(\mathbf{N}_\varepsilon^{(3)}, \mathbf{N}_\varepsilon^{(2)}, \mathbf{N}_\varepsilon^{(1)}, \mathbf{N}_\varepsilon^{(0)}\right) = \int_{-h/2}^{h/2} (\Psi_3, \Psi_2, \Psi_1, 1)\boldsymbol{\sigma}dx_3 \tag{9}$$

$$\begin{Bmatrix} \mathbf{N}_\varepsilon^{(0)} \\ \mathbf{N}_\varepsilon^{(1)} \\ \mathbf{N}_\varepsilon^{(2)} \\ \mathbf{N}_\varepsilon^{(3)} \end{Bmatrix} = \begin{bmatrix} \mathbf{A}^\varepsilon & \mathbf{B}^\varepsilon & \mathbf{B}_s^\varepsilon & \mathbf{0} \\ \mathbf{B}^\varepsilon & \mathbf{D}^\varepsilon & \mathbf{D}_s^\varepsilon & \mathbf{0} \\ \mathbf{B}_s^\varepsilon & \mathbf{D}_s^\varepsilon & \mathbf{H}_s^\varepsilon & \mathbf{0} \\ \mathbf{0} & \mathbf{0} & \mathbf{0} & \mathbf{A}_s^\varepsilon \end{bmatrix} \begin{Bmatrix} \boldsymbol{\varepsilon}^{(0)} \\ \boldsymbol{\varepsilon}^{(1)} \\ \boldsymbol{\varepsilon}^{(2)} \\ \boldsymbol{\varepsilon}^{(3)} \end{Bmatrix} \tag{10}$$

where the stiffness components are given:

$$\left(\mathbf{A}^\varepsilon, \mathbf{B}^\varepsilon, \mathbf{D}^\varepsilon, \mathbf{H}_s^\varepsilon, \mathbf{B}_s^\varepsilon, \mathbf{D}_s^\varepsilon, \mathbf{A}_s^\varepsilon\right) = \int_{-h/2}^{h/2} \left(1, \Psi_1, \Psi_1^2, \Psi_2^2, \Psi_2, \Psi_1\Psi_2, \Psi_3^2\right)\mathbf{Q}_\varepsilon dx_3 \tag{11}$$

The change in the work done $\delta\Pi_V$ due to compressive membrane loads ($N_1^0 = N_2^0 = N_{12}^0 = N^0$) is expressed as:

$$\delta\Pi_V = -\int_A N^0\left(u_{3,1}^0\delta u_{3,1}^0 + u_{3,2}^0\delta u_{3,2}^0 + 2u_{3,1}^0\delta u_{3,2}^0\right)dA \tag{12}$$

The variation of kinetic energy $\delta\Pi_K$ is calculated by:

$$\begin{aligned} \delta\Pi_K &= \frac{1}{2}\int_V \rho(\dot{u}_3\delta\dot{u}_3 + \dot{u}_2\delta\dot{u}_2 + \dot{u}_1\delta\dot{u}_1)dV \\ &= \frac{1}{2}\int_A \Big[I_2\left(\dot{u}_{3,1}^0\delta\dot{u}_{3,1}^0 + \dot{u}_{3,2}^0\delta\dot{u}_{3,2}^0\right) + K_2(\dot{\theta}_1\delta\dot{\theta}_1 + \dot{\theta}_2\delta\dot{\theta}_2) \\ &\quad I_0\left(\dot{u}_1^0\delta\dot{u}_1^0 + \dot{u}_2^0\delta\dot{u}_2^0 + \dot{u}_3^0\delta\dot{u}_3^0\right) + I_1\left(\dot{u}_1^0\delta\dot{u}_{3,1}^0 + \dot{u}_{3,1}^0\delta\dot{u}_1^0 + \dot{u}_2^0\delta\dot{u}_{3,2}^0 + \dot{u}_{3,2}^0\delta\dot{u}_2^0\right) \\ &\quad + J_1\left(\dot{u}_1^0\delta\dot{\theta}_1 + \dot{\theta}_1\delta\dot{u}_1^0 + \dot{u}_2^0\delta\dot{\theta}_2 + \dot{\theta}_2\delta\dot{u}_2^0\right) + J_2\left(\dot{u}_{3,1}^0\delta\dot{\theta}_1 + \dot{\theta}_1\delta\dot{u}_{3,1}^0 + \dot{u}_{3,2}^0\delta\dot{\theta}_2 + \dot{\theta}_2\delta\dot{u}_{3,2}^0\right)\Big]dA \end{aligned} \tag{13}$$

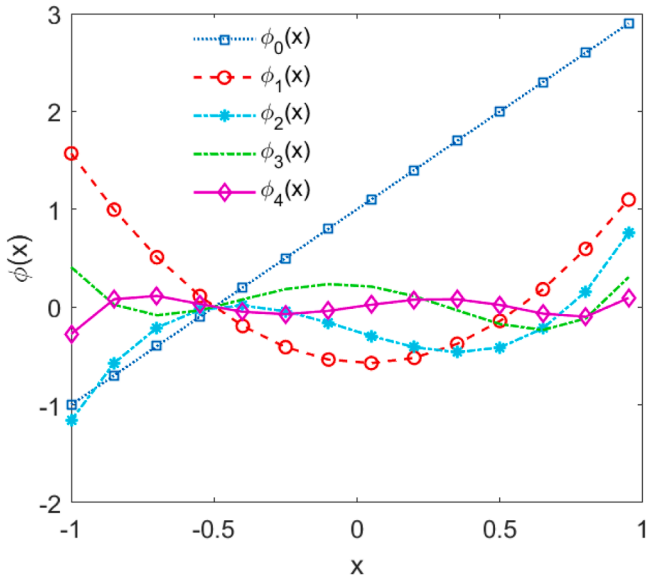

Fig. 2. The first five orthogonal polynomials

Table 1
Approximation functions of series-type solution.

BCs	$X_j(x_1)$	$Y_j(x_2)$
SSSS	$x_1(a-x_1)\phi_j$	$x_2(b-x_2)\phi_j$
CSCS	$x_1^2(a-x_1)\phi_j$	$x_2^2(b-x_2)\phi_j$
CCCC	$x_1^2(a-x_1)^2\phi_j$	$x_2^2(b-x_2)^2\phi_j$
SFSF	$x_1\phi_j$	$x_2\phi_j$

where the overdot is used to indicate the derivative of the variable with the time; K_2,J_2,J_1,I_2,I_1,I_0 are mass components of the laminated composite plate which are determined as:

$$(K_2,J_2,J_1,I_2,I_1,I_0)=\int_{-h/2}^{h/2}\left(\Psi_2^2,\Psi_1\Psi_2,\Psi_2,\Psi_1^2,\Psi_1,1\right)\rho dx_3 \tag{14}$$

3. Ritz method

The membrane and transverse displacements, as well as rotations $\left(u_1^0,u_2^0,u_3^0,\theta_1,\theta_2\right)$ can be represented through a series of shape functions in x_1- , x_2- direction ($X_i(x_1)$ and $Y_j(x_2)$) and five unknowns variables (u_{1ij},u_{2ij},u_{3ij},x_{ij},y_{ij}), expressed as follows:

$$u_2^0(x_1,x_2,t)=\sum_{i=1}^{n_1}\sum_{j=1}^{n_2}u_{2ij}(t)Y_{j,2}(x_2)X_i(x_1);u_1^0(x_1,x_2,t)$$
$$=\sum_{i=1}^{n_1}\sum_{j=1}^{n_2}u_{1ij}(t)Y_j(x_2)X_{i,1}(x_1) \tag{15a}$$

$$\theta_2(x_1,x_2,t)=\sum_{i=1}^{n_1}\sum_{j=1}^{n_2}y_{ij}(t)Y_{j,2}(x_2)X_i(x_1);\theta_1(x_1,x_2,t)$$
$$=\sum_{i=1}^{n_1}\sum_{j=1}^{n_2}x_{ij}(t)Y_j(x_2)X_{i,1}(x_1) \tag{15b}$$

$$u_3^0(x_1,x_2,t)=\sum_{i=1}^{n_1}\sum_{j=1}^{n_2}u_{3ij}(t)Y_j(x_2)X_i(x_1) \tag{15c}$$

The shape functions are pivotal in dictating the convergence rates, accuracy, and susceptibility to numerical instabilities within the Ritz solution. This critical relationship underscores the significance of meticulously crafting and analyzing shape functions, a topic detailed in prior studies ([31,34,51]). Next, the admissible orthogonal polynomial (OP) functions proposed by Bhat [52] are discussed, which are constructed using the Gram-Schmidt (GS) method [53]. These functions exhibit a rapid convergence rate, although they encounter challenges in determining the initial function. Using the GS approach is defined as follows:

$$\phi_1(x)=(x-A_1)\phi_0(x),\quad \phi_k(x)=(x-A_k)\phi_{k-1}(x)-D_k\phi_{k-2}(x) \tag{16a}$$

$$A_k=\frac{\int_c^d xw(x)\phi_{k-1}^2(x)dx}{\int_c^d w(x)\phi_{k-1}^2(x)dx};\ D_k=\frac{\int_c^d xw(x)\phi_{k-1}(x)\phi_{k-2}(x)dx}{\int_c^d w(x)\phi_{k-2}^2(x)dx} \tag{16b}$$

where $w(x)$ being the weighting function. The orthogonality is satisfied by the polynomials $\phi_k(x)$ as below:

$$\int_c^d w(x)\phi_k(x)\phi_l(x)=\begin{cases}0 & if \quad k\neq l\\ a_{kl} & if \quad k=l\end{cases} \tag{17}$$

with $w(x)=1$; $\phi_0(x)=2x+1$, and $[c,\ d]\in[-1,1]$. The first five orthogonal polynomials are shown in Fig. 2. The shape functions $X_i(x_1)$ and $Y_j(x_2)$ in Table 1 are made to satisfy the BCs in which clamped (C) and the simply-supported (S) edges are as follows:

- Clamped (C): $\theta_1=\theta_2=u_1^0=u_2^0=u_3^0=0$ at $x_1=0$, a and $x_2=0$, b
- Simply supported (S):$\theta_2=u_2^0=u_3^0=0$ at $x_1=0$, a and at $u_1^0=u_3^0=\theta_1=0x_2=0$, b

The laminated composite plate's edge conditions, a mix of simply-supported, clamped and free boundaries (SSSS, SFSF, CSCS, CCCC), are pivotal in numerical analyses. By incorporating Eq. (15) into Eqs. (8), (12), and (13), and the subsequent outcomes into Eq. (7), the characteristic motion equations are derived via the displacement vector **d**, stiffness matrix **K**and mass matrix **M** as follows:

$$\mathbf{Kd}+\mathbf{M}\ddot{\mathbf{d}}=\mathbf{0} \tag{18}$$

where

$$\mathbf{d}=\begin{bmatrix}\mathbf{u}_1 & \mathbf{u}_2 & \mathbf{u}_3 & \mathbf{x} & \mathbf{y}\end{bmatrix}^T \text{and} \mathbf{K}=\begin{bmatrix}\mathbf{K}^{11} & \mathbf{K}^{12} & \mathbf{K}^{13} & \mathbf{K}^{14} & \mathbf{K}^{15}\\ {}^T\mathbf{K}^{12} & \mathbf{K}^{22} & \mathbf{K}^{23} & \mathbf{K}^{24} & \mathbf{K}^{25}\\ {}^T\mathbf{K}^{13} & {}^T\mathbf{K}^{23} & \mathbf{K}^{33} & \mathbf{K}^{34} & \mathbf{K}^{35}\\ {}^T\mathbf{K}^{14} & {}^T\mathbf{K}^{24} & {}^T\mathbf{K}^{34} & \mathbf{K}^{44} & \mathbf{K}^{45}\\ {}^T\mathbf{K}^{15} & {}^T\mathbf{K}^{25} & {}^T\mathbf{K}^{35} & {}^T\mathbf{K}^{45} & \mathbf{K}^{55}\end{bmatrix} \tag{19}$$

Table 2
Convergence study for [0^o/90^o/90^o/0^o] plates with different BCs ($a/h=10$, $E_1/E_2=40$).

BCs	Number of series $n=n_1=n_2$					
	2	4	6	7	8	9
Normalized fundamental frequency						
SSSS	16.2797	15.5288	15.1192	15.1191	15.1192	15.1191
CSCS	21.1622	19.5302	19.2501	19.2502	19.2501	19.2501
CCCC	23.4273	22.3269	22.0249	22.0247	22.0248	22.0249
SFSF	4.1909	4.0209	4.0109	4.0110	4.0109	4.0110
Normalized critical buckling load under uniaxial compression $(N_1^0,N_2^0,N_{12}^0=1,0,0)$						
SSSS	27.1409	25.1061	23.7876	23.3042	23.3043	23.3042
CSCS	36.5583	34.8010	34.6724	34.5755	34.5757	34.5755
CCCC	46.4065	44.3619	44.1133	44.0404	44.0403	44.0404
SFSF	4.7865	4.7274	4.7109	4.7084	4.7085	4.7084

The components of **K** is formulated as:

$$K_{ijkl}^{11} = A_{11}T_{ik}^{22}S_{jl}^{00} + 2A_{16}T_{ik}^{12}S_{jl}^{10} + A_{66}T_{ik}^{11}S_{jl}^{11}$$

$$K_{ijkl}^{12} = A_{12}T_{ik}^{02}S_{jl}^{20} + A_{16}T_{ik}^{21}S_{jl}^{01} + A_{26}T_{ik}^{10}S_{jl}^{12} + A_{66}T_{ik}^{11}S_{jl}^{11}$$

$$K_{ijkl}^{\varepsilon 33} = D_{11}T_{ik}^{22}S_{jl}^{00} + D_{12}\left(T_{ik}^{02}S_{jl}^{20} + T_{ik}^{20}S_{jl}^{02}\right) + D_{22}T_{ik}^{00}S_{jl}^{22} + 4D_{66}T_{ik}^{11}S_{jl}^{11} + 4D_{16}T_{ik}^{21}S_{jl}^{01}$$
$$+4D_{26}T_{ik}^{10}S_{jl}^{21} + A_{s44}T_{ik}^{00}S_{jl}^{11} + 2A_{s45}T_{ik}^{10}S_{jl}^{01} + A_{s55}T_{ik}^{11}S_{jl}^{00} - N^0\left(T_{ik}^{11}S_{jl}^{00} + T_{ik}^{00}S_{jl}^{11} + 2T_{ik}^{10}S_{jl}^{01}\right)$$

$$K_{ijkl}^{13} = B_{11}T_{ik}^{22}S_{jl}^{00} + B_{12}T_{ik}^{02}S_{jl}^{20} + 2B_{16}T_{ik}^{21}S_{jl}^{01} + B_{26}T_{ik}^{10}S_{jl}^{12} + 2B_{66}T_{ik}^{11}S_{jl}^{11}$$

$$K_{ijkl}^{14} = B_{s11}T_{ik}^{22}S_{jl}^{00} + 2B_{s16}T_{ik}^{21}S_{jl}^{01} + B_{s66}T_{ik}^{11}S_{jl}^{11}$$

$$K_{ijkl}^{15} = B_{s12}T_{ik}^{02}S_{jl}^{20} + B_{s16}T_{ik}^{21}S_{jl}^{01} + B_{s26}T_{ik}^{10}S_{jl}^{12} + B_{s66}T_{ik}^{11}S_{jl}^{11}$$

$$K_{ijkl}^{22} = A_{22}T_{ik}^{00}S_{jl}^{22} + 2A_{16}T_{ik}^{01}S_{jl}^{21} + A_{66}T_{ik}^{11}S_{jl}^{11}$$

$$K_{ijkl}^{23} = B_{12}T_{ik}^{20}S_{jl}^{02} + B_{22}T_{ik}^{00}S_{jl}^{22} + 2B_{16}T_{ik}^{10}S_{jl}^{12} + B_{26}T_{ik}^{21}S_{jl}^{01} + 2B_{66}T_{ik}^{11}S_{jl}^{11}$$

$$K_{ijkl}^{24} = B_{s12}T_{ik}^{20}S_{jl}^{02} + B_{s16}T_{ik}^{10}S_{jl}^{12} + B_{s26}T_{ik}^{21}S_{jl}^{01} + B_{s66}T_{ik}^{11}S_{jl}^{11}$$

$$K_{ijkl}^{25} = B_{s22}T_{ik}^{00}S_{jl}^{22} + 2B_{s16}T_{ik}^{10}S_{jl}^{12} + B_{s66}T_{ik}^{11}S_{jl}^{11}$$

$$K_{ijkl}^{34} = D_{s11}T_{ik}^{22}S_{jl}^{00} + D_{s12}T_{ik}^{20}S_{jl}^{02} + 2D_{s66}T_{ik}^{11}S_{jl}^{11} + 2D_{s16}T_{ik}^{12}S_{jl}^{10}$$
$$+D_{s16}T_{ik}^{01}S_{jl}^{21} + A_{s45}T_{ik}^{01}S_{jl}^{10} + A_{s55}T_{ik}^{11}S_{jl}^{00}$$

$$K_{ijkl}^{35} = D_{s12}T_{ik}^{02}S_{jl}^{20} + D_{s22}T_{ik}^{00}S_{jl}^{22} + 2D_{s66}T_{ik}^{11}S_{jl}^{11} + D_{s16}T_{ik}^{21}S_{jl}^{01}$$
$$+2D_{s26}T_{ik}^{10}S_{jl}^{12} + A_{s45}T_{ik}^{10}S_{jl}^{01} + A_{s44}T_{ik}^{00}S_{jl}^{11}$$

$$K_{ijkl}^{44} = H_{s11}T_{ik}^{22}S_{jl}^{00} + H_{s66}T_{ik}^{11}S_{jl}^{11} + 2H_{s16}T_{ik}^{21}S_{jl}^{01} + A_{s55}T_{ik}^{11}S_{jl}^{00}$$

Table 3
Normalized fundamental frequencies of $[0^o/90^o/90^o/0^o]$ plates.

BCs	a/h	Theory	E_1/E_2				
			3	10	20	30	40
SSSS	10	TSDT [55]	7.240	9.847	12.225	13.987	15.112
		TSDT [54]	7.247	9.853	12.238	13.892	15.143
		Present	7.2137	9.8325	12.2395	13.8917	15.1192
	20	HSDT [56]	-	-	-	-	17.6620
		Present	7.4397	10.4096	13.4353	15.7603	17.6695
	25	HSDT [56]	-	-	-	-	18.0875
		Present	7.4825	10.5176	13.6504	16.0987	18.1445
CSCS	10	Present	9.8392	13.6002	16.4517	18.1279	19.2501
	20	Present	10.3734	15.1558	19.6100	22.7754	25.1996
CCCC	10	Present	12.7654	17.1590	19.8039	21.1663	22.0249
	20	Present	13.8842	20.5707	26.0621	29.5058	31.8833
SFSF	10	Present	1.4622	2.2829	3.0152	3.5623	4.0109

Table 4
Normalized fundamental frequencies of $[0^o/90^o/0^o]$ plates ($\overline{\omega}_1 = \left(\omega a^2/\pi^2\right)/\sqrt{\rho h/\left(E_2 h^3/(12(1-\nu_{12}\nu_{21}))\right)}$).

BCs	a/h	Theory	E_1/E_2				
			3	10	20	30	40
CCCC	10	HSDT [57]	-	-	-	-	7.484
		RBF-PS [58]	-	-	-	-	7.4727
		FSDT [59]	-	-	-	-	7.4106
		HSDT [56]	-	-	-	-	7.4224
		Present	4.4887	5.9410	6.7371	7.1399	7.4022
	20	HSDT [57]	-	-	-	-	11.003
		RBF-PS [58]	-	-	-	-	10.968
		FSDT [59]	-	-	-	-	10.9528
		HSDT [56]	-	-	-	-	10.9042
		Present	4.8610	7.1875	9.0084	10.1035	10.8381
	100	HSDT [57]	-	-	-	-	14.601
		RBF-PS [58]	-	-	-	-	14.4305
		FSDT [59]	-	-	-	-	14.4455
		HSDT [56]	-	-	-	-	14.3626
		Present	4.9619	7.7474	10.4816	12.6081	14.3997
CSCS	10	Present	3.5360	4.8438	5.7655	6.2794	6.6146
	20	Present	3.6949	5.3958	6.9399	8.0117	8.8148
SSSS	10	Present	2.6389	3.6286	4.4577	4.9853	5.3561
	20	Present	2.6654	3.7800	4.8782	5.7026	6.3659
SFSF	10	Present	0.5152	0.7987	1.0526	1.2421	1.3967

Table 5
Normalized fundamental frequencies of [0^o/90^o] plates.

BCs	a/h	Theory	E_1/E_2				
			3	10	20	30	40
SSSS	5	3D [60]	6.2578	6.9845	7.6745	8.1763	8.5625
		RPT [61]	6.2167	6.9836	7.8011	8.4646	9.0227
		Present	6.2170	6.9676	7.7038	8.2126	8.5594
	10	RPT [61]	-	-	-	-	10.5480
		Present	6.7995	7.7912	8.8723	9.7954	10.6125
	20	RPT [61]	-	-	-	-	11.0997
		Present	6.9819	8.0413	9.2036	10.2106	11.1161
CSCS	10	Present	9.2150	10.8820	12.5490	13.8987	15.0435
	20	Present	9.6325	11.4996	13.4143	15.0219	16.4386
CCCC	10	Present	11.9659	14.3190	16.4770	18.0981	19.3846
	20	Present	12.8105	15.6519	18.4309	20.6918	22.6332
SFSF	10	Present	1.3271	1.9078	1.7282	2.2797	2.5274

$$K_{ijkl}^{45} = H_{s12}T_{ik}^{02}S_{jl}^{20} + H_{s16}T_{ik}^{21}S_{jl}^{01} + H_{s26}T_{ik}^{01}S_{jl}^{21} + H_{s66}T_{ik}^{11}S_{jl}^{11} + A_{s45}T_{ik}^{10}S_{jl}^{01}$$

$$K_{ijkl}^{55} = H_{s22}T_{ik}^{00}S_{jl}^{22} + H_{s66}T_{ik}^{11}S_{jl}^{11} + 2H_{s16}T_{ik}^{10}S_{jl}^{12} + A_{s44}T_{ik}^{00}S_{jl}^{11} \quad (20)$$

where

$$T_{ik}^{rs} = \int_0^a \frac{\partial^r X_i}{\partial x_1^r}\frac{\partial^s X_k}{\partial x_1^s}dx_1, S_{jl}^{rs} = \int_0^b \frac{\partial^r Y_j}{\partial x_2^r}\frac{\partial^s Y_l}{\partial x_2^s}dx_2 \quad (21)$$

The components of **M** are expressed as follows:

$$M_{ijkl}^{11} = I_0T_{ik}^{11}S_{jl}^{00}, M_{ijkl}^{13} = I_1T_{ik}^{11}S_{jl}^{00}, M_{ijkl}^{14} = J_1T_{ik}^{11}S_{jl}^{00}$$

$$M_{ijkl}^{22} = I_0T_{ik}^{00}S_{jl}^{11}, M_{ijkl}^{23} = I_1T_{ik}^{00}S_{jl}^{11}, M_{ijkl}^{25} = J_1T_{ik}^{00}S_{jl}^{11}$$

$$M_{ijkl}^{33} = I_2\left(T_{ik}^{00}S_{jl}^{11} + T_{ik}^{11}S_{jl}^{00}\right) + I_0T_{ik}^{00}S_{jl}^{00}$$

$$M_{ijkl}^{35} = J_2T_{ik}^{00}S_{jl}^{11}, M_{ijkl}^{34} = J_2T_{ik}^{11}S_{jl}^{00}, M_{ijkl}^{55} = K_2T_{ik}^{00}S_{jl}^{11}, M_{ijkl}^{44} = K_2T_{ik}^{11}S_{jl}^{00} \quad (22)$$

For free vibration analysis, denoting $\mathbf{d}(t) = \mathbf{d}e^{i\omega t}$, where $i^2 = -1$ denotes the imaginary unit, the results can be determined via $(\mathbf{K} - \omega^2\mathbf{M})\mathbf{d} = \mathbf{0}$. The buckling loads can be obtained from Eq. (18) when $\mathbf{M} = 0$.

4. Optimization algorithm

In this section, three algorithms are presented to identify the fiber angle α that maximizes the critical buckling loads and frequencies of laminated composite plates, with the following objective functions.

$$\begin{aligned}&\text{Maximum}\overline{\omega} = f(\alpha_i^d)\text{or}\overline{N}_{cr} = f(\alpha_i^d)\\&\text{Subjectedto} - 90^o \le \alpha_i^d \le 90^o\end{aligned} \quad (23)$$

with d is the number of layers.

Three algorithms including differential evolution (DE), shrimp and goby association search algorithm (SGA) and balancing composite motion optimization (BCMO) are used to solve the above optimization problem.

4.1. DE algorithm

Initiated by Storn and Price [7,8], the DE algorithm has numerically shown efficacy and robustness in identifying an optimum solution throughout a defined continuous domain.

Initialization: The initial distribution of the population is created in a stochastic way as follows:

$$x_{i,j} = x_j^{\min} + rand(1,d) \times \left(x_j^{\max} - x_j^{\min}\right) \quad (24)$$

with d represents the count of design variables.

Mutation: A mutated vector $\mathbf{v}_i^t$ derives from the goal vectors $\mathbf{x}_i^t$ in the current iteration through mutation. The five frequently employed mutation choices are as follows:

$$\begin{aligned}&\text{rand}/1 : \mathbf{v}_i^t = \mathbf{v}_{T_1}^t + F\left(\mathbf{v}_{T_2}^t - \mathbf{v}_{T_3}^t\right); \text{best}/1 : \mathbf{v}_i^t = \mathbf{v}_{best}^t + F\left(\mathbf{v}_{T_1}^t - \mathbf{v}_{T_2}^t\right)\\&\text{current} - \text{to} - \text{best}/1 : \mathbf{v}_i^t = J\left(\mathbf{x}_{T_1}^t - \mathbf{x}_{T_2}^t\right) + J\left(\mathbf{x}_{best}^t - \mathbf{x}_i^t\right) + \mathbf{x}_{best}^t\\&\text{rand}/2 : \mathbf{v}_i^t = \mathbf{x}_{T_1}^t + J\left(\mathbf{x}_{T_2}^t - \mathbf{x}_{T_3}^t\right) + J\left(\mathbf{x}_{T_4}^t - \mathbf{x}_{T_5}^t\right)\\&\text{best}/2 : \mathbf{v}_i^t = J\left(\mathbf{x}_{T_3}^t - \mathbf{x}_{T_4}^t\right) + J\left(\mathbf{x}_{T_1}^t - \mathbf{x}_{T_2}^t\right) + \mathbf{x}_{best}^t\end{aligned} \quad (25)$$

where T_1, T_2, T_3, $T_4$and T_5 consist of randomly selected integer values from within the range of [1, *NP*], *NP* is a population size; J is randomly chosen [0, 1], when each of them is entirely distinct from the index i, $v_{i,j}^t$is determined:

$$v_{i,j}^t = \begin{cases} 2x_{\min,j} - v_{i,j}^t & if \quad v_{i,j}^t < x_{\min,j} \\ 2x_{\max,j} - v_{i,j}^t & if \quad v_{i,j}^t < x_{\max,j} \\ v_{i,j}^t & \text{otherwise} \end{cases} \quad (26)$$

Crossover: During this stage, a crossover mechanism enhances the variety among individual vectors $\mathbf{u}_i^t$ within the present population.

$$u_{i,j}^t = \begin{cases} u_{i,j}^t & if \quad j = L \quad or \quad rand \le [0.1,1] \\ x_{i,j}^t & \text{otherwise} \end{cases} \quad (27)$$

Selection: This process aims to pick superior individuals from the current population for the subsequent iteration.

$$\mathbf{x}_i^{t+1} = \begin{cases} \mathbf{x}_i^t & if \quad f(\mathbf{u}_i^t) \le f(\mathbf{x}_i^t) \\ \mathbf{u}_i^t & \text{otherwise} \end{cases} \quad (28)$$

4.2. SGA algorithm

Sang-To et al. [17] first has introduced SGA algorithm, which showed the efficacy in addressing high-dimensional single-objective issues of varying complexity.

The initial population:

$$B_i^{t+1} = B_i^t + \beta r_1 \otimes \left(S* - B_i^t\right) \quad (29)$$

where B is the position vector of an individual; S^* denotes the positional vector of the finest burrow; d is number of items; $\beta \in [2, 1]$ is linear function; $r_1 \in (0, 1)$.

Global Search: the mathematical modeling of signal transmission is expressed as:

$$B_{m,d}^{t+1} = r_2 \times G_{m,d}^t; \; B_{i,d}^{t+1} = r_2 \times (ub_d - lb_d) + lb_d \quad (30)$$

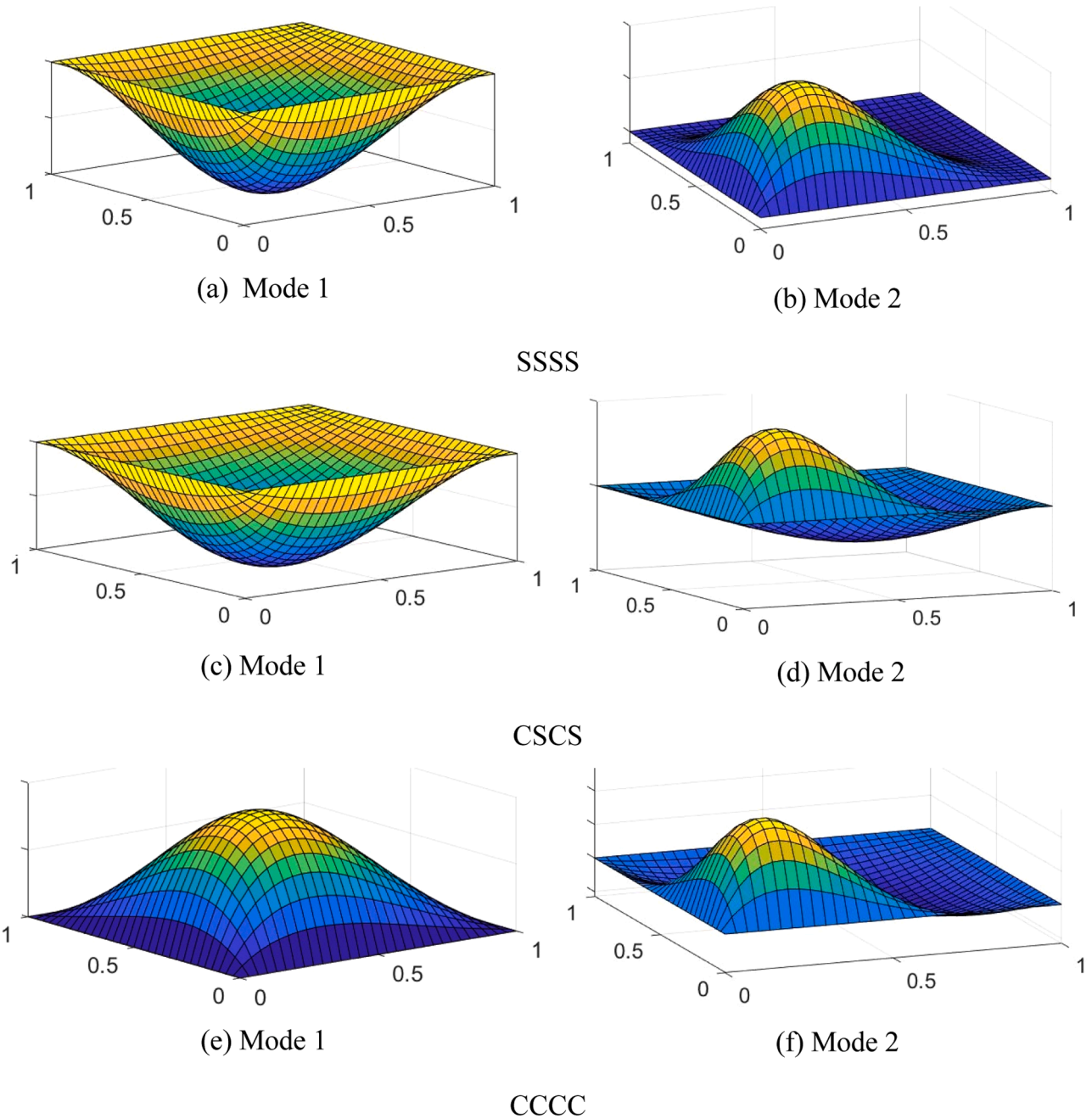

Fig. 3. Mode shapes of vibration of laminated composite plates $a/h = 10$, $E_1/E_2 = 40$, $[0^o/90^o/0^o]$, $\overline{\omega}_1 = \left(\omega a^2/\pi^2\right)/\sqrt{\rho h/\left(E_2 h^3/(12(1-\nu_{12}\nu_{21}))\right)}$

Table 6
Normalized critical buckling of $[0^o/90^o/90^o/0^o]$ plates under uniaxial compression $\left(N_1^0, N_2^0, N_{12}^0 = 1, 0, 0\right)$.

BCs	a/h	Theory	E_1/E_2				
			3	10	20	30	40
SSSS	10	HSDT [56]	5.4418	10.0208	15.4010	19.7810	23.4383
		TSDT [62]	5.3933	9.9401	15.2945	19.6644	23.3401
		TSDT [63]	5.3884	9.9303	15.2841	19.6558	23.3152
		Present	5.3600	9.9008	15.4386	19.8632	23.3042
	20	TSDT [63]	-	-	-	-	31.6975
		Present	5.6353	11.0146	18.3350	25.2412	31.7690
CSCS	10	Present	8.4138	16.2424	24.3199	30.1327	34.5755
	20	Present	9.1960	19.6748	33.1939	45.2623	56.1154
CCCC	10	Present	13.0602	24.7163	34.3922	40.1873	44.0404
	20	Present	15.2033	34.0280	56.3164	74.5690	89.8246
SFSF	10	Present	0.6486	1.5315	2.6548	3.7065	4.7084

Table 7
Normalized critical buckling of $[0^o/90^o/0^o]$ plates under biaxial compression $(N_1^0, N_2^0, N_{12}^0 = 1,1,0)$.

BCs	a/h	Theory	E_1/E_2				
			3	10	20	30	40
SSSS	10	HSDT [64]	-	4.963	7.516	9.056	10.259
		TSDT [65]	-	4.977	7.544	8.942	10.109
		TSDT [62]	-	4.916	7.448	8.820	9.9755
		TSDT [63]		4.9130	7.4408	8.7550	9.8795
		Present	2.7091	4.9492	7.5045	8.8676	10.0343
	20	TSDT [63]	-	-	-	-	13.0239
		Present	2.8325	5.5194	8.9582	11.0737	13.0866
CSCS	10	Present	4.3300	7.5574	9.8814	11.4624	12.8231
	20	Present	4.7207	9.2268	13.2198	16.5097	19.4522
CCCC	10	Present	6.7537	10.7581	13.1204	14.8401	16.2244
	20	Present	7.7957	14.2191	19.5382	23.9094	27.6485
SFSF	10	Present	0.3374	0.7598	1.2257	1.6005	1.9244

Table 8
Normalized shear buckling of $[0^o/90^o/90^o/0^o]$ plates $(N_1^0, N_2^0, N_{12}^0 = 0,0,1)$, $a/h = 10$.

BCs	E_1/E_2				
	3	10	20	30	40
SSSS	11.0219	17.9481	24.2755	28.5083	31.4874
CSCS	13.4321	21.2794	19.2607	31.1782	33.5337
CCCC	15.5753	23.7884	29.5902	33.0073	35.3192
SFSF	0.6950	1.4574	2.5695	3.6911	4.8029

with *lb* and *ub* are lower and upper boundaries. $B_{i,d}^t$ indicates the d^{th}information component of shrimp;$B_{m,d}^t$ is the d^{th}information of gobiid fish.

Local Search: The weakest candidates are placed into the top two shelters to enhance survival, concurrently bolstering the efficacy of local search process.

$$B_i^{t+1} = S_1^t \otimes (1 + \varsigma \times r_3); B_i^{t+1} = S_2^t \otimes (1 + \varsigma \times r_3) \tag{31}$$

where S_1^t, S_2^t represents the optimal positions of neighboring burrows; $\varsigma \in [2, 1]$; $r_3 \in (-1, 1)$.

More details regarding the SGA algorithm can be found in Ref. [17].

Table 9
Optimization critical buckling of symmetric square laminated composite plates with four layers ($a/h = 10$, $E_1/E_2 = 40$,$NP = 20$) under uniaxial compression $(N_1^0, N_2^0, N_{12}^0 = 1,0,0)$.

Iterations	Solution`	Max values	$\alpha^{(1)}$	α^2	$\alpha^{(3)}$	$\alpha^{(4)}$	Call function	Determinate$[0^o/90^o/90^o/0^o]$
SSSS								
500	FEM-DE [13]	30.7692	-39	42	42	-39	840	23.3042
100	Ritz-BCMO	36.9822	-37	39	39	-37	20	
	Ritz-SGA	36.9822	-37	39	39	-37	27	
	Ritz-DE	36.9822	-37	39	39	-37	50	
SFSF								
100	Ritz-BCMO	17.2807	30	-60	-60	30	20	4.7084
	Ritz-SGA	17.2807	30	-60	-60	30	27	
	Ritz-SGA	17.2807	30	-60	-60	30	50	
CSCS								
100	Ritz-BCMO	39.5512	31	-48	-48	31	20	34.5755
	Ritz-SGA	39.5512	31	-48	-48	31	27	
	Ritz-DE	39.5512	31	-48	-48	31	50	
CCCC								
100	Ritz-BCMO	44.4767	-10	85	85	-10	20	44.0404
	Ritz-SGA	44.4767	-10	85	85	-10	27	
	Ritz-DE	44.4767	-10	85	85	-10	50	

Table 10
Optimization critical buckling of square laminated composite plates with four layers ($a/h = 10$, $E_1/E_2 = 40$,$NP = 20$) under uniaxial compression $(N_1^0, N_2^0, N_{12}^0 = 1,0,0)$.

BCs	Iterations	Solution	Max values	$\alpha^{(1)}$	α^2	$\alpha^{(3)}$	$\alpha^{(4)}$	Call function
SSSS	12	Kriging-IPSO [66]	35.4351	36	-37	36	-36	20
	20	Ritz-BCMO	36.9569	37	-33	36	-39	7
		Ritz-SGA	36.9569	37	-33	36	-39	12
		Ritz-DE	36.9569	37	-33	36	-39	25
CSCS	20	Ritz-BCMO	39.3736	33	-85	33	-25	7
		Ritz-SGA	39.3736	33	-85	33	-25	12
		Ritz-DE	39.3736	33	-85	33	-25	25
CCCC	20	Ritz-BCMO	44.6772	-20	75	-70	20	7
		Ritz-SGA	44.6772	-20	75	-70	20	12
		Ritz-DE	44.6772	-20	75	-70	20	25
SFSF	20	Ritz-BCMO	17.1737	36	-16	36	-33	7
		Ritz-SGA	17.1737	36	-16	36	-33	12
		Ritz-DE	17.1737	36	-16	36	-33	25

Table 11
Optimization fundamental frequencies of square laminated composite plates with four layers ($a/h = 10$, $E_1/E_2 = 40$,$NP = 20$).

BCs	Solution	Theory	Max values	$\alpha^{(1)}$	α^{2}	$\alpha^{(3)}$	$\alpha^{(4)}$	Call function
SSSS	Asymmetric	Ritz-DE	19.1344	41	-55	43	-43	20
		Ritz-SGA	19.1344	41	-55	43	-43	7
		Ritz-BCMO	19.1344	41	-55	43	-43	5
	Symmetric	Ritz-DE	18.7588	34	-43	-43	34	20
		Ritz-SGA	18.7588	34	-43	-43	34	7
		Ritz-BCMO	18.7588	34	-43	-43	34	5
SFSF	Asymmetric	Ritz-DE	9.0532	-33	40	-39	33	20
		Ritz-SGA	9.0532	-33	40	-39	33	7
		Ritz-BCMO	9.0532	-33	40	-39	33	5
	Symmetric	Ritz-DE	9.9969	30	-37	-37	30	20
		Ritz-SGA	9.9969	30	-37	-37	30	7
		Ritz-BCMO	9.9969	30	-37	-37	30	5
CSCS	Asymmetric	Ritz-DE	21.1601	-34	77	-35	51	20
		Ritz-SGA	21.1601	-34	77	-35	51	7
		Ritz-BCMO	21.1601	-34	77	-35	51	5
	Symmetric	Ritz-DE	21.2345	48	-34	-34	48	20
		Ritz-SGA	21.2345	48	-34	-34	48	7
		Ritz-BCMO	21.2345	48	-34	-34	48	5
CCCC	Asymmetric	Ritz-DE	22.9067	47	-39	33	-49	20
		Ritz-SGA	22.9067	47	-39	33	-49	7
		Ritz-BCMO	22.9067	47	-39	33	-49	5
	Symmetric	Ritz-DE	22.9472	49	-21	-21	49	20
		Ritz-SGA	22.9472	49	-21	-21	49	7
		Ritz-BCMO	22.9472	49	-21	-21	49	5

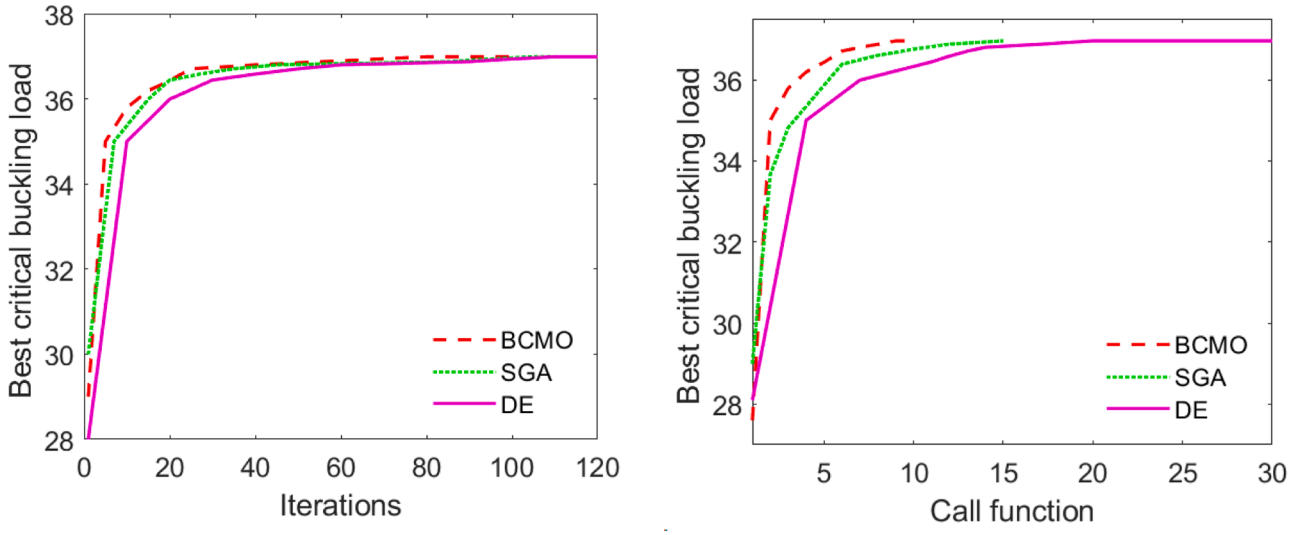

a) Symmetric layers b) Arbitrary layers

Fig. 4. Comparison of the maximum buckling load (uniaxial compression) of SSSS square laminated composite plates with size population $NP = 20$ ($E_1/E_2 = 40$)

4.3. BCMO algorithm

Le-Duc et al. [24] proposed the BCMO algorithm, which is a population-based optimization technique that aims to achieve a global optimum by skillfully balancing the composite motion properties of individual entities. The process of achieving a balance between global and local search is facilitated by employing a probabilistic model of selection, which in turn creates a mechanism for movement for each individual.

Initialization: The population is established in a random manner shows that:

$$x_i = x_j^L + rand(1,d) \times \left(x_i^U - x_j^L\right) \tag{32}$$

wherex_i^U andx_i^L are the upper and lower bounds of the i^{th} − individual; d is number of parameter applied.

Immediate global point and optimal individual: The global point x_{Oin}^t, which represents the current global optimum, is determined by the previous best point x_1^{t-1}, in relation to a trial u_1^t, utilizing the objective function.

$$x_{Oin}^t = \begin{cases} u_1^t & iff\left(u_1^t\right) < f\left(x_1^{t-1}\right) \\ x_1^{t-1} & otherwise \end{cases} \tag{33}$$

where u_1^t is calculated as follows based on data about the current generation's population:

$$u_1^t = \left(x^U + x^L\right)\Big/2 + v_{k1/k2}^t + v_{k2/1}^t \tag{34}$$

where $v_{k1/k2}^t$and $v_{k2/1}^t$ are determined using $L_{LS} = 1$as follows:

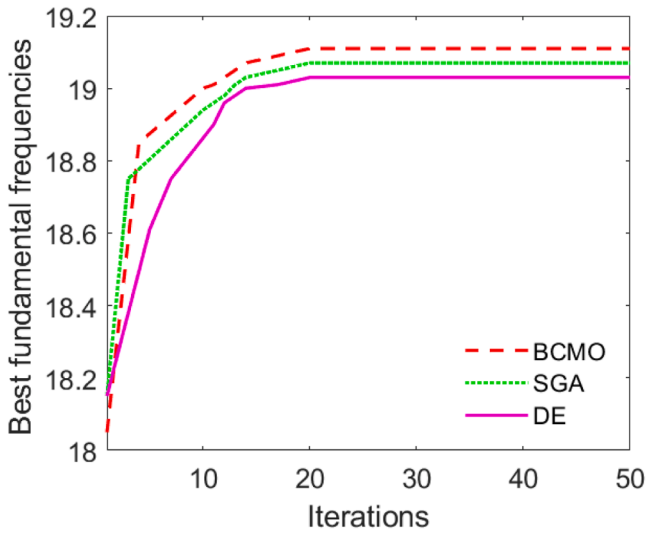

Fig. 5. Comparison of the maximum fundamental frequencies for SSSS square laminated composite plates with size population $NP = 20 (E_1/E_2 = 40)$

$$v_{i/j} = -(x_i + x_j)L_{LS} \times \begin{cases} rand(1,d) & if \quad TV_j > 0.5 \\ -rand(1,d) & otherwise \end{cases}, \tag{35}$$

Coordinated movement of individuals within the solution space: In the context of BCMO, the motion of the global search v_j which is determined:

$$v_j = -(x_j + x_{Oin})L_{GS} \times \begin{cases} e^{-\frac{1}{d}\frac{j}{NP}r_j^2} & if \quad TV_j > 0.5 \\ e^{-\frac{1}{d}\left(1-\frac{j}{NP}\right)r_j^2} & otherwise \end{cases} \tag{36}$$

whereNP is the population size; $r_j = \|x_j - x_{Oin}\|$

The probabilities for these v_{ik} cases are identical and can be calculated in the following manner:

$$G(v_{in}) = G(v_{i/j}) \times G(v_j) = 0.5 \times 0.5 = 0.25n = 1, ..., 4 \tag{37}$$

The i^{th} individual's revised position in the succeeding generation is as follows:

$$x_i^{t+1} = x_i^t + v_{i/j} + v_j \tag{38}$$

Further information regarding the BCMO algorithm is available in Ref. [24].

5. Numerical examples

Several numerical examples are conducted to explore vibration and buckling behaviors of laminated composite plates. Convergence and verification are carried out first and then DE, SGA and BCMO algorithms are employed to determine their optimal frequencies and buckling loads. The analysis involves employing the shear function $\Phi(x_3) = \cot^{-1}(h/x_3) - (16x_3^3)/(15h^3)$ ([31]). The material properties are given as:$G_{12} = G_{13} = 0.6E_2$, $G_{23} = 0.5E_2$, $v_{12} = 0.25$, $\rho = 1$ ([54]). For simplicity, the following normalized parameters are used:

$$\overline{\omega} = \frac{\omega a^2}{h}\sqrt{\frac{\rho}{E_2}}; \quad \overline{N}_{cr} = \frac{N_{cr}a^2}{h^3E_2} \tag{39}$$

To examine the convergence of current solutions, Table 2 displays the results of the square $[0^o/90^o/90^o/0^o]$ plates with $a/h = 10$ and $E_1 = 40E_2$. The outcomes are computed for four BCs (SSSS, CSCS, CCCC and SFSF) with equal series-type solutions in the $x_1 -$ and $x_2 -$ directions ($n_1 = n_2 = n$). The results indicate swift convergences, observed at $n = 6$ for fundamental frequencies and $n = 7$ for buckling loads. Therefore, these values will be utilized in the numerical examples.

5.1. Verification study

Tables 3-5 provide the fundamental frequencies of $[0^o/90^o/90^o/0^o]$, $[0^o/90^o/0^o]$ and $[0^o/90^o]$ square plates with various BCs. For SSSS

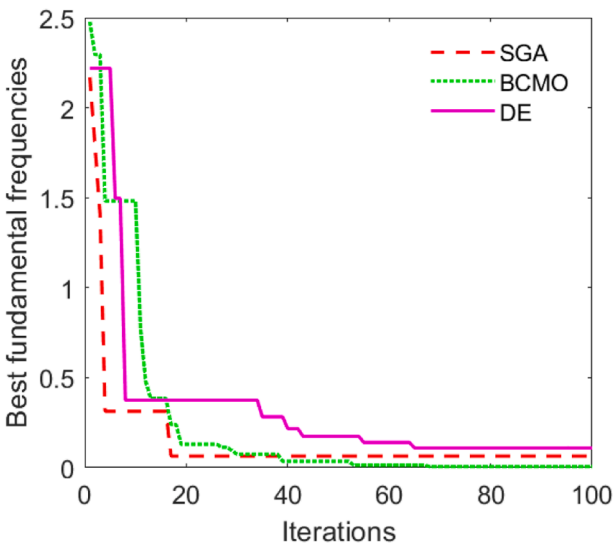

a) The fundamental frequencies

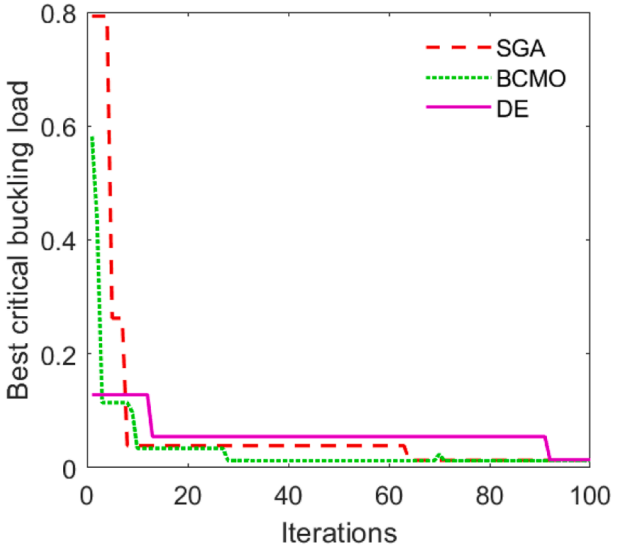

b) Critical buckling load under biaxial compression

Fig. 6. Comparison of minimum fundamental frequency and critical buckling load of SSSS square laminated composite plates with size population $NP = 20$ ($E_1/E_2 = 40$)

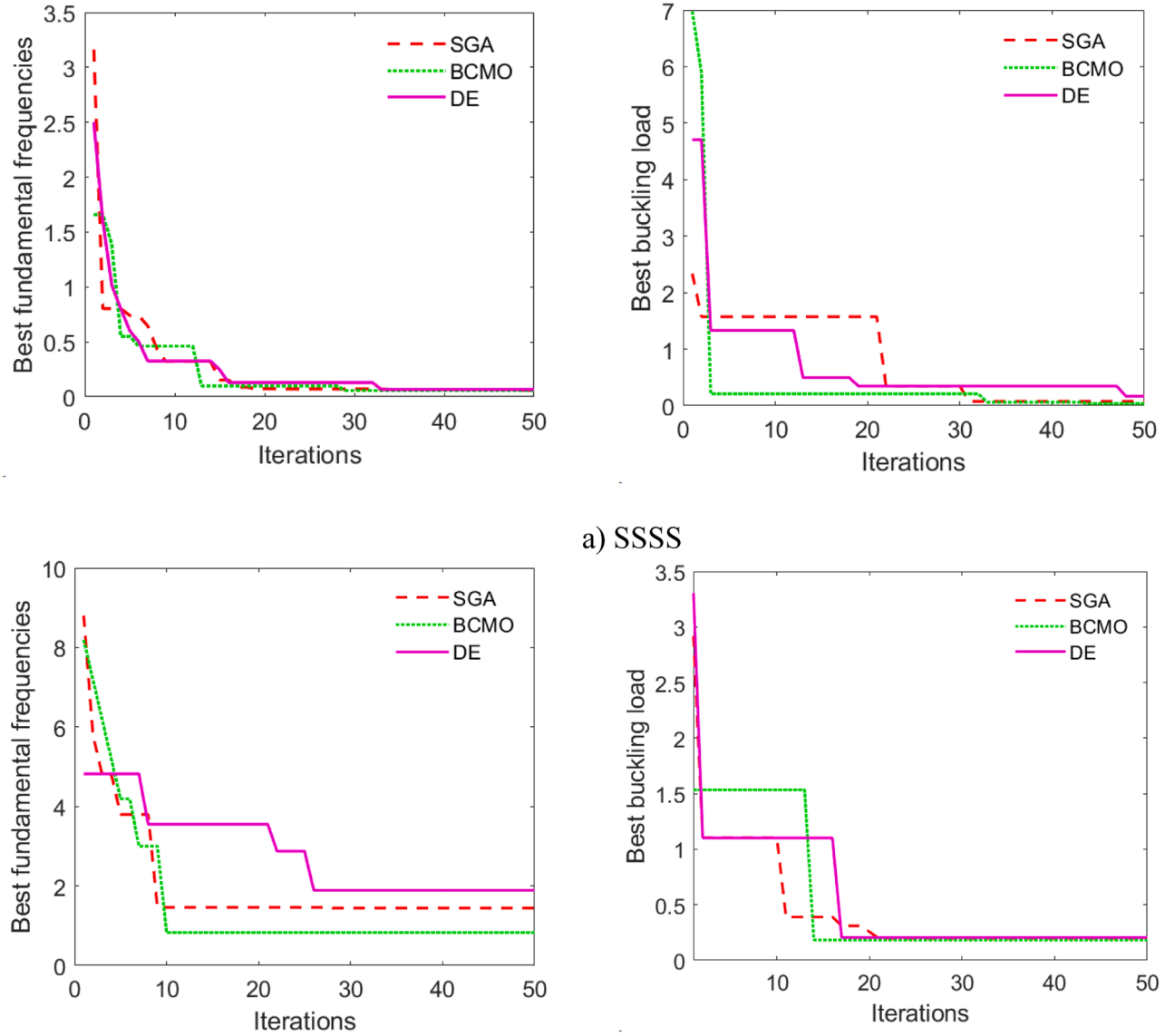

Fig. 7. Comparison of minimum fundamental frequency and critical buckling load of SSSS and CCCC square laminated composite plates with size population $NP = 50(E_1/E_2 = 40)$

plates, the obtained solutions in Table 3 are compared with those who used the third-order shear deformation theory (TSDT) ([54],[55]) with $a/h = 10$ and Thai et al. [56] using HSDT and FEM with NS-DSG3 element with $a/h = 20$ and 25. For CCCC plates, the present results in Table 4 are compared with those previously reports by Thai et al. [56], Zhen and Wanji [57], Ferreira and Fasshauer [58], Ferreira et al. [59] for case $E_1/E_2 = 40$. The results listed in Table 5 are compared with those published by Noor [60] using 3D elasticity theory with $a/h = 5$ and Thai et al. [61] using a refined plate theory (RPT) with $a/h = 5$, 10 and 20. It's evident that the present solutions exhibit strong agreement across all cases, with errors consistently below one percentage. The first two free vibration mode shapes of the square composite plates are displayed for illustration purposes in Fig. 3. Some new results are also provided in Tables 3-5 for other BCs with $a/h = 10$ and 20. It can be seen that for all BCs when modulus ratio E_1/E_2 and a/h increase, the natural frequencies increase. The critical buckling loads of $[0^o/90^o/90^o/0^o]$ plates under uniaxial compression $(N_1^0, N_2^0, N_{12}^0 = 1, 0, 0)$ and shear $(N_1^0, N_2^0, N_{12}^0 = 0, 0, 1)$ as well as of $[0^o/90^o/0^o]$ plates under biaxial compression $(N_1^0, N_2^0, N_{12}^0 = 1, 1, 0)$ are given in Tables 6-8 with different BCs. The numerical findings closely align with those reported in the literature for both uniaxial compression ([56,62,63]) and biaxial compression ([62-65]) cases. Hence, the present Ritz method is reliable for optimization vibration and buckling analysis of laminated composite plates.

5.2. Optimization study

In this section, the optimum results of the fundamental frequencies and buckling loads for uniaxial compression $(N_1^0, N_2^0, N_{12}^0 = 1, 0, 0)$ of four-layer square laminated composite plates ($a/h = 10$, $E_1/E_2 = 40$) with different BCs are investigated. Tables 9-11 show the results of three different algorithms (DE, SGA, and BCMO) with the population distribution $NP = 20$. By comparing the results from Tables 8 and 9, it is evident that the optimal responses obtained in the present study are in agreement with those reported by Ho-Huu et al. [13] using FEM-DE for

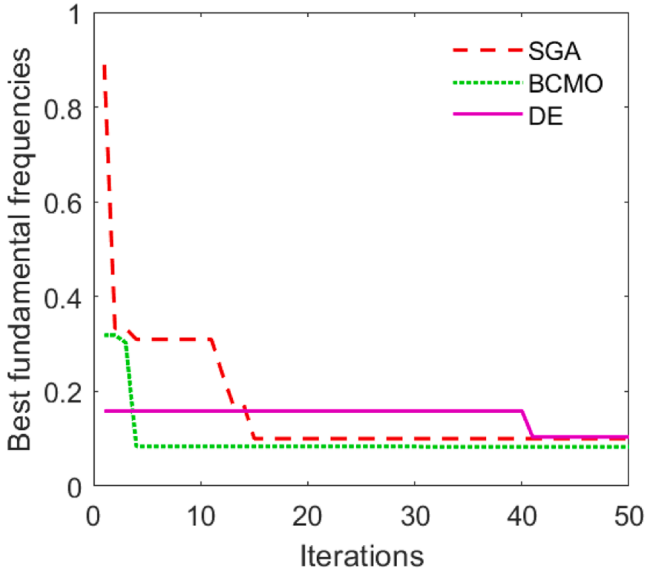

Fig. 8. Comparison of minimum fundamental frequency of CSCS square laminated composite plates with size population $NP = 50(E_1/E_2 = 40)$

symmetric lay-up and by Keshtegar et al. [66] using Kriging-IPSO for arbitrary lay-up. For minimum buckling loads and fundamental frequencies of SSSS plate, the optimal fiber angles are $[-37^o/39^o/39^o/-37^o]$ and $[34^o/-43^o/-43^o/34^o]$ for symmetric lay-ups as well as $[37^o/-33^o/36^o/-39^o]$ and $[41^o/-55^o/43^o/-43^o]$ for arbitrary ones, respectively, according to all three algorithms (BCMO, SGA, and DE). A comparative analysis of cost computation performance, involving the call function, is provided in Tables 9-11 to assess the effectiveness of the optimization algorithms. The number of call function for the BCMO algorithm is the smallest (20, 7, and 5), while the DE algorithm has the largest number (50, 25, and 20) for buckling and vibration optimization. In Table 11, the BCMO algorithm requires the fewest call function, totalling five, for optimizing fundamental frequencies. The results of the objective function (OF) for the BCMO algorithm are better than those of the SGA and DE algorithms. Additionally, new optimal results for laminated composite plates with arbitrary lay-ups and BCs are provided as a reference for future studies. To compare the efficacy of various algorithms, Figs. 4 and 5 present the convergence histories of natural frequencies and buckling loads of SSSS plates obtained using three different algorithms: DE, SGA, and BCMO. It is evident that the SGA and BCMO algorithms converge faster than the DE one. For the same number of call function, BCMO algorithm requires the fewest iterations (Fig. 4a), and for the same number of iterations, it also has the fewest call function (Fig. 4b). It should be noted that the comparison is not solely based on computational cost but extends to the effectiveness of the algorithms in achieving optimal solutions. Interestingly, while the call function of BCMO algorithm is better than SGA algorithm, their performance varies. The OF convergence histories of three algorithms for different BCs are presented in Figs. 6-8. The change in BCs from SSSS to CCCC impacts plate stiffness and subsequently affects frequencies and buckling load values. This variation is emphasized in Figs. 6 and 7, illustrating how these changes impact the numerical results produced by the algorithms. It is observed that the BCMO algorithm consistently attains the optimal solution with notably fewer iterations than the SGA and DE algorithm in nearly all cases at the maximum iteration. These findings contribute to understanding the comparative efficiency of meta-heuristic algorithms in tackling complex optimization problems in structural engineering.

6. Conclusions

This paper studies meta-heuristic optimization algorithms for vibration and buckling analysis of laminated composite plates. The theoretical framework incorporates a unified HSDT, Ritz method and three algorithms including DE BCMO, and SGA. The obtained numerical results showed an efficiency and accuracy of the present theory in predicting the responses of laminated composite plates. The numerical findings demonstrate that:

- The novel hybrid shape functions require only the first six series to achieve the convergence and numerical stability for free vibration and seven for buckling analysis.
- The performance of Ritz-BCMO and Ritz-SGA is superior to that of Ritz-DE when comparing convergence rates and computation costs
- It is observed that the BCMO algorithm consistently achieves the optimal solution with significantly fewer iterations than both the SGA and DE algorithm in nearly all cases at the maximum iteration.
- For the minimum buckling loads and fundamental frequencies of simply-supported square laminated composite plate, the optimal fiber angles are $[-37^o/39^o/39^o/-37^o]$ and $[34^o/-43^o/-43^o/34^o]$ for symmetric lay-ups as well as $[37^o/-33^o/36^o/-39^o]$ and $[41^o/-55^o/43^o/-43^o]$ for arbitrary ones, respectively.

CRediT authorship contribution statement

Van-Thien Tran: Writing – original draft, Validation, Software, Investigation. **Trung-Kien Nguyen:** Writing – review & editing, Supervision, Methodology, Conceptualization. **H. Nguyen-Xuan:** Writing – review & editing, Supervision. **Thuc P. Vo:** Writing – review & editing, Supervision.

Declaration of competing interest

The authors declare that they have no known competing financial interests or personal relationships that could have appeared to influence the work reported in this paper.

Data availability

No data was used for the research described in the article.

References

[1] Jalili N, Laxminarayana K. A review of atomic force microscopy imaging systems: application to molecular metrology and biological sciences. Mechatronics 2004;14(8):907–45.
[2] Ozevin D. 10 - Micro-electro-mechanical-systems (MEMS) for assessing and monitoring civil infrastructures. In: Wang ML, Lynch JP, Sohn H, editors. Sensor Technologies for Civil Infrastructures. Woodhead Publishing; 2014. 265–302e.
[3] Bahreyni B, Shafai C. Application of twin-beam structures for estimation of material properties and sensor fabrication. Electr. Comput. Eng., Canada. J. 2006;31:85–8.
[4] Ilic B, Craighead HG, Krylov S, W.Senarante CObe, Neuzil O. Attogram detection using nanoelectromechanical oscillators. J Appl Phys 2004:95.
[5] Bargatin I, Kozinsky I, Roukes M. Efficient electrothermal actuation of multiple modes of high-frequency nanoelectromechanical resonators. Appl Phys Lett 2007:90.
[6] Voß S. Meta-heuristics: The State of the Art. in Local Search for Planning and Scheduling. Berlin, Heidelberg: Springer Berlin Heidelberg; 2001.
[7] Storn R, Price K. Differential evolution–a simple and efficient heuristic for global optimization over continuous spaces. J. Glob. Optim. 1997;11(4):341–59.
[8] Fleetwood K. An introduction to differential evolution. In: Proceedings of Mathematics and Statistics of Complex Systems (MASCOS) One Day Symposium, 26th November; 2004.
[9] John H, Holland. Genetic algorithms. Sci Am 1992;267(1):44–50.
[10] Koza JR, Koza JR. Genetic programming: on the programming of computers by means of natural selection, 1. MIT press; 1992.
[11] Deb K, Pratap A, Agarwal S, Meyarivan T. A fast and elitist multiobjective genetic algorithm: NSGA-II. IEEE Trans. Evolut. Comput. 2002;6(2):182–97.
[12] Karakaya Ş, Soykasap Ö. Buckling optimization of laminated composite plates using genetic algorithm and generalized pattern search algorithm. Struct. Multidiscipl. Optim. 2009;39(5):477.
[13] Ho-Huu V, Do-Thi TD, Dang-Trung H, Vo-Duy T, Nguyen-Thoi T. Optimization of laminated composite plates for maximizing buckling load using improved

differential evolution and smoothed finite element method. Compos Struct 2016; 146:132–47.
[14] Kalantari M, Dong C, Davies IJ. Effect of matrix voids, fibre misalignment and thickness variation on multi-objective robust optimization of carbon/glass fibre-reinforced hybrid composites under flexural loading. Compos. Part B: Eng. 2017; 123:136–47.
[15] Drosopoulos GA, Gogos C, Foutsitzi G. Multi-objective optimization for maximum fundamental frequency and minimum cost of hybrid graphene/fibre-reinforced nanocomposite laminates. Structures 2023;54:1593–607.
[16] Dorigo M, Birattari M, Stutzle T. Ant colony optimization. IEEE Comput Intell Mag 2006;1(4):28–39.
[17] Sang-To T, Le-Minh H, Abdel Wahab M, Thanh C-L. A new metaheuristic algorithm: Shrimp and Goby association search algorithm and its application for damage identification in large-scale and complex structures. Adv. Eng. Softw. 2023;176:103363.
[18] Mirjalili S. Dragonfly algorithm: a new meta-heuristic optimization technique for solving single-objective, discrete, and multi-objective problems. Neural Comput. Appl. 2016;27(4):1053–73.
[19] Kennedy J, Eberhart R. Particle swarm optimization. In: Proceedings of ICNN'95-international conference on neural networks. IEEE; 1995.
[20] Mirjalili S, Gandomi AH, Mirjalili SZ, Saremi S, Faris H, Mirjalili SM. Salp Swarm Algorithm: A bio-inspired optimizer for engineering design problems. Adv. Eng. Softw. 2017;114:163–91.
[21] Shafei E, Shirzad A, Rabczuk T. Dynamic stability optimization of laminated composite plates: An isogeometric HSDT formulation and PSO algorithm. Compos Struct 2022;280:114935.
[22] Vosoughi AR, Darabi A, Dehghani Forkhorji H. Optimum stacking sequences of thick laminated composite plates for maximizing buckling load using FE-GAs-PSO. Compos Struct 2017;159:361–7.
[23] Vosoughi AR, Darabi A, Anjabin N, Topal U. A mixed finite element and improved genetic algorithm method for maximizing buckling load of stiffened laminated composite plates. Aerospace Sci. Technol. 2017;70:378–87.
[24] Le-Duc T, Nguyen Q-H, Nguyen-Xuan H. Balancing composite motion optimization. Inf. Sci. 2020;520:250–70.
[25] Moghaddam, F.F., R.F. Moghaddam, and M. Cheriet, Curved space optimization: a random search based on general relativity theory. arXiv preprint arXiv:1208.2214, 2012.
[26] Zheng Y-J. Water wave optimization: a new nature-inspired metaheuristic. Comput. Oper. Res. 2015;55:1–11.
[27] Ritz, W., Über eine neue Methode zur Lösung gewisser Variationsprobleme der mathematischen Physik. 2023: p. 1-61.
[28] Reddy JN. Mechanics of Laminated Composite Plates and Shells. 2nd Edition. Boca Raton: CRC Press; 2003.
[29] Zhou D, Cheung YK, Au FTK, Lo SH. Three-dimensional vibration analysis of thick rectangular plates using Chebyshev polynomial and Ritz method. Int J Solids Struct 2002;39(26):6339–53.
[30] Chen D, Yang J, Kitipornchai S. Buckling and bending analyses of a novel functionally graded porous plate using Chebyshev-Ritz method. Arch. Civil Mech. Eng. 2019;19(1):157–70.
[31] Nguyen T-K, Truong-Phong Nguyen T, Vo TP, Thai H-T. Vibration and buckling analysis of functionally graded sandwich beams by a new higher-order shear deformation theory. Compos. Part B: Eng. 2015;76:273–85.
[32] Mantari JL, Canales FG. Free vibration and buckling of laminated beams via hybrid Ritz solution for various penalized boundary conditions. Compos Struct 2016;152: 306–15.
[33] Nguyen T-K, Thai H-T, Vo TP. A novel general higher-order shear deformation theory for static, vibration and thermal buckling analysis of the functionally graded plates. J. Therm. Stress. 2020;44(3):377–94.
[34] Tran V-T, Nguyen T-K, Nguyen PTT, Vo TP. Stochastic collocation method for thermal buckling and vibration analysis of functionally graded sandwich microplates. J. Therm. Stress. 2023;46(9):909–34.
[35] Liew KM, Lam KY. A set of orthogonal plate functions for flexural vibration of regular polygonal plates. J. Vibr. Acoust. 1991;113(2):182–6.
[36] Song X, Zhai J, Chen Y, Han Q. Traveling wave analysis of rotating cross-ply laminated cylindrical shells with arbitrary boundaries conditions via Rayleigh–Ritz method. Compos Struct 2015;133:1101–15.
[37] Sun S, Cao D, Han Q. Vibration studies of rotating cylindrical shells with arbitrary edges using characteristic orthogonal polynomials in the Rayleigh–Ritz method. Int J Mech Sci 2013;68:180–9.
[38] Parashar SK, Kumar A. Three-dimensional analytical modeling of vibration behavior of piezoceramic cylindrical shells. Arch. Appl. Mech. 2015;85(5):641–56.
[39] Nguyen T-K, Sab K, Bonnet G. First-order shear deformation plate models for functionally graded materials. Compos Struct 2008;83(1):25–36.
[40] Nguyen TN, Thai CH, Nguyen-Xuan H. On the general framework of high order shear deformation theories for laminated composite plate structures: A novel unified approach. Int J Mech Sci 2016;110:242–55.
[41] Nguyen V-H, Nguyen Trung-Kien, Thai Huu-Tai, Vo Thuc P. A new inverse trigonometric shear deformation theory for isotropic and functionally graded sandwich plates. Compos. Part B: Eng. 2014;66:233–46.
[42] Aydogdu M. A new shear deformation theory for laminated composite plates. Compos Struct 2009;89(1):94–101.
[43] Mantari JL, Oktem AS, Soares CGuedes. A new higher order shear deformation theory for sandwich and composite laminated plates. Compos. Part B: Eng. 2012;43 (3):1489–99.
[44] Zhang LW, Selim BA. Vibration analysis of CNT-reinforced thick laminated composite plates based on Reddy's higher-order shear deformation theory. Compos Struct 2017;160:689–705.
[45] Thai H-T, Vo TP, Bui TQ, Nguyen T-K. A quasi-3D hyperbolic shear deformation theory for functionally graded plates. Acta Mechanica 2014;225(3):951–64.
[46] Thai T, Vo T, Bui TQ, Nguyen T-K. A quasi-3D hyperbolic shear deformation theory for functionally graded plates. Acta Mechanica 2013:225.
[47] Habib H, Tounsi A, Houari M, Bessaim A, Bedia E. New Quasi-3D hyperbolic shear deformation theory for the static and free vibration analysis of functionally graded plates. J Eng Mech 2014;140:374–83.
[48] Neves AMA, Ferreira AJM, Carrera E, Cinefra M, Roque CMC, Jorge RMN, Soares CMM. Free vibration analysis of functionally graded shells by a higher-order shear deformation theory and radial basis functions collocation, accounting for through-the-thickness deformations. Eur. J. Mech. - A/Solids 2013;37:24–34.
[49] Mantari JL, Soares CGuedes. Generalized hybrid quasi-3D shear deformation theory for the static analysis of advanced composite plates. Compos Struct 2012;94 (8):2561–75.
[50] Carrera E, Brischetto S, Cinefra M, Soave M. Effects of thickness stretching in functionally graded plates and shells. Compos. Part B: Eng. 2011;42(2):123–33.
[51] Tran V-T, Nguyen T-K, Nguyen-Xuan H, Abdel Wahab M. Vibration and buckling optimization of functionally graded porous microplates using BCMO-ANN algorithm. Thin-Walled Struct. 2023;182:110267.
[52] Bhat RB. Natural frequencies of rectangular plates using characteristic orthogonal polynomials in rayleigh-ritz method. J. Sound Vibr. 1985;102(4):493–9.
[53] Chihara TS. An Introduction to Orthogonal Polynomials. London: Gordon and Breach Science Publishers; 1978.
[54] Reddy JNJBR, editor. Mechanics of laminated composite plates- Theory and analysis. FL: CRC Press; 1997.
[55] Liu L, Chua LP, Ghista DN. Mesh-free radial basis function method for static, free vibration and buckling analysis of shear deformable composite laminates. Compos Struct 2007;78(1):58–69.
[56] Thai CH, Tran LV, Tran DT, Nguyen-Thoi T, Nguyen-Xuan H. Analysis of laminated composite plates using higher-order shear deformation plate theory and node-based smoothed discrete shear gap method. Appl. Math. Model. 2012;36(11): 5657–77.
[57] Zhen W, Wanji C. Free vibration of laminated composite and sandwich plates using global–local higher-order theory. J. Sound Vibr. 2006;298(1):333–49.
[58] Ferreira AJM, Fasshauer GE. Analysis of natural frequencies of composite plates by an RBF-pseudospectral method. Compos Struct 2007;79(2):202–10.
[59] Ferreira AJM, Castro LMS, Bertoluzza S. A high order collocation method for the static and vibration analysis of composite plates using a first-order theory. Compos Struct 2009;89(3):424–32.
[60] Noor AK. Free vibrations of multilayered composite plates. AIAA J 1973;11(7): 1038–9.
[61] Thai H-T, Kim S-E. Free vibration of laminated composite plates using two variable refined plate theory. Int J Mech Sci 2010;52(4):626–33.
[62] Thanh C-L, Ferreira AJM, Abdel Wahab M. A refined size-dependent couple stress theory for laminated composite micro-plates using isogeometric analysis. Thin-Walled Struct. 2019;145:106427.
[63] Thai CH, Ferreira AJM, Bordas SPA, Rabczuk T, Nguyen-Xuan H. Isogeometric analysis of laminated composite and sandwich plates using a new inverse trigonometric shear deformation theory. Eur. J. Mech. - A/Solids 2014;43:89–108.
[64] Khdeir AA, Librescu L. Analysis of symmetric cross-ply laminated elastic plates using a higher-order theory: Part II—Buckling and free vibration. Compos Struct 1988;9(4):259–77.
[65] Thai CH, Nguyen-Xuan H, Bordas SPA, Nguyen-Thanh N, Rabczuk T. Isogeometric analysis of laminated composite plates using the higher-order shear deformation theory. Mech Adv Mater Struct 2015;22(6):451–69.
[66] Keshtegar B, Nguyen-Thoi T, Truong TT, Zhu S-P. Optimization of buckling load for laminated composite plates using adaptive Kriging-improved PSO: A novel hybrid intelligent method. Defence Technol. 2021;17(1):85–99.

Vietnam Journal of Mechanics, Vol. 45, No. 1 (2023), pp. 36 – 59
DOI: https://doi.org/10.15625/0866-7136/17552

STATIC AND VIBRATION ANALYSIS OF FUNCTIONALLY GRADED MICROPLATE WITH POROSITIES BASED ON HIGHER-ORDER SHEAR DEFORMATION AND MODIFIED STRAIN GRADIENT THEORY

Van-Thien Tran[1], **Van-Hau Nguyen**[1,*], **Trung-Kien Nguyen**[2], **Thuc P. Vo**[3]
[1]*Faculty of Civil Engineering, Ho Chi Minh City University of Technology an Education, 1 Vo Van Ngan street, Thu Duc City, Ho Chi Minh City, Vietnam*
[2]*CIRTech Institute, HUTECH University, 475A Dien Bien Phu street, Binh Thanh district, Ho Chi Minh City, Vietnam*
[3]*School of Computing, Engineering and Mathematical Sciences, La Trobe University, Bundoora, VIC 3086, Australia*
[*]E-mail: haunv@hcmute.edu.vn

Received: 16 November 2022 / Published online: 01 March 2023

Abstract. Based on fundamental equations of the elasticity theory, a unified higher-order shear deformation theory is developed for bending and free vibration analysis of functionally graded (FG) microplates with porosities. The modified strain gradient theory is employed to capture the size effects. Bi-directional series with hybrid shape functions are used to solve the problems. Several important effects including thickness-to-material length scale parameters, side-to-thickness ratio, and boundary conditions on the deflections and natural frequencies of FG porous microplates are investigated.

Keywords: bending, vibration, functionally graded microplates, porosity, modified strain gradient theory, higher-order shear deformation theory.

1. INTRODUCTION

Microstructures have been applied in many engineering fields such as atomic force microscopes, microelectromechanical systems and nano-electromechanical systems [1,2]. The recent development of functionally graded porous (FGP) materials led to a potential application, it hence requires advanced computational methods and models especially at microscales. The study on static and dynamic responses of FGP plates and shells has attracted a number of researches with various computational methods and

models [3–14], however, those classical elasticity models could not accurately predict responses of microstructures. Therefore, advanced computations theories with material length scale parameters (MLSPs) have been developed with different approaches. A number of researches has been performed for FGP microplates in which the modified coupled stress theory (MCT) are mostly used. By considering the rotation gradient in constitutive equations, the MCT with only one MLSP is known as the simplest theory accounted for the size effects [15]. Owing to its simplicity, many size-dependent FGP microplate models with different shear deformation theories based on the MCT have been developed [16–18]. By adding strain gradients into the strain energy, the modified strain gradient theory (MST) with three MLSPs was proposed by Lam et al. [19] based on the classical strain gradient theory of Mindlin [20, 21]. This theory is more general than the MCT and it can be recovered by the MST if the effects of dilatation and deviatoric stretch gradients are neglected. By its advantages, the MST has been developed for static and dynamic of FG microplates [17,22–25]. A brief literature review showed that although many studies have been performed for static and dynamic analysis of FGP microplates using different existing shear deformation plate theories and MCT, however, the investigation based on the MST is still limited, this gap needs to be studied further.

The objective of this paper is to develop a unified framework of higher-order shear deformation theory (HSDT) for static and free vibration analyses of FGP microplates based on the MST. Hamilton's principle is used to derive the governing equations of motion, which are then solved by bi-directional series-type solutions with hybrid shape functions. Several important effects such as, thickness-to-MLSP ratio, side-to-thickness ratio, boundary conditions on the deflections and natural frequencies of FGP microplates are investigated. Some results given in this paper can be used for the future references.

2. THEORETICAL FORMULATION

Consider a rectangular FGP microplate in the coordinate system (x_1, x_2, x_3) with sides $a \times b$ and thickness h. It is supposed that the FGP microplates are composed of a metal-ceramic mixture and porosity density whose effective material properties can be approximated by the following expressions [3, 26, 27]

$$P\left(x_3\right) = \left(P_c - P_m\right)\left(\frac{2x_3 + h}{2h}\right)^p + P_m - \frac{\beta}{2}\left(P_c + P_m\right), \tag{1}$$

where P_c and P_m are the properties of ceramic and metal materials, such as Young's modulus E, mass density ρ, Poisson's ratio ν; β is the porosity volume fraction, $0 \leq \beta \ll 1$; p is the power-law index which is positive and $x_3 \in [-h/2, h/2]$.

2.1. Modified strain gradient theory (MST)

The total potential energy of the FGP microplate is obtained by

$$\Pi = \Pi_U + \Pi_V - \Pi_K, \tag{2}$$

where Π_U, Π_V, Π_K are the strain energy, work done by external forces and kinetic energy of the FGP microplates, respectively. Based on the MST, the strain energy of the system Π_U is given by

$$\Pi_U = \int_V (\boldsymbol{\sigma}\boldsymbol{\varepsilon} + \mathbf{p}\xi + \boldsymbol{\tau}\boldsymbol{\eta} + \mathbf{m}\boldsymbol{\chi}) \mathrm{d}V, \tag{3}$$

where $\boldsymbol{\varepsilon}, \boldsymbol{\chi}, \boldsymbol{\xi}, \boldsymbol{\eta}$ are strains, symmetric rotation gradients, dilatation gradient and deviation stretch gradient, respectively; $\boldsymbol{\sigma}$ is Cauchy stress; $\mathbf{m}, \mathbf{p}, \boldsymbol{\tau}$ are high-order stresses corresponding with strain gradients $\boldsymbol{\chi}, \boldsymbol{\xi}, \boldsymbol{\eta}$, respectively. The components of strain ε_{ij} and strain gradients $\xi_i, \eta_{ijk}, \chi_{ij}$ are defined as follows

$$\varepsilon_{ij} = \frac{1}{2}\left(u_{i,j} + u_{j,i}\right), \quad \xi_i = \varepsilon_{mm,i}, \quad \chi_{ij} = \frac{1}{4}\left(u_{n,mj}e_{imn} + u_{n,mi}e_{jmn}\right), \tag{4a}$$

$$\eta_{ijk} = \frac{1}{3}\left(\varepsilon_{jk,i} + \varepsilon_{ki,j} + \varepsilon_{ij,k}\right) - \frac{1}{15}\left[\left(\xi_k + 2\varepsilon_{mk,m}\right)\delta_{ij} + \left(\xi_i + 2\varepsilon_{mi,m}\right)\delta_{jk} + \left(\xi_j + 2\varepsilon_{mj,m}\right)\delta_{ki}\right], \tag{4b}$$

where δ_{ij}, e_{imn} are Knonecker delta and permutation symbol, respectively; the comma in subscript is used to indicate the partial derivative with respect to the followed variable. The components of stress are calculated from constitutive as follows

$$\sigma_{ij} = \lambda\varepsilon_{kk}\delta_{ij} + 2\mu\varepsilon_{ij}, \quad m_{ij} = 2\mu l_1^2\chi_{ij}, \quad p_j = 2\mu l_2^2\xi_j, \quad \tau_{ijk} = 2\mu l_3^2\eta_{ijk}, \tag{5}$$

where λ, μ are Lamé constants; l_1, l_2, l_3 are three MLSPs.

The work done by a transverse load q of the FGP microplates is given by

$$\Pi_V = -\int_A q u_3^0 \mathrm{d}A. \tag{6}$$

The kinetic energy of the FGP microplates Π_K is expressed by

$$\Pi_K = \frac{1}{2}\int_V \rho\left(x_3\right)\left(\dot{u}_1^2 + \dot{u}_2^2 + \dot{u}_3^2\right)\mathrm{d}V. \tag{7}$$

2.2. Unified kinematics of FGP microplates

A general HSDT kinematic of FGP microplates is derived from [28,29] as follows

$$u_1\left(x_1, x_2, x_3\right) = u_1^0\left(x_1, x_2\right) + \Phi_1\left(x_3\right)u_{3,1}^0 + \Phi_2\left(x_3\right)\varphi_1\left(x_1, x_2\right), \tag{8a}$$

$$u_2\left(x_1, x_2, x_3\right) = u_2^0\left(x_1, x_2\right) + \Phi_1\left(x_3\right)u_{3,2}^0 + \Phi_2\left(x_3\right)\varphi_2\left(x_1, x_2\right), \tag{8b}$$

$$u_3\left(x_1, x_2, x_3\right) = u_3^0\left(x_1, x_2\right), \tag{8c}$$

where $\Phi_1\left(x_3\right) = H^s\Psi\left(x_3\right) - x_3, \Phi_2\left(x_3\right) = H^s\Psi\left(x_3\right)$; u_1^0, u_2^0 and u_3^0, φ_1, φ_2 are membrane and transverse displacements, rotations around the x_2- and x_1-axis at the mid-surface of FGP microplates, respectively; H^s is the transverse shear stiffness of the FGP microplates; $\Psi\left(x_3\right) = \int_0^{x_3} \frac{f_{,3}}{\mu\left(x_3\right)} dx_3$ is a shear function; $\mu\left(x_3\right) = \frac{E\left(x_3\right)}{2\left(1+\nu\right)}$ is the shear modulus; $f\left(x_3\right)$ is a higher-order term whose first derivative satisfies the free-stress boundary condition

at the top and bottom surfaces of the plates, i.e. $f_{,3}\left(x_3 = \pm\frac{h}{2}\right) = 0$. Substituting Eq. (8) into the strains and strain gradients in Eq. (4), the strains are obtained as follows

$$\boldsymbol{\varepsilon}^{(i)} = \boldsymbol{\varepsilon}^{(0)} + \Phi_1(x_3)\,\boldsymbol{\varepsilon}^{(1)} + \Phi_2(x_3)\,\boldsymbol{\varepsilon}^{(2)}, \quad \boldsymbol{\varepsilon}^{(s)} = \Phi_3(x_3)\,\boldsymbol{\varepsilon}^{(3)}, \tag{9}$$

where $\Phi_3(x_3) = H^s\Psi_{,3}$ with $\Psi_{,3}(x_3) = \dfrac{f_{,3}(x_3)}{\mu(x_3)}$ and,

$$\begin{aligned}
\boldsymbol{\varepsilon}^{(0)} &= \begin{Bmatrix} \varepsilon_{11}^{(0)} \\ \varepsilon_{22}^{(0)} \\ \gamma_{12}^{(0)} \end{Bmatrix} = \begin{Bmatrix} u_{1,1}^0 \\ u_{2,2}^0 \\ u_{1,2}^0 + u_{2,1}^0 \end{Bmatrix}, \quad \boldsymbol{\varepsilon}^{(1)} = \begin{Bmatrix} \varepsilon_{11}^{(1)} \\ \varepsilon_{22}^{(1)} \\ \gamma_{12}^{(1)} \end{Bmatrix} = \begin{Bmatrix} u_{3,11}^0 \\ u_{3,22}^0 \\ 2u_{3,12}^0 \end{Bmatrix}, \\
\boldsymbol{\varepsilon}^{(2)} &= \begin{Bmatrix} \varepsilon_{11}^{(2)} \\ \varepsilon_{22}^{(2)} \\ \gamma_{12}^{(2)} \end{Bmatrix} = \begin{Bmatrix} \varphi_{1,1} \\ \varphi_{2,2} \\ \varphi_{1,2} + \varphi_{2,1} \end{Bmatrix}, \quad \boldsymbol{\varepsilon}^{(3)} = \begin{Bmatrix} \gamma_{13}^{(0)} \\ \gamma_{23}^{(0)} \end{Bmatrix} = \begin{Bmatrix} \varphi_1 + u_{3,1}^0 \\ \varphi_2 + u_{3,2}^0 \end{Bmatrix}.
\end{aligned} \tag{10}$$

The non-zero components of dilatation gradients $\boldsymbol{\xi} = \begin{bmatrix} \xi_1 & \xi_2 & \xi_3 \end{bmatrix}^T$ are given by

$$\boldsymbol{\xi} = \boldsymbol{\xi}^{(0)} + \Phi_1\boldsymbol{\xi}^{(1)} + \Phi_2\boldsymbol{\xi}^{(2)} + \Phi_{1,3}\boldsymbol{\xi}^{(3)} + \Phi_{2,3}\boldsymbol{\xi}^{(4)}. \tag{11}$$

The non-zero components of deviatoric stretch gradients $\boldsymbol{\eta}_{ijk}$ are given by

$$\boldsymbol{\eta} = \boldsymbol{\eta}^{(0)} + \Phi_1\boldsymbol{\eta}^{(1)} + \Phi_2\boldsymbol{\eta}^{(2)} + \Phi_3\boldsymbol{\eta}^{(3)} + \Phi_{1,3}\boldsymbol{\eta}^{(4)} + \Phi_{2,3}\boldsymbol{\eta}^{(5)} + \Phi_{3,3}\boldsymbol{\eta}^{(6)}, \tag{12}$$

where $\boldsymbol{\eta}^T = \begin{bmatrix} \eta_{111} & \eta_{222} & \eta_{333} & 3\eta_{331} & 3\eta_{332} & 3\eta_{221} & 3\eta_{112} & 3\eta_{113} & 3\eta_{223} & 6\eta_{123} \end{bmatrix}$.

The rotation gradients are expressed as follows

$$\boldsymbol{\chi} = \boldsymbol{\chi}^{(0)} + \Phi_{1,3}\boldsymbol{\chi}^{(1)} + \Phi_{2,3}\boldsymbol{\chi}^{(2)} + \Phi_{1,33}\boldsymbol{\chi}^{(3)} + \Phi_{2,33}\boldsymbol{\chi}^{(4)} + \Phi_2\boldsymbol{\chi}^{(5)}, \tag{13}$$

with $\boldsymbol{\chi}^T = \begin{bmatrix} \chi_{11} & \chi_{22} & 2\chi_{12} & \chi_{33} & 2\chi_{13} & 2\chi_{23} \end{bmatrix}$. The components of $\boldsymbol{\xi}, \boldsymbol{\eta}, \boldsymbol{\chi}$ can be seen more details in Appendix A. Furthermore, the stresses and strains of FGP microplates are related by constitutive equations as follows

$$\begin{aligned}
\boldsymbol{\sigma}^{(i)} &= \begin{Bmatrix} \sigma_{11} \\ \sigma_{22} \\ \sigma_{12} \end{Bmatrix} = \begin{bmatrix} Q_{11} & Q_{12} & 0 \\ Q_{12} & Q_{22} & 0 \\ 0 & 0 & Q_{66} \end{bmatrix} \begin{Bmatrix} \varepsilon_{11} \\ \varepsilon_{22} \\ \gamma_{12} \end{Bmatrix} = \mathbf{Q}_\varepsilon^{(i)}\boldsymbol{\varepsilon}^{(i)}, \\
\boldsymbol{\sigma}^{(o)} &= \begin{Bmatrix} \sigma_{13} \\ \sigma_{23} \end{Bmatrix} = \begin{bmatrix} Q_{55} & 0 \\ 0 & Q_{44} \end{bmatrix} \begin{Bmatrix} \gamma_{13} \\ \gamma_{23} \end{Bmatrix} = \mathbf{Q}_\varepsilon^{(o)}\boldsymbol{\varepsilon}^{(s)},
\end{aligned} \tag{14a}$$

$$\mathbf{m} = \begin{Bmatrix} m_{11} \\ m_{22} \\ m_{12} \\ m_{33} \\ m_{23} \\ m_{13} \end{Bmatrix} = 2\mu l_1^2 \begin{bmatrix} 1 & 0 & 0 & 0 & 0 & 0 \\ 0 & 1 & 0 & 0 & 0 & 0 \\ 0 & 0 & 1 & 0 & 0 & 0 \\ 0 & 0 & 0 & 1 & 0 & 0 \\ 0 & 0 & 0 & 0 & 1 & 0 \\ 0 & 0 & 0 & 0 & 0 & 1 \end{bmatrix} \begin{Bmatrix} \chi_{11} \\ \chi_{22} \\ \chi_{12} \\ \chi_{33} \\ \chi_{23} \\ \chi_{13} \end{Bmatrix} = \alpha_{\chi_6}\mathbf{I}_{6\times 6}\boldsymbol{\chi}, \tag{14b}$$

$$\mathbf{p} = \begin{Bmatrix} p_1 \\ p_2 \\ p_3 \end{Bmatrix} = 2\mu l_2^2 \begin{bmatrix} 1 & 0 & 0 \\ 0 & 1 & 0 \\ 0 & 0 & 1 \end{bmatrix} \begin{Bmatrix} \xi_1 \\ \xi_2 \\ \xi_3 \end{Bmatrix} = \alpha_\xi\mathbf{I}_{3\times 3}\boldsymbol{\xi},$$

$$\boldsymbol{\tau}=\left\{\begin{array}{c}\tau_{111}\\ \tau_{222}\\ \tau_{112}\\ \tau_{221}\\ \tau_{331}\\ \tau_{332}\\ \tau_{333}\\ \tau_{113}\\ \tau_{223}\\ \tau_{123}\end{array}\right\}=2\mu_3^2\left[\begin{array}{cccccccccc}1&0&0&0&0&0&0&0&0&0\\ 0&1&0&0&0&0&0&0&0&0\\ 0&0&1&0&0&0&0&0&0&0\\ 0&0&0&1&0&0&0&0&0&0\\ 0&0&0&0&1&0&0&0&0&0\\ 0&0&0&0&0&1&0&0&0&0\\ 0&0&0&0&0&0&1&0&0&0\\ 0&0&0&0&0&0&0&1&0&0\\ 0&0&0&0&0&0&0&0&1&0\\ 0&0&0&0&0&0&0&0&0&1\end{array}\right]\left\{\begin{array}{c}\eta_{111}\\ \eta_{222}\\ \eta_{112}\\ \eta_{221}\\ \eta_{331}\\ \eta_{332}\\ \eta_{333}\\ \eta_{113}\\ \eta_{223}\\ \eta_{123}\end{array}\right\}=\alpha_\eta\mathbf{I}_{10\times10}\boldsymbol{\eta}, \quad (14c)$$

where $\alpha_\chi=2\mu l_1^2,\alpha_\xi=2\mu l_2^2,\alpha_\eta=2\mu l_3^2$, and

$$Q_{11}=\frac{E\left(x_3\right)}{1-v^2},\ Q_{22}=\frac{E\left(x_3\right)}{1-v^2},\ Q_{12}=\frac{vE\left(x_3\right)}{1-v^2},\ Q_{44}=Q_{55}=Q_{66}=\mu=\frac{E\left(x_3\right)}{2(1+v)}. \quad (15)$$

2.3. Energy principle

In order to derive the equation of motion, Hamilton's principle is used

$$\int_{t_1}^{t_2}\left(\delta\Pi_U+\delta\Pi_V-\delta\Pi_K\right)\mathrm{d}t=0, \quad (16)$$

where $\delta\Pi_U,\delta\Pi_V,\delta\Pi_K$ are the variations of strain energy, work done by external force and kinetic energy, respectively. The variation of the strain energy of FGP microplates derived from Eq. (3) as follows

$$\begin{aligned}\delta\Pi_U=&\int_A(\boldsymbol{\sigma}\delta\boldsymbol{\varepsilon}+\mathbf{p}\delta\boldsymbol{\xi}+\boldsymbol{\tau}\delta\boldsymbol{\eta}+\mathbf{m}\delta\boldsymbol{\chi})\mathrm{d}A=\int_A\Big[\mathbf{M}_\varepsilon^{(0)}\delta\boldsymbol{\varepsilon}^{(0)}+\mathbf{M}_\varepsilon^{(1)}\delta\boldsymbol{\varepsilon}^{(1)}+\mathbf{M}_\varepsilon^{(2)}\delta\boldsymbol{\varepsilon}^{(2)}\\ &+\mathbf{M}_\varepsilon^{(3)}\delta\boldsymbol{\varepsilon}^{(3)}+\mathbf{M}_\xi^{(0)}\delta\boldsymbol{\xi}^{(0)}+\mathbf{M}_\xi^{(1)}\delta\boldsymbol{\xi}^{(1)}+\mathbf{M}_\xi^{(2)}\delta\boldsymbol{\xi}^{(2)}+\mathbf{M}_\xi^{(3)}\delta\boldsymbol{\xi}^{(3)}+\mathbf{M}_\xi^{(4)}\delta\boldsymbol{\xi}^{(4)}\\ &+\mathbf{M}_\chi^{(0)}\delta\boldsymbol{\chi}^{(0)}+\mathbf{M}_\chi^{(1)}\delta\boldsymbol{\chi}^{(1)}+\mathbf{M}_\chi^{(2)}\delta\boldsymbol{\chi}^{(2)}+\mathbf{M}_\chi^{(3)}\delta\chi^{(3)}+\mathbf{M}_\chi^{(4)}\delta\boldsymbol{\chi}^{(4)}+\mathbf{M}_\chi^{(5)}\delta\boldsymbol{\chi}^{(5)}\\ &+\mathbf{M}_\eta^{(0)}\delta\boldsymbol{\eta}^{(0)}+\mathbf{M}_\eta^{(1)}\delta\boldsymbol{\eta}^{(1)}+\mathbf{M}_\eta^{(2)}\delta\boldsymbol{\eta}^{(2)}+\mathbf{M}_\eta^{(3)}\delta\boldsymbol{\eta}^{(3)}+\mathbf{M}_\eta^{(4)}\delta\boldsymbol{\eta}^{(4)}+\mathbf{M}_\eta^{(5)}\delta\boldsymbol{\eta}^{(5)}+\mathbf{M}_\eta^{(6)}\delta\boldsymbol{\eta}^{(6)}\Big]\mathrm{d}A,\end{aligned} \quad (17)$$

where the stress resultants are given by

$$\left(\mathbf{M}_\varepsilon^{(0)},\mathbf{M}_\varepsilon^{(1)},\mathbf{M}_\varepsilon^{(2)}\right)=\int_{-h/2}^{h/2}\left(1,\Phi_1,\Phi_2\right)\boldsymbol{\sigma}^{(i)}\mathrm{d}x_3,\quad \mathbf{M}_\varepsilon^{(3)}=\int_{-h/2}^{h/2}\Phi_3\boldsymbol{\sigma}^{(o)}\mathrm{d}x_3, \quad (18a)$$

$$\left(\mathbf{M}_\xi^{(0)},\mathbf{M}_\xi^{(1)},\mathbf{M}_\xi^{(2)},\mathbf{M}_\xi^{(3)},\mathbf{M}_\xi^{(4)}\right)=\int_{-h/2}^{h/2}\left(1,\Phi_1,\Phi_2,\Phi_{1,3},\Phi_{2,3}\right)\mathbf{p}\mathrm{d}x_3, \quad (18b)$$

$$\left(\mathbf{M}_\chi^{(0)},\mathbf{M}_\chi^{(1)},\mathbf{M}_\chi^{(2)},\mathbf{M}_\chi^{(3)},\mathbf{M}_\chi^{(4)},\mathbf{M}_\chi^{(5)}\right)=\int_{-h/2}^{h/2}\left(1,\Phi_{1,3},\Phi_{2,3},\Phi_{1,33},\Phi_{2,33},\Phi_2\right)\mathbf{m}\mathrm{d}x_3, \quad (18c)$$

$$\left(\mathbf{M}_\eta^{(0)},\mathbf{M}_\eta^{(1)},\mathbf{M}_\eta^{(2)},\mathbf{M}_\eta^{(3)},\mathbf{M}_\eta^{(4)},\mathbf{M}_\eta^{(5)},\mathbf{M}_\eta^{(6)}\right)=\int_{-h/2}^{h/2}\left(1,\Phi_1,\Phi_2,\Phi_3,\Phi_{1,3},\Phi_{2,3},\Phi_{3,3}\right)\boldsymbol{\eta}\mathrm{d}x_3. \quad (18d)$$

These stress resultants can be expressed in terms of the strains and its gradients (see Appendix B for more details).

The variation of work done by transverse loads derived from Eq. (6) is given by

$$\delta\Pi_V = -\int_A q\delta u_3^0 \mathrm{d}A. \tag{19}$$

The variation of kinetic energy $\delta\Pi_K$ derived from Eq. (7) is calculated by

$$\begin{aligned}\delta\Pi_K = \frac{1}{2}\int_V \rho\left(\dot{u}_1\delta\dot{u}_1 + \dot{u}_2\delta\dot{u}_2 + \dot{u}_3\delta\dot{u}_3\right)\mathrm{d}V = \frac{1}{2}\int_A \big[I_0\left(\dot{u}_1^0\delta\dot{u}_1^0 + \dot{u}_2^0\delta\dot{u}_2^0 + \dot{u}_3^0\delta\dot{u}_3^0\right)\\ + I_1\left(\dot{u}_1^0\delta\dot{u}_{3,1}^0 + \dot{u}_{3,1}^0\delta\dot{u}_1^0 + \dot{u}_2^0\delta\dot{u}_{3,2}^0 + \dot{u}_{3,2}^0\delta\dot{u}_2^0\right)\\ + J_2\left(\dot{u}_{3,1}^0\delta\dot{\varphi}_1 + \dot{\varphi}_1\delta\dot{u}_{3,1}^0 + \dot{u}_{3,2}^0\delta\dot{\varphi}_2 + \dot{\varphi}_2\delta\dot{u}_{3,2}^0\right) + K_2\left(\dot{\varphi}_1\delta\dot{\varphi}_1 + \dot{\varphi}_2\delta\dot{\varphi}_2\right)\\ + J_1\left(\dot{u}_1^0\delta\dot{\varphi}_1 + \dot{\varphi}_1\delta\dot{u}_1^0 + \dot{u}_2^0\delta\dot{\varphi}_2 + \dot{\varphi}_2\delta\dot{u}_2^0\right) + I_2\left(\dot{u}_{3,1}^0\delta\dot{u}_{3,1}^0 + \dot{u}_{3,2}^0\delta\dot{u}_{3,2}^0\right)\big]\mathrm{d}A,\end{aligned} \tag{20}$$

where $I_0, I_1, I_2, J_1, J_2, K_2$ are mass inertias of the FGP microplates which are defined as follows

$$\left(I_0, I_1, I_2, J_1, J_2, K_2\right) = \int_{-h/2}^{h/2}\left(1, \Phi_1, \Phi_1^2, \Phi_2, \Phi_1\Phi_2, \Phi_2^2\right)\rho\mathrm{d}x_3. \tag{21}$$

3. RITZ-BASED SOLUTIONS

Based on the Ritz method, the membrane and transverse displacements, rotations $\left(u_1^0, u_2^0, u_3^0, \varphi_1, \varphi_2\right)$ of the FGP microplates can be expressed in terms of the series of approximation functions and associated values of series as follows

$$u_1^0\left(x_1, x_2\right) = \sum_{i=1}^{n_1}\sum_{j=1}^{n_2} u_{1ij}R_{i,1}\left(x_1\right)P_j\left(x_2\right), \quad u_2^0\left(x_1, x_2\right) = \sum_{i=1}^{n_1}\sum_{j=1}^{n_2} u_{2ij}R_i\left(x_1\right)P_{j,2}\left(x_2\right), \tag{22a}$$

$$u_3^0\left(x_1, x_2\right) = \sum_{i=1}^{n_1}\sum_{j=1}^{n_2} u_{3ij}R_i\left(x_1\right)P_j\left(x_2\right), \quad \varphi_1\left(x_1, x_2\right) = \sum_{i=1}^{n_1}\sum_{j=1}^{n_2} x_{ij}R_{i,1}\left(x_1\right)P_j\left(x_2\right), \tag{22b}$$

$$\varphi_2\left(x_1, x_2\right) = \sum_{i=1}^{n_1}\sum_{j=1}^{n_2} y_{ij}R_i\left(x_1\right)P_{j,2}\left(x_2\right), \tag{22c}$$

where $u_{1ij}, u_{2ij}, u_{3ij}, x_{ij}, y_{ij}$ are variables to be determined; $R_i\left(x_1\right), P_j\left(x_2\right)$ are the shape functions in x_1-, x_2-direction, respectively. As a result, five unknowns of the plate only depend on two shape functions. It should be noted that the accuracy, convergence rates and numerical instabilities of the Ritz solution depends on the selection of the shape functions, which was discussed in details in [27–32]. The functions $R_i\left(x_1\right)$ and $P_j\left(x_2\right)$ given in Table 1 are constructed to satisfy the boundary conditions (BCs) at the plate edges in which two following kinematic typical BCs are considered

- Simply supported (S): $u_2^0 = u_3^0 = \varphi_2 = 0$ at $x_1 = 0, a$ and $u_1^0 = u_3^0 = \varphi_1 = 0$ at $x_2 = 0, b$.
- Clamped (C): $u_1^0 = u_2^0 = u_3^0 = \varphi_1 = \varphi_2 = 0$ at $x_1 = 0, a$ and $x_2 = 0, b$.

Table 1. Approximation functions of series solutions with different boundary conditions [28]

Boundary conditions	Approximation functions	
	$R_j(x_1)$	$P_j(x_2)$
SSSS	$x_1(a-x_1)e^{-\frac{jx_1}{a}}$	$x_2(b-x_2)e^{-\frac{jx_2}{a}}$
CCCC	$x_1^2(a-x_1)^2e^{-\frac{jx_1}{a}}$	$x_2^2(b-x_2)^2e^{-\frac{jx_2}{b}}$
SCSC	$x_1(a-x_1)^2e^{-\frac{jx_1}{a}}$	$x_2(b-x_2)^2e^{-\frac{jx_2}{b}}$

The combination of S and C on the edges leads to the different BCs, in which SSSS, SCSC, CCCC in Table 1 are chosen to investigate in this paper. Furthermore, in order to derive characteristic equations of motion of the FGP microplates, substituting the approximations in Eq. (22) into Eqs. (20), (19), (17) and then the subsequent results into Eq. (16) lead to

$$\mathbf{K}\mathbf{d}+\mathbf{M}\ddot{\mathbf{d}}=\mathbf{F}, \tag{23}$$

where $\mathbf{d}=\begin{bmatrix}\mathbf{u}_1 & \mathbf{u}_2 & \mathbf{u}_3 & \mathbf{x} & \mathbf{y}\end{bmatrix}^T$ is the displacement vector to be determined; $\mathbf{K}=\mathbf{K}^{\varepsilon}+\mathbf{K}^{\chi}+\mathbf{K}^{\tilde{\xi}}+\mathbf{K}^{\eta}$ is the stiffness matrix which is composed of those of the strains $\mathbf{K}^{\varepsilon}$, symmetric rotation gradients $\mathbf{K}^{\chi}$, dilatation gradient $\mathbf{K}^{\tilde{\xi}}$, and deviation stretch gradient $\mathbf{K}^{\eta}$; $\mathbf{M}$ is the mass matrix, and $\mathbf{F}$ is the force vector. These components are given more details as follows

$$\mathbf{K}^{\zeta}=\begin{bmatrix}\mathbf{K}^{\zeta 11} & \mathbf{K}^{\zeta 12} & \mathbf{K}^{\zeta 13} & \mathbf{K}^{\zeta 14} & \mathbf{K}^{\zeta 15}\\ {}^{T}\mathbf{K}^{\zeta 12} & \mathbf{K}^{\zeta 22} & \mathbf{K}^{\zeta 23} & \mathbf{K}^{\zeta 24} & \mathbf{K}^{\zeta 25}\\ {}^{T}\mathbf{K}^{\zeta 13} & {}^{T}\mathbf{K}^{\zeta 23} & \mathbf{K}^{\zeta 33} & \mathbf{K}^{\zeta 34} & \mathbf{K}^{\zeta 35}\\ {}^{T}\mathbf{K}^{\zeta 14} & {}^{T}\mathbf{K}^{\zeta 24} & {}^{T}\mathbf{K}^{\zeta 34} & \mathbf{K}^{\zeta 44} & \mathbf{K}^{\zeta 45}\\ {}^{T}\mathbf{K}^{\zeta 15} & {}^{T}\mathbf{K}^{\zeta 25} & {}^{T}\mathbf{K}^{\zeta 35} & {}^{T}\mathbf{K}^{\zeta 45} & \mathbf{K}^{\zeta 55}\end{bmatrix} \text{ with } \zeta=\{\varepsilon,\tilde{\xi},\chi,\eta\}, \tag{24a}$$

$$\mathbf{M}=\begin{bmatrix}\mathbf{M}^{11} & 0 & \mathbf{M}^{13} & \mathbf{M}^{14} & 0\\ 0 & \mathbf{M}^{22} & \mathbf{M}^{23} & 0 & \mathbf{M}^{25}\\ {}^{T}\mathbf{M}^{13} & {}^{T}\mathbf{M}^{23} & \mathbf{M}^{33} & \mathbf{M}^{34} & \mathbf{M}^{35}\\ {}^{T}\mathbf{M}^{14} & 0 & {}^{T}\mathbf{M}^{34} & \mathbf{M}^{44} & \mathbf{M}^{45}\\ 0 & {}^{T}\mathbf{M}^{25} & {}^{T}\mathbf{M}^{35} & {}^{T}\mathbf{M}^{45} & \mathbf{M}^{55}\end{bmatrix}, \tag{24b}$$

$$\mathbf{F}=\begin{bmatrix}\mathbf{0} & \mathbf{0} & \mathbf{f} & \mathbf{0} & \mathbf{0}\end{bmatrix}^T, \tag{24c}$$

where the components of mass matrix $\mathbf{M}$, stiffness matrix $\mathbf{K}^{\varepsilon}$ and $\mathbf{K}^{\chi}$ can be seen in [29]. The components of stiffness matrix $\mathbf{K}^{\tilde{\xi}}$, $\mathbf{K}^{\eta}$ and load vector $\mathbf{F}$ are give in Appendix C.

It is worth to notice that for static analysis, the static responses of the FGP microplates can be obtained from Eq. (23) by ignoring inertia terms. For free vibration analysis, by denoting $\mathbf{d}(t)=\mathbf{d}e^{i\omega t}$ where ω is the natural frequency of the FGP microplates and $i^2=-1$ is imaginary unit, the natural frequencies can be derived from the following characteristic equation: $\left(\mathbf{K}-\omega^2\mathbf{M}\right)\mathbf{d}=\mathbf{0}$.

4. NUMERICAL RESULTS

In this section, numerical examples are carried out to investigate static and free vibration behaviours of FGP microplates with different BCs in which the Reddy's shear function [33] $f(x_3) = x_3 - 4x_3^3/3h^2$ is employed. They are assumed to be made of a ceramic-metal mixture whose material properties are given as follows: Al_2O_3 ($E_c = 380$ GPa, $\rho_c = 3800\ \mathrm{kg/m^3}, v_c = 0.3$), Al ($E_m = 70$ GPa, $\rho_m = 2702\ \mathrm{kg/m^3}, v_m = 0.3$). For simplification purpose, all three MLSPs are assumed to have identical values $l_1 = l_2 = l_3 = l$ and they should be determined by experimental works. For convenience, the following normalized parameters are used in the computations

$$\overline{w} = \frac{10E_c h^3}{qa^4} u_3\left(\frac{a}{2}, \frac{b}{2}\right), \quad \overline{\omega} = \frac{\omega a^2}{h}\sqrt{\frac{\rho_c}{E_c}}. \tag{25}$$

Table 2. Convergence study of series solution of Al/Al_2O_3 FGP microplates with different boundary conditions ($a/h = 10, p = 5, \beta = 0.1, h/l = \infty$)

Solution	Number of series $n = n_1 = n_2$						
	2	4	6	8	10	12	14
Normalized center deflection							
SSSS	1.1801	1.2159	1.2191	1.2182	1.2184	1.2183	1.2184
SCSC	0.7287	0.7136	0.7022	0.7016	0.7015	0.7016	0.7016
CCCC	0.4870	0.4863	0.4824	0.4828	0.4822	0.4827	0.4826
Normalized fundamental frequency							
SSSS	3.4897	3.4630	3.4560	3.4567	3.4551	3.4574	3.4573
SCSC	5.1482	4.6407	4.6179	4.6148	4.6224	4.7171	4.7172
CCCC	6.0479	5.9494	5.9035	5.8888	5.8843	5.8837	5.8838

In order to verify the convergence of present solutions, Table 2 shows the transverse center displacement and fundamental frequency of Al/Al_2O_3 FGP square microplates under a sinusoidal distributed load and with $a/h = 10, p = 5, \beta = 0.1, h/l = \infty$. The results are calculated with three types of boundary conditions (SSSS, SCSC, CCCC) and the same number of series in x_1- and x_2-direction ($n_1 = n_2 = n$). It is observed from Table 2 that the solutions converge very quickly, and the number of series $n = 12$ can be considered as a convergence point of the static and dynamic responses of the FGP microplates. Thus, this number of series will be used for numerical computations.

4.1. Static analysis

In order to verify the accuracy of the present FGP microplate model in predicting static behaviours, the first example is performed on the simply supported FG square microplates subjected to sinusoidally distributed loads without porosity effect ($\beta = 0$). Various values of the power-law index p, length-to-thickness ratio a/h, and thickness-to-MLSP ratio h/l are considered for static responses of Al/Al_2O_3 FG microplates. The

obtained results are reported in Tables 3 and 4, and compared with those derived from Thai et al. [22], Thai et al. [25] using the MST, isogeometric approach and HSDT, Zhang et al. [34] using the MST, Navier method and HSDT. It can be seen that there are good agreements between the models for different BCs, material distribution and size effects, which shows the accuracy of present approach for static behaviours.

Table 3. Normalized transverse center displacements of FGP microplates under sinusoidal load ($\beta = 0$, SSSS)

a/h	p	Theory	h/l					
			0	20	10	5	2	1
5	0.5	Present	0.5177	0.4957	0.4411	0.3065	0.1011	0.0292
		MST [22]	0.5176	0.4965	0.4426	0.3098	0.1018	0.0303
		RPT [34]	0.5198	0.4983	0.4435	0.3086	0.0997	0.0293
		IGA [25]	0.5177	0.4975	0.4457	0.3153	0.1045	0.0310
	1	Present	0.6688	0.6387	0.5625	0.3860	0.1226	0.0353
		MST [22]	0.6688	0.6399	0.5670	0.3908	0.1252	0.0369
		RPT [34]	0.6688	0.6396	0.5658	0.3879	0.1223	0.0357
		IGA [25]	0.6688	0.6412	0.5709	0.3977	0.1286	0.0378
	2	Present	0.8672	0.8261	0.7256	0.5021	0.1521	0.0442
		MST [22]	0.8671	0.8292	0.7332	0.5021	0.1580	0.0460
		RPT [34]	0.8671	0.8286	0.7313	0.4980	0.1544	0.0447
		IGA [25]	0.8671	0.8307	0.7379	0.5107	0.1627	0.0475
	4	Present	1.0411	0.9899	0.8681	0.6024	0.1898	0.0552
		MST [22]	1.0409	0.9977	0.8875	0.6159	0.1964	0.0573
		RPT [34]	1.0408	0.9967	0.8843	0.6095	0.1921	0.0558
		IGA [25]	1.0409	0.9994	0.8927	0.6263	0.2034	0.0597
	10	Present	1.2279	1.1681	1.0282	0.7443	0.2455	0.0728
		MST [22]	1.2276	1.1811	1.0609	0.7548	0.2510	0.0743
		RPT [34]	1.2269	1.1790	1.0557	0.7455	0.2454	0.0724
		IGA [25]	1.2276	1.1829	1.0668	0.7678	0.2614	0.0781
10	0.5	Present	0.4538	0.4361	0.3884	0.2747	0.0895	0.0263
		MST [22]	0.4537	0.4355	0.3887	0.2723	0.0884	0.0260
	1	Present	0.5890	0.5646	0.5003	0.3479	0.1106	0.0322
		MST [22]	0.5890	0.5640	0.5004	0.3453	0.1095	0.0320
	2	Present	0.7572	0.7258	0.6426	0.4463	0.1418	0.0412
		MST [22]	0.7573	0.7253	0.6439	0.4446	0.1407	0.0409
	4	Present	0.8814	0.8475	0.7588	0.5404	0.1797	0.0531
		MST [22]	0.8815	0.8480	0.7614	0.5405	0.1784	0.0526
	10	Present	1.0086	0.9739	0.8808	0.6497	0.2325	0.0707
		MST [22]	1.0087	0.9755	0.8879	0.6535	0.2298	0.0694

Table 4. Normalized transverse center displacements of FGP microplates under sinusoidal load with $a/h = 10$

BCs	p	Theory	h/l					
			0	20	10	5	2	1
CCCC	0.5	Present	0.1755	0.1677	0.1488	0.1032	0.0331	0.0099
		MST [22]	0.1747	0.1675	0.1492	0.1042	0.0340	0.0100
		IGA [25]	0.1773	-	0.1521	0.1068	0.0349	0.0103
	1	Present	0.2271	0.2165	0.1909	0.1306	0.0412	0.0121
		MST [22]	0.2261	0.2163	0.1951	0.1349	0.0419	0.0123
		IGA [25]	0.2295	-	0.1915	0.1318	0.0430	0.0126
	2	Present	0.2936	0.2794	0.2456	0.1673	0.0529	0.0158
		MST [22]	0.2922	0.2794	0.2472	0.1694	0.0532	0.0155
		IGA [25]	0.2967	-	0.2517	0.1733	0.0547	0.0159
	5	Present	0.3631	0.3452	0.3047	0.2124	0.0706	0.0211
		MST [22]	0.3609	0.3466	0.3100	0.2182	0.0712	0.0209
		IGA [25]	0.3676	-	0.3161	0.2233	0.0734	0.0216
	10	Present	0.4068	0.3873	0.3436	0.2437	0.0838	0.0252
		MST [22]	0.4041	0.3893	0.3582	0.2523	0.0854	0.0254
		IGA [25]	0.4121	-	0.3510	0.2584	0.0884	0.0265
SCSC	0.5	Present	0.2585	0.2477	0.2198	0.1514	0.0477	0.0139
		IGA [25]	0.2472	-	0.2122	0.1492	0.0488	0.0144
	1	Present	0.3349	0.3200	0.2823	0.1917	0.0591	0.0171
		IGA [25]	0.3201	-	0.2724	0.1886	0.0602	0.0176
	2	Present	0.4318	0.4126	0.3643	0.2480	0.0769	0.0221
		IGA [25]	0.4133	-	0.3513	0.2425	0.0768	0.0223
	5	Present	0.5256	0.5055	0.4540	0.3218	0.1059	0.0311
		IGA [25]	0.5086	-	0.4389	0.3118	0.1035	0.0306
	10	Present	0.5849	0.5646	0.5118	0.3720	0.1280	0.0382
		IGA [25]	0.5685	-	0.4961	0.3604	0.1246	0.0375

Moreover, in order to investigate effects of porosity β, material parameter p, side-to-thickness ratio a/h, size effects h/l and boundary conditions on the static responses of FGP microplates, Table 5 presents the normalized center transverse displacements with various configurations. The variations of center deflections with respect to a/h and h/l are also plotted in Fig. 1. It can be seen that the transverse displacements increase with increase of the p and h/l. The graph in Fig. 1(b) reveals that the deflections vary gradually for $h/l \leq 10$ and from $h/l = 25$ the curves become flatter and the results tend to be closed to those obtained from the classical theory $(h/l = \infty)$, which explains that the size effects on deflections of FGP microplates are not significant from $h/l > 25$.

Table 5. Normalized transverse center displacements of FGP square microplates under sinusoidal load with different boundary conditions

BCs	a/h	β	p	h/l				
				∞	10	5	2	1
SSSS	10	0.1	0.5	0.5111	0.4342	0.3025	0.0962	0.0280
			1	0.6947	0.5831	0.3964	0.1218	0.0351
			2	0.9578	0.7987	0.5365	0.1622	0.0464
			5	1.2183	1.0372	0.7244	0.2345	0.0687
			10	1.3565	1.1739	0.8523	0.2968	0.0891
		0.2	0.5	0.5822	0.4903	0.3356	0.1043	0.0301
			1	0.8456	0.6983	0.4610	0.1361	0.0387
			2	1.3214	1.0690	0.6800	0.1909	0.0536
			5	1.9318	1.5884	1.0391	0.3052	0.0870
			10	2.1828	1.8440	1.2843	0.4187	0.1231
SCSC	10	0.1	0.5	0.2906	0.2449	0.1662	0.0512	0.0149
			1	0.3939	0.3278	0.2177	0.0653	0.0187
			2	0.5436	0.4503	0.2971	0.0882	0.0249
			5	0.7016	0.5956	0.4110	0.1301	0.0373
			10	0.7870	0.6844	0.4904	0.1641	0.0483
		0.2	0.5	0.3305	0.2758	0.1841	0.0552	0.0159
			1	0.4781	0.3909	0.2525	0.0729	0.0206
			2	0.7462	0.5979	0.3749	0.1033	0.0288
			5	1.1042	0.9064	0.5905	0.1675	0.0476
			10	1.2676	1.0785	0.7459	0.2348	0.0674
CCCC	10	0.1	0.5	0.1969	0.1640	0.1100	0.0335	0.0101
			1	0.2663	0.2191	0.1439	0.0426	0.0128
			2	0.3682	0.3012	0.1962	0.0573	0.0164
			5	0.4827	0.4036	0.2735	0.0844	0.0244
			10	0.5480	0.4671	0.3281	0.1070	0.0315
		0.2	0.5	0.2233	0.1842	0.1216	0.0362	0.0104
			1	0.3219	0.2603	0.1664	0.0475	0.0135
			2	0.5018	0.3975	0.2462	0.0676	0.0210
			5	0.7550	0.6090	0.3888	0.1106	0.0313
			10	0.8832	0.7357	0.4969	0.1526	0.0440

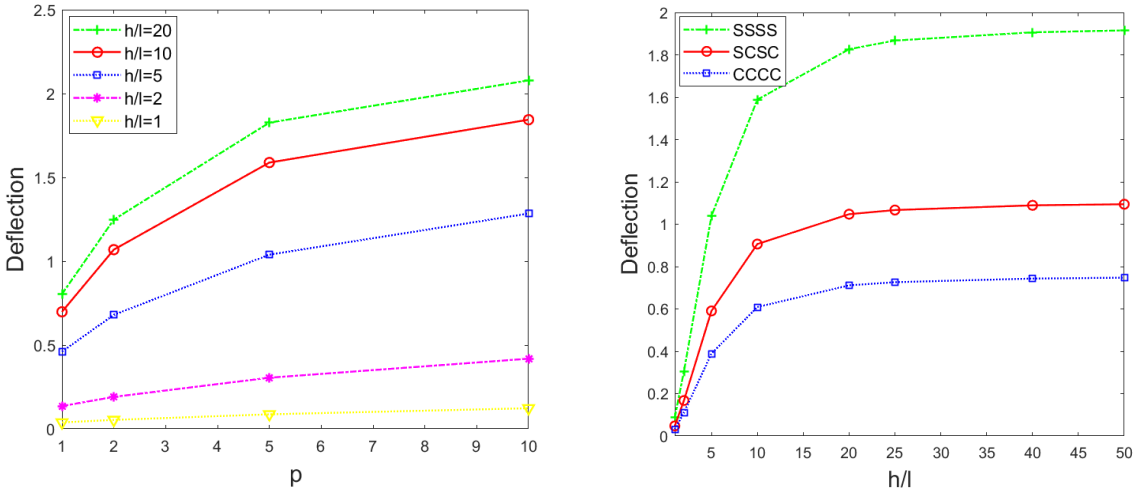

(a) SSSS (b) $p = 5$

Fig. 1. Variation of normalized center deflection with respect the power index p and thickness-to-length scale h/l of FGP microplates ($\beta = 0.2, a/h = 10$)

4.2. Free vibration analysis

In order to study the accuracy of present solutions in predicting vibration responses, Tables 6 and 7 provide the fundamental frequencies of Al/Al_2O_3 FGP microplates without porosity effects ($\beta = 0$) in which the solutions are computed for various configurations. The obtained results are compared with those derived from Thai et al. [22] and Thai et al. [25] based on the MST, IGA and HSDT, Zhang et al. [34] based on the MST and Navier procedure and a refined HSDT. It can be seen that there is no discrepancy between models. The fundamental frequencies decrease with the increase of p as expected.

Table 6. Normalized fundamental frequencies $\overline{\omega} = \omega h\sqrt{\rho_c/E_c}$ of Al/Al_2O_3 FGP square microplates ($\beta = 0$, $a/h = 10$, SSSS)

p	Theory	h/l				
		∞	10	5	2	1
0	Present	0.0577	0.0615	0.0726	0.1250	0.2283
	MST [22]	0.0577	0.0619	0.0729	0.1254	0.2297
	RPT [34]	0.0577	0.0619	0.0730	0.1258	0.2309
	IGA [25]	0.0577	0.0617	0.0725	0.1240	0.2268
0.5	Present	0.0490	0.0529	0.0626	0.1099	0.2035
	MST [22]	0.0490	0.0529	0.0633	0.1110	0.2047
	RPT [34]	0.0489	0.0529	0.0632	0.1113	0.2057
	IGA [25]	0.0490	0.0528	0.0629	0.1098	0.2023

p	Theory	h/l				
		∞	10	5	2	1
1	Present	0.0441	0.0475	0.0574	0.1014	0.1884
	MST [22]	0.0442	0.0479	0.0577	0.1024	0.1896
	RPT [34]	0.0442	0.0480	0.0578	0.1028	0.1907
	IGA [25]	0.0442	0.0478	0.0573	0.1013	0.1873
2	Present	0.0401	0.0431	0.0520	0.0926	0.1722
	MST [22]	0.0401	0.0435	0.0523	0.0930	0.1722
	RPT [34]	0.0401	0.0435	0.0524	0.0933	0.1731
	IGA [25]	0.0401	0.0434	0.0520	0.0918	0.1698
	MST [22]	0.0377	0.0404	0.0477	0.0822	0.1508
	RPT [34]	0.0377	0.0405	0.0478	0.0825	0.1514
	IGA [25]	0.0377	0.0403	0.0474	0.0810	0.1482
10	Present	0.0364	0.0388	0.0452	0.0757	0.1360
	MST [22]	0.0363	0.0387	0.0451	0.0761	0.1384
	RPT [34]	0.0364	0.0388	0.0453	0.0764	0.1390
	IGA [25]	0.0364	0.0387	0.0449	0.0750	0.1359

Table 7. Normalized fundamental frequencies of Al/Al_2O_3 FGP square microplates ($\beta = 0, a/h = 10$, CCCC and SCSC)

BCs	p	Theory	h/l					
			∞	20	10	5	2	1
CCCC	0.5	Present	8.4735	8.6614	9.1920	11.0307	18.9020	35.1640
		IGA [25]	8.4405	-	9.1227	10.8954	19.0701	35.1215
	1	Present	7.6782	7.8132	8.3908	10.0530	17.6636	32.3192
		IGA [25]	7.6251	-	8.2766	9.9597	17.6422	32.6292
	2	Present	6.9176	7.1106	7.5746	9.0783	15.9206	28.8231
		IGA [25]	6.8944	-	7.4923	9.0367	16.0977	29.8609
	5	Present	6.4231	6.5519	6.9710	8.3300	13.9971	25.9460
		IGA [25]	6.3722	-	6.8823	8.2026	14.3324	26.4157
	10	Present	6.1199	6.2784	6.6505	7.8617	13.0441	23.9971
		IGA [25]	6.1039	-	6.5602	7.7407	13.2706	24.2754
SCSC	0.5	Present	6.7197	6.8676	7.2931	8.7900	15.6599	29.0008
		IGA [25]	6.9031	-	7.4556	8.8961	15.5600	28.6567
	1	Present	6.0650	6.2057	6.6094	8.0210	14.4368	26.8247
		IGA [25]	6.2329	-	6.7605	8.1283	14.3915	26.6161
	2	Present	5.4955	5.6222	5.9858	7.2578	13.0467	24.2396
		IGA [25]	5.6405	-	6.1230	7.3744	13.1146	24.3082
	5	Present	5.1361	5.2381	5.5323	6.5758	11.4606	21.0871
		IGA [25]	5.2361	-	5.6429	6.7021	11.6480	21.4179
	10	Present	4.9452	5.0338	5.2903	6.2080	10.5865	19.3316
		IGA [25]	5.0254	-	5.3868	6.3288	10.7777	19.6645

Table 8. Normalized fundamental frequencies of Al/Al_2O_3 FGP square microplates

BCs	a/h	β	p	h/l				
				∞	10	5	2	1
SSSS	10	0.1	0.5	4.8469	5.2465	6.2753	11.1444	20.5884
			1	4.2815	4.6668	5.6497	10.2161	19.0334
			2	3.7640	4.1238	4.9947	9.1029	16.9999
			5	3.4574	3.6783	4.4653	7.8075	14.4907
			10	3.3327	3.5350	4.1840	7.0993	12.8651
		0.2	0.5	4.7972	5.2009	6.1126	11.1001	20.1158
			1	4.1121	4.5268	5.5541	10.0543	19.0057
			2	3.4064	3.7713	4.7471	8.9419	16.8823
			5	2.9323	3.2158	3.9832	7.3159	13.7288
			10	2.8148	3.0352	3.6550	6.4101	11.7388
SCSC	10	0.1	0.5	6.6598	7.2591	8.7147	15.3799	28.4118
			1	5.8920	6.4631	7.9308	14.1016	26.1753
			2	5.1741	5.6891	7.0084	12.5850	23.7134
			5	4.7171	5.1198	6.1693	10.9865	20.3606
			10	4.5305	4.8659	5.7523	9.9342	18.2235
		0.2	0.5	6.5990	7.1277	8.5988	15.1299	28.1844
			1	5.6709	6.2750	7.7094	14.0535	26.0222
			2	4.6990	5.2527	6.6405	12.5620	23.6336
			5	4.0124	4.4345	5.5079	10.2385	19.2228
			10	3.8229	4.1489	4.9977	8.8931	16.4769
CCCC	10	0.1	0.5	8.3865	9.1064	11.0009	18.7157	35.0700
			1	7.4713	8.1995	9.9376	17.5254	32.1417
			2	6.5451	7.2033	8.8372	15.7657	28.6778
			5	5.8837	6.1920	7.8150	13.3725	23.7300
			10	5.6264	6.1831	7.3008	12.0451	21.4739
		0.2	0.5	8.3202	9.1037	11.0001	18.6797	34.9638
			1	7.1684	7.9717	9.7343	17.3071	32.1207
			2	5.9501	6.6362	8.3403	15.2109	28.4556
			5	5.0257	5.6144	6.9379	11.9968	20.3562
			10	4.7414	5.2673	6.3223	10.5215	19.6228

The effect of p on the natural frequencies of Al/Al_2O_3 FGP microplates is also plotted in Fig. 2(a) for $h/l = 1, 2, 5, 10, 20, a/h = 10$ and $\beta = 0.2$. There exist large deviations of these curves, which indicate significant size effects. Moreover, the variations of fundamental frequencies with respect to h/l are displayed in Fig. 2(b). It is observed that the results decrease with the increase of h/l up to $h/l = 10$ and then the curves become flatter which indicates the size effects can be neglected.

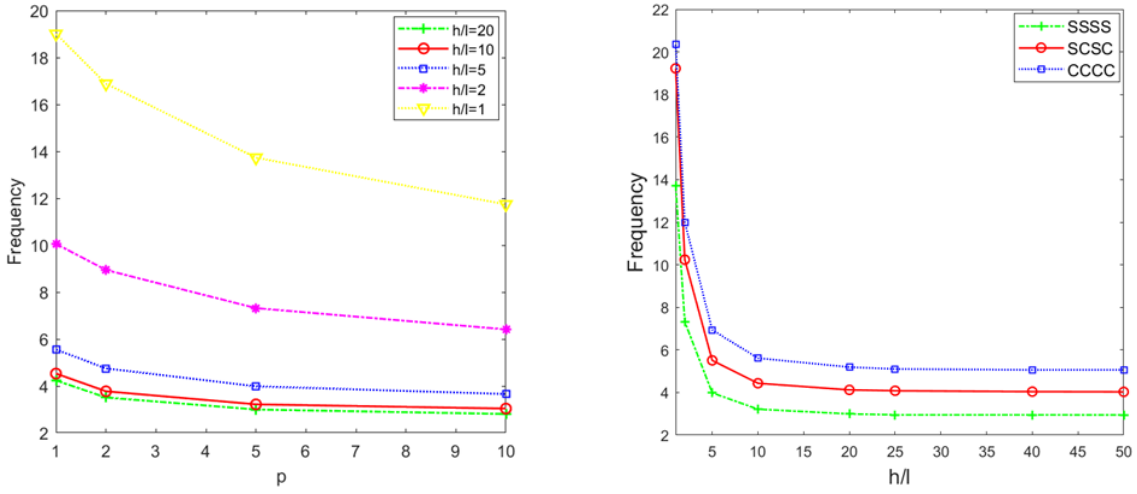

(a) SSSS (b) $p = 5$

Fig. 2. Variation of normalized fundamental frequencies with respect the power index p and thickness-to-MLSP ratio h/l $(a/h = 10, \beta = 0.2)$

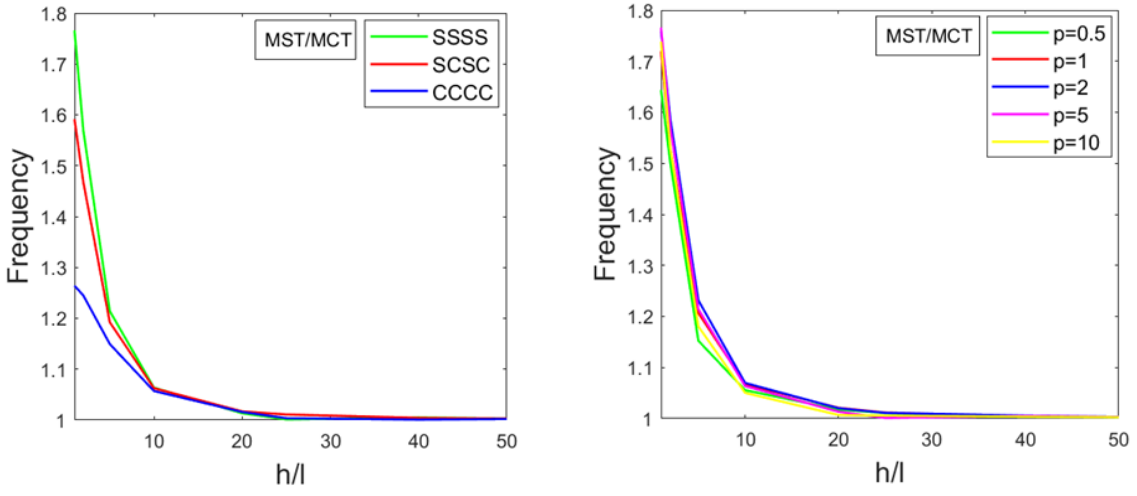

(a) $p = 5$ (b) SSSS

Fig. 3. Size effect of the MCT and MST for the normalised fundamental frequencies with respect to the length scale-to-thickness ratio h/l $(\beta = 0.2, p = 5, a/h = 10)$

In order to study further the size effects of vibration problems, Fig. 3 illustrates the ratio of fundamental frequencies computed from the MST over the MCT, which is expressed with respect to $h/l, p = 5, \beta = 0.2, a/h = 10$ and different boundary conditions. It can be observed that the MST with three MLSPs produces frequencies larger than the

MCT with one MLSP, especially when the Static and vibration analysis of functionally graded microplate with porosities based on higher-order shear deformation and modified strain gradient theory microplate thickness is close to the MLSP. It emphasizes the importance of the consideration of three components e.g. the dilatation, deviatoric stretch and symmetric part of rotation gradient tensor in the MST rather than only the symmetric part of rotation gradient tensor in the MCT when dealing with microplates. As expected, by increasing the size scale, the difference between the theories is decreased.

5. CONCLUSIONS

A unified higher-order shear deformation theory and modified strain gradient theory have been developed in this paper for static and free vibration analyses of functionally graded porous microplates. The equations of motion are derived from Hamilton's principle and series-type approximation with exponential shape functions. Numerical examples are presented to investigate effects of side-tothickness ratio, thickness-to-material length scale parameter ratio and boundary conditions on the deflections and natural frequencies of FGP microplates. The obtained results show that the size effects lead to an increase in the stiffness of the FGP microplates, consequently it decreases their transverse displacements and increases their natural frequencies. Significant differences of the present theory and modified couple stress theory are observed when the microplate thickness and MLSP is the same dimension, it shows that the dilatation and deviatoric stretch should be accounted for computations of microplates. The present theory is found to be accurate and efficient in predicting static and dynamic behaviours of FGP microplates.

DECLARATION OF COMPETING INTEREST

The authors declare that they have no known competing financial interests or personal relationships that could have appeared to influence the work reported in this paper.

FUNDING

This research received no specific grant from any funding agency in the public, commercial, or not-for-profit sectors.

REFERENCES

[1] N. Jalili and K. Laxminarayana. A review of atomic force microscopy imaging systems: application to molecular metrology and biological sciences. *Mechatronics*, **14**, (2004), pp. 907–945. https://doi.org/10.1016/j.mechatronics.2004.04.005.

[2] D. Ozevin. Micro-electro-mechanical-systems (MEMS) for assessing and monitoring civil infrastructures. In *Sensor Technologies for Civil Infrastructures*, pp. 265–302e. Elsevier, (2014). https://doi.org/10.1533/9780857099136.265.

[3] P. A. Demirhan and V. Taskin. Bending and free vibration analysis of Levy-type porous functionally graded plate using state space approach. *Composites Part B: Engineering*, **160**, (2019), pp. 661–676. https://doi.org/10.1016/j.compositesb.2018.12.020.

[4] D. Chen, J. Yang, and S. Kitipornchai. Buckling and bending analyses of a novel functionally graded porous plate using Chebyshev-Ritz method. *Archives of Civil and Mechanical Engineering*, **19**, (2019), pp. 157–170. https://doi.org/10.1016/j.acme.2018.09.004.

[5] J. Zhao, K. Choe, F. Xie, A. Wang, C. Shuai, and Q. Wang. Three-dimensional exact solution for vibration analysis of thick functionally graded porous (FGP) rectangular plates with arbitrary boundary conditions. *Composites Part B: Engineering*, **155**, (2018), pp. 369–381. https://doi.org/10.1016/j.compositesb.2018.09.001.

[6] K. Li, D. Wu, X. Chen, J. Cheng, Z. Liu, W. Gao, and M. Liu. Isogeometric Analysis of functionally graded porous plates reinforced by graphene platelets. *Composite Structures*, **204**, (2018), pp. 114–130. https://doi.org/10.1016/j.compstruct.2018.07.059.

[7] M. Dhuria, N. Grover, and K. Goyal. Influence of porosity distribution on static and buckling responses of porous functionally graded plates. *Structures*, **34**, (2021), pp. 1458–1474. https://doi.org/10.1016/j.istruc.2021.08.050.

[8] N. V. Nguyen, H. Nguyen-Xuan, D. Lee, and J. Lee. A novel computational approach to functionally graded porous plates with graphene platelets reinforcement. *Thin-Walled Structures*, **150**, (2020). https://doi.org/10.1016/j.tws.2020.106684.

[9] S. Merdaci and H. Belghoul. High-order shear theory for static analysis of functionally graded plates with porosities. *Comptes Rendus Mécanique*, **347**, (2019), pp. 207–217. https://doi.org/10.1016/j.crme.2019.01.001.

[10] A. M. Zenkour and M. H. Aljadani. Quasi-3D refined theory for functionally graded porous plates: Vibration analysis. *Physical Mesomechanics*, **24**, (2021), pp. 243–256. https://doi.org/10.1134/s1029959921030036.

[11] V. T. Long and H. V. Tung. Thermal nonlinear buckling of shear deformable functionally graded cylindrical shells with porosities. *AIAA Journal*, **59**, (2021), pp. 2233–2241. https://doi.org/10.2514/1.j060026.

[12] V. T. Long and H. V. Tung. Thermomechanical nonlinear buckling of pressurized shear deformable FGM cylindrical shells including porosities and elastically restrained edges. *Journal of Aerospace Engineering*, **34**, (2021). https://doi.org/10.1061/(asce)as.1943-5525.0001252.

[13] V. T. Long and H. V. Tung. Thermo-torsional buckling and postbuckling of thin FGM cylindrical shells with porosities and tangentially restrained edges. *Mechanics Based Design of Structures and Machines*, (2022), pp. 1–20. https://doi.org/10.1080/15397734.2022.2084752.

[14] V. T. Long and H. V. Tung. Buckling and postbuckling of functionally graded porous material nearly cylindrical shells under external lateral pressure in thermal environments. *Ships and Offshore Structures*, (2022), pp. 1–9. https://doi.org/10.1080/17445302.2022.2100666.

[15] S. Kong. A review on the size-dependent models of micro-beam and micro-plate based on the modified couple stress theory. *Archives of Computational Methods in Engineering*, **29**, (2021), pp. 1–31. https://doi.org/10.1007/s11831-021-09567-w.

[16] F. Fan, Y. Xu, S. Sahmani, and B. Safaei. Modified couple stress-based geometrically nonlinear oscillations of porous functionally graded microplates using NURBS-based isogeometric approach. *Computer Methods in Applied Mechanics and Engineering*, **372**, (2020). https://doi.org/10.1016/j.cma.2020.113400.

[17] A. Farzam and B. Hassani. Size-dependent analysis of FG microplates with temperature-dependent material properties using modified strain gradient theory

and isogeometric approach. *Composites Part B: Engineering*, **161**, (2019), pp. 150–168. https://doi.org/10.1016/j.compositesb.2018.10.028.

[18] J. Kim, K. K. Żur, and J. N. Reddy. Bending, free vibration, and buckling of modified couples stress-based functionally graded porous micro-plates. *Composite Structures*, **209**, (2019), pp. 879–888. https://doi.org/10.1016/j.compstruct.2018.11.023.

[19] D. C. C. Lam, F. Yang, A. C. M. Chong, J. Wang, and P. Tong. Experiments and theory in strain gradient elasticity. *Journal of the Mechanics and Physics of Solids*, **51**, (2003), pp. 1477–1508. https://doi.org/10.1016/s0022-5096(03)00053-x.

[20] R. D. Mindlin. Second gradient of strain and surface-tension in linear elasticity. *International Journal of Solids and Structures*, **1**, (1965), pp. 417–438. https://doi.org/10.1016/0020-7683(65)90006-5.

[21] R. D. Mindlin and N. N. Eshel. On first strain-gradient theories in linear elasticity. *International Journal of Solids and Structures*, **4**, (1968), pp. 109–124. https://doi.org/10.1016/0020-7683(68)90036-x.

[22] C. H. Thai, A. J. M. Ferreira, and H. Nguyen-Xuan. Isogeometric analysis of size-dependent isotropic and sandwich functionally graded microplates based on modified strain gradient elasticity theory. *Composite Structures*, **192**, (2018), pp. 274–288. https://doi.org/10.1016/j.compstruct.2018.02.060.

[23] C. H. Thai, A. J. M. Ferreira, and P. Phung-Van. Size dependent free vibration analysis of multilayer functionally graded GPLRC microplates based on modified strain gradient theory. *Composites Part B: Engineering*, **169**, (2019), pp. 174–188. https://doi.org/10.1016/j.compositesb.2019.02.048.

[24] C. H. Thai, A. J. M. Ferreira, T. Rabczuk, and H. Nguyen-Xuan. Size-dependent analysis of FG-CNTRC microplates based on modified strain gradient elasticity theory. *European Journal of Mechanics - A/Solids*, **72**, (2018), pp. 521–538. https://doi.org/10.1016/j.euromechsol.2018.07.012.

[25] S. Thai, H.-T. Thai, T. P. Vo, and V. I. Patel. Size-dependant behaviour of functionally graded microplates based on the modified strain gradient elasticity theory and isogeometric analysis. *Computers & Structures*, **190**, (2017), pp. 219–241. https://doi.org/10.1016/j.compstruc.2017.05.014.

[26] C.-L. Thanh, L. V. Tran, T. Q. Bui, H. X. Nguyen, and M. Abdel-Wahab. Isogeometric analysis for size-dependent nonlinear thermal stability of porous FG microplates. *Composite Structures*, **221**, (2019). https://doi.org/10.1016/j.compstruct.2019.04.010.

[27] A. M. Zenkour and M. H. Aljadani. Porosity effect on thermal buckling behavior of actuated functionally graded piezoelectric nanoplates. *European Journal of Mechanics - A/Solids*, **78**, (2019). https://doi.org/10.1016/j.euromechsol.2019.103835.

[28] T.-K. Nguyen, H.-T. Thai, and T. P. Vo. A novel general higher-order shear deformation theory for static, vibration and thermal buckling analysis of the functionally graded plates. *Journal of Thermal Stresses*, (2021), pp. 1–21. https://doi.org/10.1080/01495739.2020.1869127.

[29] V.-T. Tran, T.-K. Nguyen, P. T. T. Nguyen, and T. P. Vo. Stochastic vibration and buckling analysis of functionally graded microplates with a unified higher-order shear deformation theory. *Thin-Walled Structures*, **177**, (2022). https://doi.org/10.1016/j.tws.2022.109473.

[30] M. Aydogdu. Buckling analysis of cross-ply laminated beams with general boundary conditions by Ritz method. *Composites Science and Technology*, **66**, (2006), pp. 1248–1255. https://doi.org/10.1016/j.compscitech.2005.10.029.

[31] M. Aydogdu. Vibration analysis of cross-ply laminated beams with general boundary conditions by Ritz method. *International Journal of Mechanical Sciences*, **47**, (2005), pp. 1740–1755. https://doi.org/10.1016/j.ijmecsci.2005.06.010.

[32] J. L. Mantari and F. G. Canales. Free vibration and buckling of laminated beams via hybrid Ritz solution for various penalized boundary conditions. *Composite Structures*, **152**, (2016), pp. 306–315. https://doi.org/10.1016/j.compstruct.2016.05.037.

[33] J. N. Reddy. *Mechanics of laminated composite plates and shells*. CRC Press, (2003). https://doi.org/10.1201/b12409.

[34] B. Zhang, Y. He, D. Liu, L. Shen, and J. Lei. An efficient size-dependent plate theory for bending, buckling and free vibration analyses of functionally graded microplates resting on elastic foundation. *Applied Mathematical Modelling*, **39**, (2015), pp. 3814–3845. https://doi.org/10.1016/j.apm.2014.12.001.

APPENDIX A

The non-zero components of dilatation gradients in Eq. (11) are defined by

$$\boldsymbol{\xi}^{(0)} = \begin{Bmatrix} \xi_1^{(0)} \\ \xi_2^{(0)} \\ \xi_3^{(0)} \end{Bmatrix} = \begin{Bmatrix} u^0_{1,11} + u^0_{2,12} \\ u^0_{1,12} + u^0_{2,22} \\ 0 \end{Bmatrix}, \quad \boldsymbol{\xi}^{(1)} = \begin{Bmatrix} \xi_1^{(1)} \\ \xi_2^{(1)} \\ \xi_3^{(1)} \end{Bmatrix} = \begin{Bmatrix} u^0_{3,111} + u^0_{3,122} \\ u^0_{3,112} + u^0_{3,222} \\ 0 \end{Bmatrix}, \tag{A.1a}$$

$$\boldsymbol{\xi}^{(2)} = \begin{Bmatrix} \xi_1^{(2)} \\ \xi_2^{(2)} \\ \xi_3^{(2)} \end{Bmatrix} = \begin{Bmatrix} \varphi_{1,11} + \varphi_{2,12} \\ \varphi_{1,12} + \varphi_{2,22} \\ 0 \end{Bmatrix}, \quad \boldsymbol{\xi}^{(3)} = \begin{Bmatrix} \xi_1^{(3)} \\ \xi_2^{(3)} \\ \xi_3^{(3)} \end{Bmatrix} = \begin{Bmatrix} 0 \\ 0 \\ u^0_{3,11} + u^0_{3,22} \end{Bmatrix}, \tag{A.1b}$$

$$\boldsymbol{\xi}^{(4)} = \begin{Bmatrix} \xi_1^{(4)} \\ \xi_2^{(4)} \\ \xi_3^{(4)} \end{Bmatrix} = \begin{Bmatrix} 0 \\ 0 \\ \varphi_{1,1} + \varphi_{2,2} \end{Bmatrix}.$$

The non-zero components of deviatoric stretch gradients η_{ijk} in Eq. (12) are given by

$$\eta_{111} = \varepsilon_{11,1} - \frac{1}{5}\left(\xi_1 + 2\varepsilon_{11,1} + \gamma_{12,2} + \gamma_{13,3}\right), \tag{A.2a}$$

$$\eta_{222} = \varepsilon_{22,2} - \frac{1}{5}\left(\xi_2 + 2\varepsilon_{22,2} + \gamma_{12,1} + \gamma_{23,3}\right),$$

$$\eta_{333} = -\frac{1}{5}\left(\xi_3 + \gamma_{13,1} + \gamma_{23,2}\right), \tag{A.2b}$$

$$\eta_{112} = \eta_{211} = \eta_{121} = \frac{1}{3}\left(\varepsilon_{11,2} + \gamma_{12,1}\right) - \frac{1}{15}\left(\xi_2 + \gamma_{12,1} + 2\varepsilon_{22,2} + \gamma_{23,3}\right),$$

$$\eta_{113} = \eta_{311} = \eta_{131} = \frac{1}{3}\left(\gamma_{13,1} + \varepsilon_{11,3}\right) - \frac{1}{15}\left(\xi_3 + \gamma_{13,1} + \gamma_{23,2}\right), \tag{A.2c}$$

$$\eta_{221} = \eta_{122} = \eta_{212} = \frac{1}{3}\left(\gamma_{12,2} + \varepsilon_{22,1}\right) - \frac{1}{15}\left(\xi_1 + 2\varepsilon_{11,1} + \gamma_{12,2} + \gamma_{13,3}\right), \tag{A.2d}$$

$$\eta_{223} = \eta_{322} = \eta_{232} = \frac{1}{3}\left(\gamma_{23,2} + \varepsilon_{22,3}\right) - \frac{1}{15}\left(\xi_3 + \gamma_{13,1} + \gamma_{23,2}\right), \tag{A.2e}$$

$$\eta_{331} = \eta_{133} = \eta_{313} = \frac{1}{3}\gamma_{13,3} - \frac{1}{15}\left(\xi_1 + 2\varepsilon_{11,1} + \gamma_{12,2} + \gamma_{13,3}\right), \tag{A.2f}$$

$$\eta_{332} = \eta_{233} = \eta_{323} = \frac{1}{3}\gamma_{23,3} - \frac{1}{15}\left(\xi_2 + \gamma_{12,1} + 2\varepsilon_{22,2} + \gamma_{23,3}\right), \tag{A.2g}$$

$$\eta_{123} = \eta_{231} = \eta_{312} = \eta_{132} = \eta_{321} = \eta_{213} = \frac{1}{6}\left(\gamma_{23,1} + \gamma_{13,2} + \gamma_{12,3}\right). \tag{A.2h}$$

These components can be expressed in terms of the displacements as follows

$$\boldsymbol{\eta}^{(0)} = \frac{1}{5}\begin{Bmatrix} 2u^0_{1,11} - 2u^0_{2,12} - u^0_{1,22} \\ 2u^0_{2,22} - 2u^0_{1,12} - u^0_{2,11} \\ 0 \\ -\left(3u^0_{1,11} + 2u^0_{2,12} + u^0_{1,22}\right) \\ -\left(3u^0_{2,22} + 2u^0_{1,12} + u^0_{2,11}\right) \\ 4u^0_{1,22} + 8u^0_{2,12} - 3u^0_{1,11} \\ 4u^0_{2,11} + 8u^0_{1,12} - 3u^0_{2,22} \\ 0 \\ 0 \\ 0 \end{Bmatrix}, \quad \boldsymbol{\eta}^{(1)} = \frac{1}{5}\begin{Bmatrix} 2u^0_{3,111} - 3u^0_{3,122} \\ 2u^0_{3,222} - 3u^0_{3,112} \\ 0 \\ -3\left(u^0_{3,111} + u^0_{3,122}\right) \\ -3\left(u^0_{3,112} + u^0_{3,222}\right) \\ 3\left(4u^0_{3,122} - u^0_{3,111}\right) \\ 3\left(4u^0_{3,112} - u^0_{3,222}\right) \\ 0 \\ 0 \\ 0 \end{Bmatrix}, \tag{A.3a}$$

$$\boldsymbol{\eta}^{(2)} = \frac{1}{5}\begin{Bmatrix} 2\varphi_{1,11} - 2\varphi_{2,12} - \varphi_{1,22} \\ 2\varphi_{2,22} - 2\varphi_{1,12} - \varphi_{2,11} \\ 0 \\ -\left(3\varphi_{1,11} + 2\varphi_{2,12} + \varphi_{1,22}\right) \\ -\left(3\varphi_{2,22} + 2\varphi_{1,12} + \varphi_{2,11}\right) \\ 4\varphi_{1,22} + 8\varphi_{2,12} - 3\varphi_{1,11} \\ 4\varphi_{2,11} + 8\varphi_{1,12} - 3\varphi_{2,22} \\ 0 \\ 0 \\ 0 \end{Bmatrix},$$

$$\boldsymbol{\eta}^{(3)} = \frac{1}{5}\begin{Bmatrix} 0 \\ 0 \\ -\left(u^0_{3,11} + u^0_{3,22} + \varphi_{1,1} + \varphi_{2,2}\right) \\ 0 \\ 0 \\ 0 \\ 0 \\ 4u^0_{3,11} - u^0_{3,22} + 4\varphi_{1,1} - \varphi_{2,2} \\ 4u^0_{3,22} - u^0_{3,11} + 4\varphi_{2,2} - \varphi_{1,1} \\ 5\left(\varphi_{1,2} + \varphi_{2,1} + 2u^0_{3,12}\right) \end{Bmatrix}, \quad \boldsymbol{\eta}^{(4)} = \frac{1}{5}\begin{Bmatrix} 0 \\ 0 \\ -\left(u^0_{3,11} + u^0_{3,22}\right) \\ 0 \\ 0 \\ 0 \\ 0 \\ 4u^0_{3,11} - u^0_{3,22} \\ 4u^0_{3,22} - u^0_{3,11} \\ 10u^0_{3,12} \end{Bmatrix}, \tag{A.3b}$$

$$\boldsymbol{\eta}^{(5)} = \frac{1}{5}\begin{Bmatrix} 0 \\ 0 \\ -\left(\varphi_{1,1} + \varphi_{2,2}\right) \\ 0 \\ 0 \\ 0 \\ 0 \\ 4\varphi_{1,1} - \varphi_{2,2} \\ 4\varphi_{2,2} - \varphi_{1,1} \\ 5\left(\varphi_{1,2} + \varphi_{2,1}\right) \end{Bmatrix}, \quad \boldsymbol{\eta}^{(6)} = \frac{1}{5}\begin{Bmatrix} -\left(\varphi_1 + u^0_{3,1}\right) \\ -\left(\varphi_2 + u^0_{3,2}\right) \\ 0 \\ 4\left(\varphi_1 + u^0_{3,1}\right) \\ 4\left(\varphi_2 + u^0_{3,2}\right) \\ -\left(\varphi_1 + u^0_{3,1}\right) \\ -\left(\varphi_2 + u^0_{3,2}\right) \\ 0 \\ 0 \\ 0 \end{Bmatrix}.$$

The components of rotation gradients in Eq. (13) are expressed as follows

$$\boldsymbol{\chi}^{(0)} = \frac{1}{2}\begin{Bmatrix} u^0_{3,12} \\ -u^0_{3,12} \\ u^0_{3,22} - u^0_{3,11} \\ 0 \\ u^0_{2,11} - u^0_{1,12} \\ u^0_{2,12} - u^0_{1,22} \end{Bmatrix}, \quad \boldsymbol{\chi}^{(1)} = \frac{1}{2}\begin{Bmatrix} -u^0_{3,12} \\ u^0_{3,12} \\ u^0_{3,11} - u^0_{3,22} \\ 0 \\ 0 \\ 0 \end{Bmatrix}, \quad \boldsymbol{\chi}^{(2)} = \frac{1}{2}\begin{Bmatrix} -\varphi_{2,1} \\ \varphi_{1,2} \\ \varphi_{1,1} - \varphi_{2,2} \\ \varphi_{2,1} - \varphi_{1,2} \\ 0 \\ 0 \end{Bmatrix}, \tag{A.4a}$$

$$\chi^{(3)} = \frac{1}{2}\begin{Bmatrix} 0 \\ 0 \\ 0 \\ 0 \\ -u^0_{3,2} \\ u^0_{3,1} \end{Bmatrix}, \quad \chi^{(4)} = \frac{1}{2}\begin{Bmatrix} 0 \\ 0 \\ 0 \\ 0 \\ -\varphi_2 \\ \varphi_1 \end{Bmatrix}, \quad \chi^{(5)} = \frac{1}{2}\begin{Bmatrix} 0 \\ 0 \\ 0 \\ 0 \\ \varphi_{2,11} - \varphi_{1,12} \\ \varphi_{2,12} - \varphi_{1,22} \end{Bmatrix}. \tag{A.4b}$$

APPENDIX B

The stress resultants of the FGP microplates are expressed in terms of the strains and its gradients as follows

$$\begin{Bmatrix} \mathbf{M}^{(0)}_{\varepsilon} \\ \mathbf{M}^{(1)}_{\varepsilon} \\ \mathbf{M}^{(2)}_{\varepsilon} \\ \mathbf{M}^{(3)}_{\varepsilon} \end{Bmatrix} = \begin{bmatrix} \mathbf{A}^{\varepsilon} & \mathbf{B}^{\varepsilon} & \mathbf{B}^{\varepsilon}_s & \mathbf{0} \\ \mathbf{B}^{\varepsilon} & \mathbf{D}^{\varepsilon} & \mathbf{D}^{\varepsilon}_s & \mathbf{0} \\ \mathbf{B}^{\varepsilon}_s & \mathbf{D}^{\varepsilon}_s & \mathbf{H}^{\varepsilon}_s & \mathbf{0} \\ \mathbf{0} & \mathbf{0} & \mathbf{0} & \mathbf{A}^{\varepsilon}_s \end{bmatrix} \begin{Bmatrix} \boldsymbol{\varepsilon}^{(0)} \\ \boldsymbol{\varepsilon}^{(1)} \\ \boldsymbol{\varepsilon}^{(2)} \\ \boldsymbol{\varepsilon}^{(3)} \end{Bmatrix}, \tag{B.1a}$$

$$\begin{Bmatrix} \mathbf{M}^{(0)}_{x} \\ \mathbf{M}^{(1)}_{x} \\ \mathbf{M}^{(2)}_{x} \\ \mathbf{M}^{(3)}_{x} \\ \mathbf{M}^{(4)}_{x} \\ \mathbf{M}^{(5)}_{x} \end{Bmatrix} = \begin{bmatrix} \mathbf{A}^{x} & \overline{\mathbf{B}}^{x} & \overline{\mathbf{B}}^{x}_s & \overline{\mathbf{B}}^{x} & \overline{\mathbf{B}}^{x}_s & \mathbf{B}^{x}_s \\ \overline{\mathbf{B}}^{x} & \overline{\mathbf{D}}^{x} & \overline{\mathbf{D}}^{x}_s & \overline{\mathbf{E}}^{x} & \overline{\mathbf{E}}^{x}_s & \overline{\mathbf{F}}^{x}_s \\ \overline{\mathbf{B}}^{x}_s & \overline{\mathbf{D}}^{x}_s & \overline{\mathbf{H}}^{x}_s & \overline{\mathbf{G}}^{x}_s & \overline{\mathbf{I}}^{x} & \overline{\mathbf{J}}^{x} \\ \overline{\mathbf{B}}^{x} & \overline{\mathbf{E}}^{x} & \overline{\mathbf{G}}^{x}_s & \overline{\overline{\mathbf{D}}}^{x} & \overline{\overline{\mathbf{D}}}^{x}_s & \overline{\mathbf{K}}^{x}_s \\ \overline{\overline{\mathbf{B}}}^{x}_s & \overline{\mathbf{E}}^{x}_s & \overline{\mathbf{I}}^{x} & \overline{\overline{\mathbf{D}}}^{x}_s & \overline{\overline{\mathbf{H}}}^{x}_s & \overline{\mathbf{L}} \\ \mathbf{B}^{x}_s & \overline{\mathbf{F}}^{x}_s & \overline{\mathbf{J}}^{x} & \overline{\mathbf{K}}^{x}_s & \overline{\mathbf{L}} & \mathbf{H}^{x}_s \end{bmatrix} \begin{Bmatrix} \chi^{(0)} \\ \chi^{(2)} \\ \chi^{(3)} \\ \chi^{(4)} \\ \chi^{(5)} \end{Bmatrix}, \tag{B.1b}$$

$$\begin{Bmatrix} \mathbf{M}^{(0)}_{\eta} \\ \mathbf{M}^{(1)}_{\eta} \\ \mathbf{M}^{(2)}_{\eta} \\ \mathbf{M}^{(3)}_{\eta} \\ \mathbf{M}^{(4)}_{\eta} \\ \mathbf{M}^{(5)}_{\eta} \\ \mathbf{M}^{(6)}_{\eta} \end{Bmatrix} = \begin{bmatrix} \mathbf{A}^{\eta} & \mathbf{B}^{\eta} & \mathbf{B}^{\eta}_s & \mathbf{A}^{\eta}_s & \overline{\mathbf{B}}^{\eta} & \overline{\mathbf{B}}^{\eta}_s & \overline{\mathbf{A}}^{\eta}_s \\ \mathbf{B}^{\eta} & \mathbf{D}^{\eta} & \mathbf{D}^{\eta}_s & \mathbf{D}^{\eta}_{ts} & \overline{\mathbf{O}}^{\eta} & \overline{\mathbf{P}}^{\eta}_s & \overline{\mathbf{Q}}^{\eta}_s \\ \mathbf{B}^{\eta}_s & \mathbf{D}^{\eta}_s & \mathbf{H}^{\eta}_s & \mathbf{D}^{\eta}_{hs} & \overline{\mathbf{F}}^{\eta}_s & \overline{\mathbf{J}}^{\eta} & \overline{\mathbf{F}}^{\eta}_{hs} \\ \mathbf{A}^{\eta}_s & \mathbf{D}^{\eta}_{ts} & \mathbf{D}^{\eta}_{hs} & \mathbf{H}^{\eta}_{ts} & \overline{\mathbf{F}}^{\eta}_{ts} & \overline{\mathbf{J}}^{\eta}_{hs} & \overline{\mathbf{R}}^{\eta} \\ \overline{\mathbf{B}}^{\eta} & \overline{\mathbf{O}}^{\eta} & \overline{\mathbf{F}}^{\eta}_s & \overline{\mathbf{F}}^{\eta}_{ts} & \overline{\mathbf{D}}^{\eta} & \overline{\mathbf{D}}^{\eta}_s & \overline{\mathbf{D}}^{\eta}_{ts} \\ \overline{\mathbf{B}}^{\eta}_s & \overline{\mathbf{P}}^{\eta}_s & \overline{\mathbf{J}}^{\eta} & \overline{\mathbf{J}}^{\eta}_{hs} & \overline{\mathbf{D}}^{\eta}_s & \overline{\mathbf{H}}^{\eta}_s & \overline{\mathbf{D}}^{\eta}_{hs} \\ \overline{\mathbf{A}}^{\eta}_s & \overline{\mathbf{Q}}^{\eta}_s & \overline{\mathbf{F}}^{\eta}_{hs} & \overline{\mathbf{R}}^{\eta} & \overline{\mathbf{D}}^{\eta}_{ts} & \overline{\mathbf{D}}^{\eta}_{hs} & \overline{\mathbf{H}}^{\eta}_{ts} \end{bmatrix} \begin{Bmatrix} \boldsymbol{\eta}^{(0)} \\ \boldsymbol{\eta}^{(1)} \\ \boldsymbol{\eta}^{(2)} \\ \boldsymbol{\eta}^{(3)} \\ \boldsymbol{\eta}^{(4)} \\ \boldsymbol{\eta}^{(5)} \\ \boldsymbol{\eta}^{(6)} \end{Bmatrix}, \tag{B.1c}$$

$$\begin{Bmatrix} \mathbf{M}^{(0)}_{\xi} \\ \mathbf{M}^{(1)}_{\xi} \\ \mathbf{M}^{(2)}_{\xi} \\ \mathbf{M}^{(3)}_{\xi} \\ \mathbf{M}^{(4)}_{\xi} \end{Bmatrix} \begin{bmatrix} \mathbf{A}^{\xi} & \mathbf{B}^{\xi} & \mathbf{B}^{\xi}_s & \overline{\mathbf{B}}^{\xi} & \overline{\mathbf{B}}^{\xi}_s \\ \mathbf{B}^{\xi} & \mathbf{D}^{\xi} & \mathbf{D}^{\xi}_s & \overline{\mathbf{O}}^{\xi} & \overline{\mathbf{P}}^{\xi}_s \\ \mathbf{B}^{\xi}_s & \mathbf{D}^{\xi}_s & \mathbf{H}^{\xi}_s & \overline{\mathbf{F}}^{\xi}_s & \overline{\mathbf{J}}^{\xi} \\ \overline{\mathbf{B}}^{\xi} & \overline{\mathbf{O}}^{\xi} & \overline{\mathbf{F}}^{\xi}_s & \overline{\mathbf{D}}^{\xi} & \overline{\mathbf{D}}^{\xi}_s \\ \overline{\mathbf{B}}^{\xi}_s & \overline{\mathbf{P}}^{\xi}_s & \overline{\mathbf{J}}^{\xi} & \overline{\mathbf{D}}^{\xi}_s & \overline{\mathbf{H}}^{\xi}_s \end{bmatrix} \begin{Bmatrix} \boldsymbol{\xi}^{(0)} \\ \boldsymbol{\xi}^{(1)} \\ \boldsymbol{\xi}^{(2)} \\ \boldsymbol{\xi}^{(3)} \\ \boldsymbol{\xi}^{(4)} \end{Bmatrix}, \tag{B.1d}$$

where the stiffness components of the FGP microplates are defined as follows

$$
\begin{aligned}
&(\mathbf{A}^{\varepsilon},\mathbf{B}^{\varepsilon},\mathbf{D}^{\varepsilon},\mathbf{H}_s^{\varepsilon},\mathbf{B}_s^{\varepsilon},\mathbf{D}_s^{\varepsilon}) = \int_{-h/2}^{h/2}\left(1,\Phi_1,\Phi_1^2,\Phi_2^2,\Phi_2,\Phi_1\Phi_2\right)\mathbf{Q}_{\varepsilon}^{(i)}\mathrm{d}x_3, \quad \mathbf{A}_s^{\varepsilon} = \int_{-h/2}^{h/2}\Phi_3^2\mathbf{Q}_{\varepsilon}^{(o)}\mathrm{d}x_3,\\
&\left(\mathbf{A}^{\xi},\mathbf{B}^{\xi},\mathbf{B}_s^{\xi},\overline{\mathbf{B}}^{\xi},\overline{\mathbf{B}}_s^{\xi}\right) = \left(A^{\xi},B^{\xi},B_s^{\xi},\overline{B}^{\xi},\overline{B}_s^{\xi}\right)\mathbf{I}_{3\times3} = \int_{-h/2}^{h/2}\left(1,\Phi_1,\Phi_2,\Phi_{1,3},\Phi_{2,3}\right)\alpha_{\xi}\mathbf{I}_{3\times3}\mathrm{d}x_3,\\
&\left(\mathbf{D}^{\xi},\mathbf{D}_s^{\xi},\overline{\mathbf{O}}^{\xi},\overline{\mathbf{P}}_s^{\xi}\right) = \left(D^{\xi},D_s^{\xi},\overline{O}^{\xi},\overline{P}_s^{\xi}\right)\mathbf{I}_{3\times3} = \int_{-h/2}^{h/2}\Phi_1\left(\Phi_1,\Phi_2,\Phi_{1,3},\Phi_{2,3}\right)\alpha_{\xi}\mathbf{I}_{3\times3}\mathrm{d}x_3,\\
&\left(\mathbf{H}_s^{\xi},\overline{\mathbf{F}}_s^{\xi},\overline{\mathbf{J}}^{\xi},\overline{\mathbf{D}}^{\xi},\overline{\mathbf{D}}_s^{\xi},\overline{\mathbf{H}}_s^{\xi}\right) = \left(H_s^{\xi},\overline{F}_s^{\xi},\overline{J}^{\xi},\overline{D}^{\xi},\overline{D}_s^{\xi},\overline{H}_s^{\xi}\right)\mathbf{I}_{3\times3} = \int_{-h/2}^{h/2}\left(\Phi_2^2,\Phi_2\Phi_{1,3},\Phi_2\Phi_{2,3},\Phi_{1,3}^2,\Phi_{1,3}\Phi_{2,3},\Phi_{2,3}^2\right)\alpha_{\xi}\mathbf{I}_{3\times3}\mathrm{d}x_3,\\
&\left(\mathbf{A}^{\eta},\mathbf{B}^{\eta},\mathbf{B}_s^{\eta},\mathbf{A}_s^{\eta},\overline{\mathbf{B}}^{\eta},\overline{\mathbf{B}}_s^{\eta},\overline{\mathbf{A}}_s^{\eta}\right) = \left(A^{\eta},B^{\eta},B_s^{\eta},A_s^{\eta},\overline{B}^{\eta},\overline{B}_s^{\eta},\overline{A}_s^{\eta}\right)\mathbf{I}_{10\times10} = \int_{-h/2}^{h/2}\left(1,\Phi_1,\Phi_2,\Phi_3,\Phi_{1,3},\Phi_{2,3},\Phi_{3,3}\right)\alpha_{\eta}\mathbf{I}_{10\times10}\mathrm{d}x_3,\\
&\left(\mathbf{D}^{\eta},\mathbf{D}_s^{\eta},\mathbf{D}_{ts}^{\eta},\overline{\mathbf{O}}^{\eta},\overline{\mathbf{P}}_s^{\eta},\overline{\mathbf{Q}}_s^{\eta}\right) = \left(D^{\eta},D_s^{\eta},D_{ts}^{\eta},\overline{O}^{\eta},\overline{P}_s^{\eta},\overline{Q}_s^{\eta}\right)\mathbf{I}_{10\times10} = \int_{-h/2}^{h/2}\Phi_1\left(\Phi_1,\Phi_2,\Phi_3,\Phi_{1,3},\Phi_{2,3},\Phi_{3,3}\right)\alpha_{\eta}\mathbf{I}_{10\times10}\mathrm{d}x_3,\\
&\left(\mathbf{H}_s^{\eta},\overline{\mathbf{D}}_{hs}^{\eta},\overline{\mathbf{F}}_s^{\eta},\overline{\mathbf{J}}^{\eta},\overline{\mathbf{F}}_{hs}^{\eta}\right) = \left(H_s^{\eta},\overline{D}_{hs}^{\eta},\overline{F}_s^{\eta},\overline{J}^{\eta},\overline{F}_{hs}^{\eta}\right)\mathbf{I}_{10\times10} = \int_{-h/2}^{h/2}\Phi_2\left(\Phi_2,\Phi_3,\Phi_{1,3},\Phi_{2,3},\Phi_{3,3}\right)\alpha_{\eta}\mathbf{I}_{10\times10}\mathrm{d}x_3,\\
&\left(\mathbf{H}_{ts}^{\eta},\overline{\mathbf{F}}_{ts}^{\eta},\overline{\mathbf{J}}_{hs}^{\eta},\overline{\mathbf{R}}^{\eta}\right) = \left(H_{ts}^{\eta},\overline{F}_{ts}^{\eta},\overline{J}_{hs}^{\eta},\overline{R}^{\eta}\right)\mathbf{I}_{10\times10} = \int_{-h/2}^{h/2}\Phi_3\left(\Phi_3,\Phi_{1,3},\Phi_{2,3},\Phi_{3,3}\right)\alpha_{\eta}\mathbf{I}_{10\times10}\mathrm{d}x_3,\\
&\left(\overline{\mathbf{D}}^{\eta},\overline{\mathbf{D}}_s^{\eta},\overline{\mathbf{D}}_{ts}^{\eta},\overline{\mathbf{H}}_s^{\eta},\overline{\mathbf{D}}_{hs}^{\eta},\overline{\mathbf{H}}_{ts}^{\eta}\right) = \left(\overline{D}^{\eta},\overline{D}_s^{\eta},\overline{D}_{ts}^{\eta},\overline{H}_s^{\eta},\overline{D}_{hs}^{\eta},\overline{H}_{ts}^{\eta}\right)\mathbf{I}_{10\times10}\\
&\qquad = \int_{-h/2}^{h/2}\left(\Phi_{1,3}^2,\Phi_{1,3}\Phi_{2,3},\Phi_{1,3}\Phi_{3,3},\Phi_{2,3}^2,\Phi_{2,3}\Phi_{3,3},\Phi_{3,3}^2\right)\alpha_{\eta}\mathbf{I}_{10\times10}\mathrm{d}x_3,\\
&\left(\mathbf{A}^{\chi},\overline{\mathbf{B}}^{\chi},\overline{\mathbf{B}}_s^{\chi},\overline{\overline{\mathbf{B}}}^{\chi},\overline{\overline{\mathbf{B}}}_s^{\chi},\mathbf{B}_s^{\chi}\right) = \left(A^{\chi},\overline{B}^{\chi},\overline{B}_s^{\chi},\overline{\overline{B}}^{\chi},\overline{\overline{B}}_s^{\chi},B_s^{\chi}\right)\mathbf{I}_{6\times6} = \int_{-h/2}^{h/2}\left(1,\Phi_{1,3},\Phi_{2,3},\Phi_{1,33},\Phi_{2,33},\Phi_2\right)\alpha_{\chi}\mathbf{I}_{6\times6}\mathrm{d}x_3,\\
&\left(\overline{\mathbf{D}}^{\chi},\overline{\mathbf{D}}_s^{\chi},\overline{\mathbf{E}}^{\chi},\overline{\mathbf{E}}_s^{\chi},\overline{\mathbf{F}}_s^{\chi}\right) = \left(\overline{D}^{\chi},\overline{D}_s^{\chi},\overline{E}^{\chi},\overline{E}_s^{\chi},\overline{F}_s^{\chi}\right)\mathbf{I}_{6\times6} = \int_{-h/2}^{h/2}\Phi_{1,3}\left(\Phi_{1,3},\Phi_{2,3},\Phi_{1,33},\Phi_{2,33},\Phi_2\right)\alpha_{\chi}\mathbf{I}_{6\times6}\mathrm{d}x_3,\\
&\left(\overline{\mathbf{H}}_s^{\chi},\overline{\mathbf{G}}_s^{\chi},\overline{\mathbf{I}}^{\chi},\overline{\mathbf{J}}^{\chi}\right) = \left(\overline{H}_s^{\chi},\overline{G}_s^{\chi},\overline{I}^{\chi},\overline{J}^{\chi}\right)\mathbf{I}_{6\times6} = \int_{-h/2}^{h/2}\Phi_{2,3}\left(\Phi_{2,3},\Phi_{1,33},\Phi_{2,33},\Phi_2\right)\alpha_{\chi}\mathbf{I}_{6\times6}\mathrm{d}x_3,\\
&\left(\overline{\overline{\mathbf{D}}}^{\chi},\overline{\overline{\mathbf{D}}}_s^{\chi},\overline{\mathbf{K}}_s^{\chi},\overline{\overline{\mathbf{H}}}_s^{\chi},\overline{\mathbf{L}}^{\chi},\mathbf{H}_s^{\chi}\right) = \left(\overline{\overline{D}}^{\chi},\overline{\overline{D}}_s^{\chi},\overline{K}_s^{\chi},\overline{\overline{H}}_s^{\chi},\overline{L}^{\chi},H_s^{\chi}\right)\mathbf{I}_{6\times6}\\
&\qquad = \int_{-h/2}^{h/2}\left(\Phi_{1,33}^2,\Phi_{1,33}\Phi_{2,33},\Phi_{1,33}\Phi_2,\Phi_{2,33}^2,\Phi_{2,33}\Phi_2,\Phi_2^2\right)\alpha_{\chi}\mathbf{I}_{6\times6}\mathrm{d}x_3.
\end{aligned}
\tag{B.2}
$$

APPENDIX C

The components of stiffness matrix $\mathbf{K}^{\xi}, \mathbf{K}^{\eta}$ and load vector $\mathbf{F}$ are defined as follows

$$
\begin{aligned}
K_{ijkl}^{\xi11} &= A^{\xi}\left(T_{ik}^{33}S_{jl}^{00}+T_{ik}^{22}S_{jl}^{11}\right), \quad K_{ijkl}^{\xi12} = A^{\xi}\left(T_{ik}^{13}S_{jl}^{20}+T_{ik}^{02}S_{jl}^{31}\right),\\
K_{ijkl}^{\xi13} &= B^{\xi}\left(T_{ik}^{33}S_{jl}^{00}+T_{ik}^{13}S_{jl}^{20}+T_{ik}^{02}S_{jl}^{31}+T_{ik}^{22}S_{jl}^{11}\right),\\
K_{ijkl}^{\xi14} &= B_s^{\xi}\left(T_{ik}^{33}S_{jl}^{00}+T_{ik}^{22}S_{jl}^{11}\right), \quad K_{ijkl}^{\xi15} = B_s^{\xi}\left(T_{ik}^{13}S_{jl}^{20}+T_{ik}^{02}S_{jl}^{31}\right),\\
K_{ijkl}^{\xi22} &= A^{\xi}\left(T_{ik}^{11}S_{jl}^{22}+T_{ik}^{00}S_{jl}^{33}\right), \quad K_{ijkl}^{\xi23} = B^{\xi}\left(T_{ik}^{31}S_{jl}^{02}+T_{ik}^{11}S_{jl}^{22}+T_{ik}^{20}S_{jl}^{13}+T_{ik}^{00}S_{jl}^{33}\right),\\
K_{ijkl}^{\xi24} &= B_s^{\xi}\left(T_{ik}^{31}S_{jl}^{02}+T_{ik}^{20}S_{jl}^{13}\right), \quad K_{ijkl}^{\xi25} = B_s^{\xi}\left(T_{ik}^{11}S_{jl}^{22}+T_{ik}^{00}S_{jl}^{33}\right),\\
K_{ijkl}^{\xi33} &= D^{\xi}\left(T_{ik}^{33}S_{jl}^{00}+T_{ik}^{00}S_{jl}^{33}+T_{ik}^{31}S_{jl}^{02}+T_{ik}^{02}S_{jl}^{31}+T_{ik}^{13}S_{jl}^{20}+T_{ik}^{20}S_{jl}^{13}+T_{ik}^{11}S_{jl}^{22}+T_{ik}^{22}S_{jl}^{11}\right)\\
&\quad+\overline{D}^{\xi}\left(T_{ik}^{22}S_{jl}^{00}+T_{ik}^{20}S_{jl}^{02}+T_{ik}^{02}S_{jl}^{20}+T_{ik}^{00}S_{jl}^{22}\right),\\
K_{ijkl}^{\xi34} &= D_s^{\xi}\left(T_{ik}^{33}S_{jl}^{00}+T_{ik}^{31}S_{jl}^{02}+T_{ik}^{22}S_{jl}^{11}+T_{ik}^{20}S_{jl}^{13}\right)+\overline{D}_s^{\xi}\left(T_{ik}^{22}S_{jl}^{00}+T_{ik}^{20}S_{jl}^{02}\right),\\
K_{ijkl}^{\xi35} &= D_s^{\xi}\left(T_{ik}^{13}S_{jl}^{20}+T_{ik}^{11}S_{jl}^{22}+T_{ik}^{02}S_{jl}^{31}+T_{ik}^{00}S_{jl}^{33}\right)+\overline{D}_s^{\xi}\left(T_{ik}^{02}S_{jl}^{20}+T_{ik}^{00}S_{jl}^{22}\right),\\
K_{ijkl}^{\xi44} &= H_s^{\xi}T_{ik}^{33}S_{jl}^{00}+H_s^{\xi}T_{ik}^{22}S_{jl}^{11}+\overline{H}_s^{\xi}T_{ik}^{22}S_{jl}^{00}, \quad K_{ijkl}^{\xi45} = H_s^{\xi}T_{ik}^{13}S_{jl}^{20}+H_s^{\xi}T_{ik}^{02}S_{jl}^{31}+\overline{H}_s^{\xi}T_{ik}^{02}S_{jl}^{20},\\
K_{ijkl}^{\xi55} &= H_s^{\xi}T_{ik}^{00}S_{jl}^{33}+H_s^{\xi}T_{ik}^{11}S_{jl}^{22}+\overline{H}_s^{\xi}T_{ik}^{00}S_{jl}^{22},
\end{aligned}
\tag{C.1a}
$$

$$
\begin{aligned}
K_{ijkl}^{\eta 11} &= A^{\eta}\left(22T_{ik}^{33}S_{jl}^{00}-11T_{ik}^{31}S_{jl}^{02}-11T_{ik}^{13}S_{jl}^{20}+18T_{ik}^{11}S_{jl}^{22}+72T_{ik}^{22}S_{jl}^{11}\right)/25,\\
K_{ijkl}^{\eta 12} &= 2A^{\eta}\left(-11T_{ik}^{13}S_{jl}^{20}-11T_{ik}^{02}S_{jl}^{31}+18T_{ik}^{11}S_{jl}^{22}+18T_{ik}^{22}S_{jl}^{11}\right)/25,\\
K_{ijkl}^{\eta 13} &= B^{\eta}\left(22T_{ik}^{33}S_{jl}^{00}-11T_{ik}^{31}S_{jl}^{02}-33T_{ik}^{13}S_{jl}^{20}+54T_{ik}^{11}S_{jl}^{22}-22T_{ik}^{02}S_{jl}^{31}+108T_{ik}^{22}S_{jl}^{11}\right)/25,\\
K_{ijkl}^{\eta 25} &= B_{s}^{\eta}\left(72T_{ik}^{11}S_{jl}^{22}+22T_{ik}^{00}S_{jl}^{33}-11T_{ik}^{02}S_{jl}^{31}-11T_{ik}^{20}S_{jl}^{13}+18T_{ik}^{22}S_{jl}^{11}\right)/25-\overline{A}_{s}^{\eta}\left(7T_{ik}^{02}S_{jl}^{11}+11T_{ik}^{00}S_{jl}^{13}\right)/25,\\
K_{ijkl}^{\eta 33} &= D^{\eta}\left(22T_{ik}^{33}S_{jl}^{00}-33T_{ik}^{31}S_{jl}^{02}-33T_{ik}^{13}S_{jl}^{20}+162T_{ik}^{11}S_{jl}^{22}+162T_{ik}^{22}S_{jl}^{11}+22T_{ik}^{00}S_{jl}^{33}-33T_{ik}^{02}S_{jl}^{31}-33T_{ik}^{20}S_{jl}^{13}\right)/25,\\
&\quad-\overline{Q}_{s}^{\eta}\left(11T_{ik}^{00}S_{jl}^{13}+11T_{ik}^{13}S_{jl}^{00}+11T_{ik}^{31}S_{jl}^{00}+11T_{ik}^{00}S_{jl}^{31}+21T_{ik}^{02}S_{jl}^{11}+21T_{ik}^{11}S_{jl}^{02}+21T_{ik}^{11}S_{jl}^{20}+21T_{ik}^{20}S_{jl}^{11}\right)/25,\\
&\quad+\left(H_{ts}^{\eta}+2\overline{F}_{ts}^{\eta}+\overline{D}^{\eta}\right)\left(18T_{ik}^{22}S_{jl}^{00}-7T_{ik}^{20}S_{jl}^{02}-7T_{ik}^{02}S_{jl}^{20}+18T_{ik}^{00}S_{jl}^{22}+100T_{ik}^{11}S_{jl}^{11}\right)/25+18\overline{H}_{ts}^{\eta}\left(T_{ik}^{11}S_{jl}^{00}+T_{ik}^{00}S_{jl}^{11}\right)/25,\\
K_{ijkl}^{\eta 34} &= D_{s}^{\eta}\left(22T_{ik}^{33}S_{jl}^{00}-33T_{ik}^{31}S_{jl}^{02}-11T_{ik}^{13}S_{jl}^{20}+54T_{ik}^{11}S_{jl}^{22}-22T_{ik}^{20}S_{jl}^{13}+108T_{ik}^{22}S_{jl}^{11}\right)/25\\
&\quad-\overline{Q}_{s}^{\eta}\left(11T_{ik}^{13}S_{jl}^{00}+21T_{ik}^{11}S_{jl}^{02}\right)/25+\left(H_{ts}^{\eta}+\overline{J}_{hs}^{\eta}+\overline{F}_{ts}^{\eta}+\overline{D}_{s}^{\eta}\right)\left(18T_{ik}^{22}S_{jl}^{00}-7T_{ik}^{20}S_{jl}^{02}+50T_{ik}^{11}S_{jl}^{11}\right)/25\\
&\quad-\overline{F}_{hs}^{\eta}\left(14T_{ik}^{20}S_{jl}^{11}+11T_{ik}^{31}S_{jl}^{00}+7T_{ik}^{11}S_{jl}^{20}\right)/25+18\overline{H}_{is}^{\eta}T_{ik}^{11}S_{jl}^{00}/25,\\
K_{ijkl}^{\eta 35} &= D_{s}^{\eta}\left(108T_{ik}^{11}S_{jl}^{22}+54T_{ik}^{22}S_{jl}^{11}+22T_{ik}^{00}S_{jl}^{33}-33T_{ik}^{02}S_{jl}^{31}-11T_{ik}^{20}S_{jl}^{13}-22T_{ik}^{13}S_{jl}^{20}\right)/25\\
&\quad-\overline{Q}_{s}^{\eta}\left(21T_{ik}^{02}S_{jl}^{11}+11T_{ik}^{00}S_{jl}^{13}\right)/25+\left(H_{ts}^{\eta}+\overline{J}_{hs}^{\eta}+\overline{F}_{ts}^{\eta}+\overline{D}_{s}^{\eta}\right)\left(18T_{ik}^{00}S_{jl}^{22}-7T_{ik}^{02}S_{jl}^{20}+50T_{ik}^{11}S_{jl}^{11}\right)/25\\
&\quad-\overline{F}_{hs}^{\eta}\left(14T_{ik}^{11}S_{jl}^{20}+11T_{ik}^{00}S_{jl}^{31}+7T_{ik}^{20}S_{jl}^{11}\right)/25+18\overline{H}_{is}^{\eta}T_{ik}^{00}S_{jl}^{11}/25,\\
K_{ijkl}^{\eta 44} &= H_{s}^{\eta}\left(22T_{ik}^{33}S_{jl}^{00}-11T_{ik}^{31}S_{jl}^{02}-11T_{ik}^{13}S_{jl}^{20}+18T_{ik}^{11}S_{jl}^{22}+72T_{ik}^{22}S_{jl}^{11}\right)/25+18\overline{H}_{is}^{\eta}T_{ik}^{11}S_{jl}^{00}/25\\
&\quad+\left(H_{is}^{\eta}+2\overline{J}_{hs}^{\eta}+\overline{H}_{s}^{\eta}\right)\left(18T_{ik}^{22}S_{jl}^{00}+25T_{ik}^{11}S_{jl}^{11}\right)-\overline{F}_{hs}^{\eta}\left(11T_{ik}^{31}S_{jl}^{00}+7T_{ik}^{11}S_{jl}^{20}+11T_{ik}^{13}S_{jl}^{00}+7T_{ik}^{11}S_{jl}^{02}\right)/25,\\
K_{ijkl}^{\eta 45} &= H_{s}^{\eta}\left(36T_{ik}^{11}S_{jl}^{22}+36T_{ik}^{22}S_{jl}^{11}-22T_{ik}^{13}S_{jl}^{20}-22T_{ik}^{02}S_{jl}^{31}\right)/25-14\overline{F}_{hs}^{\eta}\left(T_{ik}^{02}S_{jl}^{11}+T_{ik}^{11}S_{jl}^{20}\right)/25\\
&\quad+\left(H_{ts}^{\eta}+2\overline{J}_{hs}^{\eta}+\overline{H}_{s}^{\eta}\right)\left(25T_{ik}^{11}S_{jl}^{11}-7T_{ik}^{02}S_{jl}^{20}\right)/25,\\
K_{ijkl}^{\eta 55} &= H_{s}^{\eta}\left(72T_{ik}^{11}S_{jl}^{22}+22T_{ik}^{00}S_{jl}^{33}-11T_{ik}^{02}S_{jl}^{31}-11T_{ik}^{20}S_{jl}^{13}+18T_{ik}^{22}S_{jl}^{11}\right)/25+18\overline{H}_{ts}^{\eta}T_{ik}^{00}S_{jl}^{11}/25\\
&\quad+\left(H_{ts}^{\eta}+2\overline{J}_{hs}^{\eta}+\overline{H}_{s}^{\eta}\right)\left(18T_{ik}^{00}S_{jl}^{22}+25T_{ik}^{11}S_{jl}^{11}\right)/25-\overline{F}_{hs}^{\eta}\left(11T_{ik}^{00}S_{jl}^{13}+7T_{ik}^{02}S_{jl}^{11}+11T_{ik}^{00}S_{jl}^{31}+7T_{ik}^{20}S_{jl}^{11}\right)/25,
\end{aligned}
\tag{C.1b}
$$

$$
f_{ij}=\int_{0}^{a}\int_{0}^{b}qX_{i}Y_{j}\mathrm{d}x_{1}\mathrm{d}x_{2},
\tag{C.1c}
$$

$$
T_{ik}^{rs}=\int_{0}^{a}\frac{\partial^{r}R_{i}}{\partial x_{1}^{r}}\frac{\partial^{s}R_{k}}{\partial x_{1}^{s}}\mathrm{d}x_{1},\qquad S_{jl}^{rs}=\int_{0}^{a}\frac{\partial^{r}P_{j}}{\partial x_{2}^{r}}\frac{\partial^{s}P_{l}}{\partial x_{2}^{s}}\mathrm{d}x_{2}.
\tag{C.1d}
$$

A General Framework of Higher-Order Shear Deformation Theory for Free Vibration Analysis of Functionally Graded Microplates

Van-Thien Tran and Trung-Kien Nguyen

Abstract This paper proposes a unified higher-order shear deformation microplate model for vibration analysis of functionally graded materials. The theory is developed from fundamental equations of the elasticity theory and modified couple stress theory, from which many different frameworks of size-dependent plate models are recovered. In order to capture the size effects, the modified couple stress theory with one independent length-scale parameter is used. The solution field is approximated by bi-directional series in which hybrid shape functions are proposed, then the stiffness and mass matrix are explicitly derived. Numerical results are presented for different configurations of material distribution, side-to-thickness ratio, size-scale-thickness ratio and boundary conditions on the natural frequencies of functionally graded microplates.

Keywords Series-type solutions · Vibration · Functionally graded microplates · Modified couple stress theory

1 Introduction

The recent development of functionally graded (FG) microplates with continuous variations of materials in a required direction led to a large potential application in engineering field. However, the behaviours of these structures at small scales require advanced computational models to capture size effects. The earlier experimental works revealed that the classical elasticity theory could not accurately predict responses of microstructures at small scale, advanced computations theories with length scale parameters have been therefore developed with different approaches. A number of researches has been performed to accurately predict static and vibration behaviours of FG microplates in which the modified coupled stress theory (MCT) is mostly used. The MCT initiated by Yang et al. [1] is known as the simplest theory

V.-T. Tran · T.-K. Nguyen (✉)
Faculty of Civil Engineering, Ho Chi Minh City University of Technology and Education, 1 Vo Van Ngan Street, Thu Duc City, Ho Chi Minh City, Viet Nam
e-mail: kiennt@hcmute.edu.vn

J. N. Reddy et al. (eds.), *ICSCEA 2021*, Lecture Notes in Civil Engineering 268,
https://doi.org/10.1007/978-981-19-3303-5_64

accounted for the size effects in which only one material length scale parameter associated with rotation gradient is accounted in the constitutive equations. Based on the MCT, many researches have been developed for static and dynamic analysis of FG microplates, only some representative references are herein cited. Tsiatas [2] investigated static analysis of isotropic micro-plates using classical plate theory (CPT). Ma et al. [3] analysed bending and free vibration responses of FG microplates using first-order shear deformation theory (FSDT). Reddy and Kim [4] presented geometrically nonlinear analysis of FG microplates based on a higher-order shear deformation theory (HSDT). Thai et al. [5, 6] studied size-dependent effects on static and vibration responses of FG microplate by using the HSDT. He et al. [7] used a refined HSDT for analysis of FG microplates. A brief literature review on the behaviours of FG microplates showed that though there is a number of studies have been performed in predicting static and dynamic behaviours of the FG microplates using the MCT with different plate theories, this complicated problem needs to be studied more further.

The objective of this paper is to propose a unified size-dependent plate model based on a general HSDT framework and MCT for analysis of FG materials. It is developed from fundamental equations of the elasticity theory and modified couple stress one. The governing equations of motions are derived from Lagrange's equations and then bi-directional series-type solutions with hybrid shape functions are proposed. Numerical results are presented for different configurations of material distribution, side-to-thickness ratio and boundary conditions on natural frequencies of the FG microplates. New results presented in this study can be of interests to the scientific and engineering community in the future.

2 Theoretical formulation

Consider a FG rectangle microplate in the coordinate system (x_1, x_2, x_3) with sides $a \times b$ and thickness h as shown in Fig. 1. The plate is composed of a mixture of ceramic and metal materials whose properties vary continuously in the thickness direction. The effective material properties of FG microplates can be approximated

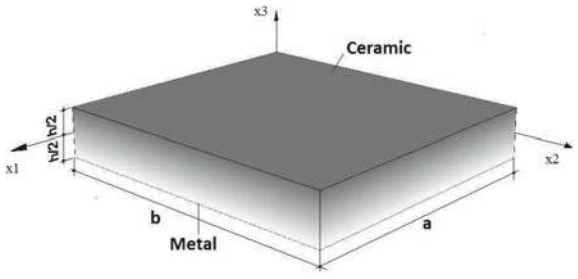

Fig. 1 Geometry of a FG microplate

by the following expressions [6, 7]:

$$P(x_3) = (P_c - P_m)\left(\frac{2x_3 + h}{2h}\right)^p + P_m \tag{1}$$

where P_c and P_m are the properties of ceramic and metal materials, respectively, such as Young's moduli E, mass density ρ, Poisson's ratio ν; p is the power-law index which is positive and $x_3 \in [-h/2, h/2]$.

2.1 Modified couple stress theory

The total potential energy of the FG microplate is obtained by:

$$\Pi = \Pi_U - \Pi_K \tag{2}$$

where Π_U, Π_K are the strain energy and kinetic energy of the FG microplate, respectively. Based on the MCT, the strain energy of the system Π_U is given by [1, 6]:

$$\Pi_U = \int_V (\boldsymbol{\sigma}\varepsilon + \mathrm{m}\boldsymbol{\chi})dV \tag{3}$$

where $\boldsymbol{\varepsilon}$, $\boldsymbol{\chi}$ are strains and symmetric rotation gradients, respectively; $\boldsymbol{\sigma}$ is Cauchy stress; $\boldsymbol{m}$ are higher-order stress corresponding with strain gradients $\boldsymbol{\chi}$. The components of strain ε_{ij} and strain gradients χ_{ij} are defined as follows:

$$\varepsilon_{ij} = \frac{1}{2}\left(u_{i,j} + u_{j,i}\right),\ \chi_{ij} = \frac{1}{4}\left(u_{n,mj}e_{imn} + u_{n,mi}e_{jmn}\right) \tag{4}$$

where e_{imn} are Knonecker delta and permutation symbol, respectively. The components of stress are calculated from constitutive equations as follows:

$$\sigma_{ij} = \lambda\varepsilon_{kk}\delta_{ij} + 2\mu\varepsilon_{ij},\ m_{ij} = 2\mu l^2\chi_{ij} \tag{5}$$

where λ, μ are Lamé constants; l is length scale parameter. The kinetic energy of the FG microplate Π_K is expressed by:

$$\Pi_K = \frac{1}{2}\int_V \rho(x_3)\left(\dot{u}_1^2 + \dot{u}_2^2 + \dot{u}_3^2\right)dV \tag{6}$$

where $\rho(x_3)$ is mass density of the FG microplate; $\dot{u}_1 = u_{1,t}$, $\dot{u}_2 = u_{2,t}$, $\dot{u}_3 = u_{3,t}$ are velocities in x_1-, x_2- and x_3- directions, respectively.

2.2 *Unified kinematics of FG microplates*

For simplicity purpose, the effects of transverse normal strain are neglected in the sequel, i.e. $u_3(x_1, x_2, x_3) = u_3^0(x_1, x_2)$ where $u_3^0(x_1, x_2)$ is transverse displacement at the mid-surface of the FG microplate. Moreover, it is supposed that the transverse shear stresses are expressed in terms of the transverse shear forces as follows:

$$\sigma_{13} = f_{,3}(x_3)Q_1(x_1, x_2), \sigma_{23} = f_{,3}(x_3)Q_2(x_1, x_2) \tag{7}$$

where $f(x_3)$ is a higher-order term whose first derivative satisfies the free-stress boundary condition at the top and bottom surfaces of the plates, i.e. $f_{,3}\left(x_3 = \pm\frac{h}{2}\right) = 0$; the comma in subscript is used to indicate the derivative of variable that follows. Additionally, transverse shear strains are linearly related to the membrane displacements $u_1(x_1, x_2, x_3)$, $u_2(x_1, x_2, x_3)$ and transverse one $u_3^0(x_1, x_2)$ by:

$$\gamma_{13} = u_{1,3} + u_{3,1}^0 = \frac{\sigma_{13}}{\mu} = \frac{f_{,3}Q_1}{\mu}, \gamma_{23} = u_{2,3} + u_{3,2}^0 = \frac{\sigma_{23}}{\mu} = \frac{f_{,3}Q_2}{\mu}, \tag{8}$$

where $\mu(x_3) = \frac{E(x_3)}{2(1+\nu)}$ is the shear modulus. Furthermore, integrating Eq. (8) in x_3- direction leads to a general displacement field of the FG microplate as follows:

$$u_1(x_1, x_2, x_3) = u_1^0(x_1, x_2) - x_3 u_{3,1}^0 + \Psi(x_3)Q_1(x_1, x_2) \tag{9a}$$

$$u_2(x_1, x_2, x_3) = u_2^0(x_1, x_2) - x_3 u_{3,2}^0 + \Psi(x_3)Q_2(x_1, x_2) \tag{9b}$$

$$u_3(x_1, x_2, x_3) = u_3^0(x_1, x_2) \tag{9c}$$

where $\Psi(x_3) = \int_0^{x_3} \frac{f_{,3}}{\mu(x_3)} dx_3$. Moreover, it is known that the shear forces can be expressed in terms of the rotation (φ_1, φ_2) and gradients of the transverse displacement as follows:

$$Q_1(x_1, x_2) = H^s\left(\varphi_1 + u_{3,1}^0\right), Q_2(x_1, x_2) = H^s\left(\varphi_2 + u_{3,2}^0\right) \tag{10}$$

where $H^s = k^s \int_{-h/2}^{h/2} \mu(x_3) dx_3$ is the transverse shear stiffness of the FG microplates; $k^s = 5/6$ is shear coefficient factor. Substituting Eq. (10) into Eq. (9) leads to a general higher-order shear deformation FG microplate theory as follows:

$$u_1(x_1, x_2, x_3) = u_1^0(x_1, x_2) + \Phi_1(x_3)u_{3,1}^0 + \Phi_2(x_3)\varphi_1(x_1, x_2) \tag{11a}$$

$$u_2(x_1, x_2, x_3) = u_2^0(x_1, x_2) + \Phi_1(x_3)u_{3,2}^0 + \Phi_2(x_3)\varphi_2(x_1, x_2) \tag{11b}$$

$$u_3(x_1, x_2, x_3) = u_3^0(x_1, x_2) \tag{11c}$$

where $\Phi_1(x_3) = H^s\Psi(x_3) - x_3$, $\Phi_2(x_3) = H^s\Psi(x_3)$. Subsituting Eq. (11) into the strains and strain gradients in Eq. (4), the strains $\boldsymbol{\varepsilon}^T = \left[\boldsymbol{\varepsilon}^{(i)}\ \boldsymbol{\varepsilon}^{(s)}\right]$ are obtained as follows:

$$\boldsymbol{\varepsilon}^{(i)} = \boldsymbol{\varepsilon}^{(0)} + \Phi_1(x_3)\boldsymbol{\varepsilon}^{(1)} + \Phi_2(x_3)\boldsymbol{\varepsilon}^{(2)},\ \boldsymbol{\varepsilon}^{(s)} = \Phi_3(x_3)\boldsymbol{\varepsilon}^{(3)} \tag{12}$$

where $\Phi_3(x_3) = H^s\Psi_{,3}$ with $\Psi_{,3}(x_3) = \frac{f_{,3}(x_3)}{\mu(x_3)}$ and,

$$\boldsymbol{\varepsilon}^{(0)} = \begin{Bmatrix} \varepsilon_{11}^{(0)} \\ \varepsilon_{22}^{(0)} \\ \gamma_{12}^{(0)} \end{Bmatrix} = \begin{Bmatrix} u_{1,1}^0 \\ u_{2,2}^0 \\ u_{1,2}^0 + u_{2,1}^0 \end{Bmatrix}, \boldsymbol{\varepsilon}^{(1)} = \begin{Bmatrix} \varepsilon_{11}^{(1)} \\ \varepsilon_{22}^{(1)} \\ \gamma_{12}^{(1)} \end{Bmatrix} = \begin{Bmatrix} u_{3,11}^0 \\ u_{3,22}^0 \\ 2u_{3,12}^0 \end{Bmatrix},$$
$$\boldsymbol{\varepsilon}^{(2)} = \begin{Bmatrix} \varepsilon_{11}^{(2)} \\ \varepsilon_{22}^{(2)} \\ \gamma_{12}^{(2)} \end{Bmatrix} = \begin{Bmatrix} \varphi_{1,1} \\ \varphi_{2,2} \\ \varphi_{1,2} + \varphi_{2,1} \end{Bmatrix} \tag{13a}$$

$$\boldsymbol{\varepsilon}^{(3)} = \begin{Bmatrix} \gamma_{13}^{(0)} \\ \gamma_{23}^{(0)} \end{Bmatrix} = \begin{Bmatrix} \varphi_1 + u_{3,1}^0 \\ \varphi_2 + u_{3,2}^0 \end{Bmatrix} \tag{13b}$$

Moreover, the symmetric rotation gradients are given by:

$$\chi_{ij} = \frac{1}{2}\left(\overline{\theta}_{i,j} + \overline{\theta}_{j,i}\right) \tag{14}$$

where $\overline{\theta}_i$ is determined in terms of the displacements u_i as follows:

$$\overline{\theta}_1 = \frac{1}{2}\left(u_{3,2} - u_{2,3}\right) = \frac{1}{2}\left(u_3, 2^0 - \Phi_{1,3}u_3, 2^0 - \Phi_{2,3}\varphi_2\right) \tag{15a}$$

$$\overline{\theta}_2 = \frac{1}{2}\left(u_{1,3} - u_3, 1\right) = \frac{1}{2}\left(-u_3, 1^0 + \Phi_{1,3}u_3, 1^0 + \Phi_{2,3}\varphi_1\right) \tag{15b}$$

$$\overline{\theta}_3 = \frac{1}{2}\left(u_{2,1} - u_1, 2\right) = \frac{1}{2}\left[u_2, 1^0 - u_1, 2^0 + \Phi_2\left(\varphi_{2,1} - \varphi_{1,2}\right)\right] \tag{15c}$$

Substituting Eq. (15) into Eq. (13), the rotation gradients are expressed as follows:

$$\boldsymbol{\chi} = \boldsymbol{\chi}^{(0)} + \Phi_{1,3}\boldsymbol{\chi}^{(1)} + \Phi_{2,3}\boldsymbol{\chi}^{(2)} + \Phi_{1,33}\boldsymbol{\chi}^{(3)} + \Phi_{2,33}\boldsymbol{\chi}^{(4)} + \Phi_2\boldsymbol{\chi}^{(5)} \tag{16}$$

where $\boldsymbol{\chi}^T = \left[\chi_{11}\ \chi_{22}\ 2\chi_{12}\ \chi_{33}\ 2\chi_{13}\ 2\chi_{23}\right]$ and,

$$\boldsymbol{\chi}^{(0)} = \frac{1}{2}\begin{Bmatrix} u_3, 12^0 \\ -u_3, 12^0 \\ u^0_{3,22} - u^0_{3,11} \\ 0 \\ u^0_{2,11} - u^0_{1,12} \\ u^0_{2,12} - u^0_{1,22} \end{Bmatrix}, \boldsymbol{\chi}^{(1)} = \frac{1}{2}\begin{Bmatrix} -u_3, 12^0 \\ u_3, 12^0 \\ u^0_{3,11} - u^0_{3,22} \\ 0 \\ 0 \\ 0 \end{Bmatrix}, \boldsymbol{\chi}^{(2)} = \frac{1}{2}\begin{Bmatrix} -\varphi_{2,1} \\ \varphi_{1,2} \\ \varphi_{1,1} - \varphi_{2,2} \\ \varphi_{2,1} - \varphi_{1,2} \\ 0 \\ 0 \end{Bmatrix} \tag{17a}$$

$$\boldsymbol{\chi}^{(3)} = \frac{1}{2}\begin{Bmatrix} 0 \\ 0 \\ 0 \\ 0 \\ -u^0_{3,2} \\ u^0_{3,1} \end{Bmatrix}, \boldsymbol{\chi}^{(4)} = \frac{1}{2}\begin{Bmatrix} 0 \\ 0 \\ 0 \\ 0 \\ -\varphi_2 \\ \varphi_1 \end{Bmatrix}, \boldsymbol{\chi}^{(5)} = \frac{1}{2}\begin{Bmatrix} 0 \\ 0 \\ 0 \\ 0 \\ \varphi_{2,11} - \varphi_{1,12} \\ \varphi_{2,12} - \varphi_{1,22} \end{Bmatrix} \tag{17b}$$

Furthermore, the stresses and strains of FG microplates are related by constitutive equations as follows:

$$\begin{aligned} \boldsymbol{\sigma}^{(i)} &= \begin{Bmatrix} \sigma_{11} \\ \sigma_{22} \\ \sigma_{12} \end{Bmatrix} = \begin{bmatrix} Q_{11} & Q_{12} & 0 \\ Q_{12} & Q_{22} & 0 \\ 0 & 0 & Q_{66} \end{bmatrix} \begin{Bmatrix} \varepsilon_{11} \\ \varepsilon_{22} \\ \gamma_{12} \end{Bmatrix} = \boldsymbol{Q}^{(i)}_{\varepsilon} \boldsymbol{\varepsilon}^{(i)}, \\ \boldsymbol{\sigma}^{(o)} &= \begin{Bmatrix} \sigma_{13} \\ \sigma_{23} \end{Bmatrix} = \begin{bmatrix} Q_{55} & 0 \\ 0 & Q_{44} \end{bmatrix} \begin{Bmatrix} \gamma_{13} \\ \gamma_{23} \end{Bmatrix} = \boldsymbol{Q}^{(o)}_{\varepsilon} \boldsymbol{\varepsilon}^{(s)} \end{aligned} \tag{18a}$$

$$\boldsymbol{m} = \begin{Bmatrix} m_{11} \\ m_{22} \\ m_{12} \\ m_{33} \\ m_{23} \\ m_{13} \end{Bmatrix} = 2\mu l_1^2 \begin{bmatrix} 1&0&0&0&0&0 \\ 0&1&0&0&0&0 \\ 0&0&1&0&0&0 \\ 0&0&0&1&0&0 \\ 0&0&0&0&1&0 \\ 0&0&0&0&0&1 \end{bmatrix} \begin{Bmatrix} \chi_{11} \\ \chi_{22} \\ \chi_{12} \\ \chi_{33} \\ \chi_{23} \\ \chi_{13} \end{Bmatrix} = \alpha_\chi \boldsymbol{I}_{6\times 6} \boldsymbol{\chi} \tag{18b}$$

where $\alpha_\chi = 2\mu l^2$, $Q_{11} = \frac{E(x_3)}{1-\nu^2}$,$Q_{22} = \frac{E(x_3)}{1-\nu^2}$, $Q_{12} = \frac{\nu E(x_3)}{1-\nu^2}$, $Q_{44} = Q_{55} = Q_{66} = \mu = \frac{E(x_3)}{2(1+\nu)}$.

2.3 Energy Principle

In order to derive the equation of motion, Hamilton's principle is used:

$$\int_{t_1}^{t_2} (\delta\Pi_U - \delta\Pi_K) dt = 0 \tag{19}$$

where $\delta\Pi_U$, $\delta\Pi_K$ are the variations of strain energy and kinetic energy, respectively. The variation of the strain energy of FG microplates derived from Eq. (3) as follows:

$$\delta\Pi_U = \int_A (\sigma\delta\varepsilon + \mathbf{m}\delta\chi)dA = \int_A \left[\mathbf{M}_\varepsilon^{(0)}\delta\varepsilon^{(0)} + \mathbf{M}_\varepsilon^{(1)}\delta\varepsilon^{(1)} + \mathbf{M}_\varepsilon^{(2)}\delta\varepsilon^{(2)} + \mathbf{M}_\varepsilon^{(3)}\delta\varepsilon^{(3)}\right.$$
$$\left.+\mathbf{M}_\chi^{(0)}\delta\chi^{(0)} + \mathbf{M}_\chi^{(1)}\delta\chi^{(1)} + \mathbf{M}_\chi^{(2)}\delta\chi^{(2)} + \mathbf{M}_\chi^{(3)}\delta\chi^{(3)} + \mathbf{M}_\chi^{(4)}\delta\chi^{(4)} + \mathbf{M}_\chi^{(5)}\delta\chi^{(5)}\right]dA \tag{20}$$

where the stress resultants are given by:

$$\left(\boldsymbol{M}_\varepsilon^{(0)}, \boldsymbol{M}_\varepsilon^{(1)}, \boldsymbol{M}_\varepsilon^{(2)}\right) = \int_{-h/2}^{h/2} (1, \Phi_1, \Phi_2)\boldsymbol{\sigma}^{(i)}dx_3, \boldsymbol{M}_\varepsilon^{(3)} = \int_{-h/2}^{h/2} \Phi_3\sigma^{(o)}dx_3 \tag{21a}$$

$$\left(\boldsymbol{M}_\chi^{(0)}, \boldsymbol{M}_\chi^{(1)}, \boldsymbol{M}_\chi^{(2)}, \boldsymbol{M}_\chi^{(3)}, \boldsymbol{M}_\chi^{(4)}, \boldsymbol{M}_\chi^{(5)}\right) = \int_{-h/2}^{h/2} (1, \Phi_{1,3}, \Phi_{2,3}, \Phi_{1,33}, \Phi_{2,33}, \Phi_2)\boldsymbol{m}dx_3 \tag{21b}$$

These stress resultants can be expressed in terms of the strains and its gradients as follows:

$$\begin{Bmatrix} \mathbf{M}_\varepsilon^{(0)} \\ \mathbf{M}_\varepsilon^{(1)} \\ \mathbf{M}_\varepsilon^{(2)} \\ \mathbf{M}_\varepsilon^{(3)} \end{Bmatrix} = \begin{bmatrix} \mathbf{A}^\varepsilon & \mathbf{B}^\varepsilon & \mathbf{B}_\mathbf{s}^\varepsilon & \mathbf{0} \\ \mathbf{B}^\varepsilon & \mathbf{D}^\varepsilon & \mathbf{D}_\mathbf{s}^\varepsilon & \mathbf{0} \\ \mathbf{B}_\mathbf{s}^\varepsilon & \mathbf{D}_\mathbf{s}^\varepsilon & \mathbf{H}_s^\varepsilon & \mathbf{0} \\ \mathbf{0} & \mathbf{0} & \mathbf{0} & \mathbf{A}_\mathbf{s}^\varepsilon \end{bmatrix} \begin{Bmatrix} \varepsilon^{(0)} \\ \varepsilon^{(1)} \\ \varepsilon^{(2)} \\ \varepsilon^{(3)} \end{Bmatrix} \tag{22a}$$

$$\begin{Bmatrix} \mathbf{M}_\chi^{(0)} \\ \mathbf{M}_\chi^{(1)} \\ \mathbf{M}_\chi^{(2)} \\ \mathbf{M}_\chi^{(3)} \\ \mathbf{M}_\chi^{(4)} \\ \mathbf{M}_\chi^{(5)} \end{Bmatrix} = \begin{bmatrix} \mathbf{A}^\chi & \overline{\mathbf{B}}^\chi & \overline{\mathbf{B}}_s^\chi & \overline{\overline{\mathbf{B}}}^\chi & \overline{\overline{\mathbf{B}}}_s^\chi & \mathbf{B}_s^\chi \\ \overline{\mathbf{B}}^\chi & \overline{\mathbf{B}}^\chi & \overline{\mathbf{D}}_s^\chi & \overline{\mathbf{E}}^\chi & \overline{\mathbf{E}}_s^\chi & \overline{\mathbf{F}}_s^\chi \\ \overline{\mathbf{B}}_s^\chi & \overline{\mathbf{D}}_s^\chi & \overline{\mathbf{H}}_s^\chi & \overline{\mathbf{G}}_s^\chi & \overline{\mathbf{I}}^\chi & \overline{\mathbf{J}}^\chi \\ \overline{\overline{\mathbf{B}}}^\chi & \overline{\mathbf{E}}^\chi & \overline{\mathbf{G}}_s^\chi & \overline{\overline{\mathbf{D}}}^\chi & \overline{\overline{\mathbf{D}}}_s^\chi & \overline{\overline{\mathbf{K}}}_s^\chi \\ \overline{\overline{\mathbf{B}}}_s^\chi & \overline{\mathbf{E}}_s^\chi & \overline{\mathbf{I}}^\chi & \overline{\overline{\mathbf{D}}}_s^\chi & \overline{\overline{\mathbf{H}}}_s^\chi & \overline{\mathbf{L}} \\ \mathbf{B}_s^\chi & \overline{\mathbf{F}}_s^\chi & \overline{\mathbf{J}}^\chi & \overline{\mathbf{K}}_s^\chi & \overline{\mathbf{L}} & \mathbf{H}_s^\chi \end{bmatrix} \begin{Bmatrix} \chi^{(0)} \\ \chi^{(1)} \\ \chi^{(2)} \\ \chi^{(3)} \\ \chi^{(4)} \\ \chi^{(5)} \end{Bmatrix} \tag{22b}$$

where the stiffness components of the FG microplates are defined as follows:

$$\left(\mathbf{A}^\varepsilon, \mathbf{B}^\varepsilon, \mathbf{D}^\varepsilon, \mathbf{H}_\mathbf{s}^\varepsilon, \mathbf{B}_\mathbf{s}^\varepsilon, \mathbf{D}_\mathbf{s}^\varepsilon\right) = \int_{-\mathbf{h/2}}^{\mathbf{h/2}} \left(\mathbf{1}, \Phi_\mathbf{1}, \Phi_\mathbf{1}^\mathbf{2}, \Phi_\mathbf{2}^\mathbf{2}, \Phi_\mathbf{2}, \Phi_\mathbf{1}\Phi_\mathbf{2}\right)\mathbf{Q}_\varepsilon^{(\mathbf{i})}\mathbf{dx_3}, A_s^\varepsilon = \int_{-h/2}^{h/2} \Phi_3^2\mathbf{Q}_\varepsilon^{(\mathbf{o})}dx_3 \tag{23a}$$

$$\mathbf{A}^\chi, \overline{\mathbf{B}}^\chi, \overline{\mathbf{B}}_s^\chi, \overline{\overline{\mathbf{B}}}^\chi, \overline{\overline{\mathbf{B}}}_s^\chi, \mathbf{B}_s^\chi = \int_{-h/2}^{h/2} \left(1, \Phi_{1,3}, \Phi_{2,3}, \Phi_{1,33}, \Phi_{2,33}, \Phi_2\right)\alpha_\chi\mathbf{I}_{6\times6}dx_3 \tag{23b}$$

$$\left(\overline{\boldsymbol{D}}^{\chi}, \overline{\boldsymbol{D}}_s^{\chi}, \overline{\boldsymbol{E}}^{\chi}, \overline{\boldsymbol{E}}_s^{\chi}, \overline{\boldsymbol{F}}_s^{\chi}\right) = \int_{-h/2}^{h/2} \Phi_{1,3}\left(\Phi_{1,3}, \Phi_{2,3}, \Phi_{1,33}, \Phi_{2,33}, \Phi_2\right)\alpha_{\chi}\boldsymbol{I}_{6\times 6}dx_3 \tag{23c}$$

$$\left(\overline{\boldsymbol{H}}_s^{\chi}, \overline{\boldsymbol{G}}_s^{\chi}, \overline{\boldsymbol{I}}^{\chi}, \overline{\boldsymbol{J}}^{\chi}\right) = \int_{-h/2}^{h/2} \Phi_{2,3}\left(\Phi_{2,3}, \Phi_{1,33}, \Phi_{2,33}, \Phi_2\right)\alpha_{\chi}\boldsymbol{I}_{6\times 6}dx_3 \tag{23d}$$

$$\left(\overline{\overline{\boldsymbol{D}}}^{\chi}, \overline{\overline{\boldsymbol{D}}}_s^{\chi}, \overline{\boldsymbol{K}}_s^{\chi}, \overline{\overline{\boldsymbol{H}}}_s^{\chi}, \overline{\boldsymbol{L}}^{\chi}, \boldsymbol{H}_s^{\chi}\right) = \int_{-h/2}^{h/2} \left(\Phi_{1,33}^2, \Phi_{1,33}\Phi_{2,33}, \Phi_{1,33}\Phi_2, \Phi_{2,33}^2, \Phi_{2,33}\Phi_2, \Phi_2^2\right) \alpha_{\chi}\boldsymbol{I}_{6\times 6}dx_3 \tag{23e}$$

The variation of kinetic energy $\delta\prod_K$ derived from Eq. (6) is calculated by:

$$\begin{aligned}
\delta\Pi_K &= \frac{1}{2}\int_V \rho(\dot{u}_1\delta\dot{u}_1 + \dot{u}_2\delta\dot{u}_2 + \dot{u}_3\delta\dot{u}_3)dV \\
&= \frac{1}{2}\int_A \Big[I_0\left(\dot{u}_1^0\delta\dot{u}_1^0 + \dot{u}_2^0\delta\dot{u}_2^0 + \dot{u}_3^0\delta\dot{u}_3^0\right) + I_1\left(\dot{u}_1^0\delta\dot{u}_{3,1}^0 + \dot{u}_{3,1}^0\delta\dot{u}_1^0 + \dot{u}_2^0\delta\dot{u}_{3,2}^0 + \dot{u}_{3,2}^0\delta\dot{u}_2^0\right) \\
&+ J_2\left(\dot{u}_{3,1}^0\delta\dot{\varphi}_1 + \dot{\varphi}_1\delta\dot{u}_{3,1}^0 + \dot{u}_{3,2}^0\delta\dot{\varphi}_2 + \dot{\varphi}_2\delta\dot{u}_{3,2}^0\right) + K_2(\dot{\varphi}_1\delta\dot{\varphi}_1 + \dot{\varphi}_2\delta\dot{\varphi}_2) \\
&+ J_1\left(\dot{u}_1^0\delta\dot{\varphi}_1 + \dot{\varphi}_1\delta\dot{u}_1^0 + \dot{u}_2^0\delta\dot{\varphi}_2 + \dot{\varphi}_2\delta\dot{u}_2^0\right) + I_2\left(\dot{u}_{3,1}^0\delta\dot{u}_{3,1}^0 + \dot{u}_{3,2}^0\delta\dot{u}_{3,2}^0\right)\Big]dA
\end{aligned} \tag{24}$$

where $I_0, I_1, I_2, J_1, J_2, K_2$ are mass components of the FG microplates which are defined as follows:

$$(I_0, I_1, I_2, J_1, J_2, K_2) = \int_{-h/2}^{h/2} \left(1, \Phi_1, \Phi_1^2, \Phi_2, \Phi_1\Phi_2, \Phi_2^2\right)\rho dx_3 \tag{25}$$

3 Series-Type Solutions of FG Microplates

Based on the Ritz method, the membrane and transverse displacements, rotations $\left(u_1^0, u_2^0, u_3^0, \varphi_1, \varphi_2\right)$ of the FG microplate can be expressed in terms of the series of approximation functions and associated values of series as follows:

$$\left\{u_1^0(x_1, x_2, t), \varphi_1(x_1, x_2, t)\right\} = \sum_{i=1}^{n_1}\sum_{j=1}^{n_2}\left\{u_{1ij}(t), x_{ij}(t)\right\}R_{i,1}(x_1)P_j(x_2) \tag{26a}$$

$$\left\{u_2^0(x_1, x_2, t), \varphi_2(x_1, x_2, t)\right\} = \sum_{i=1}^{n_1}\sum_{j=1}^{n_2}\left\{u_{2ij}(t), y_{ij}(t)\right\}R_i(x_1)P_{j,2}(x_2) \tag{26b}$$

$$u_3^0(x_1, x_2, t) = \sum_{i=1}^{n_1} \sum_{j=1}^{n_2} u_{3ij}(t) R_i(x_1) P_j(x_2) \tag{26c}$$

where $u_{1ij}, u_{2ij}, u_{3ij}, x_{ij}, y_{ij}$ are variables to be determined; $R_i(x_1)$, $P_j(x_2)$ are the shape functions in x_1-, x_2- direction, respectively. As a result, five unknowns of the plate only depend on two shape functions. It should be noted that the accuracy, convergence rates and numerical instabilities of the Ritz solution depends on the construction of the shape functions, which was discussed in details in [8–11]. The functions $R_i(x_1)$ and $P_j(x_2)$ are constructed to satisfy the boundary conditions (BCs) in which the simply-supported and clamped–clamped BCs are followed:

- Simply supported (S): $u_2^0 = u_3^0 = \varphi_2 = 0$ at $x_1 = 0, a$ and $u_1^0 = u_3^0 = \varphi_1 = 0$ at $x_2 = 0, b$
- Clamped (C): $u_1^0 = u_2^0 = u_3^0 = \varphi_1 = \varphi_2 = 0$ at $x_1 = 0, a$ and $x_2 = 0, b$

The combination of simply-supported, clamped boundary conditions on the edges of the plate leads to the different BCs as follows: SSSS, CSCS, CCSS, CCCC which will be considered in the numerical examples. Substituting Eq. (26) into Eqs.(20), (24) and then the subsequent results into Eq. (15) lead to the characteristic equations of motion of the FG microplates as follows: $\mathbf{Kd}+\mathbf{M}\ddot{\mathbf{d}} = \mathbf{0}$ where $\boldsymbol{d} = \left[\boldsymbol{u}_1\ \boldsymbol{u}_2\ \boldsymbol{u}_3\ \boldsymbol{x}\ \boldsymbol{y}\right]^T$ is the displacement vector to be determined; $\mathbf{K} = \mathbf{K}^{\varepsilon} + \mathbf{K}^{\chi}$ is the stiffness matrix which is composed of those of the strains $\mathbf{K}^{\varepsilon}$, symmetric rotation gradients $\mathbf{K}^{\chi}$; $\boldsymbol{M}$ is the mass matrix. These components are given more details as follows:

$$\mathbf{K}^{\zeta} = \begin{bmatrix} \mathbf{K}^{\zeta 11} & \mathbf{K}^{\zeta 12} & \mathbf{K}^{\zeta 13} & \mathbf{K}^{\zeta 14} & \mathbf{K}^{\zeta 15} \\ {}^{\mathrm{T}}\mathbf{K}^{\zeta 12} & \mathbf{K}^{\zeta 22} & \mathbf{K}^{\zeta 23} & \mathbf{K}^{\zeta 24} & \mathbf{K}^{\zeta 25} \\ {}^{\mathrm{T}}\mathbf{K}^{\zeta 13} & {}^{\mathrm{T}}\mathbf{K}^{\zeta 23} & \mathbf{K}^{\zeta 33} & \mathbf{K}^{\zeta 34} & \mathbf{K}^{\zeta 35} \\ {}^{\mathrm{T}}\mathbf{K}^{\zeta 14} & {}^{\mathrm{T}}\mathbf{K}^{\zeta 24} & {}^{\mathrm{T}}\mathbf{K}^{\zeta 34} & \mathbf{K}^{\zeta 44} & \mathbf{K}^{\zeta 45} \\ {}^{\mathrm{T}}\mathbf{K}^{\zeta 15} & {}^{\mathrm{T}}\mathbf{K}^{\zeta 25} & {}^{\mathrm{T}}\mathbf{K}^{\zeta 35} & {}^{\mathrm{T}}\mathbf{K}^{\zeta 45} & \mathbf{K}^{\zeta 55} \end{bmatrix} \text{ with } \zeta = \{\varepsilon, \chi\} \tag{27}$$

where the components of stiffness matrix $\mathbf{K}^{\varepsilon}$ are defined as follows:

$$K_{ijkl}^{\varepsilon 11} = A_{11}^{\varepsilon} T_{ik}^{22} S_{jl}^{00} + A_{66}^{\varepsilon} T_{ik}^{11} S_{jl}^{11},\ K_{ijkl}^{\varepsilon 12} = A_{12}^{\varepsilon} T_{ik}^{02} S_{jl}^{20} + A_{66}^{\varepsilon} T_{ik}^{11} S_{jl}^{11}$$

$$K_{ijkl}^{\varepsilon 13} = B_{11}^{\varepsilon} T_{ik}^{22} S_{jl}^{00} + B_{12}^{\varepsilon} T_{ik}^{02} S_{jl}^{20} + 2B_{66}^{\varepsilon} T_{ik}^{11} S_{jl}^{11}$$

$$K_{ijkl}^{\varepsilon 14} = B_{s11}^{\varepsilon} T_{ik}^{22} S_{jl}^{00} + B_{s66}^{\varepsilon} T_{ik}^{11} S_{jl}^{11},\ K_{ijkl}^{\varepsilon 15} = B_{s12}^{\varepsilon} T_{ik}^{02} S_{jl}^{20} + B_{s66}^{\varepsilon} T_{ik}^{11} S_{jl}^{11}$$

$$K_{ijkl}^{\varepsilon 22} = A_{22}^{\varepsilon} T_{ik}^{00} S_{jl}^{22} + A_{66}^{\varepsilon} T_{ik}^{11} S_{jl}^{11},\ K_{ijkl}^{\varepsilon 23} = B_{12}^{\varepsilon} T_{ik}^{20} S_{jl}^{02} + B_{22}^{\varepsilon} T_{ik}^{00} S_{jl}^{22} + 2B_{66}^{\varepsilon} T_{ik}^{11} S_{jl}^{11}$$

$$K_{ijkl}^{\varepsilon 24} = B_{s12}^{\varepsilon} T_{ik}^{20} S_{jl}^{02} + B_{s66}^{\varepsilon} T_{ik}^{11} S_{jl}^{11},\ K_{ijkl}^{\varepsilon 25} = B_{s22}^{\varepsilon} T_{ik}^{00} S_{jl}^{22} + B_{s66}^{\varepsilon} T_{ik}^{11} S_{jl}^{11}$$

$$K_{ijkl}^{\varepsilon 33} = D_{11}^{\varepsilon} T_{ik}^{22} S_{jl}^{00} + D_{12}^{\varepsilon}\left(T_{ik}^{02} S_{jl}^{20} + T_{ik}^{20} S_{jl}^{02}\right) + D_{22}^{\varepsilon} T_{ik}^{00} S_{jl}^{22} + 4D_{66}^{\varepsilon} T_{ik}^{11} S_{jl}^{11}$$
$$+A_{s44}^{\varepsilon} T_{ik}^{00} S_{jl}^{11} + A_{s55}^{\varepsilon} T_{ik}^{11} S_{jl}^{00}$$

$$K_{ijkl}^{\varepsilon 34} = D_{s11}^{\varepsilon} T_{ik}^{22} S_{jl}^{00} + D_{s12}^{\varepsilon} T_{ik}^{20} S_{jl}^{02} + 2D_{s66}^{\varepsilon} T_{ik}^{11} S_{jl}^{11} + A_{s55}^{\varepsilon} T_{ik}^{11} S_{jl}^{00}$$

$$K_{ijkl}^{\varepsilon 35} = D_{s12}^{\varepsilon} T_{ik}^{02} S_{jl}^{20} + D_{s22}^{\varepsilon} T_{ik}^{00} S_{jl}^{22} + 2D_{s66}^{\varepsilon} T_{ik}^{11} S_{jl}^{11} + A_{s44}^{\varepsilon} T_{ik}^{00} S_{jl}^{11}$$

$$K_{ijkl}^{\varepsilon 44} = H_{s11}^{\varepsilon} T_{ik}^{22} S_{jl}^{00} + H_{s66}^{\varepsilon} T_{ik}^{11} S_{jl}^{11} + A_{s55}^{\varepsilon} T_{ik}^{11} S_{jl}^{00}$$

$$K_{ijkl}^{\varepsilon 45} = H_{s12}^{\varepsilon} T_{ik}^{02} S_{jl}^{20} + H_{s66}^{\varepsilon} T_{ik}^{11} S_{jl}^{11},\ K_{ijkl}^{\varepsilon 55} = H_{s22}^{\varepsilon} T_{ik}^{00} S_{jl}^{22} + H_{s66}^{\varepsilon} T_{ik}^{11} S_{jl}^{11} + A_{s44}^{\varepsilon} T_{ik}^{00} S_{jl}^{11} \quad (28)$$

with noticing that:

$$T_{ik}^{rs} = \int_0^a \frac{\partial^r R_i}{\partial x_1^r} \frac{\partial^s R_k}{\partial x_1^s} dx_1,\ S_{jl}^{rs} = \int_0^a \frac{\partial^r S_i}{\partial x_2^r} \frac{\partial^s S_l}{\partial x_2^s} dx_2 \quad (29)$$

The components of stiffness matrix $\mathbf{K}^{\chi}$ are defined as follows:

$$K_{ijkl}^{\chi 11} = \frac{A^{\chi}}{4}\left(T_{ik}^{22} S_{jl}^{11} + T_{ik}^{11} S_{jl}^{22}\right),\ K_{ijkl}^{\chi 12} = -\frac{A^{\chi}}{4}\left(T_{ik}^{22} S_{jl}^{11} + T_{ik}^{11} S_{jl}^{22}\right)$$

$$K_{ijkl}^{\chi 13} = \frac{\overline{B}^{\chi}}{4}\left(T_{ik}^{02} S_{jl}^{11} - T_{ik}^{11} S_{jl}^{02}\right),\ K_{ijkl}^{\chi 14} = \frac{1}{4}\left(B_s^{\chi} T_{ik}^{22} S_{jl}^{11} + B_s^{\chi} T_{ik}^{11} S_{jl}^{22} - \overline{\overline{B}}_s^{\chi} T_{ik}^{11} S_{jl}^{02}\right)$$

$$K_{ijkl}^{\chi 15} = \frac{1}{4}\left(\overline{\overline{B}}_s^{\chi} T_{ik}^{02} S_{jl}^{11} - B_s^{\chi} T_{ik}^{22} S_{jl}^{11} - B_s^{\chi} T_{ik}^{11} S_{jl}^{22}\right),\ K_{ijkl}^{\chi 22} = \frac{A^{\chi}}{4}\left(T_{ik}^{22} S_{jl}^{11} + T_{ik}^{11} S_{jl}^{22}\right)$$

$$K_{ijkl}^{\chi 23} = \frac{\overline{\overline{B}}^{\chi}}{4}\left(T_{ik}^{11} S_{jl}^{02} - T_{ik}^{02} S_{jl}^{11}\right),\ K_{ijkl}^{\chi 24} = \frac{1}{4}\left(\overline{\overline{B}}_s^{\chi} T_{ik}^{11} S_{jl}^{02} - B_s^{\chi} T_{ik}^{22} S_{jl}^{11} - B_s^{\chi} T_{ik}^{11} S_{jl}^{22}\right)$$

$$K_{ijkl}^{\chi 25} = \frac{1}{4}\left(B_s^{\chi} T_{ik}^{22} S_{jl}^{11} + B_s^{\chi} T_{ik}^{11} S_{jl}^{22} - \overline{\overline{B}}_s^{\chi} T_{ik}^{02} S_{jl}^{11}\right)$$

$$K_{ijkl}^{\chi 33} = \frac{1}{4}\left(A^{\chi} - 2\overline{B}^{\chi} + \overline{D}^{\chi}\right)\left(T_{ik}^{00} S_{jl}^{22} - T_{ik}^{20} S_{jl}^{02} - T_{ik}^{02} S_{jl}^{20} + T_{ik}^{22} S_{jl}^{00} + 2T_{ik}^{11} S_{jl}^{11}\right)$$
$$+ \frac{1}{4}\overline{\overline{D}}^{\chi}\left(T_{ik}^{00} S_{jl}^{11} + T_{ik}^{11} S_{jl}^{00}\right)$$

$$K_{ijkl}^{\chi 34} = \frac{1}{4}\left[\left[\left(\overline{B}_s^{\chi} - \overline{D}_s^{\chi}\right)\left(T_{ik}^{20} S_{jl}^{02} - T_{ik}^{22} S_{jl}^{00} - T_{ik}^{11} S_{jl}^{11}\right) + \overline{K}_s^{\chi}\left(T_{ik}^{20} S_{jl}^{11} - T_{ik}^{11} S_{jl}^{20}\right) + \overline{\overline{D}}_s^{\chi} T_{ik}^{11} S_{jl}^{00}\right]\right.$$

$$K_{ijkl}^{\chi 35} = \frac{1}{4}\left[\left(\overline{B}_s^{\chi} - \overline{D}_s^{\chi}\right)\left(-T_{ik}^{00} S_{jl}^{22} + T_{ik}^{02} S_{jl}^{20} - T_{ik}^{11} S_{jl}^{11}\right) + \overline{\overline{D}}_s^{\chi} T_{ik}^{00} S_{jl}^{11} + \overline{K}_s^{\chi}\left(T_{ik}^{11} S_{jl}^{20} - T_{ik}^{20} S_{jl}^{11}\right)\right]$$

$$K_{ijkl}^{\chi 44} = \frac{1}{4}\left[\overline{H}_s^{\chi}\left(T_{ik}^{22} S_{jl}^{00} + 2T_{ik}^{11} S_{jl}^{11}\right) + \overline{\overline{H}}_s^{\chi} T_{ik}^{11} S_{jl}^{00}\right.$$
$$\left.-\overline{L}^{\chi}\left(T_{ik}^{11} S_{jl}^{20} + T_{ik}^{11} S_{jl}^{02}\right) + H_s^{\chi}\left(T_{ik}^{22} S_{jl}^{11} + T_{ik}^{11} S_{jl}^{22}\right)\right]$$

$$K_{ijkl}^{\chi 45} = \frac{1}{4}\left[\overline{L}^{\chi}\left(T_{ik}^{11}S_{jl}^{20} + T_{ik}^{02}S_{jl}^{11}\right) - \overline{H}_s^{\chi}\left(T_{ik}^{02}S_{jl}^{20} + T_{ik}^{11}S_{jl}^{11}\right) - H_s^{\chi}\left(T_{ik}^{11}S_{jl}^{22} + T_{ik}^{22}S_{jl}^{11}\right)\right]$$

$$K_{ijkl}^{\chi 55} = \frac{1}{4}\left[\overline{H}_s^{\chi}\left(2T_{ik}^{11}S_{jl}^{11} + T_{ik}^{00}S_{jl}^{22}\right) + \overline{\overline{H}}_s^{\chi}T_{ik}^{00}S_{jl}^{11}\right.$$
$$\left. -\overline{L}^{\chi}\left(T_{ik}^{20}S_{jl}^{11} + T_{ik}^{02}S_{jl}^{11}\right) + H_s^{\chi}\left(T_{ik}^{11}S_{jl}^{22} + T_{ik}^{22}S_{jl}^{11}\right)\right] \tag{30}$$

The components of mass matrix $\boldsymbol{M}$ are given by:

$$\begin{aligned}
&M_{ijkl}^{11} = I_0 T_{ik}^{11} S_{jl}^{00},\ M_{ijkl}^{13} = I_1 T_{ik}^{11} S_{jl}^{00},\ M_{ijkl}^{14} = J_1 T_{ik}^{11} S_{jl}^{00},\\
&M_{ijkl}^{22} = I_0 T_{ik}^{00} S_{jl}^{11},\ M_{ijkl}^{23} = I_1 T_{ik}^{00} S_{jl}^{11},\ M_{ijkl}^{25} = J_1 T_{ik}^{00} S_{jl}^{11}\\
&M_{ijkl}^{33} = I_0 T_{ik}^{00} S_{jl}^{00} + I_2\left(T_{ik}^{11} S_{jl}^{00} + T_{ik}^{00} S_{jl}^{11}\right),\ M_{ijkl}^{34} = J_2 T_{ik}^{11} S_{jl}^{00},\\
&M_{ijkl}^{35} = J_2 T_{ik}^{00} S_{jl}^{11},\ M_{ijkl}^{44} = K_2 T_{ik}^{11} S_{jl}^{00},\ M_{ijkl}^{55} = K_2 T_{ik}^{00} S_{jl}^{11}
\end{aligned} \tag{31}$$

It is worth noticing that for free vibration analysis, by denoting $\boldsymbol{d}(t) = \boldsymbol{d}e^{i\omega t}$ where ω is the natural frequency of the FG microplates and $i^2 = -1$ is imaginary unit, the natural frequency can be hence derived from the following the equation $\left(\mathbf{K} - \omega^2 \boldsymbol{M}\right)\boldsymbol{d} = \mathbf{0}$.

4 Numerical Examples

In this section, numerical examples are carried out to investigate free vibration behaviours of FG microplates with different BCs in which the shear function $f(x_3) = x_3 - 4x_3^3/3h^2$ is selected. The FG microplates are supposed to be made of ceramic material Al_2O_3 and metal one Al whose properties are given as follows: Al_2O_3 ($E_c = 380$ GPa, $\rho_c = 3800$ kg/m^3, $\nu_c = 0.3$), Al ($E_m = 70$ GPa, $\rho_m = 2702$ kg/m^3, $\nu_m = 0.3$). Preliminary convergence study of the series solution showed that the number of series $n_1 = n_2 = n = 10$ can be considered as the convergence point of the solution field, therefore this value will be used in the sequel computations. Moreover, for convenience, the following normalized parameter are used in the numerical examples:

$$\overline{\omega} = \frac{\omega a^2}{h}\sqrt{\frac{\rho_c}{E_c}} \tag{32}$$

In order to verify the accuracy of the present theory, Table 1 introduces normalized fundamental frequencies of Al/Al_2O_3 FG microplates in which the solutions are calculated with different values of the power index $p = 1, 2, 5, 10$, side-to-thickness ratio $a/h = 10, 20$, ratio of thickness-to-material scale $h/l = \infty$, 5, 2.5, 5/3, 1.25, 1, and four boundary conditions (SSSS, CSCS, CCSS, CCCC). The results obtained from the present theory with SSSS boundary condition has been compared with thosed of He et al. [7] based on the MCT and IGA-HSDT theory, Thai and Kim [6] using the IGA method, TSDT and MCT. It can be seen that there are good agreements

Table 1 Normalized fundamental frequencies of Al/Al_2O_3 FG microplates

BCs	a/h	p	Theory	h/l					
				∞	5	2.5	5/3	1.25	1
SSSS	20	1	Present	4.5141	4.9608	6.0715	7.5784	9.3065	11.1115
			TSDT-MCT [6]	4.5228	4.9568	6.0756	7.5817	9.2887	11.1042
			HSDT-MCT [7]	4.5228	4.9568	6.0756	7.5817	9.2887	11.1042
		2	Present	4.1328	4.5055	5.5080	6.8791	8.4182	10.0537
			TSDT-MCT [6]	4.1100	4.5006	5.5082	6.8661	8.4062	10.0450
		5	Present	3.8949	4.1938	5.0048	6.1394	7.4333	8.8334
			TSDT-MCT [6]	3.8884	4.2005	5.0199	6.1457	7.4397	8.8286
		10	Present	3.7641	4.0336	4.7303	5.7438	6.8892	8.1474
			TSDT-MCT [6]	3.7622	4.0323	4.7488	5.7453	6.9013	8.1494
	10	1	Present	4.4186	4.8537	5.9779	7.4863	9.1982	11.0127
			TSDT-MCT [6]	4.4192	4.8526	5.9664	7.4619	9.1537	10.9511
		2	Present	4.0071	4.4029	5.4160	6.7853	8.3177	9.9588
			TSDT-MCT [6]	4.0090	4.4006	5.4071	6.7580	8.2863	9.9101
		5	Present	3.7704	4.0825	4.9086	6.0476	7.3324	8.7213
			TSDT-MCT [6]	3.7682	4.0876	4.9169	6.0447	7.3338	8.7135
		10	Present	3.6376	3.9110	4.6355	5.6433	6.8060	8.0434
			TSDT-MCT [6]	3.6368	3.9162	4.6464	5.6487	6.8030	8.0448
CSCS	10	1	Present	5.9217	6.7270	8.6699	11.1709	13.9332	15.4952
		2	Present	5.3641	6.0886	7.8423	10.0972	12.5893	15.2033
		5	Present	5.0089	5.5972	7.0417	8.9330	11.0458	13.2752
		10	Present	4.8179	5.3319	6.6071	8.2965	10.1959	12.2104
CCSS	10	1	Present	6.2571	7.1981	9.4486	12.3090	15.4451	18.7177
		2	Present	5.6642	6.5115	8.5418	11.1216	13.9519	16.9038
		5	Present	5.2629	5.9547	7.6375	9.8094	12.2142	14.7385
		10	Present	5.0546	5.6600	7.1471	9.0888	11.2542	13.5382
CCCC	10	1	Present	7.5972	8.9737	11.9334	15.7186	19.8229	24.0786
		2	Present	6.9314	8.0884	10.8045	14.2073	18.7789	21.7420
		5	Present	6.3776	7.3691	9.6230	12.4991	15.6417	18.9349
		10	Present	6.1521	6.9859	8.9859	11.5569	14.4000	17.3824

bewteen the models. Moreover, it is observed from Table 1 that the fundamental frequencies decrease with an increase of the power index p. This can be explained by the fact that with an increase of p led to an decrease of the volume fraction of ceramic and stiffness of FG microplates. The effect of the power index p on the natural frequencies of Al/Al_2O_3 FG microplates is also plotted in Fig. 2 for different values of ratio of thickness-to-material scale $h/l = 5,\ 2.5,\ 5/3,\ 1.25,\ 1$, and SSSS boundary condition. It can be seen from this figure that the highest and lowest curves correspond to $h/l = 1$ and 5, respectively, and there are large deviations of these curves. The variations of normalized fundamental frequencies with respect to the ratio of thickness-to-material scale h/l are observed in Table 1 and Fig. 3 for Al/Al_2O_3

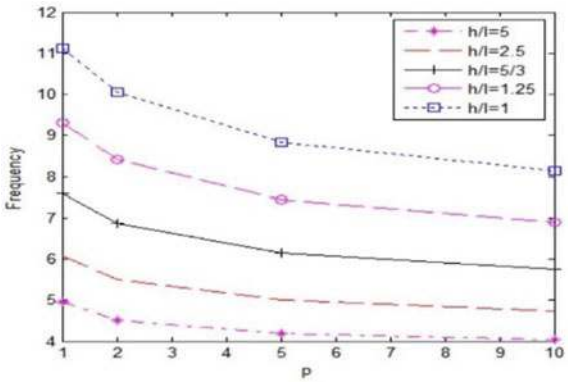

Fig. 2 Variation of normalized fundamental frequencies with respect the power index p ($a/h = 20$, SSSS)

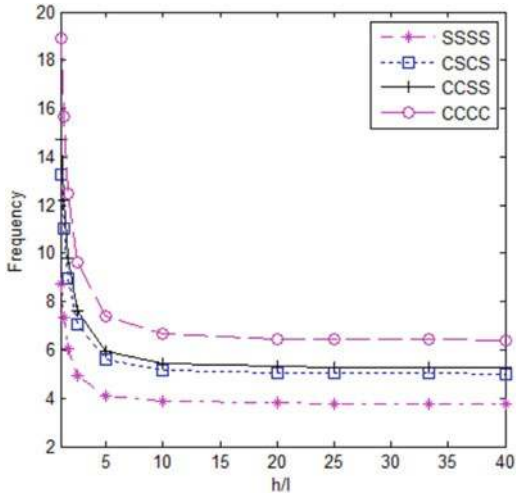

Fig. 3 Variation of normalized fundamental frequencies with respect to h/l ($p = 5, a/h = 10$)

FG microplates with $p = 5$ and $a/h = 10$. The graphs are displayed with four boundary conditions (SSSS, CSCS, CCSS, CCCC) within which it is observed that the natural frequencies decrease with the increase of h/l up to the value of $h/l = 10$ from which the curves become flatter and size effects can be hence neglected.

5 Conclusions

A unified higher-order shear deformation microplate model for vibration analysis of functionally graded materials has been proposed in this paper. The present theory is developed from fundamental equations of the elasticity theory and modified couple stress theory in which many different frameworks of size-dependent plate models could be recovered. In order to capture the size effects, the modified couple stress theory with one independent length-scale parameter is used. The solution field is approximated by bi-directional series in which hybrid shape functions are proposed, then the stiffness and mass matrix are explicitly derived. Numerical examples are investigated for different configurations of material distribution, side-to-thickness ratio, size-scale-thickness ratio and boundary conditions on the natural frequencies of FG microplates. The obtained results shows that the size effect is important and needs to be accounted for the computations. The size effect leads to an increase of the stiffness and natural frequency of the FG plates. The proposed unified size dependent plate model presents the accuracy and efficiency in predicting vibration behaviours of FG microplates.

Acknowledgements This research is funded by Vietnam National Foundation for Science and Technology Development (NAFOSTED) Under Grant No. 107.02-2018.312.

References

1. Yang F, Chong ACM, Lam DCC, Tong P (05/01 2002) Couple stress based strain gradient theory for elasticity. Int J Solids Struct 39:2731–2743
2. Tsiatas GC (2009/06/15/ 2009) A new Kirchhoff plate model based on a modified couple stress theory. Int J Solids Struct 46(13):2757–2764
3. Ma HM, Gao XL, Reddy JN (2011/08/01 2011) A non-classical Mindlin plate model based on a modified couple stress theory. Acta Mech 220(1):217–235
4. Reddy JN, Kim J (2012/02/01/ 2012) A nonlinear modified couple stress-based third-order theory of functionally graded plates. Compos Struct 94(3):1128–1143
5. Thai H-T, Vo TP (2013/02/01/2013) A size-dependent functionally graded sinusoidal plate model based on a modified couple stress theory. Compos Struct 96:376–383
6. Thai H-T, Kim S-E (2013/02/01/ 2013) A size-dependent functionally graded Reddy plate model based on a modified couple stress theory. Compos Part B: Eng 45(1):1636–1645
7. He L, Lou J, Zhang E, Wang Y, Bai Y (2015/10/15/ 2015) A size-dependent four variable refined plate model for functionally graded microplates based on modified couple stress theory. Compos Struct 130:107–115

8. Mantari JL, Canales FG (2016/09/15/ 2016) Free vibration and buckling of laminated beams via hybrid Ritz solution for various penalized boundary conditions. Compos Struct 152:306–315
9. Moreno-García P, Dos Santos JV, Lopes H (03/24 2017) A review and study on Ritz method admissible functions with emphasis on buckling and free vibration of isotropic and anisotropic beams and plates. Arch Comput Methods Eng 25:785–815
10. Nguyen T-K, Truong-Phong Nguyen T, Vo TP, Thai H-T (2015/07/01/ 2015) Vibration and buckling analysis of functionally graded sandwich beams by a new higher-order shear deformation theory. Compos Part B: Eng 76:273–285
11. Nguyen T-K, Vo TP, Nguyen B-D, Lee J (2016/11/15/ 2016) An analytical solution for buckling and vibration analysis of functionally graded sandwich beams using a quasi-3D shear deformation theory. Compos Struct 156:238–252

An Efficient Size-Dependent Computational Approach for Functionally Graded Porous Sandwich Microplates Based on Modified Couple Stress Theory

Van-Thien Tran[1], Trung-Kien Nguyen[2(✉)], and Van-Hau Nguyen[1]

[1] Faculty of Civil Engineering, Ho Chi Minh City University of Technology and Education, No. 1 Vo Van Ngan Street, Thu Duc City, Ho Chi Minh City, Vietnam
[2] CIRTech Institute, HUTECH University, 475A Dien Bien Phu, Binh Thanh District, Ho Chi Minh City, Vietnam
ntkien@hutech.edu.vn

Abstract. A unified higher-order shear deformation microplate model for free vibration analysis of functionally graded sandwich materials with porosities is proposed in this paper. The theory is developed from a general higher-order shear deformation framework and modified couple stress theory to capture the size effects. The displacements are approximated by bi-directional series of hybrid shape functions, then characteristic equations of motion are obtained by Lagrange's equations. Numerical results are presented for different configurations of material distribution, side-to-thickness ratio, size-scale-thickness ratio and boundary conditions on natural frequencies of functionally graded porous sandwich microplates.

Keywords: Series-type solutions · Vibration · Functionally graded porous sandwich microplates · Modified couple stress theory

1 Introduction

Thank to high strength-to-weight and stiffness-to-weight ratios, laminated composite sandwich materials have been used for micro- and nano-scale structures with large applications in atomic force microscopes (AFMs), micro-electromechanical systems (MEMs) and nano-electromechanical systems (NEMS). Moreover, the recent development of functionally graded porous (FGP) materials with continuous variations of constituents and a significant porosity density led to challenges in computational methods and models of FGP sandwich microplates. A number of researches have been performed with different approaches to accurately predict static and dynamic behaviours of FGP sandwich structures, only some representative references are herein cited. For behaviours of FGP sandwich plates at macroscale, Daikh and Zenkour investigated buckling and vibration responses of FGP sandwich plates using a higher-order shear deformation theory (HSDT) and analytical Navier procedure [1]. Pham and Le [2] presented static, buckling

Y.-P. Huang et al. (Eds.): GTSD 2022, LNNS 567, pp. 82–96, 2023.
https://doi.org/10.1007/978-3-031-19694-2_8

and vibration analysis of FGP sandwich plates based on a HSDT and finite element method (FEM). Tran et al. [3] analysed nonlinear vibration of FGP sandwich plates on elastic foundations subjected to blast loadings using a HSDT and Galerkin method. Zhang et al. [4] proposed free vibration and damping analysis of FGP sandwich plates based on the first-order shear deformation theory (FSDT) and Fourier-Ritz method. Tahir et al. [5] considered wave propagation of FGP sandwich plates in hygro-thermal environments based on a refined HSDT and analytical solution. Sah and Ghosh [6] examined effects of porosity distribution on free vibration and buckling of multi-directional FGP sandwich plates based on a HSDT and analytical Navier solution. Though a number of researches have been performed in predicting static and dynamic responses of FGP sandwich plates using various analytical and numerical methods, the analysis of FGP sandwich plates at micro- and nano-scales is limited. Thai et al. [7] investigated static, buckling and vibration behaviours of FGP sandwich microplates using the modified coupled stress theory (MCT) and Kriging meshfree method. Phung-Van et al. [8] optimized material distributions of FGP sandwich nanoplates using Eringen's nonlocal elasticity theory, a refined HSDT and isogeometric approach. A brief literature survey reveals that the analysis of size effects on behaviours of FGP sandwich microplates is an interesting topic that needs to be studied further.

The objective of this paper is to propose a unified size-dependent model for free vibration analysis of FGP sandwich microplates. The present theory is an extension of previous work [9] for FGP sandwich microplates by using the MCT. The governing equations of motion are derived from Lagrange's equations and then bi-directional series-type solutions with hybrid shape functions are proposed. Numerical results are presented for different configurations of material distribution, side-to-thickness ratio and different boundary conditions on natural frequencies of the FGP sandwich microplates.

2 Theoretical Formulation

Consider a FGP sandwich rectangle microplate in the coordinate system (x_1, x_2, x_3) with sides $a \times b$ and thickness h as shown in Fig. 1. The plate is composed of a homogeneous core and two functionally graded (FG) porous faces which are made of ceramic-metal materials and a porosity density. The effective material properties of FGP sandwich microplates can be approximated by the following expressions [10]:

$$P(x_3) = (P_c - P_m)V_c(x_3) + P_m - \frac{\beta}{2}(P_c + P_m) \tag{1}$$

where the volume fraction of the ceramic material $V_c(x_3)$ through the plate thickness is defined by [11]:

$$V_c(x_3) = \begin{cases} \left(\frac{z_4 - x_3}{z_4 - z_3}\right)^p, & z_3 \le x_3 \le z_4 \quad \text{FG} \quad \text{top layer} \\ 1 & z_2 \le x_3 \le z_3 \quad \text{ceramic} \quad \text{core layer} \\ \left(\frac{x_3 - z_1}{z_2 - z_1}\right)^p & z_1 \le x_3 \le z_2 \quad \text{FG} \quad \text{bottom layer} \end{cases} \tag{2}$$

where P_c and P_m are the properties of ceramic and metal materials, respectively, such as Young's moduli E, mass density ρ, Poisson's ratio ν; $\beta \leq 1$ is the porosity volume fraction; p is the power-law index.

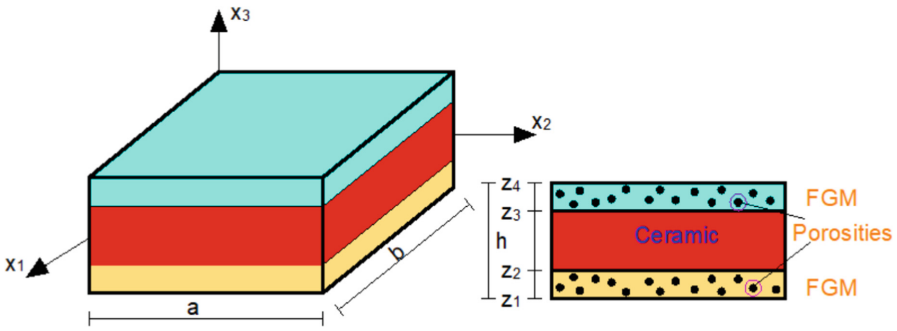

Fig. 1. Geometry of a FGP sandwich microplate

2.1 Modified Couple Stress Theory

The total potential energy of the FGP sandwich microplates is obtained by:

$$\Pi = \Pi_U - \Pi_K \tag{3}$$

where Π_U, Π_K are the strain energy and kinetic energy of the FGP sandwich microplates, respectively. Based on the MCT, the strain energy of the system Π_U is given by [12]:

$$\Pi_U = \int_V (\boldsymbol{\sigma}\boldsymbol{\varepsilon} + \mathbf{m}\boldsymbol{\chi}) dV \tag{4}$$

where $\boldsymbol{\varepsilon}$, $\boldsymbol{\chi}$ are strains and symmetric rotation gradients, respectively; $\boldsymbol{\sigma}$ is Cauchy stress; $\mathbf{m}$ are higher-order stress corresponding with strain gradients $\boldsymbol{\chi}$. The components of strain ε_{ij} and strain gradients χ_{ij} are defined as follows:

$$\varepsilon_{ij} = \frac{1}{2}\left(u_{i,j} + u_{j,i}\right), \quad \chi_{ij} = \frac{1}{4}\left(u_{n,mj}e_{imn} + u_{n,mi}e_{jmn}\right) \tag{5}$$

where e_{imn} are permutation symbol. The components of stress are calculated from constitutive equations as follows:

$$\sigma_{ij} = \lambda\varepsilon_{kk}\delta_{ij} + 2\mu\varepsilon_{ij}, \quad m_{ij} = 2\mu l^2\chi_{ij} \tag{6}$$

where λ, μ are Lamé constants; δ_{ij} are Kronecker delta; l is length scale parameter.

The kinetic energy of the FG sandwich microplates Π_K is expressed by:

$$\Pi_K = \frac{1}{2}\int_V \rho(x_3)\left(\dot{u}_1^2 + \dot{u}_2^2 + \dot{u}_3^2\right)dV \tag{7}$$

where $\rho(x_3)$ is mass density of the FGP sandwich microplates; $\dot{u}_1 = u_{1,t}$, $\dot{u}_2 = u_{2,t}$, $\dot{u}_3 = u_{3,t}$ are velocities in x_1-, x_2- and x_3- directions, respectively.

2.2 Unified Kinematics of FGP Sandwich Microplates

A general HSDT kinematic of FGP sandwich plates is derived from [9] as follows:

$$u_1(x_1, x_2, x_3) = u_1^0(x_1, x_2) + \Phi_1(x_3)u_{3,1}^0 + \Phi_2(x_3)\varphi_1(x_1, x_2) \tag{8a}$$

$$u_2(x_1, x_2, x_3) = u_2^0(x_1, x_2) + \Phi_1(x_3)u_{3,2}^0 + \Phi_2(x_3)\varphi_2(x_1, x_2) \tag{8b}$$

$$u_3(x_1, x_2, x_3) = u_3^0(x_1, x_2) \tag{8c}$$

where $\Phi_1(x_3) = H^s\Psi(x_3) - x_3$; $\Phi_2(x_3) = H^s\Psi(x_3)$; $H^s = \frac{5}{6}\int_{-h/2}^{h/2}\mu(x_3)dx_3$ is the transverse shear stiffness; $\mu(x_3) = \frac{E(x_3)}{2(1+\nu)}$ is the shear modulus; $f(x_3)$ is a higher-order term whose first derivative satisfies the free-stress boundary condition at the top and bottom surfaces of the FGP plates, i.e. $f_{,3}\left(x_3 = \pm\frac{h}{2}\right) = 0$; $\Psi(x_3) = \int_0^{x_3}\frac{f_{,3}}{\mu(x_3)}dx_3$.

Substituting Eq. (8) into the strains and strain gradients in Eq. (5), the strains $\boldsymbol{\varepsilon}^T = \left[\boldsymbol{\varepsilon}^{(i)}\ \boldsymbol{\varepsilon}^{(s)}\right]$ are obtained as follows:

$$\boldsymbol{\varepsilon}^{(i)} = \boldsymbol{\varepsilon}^{(0)} + \Phi_1(x_3)\boldsymbol{\varepsilon}^{(1)} + \Phi_2(x_3)\boldsymbol{\varepsilon}^{(2)},\ \boldsymbol{\varepsilon}^{(s)} = \Phi_3(x_3)\boldsymbol{\varepsilon}^{(3)} \tag{9}$$

where $\Phi_3(x_3) = H^s\Psi_{,3}$ with $\Psi_{,3}(x_3) = \frac{f_{,3}(x_3)}{\mu(x_3)}$ and,

$$\boldsymbol{\varepsilon}^{(0)} = \begin{Bmatrix}\varepsilon_{11}^{(0)}\\ \varepsilon_{22}^{(0)}\\ \gamma_{12}^{(0)}\end{Bmatrix} = \begin{Bmatrix}u_{1,1}^0\\ u_{2,2}^0\\ u_{1,2}^0 + u_{2,1}^0\end{Bmatrix},\ \boldsymbol{\varepsilon}^{(1)} = \begin{Bmatrix}\varepsilon_{11}^{(1)}\\ \varepsilon_{22}^{(1)}\\ \gamma_{12}^{(1)}\end{Bmatrix} = \begin{Bmatrix}u_{3,11}^0\\ u_{3,22}^0\\ 2u_{3,12}^0\end{Bmatrix} \tag{10a}$$

$$\boldsymbol{\varepsilon}^{(2)} = \begin{Bmatrix}\varepsilon_{11}^{(2)}\\ \varepsilon_{22}^{(2)}\\ \gamma_{12}^{(2)}\end{Bmatrix} = \begin{Bmatrix}\varphi_{1,1}\\ \varphi_{2,2}\\ \varphi_{1,2} + \varphi_{2,1}\end{Bmatrix},\ \boldsymbol{\varepsilon}^{(3)} = \begin{Bmatrix}\gamma_{13}^{(0)}\\ \gamma_{23}^{(0)}\end{Bmatrix} = \begin{Bmatrix}\varphi_1 + u_{3,1}^0\\ \varphi_2 + u_{3,2}^0\end{Bmatrix} \tag{10b}$$

Moreover, the symmetric rotation gradients are given by:

$$\chi_{ij} = \frac{1}{2}\left(\overline{\theta}_{i,j} + \overline{\theta}_{j,i}\right) \tag{11}$$

where $\overline{\theta}_i$ is determined in terms of the displacements u_i as follows:

$$\overline{\theta}_1 = \frac{1}{2}\left(u_{3,2} - u_{2,3}\right) = \frac{1}{2}\left(u^0_{3,2} - \Phi_{1,3}u^0_{3,2} - \Phi_{2,3}\varphi_2\right) \tag{12a}$$

$$\overline{\theta}_2 = \frac{1}{2}\left(u_{1,3} - u_{3,1}\right) = \frac{1}{2}\left(-u^0_{3,1} + \Phi_{1,3}u^0_{3,1} + \Phi_{2,3}\varphi_1\right) \tag{12b}$$

$$\overline{\theta}_3 = \frac{1}{2}\left(u_{2,1} - u_{1,2}\right) = \frac{1}{2}\left[u^0_{2,1} - u^0_{1,2} + \Phi_2\left(\varphi_{2,1} - \varphi_{1,2}\right)\right] \tag{12c}$$

Substituting Eq. (12) into Eq. (11), the rotation gradients are expressed as follows:

$$\boldsymbol{\chi} = \boldsymbol{\chi}^{(0)} + \Phi_{1,3}\boldsymbol{\chi}^{(1)} + \Phi_{2,3}\boldsymbol{\chi}^{(2)} + \Phi_{1,33}\boldsymbol{\chi}^{(3)} + \Phi_{2,33}\boldsymbol{\chi}^{(4)} + \Phi_2\boldsymbol{\chi}^{(5)} \tag{13}$$

where $\boldsymbol{\chi}^T = \left[\, \chi_{11}\ \chi_{22}\ 2\chi_{12}\ \chi_{33}\ 2\chi_{13}\ 2\chi_{23} \,\right]$ and,

$$\boldsymbol{\chi}^{(0)} = \frac{1}{2}\begin{Bmatrix} u^0_{3,12} \\ -u^0_{3,12} \\ u^0_{3,22} - u^0_{3,11} \\ 0 \\ u^0_{2,11} - u^0_{1,12} \\ u^0_{2,12} - u^0_{1,22} \end{Bmatrix},\ \boldsymbol{\chi}^{(1)} = \frac{1}{2}\begin{Bmatrix} -u^0_{3,12} \\ u^0_{3,12} \\ u^0_{3,11} - u^0_{3,22} \\ 0 \\ 0 \\ 0 \end{Bmatrix},\ \boldsymbol{\chi}^{(2)} = \frac{1}{2}\begin{Bmatrix} -\varphi_{2,1} \\ \varphi_{1,2} \\ \varphi_{1,1} - \varphi_{2,2} \\ \varphi_{2,1} - \varphi_{1,2} \\ 0 \\ 0 \end{Bmatrix} \tag{14a}$$

$$\boldsymbol{\chi}^{(3)} = \frac{1}{2}\begin{Bmatrix} 0 \\ 0 \\ 0 \\ 0 \\ -u^0_{3,2} \\ u^0_{3,1} \end{Bmatrix},\ \boldsymbol{\chi}^{(4)} = \frac{1}{2}\begin{Bmatrix} 0 \\ 0 \\ 0 \\ 0 \\ -\varphi_2 \\ \varphi_1 \end{Bmatrix},\ \boldsymbol{\chi}^{(5)} = \frac{1}{2}\begin{Bmatrix} 0 \\ 0 \\ 0 \\ 0 \\ \varphi_{2,11} - \varphi_{1,12} \\ \varphi_{2,12} - \varphi_{1,22} \end{Bmatrix} \tag{14b}$$

Furthermore, the stresses and strains of FGP sandwich microplates are related by constitutive equations as follows:

$$\begin{aligned} \boldsymbol{\sigma}^{(i)} &= \begin{Bmatrix} \sigma_{11} \\ \sigma_{22} \\ \sigma_{12} \end{Bmatrix} = \begin{bmatrix} Q_{11} & Q_{12} & 0 \\ Q_{12} & Q_{22} & 0 \\ 0 & 0 & Q_{66} \end{bmatrix} \begin{Bmatrix} \varepsilon_{11} \\ \varepsilon_{22} \\ \gamma_{12} \end{Bmatrix} = \mathbf{Q}^{(i)}_{\varepsilon}\boldsymbol{\varepsilon}^{(i)} \\ \boldsymbol{\sigma}^{(o)} &= \begin{Bmatrix} \sigma_{13} \\ \sigma_{23} \end{Bmatrix} = \begin{bmatrix} Q_{55} & 0 \\ 0 & Q_{44} \end{bmatrix} \begin{Bmatrix} \gamma_{13} \\ \gamma_{23} \end{Bmatrix} = \mathbf{Q}^{(o)}_{\varepsilon}\boldsymbol{\varepsilon}^{(s)} \end{aligned} \tag{15a}$$

$$\mathbf{m} = \begin{Bmatrix} m_{11} \\ m_{22} \\ m_{12} \\ m_{33} \\ m_{23} \\ m_{13} \end{Bmatrix} = 2\mu l^2 \begin{bmatrix} 1&0&0&0&0&0 \\ 0&1&0&0&0&0 \\ 0&0&1&0&0&0 \\ 0&0&0&1&0&0 \\ 0&0&0&0&1&0 \\ 0&0&0&0&0&1 \end{bmatrix} \begin{Bmatrix} \chi_{11} \\ \chi_{22} \\ \chi_{12} \\ \chi_{33} \\ \chi_{23} \\ \chi_{13} \end{Bmatrix} = \alpha_\chi \mathbf{I}_{6\times 6}\boldsymbol{\chi} \tag{15b}$$

where

$$\alpha_\chi = 2\mu l^2 \tag{16a}$$

$$Q_{11} = \frac{E(x_3)}{1-\nu^2},\ Q_{22} = \frac{E(x_3)}{1-\nu^2},\ Q_{12} = \frac{\nu E(x_3)}{1-\nu^2},\ Q_{44} = Q_{55} = Q_{66} = \mu = \frac{E(x_3)}{2(1+\nu)}, \tag{16b}$$

2.3 Energy Principle

In order to derive the equations of motion, Hamilton's principle is used:

$$\int_{t_1}^{t_2} (\delta\Pi_U - \delta\Pi_K)dt = 0 \tag{17}$$

where $\delta\Pi_U, \delta\Pi_K$ are the variations of strain energy and kinetic energy, respectively. The variation of the strain energy of FGP sandwich microplates derived from Eq. (4) as follows:

$$\delta\prod_U = \int_A (\boldsymbol{\sigma}\delta\boldsymbol{\varepsilon} + \mathbf{m}\delta\boldsymbol{\chi})dA = \int_A \Big[\mathbf{M}_\varepsilon^{(0)}\delta\boldsymbol{\varepsilon}^{(0)} + \mathbf{M}_\varepsilon^{(1)}\delta\boldsymbol{\varepsilon}^{(1)} + \mathbf{M}_\varepsilon^{(2)}\delta\boldsymbol{\varepsilon}^{(2)} + \mathbf{M}_\varepsilon^{(3)}\delta\boldsymbol{\varepsilon}^{(3)}$$
$$+\mathbf{M}_\chi^{(0)}\delta\boldsymbol{\chi}^{(0)} + \mathbf{M}_\chi^{(1)}\delta\boldsymbol{\chi}^{(1)} + \mathbf{M}_\chi^{(2)}\delta\boldsymbol{\chi}^{(2)} + \mathbf{M}_\chi^{(3)}\delta\boldsymbol{\chi}^{(3)} + \mathbf{M}_\chi^{(4)}\delta\boldsymbol{\chi}^{(4)} + \mathbf{M}_\chi^{(5)}\delta\boldsymbol{\chi}^{(5)}\Big]dA \tag{18}$$

where the stress resultants are given by:

$$\left(\mathbf{M}_\varepsilon^{(0)}, \mathbf{M}_\varepsilon^{(1)}, \mathbf{M}_\varepsilon^{(2)}\right) = \int_{-h/2}^{h/2} (1, \Phi_1, \Phi_2)\boldsymbol{\sigma}^{(i)}dx_3,\ \mathbf{M}_\varepsilon^{(3)} = \int_{-h/2}^{h/2} \Phi_3\boldsymbol{\sigma}^{(o)}dx_3 \tag{19a}$$

$$\left(\mathbf{M}_\chi^{(0)}, \mathbf{M}_\chi^{(1)}, \mathbf{M}_\chi^{(2)}, \mathbf{M}_\chi^{(3)}, \mathbf{M}_\chi^{(4)}, \mathbf{M}_\chi^{(5)}\right) = \int_{-h/2}^{h/2} \left(1, \Phi_{1,3}, \Phi_{2,3}, \Phi_{1,33}, \Phi_{2,33}, \Phi_2\right)\mathbf{m}dx_3 \tag{19b}$$

These stress resultants can be expressed in terms of the strains and its gradients as follows:

$$\begin{Bmatrix} \mathbf{M}_\varepsilon^{(0)} \\ \mathbf{M}_\varepsilon^{(1)} \\ \mathbf{M}_\varepsilon^{(2)} \\ \mathbf{M}_\varepsilon^{(3)} \end{Bmatrix} = \begin{bmatrix} \mathbf{A}^\varepsilon & \mathbf{B}^\varepsilon & \mathbf{B}_s^\varepsilon & \mathbf{0} \\ \mathbf{B}^\varepsilon & \mathbf{D}^\varepsilon & \mathbf{D}_s^\varepsilon & \mathbf{0} \\ \mathbf{B}_s^\varepsilon & \mathbf{D}_s^\varepsilon & \mathbf{H}_s^\varepsilon & \mathbf{0} \\ \mathbf{0} & \mathbf{0} & \mathbf{0} & \mathbf{A}_s^\varepsilon \end{bmatrix} \begin{Bmatrix} \boldsymbol{\varepsilon}^{(0)} \\ \boldsymbol{\varepsilon}^{(1)} \\ \boldsymbol{\varepsilon}^{(2)} \\ \boldsymbol{\varepsilon}^{(3)} \end{Bmatrix} \tag{20a}$$

$$\begin{Bmatrix} \mathbf{M}_{\chi}^{(0)} \\ \mathbf{M}_{\chi}^{(1)} \\ \mathbf{M}_{\chi}^{(2)} \\ \mathbf{M}_{\chi}^{(3)} \\ \mathbf{M}_{\chi}^{(4)} \\ \mathbf{M}_{\chi}^{(5)} \end{Bmatrix} = \begin{bmatrix} \mathbf{A}^{\chi} & \overline{\mathbf{B}}^{\chi} & \overline{\mathbf{B}}_s^{\chi} & \overline{\overline{\mathbf{B}}}^{\chi} & \overline{\overline{\mathbf{B}}}_s^{\chi} & \mathbf{B}_s^{\chi} \\ \overline{\mathbf{B}}^{\chi} & \overline{\mathbf{D}}^{\chi} & \overline{\mathbf{D}}_s^{\chi} & \overline{\mathbf{E}}^{\chi} & \overline{\mathbf{E}}_s^{\chi} & \overline{\mathbf{F}}_s^{\chi} \\ \overline{\mathbf{B}}_s^{\chi} & \overline{\mathbf{D}}_s^{\chi} & \overline{\mathbf{H}}_s^{\chi} & \overline{\mathbf{G}}_s^{\chi} & \overline{\mathbf{I}}^{\chi} & \overline{\mathbf{J}}^{\chi} \\ \overline{\overline{\mathbf{B}}}^{\chi} & \overline{\mathbf{E}}^{\chi} & \overline{\mathbf{G}}_s^{\chi} & \overline{\overline{\mathbf{D}}}^{\chi} & \overline{\overline{\mathbf{D}}}_s^{\chi} & \overline{\mathbf{K}}_s^{\chi} \\ \overline{\overline{\mathbf{B}}}_s^{\chi} & \overline{\mathbf{E}}_s^{\chi} & \overline{\mathbf{I}}^{\chi} & \overline{\overline{\mathbf{D}}}_s^{\chi} & \overline{\overline{\mathbf{H}}}_s^{\chi} & \overline{\mathbf{L}} \\ \mathbf{B}_s^{\chi} & \overline{\mathbf{F}}_s^{\chi} & \overline{\mathbf{J}}^{\chi} & \overline{\mathbf{K}}_s^{\chi} & \overline{\mathbf{L}} & \mathbf{H}_s^{\chi} \end{bmatrix} \begin{Bmatrix} \boldsymbol{\chi}^{(0)} \\ \boldsymbol{\chi}^{(1)} \\ \boldsymbol{\chi}^{(2)} \\ \boldsymbol{\chi}^{(3)} \\ \boldsymbol{\chi}^{(4)} \\ \boldsymbol{\chi}^{(5)} \end{Bmatrix} \tag{20b}$$

where the stiffness components of the FGP sandwich microplates are defined as follows:

$$\left(\mathbf{A}^{\varepsilon}, \mathbf{B}^{\varepsilon}, \mathbf{D}^{\varepsilon}, \mathbf{H}_s^{\varepsilon}, \mathbf{B}_s^{\varepsilon}, \mathbf{D}_s^{\varepsilon}\right) = \int_{-h/2}^{h/2} \left(1, \Phi_1, \Phi_1^2, \Phi_2^2, \Phi_2, \Phi_1\Phi_2\right)\mathbf{Q}_{\varepsilon}^{(i)} dx_3 \tag{21a}$$

$$\mathbf{A}_s^{\varepsilon} = \int_{-h/2}^{h/2} \Phi_3^2 \mathbf{Q}_{\varepsilon}^{(o)} dx_3 \tag{21b}$$

$$\left(\mathbf{A}^{\chi}, \overline{\mathbf{B}}^{\chi}, \overline{\mathbf{B}}_s^{\chi}, \overline{\overline{\mathbf{B}}}^{\chi}, \overline{\overline{\mathbf{B}}}_s^{\chi}, \mathbf{B}_s^{\chi}\right) = \int_{-h/2}^{h/2} \left(1, \Phi_{1,3}, \Phi_{2,3}, \Phi_{1,33}, \Phi_{2,33}, \Phi_2\right)\alpha_{\chi}\mathbf{I}_{6\times 6} dx_3 \tag{21c}$$

$$\left(\overline{\mathbf{D}}^{\chi}, \overline{\mathbf{D}}_s^{\chi}, \overline{\mathbf{E}}^{\chi}, \overline{\mathbf{E}}_s^{\chi}, \overline{\mathbf{F}}_s^{\chi}\right) = \int_{-h/2}^{h/2} \Phi_{1,3}\left(\Phi_{1,3}, \Phi_{2,3}, \Phi_{1,33}, \Phi_{2,33}, \Phi_2\right)\alpha_{\chi}\mathbf{I}_{6\times 6} dx_3 \tag{21d}$$

$$\left(\overline{\mathbf{H}}_s^{\chi}, \overline{\mathbf{G}}_s^{\chi}, \overline{\mathbf{I}}^{\chi}, \overline{\mathbf{J}}^{\chi}\right) = \int_{-h/2}^{h/2} \Phi_{2,3}\left(\Phi_{2,3}, \Phi_{1,33}, \Phi_{2,33}, \Phi_2\right)\alpha_{\chi}\mathbf{I}_{6\times 6} dx_3 \tag{21e}$$

$$\begin{aligned} &\left(\overline{\overline{\mathbf{D}}}^{\chi}, \overline{\overline{\mathbf{D}}}_s^{\chi}, \overline{\mathbf{K}}_s^{\chi}, \overline{\overline{\mathbf{H}}}_s^{\chi}, \overline{\mathbf{L}}^{\chi}, \mathbf{H}_s^{\chi}\right) \\ &= \int_{-h/2}^{h/2} \left(\Phi_{1,33}^2, \Phi_{1,33}\Phi_{2,33}, \Phi_{1,33}\Phi_2, \Phi_{2,33}^2, \Phi_{2,33}\Phi_2, \Phi_2^2\right)\alpha_{\chi}\mathbf{I}_{6\times 6} dx_3 \end{aligned} \tag{21f}$$

The variation of kinetic energy $\delta\prod_K$ derived from Eq. (7) is calculated by:

$$\begin{aligned} \delta\Pi_K &= \frac{1}{2}\int_V \rho\left(\dot{u}_1\delta\dot{u}_1 + \dot{u}_2\delta\dot{u}_2 + \dot{u}_3\delta\dot{u}_3\right)dV \\ &= \frac{1}{2}\int_A \Big[I_0\left(\dot{u}_1^0\delta\dot{u}_1^0 + \dot{u}_2^0\delta\dot{u}_2^0 + \dot{u}_3^0\delta\dot{u}_3^0\right) + I_1\left(\dot{u}_1^0\delta\dot{u}_{3,1}^0 + \dot{u}_{3,1}^0\delta\dot{u}_1^0 + \dot{u}_2^0\delta\dot{u}_{3,2}^0 + \dot{u}_{3,2}^0\delta\dot{u}_2^0\right) \\ &+ J_2\left(\dot{u}_{3,1}^0\delta\dot{\varphi}_1 + \dot{\varphi}_1\delta\dot{u}_{3,1}^0 + \dot{u}_{3,2}^0\delta\dot{\varphi}_2 + \dot{\varphi}_2\delta\dot{u}_{3,2}^0\right) + K_2\left(\dot{\varphi}_1\delta\dot{\varphi}_1 + \dot{\varphi}_2\delta\dot{\varphi}_2\right) \\ &+ J_1\left(\dot{u}_1^0\delta\dot{\varphi}_1 + \dot{\varphi}_1\delta\dot{u}_1^0 + \dot{u}_2^0\delta\dot{\varphi}_2 + \dot{\varphi}_2\delta\dot{u}_2^0\right) + I_2\left(\dot{u}_{3,1}^0\delta\dot{u}_{3,1}^0 + \dot{u}_{3,2}^0\delta\dot{u}_{3,2}^0\right)\Big]dA \end{aligned} \tag{22}$$

where $I_0, I_1, I_2, J_1, J_2, K_2$ are mass components of the FGP sandwich microplates which are defined as follows:

$$(I_0, I_1, I_2, J_1, J_2, K_2) = \int_{-h/2}^{h/2} \left(1, \Phi_1, \Phi_1^2, \Phi_2, \Phi_1\Phi_2, \Phi_2^2\right)\rho dx_3 \tag{23}$$

3 Series-Type Solutions of FGP Sandwich Microplates

Based on the Ritz method, the membrane and transverse displacements, rotations $\left(u_1^0, u_2^0, u_3^0, \varphi_1, \varphi_2\right)$ of the FGP sandwich microplates can be expressed in terms of the series of approximation functions and associated values of series as follows:

$$\left\{u_1^0(x_1, x_2, t), \varphi_1(x_1, x_2, t)\right\} = \sum_{i=1}^{n_1}\sum_{j=1}^{n_2}\left\{u_{1ij}(t), x_{ij}(t)\right\}R_{i,1}(x_1)P_j(x_2) \tag{24a}$$

$$\left\{u_2^0(x_1, x_2, t), \varphi_2(x_1, x_2, t)\right\} = \sum_{i=1}^{n_1}\sum_{j=1}^{n_2}\left\{u_{2ij}(t), y_{ij}(t)\right\}R_i(x_1)P_{j,2}(x_2) \tag{24b}$$

$$u_3^0(x_1, x_2, t) = \sum_{i=1}^{n_1}\sum_{j=1}^{n_2}u_{3ij}(t)R_i(x_1)P_j(x_2) \tag{24c}$$

where $u_{1ij}, u_{2ij}, u_{3ij}, x_{ij}, y_{ij}$ are variables to be determined; $R_i(x_1), P_j(x_2)$ are the shape functions in x_1-, x_2- direction, respectively. As a result, five unknowns of the FGP microplates only depend on two shape functions. It should be noted that the accuracy, convergence rates and numerical instabilities of the Ritz solution depend on the construction of the shape functions, which was discussed in details in [13, 14]. The functions $R_i(x_1)$ and $P_j(x_2)$ are constructed to satisfy the boundary conditions (BCs):

- Simply supported (S): $u_2^0 = u_3^0 = \varphi_2 = 0$ at $x_1 = 0, a$ and $u_1^0 = u_3^0 = \varphi_1 = 0$ at $x_2 = 0, b$
- Clamped (C): $u_1^0 = u_2^0 = u_3^0 = \varphi_1 = \varphi_2 = 0$ at $x_1 = 0, a$ and $x_2 = 0, b$

The combination of simply-supported and clamped BCs on the edges of the FGP microplates leads to the various BCs. In the present paper, two typical BCs (SSSS and CCCC) are considered in which the shape functions are formed from hybrid ones which are composed of admissible functions and exponential ones as follows:

- For SSSS BC: $R_j(x_1) = x_1(a - x_1)e^{-\frac{jx_1}{a}}$, $P_j(x_2) = x_2(b - x_2)e^{-\frac{jx_2}{b}}$
- For CCCC BC: $R_j(x_1) = x_1^2(a - x_1)^2e^{-\frac{jx_1}{a}}$, $P_j(x_2) = x_2^2(b - x_2)^2e^{-\frac{jx_2}{b}}$.

Substituting Eq. (24) into Eqs. (18) and (22) and then the subsequent results into Eq. (17) lead to the characteristic equations of motion of the FGP sandwich microplates as follows: $\mathbf{Kd} + \mathbf{M}\ddot{\mathbf{d}} = \mathbf{0}$ where $\mathbf{d} = \left[\mathbf{u}_1\ \mathbf{u}_2\ \mathbf{u}_3\ \mathbf{x}\ \mathbf{y}\right]^T$ is the displacement vector to be determined; $\mathbf{K} = \mathbf{K}^{\varepsilon} + \mathbf{K}^{\chi}$ is the stiffness matrix which is composed of those of the strains $\mathbf{K}^{\varepsilon}$, symmetric rotation gradients $\mathbf{K}^{\chi}$; $\mathbf{M}$ is the mass matrix. These components are given more details as follows:

$$\mathbf{K}^{\zeta} = \begin{bmatrix} \mathbf{K}^{\zeta 11} & \mathbf{K}^{\zeta 12} & \mathbf{K}^{\zeta 13} & \mathbf{K}^{\zeta 14} & \mathbf{K}^{\zeta 15} \\ {}^{T}\mathbf{K}^{\zeta 12} & \mathbf{K}^{\zeta 22} & \mathbf{K}^{\zeta 23} & \mathbf{K}^{\zeta 24} & \mathbf{K}^{\zeta 25} \\ {}^{T}\mathbf{K}^{\zeta 13} & {}^{T}\mathbf{K}^{\zeta 23} & \mathbf{K}^{\zeta 33} & \mathbf{K}^{\zeta 34} & \mathbf{K}^{\zeta 35} \\ {}^{T}\mathbf{K}^{\zeta 14} & {}^{T}\mathbf{K}^{\zeta 24} & {}^{T}\mathbf{K}^{\zeta 34} & \mathbf{K}^{\zeta 44} & \mathbf{K}^{\zeta 45} \\ {}^{T}\mathbf{K}^{\zeta 15} & {}^{T}\mathbf{K}^{\zeta 25} & {}^{T}\mathbf{K}^{\zeta 35} & {}^{T}\mathbf{K}^{\zeta 45} & \mathbf{K}^{\zeta 55} \end{bmatrix} \text{ with } \zeta = \{\varepsilon, \chi\} \tag{25}$$

where the components of stiffness matrix $\mathbf{K}^{\varepsilon}$ are defined as follows:

$$K_{ijkl}^{\varepsilon 11} = A_{11}^{\varepsilon} T_{ik}^{22} S_{jl}^{00} + A_{66}^{\varepsilon} T_{ik}^{11} S_{jl}^{11}, K_{ijkl}^{\varepsilon 12} = A_{12}^{\varepsilon} T_{ik}^{02} S_{jl}^{20} + A_{66}^{\varepsilon} T_{ik}^{11} S_{jl}^{11}$$
$$K_{ijkl}^{\varepsilon 13} = B_{11}^{\varepsilon} T_{ik}^{22} S_{jl}^{00} + B_{12}^{\varepsilon} T_{ik}^{02} S_{jl}^{20} + 2B_{66}^{\varepsilon} T_{ik}^{11} S_{jl}^{11}$$
$$K_{ijkl}^{\varepsilon 14} = B_{s11}^{\varepsilon} T_{ik}^{22} S_{jl}^{00} + B_{s66}^{\varepsilon} T_{ik}^{11} S_{jl}^{11}, K_{ijkl}^{\varepsilon 15} = B_{s12}^{\varepsilon} T_{ik}^{02} S_{jl}^{20} + B_{s66}^{\varepsilon} T_{ik}^{11} S_{jl}^{11}$$
$$K_{ijkl}^{\varepsilon 22} = A_{22}^{\varepsilon} T_{ik}^{00} S_{jl}^{22} + A_{66}^{\varepsilon} T_{ik}^{11} S_{jl}^{11}, K_{ijkl}^{\varepsilon 23} = B_{12}^{\varepsilon} T_{ik}^{20} S_{jl}^{02} + B_{22}^{\varepsilon} T_{ik}^{00} S_{jl}^{22} + 2B_{66}^{\varepsilon} T_{ik}^{11} S_{jl}^{11}$$
$$K_{ijkl}^{\varepsilon 24} = B_{s12}^{\varepsilon} T_{ik}^{20} S_{jl}^{02} + B_{s66}^{\varepsilon} T_{ik}^{11} S_{jl}^{11}, K_{ijkl}^{\varepsilon 25} = B_{s22}^{\varepsilon} T_{ik}^{00} S_{jl}^{22} + B_{s66}^{\varepsilon} T_{ik}^{11} S_{jl}^{11}$$
$$K_{ijkl}^{\varepsilon 33} = D_{11}^{\varepsilon} T_{ik}^{22} S_{jl}^{00} + D_{12}^{\varepsilon} \left(T_{ik}^{02} S_{jl}^{20} + T_{ik}^{20} S_{jl}^{02} \right) + D_{22}^{\varepsilon} T_{ik}^{00} S_{jl}^{22} + 4D_{66}^{\varepsilon} T_{ik}^{11} S_{jl}^{11}$$
$$+ A_{s44}^{\varepsilon} T_{ik}^{00} S_{jl}^{11} + A_{s55}^{\varepsilon} T_{ik}^{11} S_{jl}^{00}$$
$$K_{ijkl}^{\varepsilon 34} = D_{s11}^{\varepsilon} T_{ik}^{22} S_{jl}^{00} + D_{s12}^{\varepsilon} T_{ik}^{20} S_{jl}^{02} + 2D_{s66}^{\varepsilon} T_{ik}^{11} S_{jl}^{11} + A_{s55}^{\varepsilon} T_{ik}^{11} S_{jl}^{00}$$
$$K_{ijkl}^{\varepsilon 35} = D_{s12}^{\varepsilon} T_{ik}^{02} S_{jl}^{20} + D_{s22}^{\varepsilon} T_{ik}^{00} S_{jl}^{22} + 2D_{s66}^{\varepsilon} T_{ik}^{11} S_{jl}^{11} + A_{s44}^{\varepsilon} T_{ik}^{00} S_{jl}^{11}$$
$$K_{ijkl}^{\varepsilon 44} = H_{s11}^{\varepsilon} T_{ik}^{22} S_{jl}^{00} + H_{s66}^{\varepsilon} T_{ik}^{11} S_{jl}^{11} + A_{s55}^{\varepsilon} T_{ik}^{11} S_{jl}^{00}$$
$$K_{ijkl}^{\varepsilon 45} = H_{s12}^{\varepsilon} T_{ik}^{02} S_{jl}^{20} + H_{s66}^{\varepsilon} T_{ik}^{11} S_{jl}^{11}, K_{ijkl}^{\varepsilon 55} = H_{s22}^{\varepsilon} T_{ik}^{00} S_{jl}^{22} + H_{s66}^{\varepsilon} T_{ik}^{11} S_{jl}^{11} + A_{s44}^{\varepsilon} T_{ik}^{00} S_{jl}^{11}$$

$$T_{ik}^{rs} = \int_0^a \frac{\partial^r R_i}{\partial x_1^r} \frac{\partial^s R_k}{\partial x_1^s} dx_1, S_{jl}^{rs} = \int_0^a \frac{\partial^r S_j}{\partial x_2^r} \frac{\partial^s S_l}{\partial x_2^s} dx_2 \tag{26}$$

The components of stiffness matrix $\mathbf{K}^{\chi}$ are defined as follows:

$$
\begin{aligned}
&K_{ijkl}^{\chi 11} = \frac{A^{\chi}}{4}\left(T_{ik}^{22}S_{jl}^{11} + T_{ik}^{11}S_{jl}^{22}\right),\ K_{ijkl}^{\chi 12} = -\frac{A^{\chi}}{4}\left(T_{ik}^{22}S_{jl}^{11} + T_{ik}^{11}S_{jl}^{22}\right)\\
&K_{ijkl}^{\chi 13} = \frac{\overline{\overline{B}}^{\chi}}{4}\left(T_{ik}^{02}S_{jl}^{11} - T_{ik}^{11}S_{jl}^{02}\right),\ K_{ijkl}^{\chi 14} = \frac{1}{4}\left(B_s^{\chi}T_{ik}^{22}S_{jl}^{11} + B_s^{\chi}T_{ik}^{11}S_{jl}^{22} - \overline{\overline{B}}_s^{\chi}T_{ik}^{11}S_{jl}^{02}\right)\\
&K_{ijkl}^{\chi 15} = \frac{1}{4}\left(\overline{\overline{B}}_s^{\chi}T_{ik}^{02}S_{jl}^{11} - B_s^{\chi}T_{ik}^{22}S_{jl}^{11} - B_s^{\chi}T_{ik}^{11}S_{jl}^{22}\right),\ K_{ijkl}^{\chi 22} = \frac{A^{\chi}}{4}\left(T_{ik}^{22}S_{jl}^{11} + T_{ik}^{11}S_{jl}^{22}\right)\\
&K_{ijkl}^{\chi 23} = \frac{\overline{\overline{B}}^{\chi}}{4}\left(T_{ik}^{11}S_{jl}^{02} - T_{ik}^{02}S_{jl}^{11}\right),\ K_{ijkl}^{\chi 24} = \frac{1}{4}\left(\overline{\overline{B}}_s^{\chi}T_{ik}^{11}S_{jl}^{02} - B_s^{\chi}T_{ik}^{22}S_{jl}^{11} - B_s^{\chi}T_{ik}^{11}S_{jl}^{22}\right)\\
&K_{ijkl}^{\chi 25} = \frac{1}{4}\left(B_s^{\chi}T_{ik}^{22}S_{jl}^{11} + B_s^{\chi}T_{ik}^{11}S_{jl}^{22} - \overline{\overline{B}}_s^{\chi}T_{ik}^{02}S_{jl}^{11}\right)\\
&K_{ijkl}^{\chi 33} = \frac{1}{4}\left(A^{\chi} - 2\overline{B}^{\chi} + \overline{D}^{\chi}\right)\left(T_{ik}^{00}S_{jl}^{22} - T_{ik}^{20}S_{jl}^{02} - T_{ik}^{02}S_{jl}^{20} + T_{ik}^{22}S_{jl}^{00} + 2T_{ik}^{11}S_{jl}^{11}\right)\\
&\quad + \frac{1}{4}\overline{\overline{D}}^{\chi}\left(T_{ik}^{00}S_{jl}^{11} + T_{ik}^{11}S_{jl}^{00}\right)\\
&K_{ijkl}^{\chi 34} = \frac{1}{4}\Big[\left(\overline{B}_s^{\chi} - \overline{D}_s^{\chi}\right)\left(T_{ik}^{20}S_{jl}^{02} - T_{ik}^{22}S_{jl}^{00} - T_{ik}^{11}S_{jl}^{11}\right)\\
&\quad + \overline{K}_s^{\chi}\left(T_{ik}^{20}S_{jl}^{11} - T_{ik}^{11}S_{jl}^{20}\right) + \overline{\overline{D}}_s^{\chi}T_{ik}^{11}S_{jl}^{00}\Big]\\
&K_{ijkl}^{\chi 35} = \frac{1}{4}\Big[\left(\overline{B}_s^{\chi} - \overline{D}_s^{\chi}\right)\left(-T_{ik}^{00}S_{jl}^{22} + T_{ik}^{02}S_{jl}^{20} - T_{ik}^{11}S_{jl}^{11}\right)\\
&\quad + \overline{\overline{D}}_s^{\chi}T_{ik}^{00}S_{jl}^{11} + \overline{K}_s^{\chi}\left(T_{ik}^{11}S_{jl}^{20} - T_{ik}^{20}S_{jl}^{11}\right)\Big]\\
&K_{ijkl}^{\chi 44} = \frac{1}{4}\Big[\overline{H}_s^{\chi}\left(T_{ik}^{22}S_{jl}^{00} + 2T_{ik}^{11}S_{jl}^{11}\right) + \overline{\overline{H}}_s^{\chi}T_{ik}^{11}S_{jl}^{00}\\
&\quad - \overline{L}^{\chi}\left(T_{ik}^{11}S_{jl}^{20} + T_{ik}^{11}S_{jl}^{02}\right) + H_s^{\chi}\left(T_{ik}^{22}S_{jl}^{11} + T_{ik}^{11}S_{jl}^{22}\right)\Big]\\
&K_{ijkl}^{\chi 45} = \frac{1}{4}\Big[\overline{L}^{\chi}\left(T_{ik}^{11}S_{jl}^{20} + T_{ik}^{02}S_{jl}^{11}\right) - \overline{H}_s^{\chi}\left(T_{ik}^{02}S_{jl}^{20} + T_{ik}^{11}S_{jl}^{11}\right) - H_s^{\chi}\left(T_{ik}^{11}S_{jl}^{22} + T_{ik}^{22}S_{jl}^{11}\right)\Big]\\
&\ldots\\
&K_{ijkl}^{\chi 55} = \frac{1}{4}\Big[\overline{H}_s^{\chi}\left(2T_{ik}^{11}S_{jl}^{11} + T_{ik}^{00}S_{jl}^{22}\right) + \overline{\overline{H}}_s^{\chi}T_{ik}^{00}S_{jl}^{11} - \overline{L}^{\chi}\left(T_{ik}^{20}S_{jl}^{11} + T_{ik}^{02}S_{jl}^{11}\right)\\
&\quad + H_s^{\chi}\left(T_{ik}^{11}S_{jl}^{22} + T_{ik}^{22}S_{jl}^{11}\right)\Big]\\
&\ldots
\end{aligned}
\tag{27}
$$

The components of mass matrix $\mathbf{M}$ are given by:

$$
\begin{aligned}
&M_{ijkl}^{11} = I_0T_{ik}^{11}S_{jl}^{00}, M_{ijkl}^{13} = I_1T_{ik}^{11}S_{jl}^{00}, M_{ijkl}^{14} = J_1T_{ik}^{11}S_{jl}^{00}, M_{ijkl}^{44} = K_2T_{ik}^{11}S_{jl}^{00}\\
&M_{ijkl}^{22} = I_0T_{ik}^{00}S_{jl}^{11}, M_{ijkl}^{23} = I_1T_{ik}^{00}S_{jl}^{11}, M_{ijkl}^{25} = J_1T_{ik}^{00}S_{jl}^{11}, M_{ijkl}^{55} = K_2T_{ik}^{00}S_{jl}^{11}\\
&M_{ijkl}^{33} = I_0T_{ik}^{00}S_{jl}^{00} + I_2\left(T_{ik}^{11}S_{jl}^{00} + T_{ik}^{00}S_{jl}^{11}\right), M_{ijkl}^{34} = J_2T_{ik}^{11}S_{jl}^{00}, M_{ijkl}^{35} = J_2T_{ik}^{00}S_{jl}^{11}
\end{aligned}
\tag{28}
$$

It is worth noticing that for free vibration analysis, by denoting $\mathbf{d}(t) = \mathbf{d}e^{i\omega t}$ where ω is the natural frequency of the FGP sandwich microplates and $i^2 = -1$ is imaginary

unit, the natural frequencies can be hence derived from the following the equation: $\left(\mathbf{K} - \omega^2 \mathbf{M}\right)\mathbf{d} = \mathbf{0}$.

4 Numerical Examples

In this section, numerical examples are carried out to investigate free vibration behaviours of FGP sandwich microplates in which the shear function $f(x_3) = x_3 - 4x_3^3/3h^2$ is selected. The FGP sandwich microplates are supposed to be made of ceramic material Al_2O_3 and metal one Al whose properties are given as follows: Al_2O_3 ($E_c = 380$ GPa, $\nu_c = 0.3$,$\rho_c = 3800$ kg/m^3), Al ($E_m = 70$ GPa, $\rho_m = 2702$ kg/m^3, $\nu_m = 0.3$), $\rho_o = 1$ kg/m^3 and $E_o = 1$ GPa.The preliminary convergence study on the series solution showed that the number of series $n_1 = n_2 = n = 10$ can be considered as the convergence point of the solution field, therefore this value will be used in the sequel computations. Moreover, for convenience, the following normalized parameter is used in the numerical examples:

$$\overline{\omega} = \frac{\omega a^2}{h}\sqrt{\frac{\rho_o}{E_o}} \tag{29}$$

In order to verify the accuracy of the present theory, Table 1 introduces normalized fundamental frequencies of Al/Al_2O_3 FGP sandwich microplates in which the solutions are calculated with different values of the power index $p = 0.5, 1, 2$, side-to-thickness ratio $a/h = 10$, ratio of thickness-to-material scale $h/l = \infty, 5, 5/3, 1$, porous parameter $\beta = 0, 0.1, 0.2$.

The results obtained from the present theory with SSSS boundary condition are compared with those derived from FGP sandwich plates of Pham and Le [2] based on the FEM and HSDT, Li et al. [11] based on three-dimensional model and Ritz method, Thai et al. [15, 16] based on HSDTs and isogeometric approach, Daikh et al. [1] based on a HSDT and Navier procedure, Thai et al. [7] based on the MCT and HSDT. It can be seen that there are good agreements among the models at both macro- and micro-scales. Moreover, it is observed from Table 1 that the fundamental frequencies decrease with an increase of the power index p. This can be explained by the fact that with an increase of p led to a decrease of the volume fraction of ceramic and stiffness of FGP sandwich microplates. The variations of normalized fundamental frequencies with respect to the ratio of thickness-to-material scale h/l are observed in Fig. 2 for Al/Al_2O_3 FGP microplates with $\beta = 0.1$, $p = 2$ and $a/h = 10$. The graphs are displayed with six different types of bottom-core-top thickness ratio within which it is observed that the natural frequencies decrease with the increase of h/l up to the value of $h/l = 10$ from which the curves become flatter and size effects can be hence neglected. Moreover, Table 2 shows the normalized fundamental frequencies of FGP sandwich microplates with clamped boundary condition. The solutions are examined with those of Pham and Le [2] without size effect ($h/L = \infty$), Li et al. [11] without size and porosity effects ($h/L = \infty$, $\beta = 0$). Good agreements are again found of the theories when the effects of porosity or both size and porosity are not considered. New results on fundamental frequencies on the CCCC boundary condition can be used for benchmarks in future research.

Table 1. Normalized fundamental frequencies of Al/Al_2O_3 FGP sandwich microplates with SSSS and $a/h = 10$

p	h/l	Theory	1-0-1	2-1-2	2-1-1	1-1-1	2-2-1	1-2-1
$\beta = 0$								
0.5	∞	Present	1.4404	1.4806	1.5046	1.5160	1.5454	1.5717
		MCT [7]	1.4462	1.4861	1.5084	1.5213	1.5492	1.5766
		3D [11]	1.4461	1.4861	1.5084	1.5213	1.5493	1.5766
		IGA [15]	1.4443	1.4841	1.5064	1.5192	1.5472	1.5745
		IGA [16]	1.4519	1.4918	1.5142	1.5264	1.5543	1.5806
	5	Present	1.5944	1.6424	1.6670	1.6818	1.7121	1.7413
		MCT [7]	1.5987	1.6423	1.6643	1.6788	1.7064	1.7345
	5/3	Present	2.5059	2.5960	2.6261	2.6584	2.6965	2.7409
		MCT [7]	2.5006	2.5667	2.5900	2.6142	2.6437	2.6787
	1	Present	3.7068	3.8488	3.8888	3.9415	3.9913	4.0370
		MCT [7]	3.6872	3.7836	3.8126	3.8488	3.8885	3.9325
1	∞	Present	1.2400	1.2968	1.3343	1.3501	1.3968	1.4363
		MCT [7]	1.2449	1.3019	1.3352	1.3552	1.3975	1.4413
		3D [11]	1.2447	1.3018	1.3351	1.3552	1.3976	1.4413
		IGA [15]	1.2432	1.3001	1.3334	1.3533	1.3957	1.4393
		IGA [16]	1.2552	1.3128	1.3466	1.3653	1.4076	1.4490
	5	Present	1.3918	1.4616	1.4996	1.5204	1.5677	1.6106
		MCT [7]	1.3963	1.4612	1.4941	1.4941	1.5590	1.6038
	5/3	Present	2.2667	2.4029	2.4474	2.4949	2.5511	2.6155
		MCT [7]	2.2638	2.3729	2.4092	2.4492	2.4950	2.5512
	1	Present	3.3964	3.6121	3.6716	3.7483	3.8217	3.9149
		MCT [7]	3.3769	3.5413	3.5882	3.6486	3.7072	3.7830
$\beta = 0.1$								
2	∞	Present	0.9787	1.0532	1.1117	1.1309	1.2038	1.2616
		FEM [2]	0.9755	1.0562	1.0888	1.1292	1.1774	1.2492
		HSDT[1]	0.9825	1.0471	1.0941	1.1207	1.1826	1.2493
	5	Present	1.1326	1.2313	1.2891	1.3176	1.3893	1.4515
	1	Present	3.0104	3.3555	3.4467	3.5625	3.6703	3.8047
$\beta = 0.2$								
	∞	Present	0.9156	0.9909	1.0388	1.0659	1.1299	1.2194

(*continued*)

Table 1. (*continued*)

p	h/l	Theory	1-0-1	2-1-2	2-1-1	1-1-1	2-2-1	1-2-1
		FEM [2]	0.9118	0.9961	1.0150	1.0737	1.1150	1.2039
		HSDT [1]	0.8786	0.9549	1.0055	1.0420	1.1105	1.1915
	5	Present	1.0423	1.1644	1.2303	1.2671	1.3483	1.4212
	1	Present	2.9608	3.3527	3.4533	3.5829	3.7009	3.8479

Table 2. Normalized fundamental frequencies of Al/Al_2O_3 FGP sandwich microplates with CCCC BC and $a/h = 10$

p	h/l	Theory	1-0-1	2-1-2	1-1-1	2-2-1	1-2-1	1-8-1
$\beta = 0$								
0.5	∞	Present	2.5021	2.5699	2.6262	2.6678	2.7109	2.9006
		3D [11]	2.5259	2.5949	2.6535	2.6982	2.7498	2.9583
	10	Present	2.6160	2.6903	2.7498	2.7931	2.8377	3.0325
	5	Present	2.9269	3.0174	3.0861	3.1324	3.1833	3.3902
	2	Present	4.5152	4.6803	4.7922	4.8575	4.9368	5.2193
	1	Present	7.8188	8.1195	8.3227	8.4462	8.5852	9.0923
1	∞	Present	2.1774	2.2770	2.3658	2.4355	2.5039	2.8174
		3D [11]	2.1901	2.2910	2.3818	2.4510	2.5397	2.8625
	10	Present	2.2890	2.3985	2.4915	2.5622	2.6335	2.9498
	5	Present	2.5923	2.7272	2.8322	2.9055	2.9838	3.3085
	2	Present	4.0961	4.3460	4.5115	4.6079	4.7225	5.1290
	1	Present	7.0669	7.5054	7.8021	7.9964	8.1889	8.9382
5	∞	Present	1.6662	1.7417	1.8521	1.9726	2.1120	2.6393
		3D [11]	1.6618	1.7392	1.8579	1.9671	2.1571	2.6673
	10	Present	1.7550	1.8608	1.9835	2.1052	2.2096	2.7742
	5	Present	1.9956	2.1768	2.3309	2.4563	2.5752	3.1378
	2	Present	3.1799	3.6540	3.9423	4.1074	4.2943	4.9494
	1	Present	5.4600	6.1861	6.6639	7.0401	7.3095	8.6038
$\beta = 0.2$								
2	∞	Present	1.5633	1.7347	1.9001	2.0286	2.1612	2.7331

(*continued*)

Table 2. (*continued*)

p	h/l	Theory	1-0-1	2-1-2	1-1-1	2-2-1	1-2-1	1-8-1
		FEM [2]	–	–	1.8944	1.9680	–	–
	10	Present	1.6876	1.8789	2.0494	2.1773	2.3110	2.8768
	5	Present	2.0126	2.2537	2.4406	2.5677	2.7074	3.2634
	2	Present	3.4838	3.9376	4.2175	4.3737	4.5588	5.1840
	1	Present	5.8706	6.6405	7.1623	7.5421	7.8361	9.0762

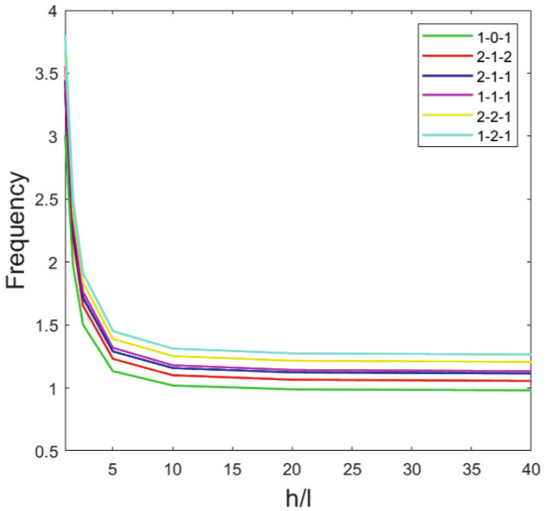

Fig. 2. Variation of normalized fundamental frequencies of Al/Al_2O_3 FGP sandwich microplates with SSSS respect to h/l ($p = 2$, $\beta = 0.1$, $a/h = 10$)

5 Conclusions

A unified higher-order shear deformation microplate model for free vibration analysis of functionally graded sandwich porous materials has been proposed in this paper. The present theory is developed from fundamental equations of the elasticity theory and modified couple stress theory. The solution field is approximated by bi-directional series in which hybrid shape functions are proposed, then the stiffness and mass matrix are explicitly derived. Numerical examples are investigated for the different configurations of material distribution, side-to-thickness ratio, size-scale-thickness ratio on the natural frequencies of FGP sandwich microplates. The obtained results show that the size effect is important and needs to be accounted for the computations. The size effect leads to an increase of the stiffness and natural frequency of the FGP sandwich plates. The proposed unified size dependent plate model presents the accuracy and efficiency in predicting vibration behaviours of FGP sandwich microplates.

References

1. Daikh, A.A., Zenkour, A.: Free vibration and buckling of porous power-law and sigmoid functionally graded sandwich plates using a simple higher-order shear deformation theory. Mater. Res. Express **6**, 115707 (2019)
2. Van Vinh, P., Huy, L.Q.: Finite element analysis of functionally graded sandwich plates with porosity via a new hyperbolic shear deformation theory. Defence Technol. (2021)
3. Quan, T.Q., Ha, D.T.T., Duc, N.D.: Analytical solutions for nonlinear vibration of porous functionally graded sandwich plate subjected to blast loading. Thin-Walled Struct. **170**, 108606 Jan 01 (2022)
4. Zhang, Y., Jin, G., Chen, M., Ye, T., Yang, C., Yin, Y.: Free vibration and damping analysis of porous functionally graded sandwich plates with a viscoelastic core. Compos. Struct. **244**, 112298 (2020)
5. Tahir, S.I., Chikh, A., Tounsi, A., Al-Osta, M.A., Al-Dulaijan, S.U., Al-Zahrani, M.M.: Wave propagation analysis of a ceramic-metal functionally graded sandwich plate with different porosity distributions in a hygro-thermal environment. Compos. Struct. **269**, 114030 (2021)
6. Kumar Sah, S., Ghosh, A.: Influence of porosity distribution on free vibration and buckling analysis of multi-directional functionally graded sandwich plates. Compos. Struct. **279**, 114795 (2022)
7. Thai Hoang, C., Ferreira, A., Lee, J., Nguyen-Xuan, H.: An efficient size-dependent computational approach for functionally graded isotropic and sandwich microplates based on modified couple stress theory and moving Kriging-based meshfree method. Int. J. Mech. Sci. **142**, (2018)
8. Phung-Van, P., Ferreira, A.J.M., Thai, C.H.: Computational optimization for porosity-dependent isogeometric analysis of functionally graded sandwich nanoplates. Compos. Struct. **239**, 112029 (2020)
9. Nguyen, T.-K., Thai, H.-T., Vo, T.P.: A novel general higher-order shear deformation theory for static, vibration and thermal buckling analysis of the functionally graded plates. J. Thermal Stress. **44**(3), 377–394 (2021)
10. Thanh, C.-L., Tran, L.V., Bui, T.Q., Nguyen, H.X., Abdel-Wahab, M.: Isogeometric analysis for size-dependent nonlinear thermal stability of porous FG microplates. Compos. Struct. **221**, 110838 (2019)
11. Li, Q., Iu, V.P., Kou, K.P.: Three-dimensional vibration analysis of functionally graded material sandwich plates. J. Sound Vibr. **311**(1), 498–515 (2008)
12. Yang, F., Chong, A.C.M., Lam, D.C.C., Tong, P.: Couple stress based strain gradient theory for elasticity. Int. J. Solids Struct. **39**, 2731–2743 (2002)
13. Nguyen, T.-K., Truong-Phong Nguyen, T., Vo, T.P., Thai, H.-T.: Vibration and buckling analysis of functionally graded sandwich beams by a new higher-order shear deformation theory. Compos. Part B: Eng. **76**, 273–285 (2015)
14. Nguyen, T.-K., Vo, T.P., Nguyen, B.-D., Lee, J.: An analytical solution for buckling and vibration analysis of functionally graded sandwich beams using a quasi-3D shear deformation theory. Compos. Struct. **156**, 238–252 (2016)
15. Thai, C.H., Kulasegaram, S., Tran, L.V., Nguyen-Xuan, H.: Generalized shear deformation theory for functionally graded isotropic and sandwich plates based on isogeometric approach. Comput. Struct. **141**, 94–112 (2014)
16. Thai, C.H., Zenkour, A.M., Abdel Wahab, M., Nguyen-Xuan, H.: A simple four-unknown shear and normal deformations theory for functionally graded isotropic and sandwich plates based on isogeometric analysis. Compos. Struct. **139**, 77–95 (2016)

HỘI CƠ HỌC VIỆT NAM

TUYỂN TẬP CÔNG TRÌNH KHOA HỌC

HỘI NGHỊ CƠ HỌC TOÀN QUỐC

LẦN THỨ XI

HÀ NỘI, 02-03/12/2022

TẬP 1. Cơ học Vật rắn biến dạng

NHÀ XUẤT BẢN KHOA HỌC TỰ NHIÊN VÀ CÔNG NGHỆ

HỘI CƠ HỌC VIỆT NAM

Tuyển tập công trình khoa học
Hội nghị Cơ học toàn quốc lần thứ XI

Hà Nội, 02-03/12/2022

Tập 1. Cơ học Vật rắn biến dạng

HÀ NỘI, 2022

Tuyển tập công trình khoa học Hội nghị Cơ học toàn quốc lần thứ XI

Hà Nội, 02-03/12/2022

Tập 1. Cơ học Vật rắn biến dạng

ISBN: 978-604-357-084-7

NHÀ XUẤT BẢN KHOA HỌC TỰ NHIÊN VÀ CÔNG NGHỆ

Trụ sở: Nhà A16, số 18 Hoàng Quốc Việt, Cầu Giấy, Hà Nội.

Điện thoại: 024 22149040 Fax: 024 37910147

Website: http://www.vap.vast.vn

BAN KHOA HỌC

Trưởng ban: Nguyễn Tiến Khiêm.

Phó Trưởng ban: Nguyễn Đình Đức, Hoàng Văn Huân, Nguyễn Xuân Hùng, Nguyễn Văn Khang, Phan Bùi Khôi, Trần Ích Thịnh, Nguyễn Đăng Tộ, Đỗ Như Tráng.

Ủy viên: Nguyễn Đông Anh, Đào Huy Bích, Nguyễn Đăng Bích, Lê Văn Cảnh, Ngô Huy Cẩn, Phạm Đức Chính, Nguyễn Thái Chung, Nguyễn Đức Cương, Nguyễn Phong Điền, Nguyễn Văn Điệp, Bùi Văn Ga, Dương Ngọc Hải, Vũ Công Hàm, Nguyễn Thế Hùng, Nguyễn Quốc Hưng, Ngô Như Khoa, Nguyễn Việt Khoa, Nguyễn Trung Kiên, Trần Văn Liên, Nguyễn Hữu Lộc, Hoàng Xuân Lượng, Nguyễn Xuân Lựu, Đào Như Mai, Nguyễn Xuân Mãn, Đinh Văn Mạnh, Trần Văn Nam, Ngô Kiều Nhi, Nguyễn Ân Niên, Nguyễn Văn Phó, Đinh Văn Phong, Khúc Văn Phú, Nguyễn Thiện Phúc, Phạm Hồng Phúc, Nguyễn Trọng Phước, Lê Quang, Vũ Duy Quang, Trần Quốc Quân, Lê Minh Quý, Ngô Văn Quyết, Nguyễn Chỉ Sáng, Đỗ Sanh, Nguyễn Hoài Sơn, Lê Lương Tài, Phạm Mạnh Thắng, Trương Tích Thiện, Bùi Quốc Tính, Vũ Quốc Trụ, Nguyễn Thời Trung, Trần Đức Trung, Trần Minh Tú, Hoàng Văn Tùng, Lã Đức Việt, Nguyễn Trung Việt, Phạm Chí Vĩnh.

BAN TỔ CHỨC

Đồng Trưởng ban: Nguyễn Đình Đức, Trần Văn Liên.

Phó Trưởng ban: Lê Văn Cảnh, Nguyễn Thị Việt Liên, Trần Văn Nam.

Ủy viên: Chu Thanh Bình, Trần Anh Bình, Lương Xuân Bính, Thái Hoàng Chiến, Phạm Hồng Công, Nguyễn Tiến Dũng, Phan Hải Đăng, Phạm Tiến Đạt, Nguyễn Phong Điền, Phạm Minh Hải, Trần Thanh Hải, Vũ Công Hàm, Hà Ngọc Hiến, Nguyễn Quang Hoàng, Hoàng Văn Huân, Phan Bùi Khôi, Đặng Bảo Lâm, Đào Như Mai, Dương Tuấn Mạnh, Phan Đăng Phong, Cao Văn Phường, Vũ Ngọc Pi, Trần Quốc Quân, Nguyễn Hoài Sơn, Nguyễn Hồng Thái, Đặng Ngọc Thanh, Châu Đình Thành, Phạm Mạnh Thắng, Nguyễn Đăng Tộ, Nguyễn Xuân Toản, Phạm Quốc Tuấn, Trần Thanh Hải Tùng.

BAN THƯ KÝ

Trưởng ban: Nguyễn Thị Việt Liên.

Ủy viên: Vũ Thị Thùy Anh, Nguyễn Tiến Cường, Phan Hải Đăng, Trần Bình Định, Trần Thị Thu Hà, Nguyễn Quang Hoàng, Đặng Bảo Lâm, Phan Thị Cẩm Ly, Đào Như Mai, Dương Tuấn Mạnh, Phùng Văn Phúc, Nguyễn Tất Thắng, Nguyễn Kim Thoa, Phạm Quốc Tuấn, Trần Ngọc Trung, Nguyễn Ngọc Vinh.

BAN BIÊN TẬP

Trưởng ban: Nguyễn Tiến Khiêm.

Với sự tham gia của: Nguyễn Tiến Cường, Phan Hải Đăng, Trần Bình Định, Nguyễn Đình Đức, Nguyễn Quang Hoàng, Hoàng Văn Huân, Nguyễn Xuân Hùng, Nguyễn Văn Khang, Phan Bùi Khôi, Đặng Bảo Lâm, Trần Văn Liên, Nguyễn Thị Việt Liên, Đào Như Mai, Phùng Văn Phúc, Nguyễn Tất Thắng, Trần Ích Thịnh, Nguyễn Đăng Tộ, Đỗ Như Tráng, Trần Ngọc Trung, Phạm Quốc Tuấn.

A BCMO-DNN algorithm for vibration optimization of functionally graded porous microplates

Van-Hau Nguyen[1], Van-Thien Tran[1] and Trung-Kien Nguyen[2,*]
[1] *Faculty of Civil Engineering, Ho Chi Minh City University of Technology and Education, 1 Vo Van Ngan street, Thu Duc district, Ho Chi Minh City, Viet Nam*
[2] *CIRTech Institute, HUTECH University, 475A Dien Bien Phu street, Binh Thanh district, Ho Chi Minh City, Viet Nam*
[*]Email: ntkien@hutech.edu.vn

Abstract. The authors propose a novel BCMO-DNN algorithm for vibration optimization of functionally graded porous microplates. The theory is based on a unified framework of higher-order shear deformation theory and modified strain gradient theory. A hybrid combination of deep learning neural network and balancing composite motion optimization is developed to solve the optimization problems and predict stochastic vibration behaviors of functionally graded porous microplates with uncertainties of material properties. The characteristic equations of motion are derived from Hamilton's principle and approximation of exponential series. Numerical results are obtained to investigate the effects of the material distribution, material length scale, porosity density and boundary conditions on natural frequencies of functionally graded porous microplates.

Keywords: Vibration, Functionally graded microplates, Modified strain gradient theory, Deep leaning neural network, Balancing composite motion optimization.

1. Introduction

The study on static and dynamic responses of functionally graded porous (FGP) plates has recently been an interesting topic attracted a number of researches with various computational methods and plate models. However practically, the behaviors of such structures at the small scale could not accurately predict by classical elasticity theories due to size effects. In order to overcome this adverse, the nonlocal elasticity theory ([1]) can be used for analysis of functionally graded nanoplates ([2]). Nevertheless, the implementation of this theory for nanostructures with different boundary conditions appears to be quite complicated. Another way to investigate the size effects is to use the modified couple stress theory (MCT) with one material length scale parameter (MLSP) or modified strain gradient theory (MST) with three MLSPs. These approaches have been employed to predict the behaviors of functionally graded microplates ([3-5]). For optimization of composite structures, meta-heuristic optimization methods based on natural phenomena are recently considered as robust and reliable approaches ([6-9]). In practice, these algorithms with dependent parameters require high computational costs. An alternative way is to use balancing composite motion optimization algorithm (BCMO) ([10]) in which no dependent parameters are required. This approach has been applied to optimize behaviors of functionally graded plates ([11, 12]). Moreover, the machine learning included artificial neural network (ANN) and deep learning neural network (DNN) has been used to material optimization of composite structures ([13-15]). Though many researches on the optimization analysis of laminated composite and functionally graded plates have been performed, as far as the authors are aware, the study on optimal behaviors of the FGP microplates with uncertain materials is still limited.

This paper aims to investigate optimal responses of natural frequencies of FGP microplates subjected to uncertainties of material properties. It is based on a unified microplate model using a general higher-order shear deformation theory and MST. A combination of BCMO-DNN is for

the first time proposed to solve the optimization problems and predict stochastic vibration behaviors of FGP microplates. The characteristic equations of motion are derived from Hamilton's principle, and Ritz-type series method is used to approximate the field variables. Numerical results are used to study effects of the material distribution, material length scale, porosity density and boundary conditions on natural frequencies of FGP microplates.

2. Theoretical formulation

Consider a rectangle FGP plate in the coordinate system (x_1, x_2, x_3) with sides $a \times b$ and thickness h. It is supposed that the FGP microplates are composed of a metal-ceramic mixture and porosity density whose effective material properties are approximated by the following expressions ([16]) :

$$P(x_3) = (P_c - P_m)\left(\frac{2x_3 + h}{2h}\right)^p + P_m - \frac{\beta}{2}(P_c + P_m) \tag{1}$$

where P_c and P_m are the properties of ceramic and metal materials, such as Young's modulus E, mass density ρ, Poisson's ratio ν; $\beta \le 1$ is the porosity volume fraction; p is the power-law index which is positive and $x_3 \in [-h/2, h/2]$.

2.1. Modified strain gradient theory

The total potential energy of the FGP microplates is composed of the strain energy Π_U and kinetic energy Π_K as follows: $\Pi = \Pi_U - \Pi_K$. Based on the MST, the strain energy Π_U is given by:

$$\Pi_U = \int_V (\boldsymbol{\sigma}\boldsymbol{\varepsilon} + \mathbf{p}\boldsymbol{\xi} + \boldsymbol{\tau}\boldsymbol{\eta} + \mathbf{m}\boldsymbol{\chi})\, dV \tag{2}$$

where $\boldsymbol{\varepsilon}, \boldsymbol{\chi}, \boldsymbol{\xi}, \boldsymbol{\eta}$ are strains, symmetric rotation gradients, dilatation gradient and deviation stretch gradient, respectively; $\boldsymbol{\sigma}$ is Cauchy stress; $\mathbf{m}, \mathbf{p}, \boldsymbol{\tau}$ are high-order stresses corresponding with strain gradients $\boldsymbol{\chi}, \boldsymbol{\xi}, \boldsymbol{\eta}$, respectively. The components of strain ε_{ij} and strain gradients $\xi_i, \eta_{ijk}, \chi_{ij}$ are defined as follows:

$$\varepsilon_{ij} = \frac{1}{2}(u_{i,j} + u_{j,i});\ \xi_i = \varepsilon_{mm,i};\ \chi_{ij} = \frac{1}{4}(u_{n,mj}e_{imn} + u_{n,mi}e_{jmn}) \tag{3a}$$

$$\eta_{ijk} = \frac{1}{3}(\varepsilon_{jk,i} + \varepsilon_{ki,j} + \varepsilon_{ij,k}) - \frac{1}{15}\left[(\xi_k + 2\varepsilon_{mk,m})\delta_{ij} + (\xi_i + 2\varepsilon_{mi,m})\delta_{jk} + (\xi_j + 2\varepsilon_{mj,m})\delta_{ki}\right] \tag{3b}$$

where δ_{ij}, e_{imn} are Knonecker delta and permutation symbol, respectively; the comma in subscript is used to indicate the derivative of variable that follows. The components of stress are calculated from constitutive equations as follows:

$$\sigma_{ij} = \lambda\varepsilon_{kk}\delta_{ij} + 2\mu\varepsilon_{ij};\ m_{ij} = 2\mu l_1^2\chi_{ij};\ p_j = 2\mu l_2^2\xi_j;\ \tau_{ijk} = 2\mu l_3^2\eta_{ijk} \tag{4}$$

where λ, μ are Lamé constants; l_1, l_2, l_3 are three MLSPs. The kinetic energy of the FGP microplates Π_K is expressed by:

$$\Pi_K = \frac{1}{2}\int_V \rho(x_3)\left(\dot{u}_1^2 + \dot{u}_2^2 + \dot{u}_3^2\right)dV \tag{5}$$

where $\rho(x_3)$ is mass density of the FGP microplates; $\dot{u}_1 = u_{1,t}$, $\dot{u}_2 = u_{2,t}$, $\dot{u}_3 = u_{3,t}$ are velocities in x_1-, x_2- and x_3-directions, respectively.

2.2. A general kinematic of FGP microplates

A general kinematic of FGP microplates is derived from ([17]) as follows:

$$u_1(x_1,x_2,x_3) = u_1^0(x_1,x_2) + \Phi_1(x_3)u_{3,1}^0 + \Phi_2(x_3)\varphi_1(x_1,x_2) \tag{6a}$$

$$u_2(x_1,x_2,x_3) = u_2^0(x_1,x_2) + \Phi_1(x_3)u_{3,2}^0 + \Phi_2(x_3)\varphi_2(x_1,x_2) \tag{6b}$$

$$u_3(x_1,x_2,x_3) = u_3^0(x_1,x_2) \tag{6c}$$

where $\Phi_1(x_3) = H^s\Psi(x_3) - x_3, \Phi_2(x_3) = H^s\Psi(x_3)$; H^s is the transverse shear stiffness of the FGP microplates; $\Psi(x_3) = \int_0^{x_3} f_{,3}/\mu(x_3)dx_3$ is a shear function; $\mu(x_3) = E(x_3)/\left(2(1+\nu)\right)$ is the shear modulus; $f(x_3)$ is a higher-order term whose first derivative satisfies the free-stress boundary condition at the top and bottom surfaces of the microplates, i.e. $f_{,3}(x_3 = \pm h/2) = 0$. Substituting Eq. (6) into the strains and strain gradients in Eq. (3), the strains $\boldsymbol{\varepsilon}^T = \left[\boldsymbol{\varepsilon}^{(i)} \quad \boldsymbol{\varepsilon}^{(s)}\right]$ are obtained as follows:

$$\boldsymbol{\varepsilon}^{(i)} = \boldsymbol{\varepsilon}^{(0)} + \Phi_1(x_3)\boldsymbol{\varepsilon}^{(1)} + \Phi_2(x_3)\boldsymbol{\varepsilon}^{(2)};\ \boldsymbol{\varepsilon}^{(s)} = \Phi_3(x_3)\boldsymbol{\varepsilon}^{(3)} \tag{7}$$

where $\Phi_3(x_3) = H^s\Psi_{,3}$ with $\Psi_{,3}(x_3) = f_{,3}(x_3)/\mu(x_3)$; the components of $\boldsymbol{\varepsilon}^{(i)}$ can be found more details in [5]. Moreover, the non-zero components of dilatation gradients $\boldsymbol{\xi} = \left[\xi_1 \quad \xi_2 \quad \xi_3\right]^T$ are given by:

$$\boldsymbol{\xi} = \boldsymbol{\xi}^{(0)} + \Phi_1\boldsymbol{\xi}^{(1)} + \Phi_2\boldsymbol{\xi}^{(2)} + \Phi_{1,3}\boldsymbol{\xi}^{(3)} + \Phi_{2,3}\boldsymbol{\xi}^{(4)} \tag{8}$$

where

$$\boldsymbol{\xi}^{(0)} = \begin{Bmatrix}\xi_1^{(0)}\\ \xi_2^{(0)}\\ \xi_3^{(0)}\end{Bmatrix} = \begin{Bmatrix}u_{1,11}^0 + u_{2,12}^0\\ u_{1,12}^0 + u_{2,22}^0\\ 0\end{Bmatrix};\ \boldsymbol{\xi}^{(1)} = \begin{Bmatrix}\xi_1^{(1)}\\ \xi_2^{(1)}\\ \xi_3^{(1)}\end{Bmatrix} = \begin{Bmatrix}u_{3,111}^0 + u_{3,122}^0\\ u_{3,112}^0 + u_{3,222}^0\\ 0\end{Bmatrix} \tag{9a}$$

$$\boldsymbol{\xi}^{(2)} = \begin{Bmatrix}\xi_1^{(2)}\\ \xi_2^{(2)}\\ \xi_3^{(2)}\end{Bmatrix} = \begin{Bmatrix}\varphi_{1,11} + \varphi_{2,12}\\ \varphi_{1,12} + \varphi_{2,22}\\ 0\end{Bmatrix};\ \boldsymbol{\xi}^{(3)} = \begin{Bmatrix}\xi_1^{(3)}\\ \xi_2^{(3)}\\ \xi_3^{(3)}\end{Bmatrix} = \begin{Bmatrix}0\\ 0\\ u_{3,11}^0 + u_{3,22}^0\end{Bmatrix};\ \boldsymbol{\xi}^{(4)} = \begin{Bmatrix}\xi_1^{(4)}\\ \xi_2^{(4)}\\ \xi_3^{(4)}\end{Bmatrix} = \begin{Bmatrix}0\\ 0\\ \varphi_{1,1} + \varphi_{2,2}\end{Bmatrix} \tag{9b}$$

The non-zero components of deviatoric stretch gradients η_{ijk} are given by:

$$\eta_{111} = \varepsilon_{11,1} - \left(\xi_1 + 2\varepsilon_{11,1} + \gamma_{12,2} + \gamma_{13,3}\right)/5, \eta_{222} = \varepsilon_{22,2} - \left(\xi_2 + 2\varepsilon_{22,2} + \gamma_{12,1} + \gamma_{23,3}\right)/5 \tag{10a}$$

$$\eta_{333}=-\left(\xi_3+\gamma_{13,1}+\gamma_{23,2}\right)/5,\eta_{112}=\eta_{211}=\eta_{121}=\left(\varepsilon_{11,2}+\gamma_{12,1}\right)/3-\left(\xi_2+\gamma_{12,1}+2\varepsilon_{22,2}+\gamma_{23,3}\right)/15 \tag{10b}$$

$$\eta_{113}=\eta_{311}=\eta_{131}=\left(\gamma_{13,1}+\varepsilon_{11,3}\right)/3-\left(\xi_3+\gamma_{13,1}+\gamma_{23,2}\right)/15 \tag{10c}$$

$$\eta_{221}=\eta_{122}=\eta_{212}=\left(\gamma_{12,2}+\varepsilon_{22,1}\right)/3-\left(\xi_1+2\varepsilon_{11,1}+\gamma_{12,2}+\gamma_{13,3}\right)/15 \tag{10d}$$

$$\eta_{223}=\eta_{322}=\eta_{232}=\left(\gamma_{23,2}+\varepsilon_{22,3}\right)/3-\left(\xi_3+\gamma_{13,1}+\gamma_{23,2}\right)/15 \tag{10e}$$

$$\eta_{331}=\eta_{133}=\eta_{313}=\gamma_{13,3}/3-\left(\xi_1+2\varepsilon_{11,1}+\gamma_{12,2}+\gamma_{13,3}\right)/15 \tag{10f}$$

$$\eta_{332}=\eta_{233}=\eta_{323}=\gamma_{23,3}/3-\left(\xi_2+\gamma_{12,1}+2\varepsilon_{22,2}+\gamma_{23,3}\right)/15 \tag{10g}$$

$$\eta_{123}=\eta_{231}=\eta_{312}=\eta_{132}=\eta_{321}=\eta_{213}=\left(\gamma_{23,1}+\gamma_{13,2}+\gamma_{12,3}\right)/6 \tag{10h}$$

Substituting the strains in Eqs. (7) and (9) into Eq. (10) leads to the expressions of deviatoric stretch gradient components in terms of the displacements as follows:

$$\boldsymbol{\eta}=\boldsymbol{\eta}^{(0)}+\Phi_1\boldsymbol{\eta}^{(1)}+\Phi_2\boldsymbol{\eta}^{(2)}+\Phi_3\boldsymbol{\eta}^{(3)}+\Phi_{1,3}\boldsymbol{\eta}^{(4)}+\Phi_{2,3}\boldsymbol{\eta}^{(5)}+\Phi_{3,3}\boldsymbol{\eta}^{(6)} \tag{11}$$

where $\boldsymbol{\eta}^T=\left[\eta_{111}\quad\eta_{222}\quad\eta_{333}\quad3\eta_{331}\quad3\eta_{332}\quad3\eta_{221}\quad3\eta_{112}\quad3\eta_{113}\quad3\eta_{223}\quad6\eta_{123}\right]$, and

$$\boldsymbol{\eta}^{(0)}=\frac{1}{5}\begin{Bmatrix}2u^0_{1,11}-2u^0_{2,12}-u^0_{1,22}\\2u^0_{2,22}-2u^0_{1,12}-u^0_{2,11}\\0\\-\left(3u^0_{1,11}+2u^0_{2,12}+u^0_{1,22}\right)\\-\left(3u^0_{2,22}+2u^0_{1,12}+u^0_{2,11}\right)\\4u^0_{1,22}+8u^0_{2,12}-3u^0_{1,11}\\4u^0_{2,11}+8u^0_{1,12}-3u^0_{2,22}\\0\\0\\0\end{Bmatrix},\boldsymbol{\eta}^{(1)}=\frac{1}{5}\begin{Bmatrix}2u^0_{3,111}-3u^0_{3,122}\\2u^0_{3,222}-3u^0_{3,112}\\0\\-3\left(u^0_{3,111}+u^0_{3,122}\right)\\-3\left(u^0_{3,112}+u^0_{3,222}\right)\\3\left(4u^0_{3,122}-u^0_{3,111}\right)\\3\left(4u^0_{3,112}-u^0_{3,222}\right)\\0\\0\\0\end{Bmatrix},\boldsymbol{\eta}^{(2)}=\frac{1}{5}\begin{Bmatrix}2\varphi_{1,11}-2\varphi_{2,12}-\varphi_{1,22}\\2\varphi_{2,22}-2\varphi_{1,12}-\varphi_{2,11}\\0\\-\left(3\varphi_{1,11}+2\varphi_{2,12}+\varphi_{1,22}\right)\\-\left(3\varphi_{2,22}+2\varphi_{1,12}+\varphi_{2,11}\right)\\4\varphi_{1,22}+8\varphi_{2,12}-3\varphi_{1,11}\\4\varphi_{2,11}+8\varphi_{1,12}-3\varphi_{2,22}\\0\\0\\0\end{Bmatrix} \tag{12a}$$

$$\boldsymbol{\eta}^{(3)}=\frac{1}{5}\begin{Bmatrix}0\\0\\-\left(u^0_{3,11}+u^0_{3,22}+\varphi_{1,1}+\varphi_{2,2}\right)\\0\\0\\0\\0\\4u^0_{3,11}-u^0_{3,22}+4\varphi_{1,1}-\varphi_{2,2}\\4u^0_{3,22}-u^0_{3,11}+4\varphi_{2,2}-\varphi_{1,1}\\5\left(\varphi_{1,2}+\varphi_{2,1}+2u^0_{3,12}\right)\end{Bmatrix},\boldsymbol{\eta}^{(4)}=\frac{1}{5}\begin{Bmatrix}0\\0\\-\left(u^0_{3,11}+u^0_{3,22}\right)\\0\\0\\0\\0\\4u^0_{3,11}-u^0_{3,22}\\4u^0_{3,22}-u^0_{3,11}\\10u^0_{3,12}\end{Bmatrix},\boldsymbol{\eta}^{(5)}=\frac{1}{5}\begin{Bmatrix}0\\0\\-\left(\varphi_{1,1}+\varphi_{2,2}\right)\\0\\0\\0\\0\\4\varphi_{1,1}-\varphi_{2,2}\\4\varphi_{2,2}-\varphi_{1,1}\\5\left(\varphi_{1,2}+\varphi_{2,1}\right)\end{Bmatrix},\boldsymbol{\eta}^{(6)}=\frac{1}{5}\begin{Bmatrix}-\left(\varphi_1+u^0_{3,1}\right)\\-\left(\varphi_2+u^0_{3,2}\right)\\0\\4\left(\varphi_1+u^0_{3,1}\right)\\4\left(\varphi_2+u^0_{3,2}\right)\\-\left(\varphi_1+u^0_{3,1}\right)\\-\left(\varphi_2+u^0_{3,2}\right)\\0\\0\\0\end{Bmatrix} \tag{12b}$$

Moreover, the symmetric rotation gradients are given by $\chi_{ij}=\left(\bar{\theta}_{i,j}+\bar{\theta}_{j,i}\right)/2$ where $\bar{\theta}_i$ is determined in terms of the displacements u_i as follows:

$$\bar{\theta}_1=\left(u_{3,2}-u_{2,3}\right)/2=\left(u^0_{3,2}-\Phi_{1,3}u^0_{3,2}-\Phi_{2,3}\varphi_2\right)/2, \bar{\theta}_2=\left(u_{1,3}-u_{3,1}\right)/2=\left(-u^0_{3,1}+\Phi_{1,3}u^0_{3,1}+\Phi_{2,3}\varphi_1\right)/2 \quad (13a)$$

$$\bar{\theta}_3=\left(u_{2,1}-u_{1,2}\right)/2=\left[u^0_{2,1}-u^0_{1,2}+\Phi_2\left(\varphi_{2,1}-\varphi_{1,2}\right)\right]/2 \quad (13b)$$

The rotation gradients are expressed as follows:

$$\boldsymbol{\chi}=\boldsymbol{\chi}^{(0)}+\Phi_{1,3}\boldsymbol{\chi}^{(1)}+\Phi_{2,3}\boldsymbol{\chi}^{(2)}+\Phi_{1,33}\boldsymbol{\chi}^{(3)}+\Phi_{2,33}\boldsymbol{\chi}^{(4)}+\Phi_2\boldsymbol{\chi}^{(5)} \quad (14)$$

where $\boldsymbol{\chi}^{(0)},\boldsymbol{\chi}^{(1)},\boldsymbol{\chi}^{(2)},\boldsymbol{\chi}^{(3)},\boldsymbol{\chi}^{(4)},\boldsymbol{\chi}^{(5)}$ are given in [5]. The stresses and strains of FGP microplates are related by constitutive equations as follows:

$$\boldsymbol{\sigma}^{(i)}=\mathbf{Q}^{(i)}_{\varepsilon}\boldsymbol{\varepsilon}^{(i)};\boldsymbol{\sigma}^{(o)}=\mathbf{Q}^{(o)}_{\varepsilon}\boldsymbol{\varepsilon}^{(s)} \quad (15a)$$

$$\mathbf{m}=\alpha_{\chi}\mathbf{I}_{6\times6}\boldsymbol{\chi},\mathbf{p}=\alpha_{\xi}\mathbf{I}_{3\times3}\boldsymbol{\xi},\ \boldsymbol{\tau}=\alpha_{\eta}\mathbf{I}_{10\times10}\boldsymbol{\eta} \quad (15b)$$

where $\alpha_{\chi}=2\mu l_1^2$, $\alpha_{\xi}=2\mu l_2^2$, $\alpha_{\eta}=2\mu l_3^2$; the reduced stiffness matrix $\mathbf{Q}^{(i)}_{\varepsilon}$ and $\mathbf{Q}^{(o)}_{\varepsilon}$ can be found in [5]; $\mathbf{m}=\left[m_{11}\quad m_{22}\quad m_{12}\quad m_{33}\quad m_{23}\quad m_{13}\right]^T$, $\mathbf{p}=\left[p_1\quad p_2\quad p_3\right]^T$ and $\boldsymbol{\tau}=\left[\tau_{111}\quad\tau_{222}\quad\tau_{112}\quad\tau_{221}\quad\tau_{331}\quad\tau_{332}\quad\tau_{333}\quad\tau_{113}\quad\tau_{223}\quad\tau_{123}\right]^T$.

2.3 Variational formulation

In order to derive the equation of motion, Hamilton's principle is used:

$$\int_{t_1}^{t_2}\left(\delta\Pi_U-\delta\Pi_K\right)dt=0 \quad (16)$$

where the variation of the strain energy $\delta\Pi_U$ of FGP microplates as follows:

$$\begin{aligned}\delta\Pi_U=&\int_A\left(\boldsymbol{\sigma}\delta\boldsymbol{\varepsilon}+\mathbf{p}\delta\boldsymbol{\xi}+\boldsymbol{\tau}\delta\boldsymbol{\eta}+\mathbf{m}\delta\boldsymbol{\chi}\right)dA=\int_A\Big[\mathbf{M}^{(0)}_{\varepsilon}\delta\boldsymbol{\varepsilon}^{(0)}+\mathbf{M}^{(1)}_{\varepsilon}\delta\boldsymbol{\varepsilon}^{(1)}+\mathbf{M}^{(2)}_{\varepsilon}\delta\boldsymbol{\varepsilon}^{(2)}+\mathbf{M}^{(3)}_{\varepsilon}\delta\boldsymbol{\varepsilon}^{(3)}\\&+\mathbf{M}^{(0)}_{\xi}\delta\boldsymbol{\xi}^{(0)}+\mathbf{M}^{(1)}_{\xi}\delta\boldsymbol{\xi}^{(1)}+\mathbf{M}^{(2)}_{\xi}\delta\boldsymbol{\xi}^{(2)}+\mathbf{M}^{(3)}_{\xi}\delta\boldsymbol{\xi}^{(3)}+\mathbf{M}^{(4)}_{\xi}\delta\boldsymbol{\xi}^{(4)}\\&+\mathbf{M}^{(0)}_{\chi}\delta\boldsymbol{\chi}^{(0)}+\mathbf{M}^{(1)}_{\chi}\delta\boldsymbol{\chi}^{(1)}+\mathbf{M}^{(2)}_{\chi}\delta\boldsymbol{\chi}^{(2)}+\mathbf{M}^{(3)}_{\chi}\delta\boldsymbol{\chi}^{(3)}+\mathbf{M}^{(4)}_{\chi}\delta\boldsymbol{\chi}^{(4)}+\mathbf{M}^{(5)}_{\chi}\delta\boldsymbol{\chi}^{(5)}\\&+\mathbf{M}^{(0)}_{\eta}\delta\boldsymbol{\eta}^{(0)}+\mathbf{M}^{(1)}_{\eta}\delta\boldsymbol{\eta}^{(1)}+\mathbf{M}^{(2)}_{\eta}\delta\boldsymbol{\eta}^{(2)}+\mathbf{M}^{(3)}_{\eta}\delta\boldsymbol{\eta}^{(3)}+\mathbf{M}^{(4)}_{\eta}\delta\boldsymbol{\eta}^{(4)}+\mathbf{M}^{(5)}_{\eta}\delta\boldsymbol{\eta}^{(5)}+\mathbf{M}^{(6)}_{\eta}\delta\boldsymbol{\eta}^{(6)}\Big]dA\end{aligned} \quad (17)$$

These stress resultants can be expressed in terms of the strains and its gradients as follows:

$$\begin{Bmatrix}\mathbf{M}^{(0)}_{\varepsilon}\\\mathbf{M}^{(1)}_{\varepsilon}\\\mathbf{M}^{(2)}_{\varepsilon}\\\mathbf{M}^{(3)}_{\varepsilon}\end{Bmatrix}=\begin{bmatrix}\mathbf{A}^{\varepsilon}&\mathbf{B}^{\varepsilon}&\mathbf{B}^{\varepsilon}_s&\mathbf{0}\\\mathbf{B}^{\varepsilon}&\mathbf{D}^{\varepsilon}&\mathbf{D}^{\varepsilon}_s&\mathbf{0}\\\mathbf{B}^{\varepsilon}_s&\mathbf{D}^{\varepsilon}_s&\mathbf{H}^{\varepsilon}_s&\mathbf{0}\\\mathbf{0}&\mathbf{0}&\mathbf{0}&\mathbf{A}^{\varepsilon}_s\end{bmatrix}\begin{Bmatrix}\boldsymbol{\varepsilon}^{(0)}\\\boldsymbol{\varepsilon}^{(1)}\\\boldsymbol{\varepsilon}^{(2)}\\\boldsymbol{\varepsilon}^{(3)}\end{Bmatrix},\begin{Bmatrix}\mathbf{M}^{(0)}_{\chi}\\\mathbf{M}^{(1)}_{\chi}\\\mathbf{M}^{(2)}_{\chi}\\\mathbf{M}^{(3)}_{\chi}\\\mathbf{M}^{(4)}_{\chi}\\\mathbf{M}^{(5)}_{\chi}\end{Bmatrix}=\begin{bmatrix}\mathbf{A}^{\chi}&\bar{\mathbf{B}}^{\chi}&\bar{\mathbf{B}}^{\chi}_s&\bar{\bar{\mathbf{B}}}^{\chi}&\bar{\bar{\mathbf{B}}}^{\chi}_s&\mathbf{B}^{\chi}_s\\\bar{\mathbf{B}}^{\chi}&\bar{\mathbf{D}}^{\chi}&\bar{\mathbf{D}}^{\chi}_s&\bar{\mathbf{E}}^{\chi}&\bar{\mathbf{E}}^{\chi}_s&\bar{\mathbf{F}}^{\chi}_s\\\bar{\mathbf{B}}^{\chi}_s&\bar{\mathbf{D}}^{\chi}_s&\bar{\mathbf{H}}^{\chi}_s&\bar{\mathbf{G}}^{\chi}_s&\bar{\mathbf{I}}^{\chi}&\bar{\mathbf{J}}^{\chi}\\\bar{\bar{\mathbf{B}}}^{\chi}&\bar{\mathbf{E}}^{\chi}&\bar{\mathbf{G}}^{\chi}_s&\bar{\bar{\mathbf{D}}}^{\chi}&\bar{\bar{\mathbf{D}}}^{\chi}_s&\bar{\bar{\mathbf{K}}}^{\chi}_s\\\bar{\bar{\mathbf{B}}}^{\chi}_s&\bar{\mathbf{E}}^{\chi}_s&\bar{\mathbf{I}}^{\chi}&\bar{\bar{\mathbf{D}}}^{\chi}_s&\bar{\bar{\mathbf{H}}}^{\chi}_s&\bar{\mathbf{L}}\\\mathbf{B}^{\chi}_s&\bar{\mathbf{F}}^{\chi}_s&\bar{\mathbf{J}}^{\chi}&\bar{\mathbf{K}}^{\chi}_s&\bar{\mathbf{L}}&\mathbf{H}^{\chi}_s\end{bmatrix}\begin{Bmatrix}\boldsymbol{\chi}^{(0)}\\\boldsymbol{\chi}^{(1)}\\\boldsymbol{\chi}^{(2)}\\\boldsymbol{\chi}^{(3)}\\\boldsymbol{\chi}^{(4)}\\\boldsymbol{\chi}^{(5)}\end{Bmatrix} \quad (18a)$$

$$\begin{Bmatrix}\mathbf{M}_\eta^{(0)}\\ \mathbf{M}_\eta^{(1)}\\ \mathbf{M}_\eta^{(2)}\\ \mathbf{M}_\eta^{(3)}\\ \mathbf{M}_\eta^{(4)}\\ \mathbf{M}_\eta^{(5)}\\ \mathbf{M}_\eta^{(6)}\end{Bmatrix}=\begin{bmatrix}\mathbf{A}^\eta & \mathbf{B}^\eta & \mathbf{B}_s^\eta & \mathbf{A}_s^\eta & \overline{\mathbf{B}}^\eta & \overline{\mathbf{B}}_s^\eta & \overline{\mathbf{A}}_s^\eta\\ \mathbf{B}^\eta & \mathbf{D}^\eta & \mathbf{D}_s^\eta & \mathbf{D}_{ts}^\eta & \overline{\mathbf{O}}^\eta & \overline{\mathbf{P}}_s^\eta & \overline{\mathbf{Q}}_s^\eta\\ \mathbf{B}_s^\eta & \mathbf{D}_s^\eta & \mathbf{H}_s^\eta & \mathbf{D}_{hs}^\eta & \overline{\mathbf{F}}_s^\eta & \overline{\mathbf{J}}^\eta & \overline{\mathbf{F}}_{hs}^\eta\\ \mathbf{A}_s^\eta & \mathbf{D}_{ts}^\eta & \mathbf{D}_{hs}^\eta & \mathbf{H}_{ts}^\eta & \overline{\mathbf{F}}_{ts}^\eta & \overline{\mathbf{J}}_{hs}^\eta & \overline{\mathbf{R}}^\eta\\ \overline{\mathbf{B}}^\eta & \overline{\mathbf{O}}^\eta & \overline{\mathbf{F}}_s^\eta & \overline{\mathbf{F}}_{ts}^\eta & \overline{\mathbf{D}}^\eta & \overline{\mathbf{D}}_s^\eta & \overline{\mathbf{D}}_{ts}^\eta\\ \overline{\mathbf{B}}_s^\eta & \overline{\mathbf{P}}_s^\eta & \overline{\mathbf{J}}^\eta & \overline{\mathbf{J}}_{hs}^\eta & \overline{\mathbf{D}}_s^\eta & \overline{\mathbf{H}}_s^\eta & \overline{\mathbf{D}}_{hs}^\eta\\ \overline{\mathbf{A}}_s^\eta & \overline{\mathbf{Q}}_s^\eta & \overline{\mathbf{F}}_{hs}^\eta & \overline{\mathbf{R}}^\eta & \overline{\mathbf{D}}_{ts}^\eta & \overline{\mathbf{D}}_{hs}^\eta & \overline{\mathbf{H}}_{ts}^\eta\end{bmatrix}\begin{Bmatrix}\boldsymbol{\eta}^{(0)}\\ \boldsymbol{\eta}^{(1)}\\ \boldsymbol{\eta}^{(2)}\\ \boldsymbol{\eta}^{(3)}\\ \boldsymbol{\eta}^{(4)}\\ \boldsymbol{\eta}^{(5)}\\ \boldsymbol{\eta}^{(6)}\end{Bmatrix},\begin{Bmatrix}\mathbf{M}_\xi^{(0)}\\ \mathbf{M}_\xi^{(1)}\\ \mathbf{M}_\xi^{(2)}\\ \mathbf{M}_\xi^{(3)}\\ \mathbf{M}_\xi^{(4)}\end{Bmatrix}\begin{bmatrix}\mathbf{A}^\xi & \mathbf{B}^\xi & \mathbf{B}_s^\xi & \overline{\mathbf{B}}^\xi & \overline{\mathbf{B}}_s^\xi\\ \mathbf{B}^\xi & \mathbf{D}^\xi & \mathbf{D}_s^\xi & \overline{\mathbf{O}}^\xi & \overline{\mathbf{P}}_s^\xi\\ \mathbf{B}_s^\xi & \mathbf{D}_s^\xi & \mathbf{H}_s^\xi & \overline{\mathbf{F}}_s^\xi & \overline{\mathbf{J}}^\xi\\ \overline{\mathbf{B}}^\xi & \overline{\mathbf{O}}^\xi & \overline{\mathbf{F}}_s^\xi & \overline{\mathbf{D}}^\xi & \overline{\mathbf{D}}_s^\xi\\ \overline{\mathbf{B}}_s^\xi & \overline{\mathbf{P}}_s^\xi & \overline{\mathbf{J}}^\xi & \overline{\mathbf{D}}_s^\xi & \overline{\mathbf{H}}_s^\xi\end{bmatrix}\begin{Bmatrix}\boldsymbol{\xi}^{(0)}\\ \boldsymbol{\xi}^{(1)}\\ \boldsymbol{\xi}^{(2)}\\ \boldsymbol{\xi}^{(3)}\\ \boldsymbol{\xi}^{(4)}\end{Bmatrix} \tag{18b}$$

The variation of kinetic energy $\delta\Pi_K$ is calculated by:

$$\begin{aligned}\delta\Pi_K=&\frac{1}{2}\int_V\rho\left(\dot{u}_1\delta\dot{u}_1+\dot{u}_2\delta\dot{u}_2+\dot{u}_3\delta\dot{u}_3\right)dV=\frac{1}{2}\int_A\Big[I_0\left(\dot{u}_1^0\delta\dot{u}_1^0+\dot{u}_2^0\delta\dot{u}_2^0+\dot{u}_3^0\delta\dot{u}_3^0\right)+K_2\left(\dot{\varphi}_1\delta\dot{\varphi}_1+\dot{\varphi}_2\delta\dot{\varphi}_2\right)\\&+I_1\left(\dot{u}_1^0\delta\dot{u}_{3,1}^0+\dot{u}_{3,1}^0\delta\dot{u}_1^0+\dot{u}_2^0\delta\dot{u}_{3,2}^0+\dot{u}_{3,2}^0\delta\dot{u}_2^0\right)+J_2\left(\dot{u}_{3,1}^0\delta\dot{\varphi}_1+\dot{\varphi}_1\delta\dot{u}_{3,1}^0+\dot{u}_{3,2}^0\delta\dot{\varphi}_2+\dot{\varphi}_2\delta\dot{u}_{3,2}^0\right)\\&+J_1\left(\dot{u}_1^0\delta\dot{\varphi}_1+\dot{\varphi}_1\delta\dot{u}_1^0+\dot{u}_2^0\delta\dot{\varphi}_2+\dot{\varphi}_2\delta\dot{u}_2^0\right)+I_2\left(\dot{u}_{3,1}^0\delta\dot{u}_{3,1}^0+\dot{u}_{3,2}^0\delta\dot{u}_{3,2}^0\right)\Big]dA\end{aligned} \tag{19}$$

where I_0,I_1,I_2,J_1,J_2,K_2 are mass components of the FGP microplates which are defined as follows:

$$\left(I_0,I_1,I_2,J_1,J_2,K_2\right)=\int_{-h/2}^{h/2}\left(1,\Phi_1,\Phi_1^2,\Phi_2,\Phi_1\Phi_2,\Phi_2^2\right)\rho dx_3 \tag{20}$$

3. Series-type solutions

Based on the Ritz method, the membrane and transverse displacements $\left(u_1^0,u_2^0,u_3^0,\varphi_1,\varphi_2\right)$ of the FGP microplates can be expressed in terms of the series of approximation functions and associated values of series as follows:

$$\left\{u_1^0,\varphi_1\right\}(x_1,x_2)=\sum_{i=1}^{n_1}\sum_{j=1}^{n_2}\left\{u_{1ij},x_{ij}\right\}R_{i,1}\left(x_1\right)P_j\left(x_2\right);\ \left\{u_2^0,\varphi_2\right\}(x_1,x_2)=\sum_{i=1}^{n_1}\sum_{j=1}^{n_2}\left\{u_{2ij},y_{ij}\right\}R_i\left(x_1\right)P_{j,2}\left(x_2\right) \tag{21a}$$

$$u_3^0(x_1,x_2)=\sum_{i=1}^{n_1}\sum_{j=1}^{n_2}u_{3ij}R_i\left(x_1\right)P_j\left(x_2\right); \tag{21b}$$

where $u_{1ij},u_{2ij},u_{3ij},x_{ij},y_{ij}$ are variables to be determined; $R_i\left(x_1\right),P_j\left(x_2\right)$ are the shape functions in x_1-, x_2- direction, respectively. It should be noted that the accuracy, convergence rates and numerical instabilities of the Ritz solution depends on the selection of the shape functions, which was discussed in details in ([5, 17]). The functions $R_i\left(x_1\right)$ and $P_j\left(x_2\right)$ are constructed to satisfy the boundary conditions (BCs) at the FGP microplate edges in which two following kinematic typical BCs are considered as follows: Simply supported (S) for $u_2^0=u_3^0=\varphi_2=0$ at $x_1=0,a$ and $u_1^0=u_3^0=\varphi_1=0$ at $x_2=0,b$; Clamped (C) for $u_1^0=u_2^0=u_3^0=\varphi_1=\varphi_2=0$ at $x_1=0,a$ and $x_2=0,b.$ The combination of S and C on the edges leads to the different BCs, in which SSSS, SCSC and CCCC are chosen to investigate in this paper. Furthermore, in order to derive characteristis equations of motion of the FGP microplates, substituting the approximations in Eq. (21) into Eq. (16) leads to:

$$\mathbf{Kd}+\mathbf{M}\ddot{\mathbf{d}}=\mathbf{0} \tag{22}$$

where $\mathbf{d}=\begin{bmatrix}\mathbf{u}_1 & \mathbf{u}_2 & \mathbf{u}_3 & \mathbf{x} & \mathbf{y}\end{bmatrix}^T$ is the displacement vector to be determined; $\mathbf{K}=\mathbf{K}^{\varepsilon}+\mathbf{K}^{\chi}+\mathbf{K}^{\xi}+\mathbf{K}^{\eta}$ is the stiffness matrix which is composed of those of the strains $\mathbf{K}^{\varepsilon}$, symmetric rotation gradients $\mathbf{K}^{\chi}$, dilatation gradient $\mathbf{K}^{\xi}$, and deviation stretch gradient $\mathbf{K}^{\eta}$; $\mathbf{M}$ is the mass matrix. These components are given more details as follows:

$$\mathbf{K}^{\zeta}=\begin{bmatrix}\mathbf{K}^{\zeta 11} & \mathbf{K}^{\zeta 12} & \mathbf{K}^{\zeta 13} & \mathbf{K}^{\zeta 14} & \mathbf{K}^{\zeta 15}\\ {}^{T}\mathbf{K}^{\zeta 12} & \mathbf{K}^{\zeta 22} & \mathbf{K}^{\zeta 23} & \mathbf{K}^{\zeta 24} & \mathbf{K}^{\zeta 25}\\ {}^{T}\mathbf{K}^{\zeta 13} & {}^{T}\mathbf{K}^{\zeta 23} & \mathbf{K}^{\zeta 33} & \mathbf{K}^{\zeta 34} & \mathbf{K}^{\zeta 35}\\ {}^{T}\mathbf{K}^{\zeta 14} & {}^{T}\mathbf{K}^{\zeta 24} & {}^{T}\mathbf{K}^{\zeta 34} & \mathbf{K}^{\zeta 44} & \mathbf{K}^{\zeta 45}\\ {}^{T}\mathbf{K}^{\zeta 15} & {}^{T}\mathbf{K}^{\zeta 25} & {}^{T}\mathbf{K}^{\zeta 35} & {}^{T}\mathbf{K}^{\zeta 45} & \mathbf{K}^{\zeta 55}\end{bmatrix};\mathbf{M}=\begin{bmatrix}\mathbf{M}^{11} & 0 & \mathbf{M}^{13} & \mathbf{M}^{14} & 0\\ 0 & \mathbf{M}^{22} & \mathbf{M}^{23} & 0 & \mathbf{M}^{25}\\ {}^{T}\mathbf{M}^{13} & {}^{T}\mathbf{M}^{23} & \mathbf{M}^{33} & \mathbf{M}^{34} & \mathbf{M}^{35}\\ {}^{T}\mathbf{M}^{14} & 0 & {}^{T}\mathbf{M}^{34} & \mathbf{M}^{44} & \mathbf{M}^{45}\\ 0 & {}^{T}\mathbf{M}^{25} & {}^{T}\mathbf{M}^{35} & {}^{T}\mathbf{M}^{45} & \mathbf{M}^{55}\end{bmatrix} \tag{23}$$

with $\zeta=\{\varepsilon,\xi,\chi,\eta\}$. It is noted that for free vibration analysis, by denoting $\mathbf{d}(t)=\mathbf{d}e^{i\omega t}$ where ω is the natural frequency of the FGP microplates and $i^2=-1$ is imaginary unit, the natural frequencies can be derived from the following characteristic equation: $\left(\mathbf{K}-\omega^2\mathbf{M}\right)\mathbf{d}=\mathbf{0}$.

4. BCMO-DNN algorithm

Optimization problem: The objective of the current optimization problem is to search for the optimal material properties of the FGP microplates that can maximize the natural frequencies subjected to several constraints. The Young's modulus and mass densities are considered as design variables. The formulation of constrained objective functions for vibration optimization can be stated as follows:

$$\text{Maximize } \bar{\omega}=f\left(E_{c,i},E_{m,i},\rho_{c,i},\rho_{m,i}\right)$$

$$\text{Subjected to } \begin{cases}\left(\mathbf{K}-\omega^2\mathbf{M}\right)\mathbf{d}=\mathbf{0}\\ E_{c,\min}\le E_{c,i}\le E_{c,\max};E_{m,\min}\le E_{m,i}\le E_{m,\max}\\ \rho_{c,\min}\le\rho_{c,i}\le\rho_{c,\max};\rho_{m,\min}\le\rho_{m,i}\le\rho_{m,\max}\end{cases} \tag{24}$$

where $E_{,\min}=E_{,\text{mean}}-10\%E_{,\text{mean}}$, $E_{,\max}=E_{,\text{mean}}+10\%E_{,\text{mean}}$, $\rho_{,\min}=\rho_{,\text{mean}}-10\%\rho_{,\text{mean}}$, $\rho_{,\max}=\rho_{,\text{mean}}+10\%\rho_{,\text{mean}}$; $E_{,\text{mean}},\rho_{,\text{mean}}$ are the mean values of Young's modulus and mass density of constituent materials, respectively.

Combination of BCMO and DNN: Initiated by Le-Duc et al. [10], BCMO is a meta-heuristic algorithm method which is inspired by the fact that the solution space is assumed to be in Cartesian coordinates and the searching movements of candidate solutions are compositely equalized in both global and local ones. In fact, a candidate solution can move closer to better ones to exploit the local regions, and move further to explore the search space. Thus, the best-ranked individual in each generation can jump immediately from space to space or intensify its current local space (the details of the algorithm can be found in [10]). Moreover, the input data from BCMO will be trained by the deep neural network (DNN), which is passed through the input layer, hidden layers and output layer. The input data is multiplied by the weights before it reaches the nodes. Each node in the subsequent layers will get the sum of the output values of the previous nodes multiplied by the associated weights, and the output data of the activation function for the sum is given as follows ([18]):

$$y_i^n = \varphi\left(x_i^n\right) = \varphi\left(\sum_{j=1}^{L_{n-1}} w_{ij}^{n-1} \times y_j^{n-1} + b_i^n\right) \tag{25}$$

where y_i^n and x_i^n are the data pair output and input of activation function of node i, respectively; w_{ij}^{n-1} are the weights between the output node i and input node j; b_i^n is the bias of node j; φ is the activation function. Furthermore, a loss function is required to evaluate the performance of the prediction model. The objective of loss function is to measure the difference between target values and predicted ones, from which during the training process, the difference between the model outputs and the target values are converged to zeros. In practice, the mean square error (MSE) [19] is commonly used to evaluate the accuracy of the prediction model, hence it will be applied in this paper.

5. Numerical results

In this section, numerical examples are carried out to investigate optimal free vibration behaviors of FGP microplates with different boundary conditions in which the shear function $f(x_3) = x_3 - 4x_3^3/3h^2$ is selected. The FGP microplates are supposed to be made of ceramic material Al_2O_3 and metal one Al whose properties are given as follows: Al_2O_3 ($E_c = 380\,\text{GPa}$, $\rho_c = 3800\,\text{kg/m}^3$, $\nu_c = 0.3$), Al ($E_m = 70\,\text{GPa}$, $\rho_m = 2702\,\text{kg/m}^3$, $\nu_m = 0.3$). For simplification purpose, all three length scale parameters are assumed to have identical values, i.e., $l_1 = l_2 = l_3 = l$. For convenience, the following normalized parameter is used in the computations: $\bar{\omega} = \omega a^2 / h\sqrt{\rho_c / E_c}$.

In order to study the effects of the side-to-thickness ratio, material length scale and boundary conditions on natural frequencies of FGP microplates. Fig. 1 displays the variation of normalized fundamental frequencies with respect to the side-to-thickness ratio a/h and length scale-to-thickness ratio h/l of Al/Al_2O_3 FGP microplates with $p = 5$, $a/h = 10$ and three boundary conditions (SSSS, SCSC, CCCC). It can be seen that the natural frequencies decrease with the increase of h/l up to the value of $h/l = 10$ from which the curves become flatter and size effects may thus be disregarded, the highest and lowest curves of interaction correspond to the CCCC and SSSS boundary conditions, respectively.

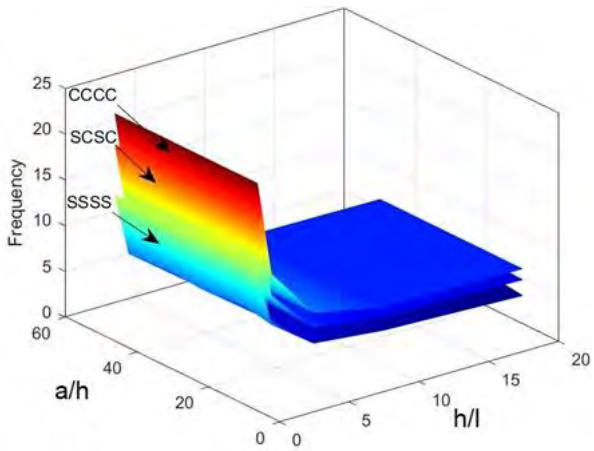

Fig. 1. Variation of normalized fundamental frequency with respect to side-to-thickness ratio a/h and length scale-to-thickness ratio h/l ($p = 5$, $\beta = 0.1$)

In order to investigate stochastic vibration responses of FGP microplates, four random variables of material properties ($E_{m,i}, E_{c,i}, \rho_{m,i}, \rho_{c,i}$) are employed with the population size $NP = 500$. These design variables are considered as input data and the first normalization of frequency are taken as output data for training samples. The data set consists of input-output pairs and training samples which are randomly generated through iterations for training in the DNN. It is noted that the DNN processing with 1000 iterations and 1 epoch for each iteration. Table 1 presents the mean and standard deviation (SD) of normalized fundamental frequencies of Al/Al_2O_3 FGP microplates. The results are calculated for two boundary conditions (SSSS, CCCC), power law-index $p = 2$, side-to-thickness ratio $a/h = 10$, porous parameters $\beta = 0.1$ and 0.2 with different values of thickness-to-MLSP ratio $h/l = 1, 2, 5, 10$. It can be seen that the statistical moments of normalized fundamental frequencies obtained from the Ritz–BCMO and BCMO-DNN show great agreements in all cases. The mean values of nondimensional fundamental frequencies for both Ritz-BCMO and BCMO-DNN are close to the deterministic result (Ritz) for all boundary conditions. As expected, the natural frequencies decrease with an increase of the ratio of material length scale parameter. Moreover, it is observed that the computational time needed by the Ritz-BCMO approach is approximately 9 times greater than that by the BCMO-DNN method, that shows the efficiency on computational cost of the BCMO-DNN algorithm.

Table 1. Mean and standard deviation of normalized fundamental frequencies of FGP microplates with $p = 2$ and $a/h = 10$

BCs	Statistical moments	Theory	h/l				Time (s)
			10	5	2	1	
SSSS	$\beta = 0.1$						
		Ritz	4.1238	4.9947	9.1029	16.9999	
	mean	Ritz-BCMO	4.0969	5.0102	9.1118	16.9679	2854
		BCMO-DNN	4.0975	5.0110	9.1130	16.9694	320
	SD	Ritz- BCMO	0.1308	0.1696	0.2578	0.4501	
		BCMO-DNN	0.1299	0.1684	0.2561	0.4468	
	$\beta = 0.2$						
		Ritz	3.7713	4.7471	8.9419	16.8823	
	mean	Ritz- BCMO	3.7733	4.7238	8.9212	16.8805	2855
		BCMO-DNN	3.7742	4.7246	8.9226	16.8829	325
	SD	Ritz- BCMO	0.1722	0.1803	0.2747	0.5207	
		BCMO-DNN	0.1714	0.1793	0.2730	0.5170	
CCCC	$\beta = 0.1$						
	mean	Ritz	7.2033	8.8372	15.7657	28.6778	
		Ritz- BCMO	7.1993	8.8144	15.7081	28.7767	2855
		BCMO-DNN	7.2006	8.8156	15.7100	28.7775	320
	SD	Ritz- BCMO	0.2404	0.2634	0.4635	0.8480	
		BCMO-DNN	0.2391	0.2614	0.4615	0.8498	
	$\beta = 0.2$						
	mean	Ritz	6.6362	8.3403	15.2109	28.4556	
		Ritz- BCMO	6.6804	8.3357	15.2698	28.2874	2856
		BCMO-DNN	6.6817	8.3370	15.2719	28.2856	323
	SD	Ritz- BCMO	0.2743	0.2846	0.4951	0.8394	
		BCMO-DNN	0.2725	0.2823	0.4918	0.8388	

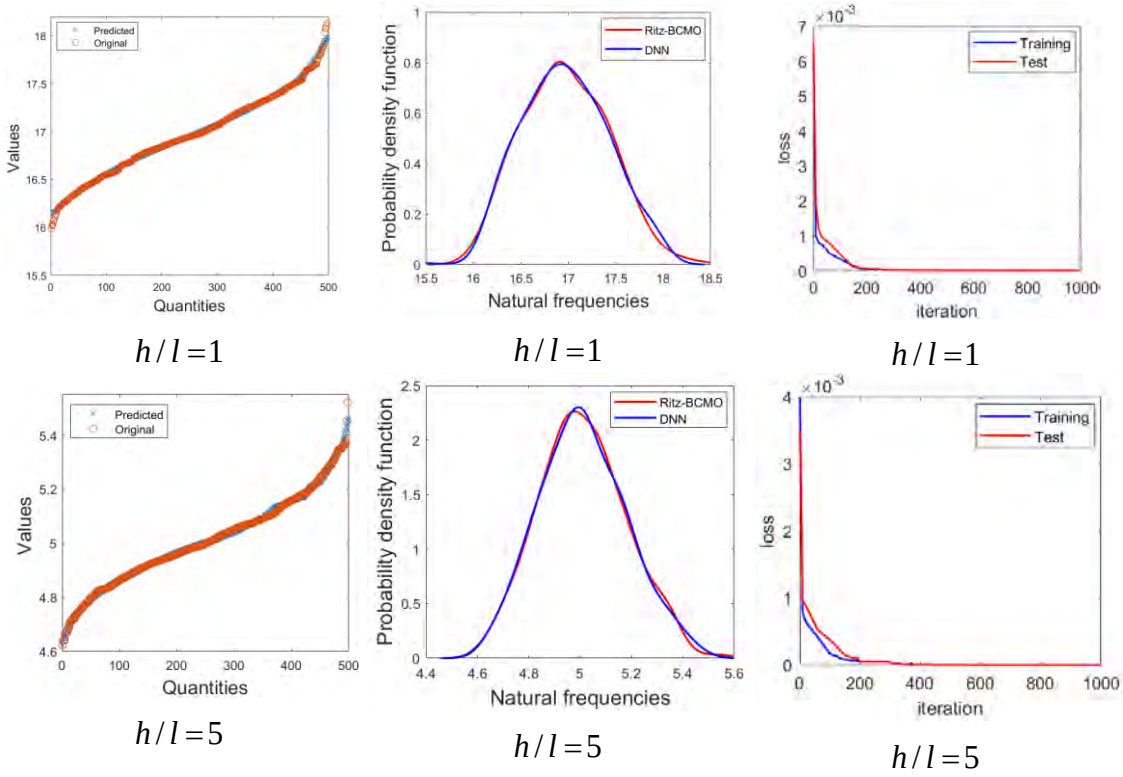

Fig. 2. Scatter plot, probability density function, and loss function of the normalized fundamental frequency for simply supported FGP microplates with $\beta=0.1$, $a/h=10$, $p=2$

In order to demonstrate the performance of present model further, Fig. 2 presents the scatter plot, probability density function and loss function of the fundamental frequency for FGP microplates with porous parameters $\beta=0.1$, $a/h=10$ and $p=2$. These graphs indicate that the present BCMO-DNN model can effectively substitute the Ritz-BCMO for stochastic analysis with accuracy and significant saving of computational time. Moreover, the MSE converges to zero after 200 iterations for both the training set and test set.

6. Conclusions

Optimal vibration behaviors of FGP microplates with uncertainties of material properties has been introduced in this paper. The theory is based on a unified framework of higher-order shear deformation theory and modified strain gradient theory. In addition, a combination of BCMO-DNN has been developed to solve the optimization problems and predict stochastic vibration responses of FGP microplates subjected to uncertainties of material properties. The effects of material distribution, material length scale, porosity density and boundary conditions on natural frequencies of FGP microplates have been investigated for both Ritz-BCMO and BCMO-DNN algorithm. Based on the obtained numerical results, the following important points can be derived:

- Present unified higher-order shear deformation theory and modified strain gradient theory are found to be accurate and efficient in predicting stochastic vibration behaviors of FGP microplates.

- Natural frequencies decrease with an increase of the porosity density and material length scale parameter.

- Proposed BCMO-DNN algorithm allows to significantly save computational costs. The computational time of natural frequencies required by the BCMO-DNN method is about 1/9 times that of the Ritz-BCMO method.

References

[1] A. C. Eringen, Nonlocal polar elastic continua, *International Journal of Engineering Science,* Vol. 10, No. 1, pp. 1-16, 1972/01/01/ 1972.

[2] A. R. Ashoori, E. Salari, and S. A. Sadough Vanini, Size-dependent thermal stability analysis of embedded functionally graded annular nanoplates based on the nonlocal elasticity theory, *International Journal of Mechanical Sciences,* Vol. 119, pp. 396-411, 2016/12/01/ 2016.

[3] A. Farzam and B. Hassani, Isogeometric analysis of in-plane functionally graded porous microplates using modified couple stress theory, *Aerospace Science and Technology,* Vol. 91, pp. 508-524, 2019/08/01/ 2019.

[4] H. X. Nguyen, T. N. Nguyen, M. Abdel-Wahab, S. P. A. Bordas, H. Nguyen-Xuan, and T. P. Vo, A refined quasi-3D isogeometric analysis for functionally graded microplates based on the modified couple stress theory, *Computer Methods in Applied Mechanics and Engineering,* Vol. 313, pp. 904-940, 2017/01/01/ 2017.

[5] V.-T. Tran, T.-K. Nguyen, P. T. T. Nguyen, and T. P. Vo, Stochastic vibration and buckling analysis of functionally graded microplates with a unified higher-order shear deformation theory, *Thin-Walled Structures,* Vol. 177, p. 109473, 2022/08/01/ 2022.

[6] G. Dhiman and V. Kumar, Spotted hyena optimizer: A novel bio-inspired based metaheuristic technique for engineering applications, *Advances in Engineering Software,* Vol. 114, pp. 48-70, 2017/12/01/ 2017.

[7] J. S. Moita, A. L. Araújo, V. F. Correia, C. M. Mota Soares, and J. Herskovits, Material distribution and sizing optimization of functionally graded plate-shell structures, *Composites Part B: Engineering,* Vol. 142, pp. 263-272, 2018/06/01/ 2018.

[8] V. M. Franco Correia, J. F. Aguilar Madeira, A. L. Araújo, and C. M. Mota Soares, Multiobjective optimization of ceramic-metal functionally graded plates using a higher order model, *Composite Structures,* Vol. 183, pp. 146-160, 2018/01/01/ 2018.

[9] D. T. T. Do, D. Lee, and J. Lee, Material optimization of functionally graded plates using deep neural network and modified symbiotic organisms search for eigenvalue problems, *Composites Part B: Engineering,* Vol. 159, pp. 300-326, 2019/02/15/ 2019.

[10] T. Le-Duc, Q.-H. Nguyen, and H. Nguyen-Xuan, Balancing composite motion optimization, *Information Sciences,* Vol. 520, pp. 250-270, 2020/05/01/ 2020.

[11] H. Thanh Duong, H. Chi Phan, T.-T. Le, and N. Duc Bui, Optimization design of rectangular concrete-filled steel tube short columns with Balancing Composite Motion Optimization and data-driven model, *Structures,* Vol. 28, pp. 757-765, 2020/12/01/ 2020.

[12] S. Khatir, S. Tiachacht, C. Le Thanh, E. Ghandourah, S. Mirjalili, and M. Abdel Wahab, An improved Artificial Neural Network using Arithmetic Optimization Algorithm for damage assessment in FGM composite plates, *Composite Structures,* Vol. 273, p. 114287, 2021/10/01/ 2021.

[13] M. Abouhamze and M. Shakeri, Multi-objective stacking sequence optimization of laminated cylindrical panels using a genetic algorithm and neural networks, *Composite Structures,* Vol. 81, No. 2, pp. 253-263, 2007/11/01/ 2007.

[14] T. T. Tran, P.-C. Nguyen, and Q.-H. Pham, Vibration analysis of FGM plates in thermal environment resting on elastic foundation using ES-MITC3 element and prediction of ANN, *Case Studies in Thermal Engineering,* Vol. 24, p. 100852, 2021/04/01/ 2021.

[15] X. Liu, F. Tao, H. Du, W. Yu, and K. J. J. o. A. M. Xu, Learning nonlinear constitutive laws using neural network models based on indirectly measurable data, Vol. 87, No. 8, p. 081003, 2020.

[16] P. A. Demirhan and V. Taskin, Bending and free vibration analysis of Levy-type porous functionally graded plate using state space approach, *Composites Part B: Engineering,* Vol. 160, pp. 661-676, 2019/03/01/ 2019.

[17] T.-K. Nguyen, H.-T. Thai, and T. P. Vo, A novel general higher-order shear deformation theory for static, vibration and thermal buckling analysis of the functionally graded plates, *Journal of Thermal Stresses*, Vol. 44, No. 3, pp. 377-394, 2021/03/04 2021.

[18] S. Makridakis *et al.*, The accuracy of extrapolation (time series) methods: Results of a forecasting competition, *Journal of Forecasting*, https://doi.org/10.1002/for.3980010202 Vol. 1, No. 2, pp. 111-153, 1982/04/01 1982.

[19] S. Makridakis et al., The accuracy of extrapolation (time series) methods: Results of a forecasting competition, Vol. 1, No. 2, pp. 111-153, 1982.